DOCTOR OF PHILOSOPHY

Rate Effect Behaviour of Different Clays from High Speed Triaxial Element Testing

Robinson, Scott

Award date:
2019

University of Dundee

School of Science
and Engineering

Rate Effect Behaviour of Different Clays from High Speed Triaxial Element Testing

Scott Robinson

A dissertation submitted for the
degree of Doctor of Philosophy
to the University of Dundee

May 2019

Declaration

This is to certify that, except where specific reference to other investigation is made, the work described in this dissertation is the result of the investigation of the candidate. All references cited have been consulted by the candidate and neither this dissertation, nor any part of it, has been presented or is currently submitted in candidature for any degree at any other university.

Scott Robinson *(Candidate)*

Dr Michael John Brown *(Supervisor)*

To Betty, Beat, Harry and Alan

Acknowledgements

Firstly, I would like to express my gratitude to my supervisor, Dr Mike Brown, for his patience, guidance, support and *extensive comments* in the completion of this thesis (as well as for finding the funding for this research from down the back of a sofa). Mike has always encouraged me to explore every avenue in search of the answers to the many questions which arose during this thesis, as well as allowing me the freedom to choose the direction of the research and it has been an honour to work with him. I can only hope that I can be as relentless and persistent as Mike in future research. I also thank all of the academic staff in the Geotechnical Research Group who have always had an open door and have all freely given advice and input at various stages of this research.

I also acknowledge the invaluable advice and assistance of Mr Martin Kierans in the Dundee Imaging Facility (DIF) and Dr Laszlo Csetenyi in the Concrete Technology Unit (CTU) with the SEM imaging, as well as the assistance of Dr Tom Dyer from the CTU in carrying out the XRD and XRF testing. Thanks are also due to the ICE Research and Development Enabling Fund for their support (Grant No. 1201) which allowed the purchase of some of the equipment used.

I would like to extend my thanks to the technical staff within the workshop in the School of Science and Engineering for their assistance in the creation of all manner of items. Most importantly, I must thank Mark Truswell for his unfailing advice, support and disaster relief in the course of the work behind this thesis, as well as for his good company in the laboratory (and for forgiving me for blocking the laboratory's drains on my first day). Without Mark's technical knowledge and skills, much of the work undertaken in the Geotechnical Research Group would simply not be possible.

The Geotechnical Research Group is truly defined by its people, and it has been a pleasure to work with each of them. Specific thanks must also go to my friends and colleagues Gertjan Meijer, Benjamin Cerfontaine, Therar Al-Baghdadi, Craig Davidson, Hamza Yakub, Katy Oakes and Hidetake Matsui who have made this experience so enjoyable (and also for the communal quests for morning coffee by which all the University's clocks could be set). I hope that our friendship will endure wherever we may be.

Most importantly I must thank my parents, Linda and Roy, for their support and patience during the completion of this thesis, and for always encouraging me to have confidence in myself and to believe that anything is possible. I can never repay them for everything that they have done for me. I must also thank Olive for always reminding me that there is light at the end of the tunnel.

Abstract

The rate effect response of three natural clays has been studied using high-speed triaxial element testing at axial strain rates up to 100,000 %/hr. Strain rate effects lead to increasing soil shear strength in fine grained soils under undrained conditions and are important for accurate predictions in a number of geotechnical applications. These include Rapid Load Testing (RLT) of piles, Free-Falling Penetrometers (FFP) and Deep Penetrating Anchors (DPA), as well as in the numerical modelling of high strain-rate activities in general. The triaxial testing used a number of techniques to improve the accuracy of the results including lubricated end platens to minimise strain localisations and a new mid-height pore pressure sensor capable of measuring rapid pore pressure changes.

Each of the three clays investigated were tested over a range of initial mean effective stresses to consider the impact of soil state and it was identified that rate effects increase with moisture content. These rate effects were shown to lead to increasing soil strength, reducing pore pressures and expanding yield envelopes. The overconsolidation ratio (OCR) was found to have no impact on the observed rate effects.

Hall effect local strain sensors were used to allow rate effects on the deviator strength to be measured throughout the strain range, from pre-yield up to the point of localisation. The rate effects were found to be highly strain dependent, with negligible rate effects observed before yield and the point of maximum rate effect occurring before 1 % shear strain. A new model for the variation of rate effects with strain across the entire measured strain range (up to the point of localisation) has been developed, which can also account for the impact of soil state and the soil properties.

The triaxial testing was combined with in-depth characterisation of the three soils, allowing the properties influencing rate effects to be determined. It was found that for the clays tested, the Specific Surface Area of the clay determined from Methylene Blue spot testing (*SSA-MB*) provided a useful rate effect indicator, with the observed rate effects increasing as the specific surface area reduces. The gradient of the critical state line (CSL) in *q-p'* space, *M*, derived at an axial strain rate of 1 %/hr was found to be another possible indicator, as *SSA* and *M* are inter-related. Additionally, *M* is more widely available than *SSA* in geotechnical studies.

Keywords: triaxial testing, high-speed, clay, rate effects, liquidity index, soil state, strain rate, viscous effects

Table of Contents

List of Tables

List of Figures

Notation

c	fitting parameter for rate effect mobilisation
c_M	membrane correction for deviator stress
c_v	coefficient of consolidation
d	representative diameter or fitting parameter for rate effect mobilisation
i	hydraulic gradient
k	soil permeability
m_v	coefficient of compressibility
n	power law rate exponent (sometimes referred to by other studies as β)
p	mean total stress
p_a	atmospheric pressure
Δp	change in mean total stress
p'	mean effective stress
p'_0	initial mean effective stress
p'_{CSL}	critical mean effective stress
p'_{max}	maximum mean effective stress
$p'_{max,app}$	apparent maximum mean effective stress due to strain rate
p'_y	mean effective stress at intersection with yield envelope
$\Delta p'$	change in mean effective stress
q	deviator stress
q_{CSL}	critical deviator stress
q_{EL}	deviator stress at the elastic limit
q_{peak}	peak deviator stress
$q_{peak,ref}$	peak deviator stress at the reference strain rate
q_{ref}	deviator stress at the reference strain rate
q_y	deviator stress at intersection with yield envelope
Δq	change in deviator stress
u	pore pressure
Δu	excess pore pressure
Δu_{si}	excess shear-induced pore pressure

$\Delta u_{dil,si}$	negative excess shear-induced pore pressure due to initial dilation
$\Delta u_{f,si}$	final excess shear-induced pore pressure
$\Delta u_{peak,si}$	excess shear-induced pore pressure at peak shear strength
$\Delta u_{peak,si,ref}$	excess shear-induced pore pressure at peak shear strength at reference rate
v	specific volume or velocity
w	moisture content

A	activity
A_{mb}	area of one methylene blue molecule
A_v	Avogadro's number
B	pore pressure response Skempton B-value
C_0	material rate dependency parameter from Martindale *et al.* (2013)
E	Young's modulus
E_{max}	maximum Young's modulus
G	secant shear modulus
G_{max}	maximum secant shear modulus
$I_{v\alpha}$	viscosity index
K_0	lateral earth pressure coefficient at rest
M	gradient of the critical state line in q-p' space
M_{app}	apparent gradient of the critical state line in q-p' space
M_M	membrane modulus
N	intercept of the normal consolidation line at 1 kPa in v-$ln(p')$ space
$P_{Kaolinite}$	proportion of Kaolinite as a percentage
P_{Illite}	proportion of Illite as a percentage
P_{Quartz}	proportion of quartz as a percentage
S_u	undrained shear strength
$S_{u,ref}$	undrained shear strength at the reference strain rate
V	normalised velocity
V_0	minimum normalised velocity at which viscous undrained rate effects occur
V_{ref}	normalised velocity at the strain rate at the transition to undrained behaviour

α	rate effect soil state (*LI*) dependency parameter
α_G	strain rate coefficient for shear stiffness
α_u	pore pressure evolution parameter
$\alpha_{\varepsilon q=1\%}$	rate effect soil state (*LI*) dependency parameter at 1 % shear strain
α_{peak}	rate effect soil state (*LI*) dependency parameter at peak strength
ε	axial strain
ε_{EL}	elastic axial strain threshold
ε_q	deviatoric shear strain
$\varepsilon_{q,EL}$	elastic shear strain threshold
$\varepsilon_{q,EL,ref}$	elastic shear strain threshold at the reference strain rate
$\varepsilon_{q,peak}$	shear strain at peak deviator stress
$\varepsilon_{q,peak,ref}$	shear strain at peak deviator stress at the reference strain rate
$\varepsilon_{q,0.7}$	shear strain at which the secant shear stiffness, *G*, has reduced to 70 % of G_{max}
$\varepsilon_{q,\lambda max}$	shear strain at which the maximum rate effect occurs
$\dot{\varepsilon}$	axial strain rate
$\dot{\varepsilon}_{corr}$	corrected axial strain rate
$\dot{\varepsilon}_q$	shear strain rate
$\dot{\varepsilon}_{q,ref}$	reference shear strain rate
$\dot{\varepsilon}_{ref}$	reference axial strain rate
γ_w	unit weight of water
η	friction ratio
δ	shear displacement
$\dot{\delta}$	shear displacement rate
κ	gradient of unload/reload line in *v-ln(p')* space
λ	rate effect per log cycle of strain rate
λ_{CSL} or λ_{NCL}	gradient of the CSL and NCL in *v-ln(p')* space
λ_{peak}	rate effect per log cycle of strain rate at peak strength
λ_{max}	maximum rate effect per log cycle of strain rate
$\lambda_{\varepsilon q=1\%}$	rate effect per log cycle of strain rate at 1 % shear strain
$\lambda_{\varepsilon q=1\%,pl}$	rate effect per log cycle of strain rate at 1 % shear strain at the plastic limit
$\Delta\lambda_{log(\varepsilon q)}$	reduction in λ per log cycle increase of strain after $\varepsilon_{q,\lambda max}$
λ'	rate effect per natural log cycle of strain rate

σ	total stress
σ_1	axial stress
σ_3	radial stress
σ'	effective stress
σ'_n	normal effective stress
σ'_v	vertical effective stress
σ'_{v0}	initial vertical effective stress
σ'_{vmax}	maximum vertical effective stress
τ	shear stress
τ_{ref}	shear stress at the reference strain rate
ϕ'_{crit}	critical effective friction angle
θ	x-ray diffraction angle
ζ	transition coefficient for modelling rate effect strain dependency
ξ_{OCR}	rate effect on normalised OCR_{app} per log cycle
$Å$	Ångström unit of length
β	shear stiffness degradation rate parameter
β_{ref}	shear stiffness degradation rate parameter at the reference strain rate
Γ	intercept of the critical state line at 1kPa in *v-ln(p')* space
Γ_o	intercept of the critical state line at 1kPa in *v-ln(p')* space at $\dot{\varepsilon}$ = 1 %/hr
Ψ	state parameter
Ψ_{ref}	state parameter at the reference strain rate
$\emptyset$	diameter

Abbreviations

1D	One Dimensional
3D	Three Dimensional
BBC	Boston Blue Clay
CAD	Computer Aided Design software (Autodesk AutoCAD)
CF	Clay Fraction
CID	Isotropically Consolidated Drained triaxial test
CIU	Isotropically Consolidated Undrained triaxial test
CPT	Cone Penetration Test
CRP	Constant Rate of Penetration test
CryoSEM	Cryogenic Scanning Electron Microscopy
CTU	Concrete Technology Unit
CSL	Critical State Line
DIA	Digital Image Analysis
DIF	Dundee Imaging Facility
DPA	Deep Penetrating Anchor
ELL	Elastic Limiting Line
ESEM	Environmental Scanning Electron Microscopy
FESEM	Field Emission Scanning Electron Microscopy
EVA	Ethyl-Vinyl Acetate
FFP	Free Falling Penetrometer
GDS	GDS Instruments Ltd
GDS ADVDPC	GDS Advanced Digital Pressure Controller
GDS DCS	GDS Dynamic Control System
GDSLAB	GDS System Control and Logging Software
GDS STDDPC	GDS Standard Digital Pressure Controller
HAT	Hymod AT ball clay
HKMC	Hong Kong Marine Clay
H71	Hyplas 71 ball clay
KLN	Kaolin

KSS	Model soil consisting of Kaolin, Sand and Silt
LI	Liquidity Index
LL	Liquid Limit
LVDT	Linear Variable Differential Transformer
MB	Methylene Blue
MCC	Modified Cam Clay
N_2 BET	Nitrogen adsorption Brunauer Emmett Teller method for specific surface area
NCL	Normal Consolidation Line
OCR	Overconsolidation Ratio
OCR_{app}	Apparent Overconsolidation Ratio due to strain rate
$OCR_{app,ref}$	Apparent Overconsolidation Ratio at the reference strain rate
PI	Plasticity Index
PID	Proportional, Integral and Differential feedback loop
PL	Plastic Limit
PPT	Pore Pressure Transducer
PSD	Particle Size Distribution
PTFE	Polytetrafluoroethylene
RLT	Rapid Load Testing
SEM	Scanning Electron Microscopy
SSA	Specific Surface Area
SSA-MB	Specific Surface Area from Methylene Blue spot testing
TD	Triaxial Drained
TU	Triaxial Undrained
UKAS	United Kingdom Accreditation Service
XRD	X-ray Diffraction analysis
XRF	X-ray Fluorescence analysis

1. Introduction

1.1. Preface

In contrast to sands, fine grained soils such as clays exhibit significant viscous effects which lead to increasing soil undrained shear strength with strain rate. The accurate assessment of rate effects is critical in a wide range of geotechnical activities where high shear strain rates occur. Rate effects currently pose a significant uncertainty for geotechnical projects and an improved understanding of these effects could allow more efficient design and project scheduling. Rate effects are normally expressed as the increase in a soil's strength at a high strain rate of interest, relative to the soil strength at a static reference strain rate and are generally accepted to range from a 5 to 20 % increase in strength per log cycle increase in strain rate.

The most commonly used assumption in terms of rate effects is a 10 % increase in shear strength per log cycle of strain rate. However, in such simplistic assumptions the impact of soil state and variations between different soils are not accounted for. This can be compounded by the fact that many activities where rate effects are relevant, such as Deep Penetrating Anchors (DPA), are several orders of magnitude faster than the testing carried out to characterise the soil in question. In this case, an error in the estimation of the rate effect per log cycle of 5 % could lead to a 25 % error in the soil's shear strength when a DPA is installed for example.

The applications where rate effects are relevant are numerous, ranging from Statnamic or rapid load pile testing (RLT), through to offshore applications such as seabed characterisation using pushed or dropped penetrometers or cable installation using seabed ploughing. Increasingly, there is also a need for models to allow rate effects to be fully accounted for in numerical analysis of high strain rate activities.

There are a number of issues which raise the need to predict rate effects using easily obtainable parameters, such as the availability of the specialist high-speed testing equipment required for rate effect characterisation. This equipment is often costly and there are still numerous technical challenges surrounding accurate instrumentation and measurement of soil behaviour in high strain rate tests. To overcome this, the ability to predict the rate effect

response of soils using easily available soil characterisation parameters would be of use to both industry and researchers. This task is the focus of the programme of high-speed triaxial element testing carried out in this study.

1.2. Element Testing

To study the impact of rate effects across a wide range of aspects of soil response, a programme of high speed triaxial testing has been carried out on three different clays at a wide range of axial strain rates up to 180,000 %/hr, and at initial mean effective stresses ranging from 300 to 1350 kPa. These specimens were reconstituted from powdered natural clays, to allow full control over the specimen's stress history and provide the required specimen quality to allow the rate effects to be accurately identified. The three clays exhibited significantly different rate effects, allowing influencing factors to be identified. A number of developments to the existing high speed triaxial testing apparatus have also been made to improve the accuracy of the test data.

The testing has allowed the impact of rate effects on the soil response from small to large strains to be identified, and a number of improvements to geotechnical models are proposed to allow better modelling of high strain rate behaviour. The impact of rate effects on the critical state framework is also investigated. Key parameters which can be indicators of soil rate effect behaviour are suggested, along with methods for modelling rate effects using these parameters. Advanced techniques have also been used to investigate potential causes behind rate effects.

1.3. Aims and Objectives

The aim of this research was to examine and identify the factors which influence rate effects such that they may be more accurately accounted for in a wide range of geotechnical activities from numerical modelling through to real world applications.

The objectives which were identified to allow this aim to be achieved were:

1. To carry out a programme of high speed triaxial element testing on a range of clays which exhibit substantially varying rate effect responses.

2. To determine how the magnitude of rate effects in a given clay are influenced by the soil state, identify which specific aspects of soil state control the rate effects and develop methods to model and predict the impact of state on the observed rate effects.
3. To examine whether the impact of rate effects in *q-p'* and *v-ln(p')* space can be modelled in the critical state framework and propose modifications to this framework if necessary.
4. To determine the variation of rate effects with shear strain and propose a method for predicting and modelling the rate effect which will occur at any given strain level.
5. To investigate the mechanism by which rate effects occur, using a range of techniques including Scanning Electron Microscopy.
6. To investigate the variation of rate effects between several different clays and identify the material properties which cause this variation between different soils.
7. To develop methods for predicting rate effect behaviour from easily obtainable parameters.

1.4. Thesis Structure

The literature review in Chapter 2 examines the current approaches for estimating rate effects, along with their limitations. The available information on the factors which influence rate effects is presented, and cases where this evidence is conflicting are highlighted. The chapter concludes by summarising the areas which have been identified as key aspects which should be investigated in this study.

Chapter 3 presents the methodology to be used for the high speed triaxial testing, along with the other advanced techniques used to characterise the clays, including X-ray diffraction (XRD) analysis and Scanning Electron Micoscopy (SEM). Special focus is given to the adaptations made to the apparatus to ensure accurate measurements at high strain rates, and techniques which have been used to minimise errors in the element testing programme. The standard material characterisations for each of the three clays are also summarised.

Chapter 4 describes the results of the large strain high speed triaxial testing undertaken on Kaolin from a total stress perspective and identifies the key aspects of the soil response which are altered by rate effects. Methods for modelling these changes are investigated, along with techniques for predicting the magnitude of rate effects which occur in Kaolin at shear strains greater than 1 %.

Chapter 5 attempts to model the rate effect behaviour of Kaolin in terms of its pore pressure response. The results are put in an effective stress framework and the implications of high strain rate testing for the critical state framework are considered.

The mobilisation of rate effects in Kaolin from extremely small strains are considered in Chapter 6 using local strain measurements. The impact of rate effects on yield behaviour is considered and the implications of rate effects for commonly used stiffness degradation models are investigated. An integrated method for modelling rate effects in Kaolin at any given strain level and soil state is also presented.

Chapter 7 presents the findings of the investigations into the mechanism behind rate effects and considers the implications of these findings for potential mechanisms previously suggested by other studies. Focus is also given to the results of the Scanning Electron Microscopy (SEM) of triaxial specimens subjected to varying axial strain rates.

The variation in rate effects between the three clays tested is presented in Chapter 8, and the usefulness of parameters which have previously been suggested as potential rate effect indicators is discussed. Easily obtainable soil parameters which are correlated with the measured rate effects in the three clays tested are identified, and the implications for these parameters in terms of the underlying mechanism are considered.

Chapter 9 concludes by summarising the findings of this research, whilst Chapter 10 identifies avenues for future research and areas for improvement which would allow the understanding of rate effects to be further advanced.

2. Literature Review

To inform the testing programme, there is a need to understand which aspects of soil behaviour are affected by rate effects, as well as whether there are any known factors which influence the rate effect response of the soil. A brief overview of the main methods used for investigating rate effects is first discussed to provide a background to the review which follows. To provide insight into the different strain rate ranges considered in the literature, the strain rate range used (in %/hr) is provided, where possible, when each study is first discussed. If this is not available, the penetration velocity, v, or the displacement rate, $\dot{\delta}$, is provided instead.

2.1. Rate Effect Investigation Methods

Several common approaches for determining a soil's rate effect response exist. These can be broadly split into laboratory testing techniques - where the rate effect response of a soil element is directly measured - and field methods, where the rate effect response of the soil is measured indirectly by its influence on the capacity or resistance of the application in question. Laboratory tests where rate effects are important include element testing such as triaxial tests (Sheahan *et al.*, 1996) and also shear-based tests including direct shear (Steenfelt, 1993) or ring shear apparatus (Lupini *et al.*, 1981; Tika *et al.*, 1996). Rate effects are also an important consideration in simpler laboratory tests which measure undrained shear strengths (e.g. shear vane tests such as Biscontin and Pestana, 2001) and also in laboratory cone tests where correlations between penetration depth and undrained shear strength are important (Stone and Phan, 1995; O'Kelly *et al.*, 2018).

Examples of field applications where rate effects are determined include cone penetration tests (CPT) (Brown and Hyde, 2008b), free-falling penetrometers (FFP) (Chow *et al.*, 2017), and deep penetrating anchors (DPA) (O'Loughlin *et al.*, 2013) as well as rapid load testing (RLT) of piles (Brown *et al.*, 2006).

2.1.1. Rate Effects in Laboratory Testing

Element testing approaches used to investigate rate effects include triaxial tests, shearbox testing and ring shear apparatus. Examples of rate effect studies which have used triaxial testing include Sheahan *et al.* (1996) and Zhu and Yin (2000). Typical maximum axial strain rates using conventional triaxial apparatus are in the range of $\dot{\varepsilon}$ = 10 to 50 %/h, however, high speed triaxial apparatus can achieve $\dot{\varepsilon}$ = 180,000 to 360,000 %/hr (Quinn, 2013; Balderas-Meca,

2004). Triaxial studies can be used to consider rate effects at strains up to $\varepsilon \approx 20$ %, with the lower limit of the accurately measurable strains being determined by local strain measurement apparatus (Clayton and Khatrush, 1986). In practice, the useful strain range is limited to the strain at which the triaxial specimen localises and ceases to behave as a uniform soil element. This localisation strain is dependent on the test conditions and soil properties but is typically of the order of $\varepsilon \approx 10$ to 20 % (Sheahan *et al.*, 1996). Triaxial tests also have the advantage of mid-height pore pressure measurements which allow the calculation of effective stress during shearing.

Examples of the use of shearbox testing (direct shear) to investigate rate effects include Steenfelt (1993) [$\dot{\delta}$ = 0.0001 to 28 mm/s]. Due to the localised nature of direct shear tests, studies using this approach tend to focus on rate effects at large strain levels, ranging from peak shear stress (which typically occurs at $\varepsilon \approx 1$ to 5 %) to residual behaviour. Ring shear apparatus is often used to consider rate effects at even greater strain levels using shear displacements of up to δ = 5000mm (e.g. Tika *et al.*, 1996; Lemos and Vaughan, 2000) [$\dot{\delta}$ = 0.0002 to 103 mm/s]. Due to the lack of a physical limit on the displacement that can be applied, ring shear testing allows the application of tests at multiple shear strain rates on the same specimen. Both shearbox and ring shear tests have the limitation that estimation of the actual shear strain rates and strain applied is problematic due to the indeterminacy of the thickness of the shear band on which the soil specimen shears. The localised nature of the shearing also means that control of the drainage conditions and measurement of pore pressures in the test are also problematic (Meehan *et al.*, 2008).

2.1.2. Rate Effects in Field Applications

Free falling penetrometers (FFP), cone penetrometer testing (CPT) and deep penetrating anchors (DPA) are commonly used field applications where rate effects are significant. Due to the high shear strain rates which occur in these instances, accurate rate effect parameters are essential for deriving the static soil response to the penetrometer as well as the prediction of penetration depth in DPA. To provide this information, a number of rate effect laboratory studies have investigated penetrometer response at high strain rates (e.g. Chow *et al.*, 2017; Morton *et al.*, 2016; Boukpeti *et al.*, 2012; Nanda *et al.*, 2017) using both centrifuge and 1g modelling. In terms of the investigation of rate effects, penetrometer studies are advantageous in testing soft soils with high liquidity indexes which would be problematic to study using

element testing. Due to their nature, penetrometer studies consider rate effects at extremely high strains although the strain levels (and hence strain rates) applied are difficult to quantify and are further complicated by localisations which occur around the penetrometer (Zhou and Randolph, 2007). This makes comparison of penetrometer rate effects with rate effects derived from element testing difficult.

Whilst free falling penetrometer (FFP) tests are easy to conduct in the field, their interpretation has a number of complications. Foremost of these is that different rate effects are observed on the tip resistance and side friction, with many studies (e.g. Steiner *et al.*, 2014) [up to v = 5000 mm/s] reporting notably higher rate effects on side friction (up to 45 % per log cycle) than on tip resistance. This effect is not unique to FFP and has also been reported in constant rate CPT tests (Dayal and Allen, 1975; Brown and Hyde, 2008b) as well as rapid load tests (RLT) on piles (Brown, 2004). Early studies suggested that these variations were due to potential influences of the different shearing mechanisms on the soil's rate effect response (Dayal and Allen, 1975) [v = 1.3 to 811 mm/s], however, improved understanding of penetrometer behaviour now suggests that the high side friction rate effects are due to dynamic inertial effects in the surrounding soil causing high lateral stresses on the penetrometer sides (Chow *et al.*, 2017) [v = 1 to 10,000 mm/s]. An example of one of these effects is described by Chow *et al.* (2017) as additional lateral stress (and hence friction) generated as soil is accelerated horizontally outwards as the penetrometer advances into the soil. Corrections for these inertial effects have not yet been devised. The implications of this are that side friction rate effects are an area where further research is required to confirm whether the high rate effects are real, or due to other mechanistic or inertial issues. Further qualitative evidence of this is the fact that reported FFP tip rate effects (Steiner *et al.*, 2014) are relatively consistent with the range of rate effects observed in element testing of 5 to 20 % per log cycle (Nanda *et al.*, 2017) whilst reported side friction rate effects are far higher (Brown, 2004).

Due to the high shear strain rates achieved, RLT pile testing is another application where rate effects have been studied (Brown and Hyde, 2008a) [up to v = 364 mm/s]. RLT pile testing involves the use of fast burning fuel to accelerate a mass above the pile head, with the reaction of this force being used to test the pile's behaviour. Rate effects are derived by comparing the resistance of the pile from the RLT test (after inertial effects are accounted for) with a static constant rate of penetration (CRP) test carried out on the same pile. If the pile is instrumented

with strain gauges over its length, the overall rate effect response of the pile can be broken down and the rate effects on the pile shaft can be analysed over its length (Brown, 2004). This has the advantage of allowing the effect of the varying soil properties over the pile length on the observed rate effects to be considered. As with penetrometer testing, rate effects on the shaft resistance are reported to be higher than pile tip rate effects (Brown, 2004). Unlike penetrometer studies, RLT rate effect studies allow the mobilisation of rate effects with strain (or in this case pile head displacement) to be investigated, although comparison with element testing is still complicated by difficulties associated with the quantification of the strain level applied by the pile and the identification of the failure mechanism around the pile itself.

2.2. Impact of Rate Effects on Shear Strength

Before considering the influence of rate effects, it is important to differentiate viscous rate effects (where the soil strength increases with shear strain rate in undrained conditions) from drainage effects (Figure 2-1). The mechanism behind viscous rate effects has not yet been conclusively identified and is still poorly understood (Kwok and Bolton, 2010). Finnie and Randolph (1994) defined a normalised velocity, V, used to determine the points of transition between the different drainage regimes (Equation 2-1).

$$V = \frac{vd}{c_v} \tag{2-1}$$

where v is the relevant velocity, d is a characteristic length often taken either as the diameter of the object or a drainage path length and c_v is the coefficient of consolidation

At normalised velocities below a value of $V \approx 0.01$, the soil exhibits a drained response and there is sufficient time for full dissipation of evolved pore pressure. Up to a normalised velocity of $V \approx 30$, the increasing velocity allows less time for dissipation leading to a reduction in shear strength until the soil becomes fully undrained. Beyond $V \approx 30$, viscous rate effects dominate, and the soil shear strength is observed to increase with strain rate. These approximate values for the transition between drained to partially drained and partially drained to undrained behaviour of $V \approx 0.01$ and $V \approx 30$ respectively, are relatively constant regardless of the soil type used, whether sand or clay (Steiner *et al.*, 2014). Randolph and Hope (2004) [v = 0.005 to 1 mm/s] proposed that the variation of rate effect throughout the drained to undrained range shown in Figure 2-1 can be captured by Equation 2-2.

$$\frac{q}{q_{ref}} = \left(1 + \frac{b}{1 + cV^{d}}\right)\left\{1 + \frac{\lambda}{ln(10)}\left[sinh^{-1}\left(\frac{V}{V_0}\right) - sinh^{-1}\left(\frac{V_{ref}}{V_0}\right)\right]\right\} \quad (2\text{-}2)$$

where b, c and d are curve fit parameters, V_0 and V_{ref} determine the transition point to undrained behaviour, and λ represents that undrained viscous rate effects.

It is the undrained viscous rate effect which is the focus of this thesis. However, one additional question relating to viscous rate effects in the drained and partially drained regions which will also be considered is whether viscous rate effects still exist in these regions but are masked by the far greater drainage effects. This is a question which is often not considered in related rate effect studies such as CPT testing (e.g. Chung *et al.*, 2006; Lehane *et al.*, 2009; Colreavy *et al.*, 2016).

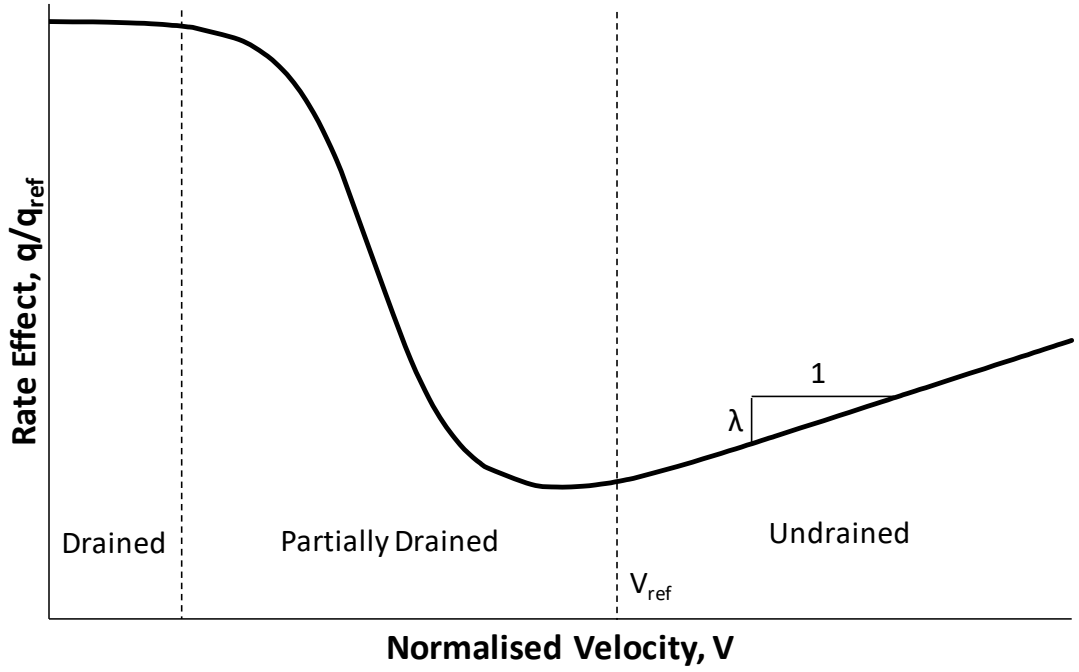

Figure 2-1 – Schematic of the variation of rate effect with normalised velocity (after Randolph and Hope, 2004)

2.2.1. Definition of Rate Effects

The rate effect on the observed shear strength is commonly defined in its simplest form as the shear strength at an elevated strain rate relative to the shear strength at a chosen static strain rate (Steiner *et al.*, 2014) as shown in Equation 2-3.

$$Rate\ effect = \frac{\tau}{\tau_{ref}}\ or\ \frac{q}{q_{ref}} \tag{2-3}$$

Three forms for the variation of the rate effect with strain rate (Equations 2-4, 2-5 and 2-6) have been proposed; semi-logarithmic relationships (e.g. Kulhawy and Mayne, 1990), power laws (e.g. Zhu and Randolph, 2011) and an inverse hyperbolic sine relationship (e.g. Eyring, 1936; Randolph and Hope, 2004; Chung *et al.*, 2006). Of these, the semi-logarithmic (Equation 2-4) and power laws (Equation 2-5) are by far the most commonly used, with the semi-logarithmic form more predominant in element testing studies (Sheahan *et al.*, 1996; Zhu and Yin, 2000), whilst power laws tend to be preferred in field applications such as penetrometer testing (Morton *et al.*, 2016) and rapid load pile testing (RLT) (Brown and Hyde, 2008a). This is due to the fact that in examples such as penetrometer testing and deep penetrating anchor installation, deviations from the semi-logarithmic rate effect relationship can be observed when the range of strain rates is large (typically more than 3 orders of magnitude), which are better captured using a power law (Chow *et al.*, 2017; O'Loughlin *et al.*, 2013; Biscontin and Pestana, 2001).

$$Rate\ effect\ = 1 + \lambda log\left(\frac{\dot{\varepsilon}}{\dot{\varepsilon}_{ref}}\right) \tag{2-4}$$

$$Rate\ effect = \left(\frac{\dot{\varepsilon}}{\dot{\varepsilon}_{ref}}\right)^{\beta} \tag{2-5}$$

$$Rate\ effect = 1 + \lambda' arcsinh\left(\frac{\dot{\varepsilon}}{\dot{\varepsilon}_{ref}}\right) \tag{2-6}$$

where $\lambda' \approx \frac{\lambda}{ln(10)}$ *for* $\frac{\dot{\varepsilon}}{\dot{\varepsilon}_{ref}} > 1$ (Steiner *et al.*, 2014)

and $\frac{\dot{\varepsilon}}{\dot{\varepsilon}_{ref}}$ may be replaced by $\frac{v}{v_{ref}}$ in field application studies in each of these three equations

Figure 2-2 shows a comparison of the forms of each of these relationships, with the parameters selected such that each relationship has approximately the same gradient between $\dot{\varepsilon}/\dot{\varepsilon}_{ref}$ = 1 to 10, in order to allow easier comparison. Beyond $\dot{\varepsilon}/\dot{\varepsilon}_{ref}$ = 1, the inverse hyperbolic relationship (Equation 2-6) is essentially similar in form to the semi-logarithmic relationship (Equation 2-4), although with a lower limit on the rate effect which is restricted to $q/q_{ref} > 1$. This makes the inverse hyperbolic relationship unsuitable for considering undrained viscous rate effects at low

strain rates below the reference strain rate, $\dot{\varepsilon}_{ref}$ (often taken as 1 %/hr). In contrast, the power law (Equation 2-5) predicts higher rate effects at higher normalised strain rates, which is the reason that it is often preferred in penetrometer testing, where extremely high shear strain rates occur.

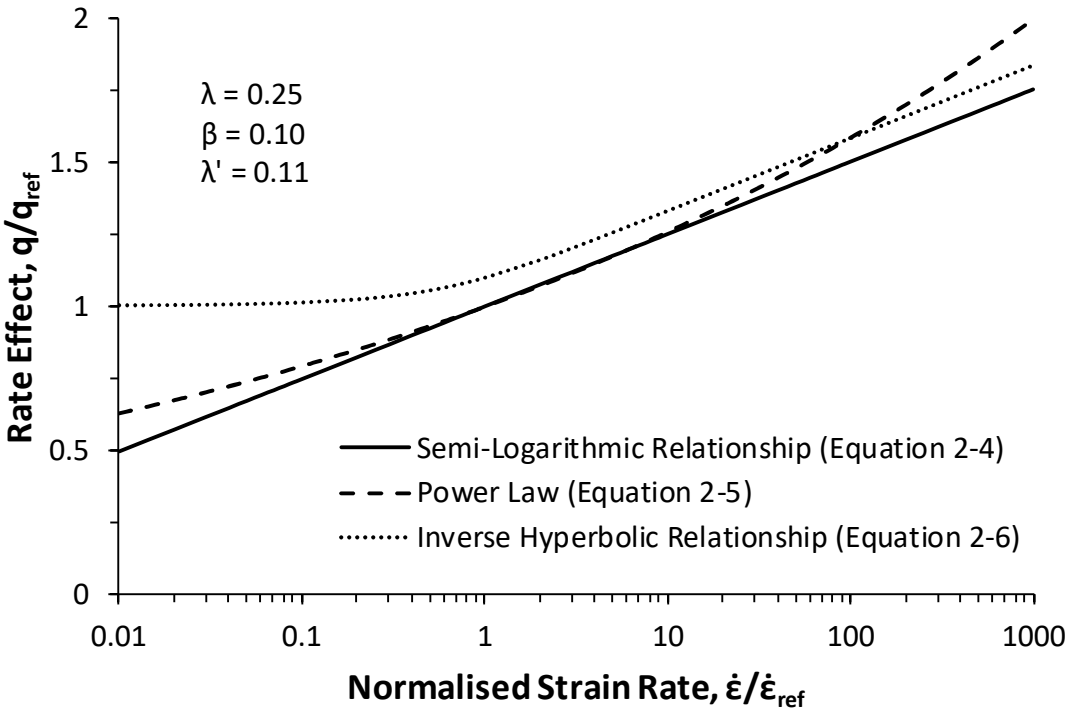

Figure 2-2 – Comparison of the three most commonly used rate effect relationships

The most commonly quoted assumption for rate effects on shear strength is that of Kulhawy and Mayne (1990) [$\dot{\varepsilon}$ = 0.001 to 10,000 %/hr] which suggests, based on data from the testing of 26 different clays in triaxial compression, that the rate effects observed in clays may be approximated as a 10 % increase in peak shear strength per log cycle increase of strain rate (λ = 0.1) (Figure 2-3). Kulhawy and Mayne (1990) considered rate effects over 7 orders of magnitude of axial strain rate, however, few of the clays were tested over this full rate range, and there is little data in the high strain rate range ($\dot{\varepsilon}$ > 100 %/hr). Additionally, the study does not provide any information on the state of the samples, such as moisture content or overconsolidation ratio. Closer examination of Figure 2-3 also shows that a number of the clays tested display both higher and lower rate effects than the 10 % per log cycle recommendation, such as Lyndhurst clay which has a rate effect of approximately 17 % per log cycle and Vicksburg clay which shows a rate effect of approximately 6 % per log cycle. This suggests that there are potentially material dependent controls, which are not considered in the study along

with potential soil state effects. The apparent lack of scatter in Figure 2-3 is due to the normalisation of all of the data at an axial strain rate of 1 %/hr, which is in the middle of the strain rate range considered and has the effect of bringing the data sets closer together, despite the variations in rate effects between the different clays.

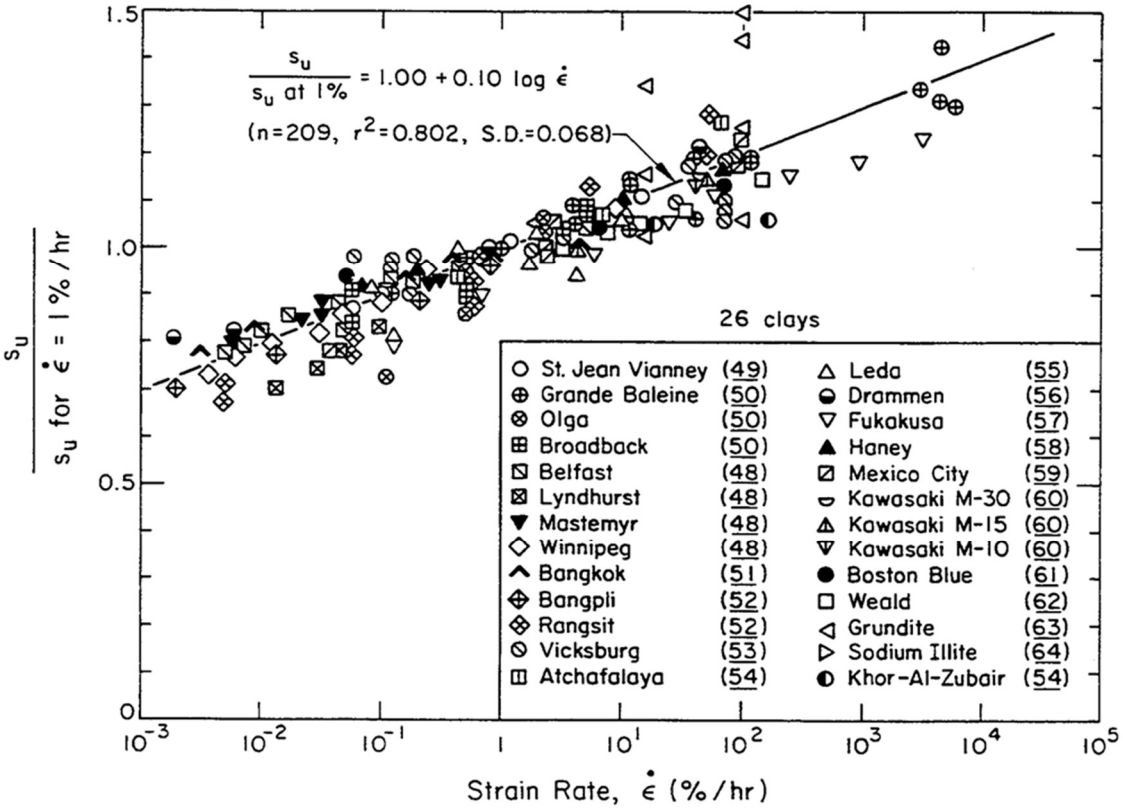

Figure 2-3 – Graph of rate effect on undrained shear strength with axial strain rate for 26 different clays (Kulhawy and Mayne, 1990)

In reality, rate effects typically vary from 5 to 20 % per log cycle (Nanda *et al.*, 2017), although there are a number of exceptions to this. Examples of studies where notably higher rate effects have been observed include Steenfelt (1993) and Diaz-Rodriguez and Martinez-Vasquez (2005). Steenfelt (1993) [$\dot{\delta}$ = 0.0001 to 28 mm/s] observed undrained rate effects of over 30 % per log cycle in large scale shear testing and field testing of Storebaelt clay till at rates of up to 100 m/hr (28 mm/s). Diaz-Rodriquez and Martinez-Vasquez (2005) [$\dot{\epsilon}$ = 1 to 800 %/hr] found even higher rate effects of up to 41 % per log cycle in triaxial testing of Mexico City soil, highlighting that generic assumptions of strain rate effects in clays should be treated with caution and demonstrating the need for a better understanding of the factors which influence the rate effect magnitude.

Some of the earliest investigation of strain rate effects was carried out by Whitman (1957) who first defined the term 'strain-rate effect'. Whitman (1957) carried out rapid strain-rate controlled triaxial tests on a range of predominantly clayey specimens at axial strain rates ranging from 108 to 3600000 %/hr. The rate effects observed varied substantially, from 6 to 22 % per log cycle. The study highlights the fact that different clayey soils exhibit differing strain rate effects, however, as each of the soil types were tested at different moisture contents and states, identification of the influencing parameters was not possible. Equipment limitations also mean that it was likely that there were issues maintaining constant strain rates at high strain rates.

In the literature review, a number of factors were identified which it has been suggested influence the magnitude of observed rate effects in clays; soil state (including moisture content or liquidity index), stress history (namely overconsolidation ratio) and the Atterberg limits. The evidence proposed thus far for each of these aspects will be considered in the following sections.

2.2.2. Influence of Moisture Content

One of the first studies to suggest a link between strain rate effects and moisture content (or liquidity index) was Dayal and Allen (1975). Using model cone penetrometer testing (CPT) at penetration rates from 1.3 to 810 mm/s in a remoulded clay at a range of moisture contents, Dayal and Allen (1975) observed extremely high cone resistance rate effects of 150 % per log cycle at moisture contents beyond the liquid limit of the clay. The study examined rate effects at a range of undrained shear strengths, which were achieved by varying the moisture content of the remoulded clay. A clear trend of increasing rate effects with reducing shear strength (or increasing moisture content) was also observed (Figure 2-4), although sufficient information to identify the rate effect variation with moisture content or liquidity index was not available. A number of other studies show similar high rate effects in soils above the liquid limit, such as Abelev and Valent (2013) which showed rate effects ranging from 60 to 100 % per log cycle at liquidity indexes ranging from 150 % to 300 % based on shear vane tests on Gulf of Mexico clay. However, it should be noted that when investigating rate effects at high liquidity indexes, the reference undrained shear strengths would be likely to be very low, which would increase the variability of the measured rate effects.

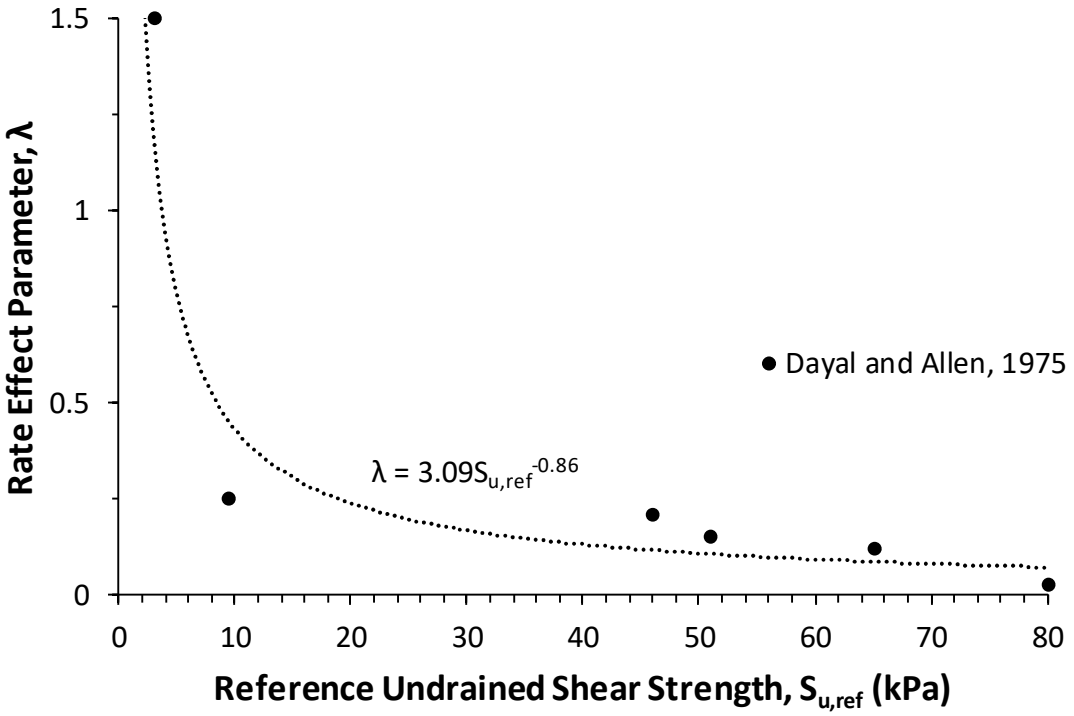

Figure 2-4 – Variation of λ with undrained shear strength based on constant rate model cone penetrometer testing of remoulded pottery clay (Dayal and Allen, 1975)

More recently, Brown and Hyde (2008a) [up to v = 364 mm/s] reported significant increases in rate effects with moisture content from RLT pile testing in Grimsby till, using instrumented piles such that the rate effect on the shaft resistance can be calculated at several locations along the length of the pile (Figure 2-5). Whilst the study used a power law, interpretation of the data indicates rate effects ranging from $\lambda \approx 0$ to $\lambda = 0.21$ as the moisture content, w, increases from 19 to 25 %.

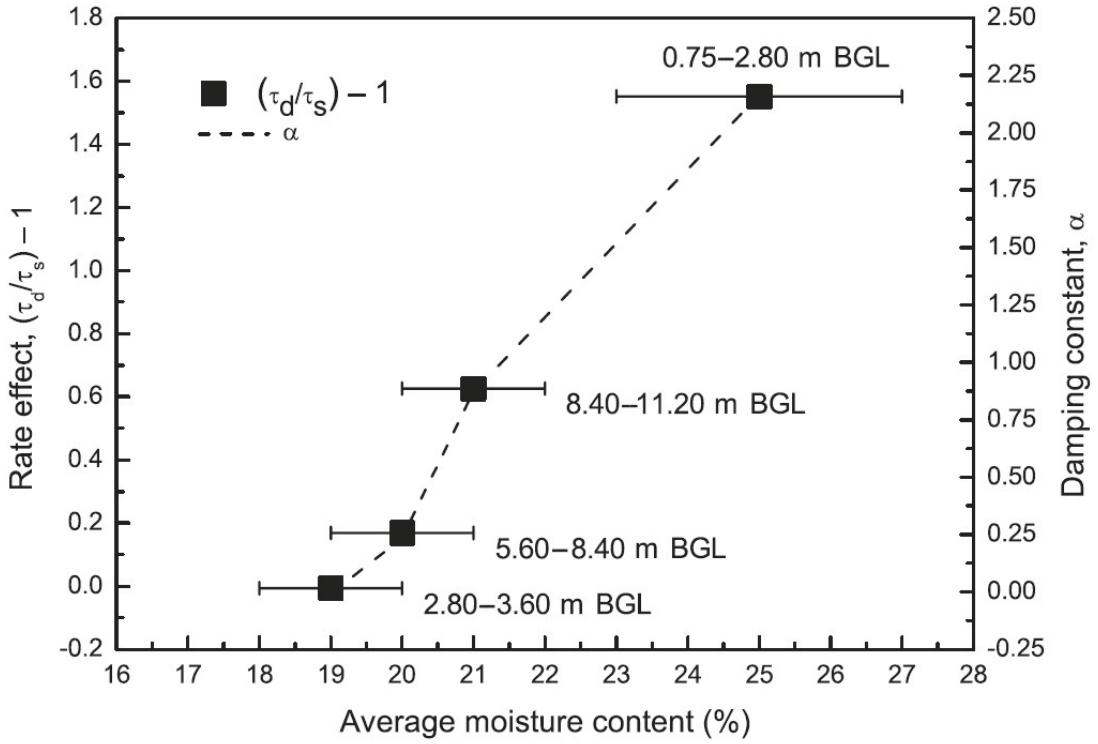

Figure 2-5 – Variation of rate effect on shaft resistance with moisture content from RLT pile tests in Grimsby glacial till (Brown and Hyde, 2008a)

A similar variation of rate effect with undrained shear strength was also identified by Briaud and Garland (1985) using data from 152 laboratory tests (Figure 2-6) on a variety of clays, although a power law was again used in this case. In each of the studies discussed, the observed rate effects are variously correlated with the undrained shear strength, liquidity index or moisture content. In reality, these parameters are inter-related and are controlled by the moisture content of the specimen, highlighting the need to compare rate effect studies using the same controlling variable (i.e. moisture content). Briaud and Garland (1985) identified rate effect correlations with a power law exponent, *n*, (Equations 2-7 to 2-9) for all three of these, however, the scatter in each of the correlations is significant and no one relationship is clearer than the others.

$$n = 0.096 S_{u,ref}^{-0.15} \quad (2\text{-}7)^*$$

$$n = 0.028 + 0.0006w \quad (2\text{-}8)$$

$$n = 0.036 + 0.046LI \quad (2\text{-}9)$$

* Equation 2-7 has been re-fitted to the data from Briaud and Garland (1985) after conversion of $S_{u,ref}$ from imperial units to kPa using the same form originally proposed by the authors.

In many rate effect studies, such as Dayal and Allen (1975) and Sheahan *et al.* (1996), specimen moisture content information is often not included, which complicates the study of the effect of soil state.

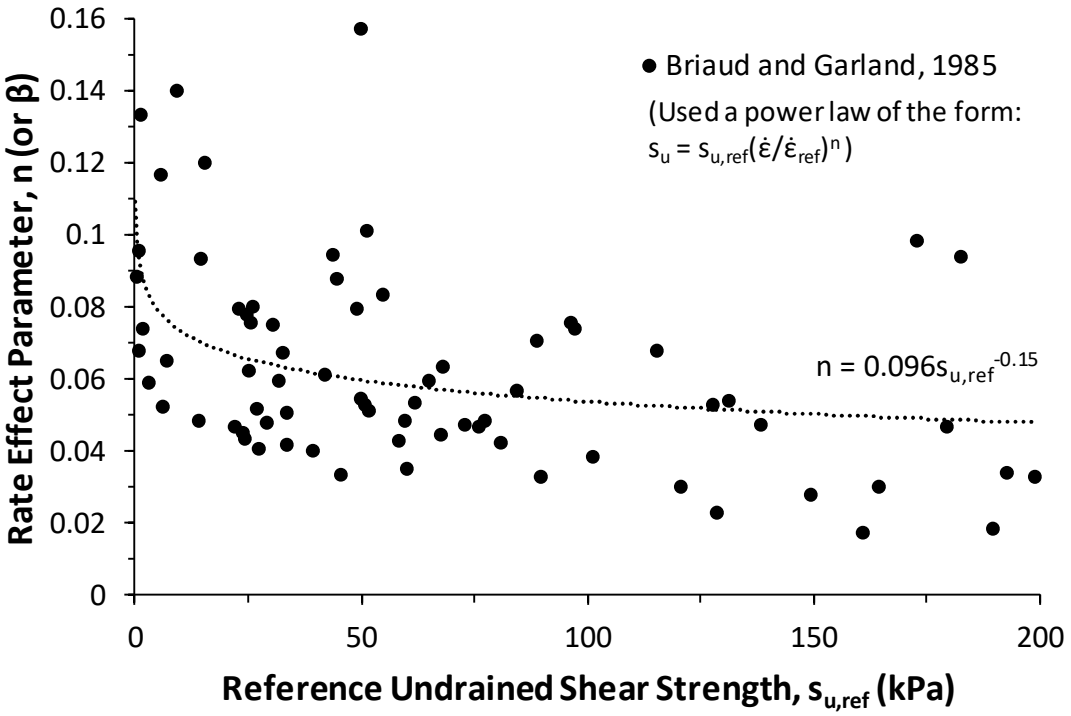

Figure 2-6 – Variation of *n* (or *β*) with undrained shear strength based on 152 laboratory tests on a variety of clays (Briaud and Garland, 1985)

Bea (1982) suggested a correlation between Liquidity Index (*LI*) and rate effects for Gulf of Mexico clay (Equation 2-10) based on triaxial testing, which attempts to capture the significant (non-linear) increase in rate effects as the liquidity index increases.

$$\lambda = \frac{OCR}{S_u / \sigma'_v} exp\left(\frac{LI - 2}{0.42}\right) \quad (2\text{-}10)$$

where OCR = 1 and S_u/σ'_v = 0.25 for the Gulf of Mexico clay tested

The general exponential trend of this relationship can also be seen in a number of other studies including Chow and Airey (2011) [*v* = 4750 to 12220 mm/s] using model free-falling penetrometers (FFP) in Kaolin and also in analysis of data from Diaz-Rodriguez and Martinez-

Vasquez (2005) shown in Figure 2-7. Hence, the literature review suggests there is a consensus on the trend in rate effect increase with *LI* (or moisture content), but not yet agreement on the models to capture this behaviour. This is an area where further research is required.

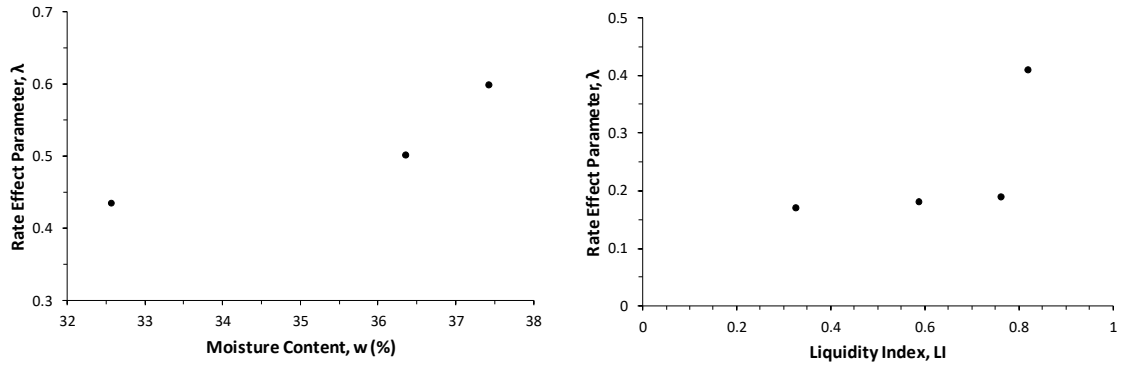

(a) (b)

Figure 2-7 – (a) Variation of λ with moisture content from FFP tests in Kaolin (Chow and Airey, 2011) (b) Variation of λ with liquidity index from triaxial tests on Mexico City soil using data from Diaz-Rodriguez and Martinez-Vasquez (2005)

A further question that then arises is what happens to rate effects at the plastic limit? This issue was considered by Stone and Phan (1995) [v = 1 to 3 mm/s] in motorised laboratory cone tests at constant penetration rates, aimed at developing an alternative approach for determining a soil's plastic limit. Comparing load-penetration curves at the plastic limit in Kaolin at two different rates (1 and 3 mm/s), it can be seen that at the elevated rate, there is a consistent increase in penetration force compared to the reference rate of 1 mm/s (Figure 2-8). Taking a penetration depth of 25 mm as the comparison point, the observed rate effect is 12 % per log cycle, suggesting (contrary to the assertion of the authors) that significant rate effects do exist at the plastic limit. Examination of data from Bea (1982) showing the variation of λ with *LI*, also indicates that λ tends to towards a value of around 0.08 at the plastic limit (Figure 2-9), although the study does not have data below *LI* = 0.2. This is similar to the value identified from Stone and Phan (1995) suggesting that rate effects may be approximately in this range ($\lambda \approx 0.08$ - 0.12) near the plastic limit. This may offer an explanation to the average value of λ = 0.1 found in the study of 26 different clays by Kulhawy and Mayne (1990) as these studies were conducted using field samples which may be near to the plastic limit for some of the soils.

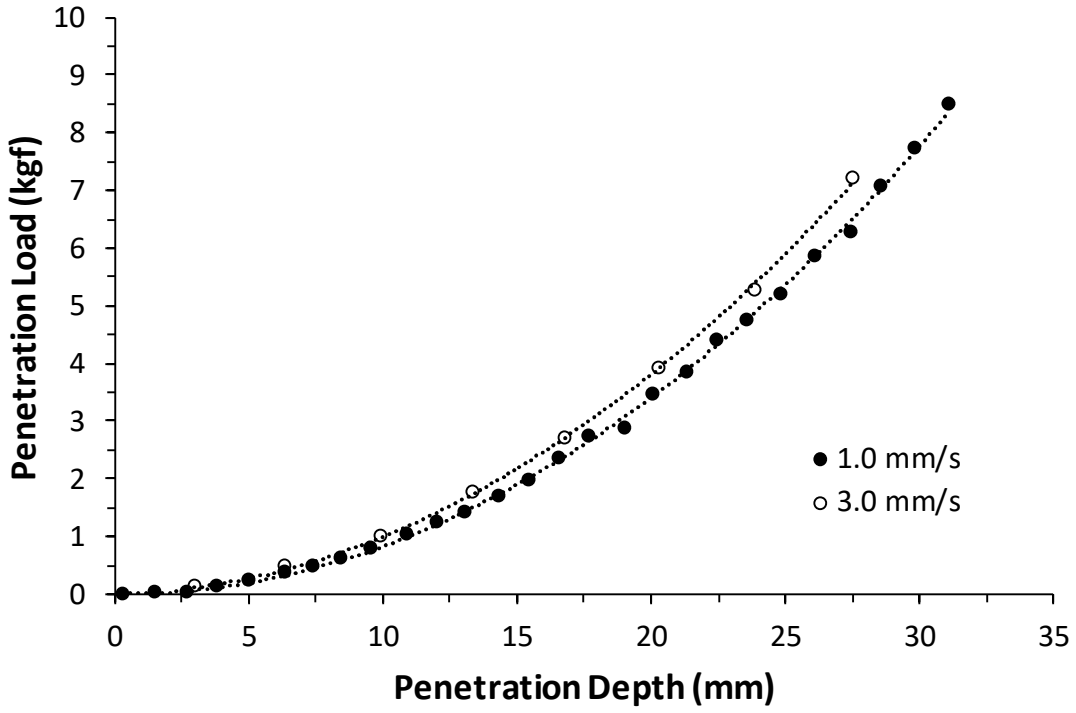

Figure 2-8 – Effect of penetration rate on penetration load for constant rate laboratory cone tests at the plastic limit in Kaolin (Stone and Phan, 1995)

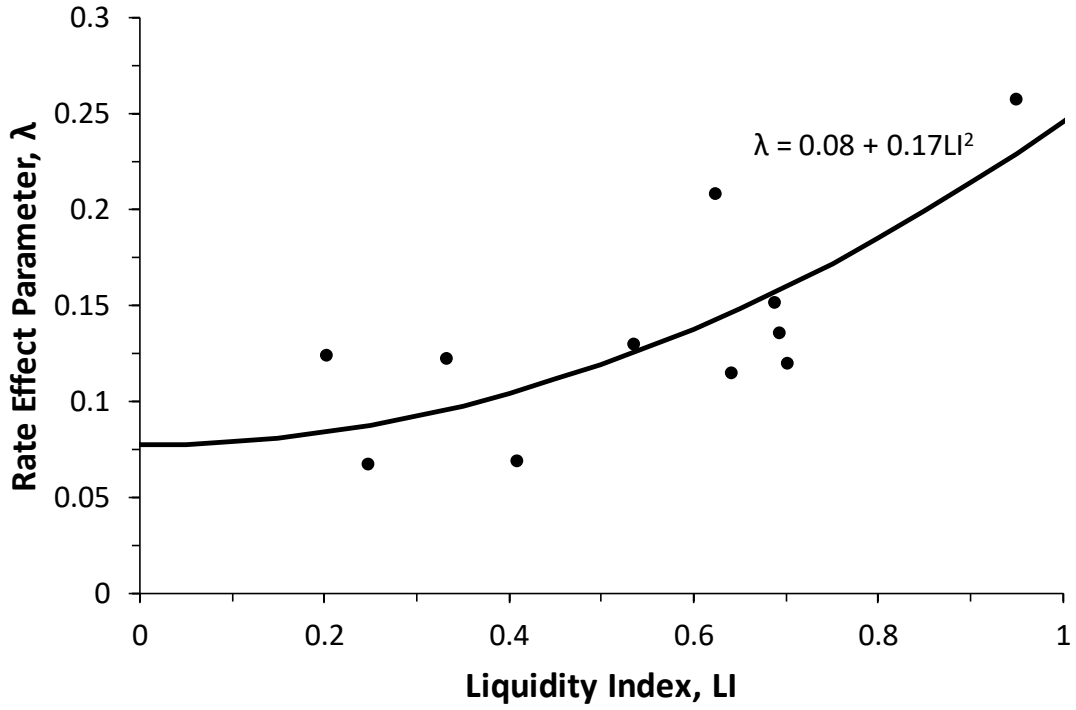

Figure 2-9 – Variation of λ with liquidity index in Gulf of Mexico clay using data from Bea (1982)

2.2.3. Influence of Overconsolidation Ratio

In contrast to the effect of liquidity index or moisture content on rate effects, where there is a general consensus on the trend, the literature on the effect of overconsolidation ratio (OCR) is conflicting. Two early studies highlight this; Briaud and Garland (1985) and Graham *et al.* (1983). Briaud and Garland (1985) identified a trend of increasing viscous exponent, *n*, (identical to the parameter β used in the power law shown previously in Equation 2-5) with OCR, considering OCRs from 1 to 25 in laboratory testing, suggesting an increase in rate effects with OCR (Figure 2-10). However, the scatter in the data is significant, and no information is given by the authors as to whether the specimens were at similar specific volumes or if the effective stress was comparable in all of the tests. Graham *et al.* (1983) [$\dot{\varepsilon}$ = 0.003 to 10 %/hr] also investigated the impact of OCR on rate effects, but instead found no clear trend with the data, if anything, suggesting a small reduction in rate effects with OCR (Figure 2-11). However, the axial strain rates used by Graham *et al.* (1983) were limited to $\dot{\varepsilon}$ = 10 %/hr and, as with other studies, the impact of soil state or moisture content was not considered.

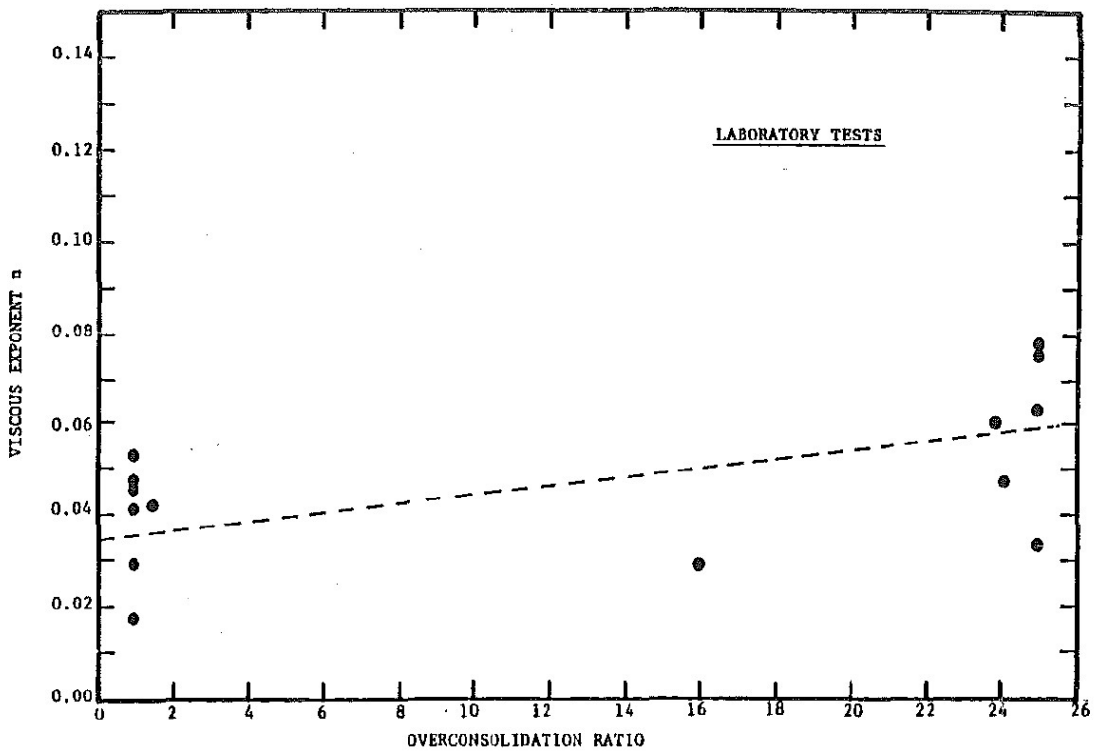

Figure 2-10 – Variation of viscous exponent, *n*, with overconsolidation ratio based on 14 laboratory tests (Briaud and Garland, 1985)

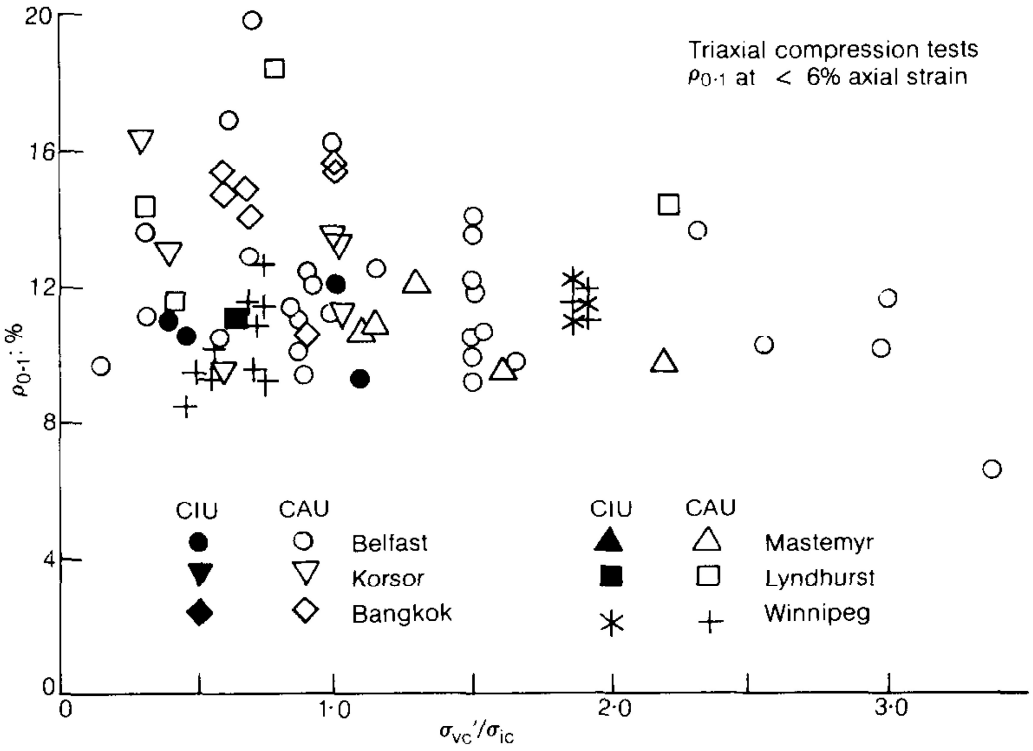

Figure 2-11 – Variation of rate effect per log cycle with OCR for 6 clays in triaxial compression (Graham *et al.*, 1983)

The reason for the varying findings on the influence of OCR on rate effects is likely due to differences in moisture content depending on the way that the overconsolidated specimen has been prepared. The specimen can be overconsolidated (Equation 2-11) in two different ways, which both result in changes in moisture content. When varying OCR, studies generally keep either the maximum consolidation stress, p'_{max}, or alternatively, the stress at the start of shearing, p'_0, constant throughout the test programme. As shown in Figure 2-12(a), if a study prepares overconsolidated specimens at the same p'_{max}, the specific volume increases slightly with OCR due to more swelling on the unload line (e.g. Sheahan *et al.*, 1996). If p'_0 is kept constant whilst varying OCR (Figure 2-12(b)), the specific volume of the specimen will reduce significantly with OCR due to greater consolidation on the NCL (e.g. Zhu and Yin, 2000). As the moisture content (and hence specific volume) is known to influence rate effects this means that studies which investigate the influence of OCR, could incorrectly find that overconsolidation either increases or reduces rate effects if the influence of moisture content is not accounted for.

$$OCR = \frac{p'_{max}}{p'_0} \tag{2-11}$$

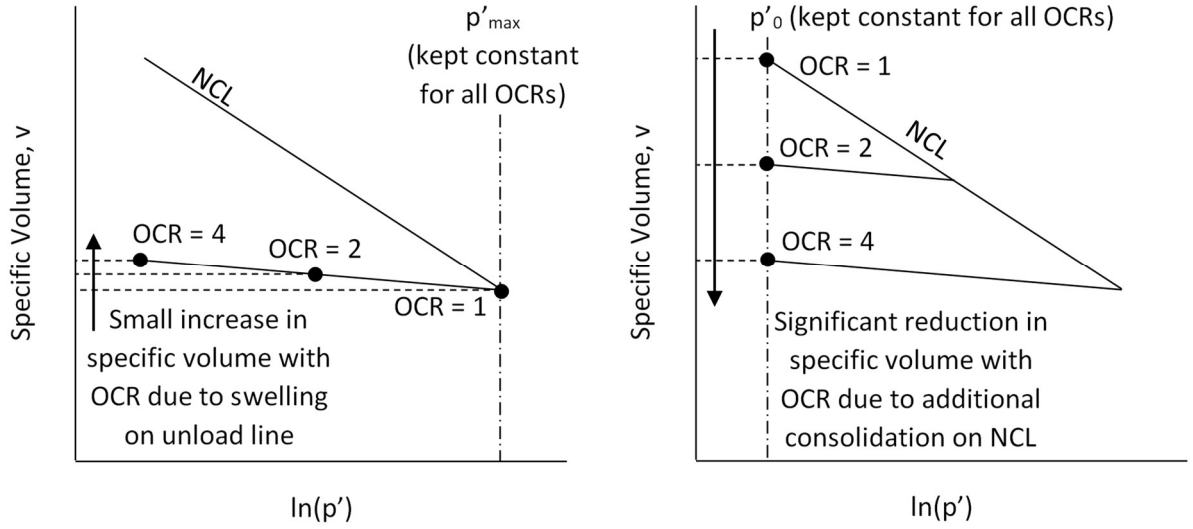

Figure 2-12 – Changes in specific volume (or moisture content) during overconsolidation (a) by maintaining a constant p'_{max} for all specimens and (b) by maintain a constant p'_0 for all specimens

Prime examples of this issue include Sheahan *et al.* (1996) and Zhu and Yin (2000). Sheahan *et al.* (1996) [$\dot{\epsilon}$ = 0.05 to 50 %/hr] carried out undrained triaxial tests on Boston Blue Clay (Figure 2-13(a)) at OCRs ranging from 1 to 8 by varying the vertical effective stress at the start of the test, σ'_{v0} (the specimens were K_0 consolidated) in a similar manner to that shown in Figure 2-12(a). Figure 2-13(b) shows the variation of the rate effect between axial strain rates of 5 to 50 %/hr (the only rate range where data is available for all OCRs) with OCR. As can be seen, there is no obvious trend in rate effect with OCR, despite the small increases in moisture content with increasing OCR. This is in part due to the fact that the tests at OCR = 1 were consolidated to a far lower effective stress (σ'_{vmax}) than the other OCRs (Table 2-1), meaning that it is at a far higher moisture content, which explains why the highest rate effects are seen at OCR = 1. There is insufficient information in Sheahan *et al.* (1996) to identify the moisture content of each of the OCRs tested, meaning that this anomaly cannot be accounted for, and the impact of moisture content cannot be separated from any potential influence of OCR. This highlights the importance of presenting information on the soil state in rate effect studies. The results of Sheahan *et al.* (1996) are also complicated by the varying degree of anisotropy at each OCR as the specimens were K_0 consolidated, although it is noted that Graham *et al.* (1983) found no impact of anisotropy on the magnitude of observed rate effects.

Table 2-1 – Stresses used to achieve different OCRs by Sheahan *et al.* (1996)

OCR	Maximum vertical consolidation stress, σ'_{vmax} (kPa)	Vertical stress at start of shearing, σ'_{v0} (kPa)
1	290	290
2	585	292
4	585	146
8	585	74

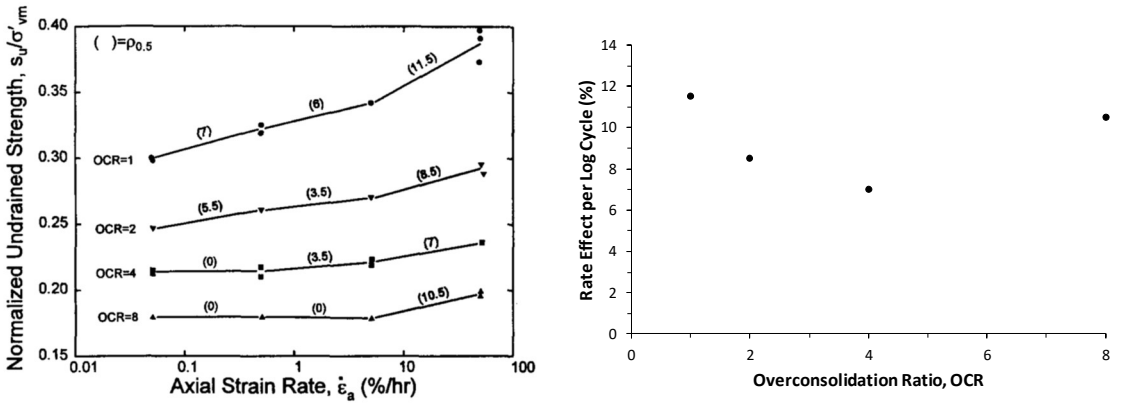

(a) (b)

Figure 2-13 – (a) Rate effects based on triaxial testing of Boston Blue Clay (BBC) at varying OCR and (b) variation of rate effect per log cycle with OCR in the axial strain rate range of 5 to 50 %/hr (the only strain rate range where data is available for all OCR's) from Sheahan *et al.* (1996)

Zhu and Yin (2000) [$\dot{\varepsilon}$ = 0.15 to 15 %/hr] used triaxial testing on Hong Kong Marine clay where the OCRs were achieved by instead varying p'_{max}, with p'_0 being kept constant (Table 2-2), meaning that the moisture content reduced substantially with OCR. This is further complicated by the fact that a different value of p'_0 was used for the tests at OCR = 1. As with Sheahan *et al.* (1996), there is no trend in rate effect variation with OCR (Figure 2-14(a)). Whilst moisture content information is not published in Zhu and Yin (2000), there is sufficient material characterisation to estimate the moisture content at each OCR using the stress history. Once the moisture content is accounted for, it can be seen that the expected trend of increasing rate effect with moisture content is present, regardless of the OCR of the specimens (Figure 2-14(b)). This suggests that rate effect variations seen in Zhu and Yin (2000) are not due to OCR, but moisture content differences between the specimens.

In summary, several studies find no impact of OCR on rate effects, and the majority of those that have reported changes in rate effects with OCR can be explained by the variation in moisture content between the specimens. This suggests that OCR has no significant influence on the magnitude of rate effects.

Table 2-2 – Mean effective stresses used to achieve varying OCRs in Zhu and Yin (2000)

OCR	Maximum consolidation stress, p'_{max} (kPa)	Stress at start of shearing, p'_0 (kPa)	Moisture content, w
1	400	400	0.335
2	200	100	0.399
4	400	100	0.358
8	800	100	0.317

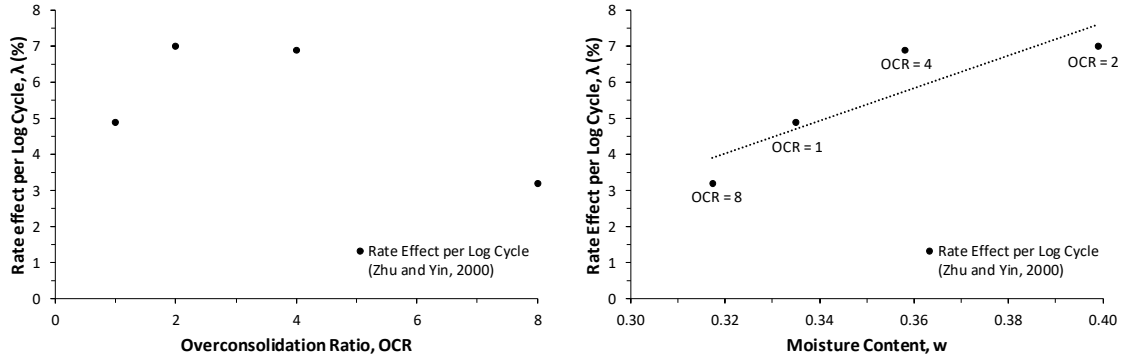

(a) (b)

Figure 2-14 – (a) Variation of rate effect with OCR and (b) variation of rate effect with moisture content from compressive triaxial tests on Hong Kong Marine clay reported by Zhu and Yin (2000)

2.2.4. Correlations between Atterberg Limits and Rate Effects

As a commonly used correlation for soil properties, the potential of the Atterberg limits as an indicator of rate effects has been investigated by several studies. These have tended to be review-based studies due to the fact that a large number of tests on multiple soils are required. Graham *et al.* (1983) collated the results of triaxial testing on 7 different clays (Figure 2-15) and found no correlation between plasticity index and rate effects. This is despite the fact that significant rate effect variations are observed between tests conducted on the same clay,

underlining the importance of accounting for the soil's state. The specimens used by Graham *et al.* (1983) were undisturbed field samples which were anisotropically reconsolidated to varying values of OCR and tested at relatively low axial strain rates of up to $\dot{\epsilon}$ = 10 %/hr. Hence, the results shown in Figure 2-15 include changing moisture content and OCR as well as the plasticity index, which may explain the scatter in the data.

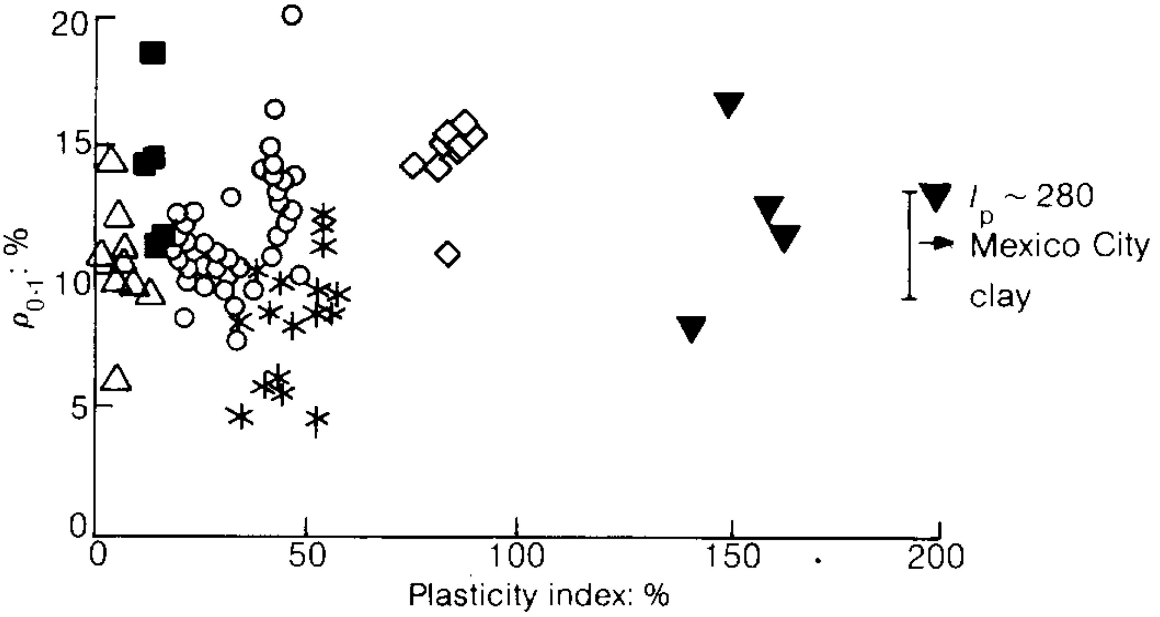

Figure 2-15 – Variation of rate effect parameter with plasticity index from triaxial testing on 7 clays (Graham *et al.*, 1983)

Briaud and Garland (1985) reported an increase in the viscous exponent, n, (identical to β, meaning an increase in rate effect) with plasticity index (Figure 2-16 and Equation 2-12), however, there is a significant amount of scatter in the data and the trend is far from clear. As with Graham *et al.* (1983), a potential cause of the scatter is that the plasticity index correlation does not account for the changes in soil state or moisture content in the study, which it is already known would influence the rate effect. The reason suggested for the correlation was that rate effects may be due to the viscosity of adsorbed water at clay particle contacts, and that these adsorbed layers would be expected to be thicker in clays of higher plasticity. Brown (2008) also proposed a similar rate effect relationship with plasticity index (Equation 2-13) where α is a rate effect damping coefficient used in RLT pile analysis, but only as such

correlations were available and specific on site moisture contents or specific volumes are often not published.

$$n = 0.035 + 0.00066\,PI \quad (2\text{-}12)$$

$$\alpha = 0.03PI + 0.5 \quad (2\text{-}13)$$

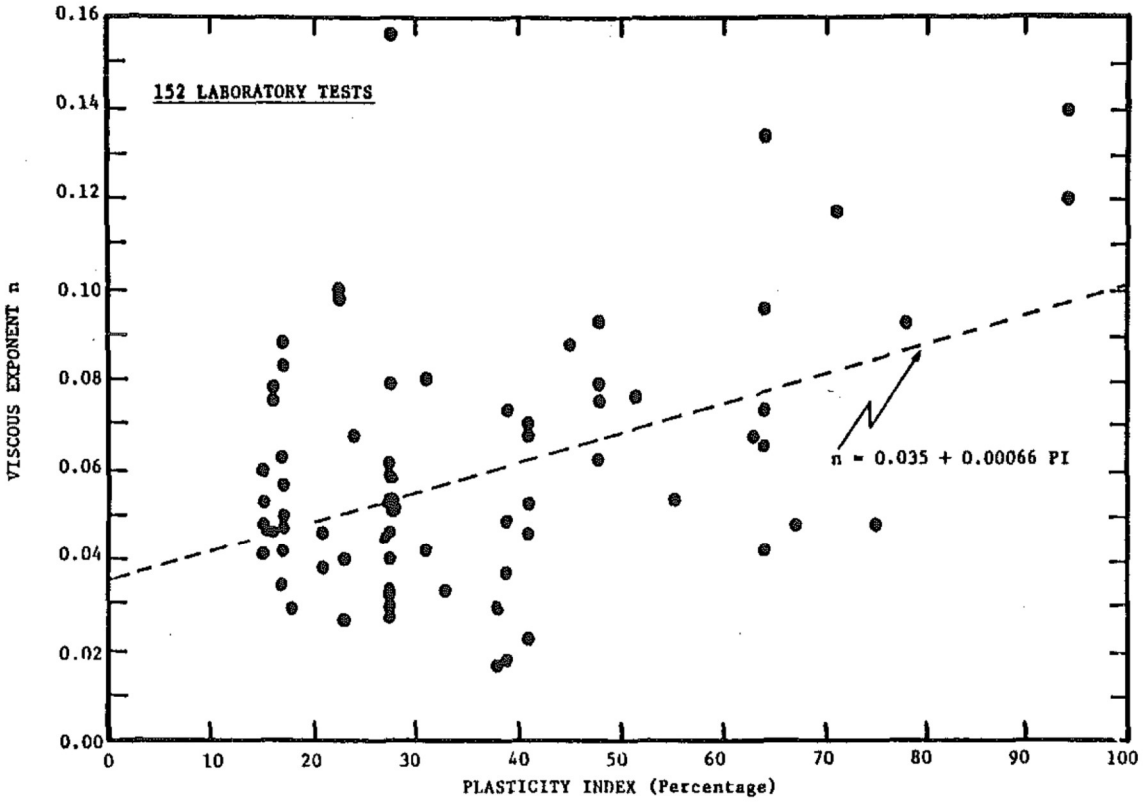

Figure 2-16 – Variation of viscous exponent, *n*, (equivalent to β) with plasticity index from 152 laboratory tests on clays (Briaud and Garland, 1985)

As for correlations with the liquid limit, the evidence is more limited. Krieg and Goldscheider (1998) identified an increase in rate effects from 4.7 to 15 % per log cycle with the logarithm of liquid limit using soils ranging from silt through to organic clay (Figure 2-17). However, as with other studies, the soil state is not taken into account, meaning that the moisture content used for each of the specimens may impact on these findings. No underlying reason or mechanism for the correlation between liquid limit and rate effects was proposed.

Overall, there is some evidence that both the plasticity index and liquid limit may be indicators of rate effects in clays, but further research is required to confirm if the observed correlations are due to variations in soil state in these studies. Another possible factor in the conflicting results is the variability in the determination of the plastic limit using the conventional thread-rolling approach (O'Kelly *et al.*, 2018).

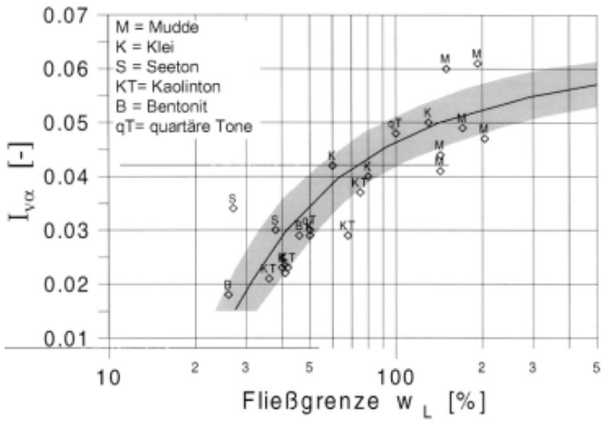

Figure 2-17 – Variation of rate effect per natural log cycle of strain rate, $I_{v\alpha}$, with liquid limit (Krieg and Goldscheider, 1998)

2.2.5. Strain Level Dependence of Rate Effects

The behaviour discussed this far has covered rate effects at peak strength, which is a useful analysis approach if the application concerned is dependent on the maximum shear resistance at high strain rates. However, to model rate effects at a more fundamental level (e.g. to inform constitutive models), there is a need to consider rate effect variations with strain level.

Before considering the dependence of rate effects on strain, it is worthwhile to briefly summarise the static soil response with strain under normally consolidated conditions and to define some of the key terms which will be discussed. Figure 2-18 presents a schematic example of soil behaviour with strain in three key spaces; q-ε_q, G-$log(\varepsilon_q)$ and q-p'. Some aspects of the figure are exaggerated for clarity. Soil initially displays an (almost) purely elastic response, as shown in Figure 2-18 (a), with near-constant stiffness up until the point where the soil yields. Various definitions exist for the point of yield, but the definition used in this study is the limit of the linear elastic zone referred to by Jardine (1992) as the "Zone 1" limit. This yield point occurs at a deviatoric yield stress denoted q_{EL} and at a yield strain denoted the

elastic shear strain threshold ($\varepsilon_{q,EL}$), after which the soil continues to tend towards the critical deviator stress, q_{CSL}, before failure (or localisation) occurs. $\varepsilon_{q,EL}$ typically occurs at strains of the order of ε_q = 0.001 to 0.01 % (Santagata *et al.*, 2007; Lo Presti *et al.*, 1996). This same behaviour, in terms of the shear modulus degradation, is shown in Figure 2-18 (b), with the soil's initial elastic behaviour being represented by a region of constant (maximum) shear modulus, G_{max}. After $\varepsilon_{q,EL}$, the shear modulus reduces with increasing strain as the soil yields. In Figure 2-18 (c), the soil specimen starts at an initial mean effective stress, p'_0, before moving vertically towards the static Zone 1 (elastic) yield envelope, at which q_{EL} (and hence $\varepsilon_{q,EL}$) occurs. After this point, significant pore pressures begin to develop due to shearing, and combined with the increasing deviator stress, this causes the specimen to tend towards the critical state line (CSL) with increasing strain. The CSL is reached at a deviator stress of q_{CSL} and a corresponding mean effective stress of p'_{CSL}. Strain dependent behaviour is often referred to as being either small strain or large strain. For the purpose of defining these terms, small strain refers to soil behaviour below ε = 0.1 %, and large strain refers to behaviour at strains greater than this. This is in keeping with the recommendations of Santagata *et al.* (2007) and Atkinson (2000), such that the small strain range includes yield behaviour and the subsequent pronounced non-linearity.

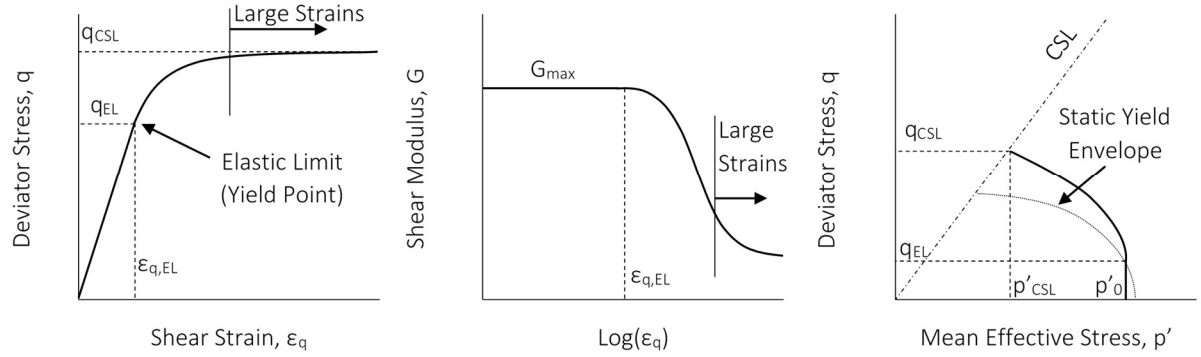

Figure 2-18 – Static (slow-rate) behaviour of clay with increasing strain in terms of (a) stress-strain response, (b) stiffness degradation with strain and (c) yield behaviour in *q-p'* space

One of the earliest reports of the strain dependency of rate effects was given by Akai *et al.* (1975) [$\dot{\varepsilon}$ = 0.12 to 3000 %/hr] using triaxial testing, which found that rate effects mobilise as strain increases to an axial strain of ε = 1 %, before an approximately constant value is reached

(Figure 2-19). Due to the limitations of the analysis methods and equipment capabilities at that time, the number of strain levels compared is limited, however, the results do highlight the key areas of strain dependence which need to be reviewed. These areas are the mobilisation of rate effects up to the maximum rate effect (which Akai *et al.* (1975) reported to be around ε = 1 %) and also whether rate effects change with increasing strain after the maximum rate effect has been reached.

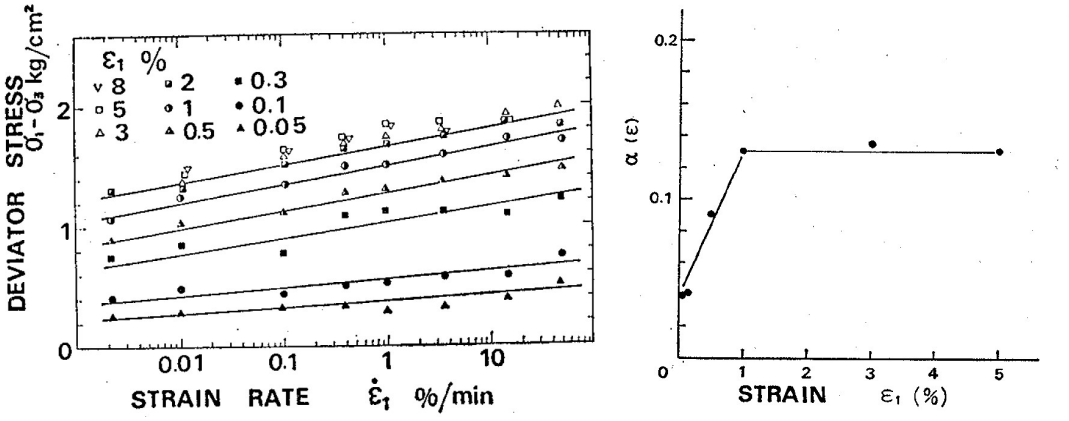

(a) (b)

Figure 2-19 – (a) Variation of deviator stress with axial strain rate for various strain levels (b) change in rate effect per log cycle, λ, with axial strain, both from Akai *et al.* (1975)

First considering rate effect mobilisation, a number of studies consider the impact of strain rate at strain levels below the soil's yield point. Sorensen *et al.* (2010) [$\dot{\varepsilon}$ = 0.006 to 0.023 %/hr] demonstrated using 'isotache' triaxial testing (where varying strain-rate steps are successively applied to the same specimen), with local small strain measurements on London Clay, that no distinguishable rate effects were observed on the soil's stiffness at small strains below the elastic yield threshold, $\varepsilon_{q,EL}$ (Figure 2-20(a)). This suggests that for any given strain level below $\varepsilon_{q,EL}$, the deviator stress appears rate independent. Sorensen *et al.* (2010) considered only low axial strain rates of up to 0.023 %/hr, however a number of other studies including Shibuya *et al.* (1996), Mukabi and Tatsuoka (1999) and Santagata *et al.* (2007) confirmed this finding at axial strain rates up to 84 %/hr using a variety of clays (Figure 2-20(b)). Santagata *et al.* (2005) [$\dot{\varepsilon}$ = 0.1 to 4 %/hr] showed that this apparent rate independence of the initial modulus applies to both normally consolidated and overconsolidated soils, as shown in the stress-strain plots in Figure 2-21. This was done using triaxial tests on Boston Blue Clay (BBC), with high resolution local strain measurements from an LVDT system. In Figure 2-21(a), the initial moduli are

consistent up to strain of approximately 0.002 %, after which the specimens begin to yield. In Figure 2-21(b), the overconsolidated specimens have higher yield strains which are outside the range shown in the graph, and the moduli are consistent throughout the visible data.

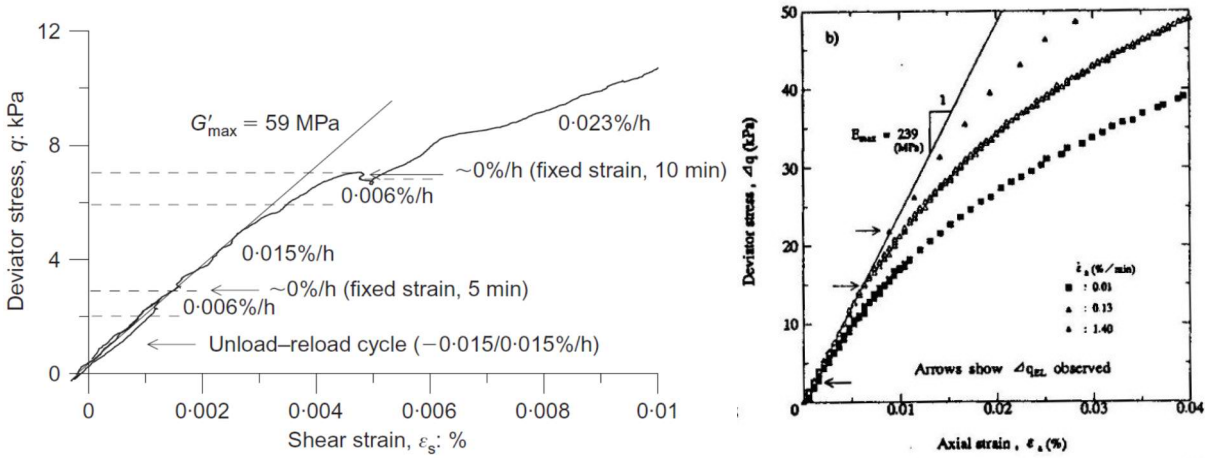

(a) (b)

Figure 2-20 – (a) Graph of deviator stress against shear strain for isotache triaxial testing on London clay (Sorensen *et al.*, 2010) and (b) graph of deviator stress against axial strain for monotonic triaxial testing on NSF clay (Shibuya *et al.*, 1996)

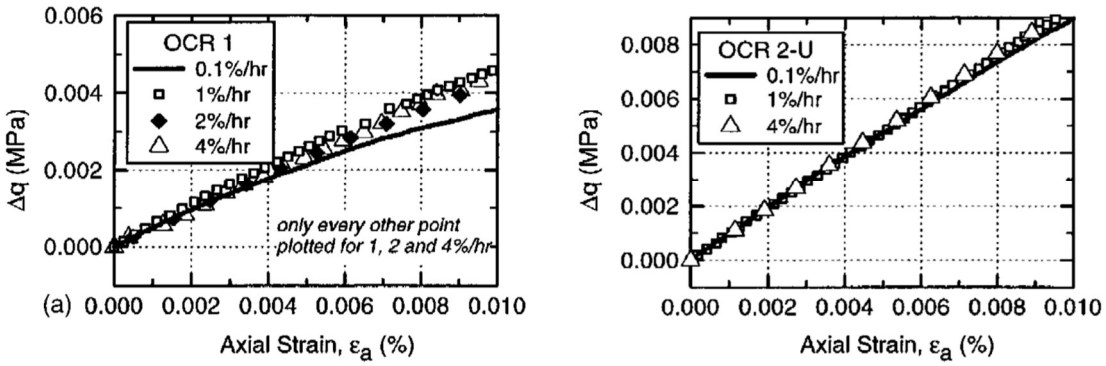

(a) (b)

Figure 2-21 – Graph of deviator stress against axial strain (a) for normally consolidated and (b) overconsolidated triaxial tests on Boston Blue Clay, showing the rate independence of the Young's Modulus (Santagata *et al.*, 2005)

Interestingly, Shibuya *et al.* (1996) and Santagata *et al.* (2007) also found that the elastic shear strain threshold increased with axial strain rate (Figure 2-20(b) and Figure 2-22(a)). Shibuya *et al.* (1996) [$\dot{\varepsilon}$ = 0.6 to 84 %/hr] suggested that $\varepsilon_{q,EL}$ varied according to Equation 2-14 for NSF clay. Santagata *et al.* (2007) [$\dot{\varepsilon}$ = 0.1 to 4 %/hr] presented the same behaviour in terms of

stiffness degradation, with the initial Young's Modulus, E_{max}, remaining constant until the elastic strain threshold, which is shown to increase with strain rate (from $\varepsilon_{EL} \approx 0.001$ at $\dot{\varepsilon} = 0.1$ %/hr up to $\varepsilon_{EL} \approx 0.005$ at $\dot{\varepsilon} = 4$ %/hr) before the stiffness degrades.

$$\varepsilon_{q,EL} \propto \sqrt{\frac{\Delta\varepsilon_a}{\Delta t}} \tag{2-14}$$

The increase in the elastic yield point in terms of the elastic yield stress, q_{EL}, with strain rate was also previously reported by O'Reilly *et al.* (1989) [$\dot{\varepsilon}$ = 0.06 to 24 %/hr] and was found to increase linearly with the logarithm of shear strain rate (Equation 2-15). As shear stiffness would appear to be rate independent up to the yield point, this means that $\varepsilon_{q,EL}$ would also be proportional to $log(\dot{\varepsilon}_q)$.

$$q_{EL} \propto \varepsilon_{q,EL} \propto log(\dot{\varepsilon}_q) \tag{2-15}$$

These two forms of equation provide very different trends in terms of $\varepsilon_{q,EL}$, with Equation 2-14 suggesting far higher values at high strain rates and further research is required to identify which of these forms is correct. However, it is noted that O'Reilly *et al.* (1989) used a greater strain rate range and number of specimens, which would increase confidence in the correlation.

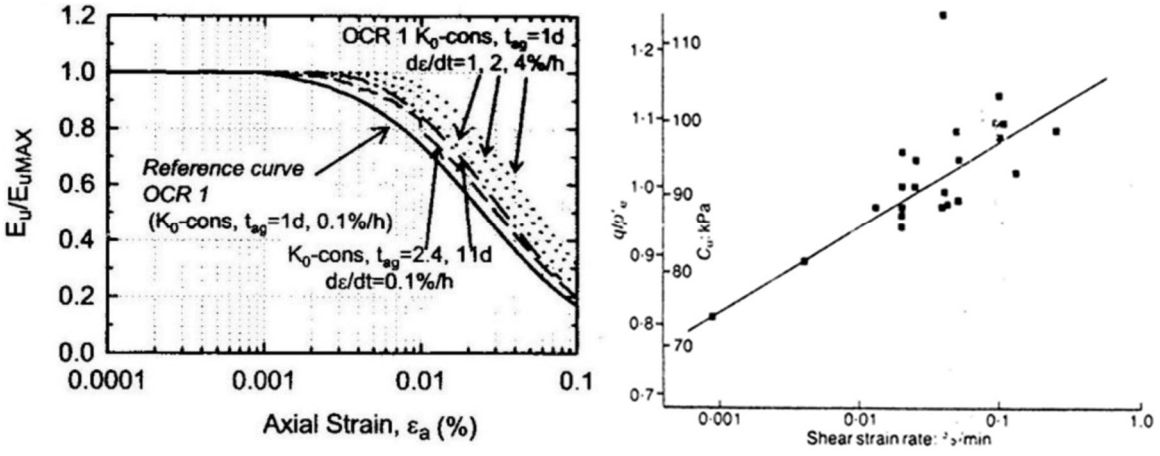

(a) (b)

Figure 2-22 – (a) Degradation of normalised stiffness with axial strain at varying axial strain rates for Boston Blue Clay (Santagata *et al.*, 2007) and (b) increase in normalised deviator stress at yield with shear strain rate (O'Reilly *et al.*, 1989)

O'Reilly *et al.* (1989) suggested that the increase in yield stress with shear strain rate is due to the expansion of the yield envelope with strain rate, with the yield envelope defining the point of onset of plastic strain. It was proposed that the 'viscous' yield envelope is dependent on the shear strain rate applied to the specimen and is coincident with the static yield envelope when the strain rate is sufficiently low (Figure 2-23). Similar increases in the yield envelope (Figure 2-24(a)) with axial strain rate were also observed by Graham *et al.* (1983) and Leroueil and Marques (1996). However, research has not yet clearly identified if existing forms of the static yield envelope (e.g. Modified Cam Clay) can adequately capture the yield envelope at high strain rates, and no models for the magnitude of expansion of the yield envelope have yet been identified from experimental data. Tatsuoka and Shibuya (1992) and Di Benedetto and Tatsuoka (1997) defined the initial elastic modulus of the soil as the Elastic Limiting Line (ELL) (Figure 2-24(b)), which cannot be exceeded, leading to the observed increases in $\varepsilon_{q,EL}$ as the yield envelope expands. The reason that rate effects are negligible below the elastic limit is poorly understood, however, if the ELL is considered to be a fundamental maximum stiffness (for the given initial soil conditions) which cannot be exceeded, then by definition no rate effect would be possible below the elastic limit. This is due to the fact that this would require a deviator stress higher than the ELL would allow.

Given that the literature suggests that rate effects are negligible below the elastic limit and that the elastic limit increases with strain rate, rate effects must mobilise at some point between yield (which occurs at $\varepsilon_q \approx 0.001$ to 0.01 %) and the point of maximum rate effect near 1 % strain. Few studies have considered this aspect of rate effects, and the only study identified was Lo Presti *et al.* (1996), which collated data from a number of sources, as well as tests conducted by the authors on Pisa and Augusta clays. Lo Presti *et al.* (1996) considered the change in a strain rate parameter, α, (which is proportional to the rate effect per log cycle, λ) with strain level (Equation 2-16).

$$\alpha(\varepsilon_q) = \frac{\Delta G(\varepsilon_q)}{\Delta(\log \dot{\varepsilon}_q) G(\varepsilon_q, \dot{\varepsilon}_{q,ref})} \tag{2-16}$$

where G is the secant shear modulus at any given shear strain, ε_q, and shear strain rate, $\dot{\varepsilon}_q$.

The study comprised of both high plasticity clay and low plasticity clay. It was shown that α increases from a near zero value after yield near $\varepsilon_q = 0.001$ %, to a value which appears to be

dependent on the plasticity of the clay. Considering the low plasticity clays (on the lower curve of points in Figure 2-25) where there are the most data, it can be seen that a maximum rate effect of α = 0.1 is reached near a value of ε_q = 1 %. This is in keeping with the findings of Akai *et al.* (1975), which also found the maximum rate effect is reached near 1 % strain. A similar trend in rate effect mobilisation with strain was also observed by Brown (2008) from RLT pile testing, although issues correlating the pile displacements back to strain level complicate the comparison.

No studies have yet proposed models for capturing this mobilisation of rate effects, and additionally experimental data on rate effect mobilisation using accurate local strain measurements is not available in the literature.

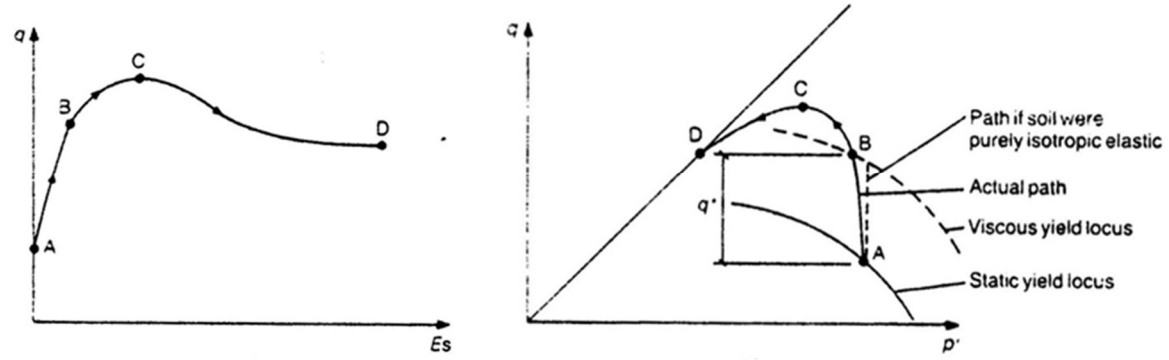

(a) (b)

Figure 2-23 – Schematic of yield behaviour of rapidly loaded specimens showing enlarged 'viscous' yield envelope (a) in terms of stress-shear strain response and (b) in *q-p'* space (O'Reilly *et al.*, 1989)

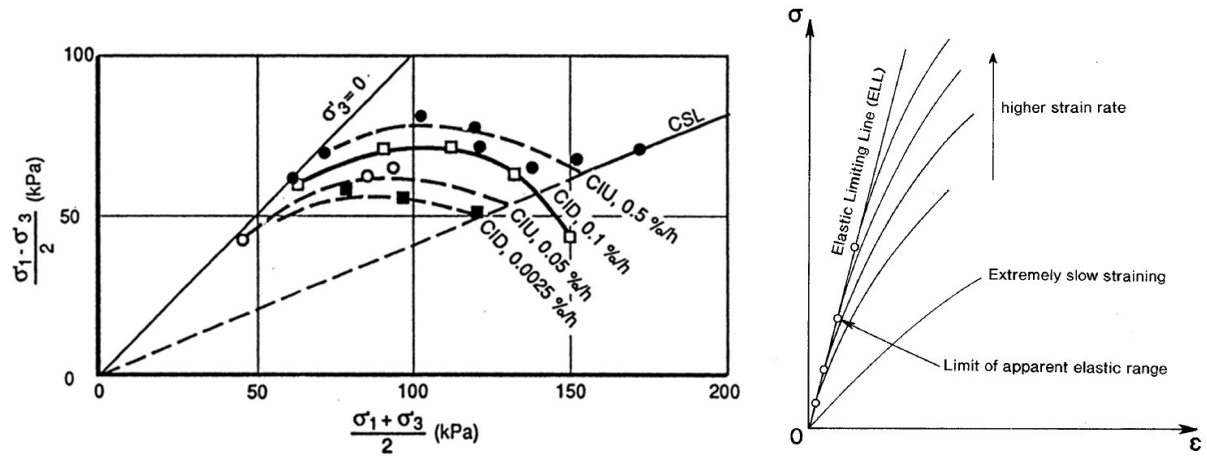

(a) (b)

Figure 2-24 – (a) Expansion of yield envelope with axial strain rate (Leroueil and Marques, 1996) and (b) definition of the Elastic Limiting Line (ELL) and its impact on yield strain (Di Benedetto and Tatsuoka, 1997)

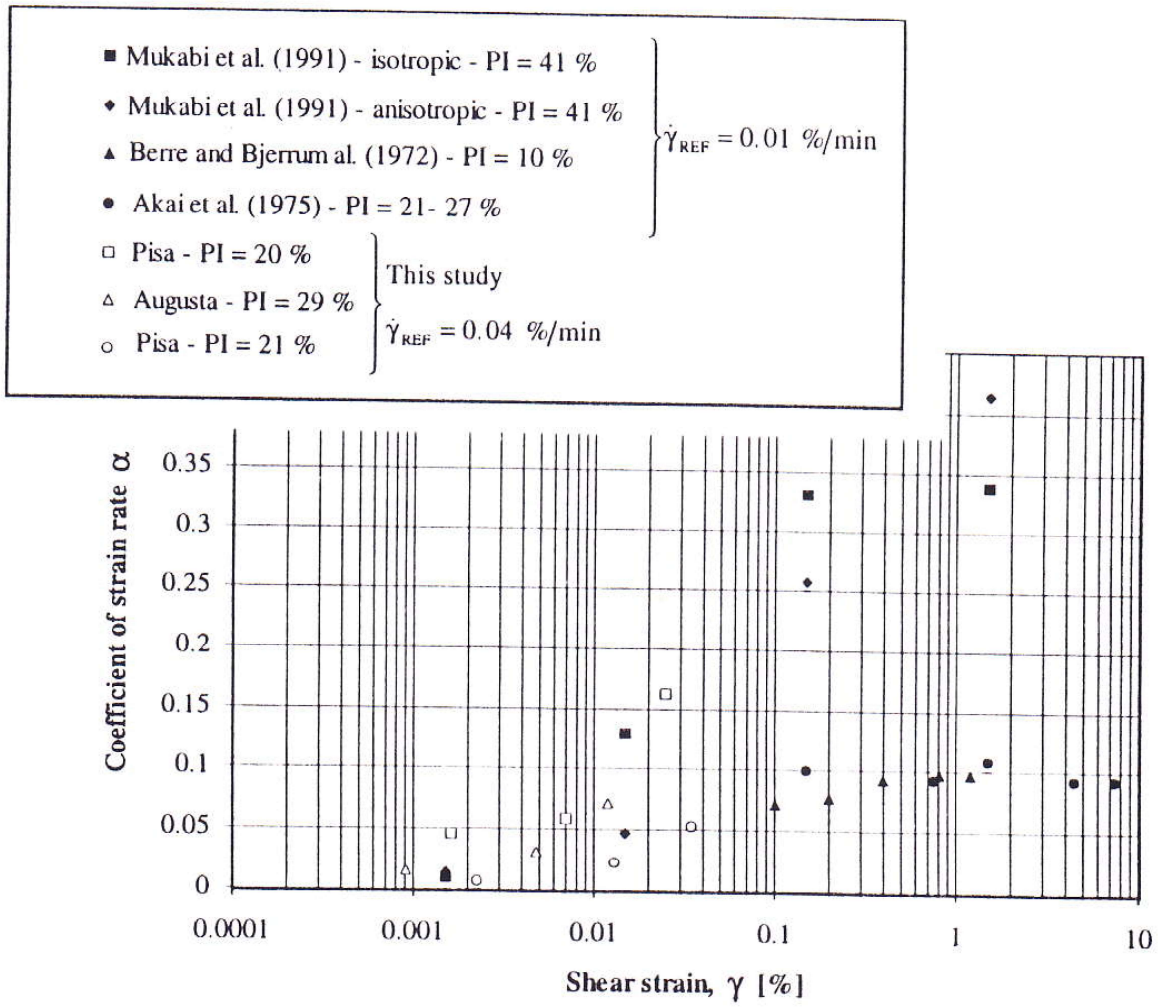

Figure 2-25 – Mobilisation of rate effects with shear strain (Lo Presti *et al.*, 1996)

The final aspect of the strain dependence of rate effects is whether rate effects change with increasing strain after the maximum rate effect has been reached. Balderas-Meca (2004) [$\dot{\varepsilon}$ = 2 to 360,000 %/hr] modelled rate effects for a Kaolin, Sand and Silt mixture (KSS) using a power law (Equation 2-17) with two parameters; a damping coefficient, α, and an exponent, β. It was found that the maximum rate effects were observed at an axial strain of approximately 0.3 %, after which α reduced with strain (Figure 2-26(a)).

$$\frac{q_d}{q_s} = 1 + \alpha(\varepsilon)\left(\frac{\Delta V}{V_0}\right)^{\beta} - \alpha(\varepsilon)\left(\frac{V_{ref}}{V_0}\right)^{\beta} \quad (2\text{-}17)$$

where the exponent, β, is kept constant at a value of 0.20 and the damping coefficient, α, increases with rate effects.

Graham *et al.* (1983) also observed that the rate effect per log cycle, λ, degraded with increasing strain at axial strains greater than 3 % (Figure 2-26(b)). This trend occurred for both normally consolidated and overconsolidated specimens. These two studies differ in that Balderas-Meca (2004) suggested that rate effects stop degrading after an axial strain of 3 % is reached, whereas Graham *et al.* (1983) showed that rate effect degradation continues throughout the entire strain range measured. Potential reasons for this inconsistency include the different types of rate effect models (power and semi-log) used in the respective studies or possibly real differences in the rate effect responses of KSS (used in Balderas-Meca, 2004) and Belfast clay (used in Graham *et al.*, 1983). It is also important to note that the reductions in the undrained rate effect with increasing strain shown by these two studies are different from those described by studies such as Tika *et al.* (1996) (ring-shear testing at displacements of up to 4000 mm) where the changes are partly due to drainage and volume changes occurring.

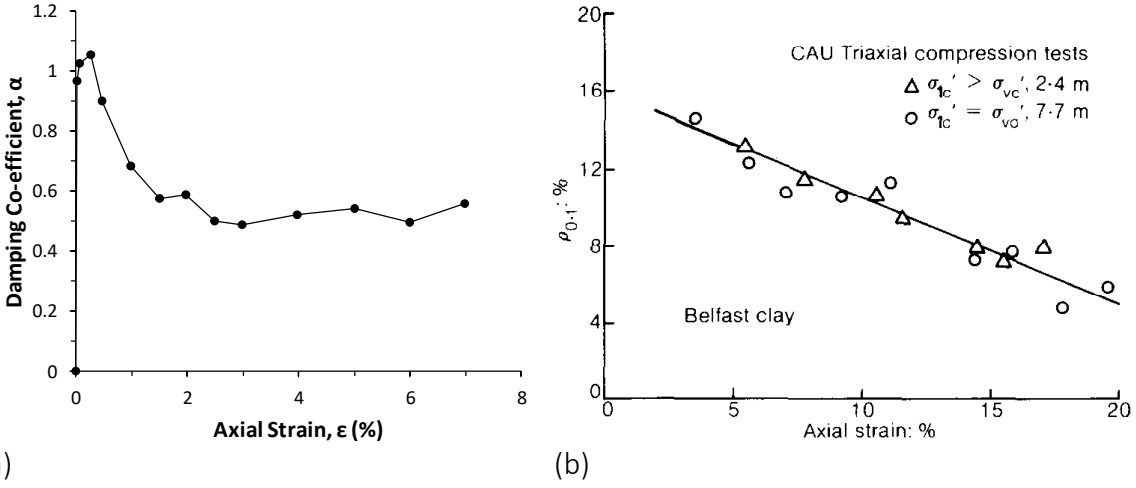

(a) (b)

Figure 2-26 – (a) Variation of damping coefficient, α, with axial strain for triaxial tests on KSS clay (Balderas-Meca, 2004) and (b) variation of rate effect per log cycle, λ, with axial strain for triaxial tests on Belfast clay (Graham *et al.*, 1983)

In summary, the literature review suggests that rate effects are negligible below the elastic yield strain, which is rate dependent, before mobilising up to a strain of approximately ε = 1 % at which the maximum rate effect is observed. After this point, rate effects appear to degrade with increasing strain. Given that a soil's peak strength may occur at a strain of the order of anywhere from ε = 1 to 5 % (Sheahan *et al.*, 1996), this raises the question of whether the commonly used (Sheahan *et al.,* 1996; Zhu and Yin, 2000) approach of using peak strength as

the comparison point to calculate rate effects is the best approach. A consequence of this is that if two soils with the same maximum rate effect are compared, they could be calculated to have different rate effects at peak strength depending on the strain level at which their peak strength occurs. This highlights the importance of using strain-based rate effect definitions, such as those used by Lo Presti *et al.* (1996).

2.3. Rate Effects on Pore Pressure Evolution

The strain rate dependency of pore pressures generated during shearing was identified by Richardson and Whitman (1963) who showed, comparing undrained triaxial tests on normally consolidated Mississippi River Valley clay at axial strain rates of 0.12 and 60 %/hr, that measured pore pressures reduced with increasing strain rate (Figure 2-27). This effect was attributed to an increased tendency for the soil to dilate at high strain rates, due to increased resistance to movement between adjacent clay particles. This reduction in pore pressure with strain rate has been reported by a number of studies including Sheahan *et al.* (1996), Zhu and Yin (2000), Santagata *et al.* (2007) and Svoboda and McCartney (2014(a)).

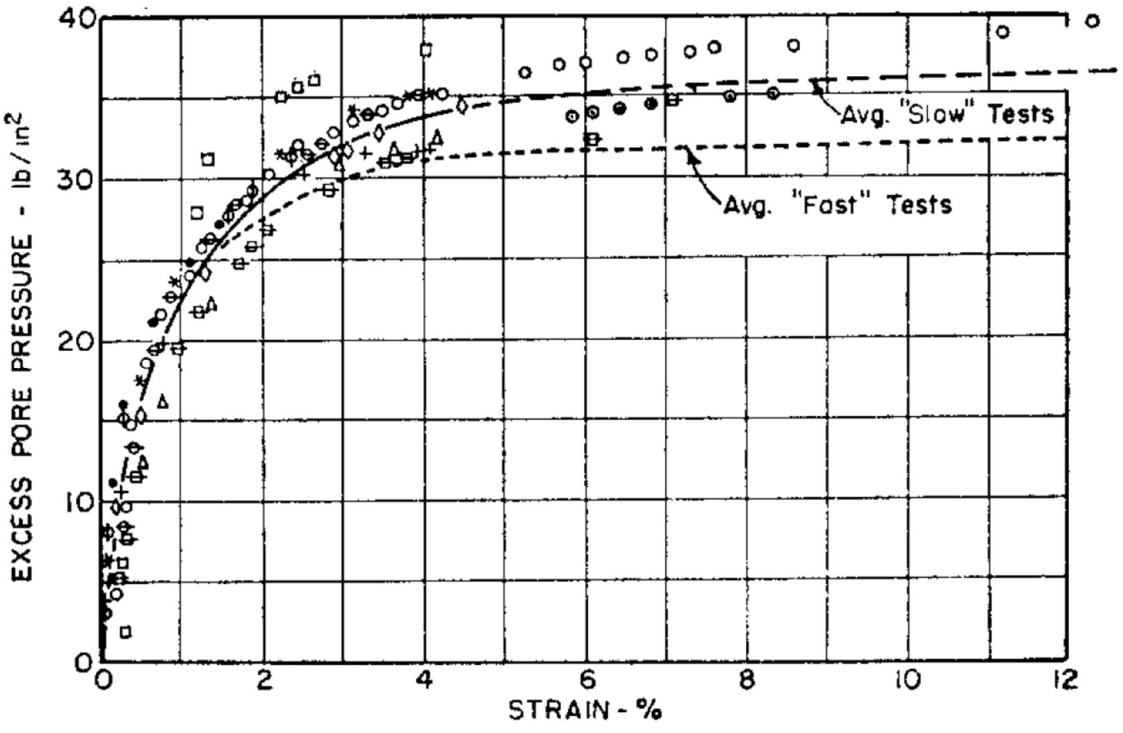

Figure 2-27 – Development of pore pressure with strain at $\dot{\epsilon}$ = 0.12 and 60 %/hr in Mississippi River Valley clay (Richardson and Whitman, 1963) [1 lb/in^2 = 6.89 kN/m^2]

One of the limitations in the study by Richardson and Whitman (1963) was that the number of strain rates was limited to only two, meaning that the question of the manner in which pore

pressures reduce with strain rate could not be considered. Zhu and Yin (2000) studied the relationship between pore pressures and strain rate in more detail and identified that for both normally and overconsolidated soils, the pore pressure at peak deviator stress reduced linearly with the logarithm of axial strain rate (Figure 2-28(b)). Comparison of whether overconsolidated soils exhibit greater reductions in pore pressure with strain rate in Zhu and Yin (2000) is once again complicated by differences in the soil state/liquidity index between the various OCRs tested, in a similar way to that previously discussed in the analysis of rate effects on the deviator stress. Zhu and Yin (2000) considered both compression and extension, which is the reason for the differences between the positive and negative axial strain rates in Figure 2-28 (a). This is illustrated in Figure 2-28 (c), although only compression is considered in this study.

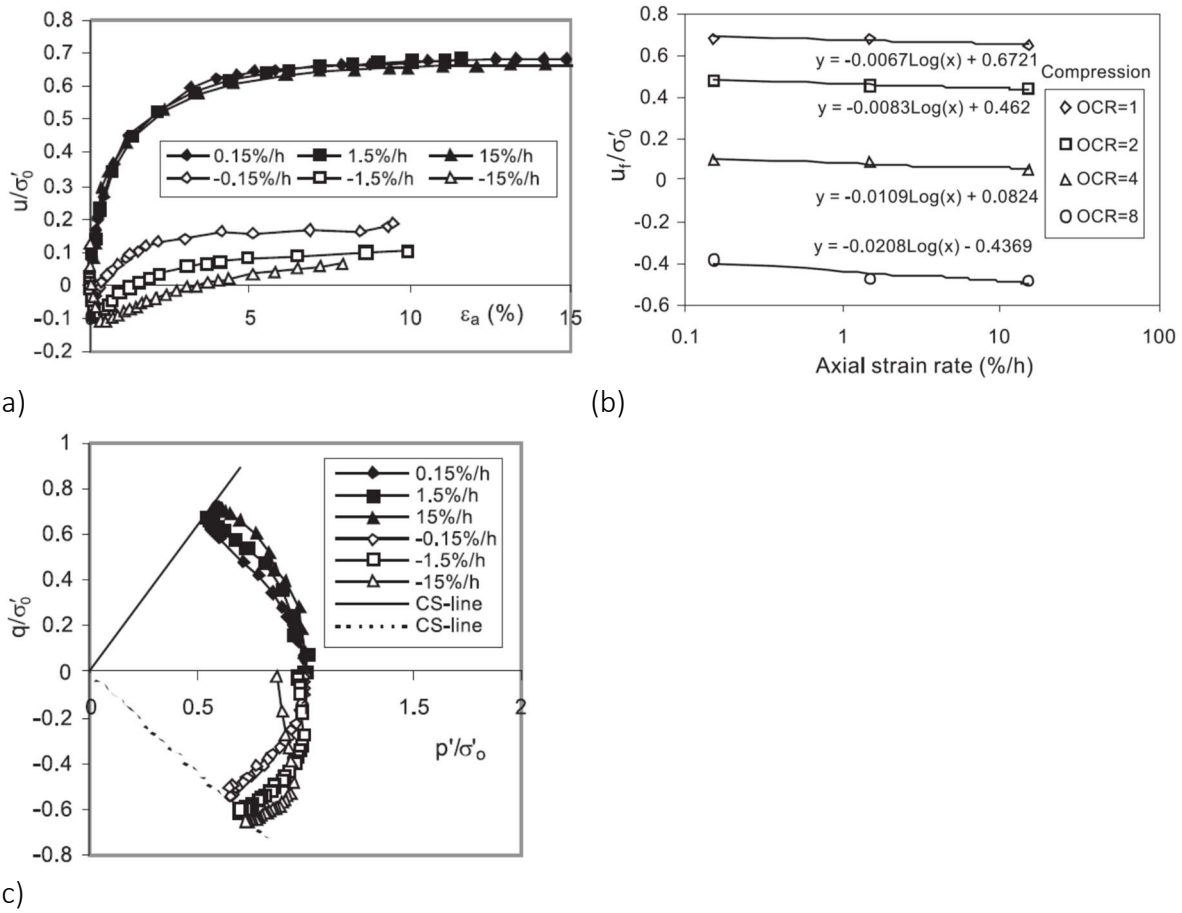

Figure 2-28 – (a) Variation of pore pressure with strain at varying axial strain rates for OCR = 1 (b) variation of pore pressure at peak deviator stress with axial strain rate and (c) effective stress paths for both triaxial compression and extension of normally consolidated Hong Kong marine clay (Zhu and Yin, 2000)

The reductions observed in pore pressure with strain rate in Zhu and Yin (2000) are comparatively small, and important reasons for this are suggested by Sheahan *et al.* (1996). When considering undrained triaxial testing at varying strain rates, the deviator stress and pore pressure response is intrinsically linked. As the deviator stress increases with strain rate, this leads to corresponding increases in the mean total stress, *p*, acting on the specimen (Equation 2-18) causing an increase in the pore pressure, *u*, which is unrelated to any pore pressures generated by shear-induced dilatant or contractive tendencies. This increase in pore pressure due to the increasing total stress with strain rate partly offsets the observed reductions in pore pressures in studies such as Zhu and Yin (2000).

$$p = \frac{\sigma_1 + \sigma_2 + \sigma_3}{3} \tag{2-18}$$

Sheahan *et al.* (1996) proposed that when analysing the impact of rate effects on pore pressures, shear-induced pore pressures (Equation 2-19) should instead be considered, as this definition accounts for issues associated with the changing total stress and is more representative of the true soil behaviour. Using this definition, it was shown that shear-induced pore pressures also reduce with *log(ε̇)*, although the reductions are greater in magnitude than those found using the conventional definition of pore pressure (Figure 2-29). The deviations from this rule at OCR = 4 and 8 shown are due to the fact that Sheahan *et al.* (1996) found that in Boston Blue Clay, highly overconsolidated specimens exhibited no rate effects below axial strain rates of approximately 5 %/hr.

$$\Delta u_{si} = \Delta u - \Delta p \text{ for any given strain where } \Delta p = \frac{\Delta\sigma_1 + \Delta\sigma_2 + \Delta\sigma_3}{3} \tag{2-19}$$

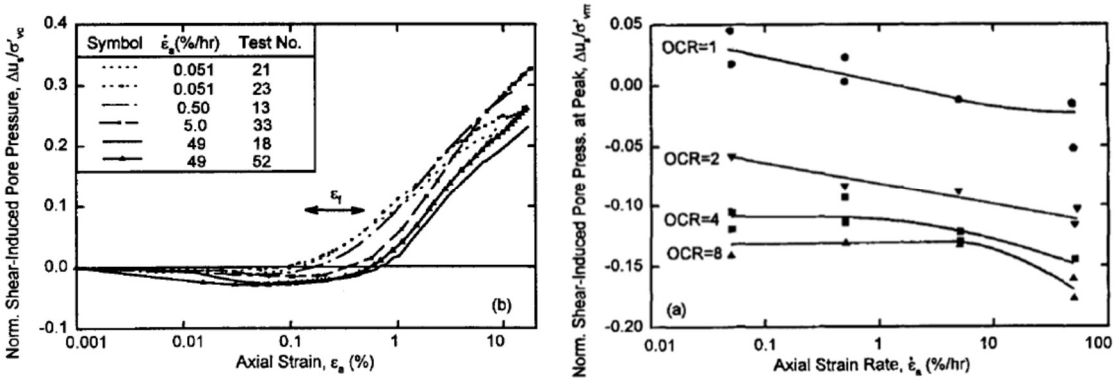

(a) (b)

Figure 2-29 – (a) Evolution of shear-induced pore pressure with axial strain rate at OCR = 1 and (b) variation of shear-induced pore pressure at peak deviator stress with axial strain rate in triaxial testing of Boston Blue Clay (Sheahan *et al.*, 1996)

The usefulness of this definition of pore pressure has been highlighted by its use in a number of rate effect studies, such as Katti *et al.* (2003) and Santagata *et al.* (2007). In particular, Santagata *et al.* (2007) [$\dot{\varepsilon}$ = 0.1 to 4 %/hr] showed that the use of shear-induced pore pressures is beneficial when analysing rate effects at small strains, as they are more closely related to the true response of the soil, with the onset of pore pressure development coinciding with the observed yield points (Figure 2-30).

However, a number of issues remain to be resolved in terms of the response of pore pressures to strain rate. Foremost of these is that current studies have considered only rate effects on pore pressures at the peak deviator stress, and there is a need to understand the impact of rate effects on pore pressures across the entire strain range if rate effects are to be more accurately modelled. Additionally, no studies have considered pore pressures at axial strain rates above 50 %/hr, primarily due to issues in pore pressure transducer response times. Just as many studies report that it is necessary to investigate rate effects on the deviator stress at strain rates close to those in the desired application in question, it would be questionable to use rate effect data on pore pressure from low strain rates and extrapolate this forward to higher strain rates. Hence, there is a need for further investigation of the rate effect on pore pressures at significantly higher strain rates.

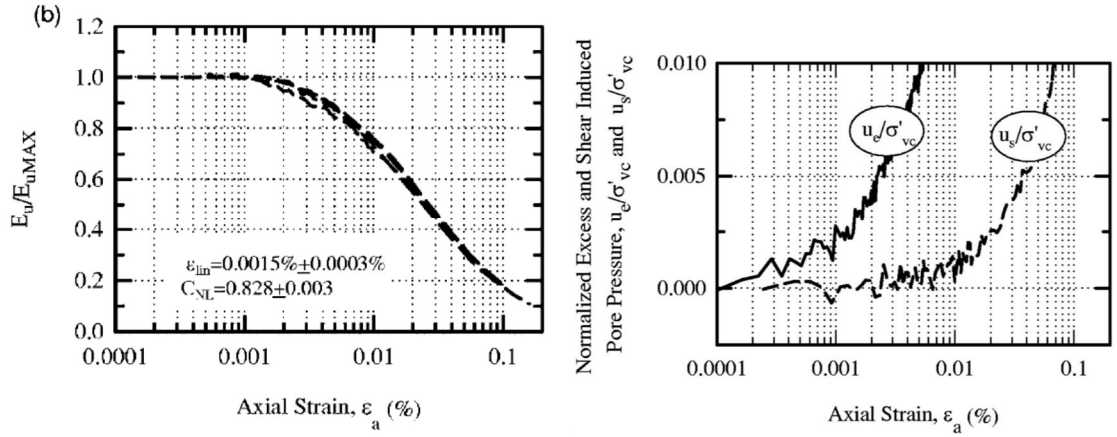

(a) (b)

Figure 2-30 – (a) Stiffness degradation curve showing yield behaviour of Boston Blue Clay and (b) evolution of both pore pressure and shear-induced pore pressure with strain in the corresponding triaxial test (Santagata *et al.*, 2007)

2.4. Critical State Behaviour at Varying Strain Rates

The literature suggests that at axial strains beyond 1 %, rate effects reduce with increasing strain. However, significant rate effects are still observed at large strains (up to ε = 10 %) in several studies (e.g. Balderas-Meca, 2004). This suggests that even at strains where the soil would be expected to be tending towards the critical state, rate effects still occur and need to be considered.

The impact of increasing strain rate on the critical state line in *q-p'* space was considered by Nakase and Kamei (1986) using triaxial testing of sand-Kawasaki clay mixtures prepared to achieve plasticity indexes ranging from 10 to 30 % at axial strain rates from 0.42 to 42 %/hr. It was found that the deviator stress at which the specimens reached critical state increased with increasing strain rate, but that there was also a corresponding reduction in pore pressure which increased the mean effective stress, *p'*. This resulted in the specimens all tending towards the same critical state line, regardless of their strain rate (Figure 2-31(a)).

More recently, Li and Baudet (2016) investigated rate effects on the critical state line in reconstituted Kaolin. Using triaxial tests at axial strain rates up to 10 %/hr, Li and Baudet (2016) also showed no impact of strain rate on the critical state line in *q-p'* space (Figure 2-31(b)). The gradient of the CSL in *v-ln(p')* space, λ_{CSL}, was also found to be rate independent as shown in Figure 2-32, although there is a reasonable amount of scatter in the data. The variation in the critical state parameters *M* and *Γ* with axial strain rate from Li and Baudet (2016) is also shown

in Figure 2-33, with no clear change in these parameters being visible over the low strain rate range studied.

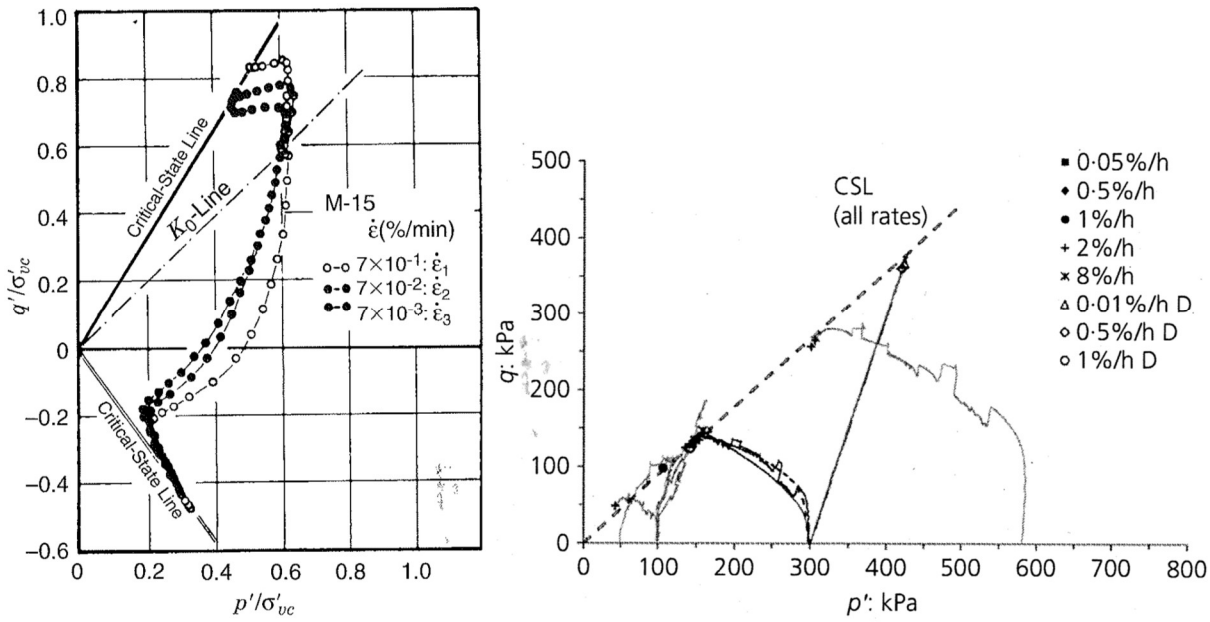

(a) (b)

Figure 2-31 – (a) Impact of axial strain rate on the critical state line for a reconstituted sand and Kawasaki clay mixture with *PI* = 15 % (Nakase and Kamei, 1986) and (b) impact of axial strain rate on the critical state line in *q-p'* space for Kaolin (Li and Baudet, 2016)

However, only a few studies investigating the impact of rate effects on the critical state line have been identified, and none of these consider axial strain rates higher than 50 %/hr. This means that there is currently no evidence of critical state behaviour at the high strain rates which are likely to occur in some field applications, most likely due to the difficulties in obtaining reliable rapid pore pressure measurements as previously mentioned.

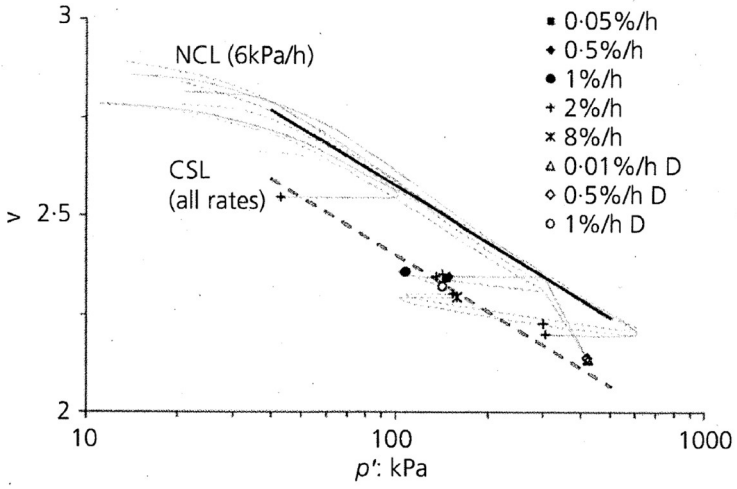

Figure 2-32 – Influence of axial strain rate on the critical state line in *v-ln(p')* space for Kaolin (Li and Baudet, 2016)

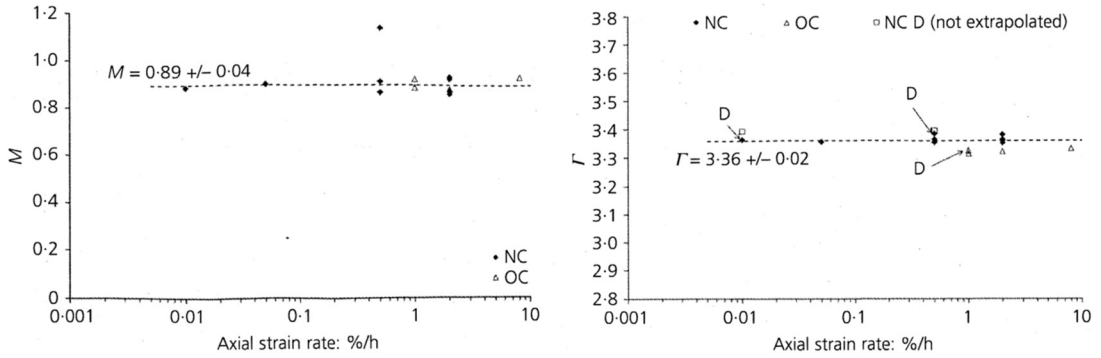

(a) (b)

Figure 2-33 – (a) Variation of the critical state gradient in *q-p'* space, *M*, with axial strain rate and (b) variation of the critical state intercept in *v-ln(p')* space, *Γ*, with axial strain rate in Kaolin (Li and Baudet, 2016)

2.5. Summary of Literature Review

The existing literature has highlighted key information on the current understanding of rate effects, along with several areas which require further research. The key points of the review are as follows:

- Rate effects are studied using a wide variety of methods, each suited to the study of specific aspects of rate effects, and in field applications care must be exercised when comparing rate effects with element testing studies (e.g. high side-friction rate effects in CPT tests).
- Strain rate effects typically range from 5 to 20 % per log cycle, but a number of exceptions to this rule have been observed near the liquid limit where rate effects can be up to 150 % per log cycle.
- The studies considered show a consensus that rate effects increase with moisture content or liquidity index, although there is no agreement on which of these parameters is the most appropriate variable for comparison or the models for capturing this effect.
- The evidence for the influence of OCR on rate effects is conflicting, but this can be explained by moisture content variations in specimen preparation, suggesting the OCR itself has no observable impact on rate effects.
- The literature is conflicting as to whether Atterberg limits are a good indicator of the magnitude of rate effects, and further research is required to clarify this.
- Rate effects are highly strain level dependent, with rate effects only mobilising after the yield point (which itself is rate dependent), reaching the maximum rate effect at axial strains of the order of 1 %.
- Beyond the point of maximum rate effect, rate effects have been found to reduce with increasing strain, although further research is required to identify how this rate effect degradation may be modelled and the factors which control it.
- Pore pressures at peak deviator stress appear to reduce with $log(\dot{\varepsilon})$ and it is important to consider the shear-induced pore pressures rather than the excess pore pressures. No studies have considered pore pressure response at high strain rates.
- Current research on the effect of rate effects on the critical state parameters is limited and no studies have considered axial strain rates higher than 50 %/hr, although no

changes in the critical state parameters have been observed at the low strain rates considered.

3. Methodology

3.1. High Speed Triaxial Testing

3.1.1. Introduction

The variability in the findings of previous studies considered in the literature review, such as the conflicting conclusions on the effect of OCR, highlights the importance of careful control of the factors which may influence the soil's rate dependent behaviour. Triaxial testing allows accurate control of the soil specimen's state and coupled with the fact that the University of Dundee has the capability to carry out high speed triaxial testing this was felt to be the most appropriate method for investigating rate effects. Due to the need for control over the specimen's stress history, reconstituted samples from three powdered clays were used.

3.1.2. Considerations in High Speed Triaxial Testing

Given that high speed triaxial testing was to be used, there were two key areas which required further consideration to ensure the accuracy of the experimental results; uniformity of the specimen during shearing and the rapid measurement of pore pressures. A brief review of the literature on these considerations follows, to inform the subsequent discussion of the triaxial testing methodology.

Conventional triaxial apparatus uses relatively rough frictional platens at the top and base of the specimens, and this friction has the effect of restraining the top and bottom ends of the triaxial specimen during shearing. This leads to non-uniform deformation of the specimen during shearing, an uneven distribution of both stress and pore pressure as well as barrelling of the specimen (Rowe and Barden, 1964). Due to these non-uniformities, 'dead zones' form within the specimen as the specimen localises on shear planes as shown in Figure 3-1(a), making accurate deviator stress and pore pressure measurements difficult to achieve.

To overcome these issues, Rowe and Barden (1964) proposed the use of lubricated ends which consist of enlarged smooth platens and a layer of grease covered with rubber membrane Figure 3-1(b). This has the effect of reducing end friction significantly such that it becomes negligible, meaning that the specimen would maintain an approximately cylindrical shape during shearing. This improves the accuracy of deviator stress calculations as well as allowing

a more even distribution of both stress and pore pressure. Rowe and Barden (1964) found that using lubricated end platens prevented the premature localisation of triaxial specimens, allowing the measurement of deviator stresses to significantly higher strain levels. In Figure 3-2 it can be seen that without lubricated ends, the specimen localises at a strain of less than ε = 10 %, whilst no localisation is observed when the lubricated end platens were used. These findings have been confirmed by a number of studies (e.g. Sheng *et al.*, 1997) including several triaxial strain rate effect studies where the even distribution of stress and pore pressure is essential for accurate measurements (Fourie and Xiaobi, 1991; Sheahan *et al.*, 1996). However, one disadvantage of the use of lubricated end platens is that the grease and membrane layers introduce additional compliance into the strain applied by the platens, reducing the accuracy of strain measurements at small strains (Fourie and Xiaobi, 1991). For this reason, it is recommended that local on-sample strain measurements are used. In summary, lubricated end platens are essential to ensure the accuracy of measured deviator stresses and pore pressures in triaxial testing by preventing inhomogeneity due to end friction, although the use of local strain measurements is recommended if lubricated end platens are used.

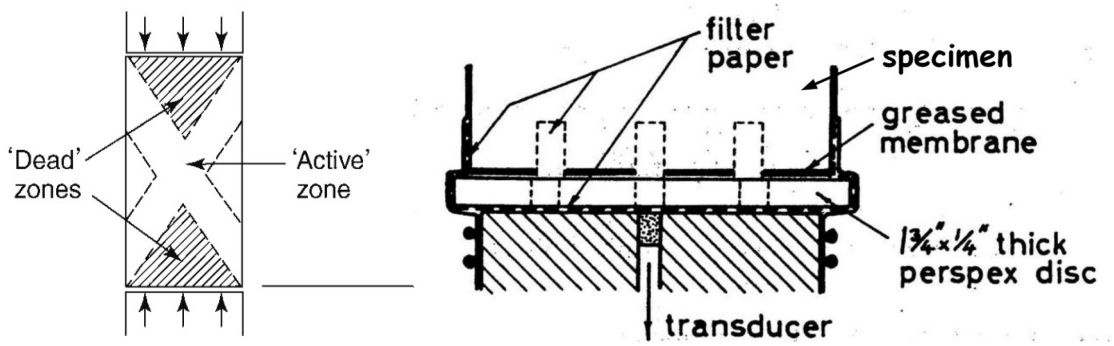

Figure 3-1 – (a) 'Dead' zones created by frictional end restraint in triaxial specimens (Head and Epps, 2011) and (b) lubricated end platen arrangement proposed by Rowe and Barden (1964)

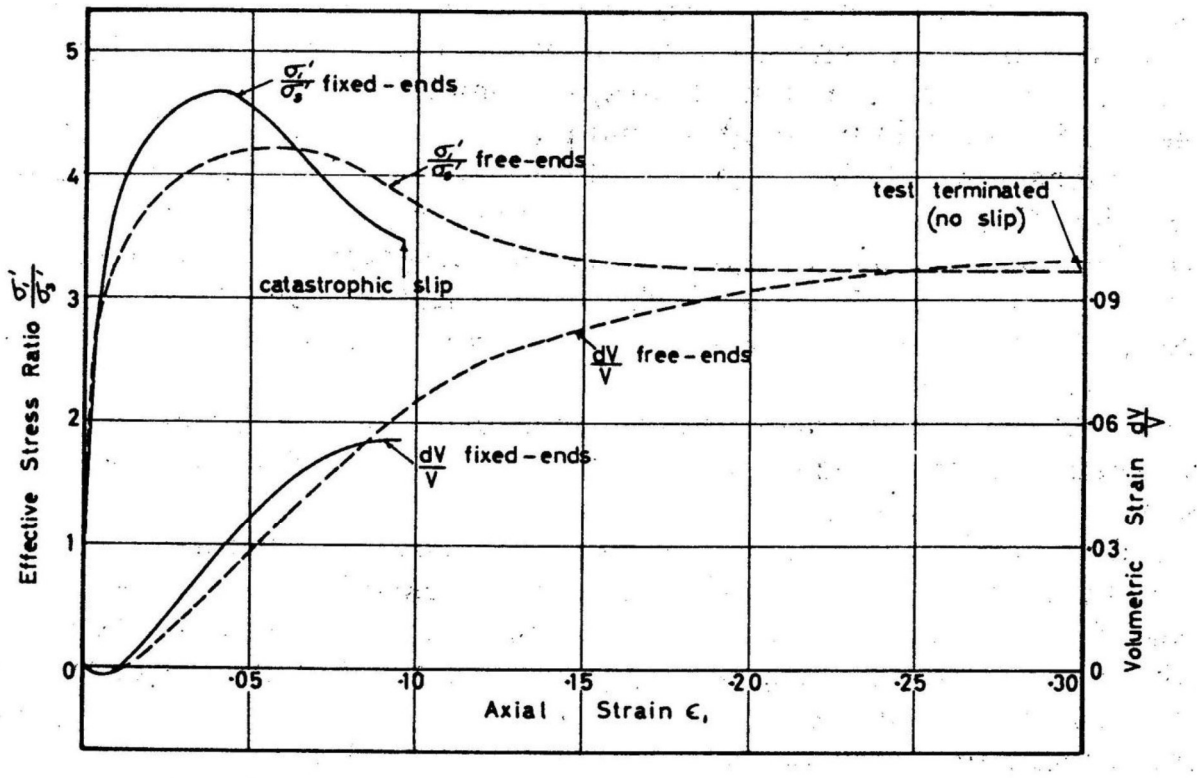

Figure 3-2 – Influence of lubricated ('free') ends on the stress-strain response of a triaxial specimen (Rowe and Barden, 1964)

Obtaining reliable pore pressure measurements is one of the most important challenges in high speed triaxial testing (Anderson, 1993) and this is one of the main reasons that effective stress behaviour at high strain rates is not often considered. In conventional static triaxial testing, time is available for pore pressures to equalise throughout the specimen and also for the pore pressure to fully mobilise the external (base) pore pressure transducer commonly used (O' Reilly, 1991). However, in high strain rate triaxial tests on clays, the specimen is fully undrained and it is assumed that there is no time for local drainage within the specimen to occur. This means that pore pressures must be measured directly on the specimen (rather than by external base pore pressure transducers located outside of the cell). The lack of time for pressure equalisation by local drainage also means that it is important that the pore pressure generation is uniform and homogenous throughout the specimen (hence the need for lubricated end platens as discussed previously) (Fourie and Xiaobi, 1991).

A number of studies have considered the response times of pore pressure measurement systems. O'Reilly (1991) conducted a comparison of conventional base pedestal pore pressure

measurements and measurements from a pore pressure probe consolidated into the specimen at mid-height (Figure 3-3). The comparison used five specimens, denoted A to E, with both types of transducer fitted, which were subjected to cyclic changes in the cell pressure. It was found that base pore pressure measurements did not provide a full response beyond 0.001 Hz (cycle/test time of 1000 seconds), whilst the mid-height pressure transducer was capable of providing a full response at up to approximately 0.1 Hz (cycle/test time of 10 seconds). The response of mid-height transducers has been researched more recently by Fourie and Xiaobi (1991) and Sheahan *et al.* (1996) which found that on sample mid-height pressure transducers can provide a full pore pressure response within 5 to 7 seconds.

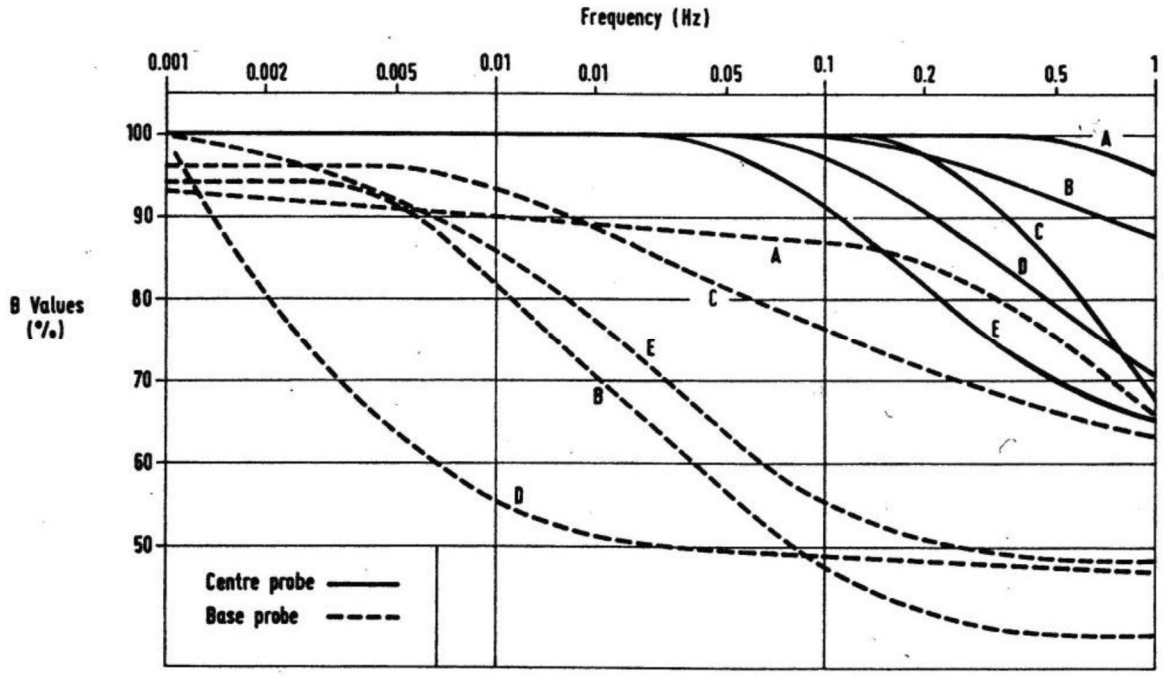

Figure 3-3 – Comparison of response times of base and internal mid-height pore pressure transducers (O'Reilly, 1991)

The need for rapid pore pressure measurements is highlighted by Quinn and Brown (2011) which compared pore pressures measured on the surface of a triaxial specimen at mid-height with those measured at the centre of the specimen using a hollow cylindrical extension piece to the surface transducer (Figure 3-4) at an axial strain rate of $\dot{\varepsilon}$ = 180,000 %/hr (test duration of 0.5 seconds). The internal probe measured extremely high pressures which tended towards the cell pressure, whilst the surface measurements showed only a small response. Closer inspection of the internal probe and its associated sealing details suggests that leakage of the cell water into the probe occurred when the specimen was subjected to shearing, causing the

high pore pressure measurements. Conversely, the response time of the Druck PDCR 81 sample surface pore pressure transducer is 2 to 3 seconds (GDS Instruments, 2014) which was longer than the test duration of 0.5 seconds, explaining the low surface pore pressure readings. As the best possible response times using the currently available mid-height pressure transducers have been shown to be longer than the duration of the highest strain rate tests which will be used in this testing (0.5 seconds), there is a need to develop a new rapid mid-height pore pressure sensor with a significantly faster response time.

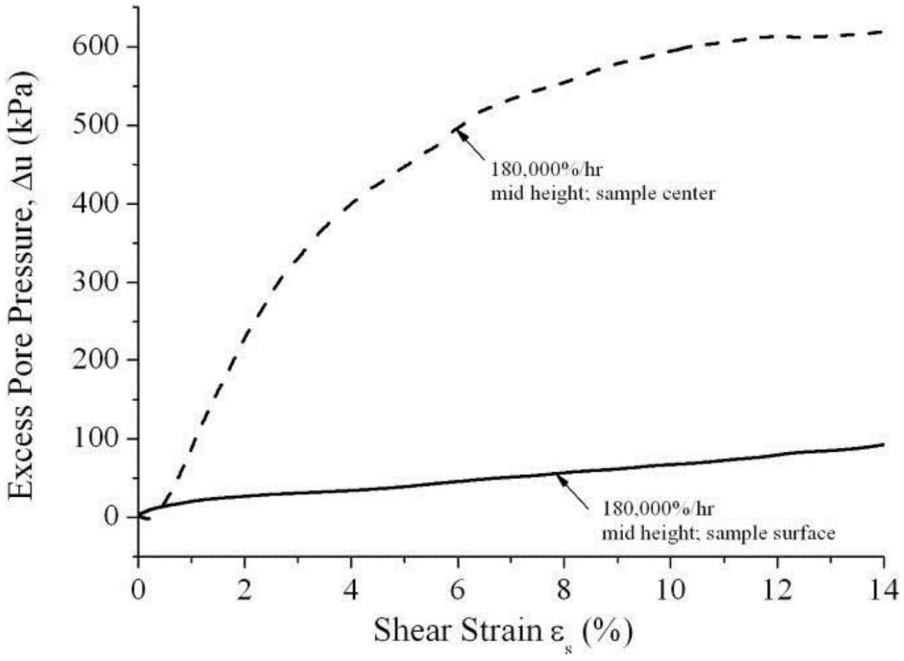

Figure 3-4 – Comparison of internal and surface pore pressure measurements from high speed triaxial testing of Kaolin at $\dot{\varepsilon}$ = 180,000 %/hr (Quinn and Brown, 2011)

3.1.3. Experimental Setup

The triaxial testing was carried out using a modified GDS MiniDYN triaxial rig (Figure 3-5(a)) specially modified by the manufacturer to allow high strain-rate monotonic triaxial testing (GDS Instruments, 2018; Quinn, 2013). The system is capable of testing standard 200 mm (h) x 100 mm (Ø) triaxial samples at displacement rates of up to 100 mm/s, equivalent to an axial strain rate of 180,000 %/hr. The system is located in a dedicated element testing laboratorywhich is enclosed and separate from the main laboratory to minimise air flow and disturbance. The room temperature is thermostatically controlled to within the range of 20 to 25 °C as required by BS1377.

The system is an electromechanical MiniDyn triaxial apparatus adapted by incorporating a significantly higher gearing ratio to allow faster displacement rates to be applied by the actuator. The system applies load to the triaxial specimen via the bottom platen, with global displacements measured by an encoder to a resolution of 1.3 µm. The actuator is backlash free such that there is negligible mechanical compliance between the motor and the bottom platen. A set of GDS local Hall effect transducers were used to measure small strains on-specimen (Figure 3-5(b)). The set consisted of 2 axial transducers and 1 radial transducer to allow axial and radial strains to be calculated. The lightweight Hall effect transducers had a resolution of 0.1 µm, but with the added advantage of removing bedding errors normally associated with imperfections in the interface between the specimen and the platens (Clayton and Khatrush, 1986).

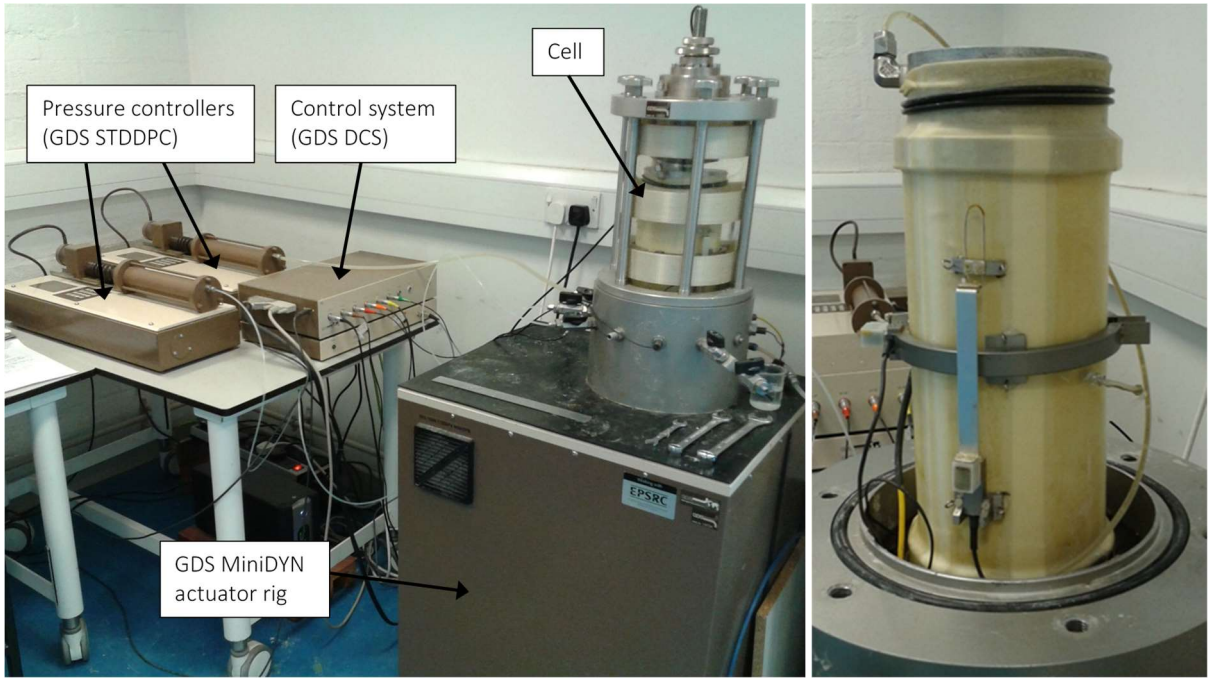

(a) (b)

Figure 3-5 – (a) Image showing the high speed triaxial system and (b) a photo of the lubricated end platen triaxial setup with local Hall effect transducers

The axial force applied to the specimen was measured by a GDS Type 9 submersible load cell with a range of 5 kN and a measurement resolution of 0.5 N. The submersible nature of the load cell meant that it was not necessary to correct the measured axial forces for changes in cell pressure. Cell and back pressures were applied by two GDS Standard Digital Pressure Controllers (GDS STDDPC) capable of applying pressures of up to 3000 kPa with an accuracy of ± 1 kPa. The triaxial cell is capable of withstanding pressures of 1700 kPa.

Two docking arrangements were used for the top cap; a half-ball connection and a suction cap connection. The half-ball connection (Figure 3-6(a)) was used for the majority of the triaxial tests, as it minimised disturbance of the sample during docking (Gasparre, 2005; Quinn, 2013). The suction cap system (Figure 3-6(b)) was reserved for specimens which experienced larger volume changes during consolidation and hence would have had excessive lateral movement of the top-cap. The additional restraint provided by the suction cap was necessary to maintain a cylindrical specimen in these cases. When the suction cap arrangement was used, the suction cap was docked immediately after the installation of the specimen in the triaxial cell and the system was set to maintain zero force on the load cell throughout the saturation and consolidation stages such that the suction cap only acted as a guide to the top cap (preventing lateral movement and rotation).

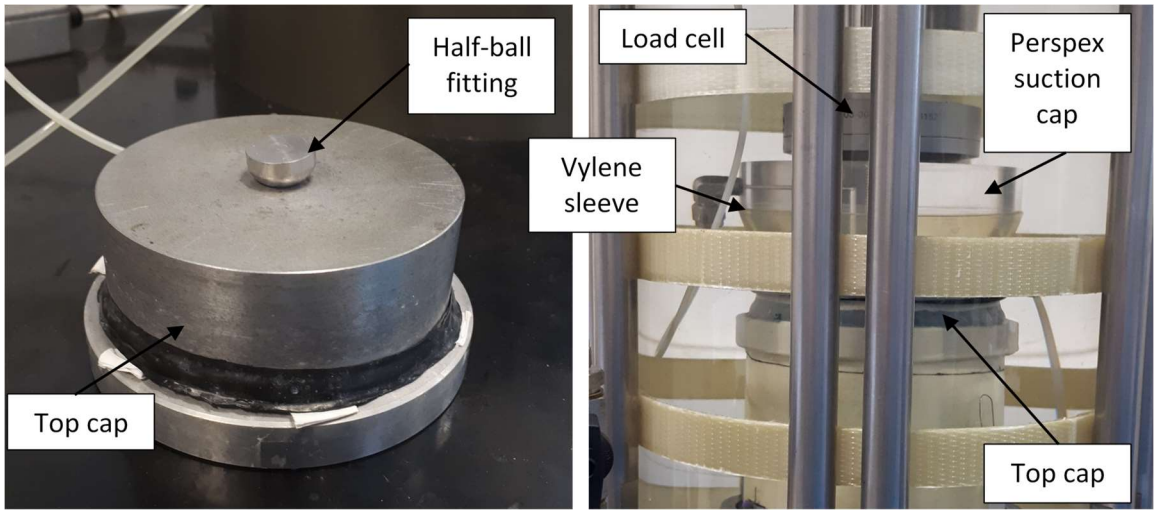

(a) (b)

Figure 3-6 – (a) Top cap with half-ball fitting and (b) suction cap docking arrangement within triaxial cell

The use of suction caps can, in certain cases, cause disturbance of the specimen due to the enforced alignment of the top cap. These issues were discussed in detail by Gasparre (2005). On docking with the specimen, the suction cap induces a small rotation of the top surface of the specimen as the top cap aligns with the horizontal surface of the suction cap, causing disturbance. This effect is especially important in natural, structured specimens, and is one of the reasons the Gasparre (2005) recommended the use of a half-ball fitting. However, the use suction caps here differs from Gasparre (2005) in a number of ways which mitigate this issue. Firstly, the specimens used here are reconstituted specimens for which the importance of structure is less significant, and Gasparre (2005) also used standard suction caps for the triaxial

testing of the reconstituted specimens rather than a half-ball fitting. Secondly, the suction cap docking process used here is to dock the specimen before filling the triaxial cell with water, such that the suction cap is already connected prior to both saturation and final consolidation. As all of the specimens were reconsolidated (to at least twice the mean effective stress used in the initial 1D consolidation, discussed later) this means that any disturbance from docking would be removed during the consolidation process. Gasparre (2005) was unable to successfully use this process as it requires precise control to maintain zero axial load during consolidation to prevent deviator stresses from occurring, which was not possible with the hydraulic triaxial system used. In this study, the GDS electro-mechanical triaxial system was capable of maintaining zero axial load on the specimen using a high-speed load control feedback loop, which was able to maintain zero change in axial force on the specimen during consolidation to within ±0.5 N ($\Delta\sigma_1$ < ±0.06 kPa).

The system control and logging was provided by a GDS Dynamic Control System (GDS DCS). This operates in two distinct modes; static and dynamic. In tests with a duration greater than 3 minutes, the system operates in static mode where the PC sends commands to the apparatus every 2-3 seconds and reads the transducers on the same frequency. In tests with shorter durations the dynamic mode is used. In this case, the details of the required displacements for the test are transferred to the GDS DCS and the test is run by the hardware using a PID control loop, with a common control and logging frequency of 10,000 Hz per channel.

One of the notable developments of the system in comparison with previous work at the University of Dundee is the adaptation to include lubricated end platens of a similar design to that proposed by Rowe and Barden (1964). The reasoning for this change was that, as found in the review previously given, the friction at the specimen ends results in inhomogeneity and 'dead zones' within the specimen which lead to premature localisation (Head and Epps, 2011). The enlarged 115 mm platens are made of polished aluminium to minimise both weight and friction and are covered by a thin layer of silicone grease (Figure 3-7(a)). A circular latex disc with slits to minimise hoop stress in the membrane and reduce sliding resistance is positioned on top of the silicone grease (Figure 3-7(b)). This design reduces end friction to a negligible level and ensures a uniform stress distribution in the sample (Head and Epps, 2011).

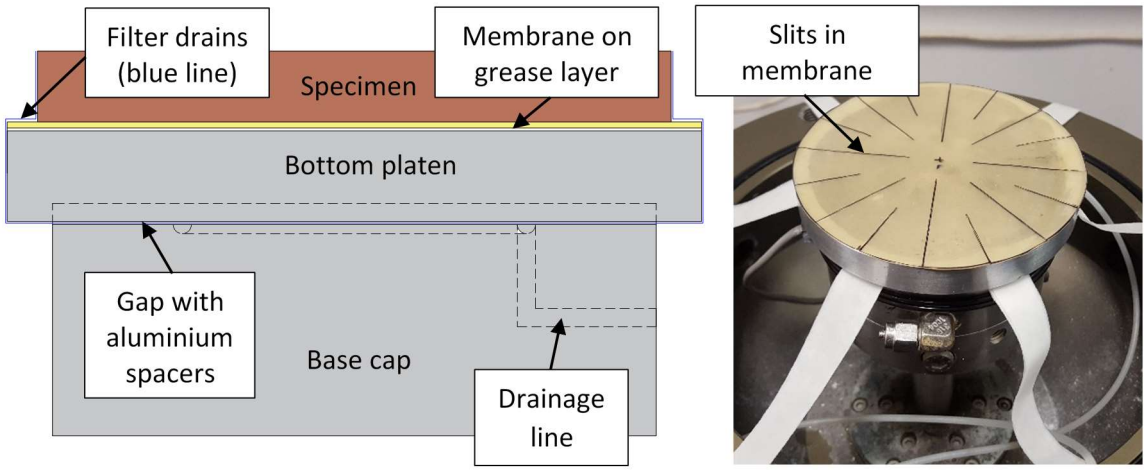

Figure 3-7 – (a) Diagram of lubricated end platen setup used and (b) of bottom lubricated end platen

Comparison of two preliminary tests highlights the importance of this change. Figure 3-8 shows two similar undrained triaxial tests; one with lubricated end platens and one using the standard triaxial setup. As can be seen, the test using the standard setup localises significantly earlier, and does not reach the full peak deviator stress. In contrast, the test using the lubricated end platen maintains the peak deviator stress to higher strain levels. The oscillations in these early tests are caused by PID control issues as they are high speed (discussed later in Section 3.2.5).

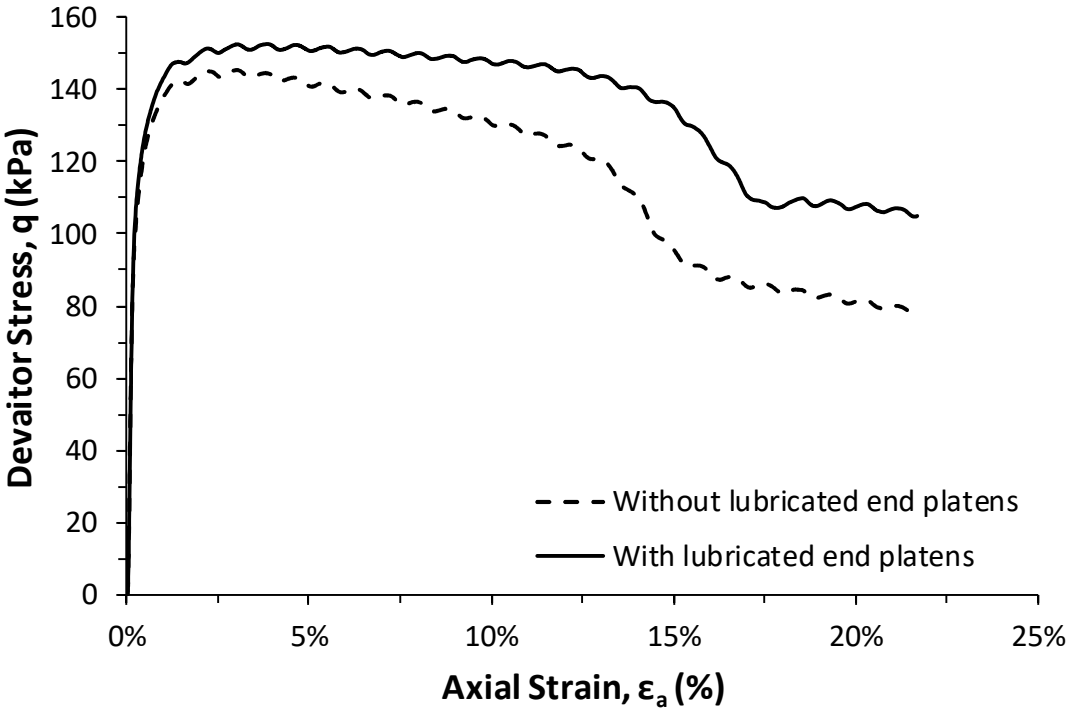

Figure 3-8 – Impact of lubricated ends on stress-strain response (isotropically consolidated Kaolin consolidated to an initial mean effective stress of p'_0 = 300 kPa and axially compressed at a strain rate of 100,000 %/hr)

Due to the addition of lubricated end platens, side filter drains were required to allow specimen consolidation. Two types of side filter drains are generally used; vertical drains and spiral drains (Head and Epps, 2014). Spiral drains are generally considered to be advantageous due to the fact that they have a smaller reinforcing effect on the measured soil deviator stress. However, due to the complex experimental setup used here, it was not possible to use these, and vertical drains were used instead. Head and Epps (2014) highlight that vertical drains may require a correction to the measured deviator stresses to account for the reinforcing and that the key factor is the specimen surface area covered by the drains which should not exceed 50 %.

An adapted method was used where 6 equidistant vertical filter drains 12 mm wide were placed around the side surface of the specimen, each consisting of three layers of Fisher Scientific qualitative filter paper equivalent to Whatman Grade No 1. This allowed a significantly reduced surface area of 23 %, whilst still providing the required drainage characteristics by increasing the flow area of the filter drains. For a standard 100 mm triaxial specimen, with the conventional filter drain layout covering 50 % of the surface area, a correction of no more than 3 kPa to the deviator stress would be required (Head and Epps, 2011). Hence, for the lower reinforced area used here, a significantly lower correction would be expected. On this basis, the effect of the filter paper strips would be significantly less than 2 % of the peak deviator strength of the specimen and no correction was applied.

The filter paper drains were connected to the drainage lines on both the top and bottom platens such that drainage could occur at both ends of the specimen. This was to minimise both the consolidation times and the maximum vertical pore pressure differential in the specimen.

Another complication generated by the use of lubricated end platens is that pore pressure measurements are not possible at the base of the specimen. Quinn (2013) used a GDS mid-height pore pressure transducer to measure the pore pressures on the surface of the sample. This was based around a Druck PDCR-81 miniature pore pressure sensor (which is no longer manufactured) fitted with a ceramic filter. However, even with careful installation and specimen saturation, the response time of this transducer is limited to 2-3 seconds in clay (GDS Instruments, 2014). Given that the shortest triaxial test duration used in this investigation is 0.5 seconds, an improved solution was required.

A new mid-height pore pressure transducer was developed which is capable of rapidly responding to pore pressure changes (See Figure 3-9). The transducer uses a Honeywell 24PCGFA6G pressure sensor with a 1700 kPa measurement range as the sensing unit. This is fitted with a 63 µm stainless steel mesh to improve the response time by eliminating the ceramic filter, which is known to account for almost all of the delay in the response time (Bertalot, 2013). The mesh was covered by filter paper which was held in place by a rubber O-ring when in use. The sensor unit is encased in a layer of epoxy resin and coated in a solvent-based liquid rubber (Performix Plastidip) to waterproof it. The gauge reference pressure for the sensor was provided by an air vent through the cable shielding to atmospheric pressure.

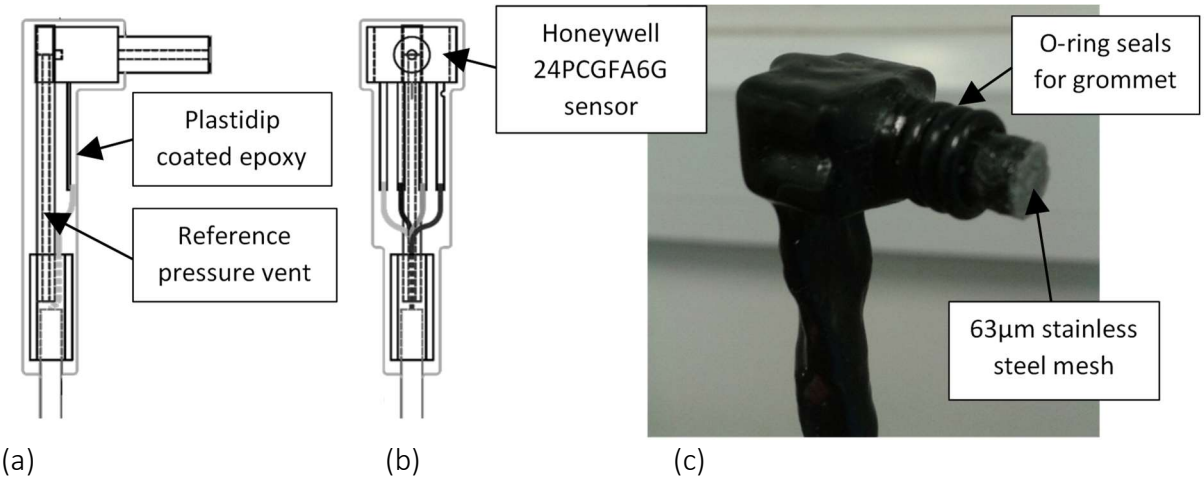

Figure 3-9 – New rapid mid-height pore pressure transducer; (a) side view, (b) front view and (c) photo of the complete transducer

To test the response time of the transducer, it was mounted on an actual clay specimen, consolidated to an isotropic effective stress of 300kPa and an external pressure vessel was used to apply rapid changes to the cell pressure by opening a valve between them. The cell pressure was logged by a Sherbourne P102 pressure sensor connected to the cell and by comparing the change in cell pressure with the change in measured pore pressure (Figure 3-10) it was possible to determine the *B* value of the sample against time in a similar manner to that described by Overy (1982) and O'Reilly (1991). For the initial few milliseconds the transducer is affected by pressure shockwaves created by the opening of the valve (causing the oscillations seen in Figure 3-10), but after this, the sensor provides an 85 % pore pressure response within 4 milliseconds and a 95 % response within 50 milliseconds (See Figure 3-11).

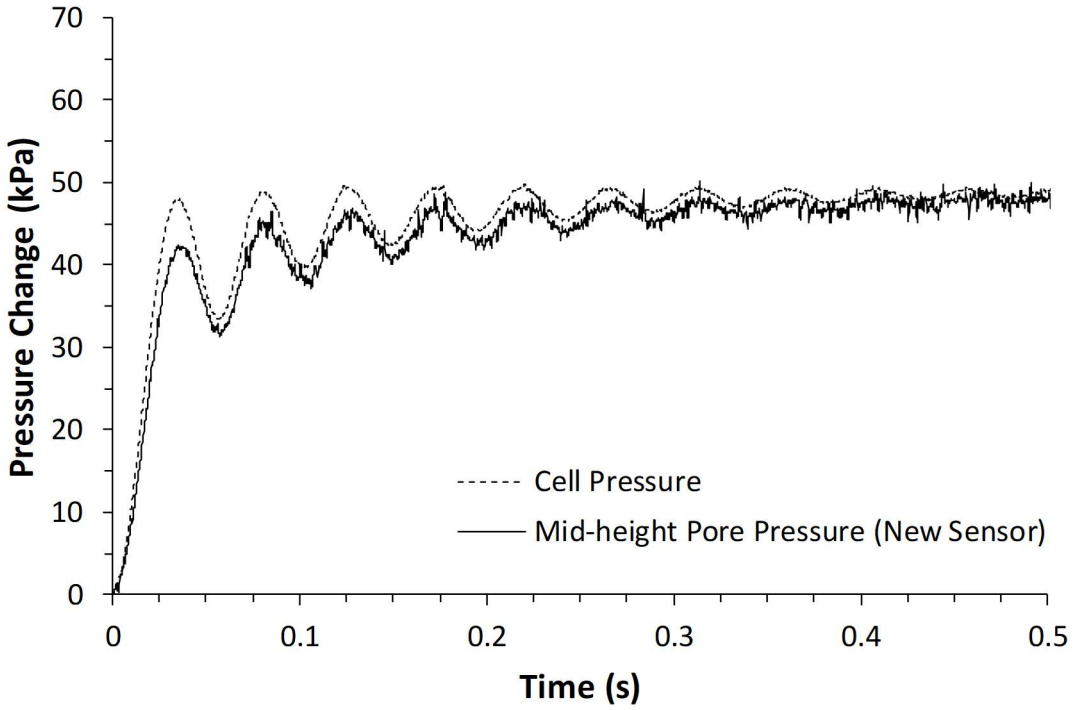

Figure 3-10 – Comparison of cell pressure and mid-height pore pressure response to rapid change

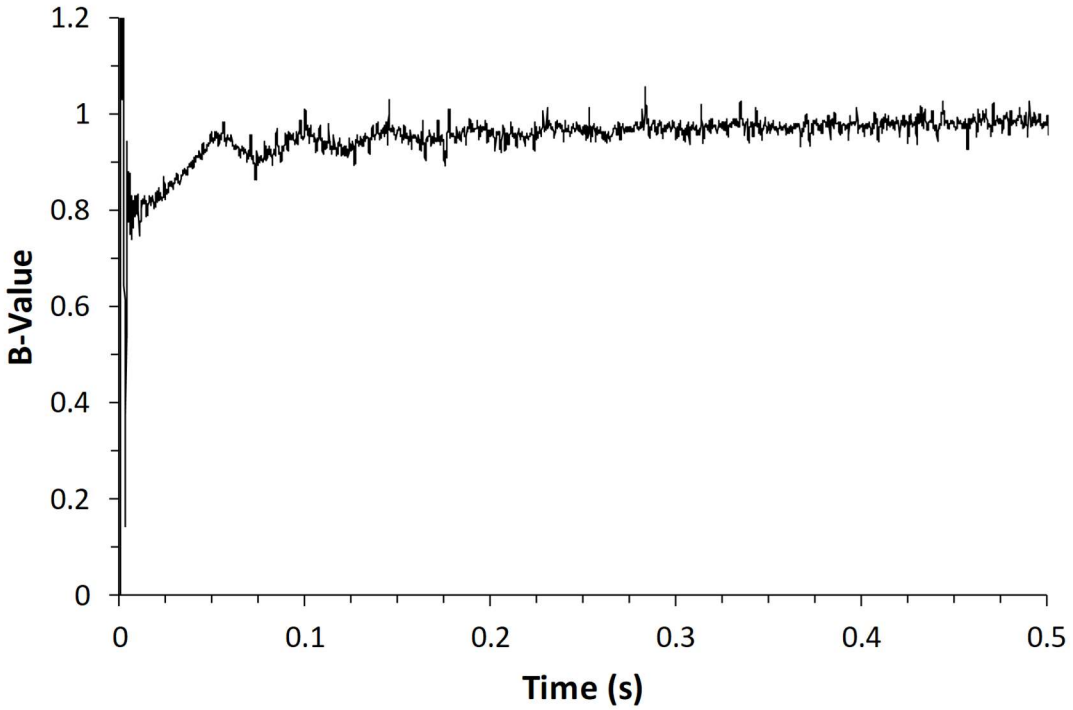

Figure 3-11 – Measured *B* value from new mid-height PPT against time

3.1.4. Specimen Preparation

The triaxial specimens were prepared in a one-dimensional consolidation apparatus consisting of compressed-air driven pistons applying pressure to slurry in 105 mm diameter aluminium sampling tubes with porous stone discs allowing drainage at both ends (See Figure 3-12). All of the clays were prepared at a moisture content of 125 % by mixing dry powdered clay (supplied by Imerys Minerals) with de-aired de-ionised water, for a period of 1 hour to ensure that all particle agglomerations were completely broken down. The de-ionised water was provided by an Elga Vision 250 De-ioniser which removes impurities from the water using a filtration system and ensures a neutral pH of 7. This is an important consideration for reconstituted samples, as the pore fluid used and its pH can significantly alter the consolidation and flocculation behaviour of clays by the addition of ions and counter-ions which influence the electrochemical interaction of the particles (Mitchell and Soga, 2005). The effectiveness of the de-ioniser was confirmed using a calibrated Oakton Ecotestr 2 pH Meter, capable of measuring the pH to +/- 0.1 pH. Prior to de-ionising the water supply was found to be 8.1 pH (+/- 0.3 pH) whilst after de-ionising the water was confirmed to be 7.0 pH (+/- 0.1 pH). The purified water was also passed through a sprinkler in a vacuum tank at a pressure of - 90 kPa (gauge), and the vacuum was held for a further hour to ensure full air removal.

Following this, the slurry was placed into the cylindrical aluminium consolidation tubes (400 mm in length x 105 mm internal Ø) with porous stones at either end. These were covered by circles of Fisher Scientific qualitative filter paper (equivalent to Whatman grade No. 1) to prevent the clay from clogging the drainage paths.

To allow the specimens to be removed from the consolidation tubes after consolidation without disturbance, it was necessary to use a lubricant to prevent the clay from adhering, however, there were issues associated with this that required to be considered. Conventionally, a thin layer of silicone grease would be used but its high viscosity meant that one of the clays being tested still experienced disturbance on removal due to its low strength at the consolidation pressure and high moisture content. Less viscous lubricants could have been used but concerns existed that these may be more easily absorbed into the specimen leading to changes in their permeability and electrochemical behaviour. The solution adopted was to use a dry film PTFE lubricant (WD40 Specialist Anti-friction Dry PTFE Lubricant) as this was found to prevent adhesion whilst also ensuring that the specimen permeability and

properties were unaffected. The lubricant was applied in spray form in two coats which were allowed to dry for at least an hour to ensure the solvents were fully evaporated and only the inert PTFE film remained.

Figure 3-12 – 1D consolidation apparatus

Next the consolidation tube was placed into the 1D consolidation apparatus and the force applied to the sample via the actuator was controlled using an air pressure regulator. Due to the fact that the pressure applied using the pressure regulator did not reflect the pressure experienced by the specimen due to piston friction, the pressure applied to the sample was instead monitored using a pore pressure transducer connected to a digital pressure meter whilst the pressure was applied. This assumed that as the clay was above the liquid limit, the lateral earth pressure coefficient, K_0, would be equal to 1.

The clays were then consolidated for the times as shown in Table 3-1 at a vertical effective stress of 200 kPa (equivalent to a mean effective stress of $p' \approx 150$ kPa) as this was the pressure required to ensure an easy to handle specimen for all of the clays to be used. The end of consolidation was confirmed by re-connecting the pore pressure transducer to the sample and monitoring the pressure for an hour to confirm that no pore pressure gradient remained.

Table 3-1 – Varying 1D consolidation times required to create handleable specimens

Clay	*Speswhite Kaolin*	*Hyplas 71*	*Hymod AT*
1D Consolidation Time (Days)	3	7	10

The values of p' resulting from the applied 200 kPa vertical effective stress (Table 3-2) were based on the assumption of K_0 conditions and K_0 was in turn estimated using Equation 3-1. ϕ'_{crit} was calculated from the measured values of the critical state gradient in q-p' space, M, presented later in this chapter using Equation 3-2.

$$K_0 = 1 - \sin\phi \tag{3-1}$$

$$\phi'_{crit} = \sin^{-1}\left(\frac{3M}{6+M}\right) \tag{3-2}$$

Table 3-2 – K_0 values used to estimate mean effective stress due to 1D consolidation

Clay	*Speswhite Kaolin*	*Hyplas 71*	*Hymod AT*
Critical Friction Angle, ϕ'_{crit} (°)	22	20	15
Lateral Earth Pressure Coefficient, K_0	0.63	0.65	0.74
p' resulting from 1D consolidation (kPa)	150	154	165

The air pressure was then removed from the actuator and the consolidation tube was placed onto a Clockhouse Engineering hydraulic jack fitted with an attachment which was threaded to secure the tube and which had a 100 mm circular platen to extrude the specimen. A visual inspection was carried out on the specimen to check for any imperfections such as air bubbles or edge disturbance from the extrusion process. The specimen was then trimmed to 200 mm in height using a guide to ensure a level cut, and the exact specimen dimensions and weight were recorded. The trimmings were also taken as a moisture content sample to provide information about the initial state of the specimen, which was then transferred to the triaxial cell.

3.1.5. Sample and Equipment Setup

Before the testing programme was carried out, all of the transducers and apparatus were first calibrated. Full details of the calibration processes used are described in Appendix 2. For the load cell and cell pressure controller, UKAS traceable calibration data was available. These calibrations were confirmed using laboratory weights and an external pressure transducer respectively. All other pressure controllers and pressure transducers were calibrated to match the cell pressure controller for consistency. The axial displacement of the bottom platen was based on the manufacturer's original calibration and confirmed using a digital caliper. The Hall effect sensors were in turn calibrated to match the bottom platen displacements.

The first step in installing the specimen in the triaxial rig was to prepare the apparatus itself. An important stage of this was to de-air all of the drainage lines with de-ionised de-aired water to ensure the volume change measurements from the pressure controllers were accurate. This was done by emptying and refilling the GDS STDDPC's and applying a pressure of 100 kPa to the back pressure and cell pressure lines with the valves to the platens closed. The back pressure and cell pressure valves were then repeatedly opened and closed to dislodge any air trapped in voids.

The six saturated filter paper strips were first positioned on the bottom platen, connecting with the platen drainage ring. Six aluminium spacers of 0.4 mm thickness (equivalent to the measured combined thickness of the three layers of filter paper) were then placed in spaces in between to ensure that the load from the specimen was not transferred via the compressible paper, preventing excessive compliance (Figure 3-7(a)). An aluminium disc of 100 mm diameter and 3 mm thickness with a locating hole was used to centre the assembly and secure it against lateral movement. The smooth aluminium bottom platen was then placed over the aluminium disc and 0.5 g of silicone grease was applied to the surface, onto which a circular disc of latex with radial slits similar to the arrangement suggested by Rowe and Barden (1964) to relieve radial stress was placed.

The process for the top cap was similar with the exception that the assembly was held together by a stainless steel screw to allow the top platen with the filter paper drains and membrane to be secured to the top cap in advance and placed in one piece.

Next the membrane was prepared by trimming it to 320 mm in length and creating a 5 mm Ø hole at the mid-height for the mid-height pore pressure transducer, which was then covered with adhesive tape to allow a vacuum to be used to place the membrane during installation (as described below). The pore pressure transducer itself was de-aired by placing it in a container of de-aired de-ionised water in a vacuum chamber at a pressure of -90 kPa for 12 hours after which the grommet and O-ring seals were applied before storing it in water until required.

The specimen was then placed on the bottom platen and the filter paper drains lifted into position on the side of the sample and temporarily pinned in place on the top end. The membrane was placed in a vacuum mould and a small vacuum of -5 kPa was applied to fully stretch the membrane, before placing it onto the sample and removing the mould. To seal the sample base, two o-rings were positioned over the membrane at the bottom platen and the pins securing the filter paper drains were removed. These were then trimmed and the top cap with the corresponding filter paper drain connections was placed on the sample, allowing two-way drainage to occur. Finally, the top cap O-rings were placed to seal the sample.

To ensure good contact between the mid-height PPT and the specimen, the PPT was placed through the hole in the membrane and any air gently pressed out. An indicator of a good connection was the measurement of the suction within the clay on the PPT immediately after placement. A thin layer of hydrophobic rubberised cyanoacrylate was applied to the edges of the membrane and grommet and an O-ring was pressed into this to create a reliably watertight seal around the PPT.

At this stage, the Hall effect transducers were attached if the test was investigating small strain behaviour. This was done by first carefully marking the position of the radial magnet and chip holder on the membrane around the mid-height before loosely positioning the holders using pins pushed gently through the membrane, leaving a small (3-4 mm) gap between the holder and the membrane. Next a small amount of rubberised cyanoacrylate was applied around the circumference of the pin before pressing the holder and pin completely into position. The process was repeated for the vertical Hall effect transducers, taking care to ensure that they were positioned directly opposite on the sample. One hour was allowed for the adhesive to dry before the magnets and chips were adjusted to fine tune their positions to utilise the full

range of measurement by predicting the expected movement during consolidation so that the magnet will be at the start of the acceptable measurement range during shearing.

A non-linear look-up table calibration was used to maximise the measurement range of the Hall effect transducers, however, despite this, the large volume changes experienced in some of the higher consolidation pressure tests meant that the magnet would need to be started beyond the edge of the Hall effect chip in order to be in the correct position at the beginning of the shearing stage. Adjustment after the consolidation stage was complete was considered, however, the process of removing the cell pressure led to cavitation of the sample which was difficult to restore to saturation. To overcome this, a small aluminium extension piece was made, consisting of two aluminium fins to restrain the magnet laterally, and an aluminium base on which it can slide vertically onto the magnet, allowing a greater range of movement (See Figure 3-13). As the extension set was made from aluminium (which is non-magnetic), it was found to have no impact on the calibration of the Hall effect set.

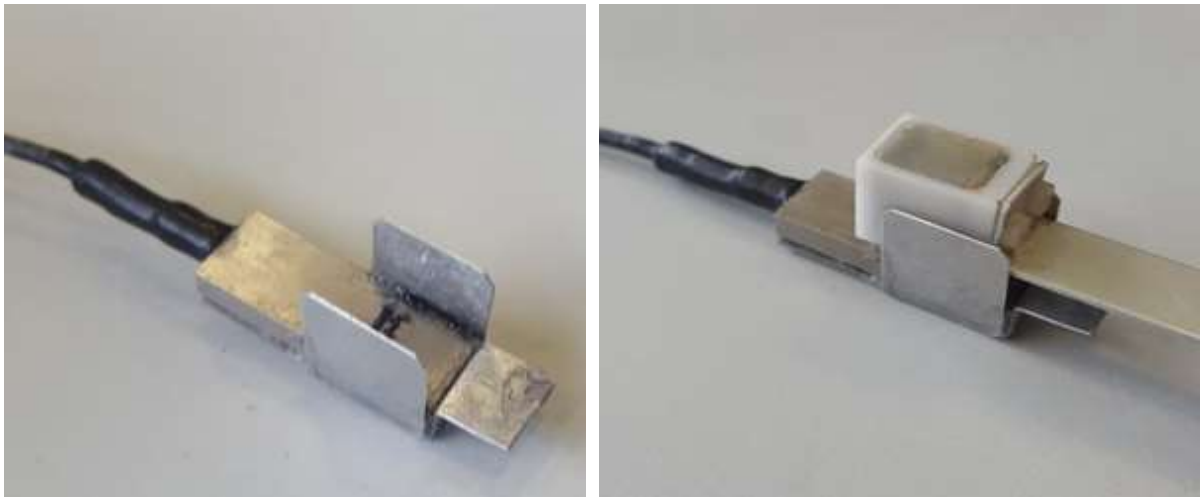

Figure 3-13 – Axial Hall effect transducer with the modified aluminium extension fins (with and without magnet)

Once the specimen installation was complete, it was inspected for any potential punctures in the membrane and then either the half-ball cap was placed in the recess of the top-cap, or the suction cap Vylene seal was secured to the top cap with a small amount of silicone grease.

3.1.6. Test Preparation Procedure

With the specimen ready, the cell outer chamber was placed and the half-ball docked with the load cell to a force of 0.001 kN (the smallest reliably controllable load possible) at which point the global displacement transducer was set to zero, before being undocked by 10 mm to remove any axial load during saturation. In the cases previously described where the suction cap was required to prevent non-uniform specimen deformation, the load was controlled by the GDS DCS at 0.001 kN whilst a small (-5 kPa) vacuum was applied until the connection was sealed. This was increased to a vacuum of -95 kPa and held until the cell was pressurised beyond 100 kPa. In this case, the load was then maintained at 0.001 kN for the remainder of the test (until the shearing stage commenced) such that the bottom platen moved to compensate for the change in the axial height of the specimen during consolidation.

After docking, the cell was filled with water controlled at room temperature (22 °C) by a mixer system, taking care to ensure that no air was trapped in the cell. To saturate the specimen, the cell pressure and back pressure were gradually raised to 300 kPa and 250 kPa respectively over the course of two hours. These pressures were maintained to drive any air remaining in the specimen from mixing or installation into saturation in the water (Head and Epps, 2014). Once the saturation was complete the pore pressure measurements were monitored to ensure that they were stable before the *B* value (Equation 3-3) was checked to measure the degree of saturation of the specimen. This was done by closing the valves on the back-pressure lines, applying a cell pressure increase of 50 kPa and measuring the change in the pore pressure recorded from the mid-height PPT. The minimum *B* value achieved in any of the tests was 0.971, indicating that the saturation process consistently achieved high degrees of saturation. To maintain this, a back pressure of 300 kPa was used throughout the test.

$$B = \frac{\Delta u}{\Delta \sigma_3} \tag{3-3}$$

Next the cell pressure was increased to provide the desired total stress, taking into account the 300 kPa back pressure, before the valves on the back pressure lines were opened to allow drainage. Specimens were allowed to consolidate for at least 24 hours or until mid-height pore pressures had dissipated to within ± 0.3 kPa (the accuracy of the PPT) of the applied back pressure. A further 24 hours were then allowed to ensure full pore pressure dissipation.

3.1.7. Testing Procedure

At this point, for undrained tests, the back pressure valve was closed to prevent any further volume change. The specimen was than sheared at a constant displacement rate, whilst the cell pressure controller maintained a constant cell pressure. The balanced ram system also ensured that the cell volume change during shearing was minimal. Tests investigating small strain behaviour were subjected to an axial displacement of 3 mm which was the minimum displacement possible when using the maximum displacement rate, and for tests examining large strain behaviour a shear displacement of 40 mm was applied. The main reason for the use of axial displacements of only 3 mm for the small strain tests is that if larger strains were applied, there was a risk of damage to the local strain Hall effect sensors which were used. This meant that the small strain and large strain tests had to be conducted on separate specimens. This also allowed the 1000 measured data points recorded during high speed tests to be focussed in the small strain range during the small strain tests. The 40 mm displacement corresponds to approximately 20 % strain depending on the specimen initial height and was selected to ensure that post localisation behaviour was observed without causing the specimen to come into contact with the cell wall. Cell pressures were maintained following the end of the test.

At the end of testing, the bottom platen was retracted at a constant rate of 1 mm/min to remove any remaining axial load on the specimen in a controlled manner and minimise any disturbance. If the suction cap setup was used, then the pressure inside the suction cap was vented to atmosphere whilst the bottom platen was retracted, allowing it to release. The cell pressure was then lowered to atmospheric pressure over a period of 15 minutes before the water was drained and the cell lid removed. The specimen was then disassembled and its diameter measured at the top, bottom and middle and three equidistant height measurements were taken to provide the final specimen dimensions. The specimen was then weighed before being split into two semi cylinders from which the angle and position of the shear plane was recorded. Finally, three moisture content samples were cut from the top, middle and bottom of the specimen which were then weighed and dried in an oven at a temperature of 105 °C for 24 hours.

3.2. Sources of Error and Mitigation

Throughout the testing, a number of concerns were dealt with, and due to their potential for impact on the results of the triaxial testing, they are discussed in more detail in this section.

3.2.1. Sample Eccentricity

As the samples being tested are reconstituted samples, a significant amount of volume change occurs during consolidation. In tests using the suction cap connection, the specimen retains a cylindrical shape due to the fact that rotation of the top-cap is prevented. However, where the half-ball connection is used, this allows rotation and lateral movement of the samples during consolidation. A consequence of this is that the load from the specimen may be transferred to the load cell eccentrically which may cause an incorrect load to be measured depending on the arrangement of the internal strain gauges.

To check whether this is an issue for the system used, an investigation was undertaken into the impact of eccentric loading. This was done by using a series of weights and varying the centre of loading across the load cell in four directions (0°, 90°, 180° and 270°) as shown in Figure 3-14(a). It was found that for all of the directions, provided the centre of loading was within 10 mm of the centre of the load cell, the load cell recorded the true applied load. Beyond this radius, the recorded load varied depending on the direction of the eccentricity (Figure 3-14(b)).

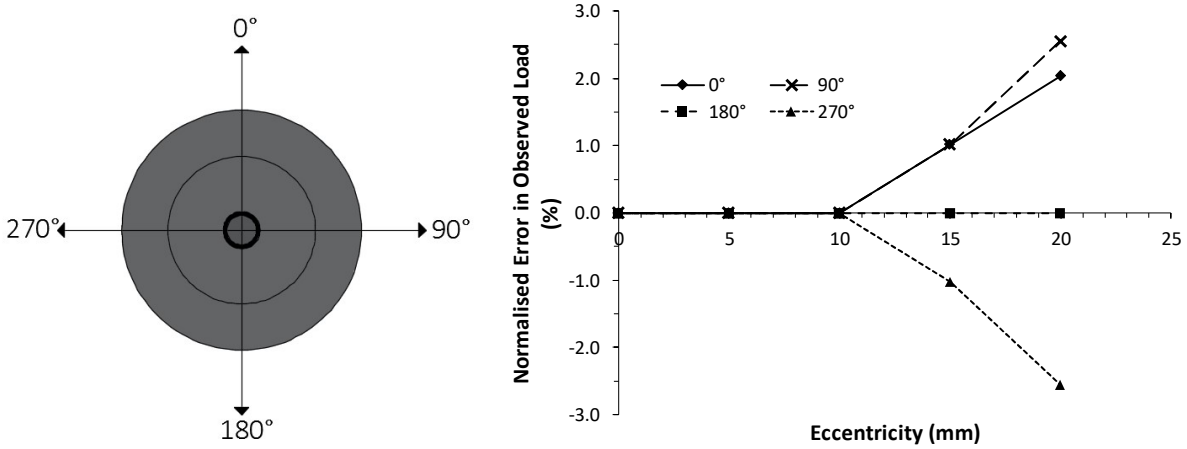

Figure 3-14 – (a) Directions tested for effect of loading eccentricity and (b) impact of eccentricity on recorded load

In order to be conservative, a limit on the eccentricity of 5 mm was adopted and marked onto the load cell. Any specimens which exceeded this limit were disregarded, however, the vast majority of samples were within the tolerance.

3.2.2. Sample Leakage

Sample leakage is an issue which affects all triaxial testing to some degree. Leroueil *et al.* (1988) demonstrated that the sample leakage varies depending a number of factors such as the membrane used, the sealing details and the cell fluid type (Head and Epps, 2014). For operational reasons, standard latex membranes were required to be used, along with water as the cell fluid. In order to minimise the leakage, several techniques were adopted. The most significant of these was the maintenance of the triaxial caps to ensure a smooth surface onto which a seal could be made, which is important as the environment within a triaxial cell is highly corrosive due to the presence of dissolved air in the cell water and the variety of metals used in its construction which may cause galvanic corrosion. To further limit the leakage at the caps, two O-rings were used to secure the membrane.

Points of leakage were identified from preliminary tests, with the most significant being the locations where the Hall effect local strain transducers and mid-plane pore pressure transducer were applied. The manufacturer specified sealing detail for the Hall effects consisted of a layer of silicone sealant between the Hall effect mounting pads and the latex membrane in order to seal around the fixing pins which penetrate into the specimen. However, this led to several issues which had implications for the testing. Firstly, the silicone led to flexibility between the fixing pins, which are smaller than their fixing holes, and the mounting pads. Secondly, the large amount of consolidation which occurs in reconstituted triaxial testing meant that the comparatively weak bond between the latex and silicone was often broken, allowing leakage into the specimen. The silicone also required long periods of time to cure (24 to 48 hours). Many of these issues are not important when testing static, intact specimens but for the more aggressive conditions imposed by the high speed testing undertaken here, they required to be addressed.

Numerous sealing alternatives including cyanoacrylate, silane-modified polymer and polychloroprene adhesives were tried, but none exhibited the required characteristics. The solution adopted was to use a rubberised cyanoacrylate (Loctite PowerFlex), as cyanoacrylates

were found to be the only adhesives which bonded well to the latex and the rubber additives prevented brittle failure of the seal. This was confirmed by visual inspection of the seals, which remained intact even after large strains were applied to the specimen.

Similar issues were found with the pore pressure transducer, which the manufacturer recommended sealing using a grommet which was provided and a layer of silicone sealant. Here, sealing the re-usable silicone grommet to the latex membrane with rubberised cyanoacrylate was not possible as this would have damaged it. Instead, disposable grommets were moulded for each individual test. These were made using Ethyl-Vinyl Acetate (EVA) thermoplastic adhesive (Bosch Precision Glue), which was placed into a two-part aluminium mould greased with high temperature silicone grease in order to create a flexible grommet (See Figure 3-15). The mould was then heated to 130°C in an oven for an hour, and the viscous nature of the adhesive at this temperature ensured that the grommet was free from trapped air. The grommet was then secured between two O-rings and attached to the latex membrane using a layer of rubberised cyanoacrylate. Using these methods, the resulting triaxial specimens were found to be reliably watertight.

(a) (b)

Figure 3-15 – (a) Thermoplastic EVA grommet for mid-height PPT and (b) two-part aluminium mould

3.2.3. Balanced Ram Operation

The triaxial cell is fitted with a balanced ram (GDS Instruments, 2018) to prevent the cell pressure from increasing as the ram is actuated into the cell by removing an amount of fluid from the main cell equal to the volume displaced by the ram. However, the balanced ram cannot perfectly account for the entire volume of displaced water and in this case the system relies on the cell pressure controller to maintain constant cell pressure. However, as noted

previously, the static feedback loop which always controls the pressure controllers is limited to a 2-3 second response time. A consequence of this is that in rapid ($\dot{\epsilon}$ > 10,000 %/hr) dynamic tests, for which this response time becomes significant in relation to the test duration, the cell pressure controller cannot be relied upon to maintain a constant cell pressure. Additionally, the cell pressure controller logging was also subjected to this delay, meaning that the recorded cell pressures were also incorrect.

To determine the magnitude of the cell pressure change exerted by the balanced ram, a series of tests at differing displacement speeds were carried out by connecting an external pressure transducer to the cell fluid. In each case, the test was run without a specimen installed in the cell, and the ram was actuated as it would be when carrying out the shearing stage, whilst the cell pressures changes were logged throughout. The target starting cell pressure used for each investigation was 1000 kPa and once the starting pressure was reached, the cell pressure controller was de-activated and the cell pressure was monitored to ensure that there was no dissipation prior to the application of displacement. Figure 3-16 shows the recorded cell pressures during investigations carried out at actuator displacement rates corresponding to triaxial samples being sheared at axial strain rates of 100 %/hr and 180,000 %/hr. This shows that the response of the balanced ram is comparable over the strain rates used, with the system over-compensating for the volume added to the cell by the actuator leading to a small reduction in cell pressure. The pressure change was directly proportional to the change in actuator displacement, however, this pressure change was dependent on number of factors such the stiffness of the cell and also the bulk modulus of the cell fluid (both of which are dependent on the applied cell pressure). Additionally, it was not possible to investigate the impact of the soil specimen on the pressure changes due to the balanced ram. To overcome these issues, an external cell pressure transducer was added to the test setup to allow the cell pressure to be accurately logged via the GDS DCS throughout the test programme.

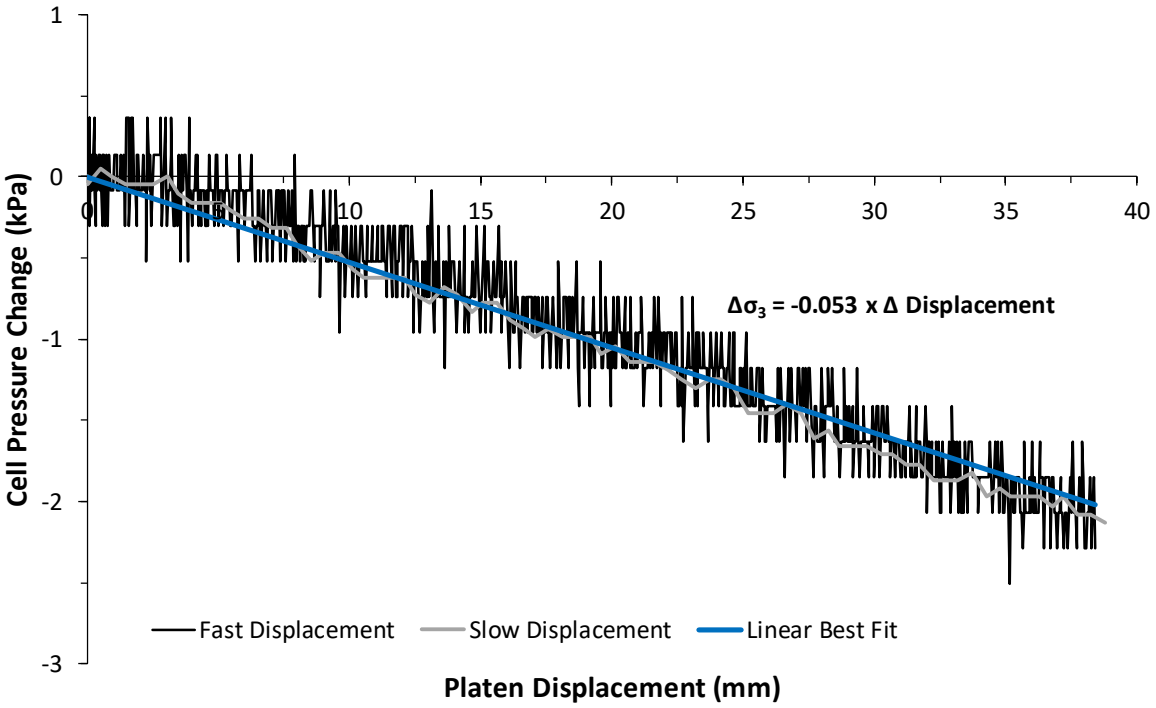

Figure 3-16 – Graph of cell pressure change against platen displacement without a specimen installed

3.2.4. Correction for Signal Conditioning Lag

Given the high speed of the triaxial tests undertaken and the fact that the small strain range is of interest, the accuracy and quality of the data recording is especially important, not only in terms of having sufficient sampling frequency, but also in terms of the data synchronisation. Whilst all of the key parameters (load, global strain, local strain and pore pressures) are recorded through the high speed GDS DCS (Dynamic Control System), initial tests revealed that the recorded data experienced acquisition delays. The impact of this was that during the early stages of the tests, the initial shear modulus, G_{max}, appeared significantly less than expected based on similar work (Chow and Airey, 2013). It was suspected that the cause was a lag in the signal amplifier as the delay was most evident in the transducer with the highest gain setting, the load cell.

To account for this delay in recording the load, the global strain measurement (from the bottom platen) was defined as the data to which the load would be synchronised, as this is digitally recorded via an encoder attached to the drive stepper motor, and as such, does not require amplification. Due to the non-linear nature of the soil response observed, it was not possible to re-synchronise the data by inspection of the triaxial test data, so further testing was required. Conventionally, to check if triaxial equipment is performing correctly, a cylindrical rubber or polymer block with a known stiffness would be placed into the apparatus to confirm that the stiffness measurements are as expected, however, this was not possible as these materials exhibit strain rate dependence. A non-rate dependent method for confirming the stiffness measurements at high speed was required. So instead, a strip of spring steel with dimensions 120 x 20 x 1.2 mm was set up on a support in the apparatus as shown in Figure 3-17, which in turn was mounted on the bottom platen. The triaxial cell was fitted over the apparatus as normal such that the load cell could dock with the half-ball fitting sitting in the middle of the spring steel element.

The spring steel was selected as it is known to be rate independent (Rae *et al.*, 2009), has a high yield limit so as to provide a completely linear stiffness response and has a known Young's Modulus of 210 to 215 GPa. In all tests using the spring steel, a displacement of 5 mm was applied as this was known to be less than the yield limit for the specimen. To provide a reference stiffness, this displacement was first applied at a rate corresponding to a triaxial test carried out at 1 %/hr (0.03 mm/min). At this rate, any delay would be insignificant as the delay

was estimated to be of the order of 10 ms and the logging frequency was every 3 seconds (corresponds to a maximum error in the stiffness of 0.3 %, rapidly reducing with strain). The displacement rate was then increased to the maximum rate used in the triaxial tests (100 mm/s) which resulted in a clear reduction in the recorded stiffness of the spring steel at small strains (Figure 3-18). To identify the delay causing this, a numerical solver was used to identify the lag which, when accounted for, restored the stiffness to the expected reference value. The delay was found to be constant at 5.8 ms for all of the displacement rates investigated and this correction was retrospectively applied to all of the load cell data by re-synchronising it accordingly. After correction, the measured Young's Modulus for all tests coincided at 214 GPa, within the expected range for the spring steel.

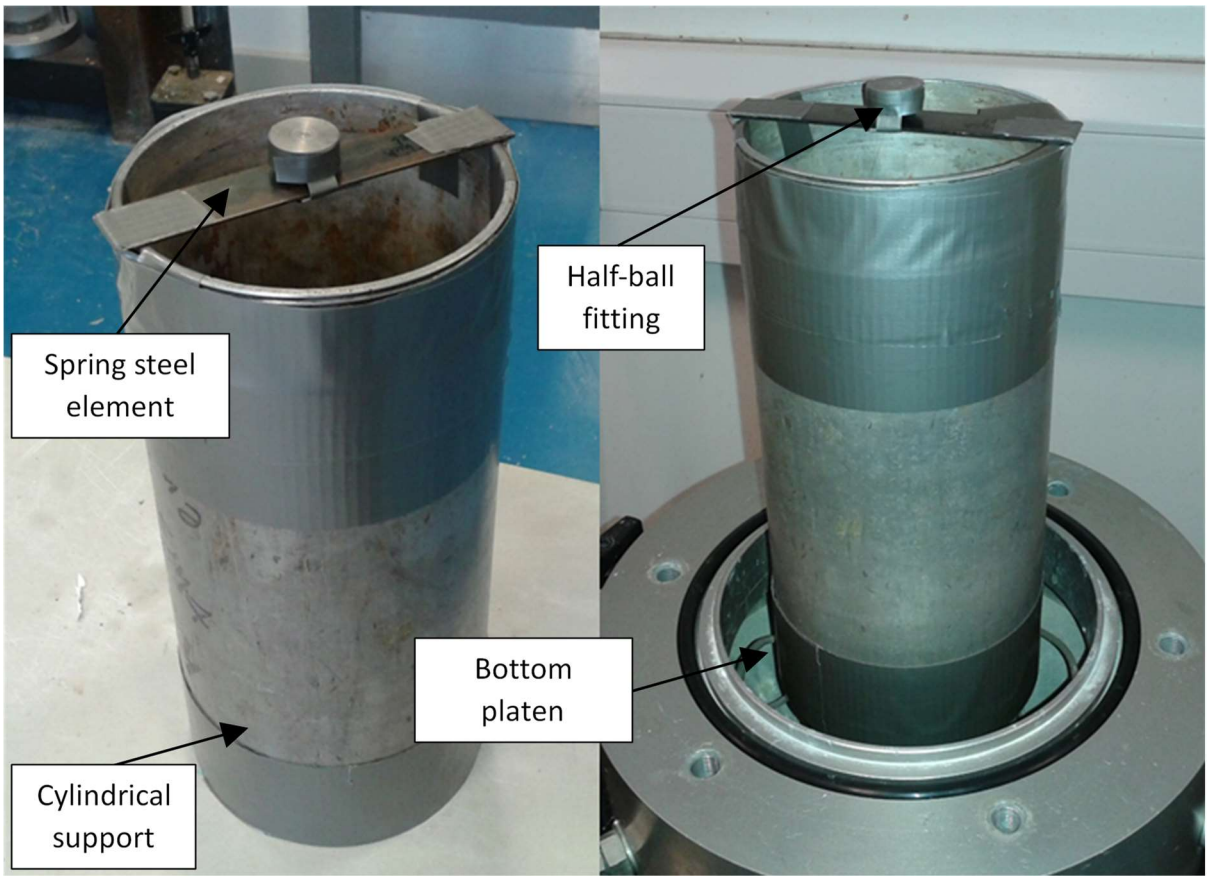

Figure 3-17 – Setup of spring steel test piece in triaxial apparatus used to identify delays in load cell measurements by providing a 'specimen' with a rate independent stiffness

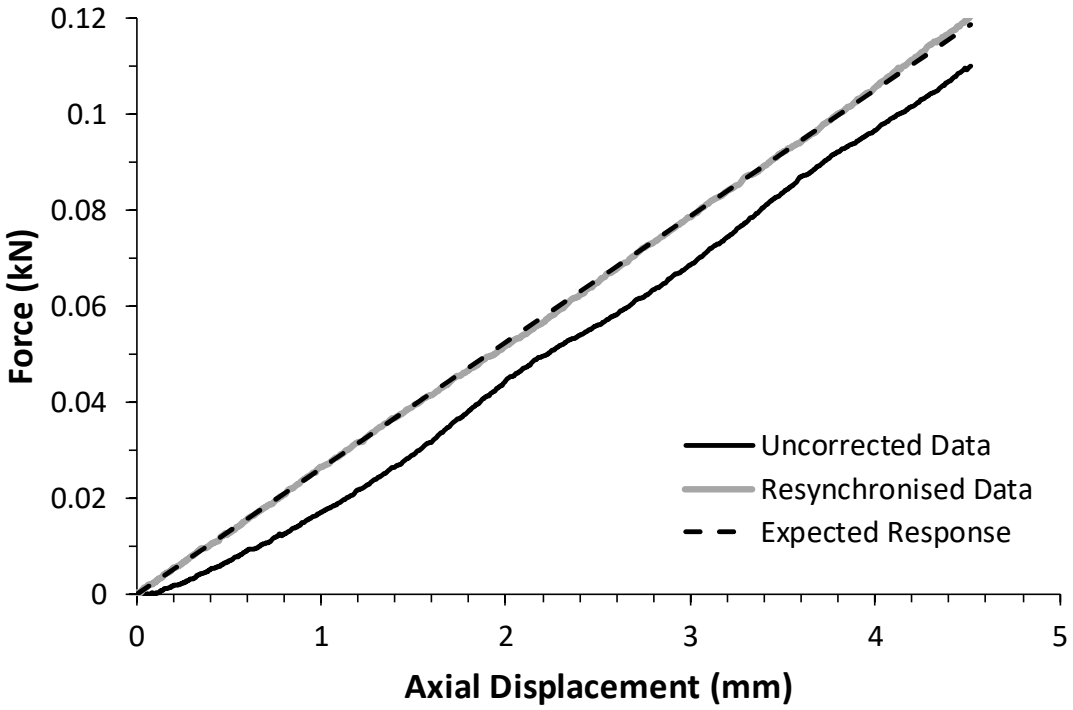

Figure 3-18 – Resynchronisation of load cell data from tests on spring steel element at 100 mm/s

A similar lag was observed in the Hall effect transducers, so a similar procedure was used to synchronise these to match the global displacement. To achieve this, the mounting pad holding the Hall effect chip was attached directly to the displacement ram using cyanoacrylate adhesive and the magnet arm was clamped to a cross-bar fixed across the cell base, providing a rigid mounting. The Hall effect chips were then aligned to ensure that they would not jam during displacement. A series of short (3 mm) displacement motions were then applied to the Hall effect over a range of displacement rates corresponding to axial strain rates of 1 %/hr to 180,000 %/hr in a 200 mm specimen. By comparing the recorded global and local displacements it was possible to determine the lag between them using a numerical solver, as before. As with the load cell, it was found that it was possible to correct for the delay by using a straightforward time offset, which was constant at 4.0 ms. This process was repeated for each of the Hall effect transducers and each time the same offset successfully corrected for the delay, indicating that the delay is not related to the order in which the transducers are sampled by the GDS DCS and is most likely related to the time required for amplification of the signal. As a result, the slightly lower lag in the Hall effects is in line with expectations as they use lower gain settings than the load cell.

3.2.5. Dynamic Displacement Application

A key aspect which is crucial to the accuracy of the high speed triaxial testing is the manner in which the displacement control signal or waveform is applied. As discussed previously, the GDS system uses two control systems for applying these; a static method suitable for axial strain rates up to 300 %/hr and a dynamic method which is used for rates that exceed this threshold.

When the static control system is in use, the triaxial rig is directly controlled by the computer, which sets required displacement targets every three seconds via the GDS DCS which controls the motor in order to achieve these targets. In this way, a linear displacement control signal is applied, as acceleration effects are negligible at such low speeds.

The dynamic control system operates in an entirely different way, as the GDSLAB software loads the required waveform for the entire displacement motion into the GDS DCS prior to the displacement application. The GDS DCS then autonomously controls the displacement application using a PID feedback loop between the motor and encoder which has a control frequency of 10,000 Hz. Within this system, two manufacturer-supplied PID gain settings were used; one for axial strain rates between 300 %/hr and 100,000 %/hr and another for strain rates exceeding 100,000 %/hr (up to the maximum possible strain rate of 180,000 %/hr). The primary issues with the dynamic control system are that due to the higher velocities involved, the manner in which the displacement system accelerates to the required velocities needs to be considered, alongside issues with maintaining a stable displacement motion at such high strain rates.

As with any system, the triaxial rig has a maximum acceleration which determines how quickly it can reach the required constant velocity. This means that a completely linear displacement waveform cannot be used as this means that the initial displacement demanded by the control system is greater than that physically achievable by the triaxial rig. The result of this is that the rig overcompensates for this and subsequently overshoots the required displacement, causing oscillations due to the fact that the PID gain settings are necessarily high (See Figure 3-19). This had a significant impact on the observed readings from the load cell and raised concerns of influencing the soil strength due to the accumulated strains from the oscillation cycles.

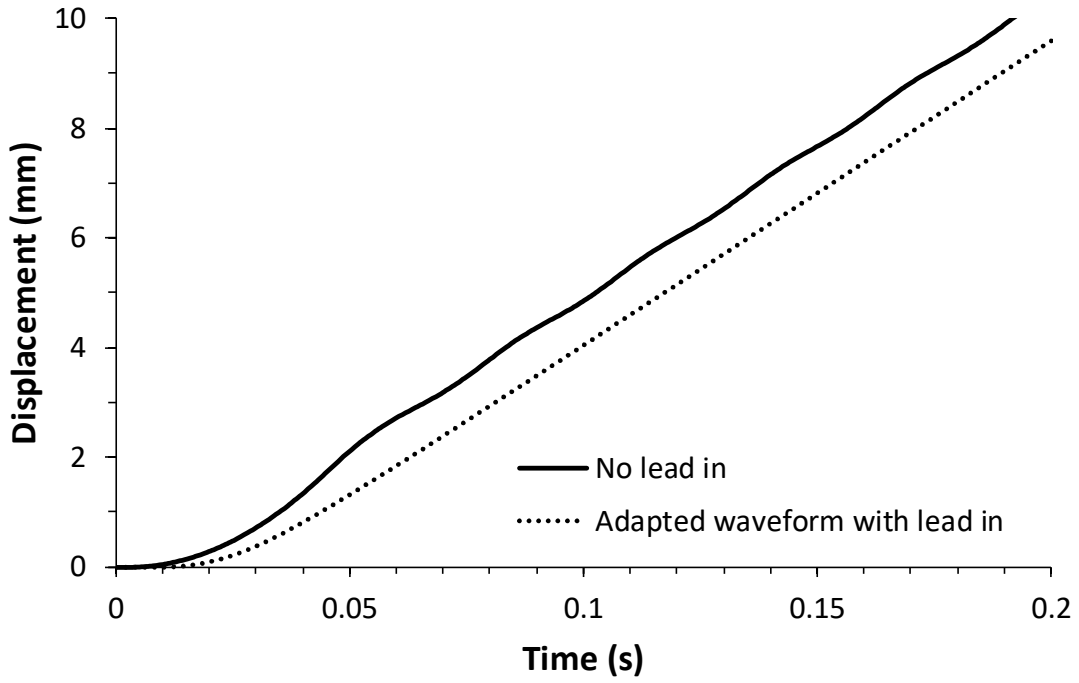

Figure 3-19 – Actuator response to request for linear displacement at 50 mm/s with and without lead-in stage

To overcome these issues, it was necessary to understand how PID control systems reach their targets. A PID controller reaches equilibrium (the constant motor rate that meets the displacement demand requirement) by overshooting and undershooting the demand requirement until the oscillation dissipates. In normal applications, there is time for this dissipation to occur, however, due to the short test durations involved this is not the case in a high speed triaxial test. One solution would be to reduce the gain settings, however, this would mean that the system would be insufficiently responsive and cause the acceleration to be spread over a large part of the motion, which is undesirable in a constant rate of strain test.

An analysis of the recorded displacement data from the initial section of several tests identified that the machine has a maximum acceleration of 1.90 m/s^2. This was investigated for the different gain settings and was found to be independent of the gain settings used.

A new waveform which accelerates at the maximum possible acceleration to the required constant velocity was written for the control system. This prevents the initial overshoot observed previously by not exceeding the machine's capabilities, leaving the rig at the correct motor rate for the constant velocity test at the end of acceleration with near-zero error

between the demand and system response. The new waveform also ensures that as much as possible of the test is carried out at the desired constant velocity, with the portion of the test where acceleration is occurring limited to 2 % even in the highest strain rate test. This is due to the fact that even at $\dot{\varepsilon}$ = 100,000 %/hr (≈ 50 mm/s), a constant displacement rate is achieved after approximately 0.8 mm travel, out of a total typical displacement of 40 mm during a triaxial test. The recorded displacement data confirmed that this approach provided a stable displacement profile, which matched the requested waveform (See Figure 3-19).

Clearly, this meant that the waveform required for each test would be a function of the maximum displacement applied and the strain rate. To deal with this, a spreadsheet was written to automatically produce the required waveform for each test based on these criteria.

3.2.6. Membrane Correction

Membrane corrections have also been applied as recommended by Henkel and Gilbert (1952) as shown in Equation 3-4. The membrane modulus, M_M, was experimentally derived for the specific batch of membranes used (0.32 mm thick on average) and was found to be 0.54 N/mm. This was done following the process described by Head and Epps (2011), whereby a strip of the membrane is placed between two hangers onto which a series of weights are connected and the change in length is measured using Vernier calipers. The membrane correction shown in Figure 3-20 was deducted from each of the measured deviator stresses. No corrections have been applied to account for the shear plane formation due to the difficulties involved in the selection of the exact strain at which localisation occurs.

$$c_M = \frac{0.4 M_M \varepsilon (100 - \varepsilon)}{D} \tag{3-4}$$

where c_M is the membrane correction in kPa

ε is the axial strain applied in %

M_M is the modulus of the membrane in N/mm width

D is the initial membrane diameter in mm

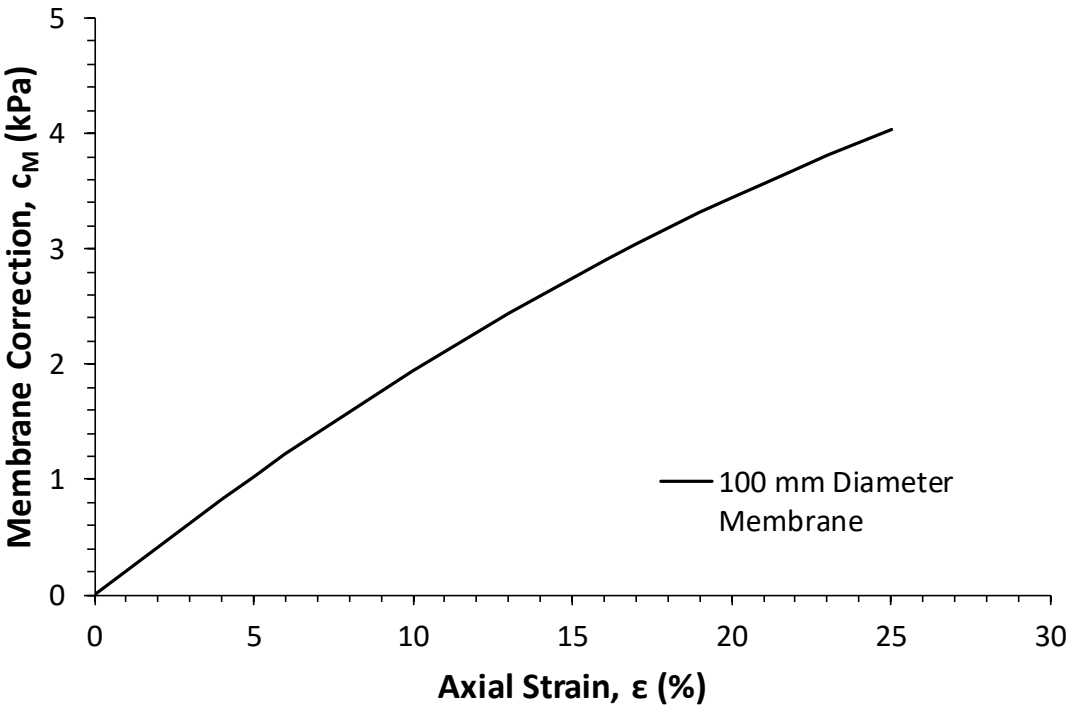

Figure 3-20 – Membrane correction applied to deviator stresses for a 100 mm membrane

3.3. Material Characterisation

Material characterisation was carried out on the three powdered clays used in the investigation namely Kaolin, Hyplas 71 and Hymod AT, all of which were produced by Imerys Minerals. These three clays were selected from a range of powdered clay samples provided by the supplier (Clayman Supplies, Chichester). Plastic and liquid limit tests were conducted on each of the samples, to give an indication of which clays would be likely to have different material properties and behaviour. The Atterberg limits are often correlated with specific material properties and the three clays used were chosen to provide the best range of plasticity indexes possible. Full details of the exact source deposits, specific quarry sites and supplier details are given in Appendix 1. The material characterisation techniques which are non-standard are described in detail in this section. All other characterisation was in accordance with BS1377.

3.3.1. Critical State Parameters

To determine the critical state parameters of the three soils, a series of 10 undrained (CIU) 38 mm triaxial tests were conducted at initial mean effective stresses ranging from 300 kPa to 1350 kPa (each with a back pressure of 300 kPa). The specimens were prepared from slurry using the same 1D consolidation process as the 100 mm specimens, but were re-sampled using 38 mm triaxial sampling tubes. These tests were conducted at a constant (static) axial strain

rate of $\dot{\varepsilon}$ = 1 %/hr in a Bishop and Wesley type hydraulic stress path cell. A half-ball fitting was used to minimise docking disturbance. The results of the critical state characterisation in terms of the *q-p*' and *v-ln(p')* response are shown for each soil in Figure 3-21, Figure 3-22 and Figure 3-23. The critical state parameters are shown in Table 3-3. It was found that the highest critical friction ratio, *M*, was for Kaolin (*M* = 0.851) and the lowest for Hymod AT (*M* = 0.569).

Table 3-3 – Critical state parameters for the three clays used

Parameter	Kaolin	Hyplas 71	Hymod AT
CSL Gradient in q-p' Space, M	0.851	0.785	0.569
CSL Gradient in v-ln(p') Space, λ	0.168	0.101	0.180
Intercept of NCL in v-ln(p') Space, N	3.101	2.328	3.125
Intercept of CSL in v-ln(p') Space, Γ	2.988	2.268	3.038
Gradient of Unload Line in v-ln(p') Space, κ	0.021	0.046	0.077

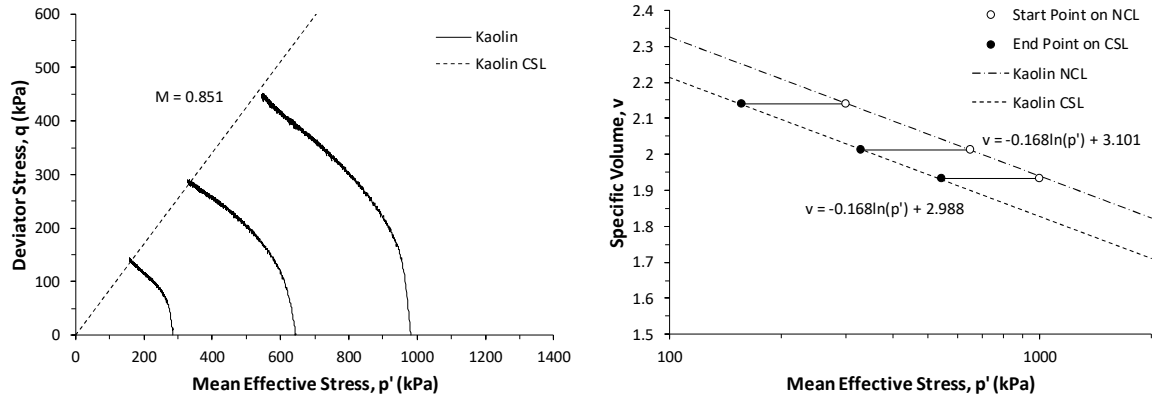

(a) (b)

Figure 3-21 – Critical state behaviour of Kaolin (a) in *q-p'* space and (b) in *v-ln(p')* space

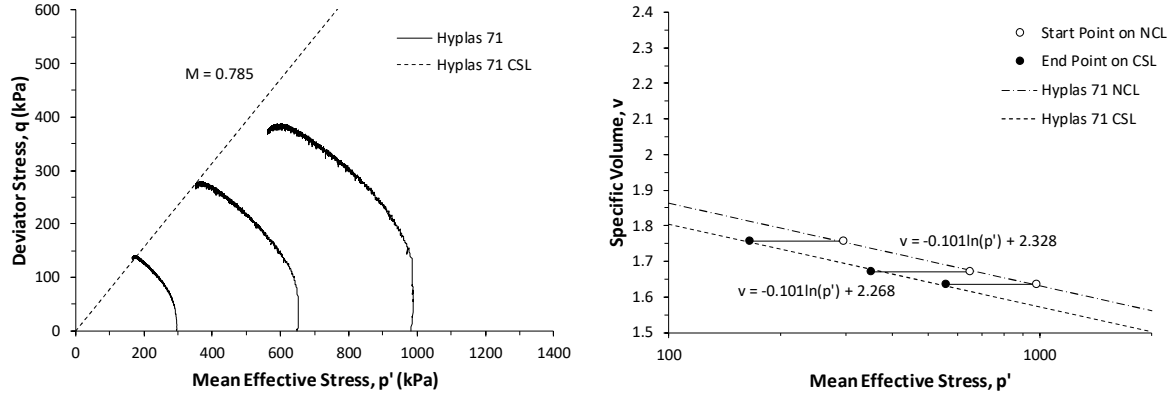

(a) (b)

Figure 3-22 – Critical state behaviour of Hyplas 71 (a) in *q-p'* space and (b) in *v-ln(p')* space

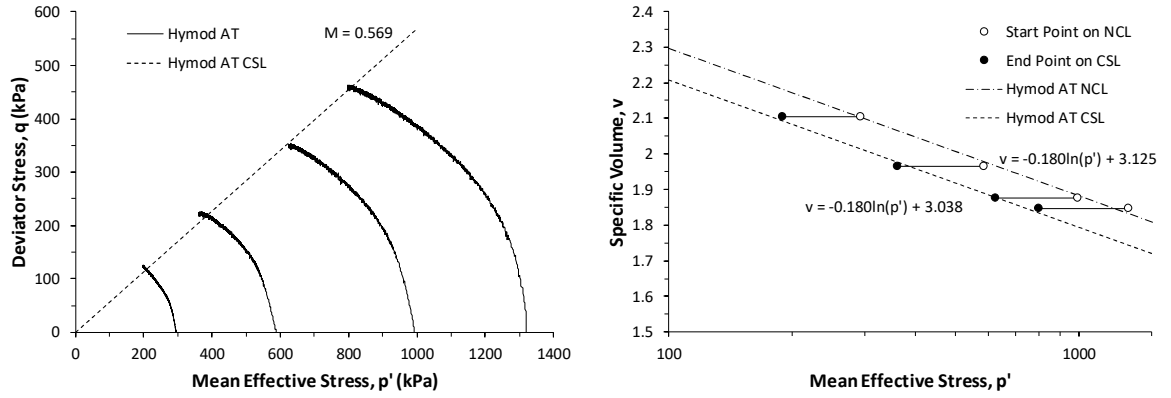

(a) (b)

Figure 3-23 – Critical state behaviour of Hymod AT (a) in *q-p'* space and (b) in *v-ln(p')* space

The state parameter at this conventional reference axial strain rate of 1 %/hr (denoted Ψ_{ref}) can be defined as shown in Equation 3-5 (Muir Wood, 1990; Atkinson, 2007). In the simplest terms it represents the difference between the initial specific volume before shearing is commenced and the specific volume at the same p' on the CSL which the specimen tends towards. Some studies alternatively refer to this state parameter as S_v.

$$\Psi_{ref} = v - v_{csl} \tag{3-5}$$

For the case of normally consolidated specimens, the initial specific volume will always lie on the NCL. As the state parameter represents the vertical distance between the initial state and the critical state in *v-ln(p')* space, this means that Equation 3-5 resolves to Equation 3-6. The idea of a state parameter for each clay is a useful one as (for normally consolidated conditions) it represents a measure of the dilatancy or contractiveness of the clay which is independent of the initial soil state (or initial mean effective stress). The state parameters under normally consolidated conditions for each of the three clays tested are shown in Table 3-4.

$$\Psi_{ref} = N - \Gamma \tag{3-6}$$

Table 3-4 – State parameter for normally consolidated conditions for each clay

Soil	*Kaolin*	*Hyplas 71*	*Hymod AT*
Ψ_{ref} #	0.113	0.06	0.087

For normally consolidated conditions

Figure 3-24 shows the unload-reload behaviour of the three clays tested, along with the derived values of κ. The values ranged from 0.021 for Kaolin to 0.077 for Hymod AT. It should be noted that κ was derived at mean effective stresses from 108 to 650 kPa for Kaolin, whilst κ values for Hyplas 71 and Hymod AT were obtained at mean effective stresses from 300 to 1350 kPa. This is due to the fact that κ for Hyplas 71 and Hymod AT was obtained from isotropic swelling of 38 mm diameter triaxial specimens from p'_0 = 1350 kPa, compared to isotropic swelling of a 100 mm diameter triaxial specimen from p'_0 = 650 kPa for Kaolin.

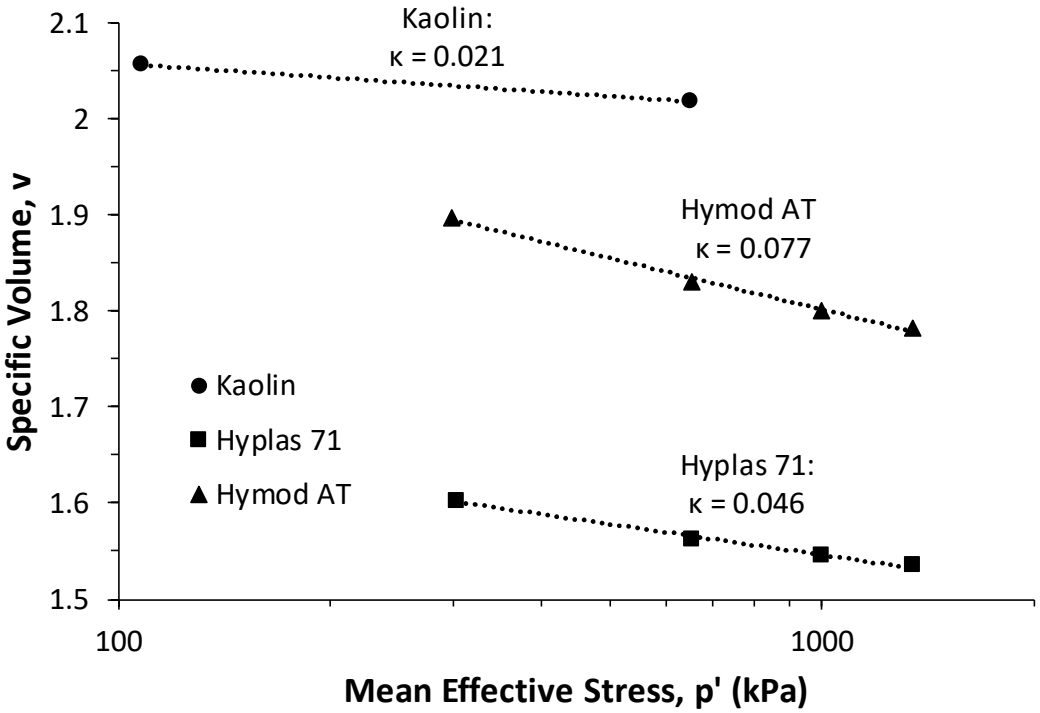

Figure 3-24 – Unload-reload lines in *v-ln(p')* space for each of the three clays showing the corresponding values of κ

3.3.2. Permeability

A series of nine triaxial permeability tests were also conducted using the 38 mm stress path cell. For each soil, three isotropically consolidated specimens were prepared at initial mean effective stresses ranging from 300 to 1000 kPa in the same manner as for the CSL characterisation tests, with a back pressure of 300 kPa. An additional pressure controller was used to apply a pressure difference between the top and bottom caps as shown in Table 3-5. The pressure difference of 30 kPa was used in all tests and was maintained for 24 hours for steady-state flow conditions to be reached. Based on the steady-state volumetric flow rate measured by the pressure controller, the permeability was determined using Equation 3-7. The results of the permeability testing are shown in Figure 3-25. Kaolin was found to be substantially more permeable than the other two clays, whilst Hyplas 71 and Hymod AT displayed similar permeabilities despite the significant differences in their specific volumes.

$$k = \frac{v}{i} \text{ where:} \tag{3-7}$$

$$v = \frac{volumetric\ flow\ rate}{cross\text{-}sectional\ area\ of\ specimen} \text{ and } i = \frac{head\ difference}{length\ of\ specimen}$$

Table 3-5 – Pressures used for triaxial permeability tests

Test	1	2	3
Cell Pressure (kPa)	600	950	1300
Back Pressure (kPa)	300	300	300
Effective Stress, p' (kPa)	300	650	1000
Pressure Difference of Flow (kPa)	30	30	30

3.3.3. Particle Size Distribution

To determine the particle-size distribution of the clays (and hence the clay fractions), hydrometer tests were conducted on each soil in accordance with BS1377. Kaolin displayed a close-graded particle size distribution with a clay fraction (< 2 µm) of 82 %. Both the Hyplas 71 and Hymod AT were open-graded, with clay fractions of 65 % and 95 % (Figure 3-26).

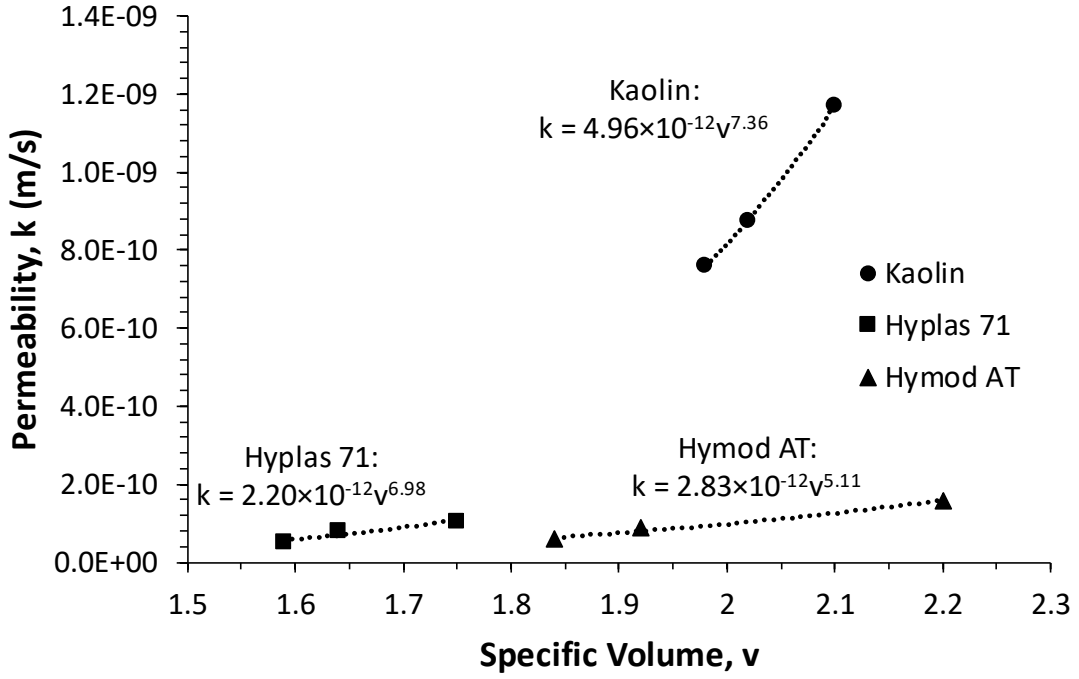

Figure 3-25 – Variation of the permeabilities of the three clays tested at different specific volumes

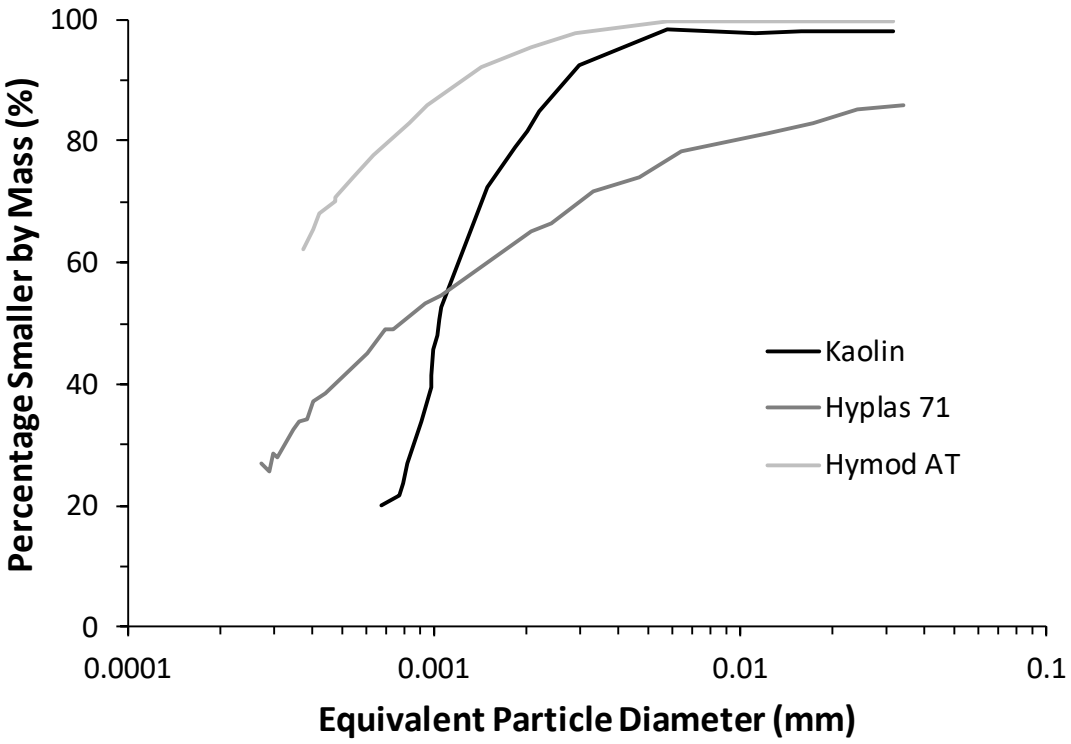

Figure 3-26 – Particle size distributions from hydrometer testing for the three clays used

3.3.4. Specific Surface Area

The specific surface area of the clays being tested was considered an important characteristic as the specific surface area has been shown to have a significant impact on the clays' plasticity index and liquid limit (Yukselen-Aksoy and Kaya, 2013) which has previously been used to estimate potential rate effects behaviour (Brown and Powell, 2013, Krieg and Goldscheider, 1998). It is also closely interrelated with the charge density and impacts on the behaviour of the layer of adsorbed ions which has been suggested as a potential explanation of the cause of rate effects (Santamarina, 2005).

The manufacturer of the three clays tested, Imerys Minerals, provided specific surface areas based on N_2 BET testing. However, N_2 BET testing is based on the absorption of gas onto the surface of dried clay, which raises two issues. Firstly, the surface areas measured will be based on the dry clay particles, which means that any effect from swelling will not be taken into account. Secondly, clay particles have a tendency to form flocs which will remain after drying and due to the small size of the clay particles, the gas may not be able to enter these flocs and measure the true surface area. Both of these considerations mean that the manufacturer's data is likely to underestimate the clays' specific surface areas (*SSA*). Yukselen-Aksoy and Kaya

(2013) also highlighted the fact that *SSA* from N_2 BET testing correlate poorly with other soil properties that may be of interest in this investigation.

To provide a more accurate measurement of the *SSA* of the clays, methylene blue (MB) absorption tests were carried out as this method uses saturated samples and the methylene blue particles are small enough to penetrate any flocs and fully cover all of the clay particles. The method relies on the positively charged methylene blue particles coating the clay particles, enabling the surface area to be calculated based on the amount of methylene blue required to achieve this.

To prepare the clay sample, the clay was dried at 105 °C for 24 hours to remove any moisture present, before mixing 10 g of clay into 30 ml of de-aired, de-ionised water. 1 g of pure methylene blue ($C_{16}H_{18}ClN_3S$) was also mixed with 200 ml of de-aired, de-ionised water to prepare the dye solution. The dye was then added in 0.5 ml increments to the clay solution and thoroughly mixed to ensure that the dye was fully absorbed onto the surface of the clay. After each increment a small drop of the clay solution was then placed onto a sheet of filter paper which drew the moisture from it. If not all of the clay had been covered by methylene blue (MB), no dye was observed in the water drawn into the surrounding filter paper. This process was continued until a faint stain surrounding the soil was observed on the filter paper, indicating that the soil was entirely covered and could no longer absorb more methylene blue, leaving any excess methylene blue in the free water present in the solution. As the area of methylene blue added was known at this point the specific surface area of the clay could be determined using Equation 3-8 (Santamarina *et al.*, 2002).

$$S_s = \frac{1}{319.87}.\frac{1}{200}(0.5N)A_v A_{mb}\frac{1}{10} \quad \text{where:} \tag{3-8}$$

N is the number of increments of methylene blue required

A_v is the Avogadro's number (6.02 x 10^{23}/mol)

A_{mb} is the area of one methylene blue molecule (130 Å^2)

The specific surface areas determined are shown in Table 3-6 along with the manufacturer's *SSA* data from N_2 BET testing. Comparison of these values shows that as expected, the manufacturer data from N_2 BET testing significantly underestimates the *SSA* of the clays by a factor of approximately 3 times.

Table 3-6 – Specific surface areas for the soils investigated

Soil	Number of MB Increments, N	SSA from MB Tests (m^2/g)	SSA from N_2 BET (m^2/g)
Kaolin	60	36.7	14
Hyplas 71	87	53.2	19
Hymod AT	172	105.2	34

3.3.5. Mineralogical and Oxide Composition

Given that the rate effect observed in clays is a micro-scale effect, a clear understanding of the composition of the clay in terms of its mineralogical makeup is essential. The composition of the clays was investigated by X-ray diffraction (XRD) to determine the mineralogy and X-ray fluorescence to consider the oxide composition.

The XRD tests were conducted in a Hilton-Brooks XRD system using randomly orientated samples of dried clay powder. The only preparation of the powder consisted of drying in a soils oven at a temperature of 105 °C for 24 hours to ensure that all moisture had been removed. No other treatment was applied to ensure that the XRD sample reflected the clay used in the triaxial testing.

The output consisted of XRD traces providing the diffraction intensity at varying diffraction angles (2θ) as shown in Figure 3-27, Figure 3-28 and Figure 3-29. Rietveld analysis (Rietveld, 1969) was then used to estimate the contribution to the diffraction intensity from each mineral present in the clay and to derive the relative proportions of the minerals. Based on this analysis, it was indicated that the three clays all consisted of three main minerals; Kaolinite, Quartz and Illite. To confirm the output from the Rietveld analysis, a manual check on the XRD traces was carried out to confirm that these three minerals could account for all of the observed peaks based on data from Mitchell and Soga (2005) and Moore and Reynolds (1997). Each peak in the range of $10° < 2\theta < 40°$ was identified and accounted for. Peaks beyond 40° were not able to be considered due to the fact that in this range a number of potential sources were possible for each peak. In any case, these would have been secondary reflections, and the primary reflections would have been identified within the range considered. Another consideration was that due to the platy nature of most clay minerals, the XRD samples would have a tendency

towards a preferred particle orientation despite the fact that they were prepared in a randomly orientated manner. This was one of the reasons that Rietveld refinement was felt suitable for the analysis of the XRD results, as it includes a correction of the observed intensities that can account for moderate preferred orientation (Rietveld, 1969).

The output from the Rietveld analysis is shown in Table 3-7. As can be seen the clays exhibit a good variation in mineralogical composition and contain substantially different proportions of the three minerals.

Table 3-7 – Mineralogical composition of the three clays used

Mineral	Speswhite Kaolin	Hyplas 71	Hymod AT
Kaolinite (%)	80	28	42
Illite (%)	18	28	40
Quartz (%)	2	44	18

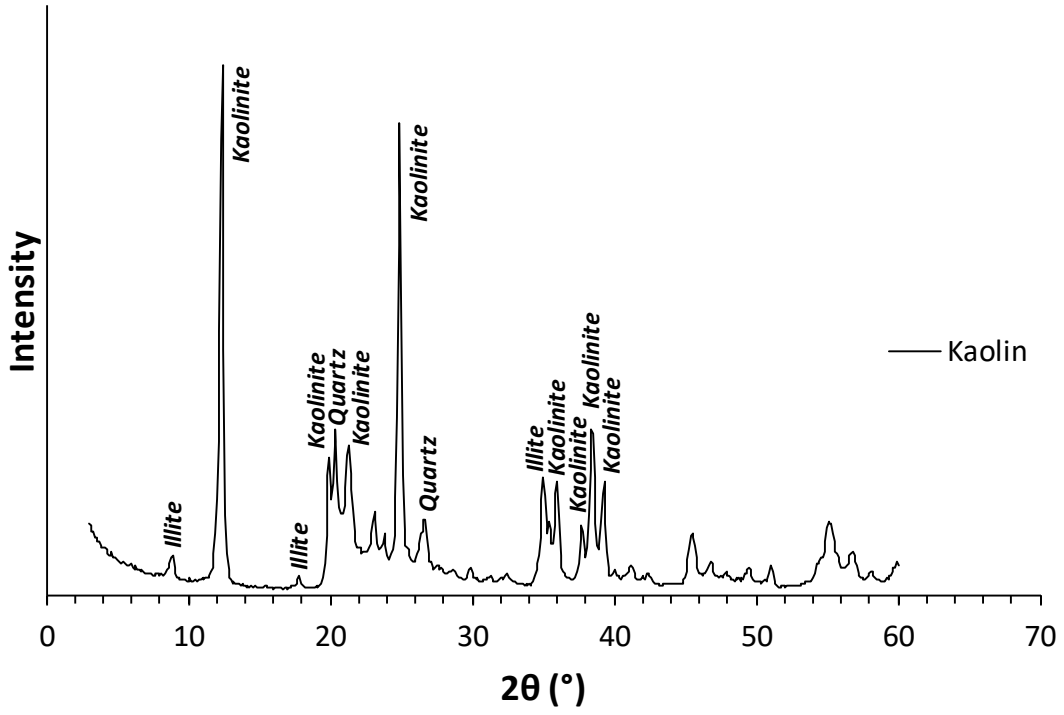

Figure 3-27 – Annotated x-ray diffraction (XRD) spectrum for Kaolin

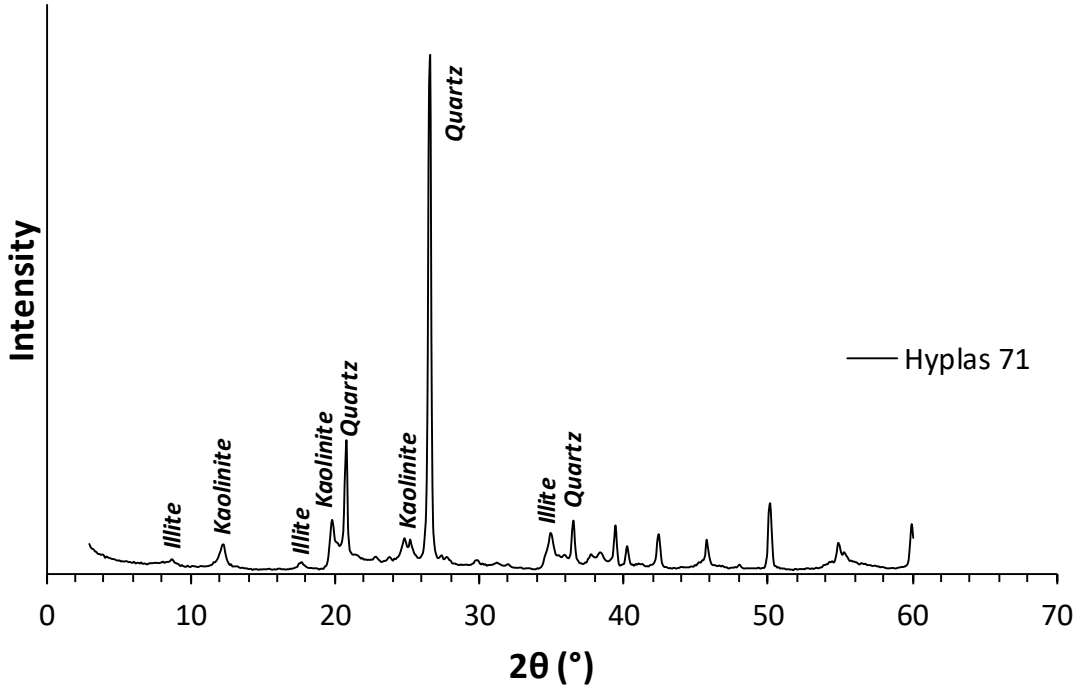

Figure 3-28 – Annotated x-ray diffraction (XRD) spectrum for Hyplas 71

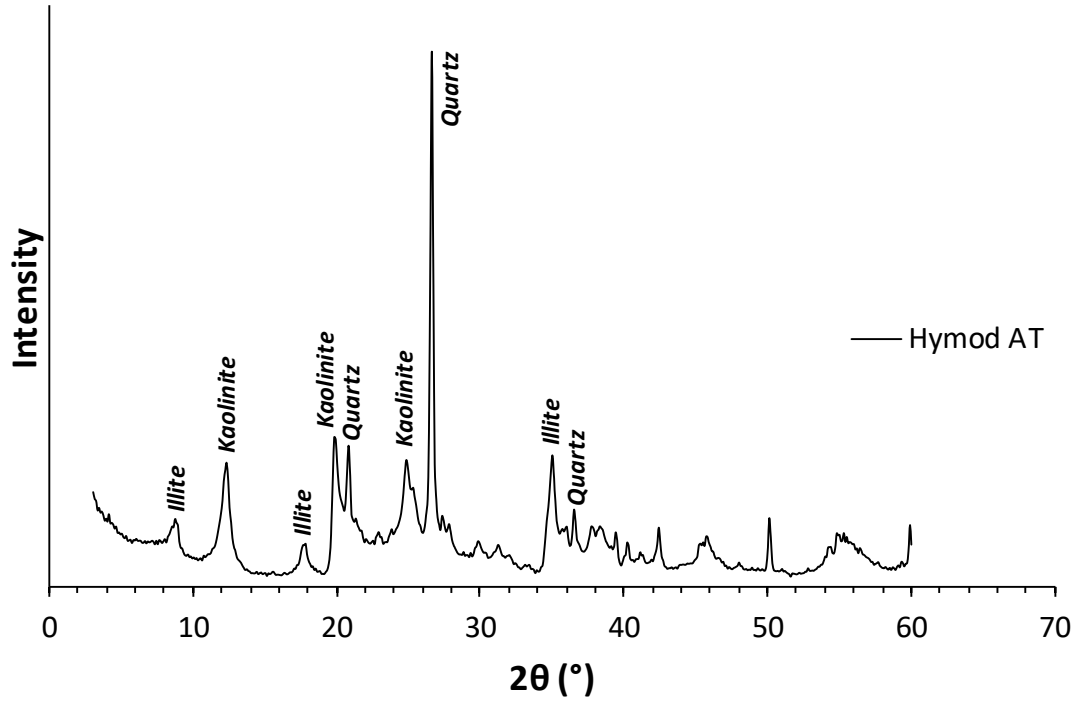

Figure 3-29 – Annotated x-ray diffraction (XRD) spectrum for Hymod AT

The x-ray Fluorescence analysis was conducted on a Philips PW 2424 X-ray Fluorescence Spectrometer. The XRF analysis works on the basis that when the sample is exposed to high energy x-rays, at an atomic level, an electron is released from the inner atomic shell. When the electron is replaced by an electron from the higher energy outer layer, the difference in energy is released as x-rays of a wavelength specific to the oxide element.

The samples were prepared by first pressing the clay in a 27 mm diameter mould to form the XRF sample. The sample was then analysed in the spectrometer. The results of this analysis are shown in Figure 3-30 and Table 3-8.

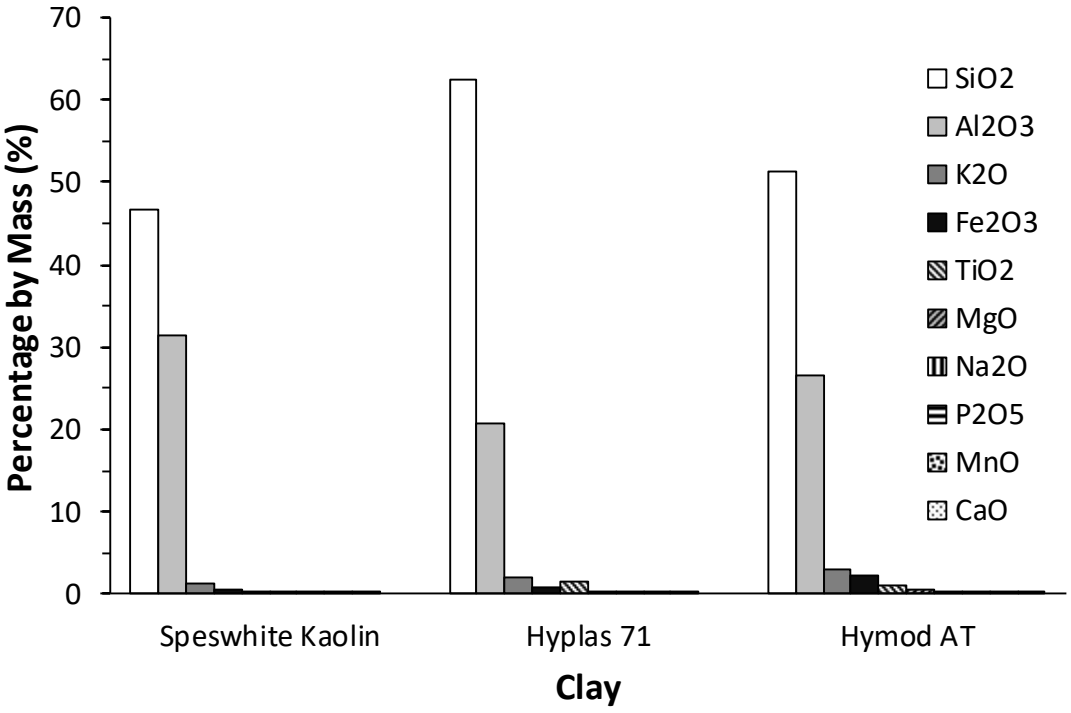

Figure 3-30 – Graph showing relative proportions of the major oxides in the three clays used

Table 3-8 – Major oxide composition of the three clays used

Major Oxide	Speswhite Kaolin	Hyplas 71	Hymod AT
Silicon Dioxide, SiO_2 (%)	46.62	62.49	51.31
Aluminium Oxide, Al_2O_3 (%)	31.52	20.66	26.48
Potassium Oxide, K_2O (%)	1.39	2.01	3.01
Iron Oxide, Fe_2O_3 (%)	0.70	0.85	2.28
Titanium Dioxide, TiO_2 (%)	0.02	1.61	1.16
Magnesium Oxide, MgO (%)	0.25	0.40	0.50
Sodium Oxide, Na_2O (%)	0.06	0.34	0.38
Phosphorus Pentoxide, P_2O_5 (%)	0.09	0.06	0.05
Manganese Oxide, MnO (%)	0.01	0.01	0.01
Calcium Oxide, CaO (%)	Trace	Trace	0.17

3.3.6. Scanning Electron Microscopy

One of the key objectives of the research is to try to identify the mechanism by which rate effects operate. An important issue raised by rate effects is whether or not the mechanism has any impact on the structure of the clays or *vice versa*. To investigate this, a programme of Scanning Electron Microscopy (SEM) was carried out on a number of the specimens tested. The SEM imaging was undertaken at the Dundee Imaging Facility (DIF) at the University of Dundee, using a Hitachi S-4700 Field Emission Scanning Electron Microscope.

Numerous techniques had been used in previous studies, and the method to be used depends on the soil type, facilities available and the aims of the study. In this case, the aim was to image the undisturbed structure of the reconstituted clay which had previously been subject to shearing in the triaxial apparatus. However, the fact that the clay is saturated causes several issues. Firstly, the delicate nature of the clay following shearing means that the process of cutting the SEM sample can destroy the sample's structure. Secondly, the process of preparing the samples for imaging can cause structural change as the sample is dried. These considerations were a key factor in selecting the SEM technique used.

Environmental SEM (ESEM) has been used previously to investigate the overall structure of clays and has the advantage of observing the clay in its undisturbed hydrated state (Monroy *et*

al., 2010). However, one of the limitations of ESEM is that the analytical precision of the image is 50 times less than that of Field Emission SEM (FESEM) which has a precision of 2-5 nm (Reeves *et al.*, 2006). This means that imaging would be restricted to a magnification of roughly 600 times and the desired observation of particle level interaction would not be possible. Cryogenic SEM (CryoSEM) involves imaging the sample whilst frozen (Karimi-Lotfabad and Gray, 2000), and whilst the facilities for this were available at DIF, each sample would have had to be imaged individually shortly after completing the triaxial test making this option impractical. As a result, the investigation was carried out using FESEM with an adapted sample preparation method to provide high quality undisturbed samples.

To overcome the issues discussed, the SEM sample was cut from areas of interest in the clay specimen using a sharp knife coated with a dry film of PTFE to minimise the disturbance during cutting. This prevented the clay from adhering to the blade, which had been visible as the cause of sample disturbance in previous attempts. To prevent structural change during drying a fast freezing method was selected to dry the sample. A key part of this was that the sample was sufficiently small in size (a 3 mm cube) such that it could freeze uniformly (Holzer *et al.*, 2010). The samples were then placed in a test tube and rapidly frozen by immersing the test tube in liquid nitrogen using a Dewar flask. Whilst being kept in the liquid nitrogen, the test tube was subjected to a 99 % vacuum, and the nitrogen was allowed to evaporate over 24 to 48 hours. Due to the high vacuum, the ice in the sample transitions directly to gas by sublimation below 0 °C as the nitrogen evaporates, without causing structural change.

The dried sample was then fractured to expose the undisturbed sample within. However, the process of fracturing can leave debris on the sample surface. To remove this, the surface was repeatedly peeled using adhesive tape ten times (Mitchell and Soga, 2005). An unpeeled anisotropic sample was also imaged for comparison. As can be seen in Figure 3-31, the unpeeled sample has debris sitting flat on the surface orientated with the fracture, whilst the expected anisotropic structure is clearly visible on the peeled sample.

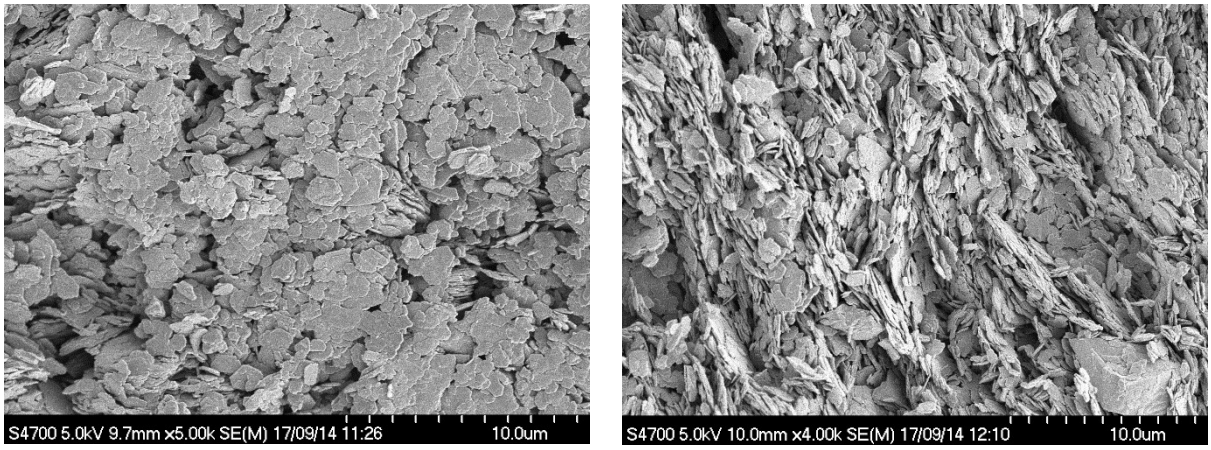

Figure 3-31 – Comparison of unpeeled (L) and peeled (R) SEM sample images of anisotropically consolidated Kaolin at 4000x magnification

The sample was then mounted on an SEM specimen holder using epoxy resin as shown in Figure 3-32. In line with the recommendations of Huggett and Shaw (1997), the samples were coated with gold-palladium to a thickness of 30 nm using a Cressington sputter coater to prevent them becoming charged during the imaging process, before being transferred to the microscope for imaging. The use of a conventional gold coating would not have been possible as the small size of the clay particles means that the features of the particles would have been obscured by the coarser gold coating. The use of the finer gold-palladium coating overcomes these limitations.

The samples were then each imaged in two locations at a variety of magnifications ranging from 30 to 40,000 times to allow different levels of structure to be observed. Due to the equipment-specific nature of the actual SEM imaging process, this is not described in detail here. The results of the SEM imaging will be discussed in Chapter 7 and the influence of the material properties on the rate effect behaviour of the three clays will be considered in Chapter 8.

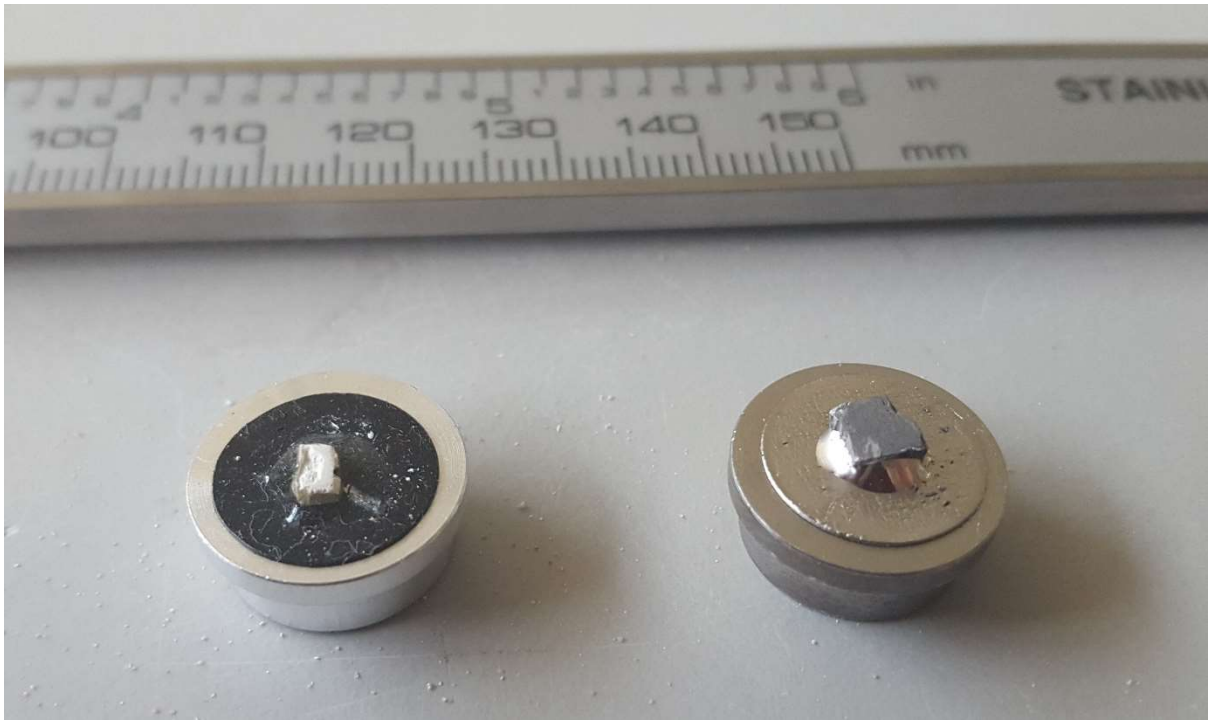

Figure 3-32 – SEM Kaolin sample mounted on holder using epoxy (L) and after sputter coating (R)

3.3.7. Summary of Material Characterisation

The results of the characterisation tests on the three clays are summarised in Table 3-9 below.

Table 3-9 – Summary of material parameters for each clay

Property	Kaolin	Hyplas 71	Hymod AT
Plastic Limit, PL (%)	32.5	20.9	29.7
Liquid Limit, LL (%)	65.0	45.5	79.0
Plasticity Index, PI (%)	32.5	24.6	49.3
Clay Fraction, CF (%)	82	65	95
Activity, A (%)	39.6	37.8	51.9
Specific Surface Area (MB), SSA (m^2/g)	36.7	53.2	105.2
Permeability, k (m/s) *	$0.76x10^{-9}$ to $1.17x10^{-9}$	$0.51x10^{-10}$ to $1.05x10^{-10}$	$0.59x10^{-10}$ to $1.56x10^{-10}$
NCL Gradient, λ_{NCL}	0.168	0.101	0.180
Unload/Reload Line Gradient, κ	0.021	0.046	0.077
NCL Intercept, N $^+$	3.101	2.328	3.125
CSL Intercept, Γ $^+$	2.988	2.268	3.038
Gradient of CSL in q-p' space, M	0.851	0.785	0.569
Reference State Parameter, Ψ_{ref} #	0.113	0.06	0.087
Proportion of Kaolinite (%)	80	28	42
Proportion of Illite (%)	18	28	40
Proportion of Quartz (%)	2	44	18

* At effective stresses ranging from p' = 300 to 1000 kPa

$^+$ Intercept defined as the specific volume, v, at p' = 1 kPa

\# For normally consolidated conditions

4. Rate Effects in Kaolin at Large Strains

As discussed in Chapter 1, the main focus of this thesis is the undrained viscous rate effects which cause an increase in shear strength with strain rate. However, a number of issues were required to be investigated before the main programme of undrained triaxial testing could be undertaken.

Firstly, the reference strain rate required to be selected. A number of different approaches for defining the reference rate are used in the literature, and different reference strain rates can lead to either higher or lower rate effects being calculated. This issue is complicated further by the fact that at sufficiently slow rates, drainage effects can influence the strength of the triaxial specimen. Even if the test is conducted under constant volume conditions (artificially undrained), local redistribution of pore fluid can have an influence on the specimen's behaviour at these slow rates. If these effects are to be avoided in the main undrained testing programme, the lowest strain rate used must be no lower than the strain rate at which the specimen is truly undrained (i.e. has insufficient time for any drainage to occur). Hence an understanding of the behaviour of Kaolin through the drained, partially drained and undrained regimes is required. The question also exists as to whether partial drainage conditions have an impact on the magnitude of viscous rate effects.

To inform these decisions and determine the selection of the main undrained testing programme, a series of drained tests were first conducted on Kaolin under drained (valves open) conditions over a wide range of axial strain rates from 0.1 to 180,000 %/hr.

4.1. Drained Testing

One of the key decisions to be made in determining the main experimental programme was the selection of the reference strain rate by which other strain rates are normalised. The review of reference strain rate selection methods carried out by Chow and Airey (2011) identified that many of the prominent rate effect studies have used different definitions of the reference point. These are summarised below along with references to typical studies which have used the corresponding definition:

- The lowest strain rate considered in the testing programme (Dayal and Allen, 1975)

- An axial strain rate of 1 %/hr or the closest available strain rate [using artificially undrained testing - drainage valves closed] (Kulhawy and Mayne, 1990; Sheahan *et al.*, 1996)
- The strain rate at which the specimen becomes fully undrained [if drainage is permitted when the time for consolidation allows – drainage valves open] (Randolph and Hope, 2004; Lehane *et al.*, 2009)

All of these approaches have an impact on the derived rate effects, with higher reference strain rates leading to lower calculated rate effects (in undrained conditions). This is due to the fact that a higher reference strain rate will usually be accompanied by a higher reference deviator stress; the value by which all other deviator stresses will be normalised (Chow and Airey, 2013). Hence, it is important that the reference strain rate selected is justifiable. As mentioned in the literature review, a number of other issues also arise including the potential impact of drainage and partial consolidation on viscous rate effects and whether artificially undrained conditions at low strain rates can be considered comparable to truly undrained conditions created by high strain rates. This is especially true if there is a strain rate below which viscous rate effects reduce or cease to exist (Dayal and Allen, 1975; Sheahan *et al.*, 1996). To inform this choice, a range of tests were carried out considering drained conditions (back pressure valve open) across a wide range of axial strain rates from 0.1 to 180,000 %/hr, as well as a small number of artificially undrained tests (See Table 4-1). The tests were also intended to investigate the performance of the high-speed triaxial system across the full range of strain rates possible and inform the selection of the strain rates to be used in the main testing programme. These tests were conducted using the triaxial methodology (with a half-ball fitting) set out in Chapter 3 using 100 mm diameter reconstituted specimens of normally consolidated Kaolin.

Abbreviations used in the test designations are summarised below:

KLN = Kaolin (Test Material Abbreviation)

TD = Triaxial Drained (Drainage valve open)

TU = Triaxial Undrained (Drainage valve closed)

Final Number = Test Number

Table 4-1 – List of drained tests conducted on Kaolin

Test Designation	*Test Type**	*Liquidity Index, LI*	*Mean Effective Stress, p'_0 (kPa)*	*Axial Strain Rate, $\dot{\varepsilon}$ (%/hr)*	*Back Pressure (kPa)*	*Back Valve State*	*Normalised Velocity, V (vd/c_v)*
KLN-TD-1	CID	0.32	300	0.1	300	Open	0.004
KLN-TD-2	CID	0.32	300	1	300	Open	0.037
KLN-TD-3	CID	0.32	300	10	300	Open	0.372
KLN-TD-4	CID	0.32	300	100	300	Open	3.724
KLN-TD-5	CID	0.32	300	300	300	Open	11.17
KLN-TD-6	CID	0.32	300	1000	300	Open	37.24
KLN-TD-7	CID	0.32	300	10000	300	Open	372.4
KLN-TD-8	CID	0.32	300	100000	300	Open	3724
KLN-TD-9	CID	0.32	300	180000	300	Open	6704
KLN-TD-10	CID	0.18	650	1	300	Open	0.023
KLN-TD-11	CID	0.18	650	10	300	Open	0.233
KLN-TD-12	CID	0.18	650	100	300	Open	2.340
KLN-TD-13	CID	0.18	650	1000	300	Open	23.40
KLN-TD-14	CID	0.18	650	10000	300	Open	234.0
KLN-TD-15	CID	0.18	650	100000	300	Open	2340
KLN-TU-1	CIU	0.32	300	1	300	Closed	0.037
KLN-TU-2	CIU	0.32	300	100	300	Closed	3.724

*Test type indicated does not take account of rate dependent changes in drainage conditions

4.1.1. Drained Testing Results

Figure 4-1 shows the results of the drained tests conducted at p'_0 = 300 kPa in terms of deviator stress against shear strain. The definition of shear strain used in deriving the results throughout this thesis is that of triaxial deviatoric shear strain as shown in Equation 4-1 (Muir Wood, 1990).

$$\Delta\varepsilon_q = \frac{2(\Delta\varepsilon_a - \Delta\varepsilon_r)}{3} \tag{4-1}$$

This has the advantage that, for undrained conditions, axial strain and shear strain are equal. Starting with the slowest rate considered of $\dot{\varepsilon}$ = 0.1 %/hr, as the strain rate is increased, an

overall reduction in the deviator stress is observed up to a rate of $\dot{\varepsilon}$ = 300 %/hr, with the tests at 0.1, 1 and 10 %/hr strain hardening without displaying a distinct peak deviator stress. This is due to the fact that these tests are likely to be in a partially drained state during shearing, with reducing time for drainage to occur at higher strain rates. Beyond this axial strain rate (300 %/hr), viscous effects are observed leading to an increase in the measured deviator stresses. It is important to note these two effects are distinct and must be differentiated between, however the questions of whether drainage has an impact on viscous rate effects and if there is a point below which viscous effects are no longer observed (such as in Sheahan *et al.* (1996)) warrant further consideration.

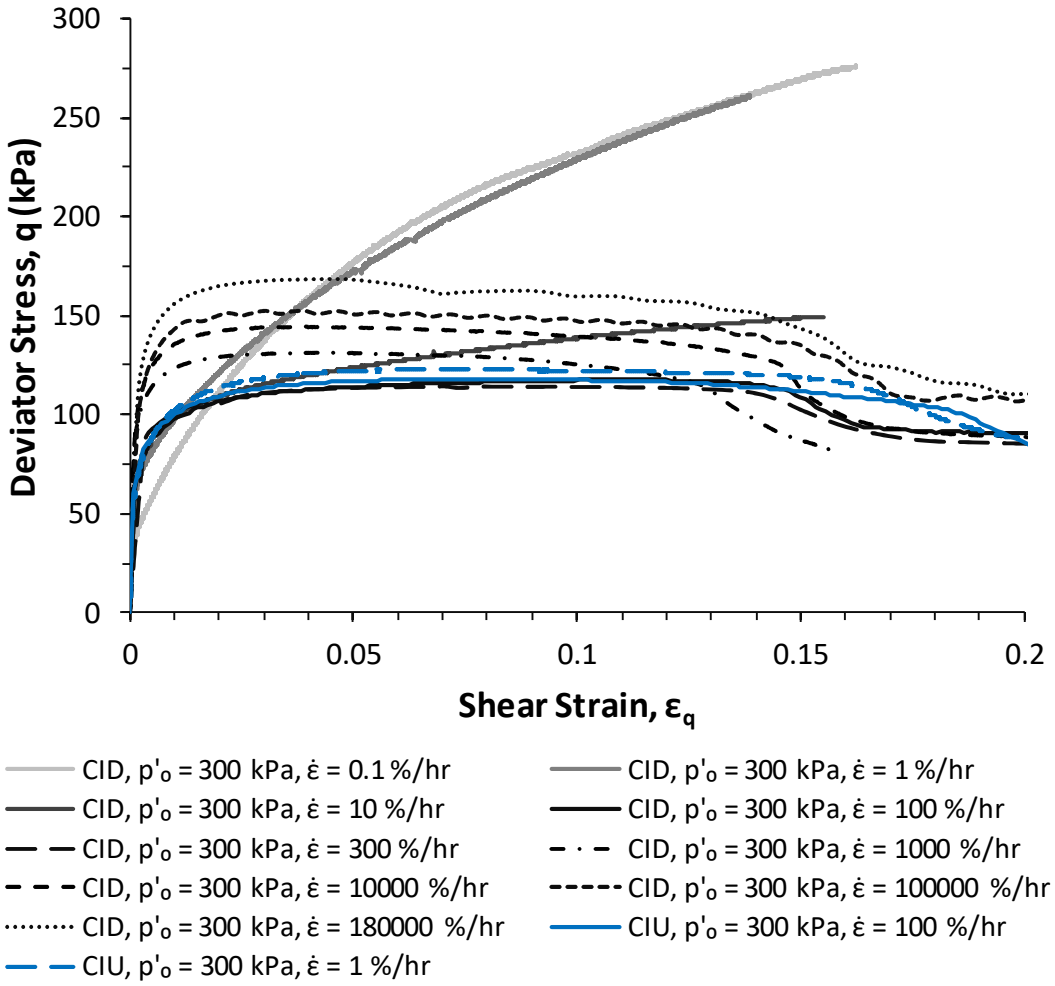

Figure 4-1 – Deviator stress against strain for drained tests at various axial strain rates conducted using Kaolin at p'_o = 300 kPa

Similar behaviour is observed for the tests conducted at p'_0 = 650 kPa (See Figure 4-2), although in this case, all tests displayed peak deviator stresses even if this was at much larger strains

than would normally be anticipated. The differences in behaviour between the tests at p'_0 = 300 kPa and 650 kPa are likely to be due to the fact that at p'_0 = 650 kPa, the permeability of the specimens was lower possibly allowing the shear plane to form.

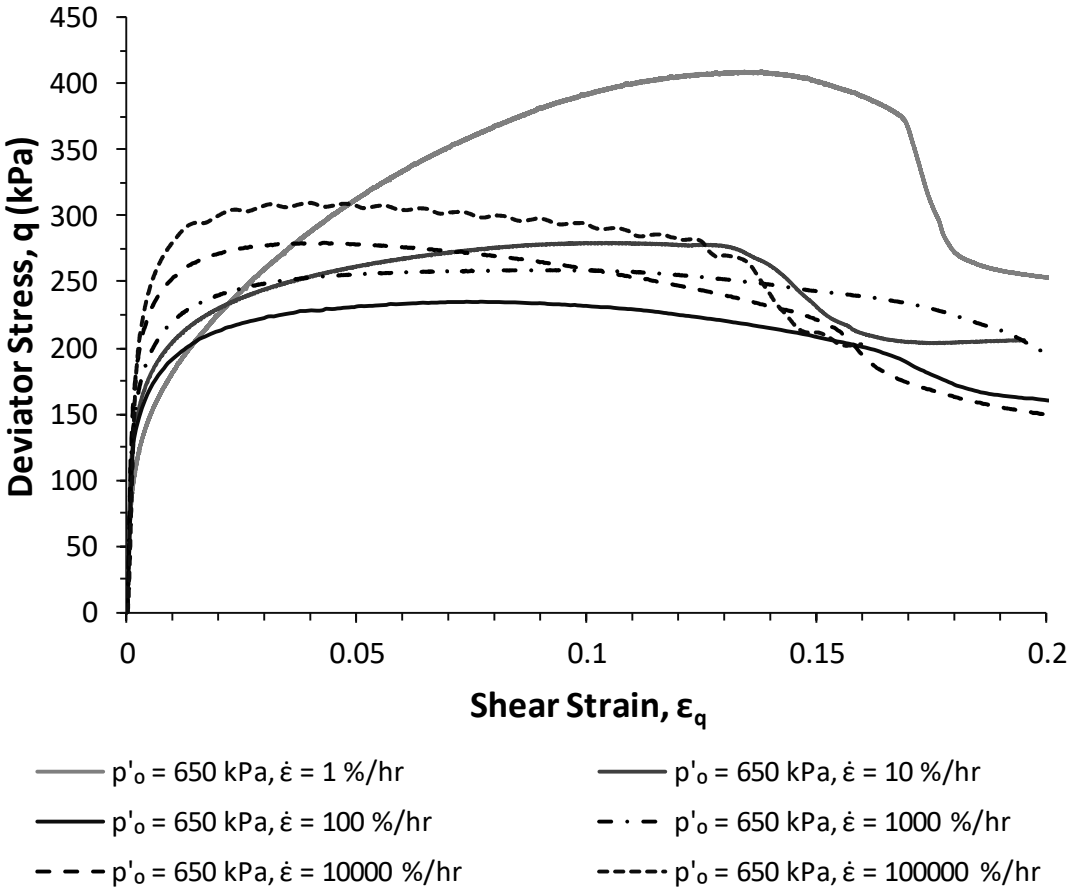

Figure 4-2 – Deviator stress against strain for drained tests conducted at various axial strain rates using Kaolin at p'_o = 650 kPa

4.1.2. Model Fitting at Peak Deviator Stress

To investigate the response of Kaolin across the strain rate range, and to allow the points of interest (the transition points from drained to partially drained and partially drained to undrained) to be determined quantitatively, the model (Equation 4-2) proposed by Randolph and Hope (2004) will be used. For any soil at a given soil state, the model allows a relationship between the normalised deviator stress, q, and strain rate to be determined. It should be noted that by definition, for this model the reference deviator stress used for normalisation is the

point at which the soil response first becomes fully undrained. Finnie and Randolph (1994) suggested that this point occurs at a normalised velocity of approximately 30.

$$\frac{q}{q_{ref}} = \left(1 + \frac{b}{1 + cV^{d}}\right)\left\{1 + \frac{\lambda}{ln(10)}\left[sinh^{-1}\left(\frac{V}{V_0}\right) - sinh^{-1}\left(\frac{V_{ref}}{V_0}\right)\right]\right\} \quad (4\text{-}2)$$

Where the normalised velocity $V = \frac{vd}{c_v}$ (Finnie and Randolph, 1994)

Values of c_v for the Kaolin used in this study to determine the normalised velocity, V, are shown in Table 4-2. These values have been calculated using Equation 4-3 using the measured permeability values presented in Chapter 3. The values for m_v were determined for a 100 kPa stress increment for each value of p'_0 (eg from p' = 250 to 350 kPa for p'_0 = 300 kPa) from volumetric strain measurements during isotropic consolidation of a 100 mm diameter triaxial specimen.

$$c_v = \frac{k}{m_v \gamma_w} \quad (4\text{-}3)$$

Table 4-2 – Coefficients of consolidation for the Kaolin used in this study

Initial Mean Effective Stress, p'_0 (kPa)	Permeability, k (m/s)	Coefficient of compressibility, m_v (m^2/kN)	Coefficient of consolidation, c_v (m^2/year)
300	1.14×10^{-9}	15.6×10^{-5}	23.5
650	8.5×10^{-10}	7.31×10^{-5}	37.4
1000	7.3×10^{-10}	4.88×10^{-5}	48.1
1350	6.6×10^{-10}	3.75×10^{-5}	56.6

Additionally, the deviator stresses used for the analysis are the peak deviator stresses. The first component of the model deals with drainage effects and the second part the undrained viscous effects. It is important to note that whilst Equation 4-2 uses an inverse hyperbolic relationship (discussed in the Literature Review) which normally considers the rate effect per natural log cycle (ln), it is already modified such that the viscous rate effect input parameter, λ, is the rate effect per log cycle ($\log_{10}$) which is more commonly used.

In this model, *b*, *c* and *d* are empirical curve-fitting parameters which are associated with the drained and partially drained ranges, whilst λ, V_0 and V_{ref} determine the viscous response and the point of transition from partially drained to undrained behaviour. It should be noted that the *d* term referred to in the normalised velocity by Finnie and Randolph (1994) instead refers to the specimen drainage path length (or a characteristic length relating to drainage in other applications).

The peak deviator stresses (or final deviator stress if peak was not achieved) were determined from the stress-strain curves shown in Figure 4-1 and Figure 4-2 and these were normalised by the lowest peak deviator stress observed (the specimens tested at $\dot{\varepsilon}$ = 300 %/hr for p'_0 = 300 kPa and at $\dot{\varepsilon}$ = 100 %/hr for p'_0 = 650 kPa). Next, least mean square regression was used to fit the model of Randolph and Hope (2004) to the experimental data from the CID tests at each effective stress, resulting in two 'backbone curves' shown in Figure 4-3. The parameters resulting from this fitting process are shown in Table 4-3. For each fit, the parameters which represent the points below which viscous rate effects cease, V_0, and the point at which fully undrained behaviour is achieved, V_{ref}, were set to be equal (as per Randolph and Hope, 2004).

From the derived parameters, it can be seen that the transition to fully undrained behaviour occurs at a normalised velocity, V_{ref}, of between 8.2 and 3.1 (for p'_0 = 300 kPa and 650 kPa respectively), with this value reducing at higher effective stresses. In terms of axial strain rates, this corresponds to $\dot{\varepsilon}$ = 132 %/hr and 220 %/hr, justifying the selection of the reference rates by which other deviator stresses are normalised. These values for V_{ref} compare well with the value of V_{ref} = 8 determined by Lehane *et al.* (2009) using centrifuge testing of T-bar penetrometers, also in Kaolin. This is likely to be due not only the fact that a similar material was used, but also the fact that Lehane *et al.* (2009) used a similar typical stress in the penetrometer testing (σ'_v = 300 kPa) to the tests conducted at p'_0 = 300 kPa here (V_{ref} = 8.2). However, the values found are notably lower than the value for the transition to undrained behaviour suggested by Finnie and Randolph of V_{ref} = 30. This highlights the fact that despite its normalisation, the soil type and voids ratio still have some impact on the normalised velocity, V_{ref}, at which undrained behaviour occurs.

Additionally, the model fit at p'_0 = 650 kPa shows lower overall rate effects in terms of the fully drained response, reducing from 2.34 at p'_0 = 300 kPa down to 1.80. This is most likely due to

the fact that the tests at p'_o = 300 kPa have more scope for consolidation and drainage during shearing because of the lower initial mean effective stress, as well as a lower reference deviator stress, q_{ref}. Thus, for higher consolidation pressures, there is lower potential for drainage-related rate effects when moving from drained to undrained behaviour. For the case of the tests at p'_0 = 650 kPa, no test was carried out at $\dot{\varepsilon}$ = 0.1 %/hr and more tests in the drained range (V < 0.01) would be required to determine the fully drained value of q/q_{ref} with greater certainty.

It is important to separate these drainage related rate effects from the viscous rate effects which are the main focus of this thesis. From the fitting process, the viscous rate effects were found to be greatest at the lowest effective stress ranging from λ = 13.8 % per log cycle at p'_0 = 300 kPa to 10.9 % at p'_0 = 650 kPa, suggesting that viscous rate effects may reduce with increasing initial mean effective stresses (or reducing moisture content/specific volume). This would suggest that soil state is a key variable to be investigated.

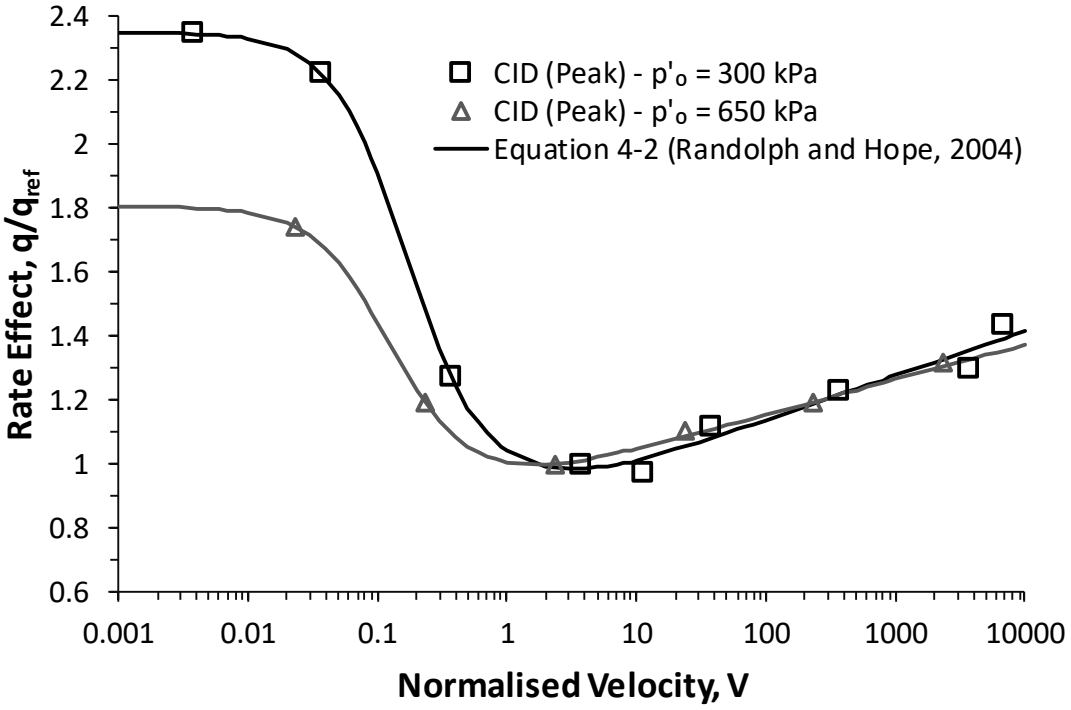

Figure 4-3 – Rate effect 'backbone' curve for Kaolin at p'_o = 300 and 650 kPa based upon peak deviator stress

Table 4-3 – Fitting parameters determined using model of Randolph and Hope (2004) (Equation 4-2) at peak deviator stress

p'_o (kPa)	*b*	*c*	*d*	*λ*	V_o	V_{ref} *(Equivalent $\dot{\varepsilon}$ in brackets)*
300	1.48	15.1	1.5	0.138	8.2	8.2 (220 %/hr)
650	0.88	24.6	1.5	0.109	3.1	3.1 (132 %/hr)

4.1.3. Model Fitting at Varying Strain Levels

Up until this stage, the model proposed by Randolph and Hope (2004) has been used to consider the variation in peak deviator stresses, but this raises issues of comparability between these selected points, given that the strains at which peaks were displayed ranged from 3 to 16 % shear strain. To allow the rate effects at varying strain levels to be considered and compared, the process used to fit the model to the peak deviator stresses was repeated, using the deviator stresses extracted at 1, 2, 5 and 10 % shear strain from the CID tests at p'_o = 300 kPa (See Figure 4-4). These results are based on external (global) strain measurements, however, rate effects at smaller strain levels are also considered in detail using local strain measurements in Chapter 6.

This allows comparison with the parameters derived from peak deviator stresses. One of the key parameters of interest, V_{ref}, was found to increase with strain level (See Table 4-4) ranging from a value of 4.0 at 1 % strain to 11.0 at 10 % strain. This is due to the fact that at higher strain levels more time elapses during which drainage can occur and excess pore pressures can dissipate, especially given the fact that the highest rate of pore pressure evolution occurs at lower strains. Hence the normalised velocity at which a specimen becomes undrained is strain level dependent. The value from the peak model (8.2) also compares well with the V_{ref} determined at 5 % strain of 8.0, most likely due to the fact that 5 % strain is reasonably close to the average strain at which peak occurs. Additionally, this strain dependence (combined with the voids ratio dependence found earlier) highlights the limitations of using a constant value of V_{ref} for a particular soil (as in Finnie and Randolph (1994) and Randolph and Hope (2004)).

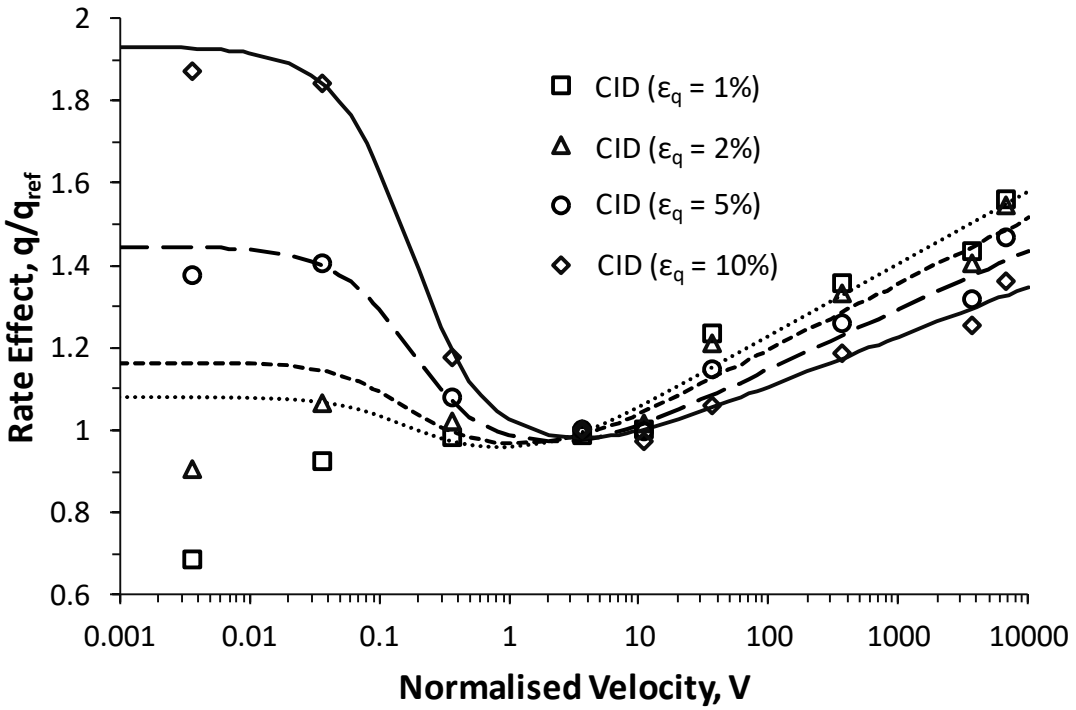

Figure 4-4 – Rate effect 'backbone' curve for Kaolin at p'_o = 300 kPa at various strain levels

Table 4-4 – Fitting parameters determined using model of Randolph and Hope (2004) (Equation 4-2) at various strain levels for p'_o = 300 kPa

Strain, ε_q (%)	*b*	*c*	*d*	*λ*	V_0	V_{ref} *(Equivalent $\dot{\varepsilon}$ in brackets)*
1	0.16	15.0	1.5	0.175	4.0	4.0 (107 %/hr)
2	0.24	15.0	1.5	0.160	5.0	5.0 (134 %/hr)
5	0.53	14.0	1.5	0.145	8.0	8.0 (215 %/hr)
10	1.02	14.0	1.5	0.121	11.0	11.0 (295 %/hr)

The viscous rate effects determined from the model fitting at each strain level are also of a similar magnitude to the 13.8 % per log cycle determined from the peak values. However, the viscous rate effect was shown to reduce with increasing strain level, ranging from 17.5 % per log cycle at 1 % strain down to 12.1 % at 10 % strain. This is in keeping with the findings of Sheahan *et al.* (1996) who also found reducing rate effects at greater strains. This suggests that

strain level variations in viscous rate effects should be a key consideration in the main testing programme.

From Figure 4-4, it can be seen that whilst the model of Randolph and Hope (2004) provides a good level of fit to the data points near and beyond the transition to undrained behaviour ($V \approx$ 5 to 10), at normalised velocities lower than $V \approx 0.1$ reductions are observed in the rate effect, q/q_{ref}, which are not accounted for in the model. This suggests that viscous rate effects may also exist below the transition point to undrained behaviour, leading to the model being unable to match the measured data. This is not a criticism of the model, as it was designed for use in modelling soil strength in t-bar and penetrometer tests, where the strains which occur are very large. However, it is useful to discuss the reasons for the observed differences such that a model that can account for them may be developed.

The difference is due to the fact that Randolph and Hope (2004) suggest that the point below which viscous rate effects become negligible, V_o, is at or near V_{ref}. This is in contrast to artificially undrained triaxial studies such as Sheahan *et al.* (1996) which found that viscous rate effects do exist at strain rates corresponding to the partially drained range. Other studies have indicated that viscous rate effects do occur in the partially drained range such as Lehane *et al.* (2009) using T-bar penetrometer testing. Lehane *et al.* (2009) states that viscous rate effects exist in the partially drained and undrained ranges, but become negligible when the soil becomes fully drained. It is worth noting that the fully drained range corresponds to normalised velocities below $V = 0.01$, and in this study, there is insufficient information to comment on the suggestion by Lehane *et al.* (2009) that viscous effects are negligible in this range.

4.1.4. Improvement of Existing Drained Rate Effect Model

Figure 4-5 shows the viscous rate effect assumed by Randolph and Hope (2004), marked 'A', along with the expected viscous rate effects based on the literature review which extend into the partially drained range ('B'). The impact on the model by Randolph and Hope (2004) ('C') of extending the viscous rate effects into the drained and partially drained range by lowering the value of V_o to 0.0001 (below the lowest normalised velocity tested here) is marked as 'D'. This shows the model outputs lower values of q/q_{ref} than those expected which are shown by the line marked 'E'. The reason for this is related to the way in which the model is formulated.

As the authors intended the drainage related rate effect component and the viscous rate effect to be separate and occur at mutually exclusive normalised velocities, these terms are multiplied together in Equation 4-2. This leads to the viscous rate effect being multiplied by the drainage related rate effect term when it is extended into the partially drained range.

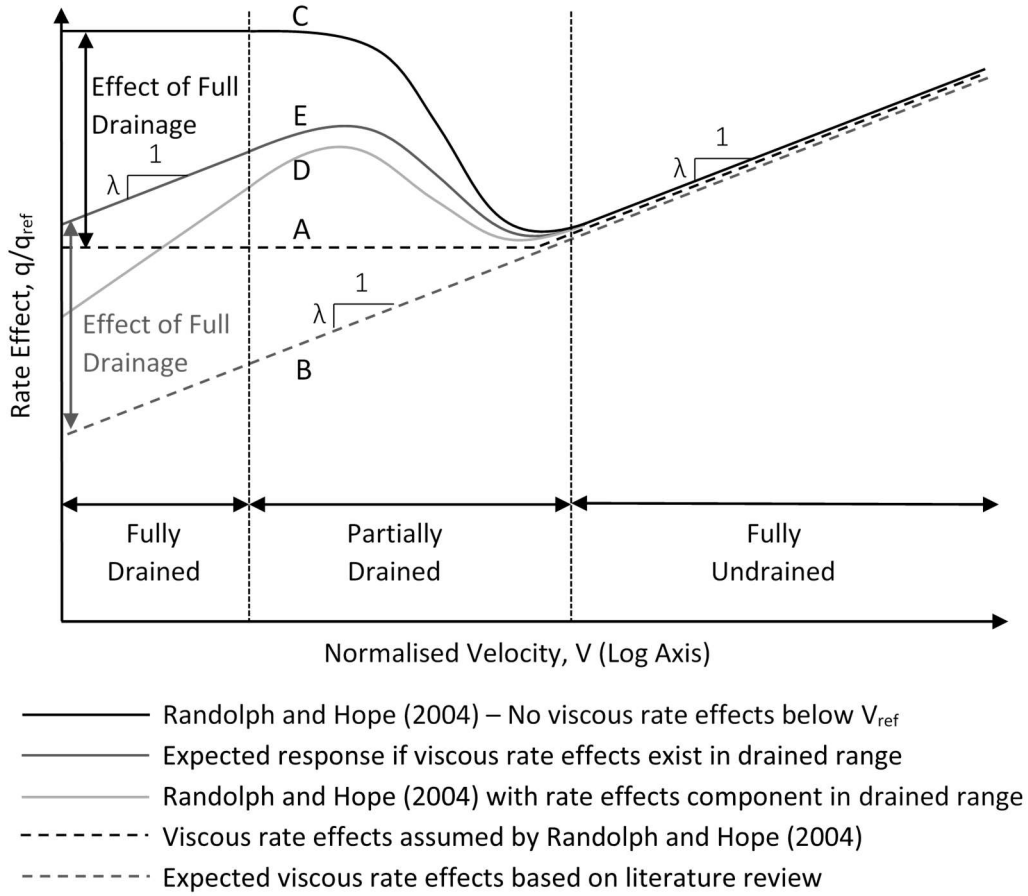

Figure 4-5 – Impact of viscous rate effect assumptions on the model by Randolph and Hope (2004)

To overcome these issues, Equation 4-2 may be simply reformulated to Equation 4-4, where the two terms are added rather than multiplied. This has no impact on the model other than to resolve the issue in question.

$$\frac{q}{q_{ref}} = 1 + \frac{b}{1+cV^d} + \frac{\lambda}{ln(10)}\left[sinh^{-1}\left(\frac{V}{V_0}\right) - sinh^{-1}\left(\frac{V_{ref}}{V_0}\right)\right] \quad (4\text{-}4)$$

Using this revised equation, the fitting process for the tests at p'_o = 300 kPa at each of the selected strain levels has been repeated (See Figure 4-6). As can be seen, the model now fits the partially drained range well, and the new parameters derived are shown in Table 4-5. There is little impact on the key parameters which represent the undrained region in comparison to

the original model by Randolph and Hope (2004), including the viscous rate effect per log cycle, and also V_{ref}. However, the modified model displays a significantly improved fit in the partially drained range now that the potential viscous rate effects in this range suggested by Lehane *et al.* (2009) are accounted for. Equation 4-4 may be more suited than the model of Randolph and Hope (2004) to applications where capturing partially drained rate effects at specific strain levels is of interest. However, further research is required before it should be extended into the fully drained range.

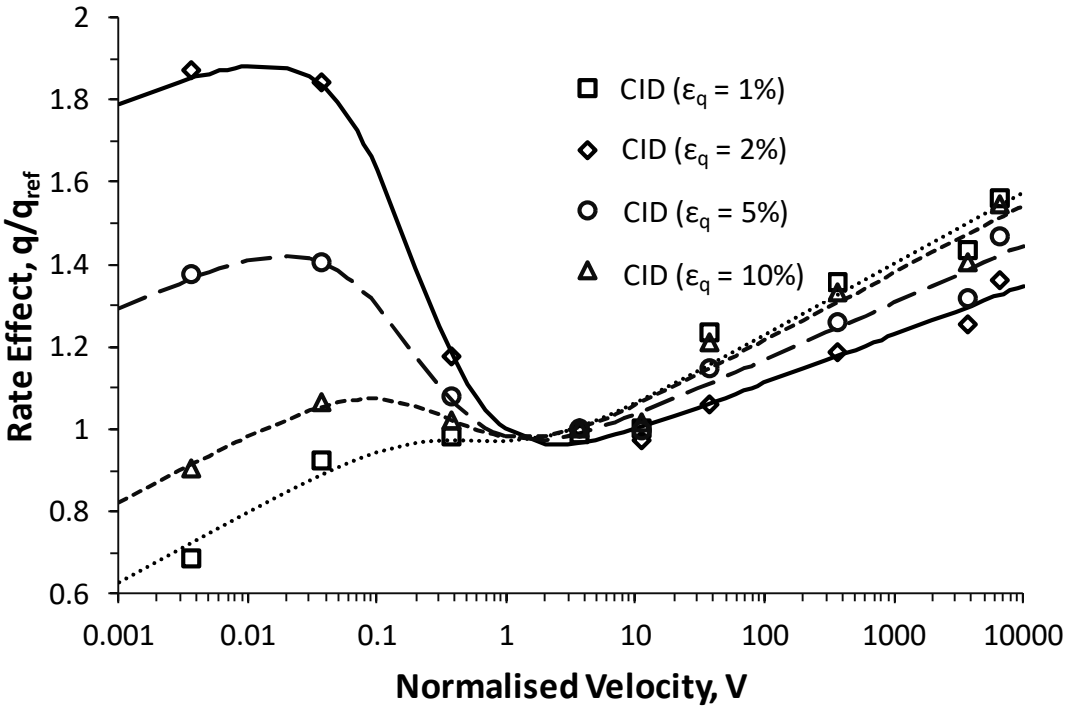

Figure 4-6 – Rate effect 'backbone' curve for Kaolin at p'_o = 300 kPa using modified model (Equation 4-4) at various strain levels

Table 4-5 – Fitting parameters determined using Equation 4-4 at various strain levels for p'_o = 300 kPa

Strain, ε_q (%)	*b*	*c*	*d*	λ	V_o	V_{ref} *(Equivalent $\dot{\varepsilon}$ in brackets)*
1	0.26	2.0	1.2	0.173	0.0001	4.8 (128 %/hr)
2	0.43	3.5	1.2	0.164	0.0001	4.9 (131 %/hr)
5	0.82	7.9	1.2	0.139	0.0001	6.2 (166 %/hr)
10	1.27	9.1	1.3	0.118	0.0001	11.4 (306 %/hr)

The parameters that define the rate effect 'backbone' curve are in themselves a useful output from this study, especially given the prominence of the use of Kaolin as a laboratory test soil for investigating rate effects using free-falling penetrometers (e.g. Chow and Airey, 2013). Figure 4-7 shows the variation in these parameters with strain for Kaolin at p'_0 = 300 kPa, showing that the parameters may be represented by Equations 4-5, 4-6, 4-7 and 4-8. The variation of the viscous rate effect parameter, λ, derived using the fitting process with strain is shown in Figure 4-8, and can be represented by Equation 4-9. The trend of reducing viscous rate effects with shear strain is clear, suggesting that this is an important aspect to be considered in the main testing programme. One point to note however, is that as these parameters have been obtained using fitting of Equation 4-4, the values of λ have been derived in conjunction with the partially drained parameters (*b, c, d,* V_{ref}) and the value of λ found was sensitive to small changes in these parameters.

$$b = log(\varepsilon_q) + 0.2 \quad (4\text{-}5)$$

$$c = 7.6\,log(\varepsilon_q) + 1.8 \quad (4\text{-}6)$$

$$d = 0.1\,log(\varepsilon_q) + 1.2 \quad (4\text{-}7)$$

$$V_{ref} = 4.1e^{0.1\varepsilon_q} \quad (4\text{-}8)$$

$$\lambda = 0.18 - 0.05log(\varepsilon_q) \quad (4\text{-}9)$$

where ε_q is in percent

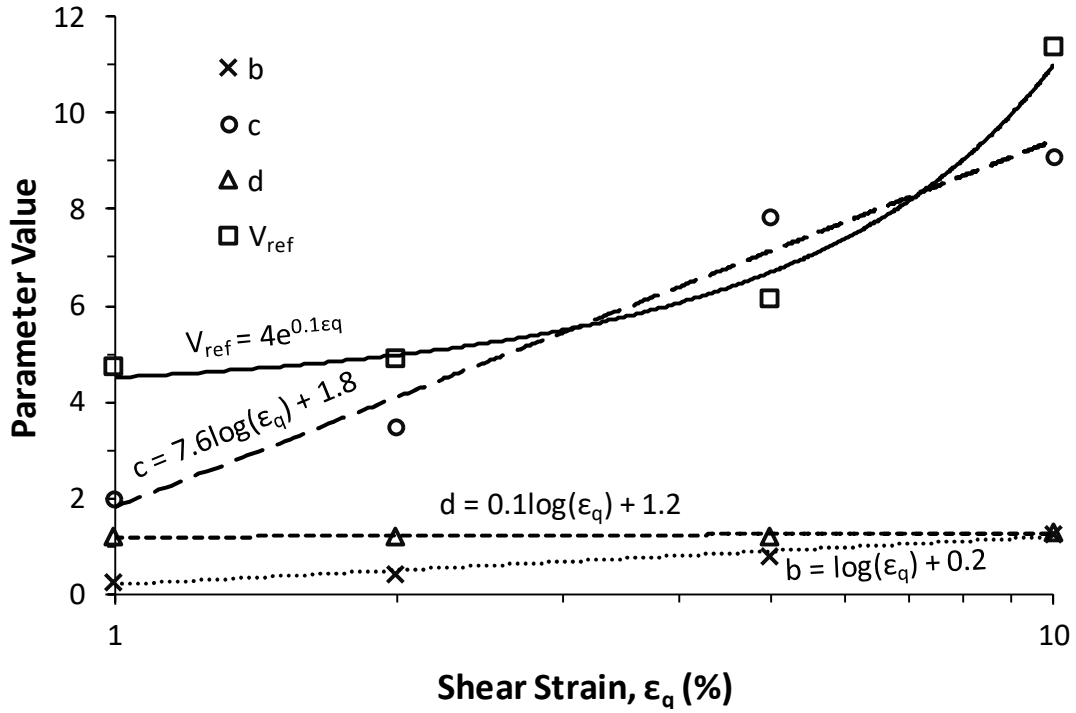

Figure 4-7 – Variation of key parameters for Equation 4-4 with strain for Kaolin at p'_0 = 300 kPa

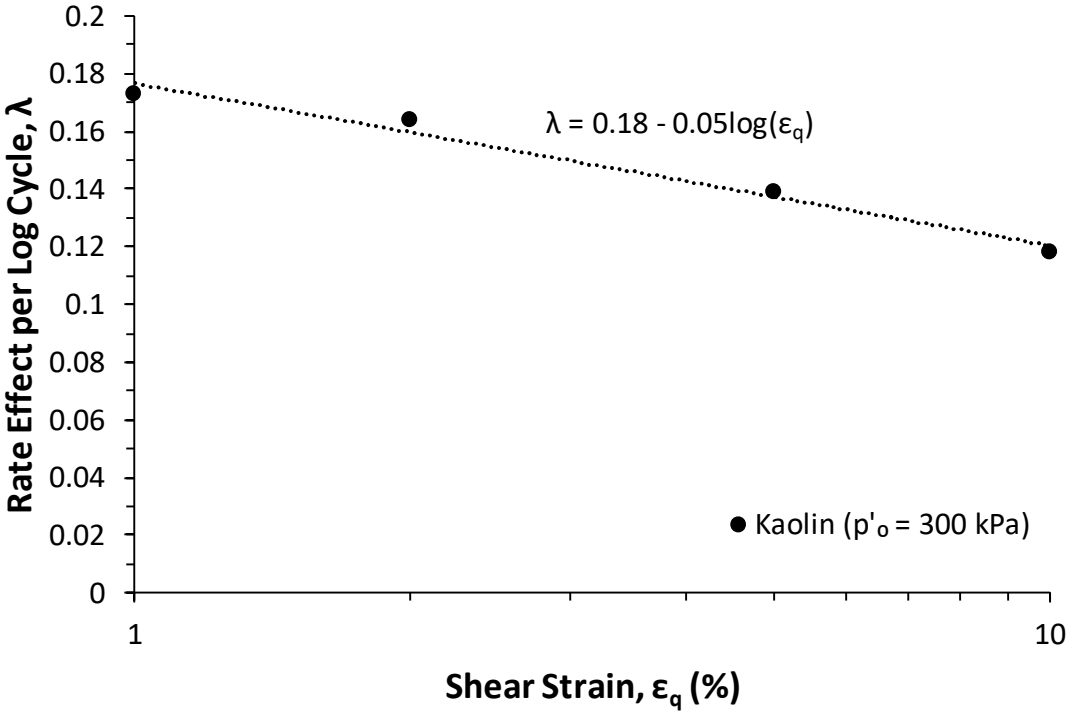

Figure 4-8 – Variation of rate effect per log cycle with shear strain in Kaolin at p'_0 = 300 kPa (derived using Equation 4-4)

4.1.5. Impact of Local Drainage on Artificially Undrained Tests

One important consideration in selecting the test types and conditions to be used in the main programme is the impact of using tests which are made artificially undrained by closing the back pressure valves at strain rates where partial or full drainage would ordinarily have occurred. Several studies have used this approach, such as Sheahan *et al.* (1996). However, even in tests where measures to mitigate specimen localisation caused by end friction have been used, clay specimens would still be expected to have some inhomogeneity. This is due to the fact that lubricated end platens do not completely eliminate the effects of end friction (as no current approach can), but minimise it such that the shearing is uniform across the majority of the length of the specimen. In doing this, premature localisation of the specimen is prevented. However, in reality there will be an area immediately adjacent to the end platens where there is slightly less shearing than the middle of the specimen (and hence less pore pressure generation). In tests where the strain rate is sufficient for the response to be fully undrained, there would be no time for the true (mid-height) pore pressure to dissipate to the

ends of the specimen. However, if the strain rate is in the partially drained range, then the pore pressures in the middle of the specimen may be able to dissipate to the specimen ends, regardless of whether or not the back pressure valves are closed. This localised drainage of pore pressure would lead to an increase in the effective stress and increases in the measured deviator stress.

To investigate this issue, two artificially undrained CIU tests were conducted at an initial mean effective stress of 300 kPa at axial strain rates of 1 %/hr (partially drained range) and 100 %/hr (beginning of fully undrained range). Figure 4-9 shows the results of these tests at peak deviator stress (for both drained [CID] and undrained [CIU] conditions), as well as the deviator stress at strains of 0.25 and 0.5 % in undrained conditions (CIU). If no local drainage were to occur, then the observed peak rate effect from the CIU tests would fall on the line expected for the undrained viscous behaviour. As can be seen, the CIU test conducted at $\dot{\varepsilon}$ = 100 %/hr (V = 3.7) agrees well with the tests conducted with the back valves open. However, for the CIU test conducted at $\dot{\varepsilon}$ = 1 %/hr (V = 0.04), higher than expected peak deviator stresses are observed, suggesting that a strength increase due to localised drainage may be occurring. To consider if this strength increase is due to localised drainage, the normalised rate effects derived using deviator stresses determined at 0.25 and 0.5 % strain are also shown. If the strength increase is due to localised drainage, then this effect would be expected to be increase with strain level as higher strains would allow more time for drainage to occur. The observed rate effects from the CIU tests shown in Figure 4-9 were found to increase with strain, providing some confirmation that localised drainage may be the cause. This raises issues surrounding the viscous rate effects derived from studies using artificially undrained testing where strain rates in the partially drained range have been used, especially where lubricated end platens were not used. This suggests that in studies where undrained rate effect investigation has been conducted at strain rates where the specimen would normally be drained by closing the drainage valve, localised drainage may still occur within the specimen. This would in turn affect the measured deviator stresses and rate effects. For this reason, it is recommended that the lowest strain rate used in a rate effect study should be at least the strain rate corresponding to the transition to undrained behaviour (i.e. V_{ref}).

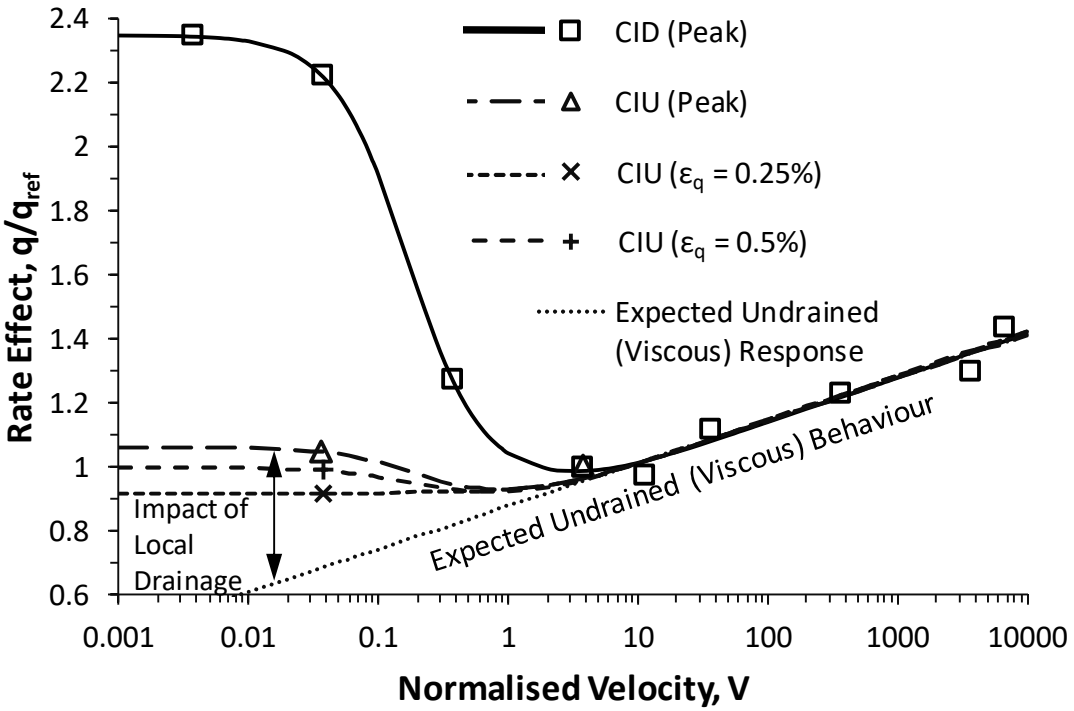

Figure 4-9 – Impact of artificially undrained conditions at strain rates below the reference velocity at p'_0 = 300 kPa (shown fitted with Equation 4-2)

4.1.6. Recommendations for Main Undrained Testing Programme

The key findings from the drained rate effect testing are summarised below:

- The transition to undrained behaviour has been found to occur at $V_{ref} \approx 4$ to 11 depending on the effective stress and strain level in question
- Viscous rate effects have been shown to exist in the partially drained range
- Care should be taken when selecting peak deviator stresses as the point of comparison for rate effects, as this leads to comparison being made between substantially different strain levels.
- Fitting of the model of Randolph and Hope (2004) suggests that rate effects may reduce with increasing initial mean effective stress and increasing strain level
- Using artificially undrained CIU tests in the partially drained strain rate range leads to undesirable deviator stress increases potentially due to localised drainage

4.2. Undrained Testing – Impact on Deviator Stress

Based on the drained testing, a programme of large strain undrained triaxial testing on kaolin was undertaken as shown in Table 4-6. The axial strain rates selected range from 1000 %/hr to 100,000 %/hr in order to ensure that all of the tests are in the fully undrained range, avoiding localised drainage issues. A wide range of effective stresses from 300 kPa up to 1350 kPa have been used to further investigate the p'_0 dependence of rate effects suggested by the drained tests. A limited number of overconsolidated tests at OCR = 6 have also been carried out to consider if OCR influences viscous rate effects. The number of OCR tests has been limited due to time constraints on the testing programme.

Table 4-6 – List of large strain CIU tests conducted on Kaolin specimens

Test Designation	*Test Type**	*Liquidity Index*	*Mean Effective Stress, p'_o (kPa)*	*Axial Strain Rate, $\dot{\varepsilon}$ (%/hr)*	*Drainage Valve State*	*OCR*	*Volumetric Strain during Consol., ε_{vol} (%)*
KLN-TU-L1	CIU	0.32	300	1000	Closed	1	8.9
KLN-TU-L2	CIU	0.32	300	10000	Closed	1	9.1
KLN-TU-L3	CIU	0.32	300	100000	Closed	1	7.2
KLN-TU-L4	CIU	0.18	650	1000	Closed	1	15.8
KLN-TU-L5	CIU	0.18	650	10000	Closed	1	14.4
KLN-TU-L6	CIU	0.18	650	100000	Closed	1	17.3
KLN-TU-L7	CIU	0.10	1000	1000	Closed	1	23.0
KLN-TU-L8	CIU	0.10	1000	10000	Closed	1	23.7
KLN-TU-L9	CIU	0.10	1000	100000	Closed	1	20.4
KLN-TU-L10	CIU	0.02	1350	1000	Closed	1	26.7
KLN-TU-L11	CIU	0.02	1350	10000	Closed	1	28.8
KLN-TU-L12	CIU	0.02	1350	100000	Closed	1	22.5
KLN-TU-L13	CIU	0.22	108 (p'_{max} = 650 kPa)	300	Closed	6	-
KLN-TU-L14	CIU	0.225	108 (p'_{max} = 650 kPa)	180000	Closed	6	-

4.2.1. Stress-Strain Behaviour

Figure 4-10 shows the stress-strain curves for 12 CIU triaxial tests on Kaolin. These were carried out at four initial mean effective stresses ranging from 300 kPa to 1350 kPa and axial strain rates from 1000 %/hr to 100,000 %/hr. The lowest strain rate used was 1000 %/hr as this is the lowest strain rate possible using the triaxial rig's dynamic control system, as discussed in the Methodology (Chapter 3). Tests lower than this rate, which are run using the static control system, record data points only every 3 seconds (compared to a fixed 1000 datapoints per test in the dynamic control method) which was insufficient for the analysis which follows. Whilst axial strain rates up to 180,000 %/hr were achievable, far greater control was possible by slightly reducing the maximum strain rate used to 100,000 %/hr (which makes little difference on the log axis used when considering rate effects). The deviator stresses shown are derived from the axial force measurements using Equation 4-10. A cylindrical deformation has been assumed throughout, as the use of lubricated end platens meant that a broadly cylindrical specimen shape was maintained during the test.

$$q = \sigma_1 - \sigma_3 \tag{4-10}$$

where:

σ_1 is the axial stress

σ_3 is the radial stress

From Figure 4-10, the main impacts of varying strain rates can be seen. As would be expected, each increase in strain rate is marked by an increase in deviator stress, when compared to other tests at the same initial mean effective stress. A shift in the strain at which peak deviator stress occurs is also observable with this strain appearing to reduce with increasing strain rate, indicating that rate effects may vary with strain level and are not constant throughout the test. Beyond 12 % axial strain, the specimens were observed to localise as a shear plane formed, with the strain at which this occurred varying significantly. There was no clear trend in the strain level at localisation in relation to strain rate.

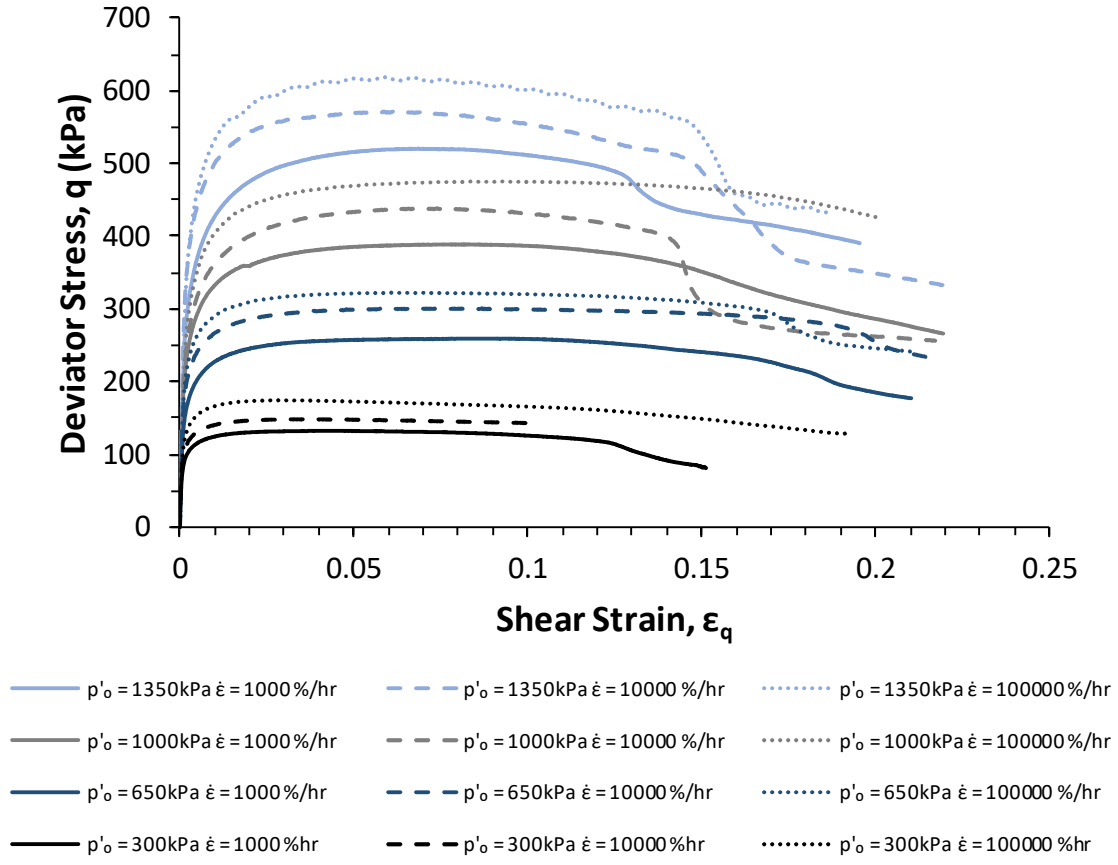

Figure 4-10 – Variation of deviator stress with shear strain at different initial mean effective stresses showing the influence of axial strain rate

4.2.2. Rate Effects on Peak Deviator Stress

In the consideration of rate effects, the two most prominent forms of models (identified in the literature review) used in undrained conditions to capture the response of deviator stress to varying strain rate are a power law (e.g. O'Loughlin *et al.*, 2009) or a semi logarithmic variation with strain rate such as that used in Sheahan *et al.* (1996) (See Equation 4-11 and Equation 4-12). The key factor in selecting the model to be used here was whether the rate effects were found to vary linearly in log-log space (as in Equation 4-11) or semi-log space (as in Equation 4-12).

$$\frac{q}{q_{ref}} = \left(\frac{\dot{\varepsilon}}{\dot{\varepsilon}_{ref}} \right)^{\beta} \tag{4-11}$$

where β is the rate exponent

$$\frac{q}{q_{ref}} = 1 + \lambda log\left(\frac{\dot{\varepsilon}}{\dot{\varepsilon}_{ref}}\right) \quad (4\text{-}12)$$

where λ is the increase in $\frac{q}{q_{ref}}$ per log cycle

Figure 4-11 shows the peak deviator stresses extracted from the stress-strain behaviour in Figure 4-10 for each strain rate. Comparison of the methods in Equations 4-11 and 4-12 found that the increase in deviator stress was best modelled using a semi-log relationship. This comparison was done prior to the deviator stresses being normalised, as normalising by a reference deviator stress, which in itself has a variability associated with it, led to increased scatter of the data points making the form of the relationship harder to determine. In the equations shown in Figure 4-11, the coefficient represents the absolute increase in deviator stress (in kPa) per log cycle increase in strain rate and the constant represents the intercept of the equation at a shear strain rate of 1 %/hr. As shown, the absolute increase in peak deviator stress per log cycle is greater at higher effective stresses, ranging from 20.8 kPa/log cycle at p'_0 = 300 kPa to 50.9 kPa/log cycle at p'_0 = 1350 kPa (although when deriving λ, this will reduce with p'_0 as q_{ref} also increases). The data points were found to have a standard deviation of 3.1 kPa, which was relatively constant for all of the initial mean effective stresses tested. Assuming that 95 % of the data points will lie within two standard deviations (SD), this indicates that the 95 % confidence limit for q_{peak} ranges from +/- 4.6 % at p'_0 = 300 kPa to +/- 1.2 % at p'_0 = 1350 kPa. Examination of the errors showed that the assumption of a normal error distribution was suitable in this case. Also shown in Figure 4-11 for comparison are the peak deviator stresses from the CID tests presented in Section 4.1 at p'_0 = 300 kPa and 650 kPa (which will also be undrained at the shear strain rates covered by Figure 4-11) to demonstrate the repeatability of the triaxial testing conducted. The datapoints at $\dot{\varepsilon}_q$ = 1000 %/hr for these CID tests are not visible as they overlap with the corresponding CIU tests.

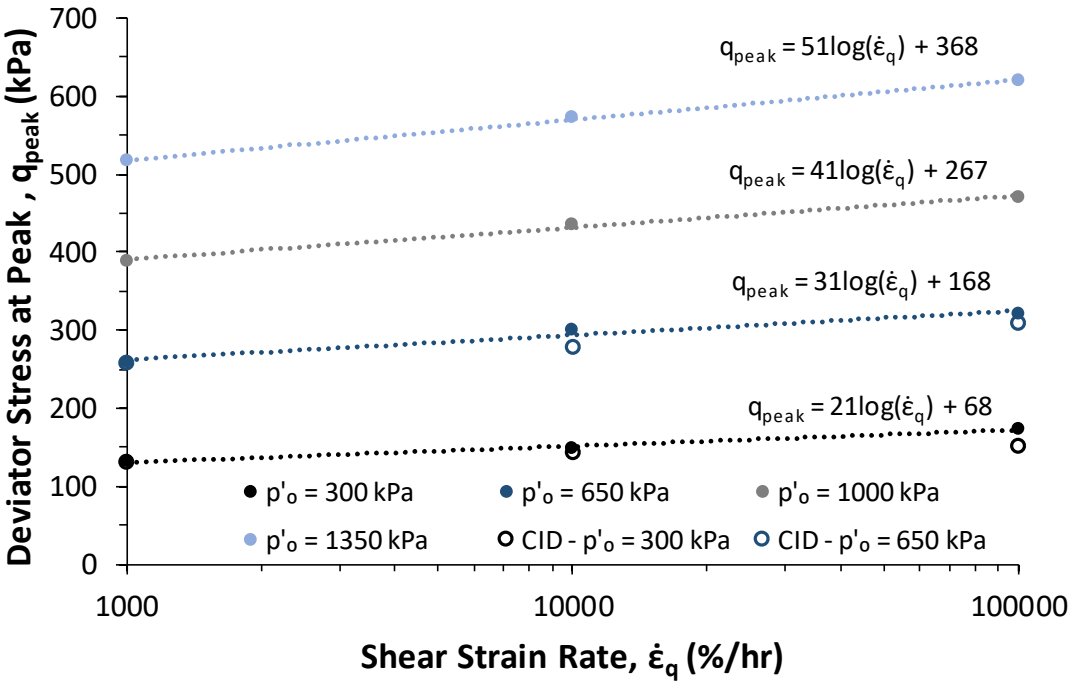

Figure 4-11 – Variation of peak deviator stress with shear strain rate for CIU specimens prepared at initial mean effective stresses ranging from p'_0 = 300 to 1350 kPa (including comparison with CID testing datapoints from Section 4.1 to demonstrate repeatability).

To enable the normalised rate effect per log cycle to be determined, it is necessary to normalise the peak deviator stresses by a reference stress, in this case the peak deviator stress at an shear strain rate of 1000 %/hr (and the corresponding initial mean effective stress). The horizontal axis has also been normalised by the lowest shear strain rate of 1000 %/hr, such that the lowest normalised strain rate will be 1; the intercept of the semi logarithmic relationship (Figure 4-12). This enables the normalised rate effect per log cycle, λ, to be determined from the gradient of the best fit line through all of the tests (at each initial effective stress). Figure 4-12 shows the values of λ ranging from 0.160 at the lowest effective stress down to 0.099 at the highest effective stress of p'_0 = 1350 kPa (close to the plastic limit, *LI* = 0.02), which is within the typical range for λ of 0.1 to 0.2 suggested by Einav and Randolph (2005) and Sheahan *et al.* (1996). This reduction in λ with increasing effective stress (or reducing moisture content) is consistent with several previous studies considered in the literature review (Briaud *and Garland, 1985*; Chow and Airey, 2013; Bea 1982), which all identified the same trend. However, it should be noted that these studies have provided little insight into the form of the relationship between moisture content (as an indicator of initial

effective stress) and rate effects. As can be seen, there is greater variability in the tests conducted at lower effective stresses, due to the fact that the absolute error in q_{peak} is more significant in percentage terms because of the lower value of the reference deviator stress, $q_{peak,ref}$.

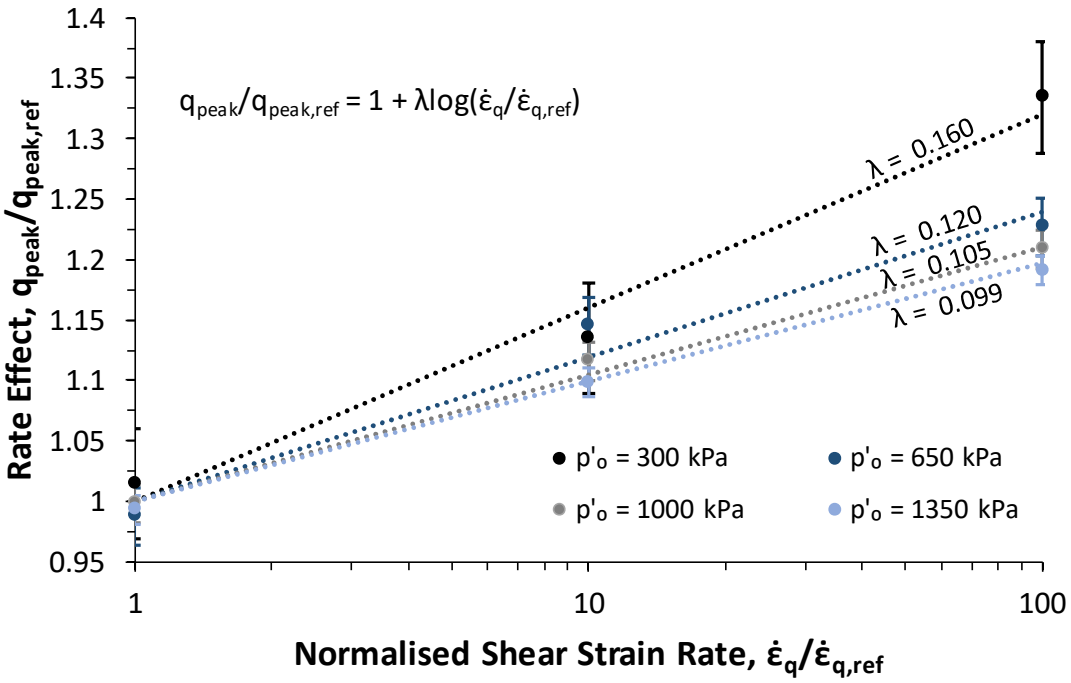

Figure 4-12 – Determination of normalised rate effects at peak strength for normally consolidated Kaolin at mean effective stresses from 300 to 1350 kPa ($\dot{\varepsilon}_{q,ref}$ = 1000 %/hr)

Another normalisation that is less commonly used is to normalise the deviator stress by the initial consolidation pressure, in this case p'_0. This is the approach used in studies such as Sheahan *et al.* (1996) and Bea (1982). The purpose of this normalisation is to attempt to remove variations in strength which occur due to differing consolidation pressure, as it is conventionally expected in static testing that soils display an approximately linear correlation between initial consolidation pressure and peak deviator stress. Figure 4-13 shows the same data which has previously been normalised by q_{ref}, but now normalised by p'_0. A key point to note is that for this study, the normalisation does not bring together the peak deviator stresses observed at the reference strain rate. This is due to the fact that the reference shear strain rate here is 1000 %/hr which is significantly higher than the conventional static reference axial strain rate of 1 %/hr (Kulhawy and Mayne, 1990). A result of this is that in this study, there is

still a significant rate effect component (i.e. the rate effects which may already be developed between the static rate of 1 %/hr and the slowest test at 1000 %/hr) at the reference strain rate, which varies between the differing moisture contents. However, it is a common form of normalisation used and is worthwhile to present. Sheahan *et al.* (1996) tested at significantly lower axial strain rates, (0.05 to 50 %/hr) which may explain why this normalisation was successful in that case as the strain rates used were closer to 'static' rates typically taken to be $\dot{\varepsilon}$ = 1 %/hr. Another consequence of this is that the rate effects per log cycle determined using this normalisation are artificially lower than those determined using q_{ref}, as shown in Figure 4-12. This is due to the fact that for any given test p'_0 is significantly greater than q_{ref} (q_{peak} is approximately one third of p'_0 for kaolin in 'static' conditions). This means that some of the results of studies such as Sheahan *et al.* (1996) and Bea (1982) may need to be adjusted before comparisons can be carried out, although it is noted that the authors do account for this fact in their final analyses. Hence, in all cases discussed in this study, q_{ref} will be used as the normalisation method.

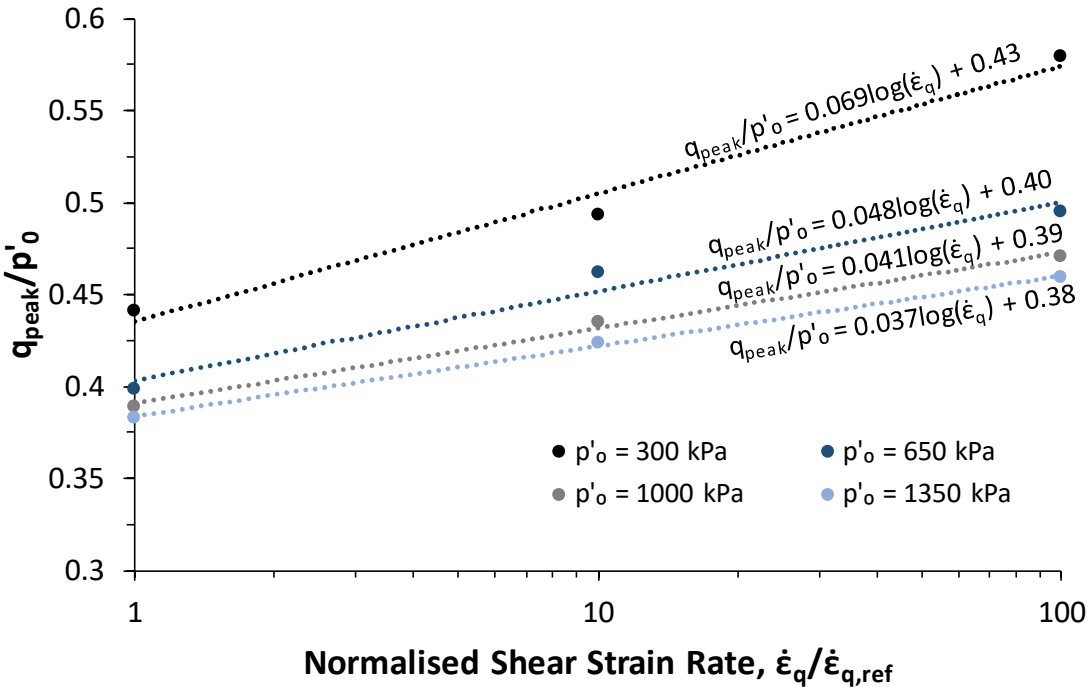

Figure 4-13 – Determination of rate effects per log cycle when normalising by p'_0 at initial mean effective stresses from 300 to 1350 kPa

As discussed, several studies have highlighted the impact of varying moisture content on rate effects. Examples include Chow and Airey (2013) based on free falling penetrometers, Briaud

and Garland (1985) and Bea (1982), both based on triaxial testing. Of these, the only studies to propose the form of the relationship between λ and moisture content are Briaud and Garland (1985) and Bea (1982). This is complicated further by the fact that Briaud and Garland (1985) used a power law to model rate effects, making the relationship difficult to compare with this study (raw data was also not presented by Briaud and Garland (1985)). Figure 4-14 shows the variation of λ determined from Figure 4-12 with liquidity index (See Equation 4-13) rather than effective stress. The rate effect per log cycle at peak deviator strength has been denoted λ_{peak}.

Liquidity index is a useful normalisation in terms of the moisture content as it defines the intercept of the y-axis as the plastic limit. Analysis of data from other studies in the literature review (Stone and Phan, 1995; Chow and Airey, 2011; Bea, 1982) indicates that there is little variation in the rate effect below the plastic limit, making this a useful reference point. As can been seen, the data from this study supports this assumption, with the change in λ_{peak} reducing as the plastic limit is approached, reaching a value of 9.9 % at a liquidity index of 0.02. It was found that the data could be best modelled using an equation of the form shown in Equation 4-14 such that λ_{peak} varies with the square of liquidity index. Where possible, correlations with specific volume, v, will also be provided to make the results more easily applied in areas such as numerical modelling. This was done by substitution of the correlation between LI and v (Equation 4-15) which for Kaolin resolves to Equation 4-16.

$$LI = \frac{w - PL}{LL - PL} \tag{4-13}$$

where w is the average moisture content of the tests at any given effective stress; PL is the plastic limit and LL is the liquid limit.

$$\lambda_{peak} = \lambda_{peak,PL} + \alpha_{peak} LI^2 \tag{4-14}$$

where $\lambda_{peak,PL}$ is the normalised rate effect per log cycle on peak deviator stress at the plastic limit; α_{peak} is a coefficient and LI is the liquidity index.

$$LI = \frac{v - 1}{2.65PI} - \frac{PL}{PI} \tag{4-15}$$

where PL is the plastic limit and PI is the plasticity index

$$LI = 1.16v - 2.16 \quad \textit{for Kaolin} \tag{4-16}$$

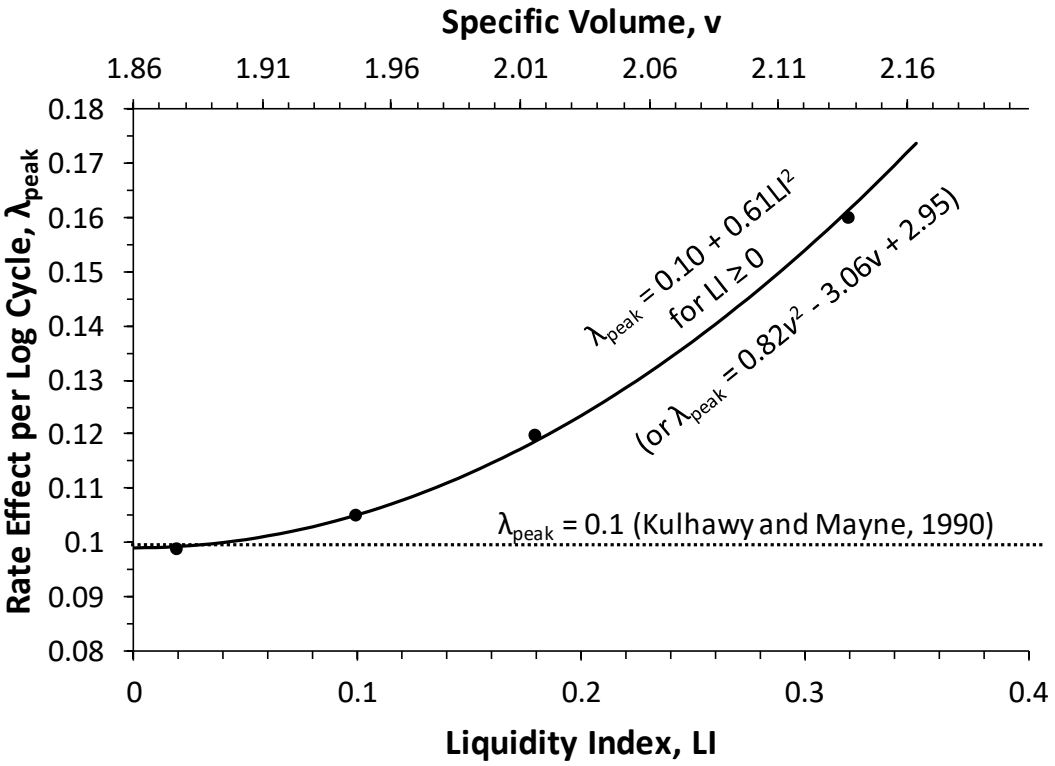

Figure 4-14 – Variation of rate effect at peak strength with liquidity index (and specific volume) for normally consolidated Kaolin

For normally consolidated kaolin, $\lambda_{peak,PL}$ and α_{peak} were found to be 0.10 and 0.61 respectively. The most commonly cited reference in relation to strain rate effects is that of Kulhawy and Mayne (1990) which suggests a constant value of λ_{peak} of 0.1. One of the main reasons that Kulhawy and Mayne (1990) is relied upon is that it consists of the analysis of a large number of tests on 26 clays using real field samples. However, as identified in the literature review, the study does not take account of any liquidity index variation. Liquidity index data for the tests analysed is not presented in Kulhawy and Mayne (1990), however, many of the field samples are overconsolidated and likely to be closer to the plastic limit, skewing the data towards the lower range of observed rate effects and potentially explains why rate effects are often quoted as being 10 % per log cycle. On this basis, the suggested value of 0.1 compares well to the rate effect determined near the plastic limit in this study of 0.10. Given that clays analysed by Kulhawy and Mayne (1990), such as Lyndhurst clay, exhibited rate effects of up to 17 % per log cycle, the rate effect observed at the highest liquidity index tested of 16 % per log cycle appears reasonable.

There are no other published relationships between λ and liquidity index for comparable Kaolin currently available, as Bea (1982) tested Gulf of Mexico Clay (GMC) and Chow and Airey (2011) used Kaolin with substantially different properties to that used here. However, it is still useful at this stage to validate the form of the proposed relationship to confirm if it is able to model the derived rate effects from these studies, despite the fact that the magnitude of the rate effects may vary. This will be an important consideration once multiple soil types are included in the framework. Figure 4-15 shows the rate effects from Bea (1982) and Chow and Airey (2011) against liquidity index. Bea (1982) found that the rate effects for Gulf of Mexico clay (GMC) could be modelled by Equation 4-17.

$$\lambda = \frac{OCR}{S_u / \sigma'_v} e^{\left(\frac{LI-2}{0.42}\right)} \tag{4-17}$$

where OCR is the overconsolidation ratio (the tests by Bea (1982) were normally consolidated)

S_u/σ'_v is the ratio of undrained shear strength to vertical effective stress (0.25 for GMC)

LI is the liquidity index.

This means that Equation 4-17 resolves to Equation 4-18:

$$\lambda = 4e^{\left(\frac{LI-2}{0.42}\right)} \text{ for normally consolidated Gulf of Mexico Clay} \tag{4-18}$$

LI^2 relationships have been fitted to both of these studies to check if this form is suitable. As shown in Figure 4-15, the proposed LI^2 relationships (shown by the dotted lines) can closely replicate the rate effect variation determined by both Bea (1982) and Chow and Airey (2011) indicating that it is suitable for modelling rate effects in multiple soils. In fact, the LI^2 relationship provides a better fit to the data from Bea (1982) up to LI = 1 than Equation 4-18 proposed by the authors (which is also shown in Figure 4-15). Interestingly, the value of $\lambda_{peak,pl}$ of 0.08 derived from the the data from Bea (1982) supports the idea that near the plastic limit, rate effects are more likely to be close to the value of λ = 0.1 suggested by Kulhawy and Mayne (1990).

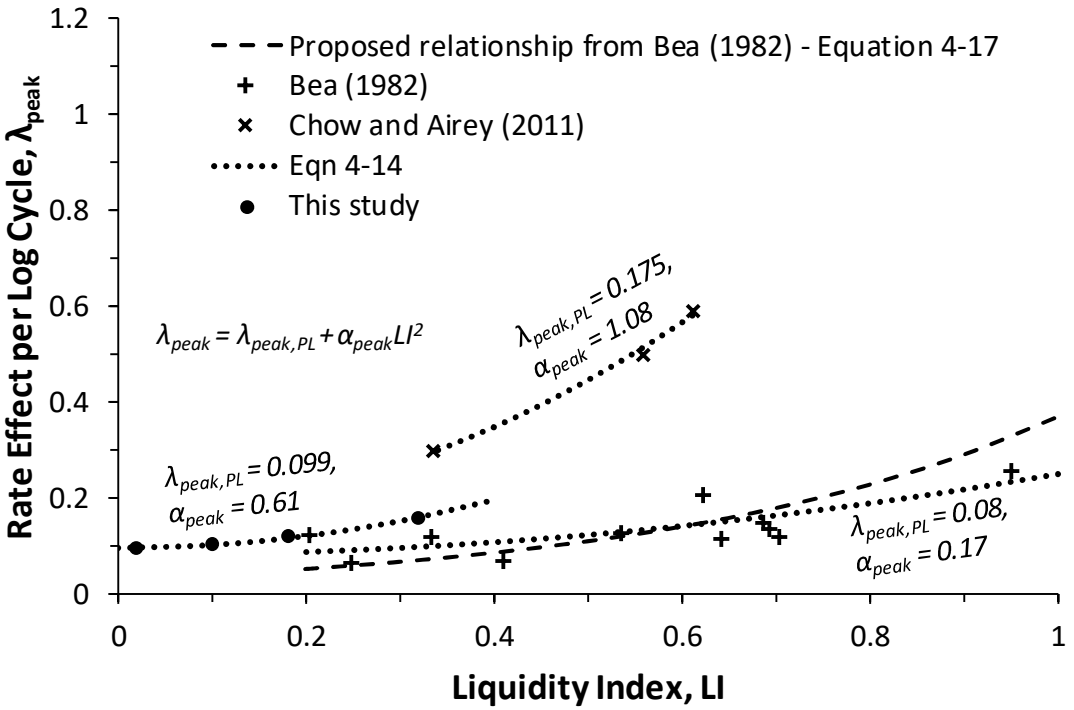

Figure 4-15 – Comparison of LI^2 relationship with peak rate effects from other studies

4.2.3. Influence of Overconsolidation Ratio

Based on the literature review, the evidence of the influence of overconsolidation ratio on rate effects has been variable. Examples include Briaud and Garland (1985) which found that rate effects increased with overconsolidation ratio (OCR), whilst Sheahan *et al.* (1996), Lehane *et al.* (2009) and Graham *et al.* (1983) found no impact of OCR on rate effects. To consider this issue further, additional tests on Kaolin specimens at an OCR of 6 were conducted (See Figure 4-16). These tests were conducted in the same manner as the normally consolidated tests, with the exception of an additional swelling stage were the effective stress was reduced from p'_{max} = 650 kPa to p'_0 = 108 kPa.

Using the same process previously described, the rate effect per log cycle, λ, was found to be 12.7 % for an OCR of 6. Initial inspection would suggest that, as this value is greater than the rate effect observed at a similar maximum effective stress in normally consolidated Kaolin (λ = 12.0 %), then overconsolidation slightly increases the observed rate effects. However, when compared at the same liquidity index (i.e. similar specific volume or moisture content), it is clear that the overconsolidated testing fits well with the previously determined relationship

between λ and *LI* from normally consolidated testing (See Figure 4-17). This indicates that the slight increase in rate effect is likely to be due to the increase in liquidity index which occurs during the swelling phase and when compared at the same liquidity index, overconsolidation has no observable impact on the measured rate effects. Figure 4-18 also shows the rate effects from the OC and NC tests plotted against effective stress, highlighting the difference in the observed OC rate effects when liquidity index is not taken into account.

This finding supports the conclusion identified in the literature review that after the effect of changes in liquidity index are taken into account, there is no observable influence of OCR on rate effects at peak strength. The literature review covered all of the available OCR rate effect studies with sufficient information including Graham *et al.* (1983), Briaud and Garland (1985), Sheahan *et al.* (1996), Zhu and Yin (2000) and Lehane *et al.* (2009). All of these either found no influence of OCR, or changes with OCR which can be explained by changes in liquidity index between the specimens (discussed in detail previously in Chapter 2).

The key point to note, as shown in Figure 4-18, is that despite a significant change in stress history compared to the normally consolidated samples, the tests at OCR = 6 display only slightly higher rate effects than the test at the same p'_{max} of 650 kPa. Additionally, this small difference can be explained by the small increase in liquidity index which occurs by swelling during overconsolidation, as shown in Figure 4-17. This suggests that the controlling variable for rate effects is the current soil state (whether specific volume, voids ratio or liquidity index are used as a comparator), rather than the specimen's stress history in terms of OCR. Given these findings and their consistency with other studies after re-evaluation, along with the need to focus the scope of this study, further investigation of rate effects in overconsolidated specimens was not carried out.

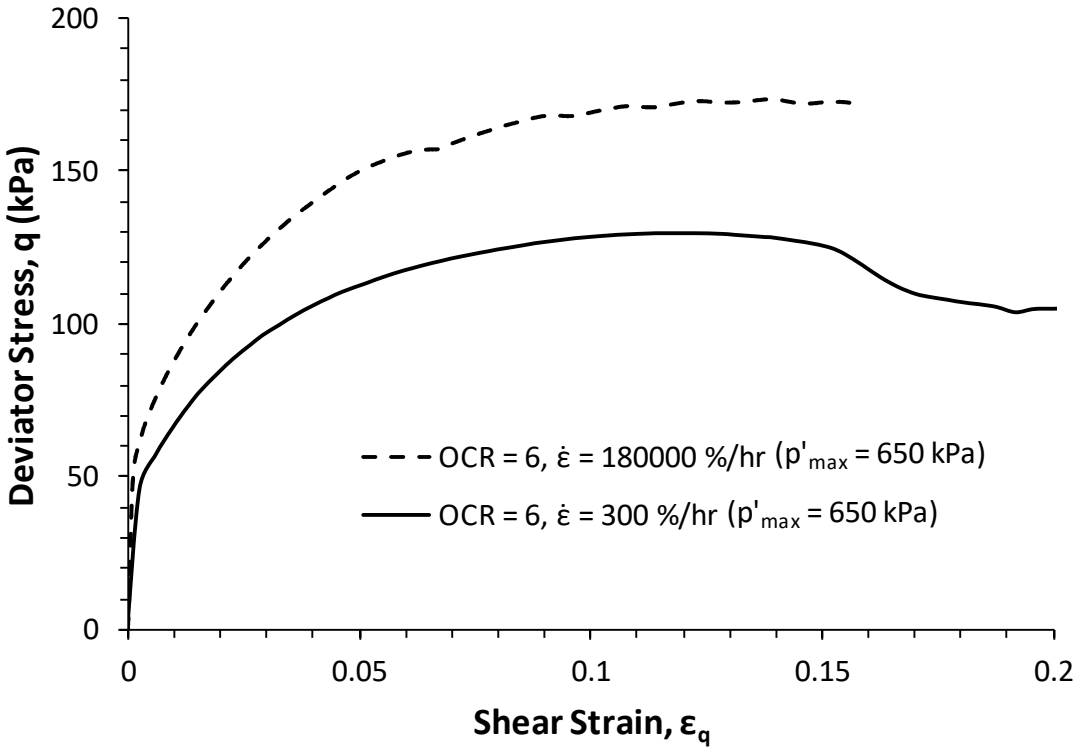

Figure 4-16 – Graph of deviator stress against shear strain for overconsolidated tests on Kaolin (*LI* = 0.225)

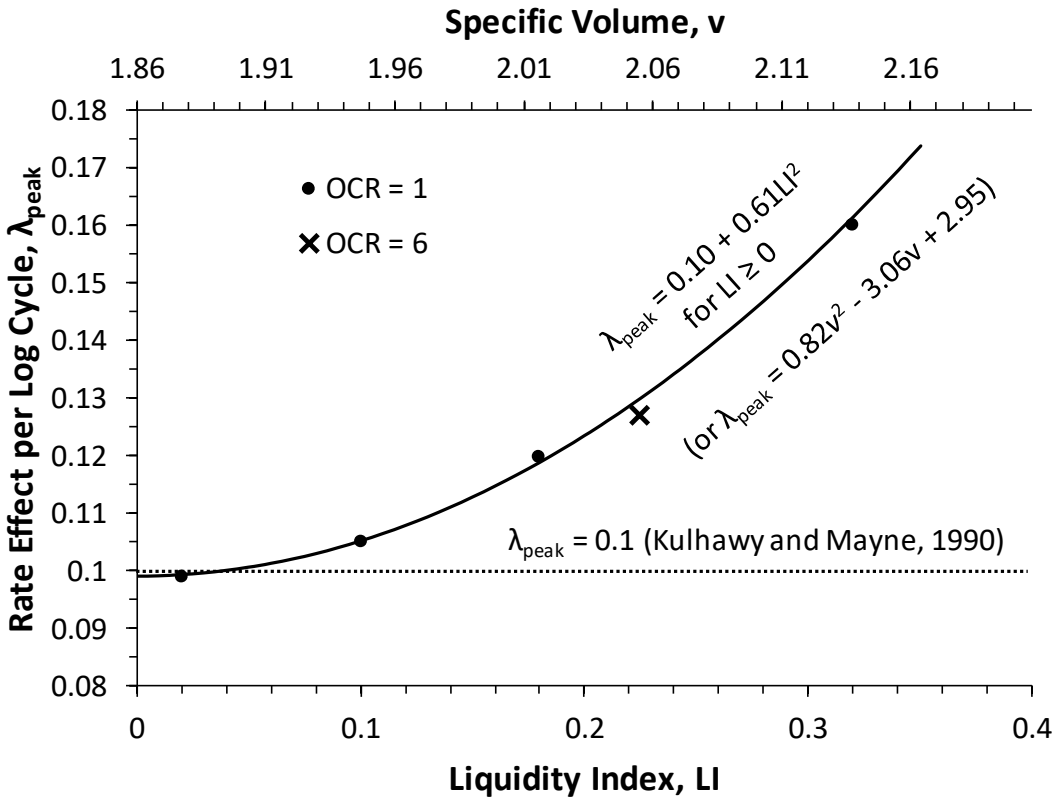

Figure 4-17 – Impact of OCR on rate effects when using Liquidity Index as a comparison

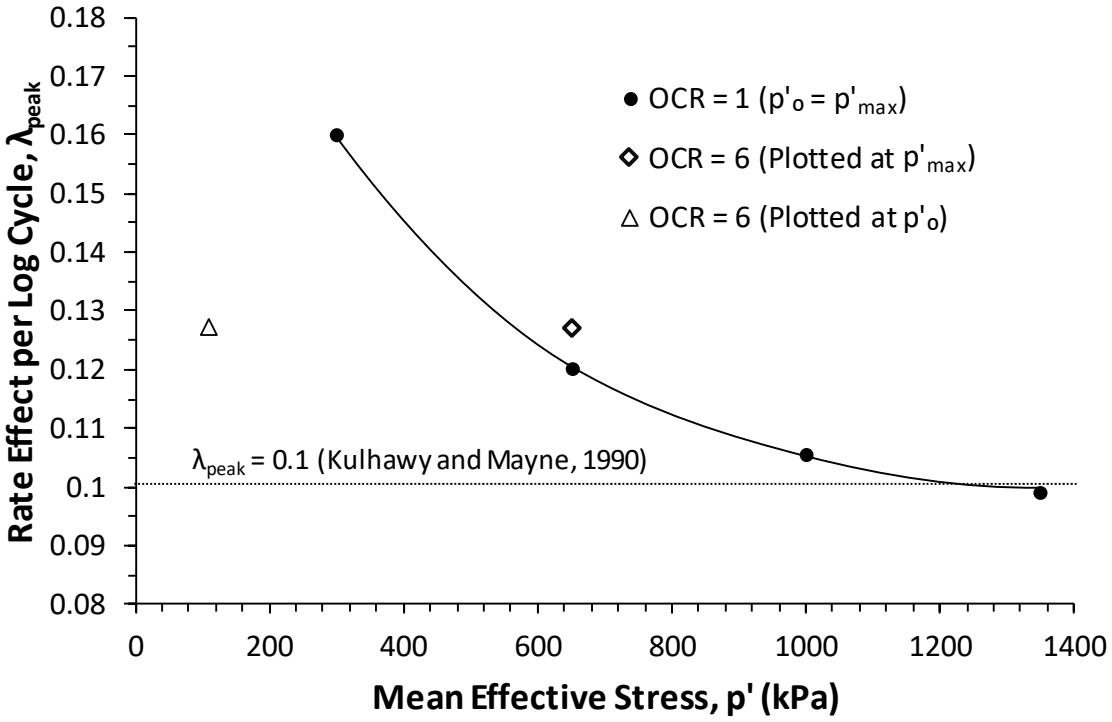

Figure 4-18 – Impact of OCR on rate effects when using effective stress as a comparison

4.2.4. Rate Dependence of Strain at Peak Strength

All of the deviator stresses considered in analysis up to this point in the thesis have been defined at peak, as has been the normal practice in the vast majority of rate effects studies. However, one issue which arises using this approach is the fact that the strain at which the peak deviator stress occurs is in itself influenced by the strain rate, meaning that the definition of the strain at peak is not consistent. Figure 4-19 shows the variations in the strain at which peak strength occurs for each axial strain rate and initial mean effective stress, p'_0, with the strain at peak ranging from 3.2 to 8.7 % shear strain (Table 4-7). There is a clear trend showing that this strain reduces with increasing strain rate. The strain at peak is also influenced by the initial mean effective stress, with the tests at p'_0 = 650 kPa and 1000 kPa exhibiting the highest strains at peak strength. The strain at peak for the test carried out at p'_0 = 1000 kPa and $\dot{\varepsilon}$ = 100000 %/hr is not shown as this data point was found to be an outlier, with the strain at peak being almost double the expected value. This issue is believed to be specific to the individual test. The reason for the 'bell-shaped' curve caused by effective stress dependence is not clear. One possibility is that the effectiveness of the lubricated end platens is reduced at the highest effective stress of p'_0 = 1350 kPa, but there is currently no evidence to suggest this. If this were to be the case, then the relationship could tend to a plateau beyond p'_0 = 1000 kPa.

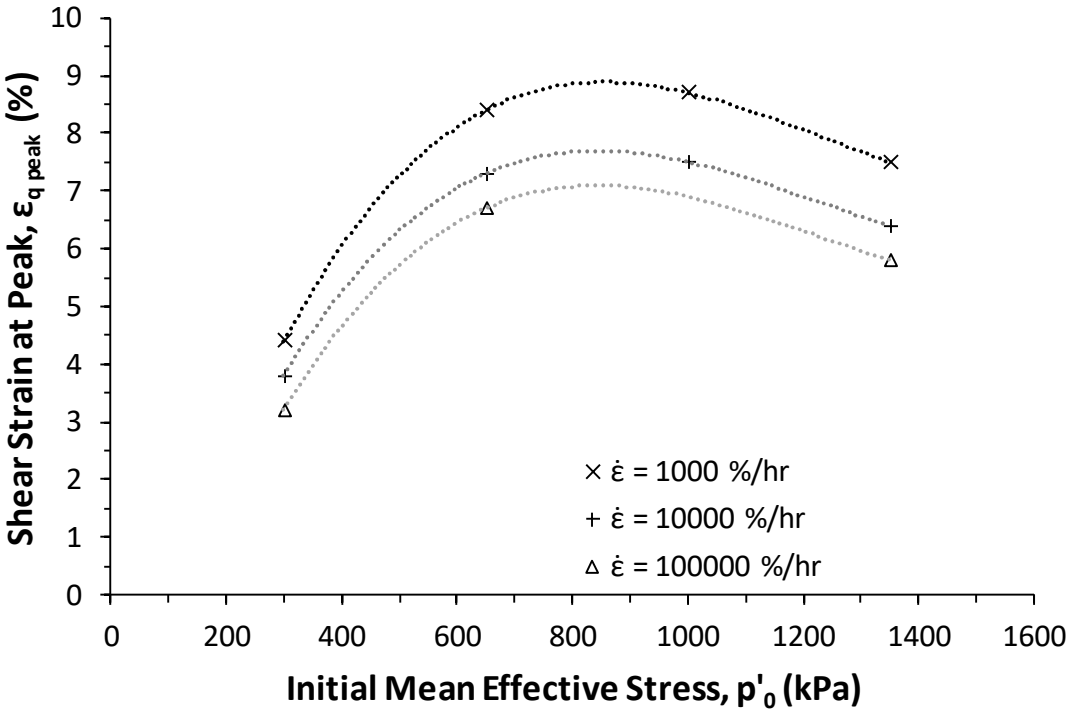

Figure 4-19 – Variation in strain at peak strength with effective stress for varying axial strain rates in Kaolin

Table 4-7 – Strain at which peak strength occurs

Axial Strain Rate (%/hr)	Initial Mean Effective Stress, p'$_0$ (kPa)			
	300	*650*	*1000*	*1350*
1000	4.4 %	8.4 %	8.7 %	7.5 %
10000	3.8 %	7.3 %	7.5 %	6.4 %
100000	3.2 %	6.7 %	-	5.8 %

Figure 4-20 shows the strain at peak, which has been normalised by the corresponding strain at peak at the reference shear strain rate of 1000 %/hr, in an attempt to account for the fact that there is clearly an impact of initial effective stress/moisture content, as well as any variation related to the change in strain rate. Using this normalisation, a clear trend can be seen in the normalised strain at peak which reduces linearly by approximately 12 % per log cycle increase in strain rate. This was found to be consistent across all of the effective stresses and moisture contents investigated, indicating that the normalisation appears to successfully account for the impact of p'_0 and moisture content on the strain at peak. The relationship

between strain at peak and shear strain rate for Kaolin was found to be as shown in Equation 4-19.

$$\frac{\varepsilon_{q,peak}}{\varepsilon_{q,peak,ref}} = 1 - 0.12 log\left(\frac{\dot{\varepsilon}_q}{\dot{\varepsilon}_{q,ref}}\right) \quad (4\text{-}19)$$

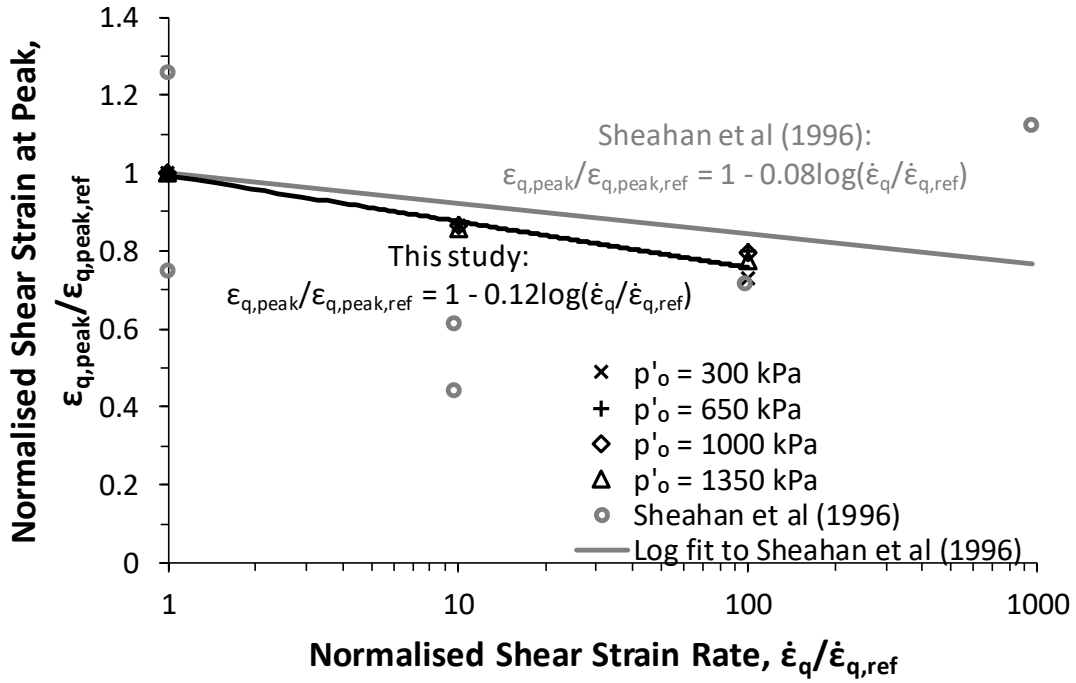

Figure 4-20 – Variation of normalised strain at peak with normalised shear strain rate from this study (Kaolin) compared with Sheahan *et al.* (1996) (Boston Blue Clay)

Few other studies have considered the impact of strain rates on strain at peak, making comparison of this finding difficult. Sheahan *et al.* (1996) considered the impact on strain at peak using triaxial testing of Boston Blue Clay (BBC), and the strains at peak from this study are also shown in Figure 4-20, although it should be noted that this data is from substantially lower axial strain rates (0.05 to 50 %/hr). Plotting a relationship of the same form as Equation 4-19 through the data from Sheahan *et al.* highlights that there is a general reduction in $\varepsilon_{q,peak}$ with strain rate, with the reduction per log cycle being less than the reduction observed in Kaolin. This would seem reasonable, as the BBC was found to have lower rate effects in terms of deviator stress as well.

However, the data from Sheahan *et al.* (1996) also has an order of magnitude more variability. One potential reason for this is the test setup used. Sheahan *et al.* (1996) used an adapted

method for implementing the lubricated end platens which are essential for ensuring the homogeneity of the specimens and preventing premature localisation. The method used by Sheahan *et al.* (1996) excludes the latex membrane which normally separates the greased smooth platen from the specimen. Tests to consider the impact of this approach found that in these circumstances, some of the lubricating grease was absorbed into the specimen which could lead to an increase in end friction. This would mean that they could behave in a similar manner to smooth end platens rather than true lubricated end platens, potentially leading to premature localisation of the samples. Tests where Sheahan *et al.* (1996) noted issues occurred have been excluded from Figure 4-20. Due to the low axial strain rates (up to 50 %/hr) used by Sheahan *et al.* (1996), another possible explanation for the variability could be local drainage within the triaxial specimens, as discussed previously.

Mun *et al.* (2016) also considered the influence of strain rate on the strain at peak strength (which was referred to as the point of 'failure') based on triaxial testing of compacted clay from Boulder, Colorado, at axial strain rates from 6 to 6000 %/hr. Figure 4-21 shows that as found in this study, where a peak strength was observed, the strain at which this occurred reduced with increasing strain rate. This can be seen for the tests conducted at moisture contents of 11.5 and 13.5 %. For the tests at higher moisture contents, no peak strength was observed before the end of the tests at ε_q = 15 %. It should, however, be kept in mind that the tests conducted by Mun *et al.* (2016) had varying degrees of saturation and hence it is difficult to draw conclusions from the study other than that the strain at peak reduces with strain rate.

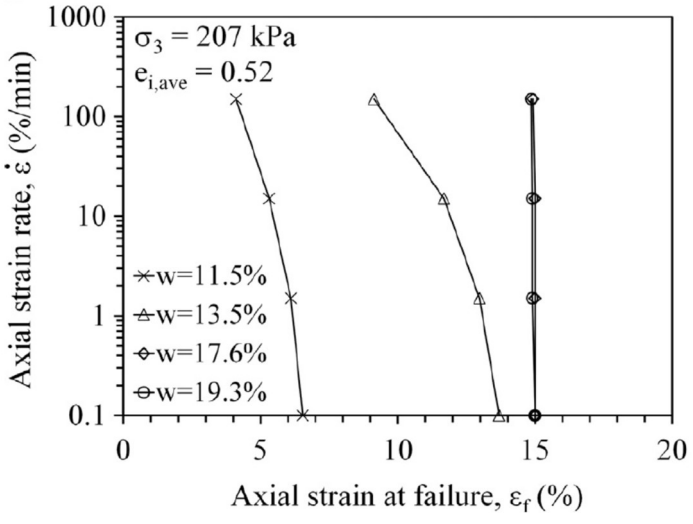

Figure 4-21 – Variation of strain at peak strength with axial strain rate for compacted Boulder Clay (Mun *et al.*, 2016) at varying moisture contents

4.2.5. Strain Dependence of Rate Effects

The results discussed in this chapter considered the large strain (externally measured) deformation of the specimens and the results of the tests conducted using local (on-sample) small strain measurement are considered in Chapter 6. However, the large strain data can still provide useful insight into how rate effects mobilise throughout the entire strain range measured, whereas the tests using local strain measurements are limited to the consideration of axial strains of up to ε = 1.5 % due to the equipment limitations discussed in Chapter 3.

Figure 4-22 shows the stress-strain response of the specimens tested at each of the four initial mean effective stresses, annotated with the yield points, (defined as the elastic shear strain threshold, $\varepsilon_{q,EL}$) and observed initial shear secant moduli based on the global displacement measurements in a similar manner to Shibuya *et al.* (1996). From this, it can be seen that the yield point at the reference strain rate (at each of the effective stresses) marks a clear transition point above which rate effects begin to mobilise, as also found by Shibuya *et al.* (1996) and Lo Presti *et al.* (1996). Below this yield point, negligible variation can be seen between the stress-strain curves at the various strain rates. Several previous studies have also reported the rate independence of deviator stress below the yield point (Mukabi and Tatsuoka, 1999; Santagata, 2008). It is only beyond this point that strain rate dependent differences in the deviator stresses start to be seen (in large strain measurements). This appears to be due to the fact that the increased strain rate results in yield of the sample occurring at a higher strain, similar to the findings of Shibuya *et al.* (1996). Coupled with the fact that no change is observed in the initial stiffness, the higher deviator stresses result. As the slowest (1000 %/hr) axial strain rate test yields, the two faster strain rate tests (10,000 and 100,000 %/hr) continue at the initial stiffness generating a difference in deviator stress between the two faster rates and the reference strain rate. This continues until the next slowest rate (10,000 %/hr) yields, whilst the fastest rate (100,000 %/hr) maintains the initial stiffness resulting in further deviator stress variations between them. Due to the limitations of the global strain measurements, quantitative analysis of the yield behaviour of the specimens has not been carried out here, as the intervals between the data points prevent accurate identification of the yield points. This aspect will be discussed further in the small strain behaviour chapter (Chapter 6).

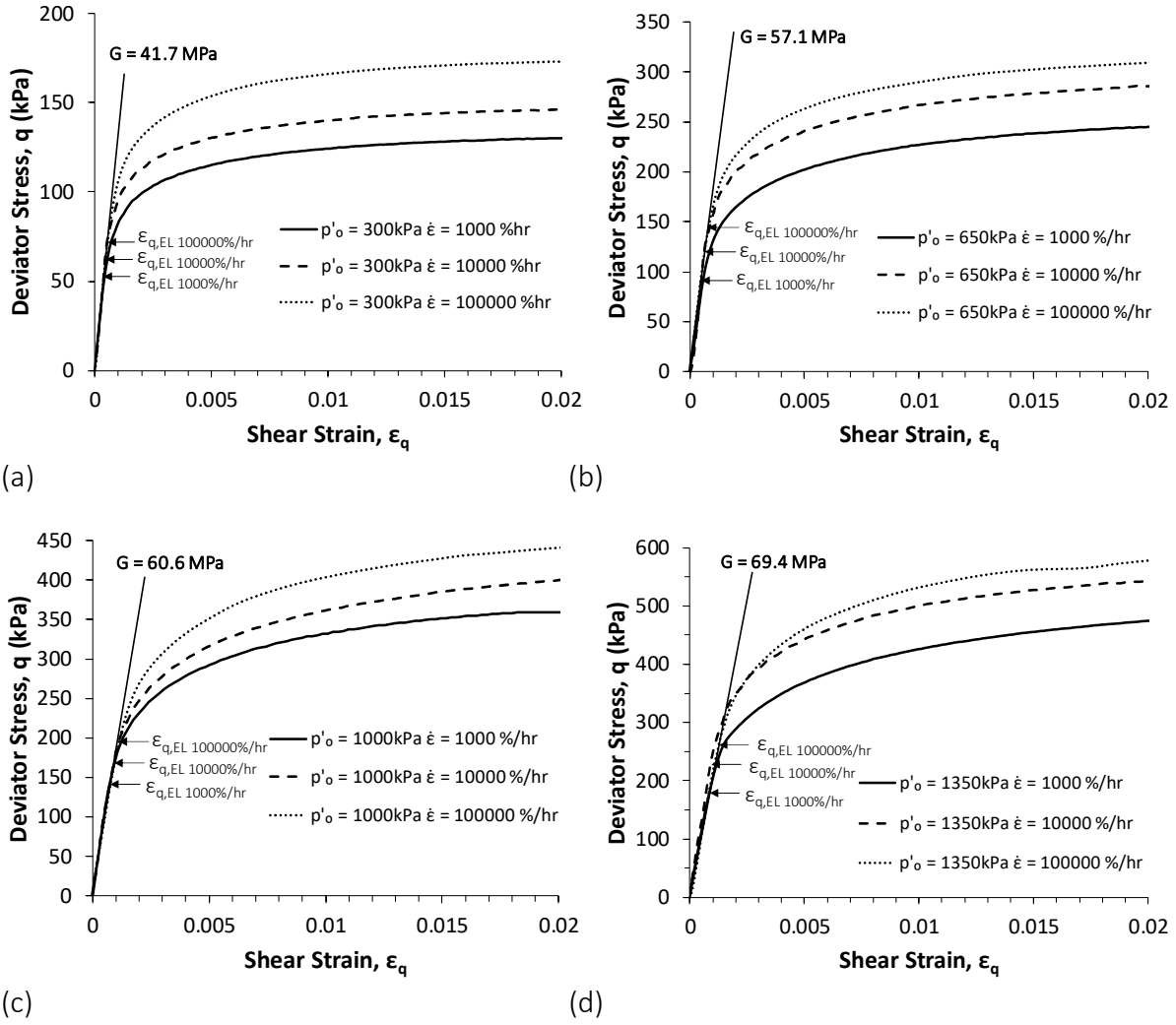

Figure 4-22 – Effect of axial strain rate on the stress-strain response of Kaolin from global strain measurements at (a) p'_0 = 300 kPa, (b) 650 kPa, (c) 1000 kPa and (d) 1350 kPa

Discussion of the rate effect per log cycle, λ, up to this point in the discussion has used a definition of peak strength as the point of interest. However, by instead defining the rate effects at a given strain level, the variation of λ with strain can be considered. Figure 4-23 shows this variation, which has been determined following the same process as that used for the analysis of peak strength rate effects, but with a strain-based definition. Several features of the strain response are clear; after rate effects begin to mobilise following the yield of the specimen at the reference strain rate, the rate effects reach a maximum value, denoted λ_{max}, before beginning to degrade. The shear strain at which λ_{max} occurs has been denoted $\varepsilon_{q,\lambda max}$. This degradation continues until a strain of between 8 and 10 % is reached, at which point the rate effect deviates from the preceding trend due to sample localisation and the beginning of

visible shear plane formation. As previously discussed in Section 4.2.1, there is no observable trend in the strain where localisation occurs with strain rate, meaning that any of the three tests at each effective stress may localise first. If a localisation forms first in the slowest (reference) test this causes an increase in λ after 8-10 % strain, whilst if a higher strain rate test localises first then a reduction in λ is observed. Rate effects have not been calculated beyond 10 % strain as after this point, the localisations lead to large variations in the deviator stresses that are strain rate independent. This means that it is no longer reasonable to use λ to represent the rate effects beyond this point, as λ is dependent on a linear correlation between $log(\dot{\varepsilon})$ and deviator stress. The rate effects at an effective stress of 1350 kPa show oscillations which started beyond $\varepsilon_{q,\lambda max}$. These are due to the fact that axial displacement gain control issues were experienced in the test at $\dot{\varepsilon}$ = 100,000 %/hr, resulting in reduced axial strain rate control leading to the observed variations in λ with strain. Figure 4-23 also highlights the influence of soil state (determined by p'_0) on rate effects throughout the strain range, not just at peak strength.

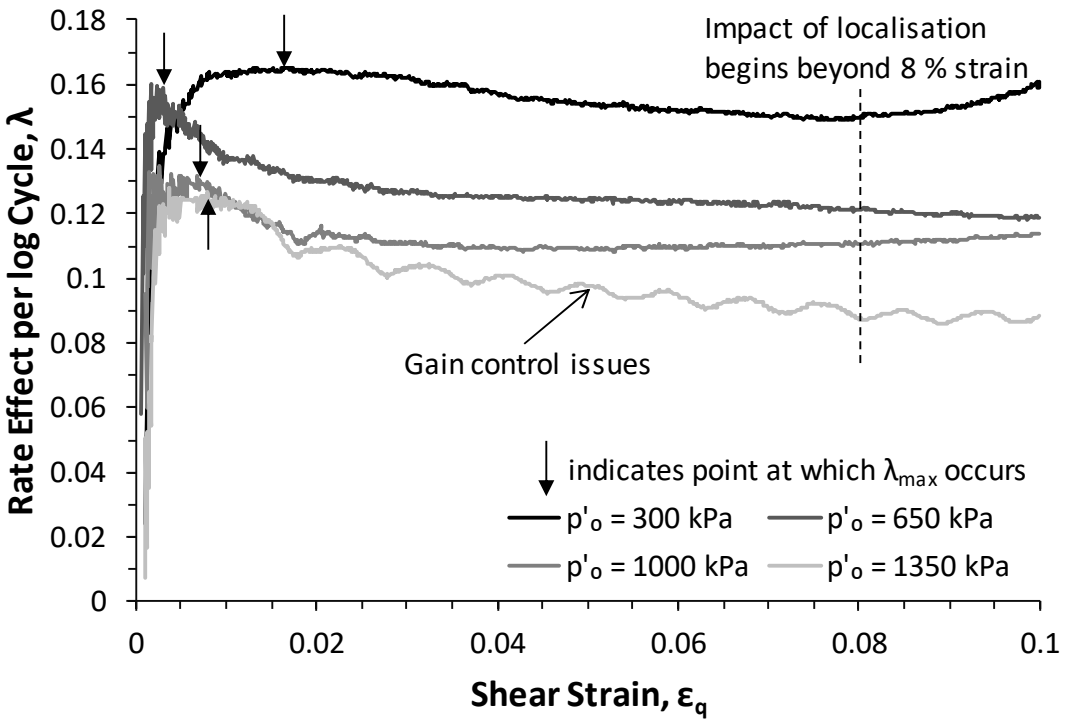

Figure 4-23 – Variation in rate effect with strain by defining λ using strain level rather than at peak strength

Table 4-8 shows the shear strains at which the maximum rate effects were observed for each of the four effective stresses. These varied from 0.33 to 1.78 %. On average, the shear strain at which the maximum rate effect occurred was 0.92 %. There is some evidence that this value for the shear strain at λ_{max} of approximately 1 % is relatively constant based on Lo Presti *et al.* (1996). This study found that the maximum strain rate coefficient, α, determined from resonant column testing was shown to occur near ε_q = 1 % for a wide range of clays with plasticity indexes ranging from 10 to 40 %.

Table 4-8 – Strain at which maximum rate effect occurs for Kaolin (based on external strain measurements)

p'_o (kPa)	*300*	*650*	*1000*	*1350*	*Average*
Strain at λ_{max}, $\varepsilon_{q,\lambda max}$ (%)	1.78	0.33	0.71	0.87	0.92

In order for the variation of rate effects at large strains to be modelled, one feature which is of interest is the manner in which rate effects degrade beyond the point of maximum rate effect, λ_{max}. Figure 4-24 shows a typical $\lambda - \varepsilon_q$ variation, plotted semi logarithmically, which shows that beyond $\varepsilon_{q,\lambda max}$ rate effects appear to degrade linearly with $log(\varepsilon_q)$. Considering all of the effective stresses investigated, a linear degradation of λ with $log(\varepsilon_q)$ was found to provide the best overall fit to the measured data.

The two key parameters in defining a semi-logarithmic relationship are the value at the intercept with the y axis (at a value of x = 1) and the change per log cycle. Conveniently, in this case, these correspond to the value of the rate effect at ε_q = 1 %, which is the approximate location of the maximum rate effect, λ_{max}, and the change from this point to ε_q = 10 %, which is typically close to the final point before localisation occurs. This means that it may be possible to model the strain dependent degradation of rate effects in the strain range from 1 to 10 % using Equation 4-20. The two rate effect parameters which require to be determined have been denoted $\lambda_{\varepsilon q=1\%}$ and $\lambda_{\varepsilon q=10\%}$ respectively.

$$\lambda = \lambda_{\varepsilon q=1\%} - (\lambda_{\varepsilon q=1\%} - \lambda_{\varepsilon q=10\%}) log(\varepsilon_q) \quad (4\text{-}20)$$

where:

ε_q is in percent

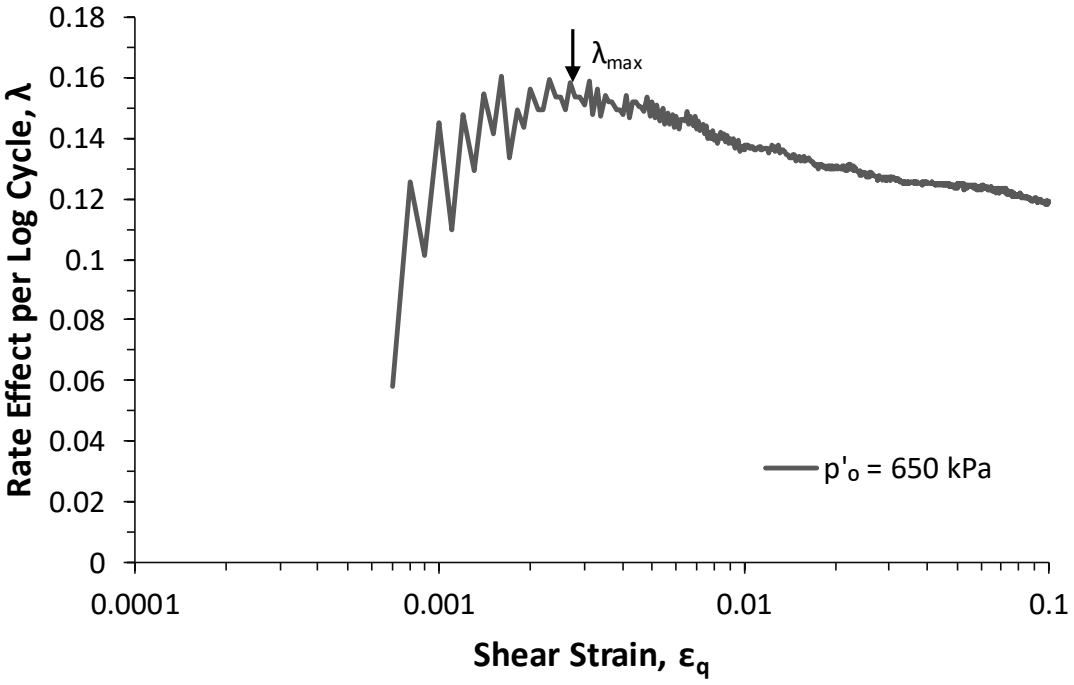

Figure 4-24 – Form of rate effect degradation after maximum rate effect at p'_0 in Kaolin

The measured rate effects per log cycle, λ, at each of the effective stresses used are shown in Figure 4-25 at both ε_q = 1 % and 10 %, which highlights the reduction in rate effects with increasing strain. Figure 4-26 shows the variation of these two key parameters with liquidity index in a similar manner to that used to show the variation of λ_{peak} with liquidity index previously. Where localisations have affected the measured rate effects before ε_q = 10 %, the final point before the onset of localisation has been used instead of ε_q = 10 % in Figure 4-25. The datapoint for p'_0 = 1350 kPa (LI = 0.02) at ε_q = 10 % has been removed due to the previously discussed gain control issues which affected one of the specimens. A least mean square regression has been used to determine the best fit of an LI^2 relationship to the measured rate effects at both ε_q = 1 % (max rate effect) and ε_q = 10 %. The relationship between λ_{peak} and LI determined previously is also included for comparison, highlighting the fact that care should be taken when using λ_{peak}, particularly at conditions close to the plastic limit where values of λ_{peak} are lower than the range of values determined using a consistent strain based definition. The rate effects at 1 % and 10 % shear strain can be represented by Equation 4-21 and Equation 4-22. Substituting these into Equation 4-20 shows that the rate effect in Kaolin (at large strains beyond 1 % shear strain) at any liquidity index and strain level can be represented by Equation 4-23.

$\lambda_{\varepsilon q=1\%} = 0.120 + 0.43LI^2$ (4-21)

$\lambda_{\varepsilon q=10\%} = 0.109 + 0.39LI^2$ (4-22)

where the constant represents the value at the plastic limit, λ_{pl}, which is the intercept with the y-axis at $LI = 0$.

$\lambda = 0.120 + 0.43LI^2 - (0.011 + 0.04LI^2)log(\varepsilon_q)$ (4-23)

where ε_q is in percent

Figure 4-27 shows the fit of the above model (dashed lines) to each of the liquidity index/effective stresses tested, represented by the dashed lines. As can be seen, the model provides a reasonable approximation of the measured data with the difference in λ not typically exceeding 0.75 %, with the exception of the 1350 kPa tests where gain control issues were experienced.

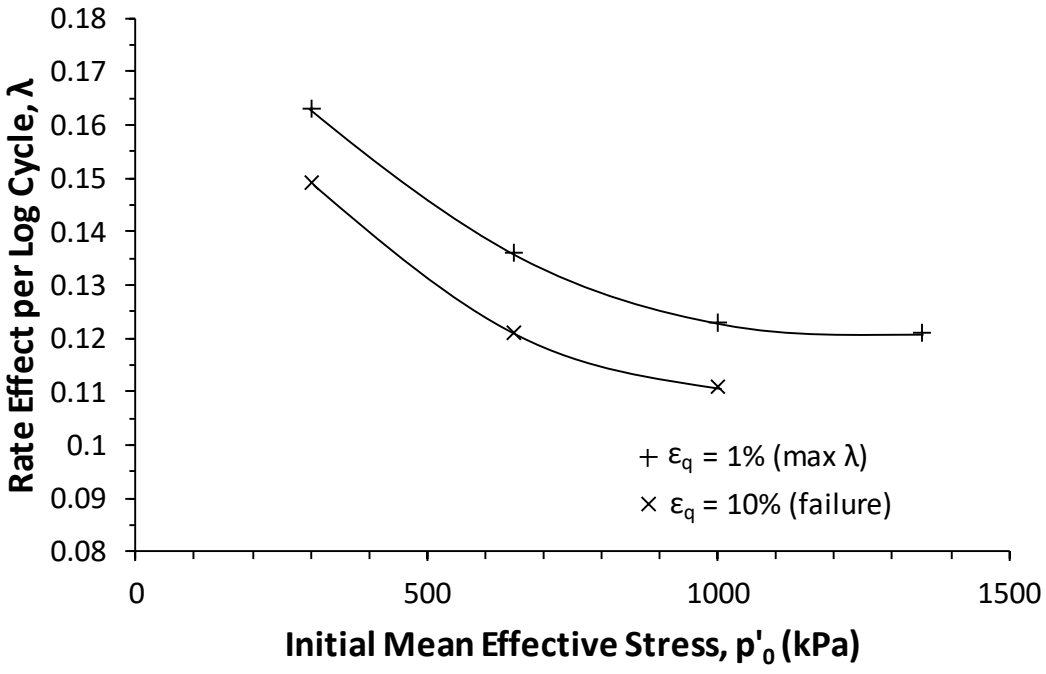

Figure 4-25 – Variation of rate effects at 1 % and 10 % strain with p'_0 for normally consolidated Kaolin

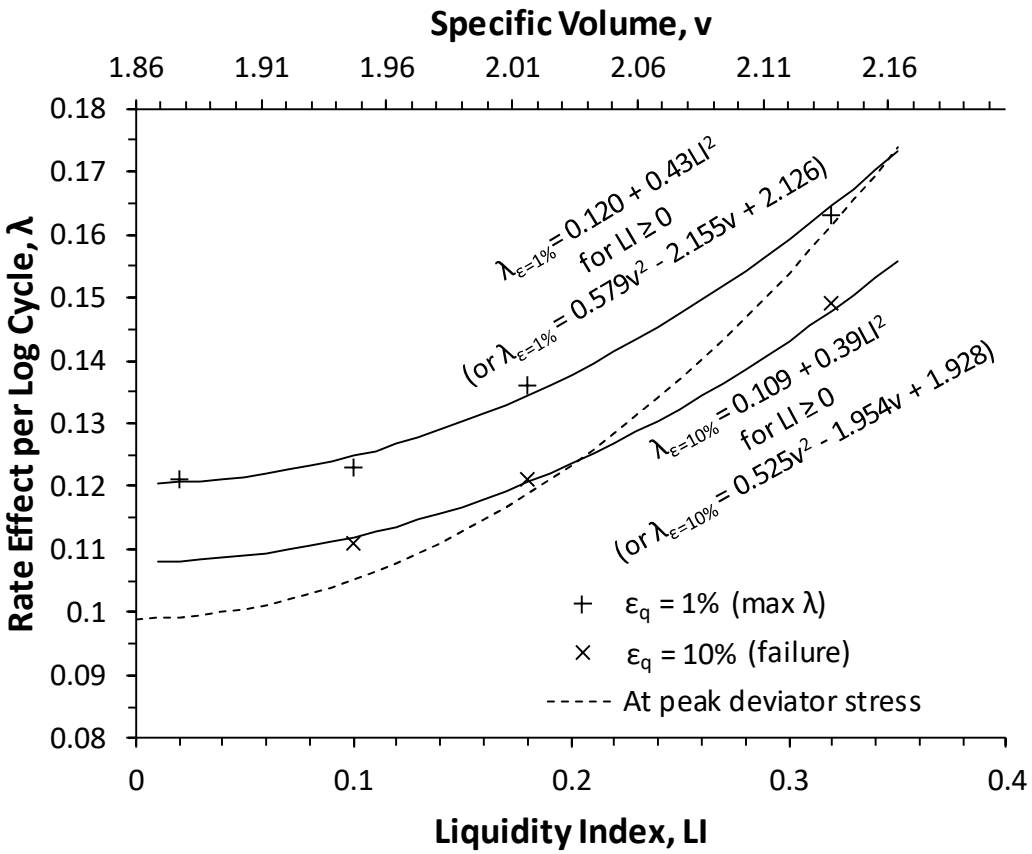

Figure 4-26 – Variation of rate effects at 1 % and 10 % strain with liquidity index in Kaolin

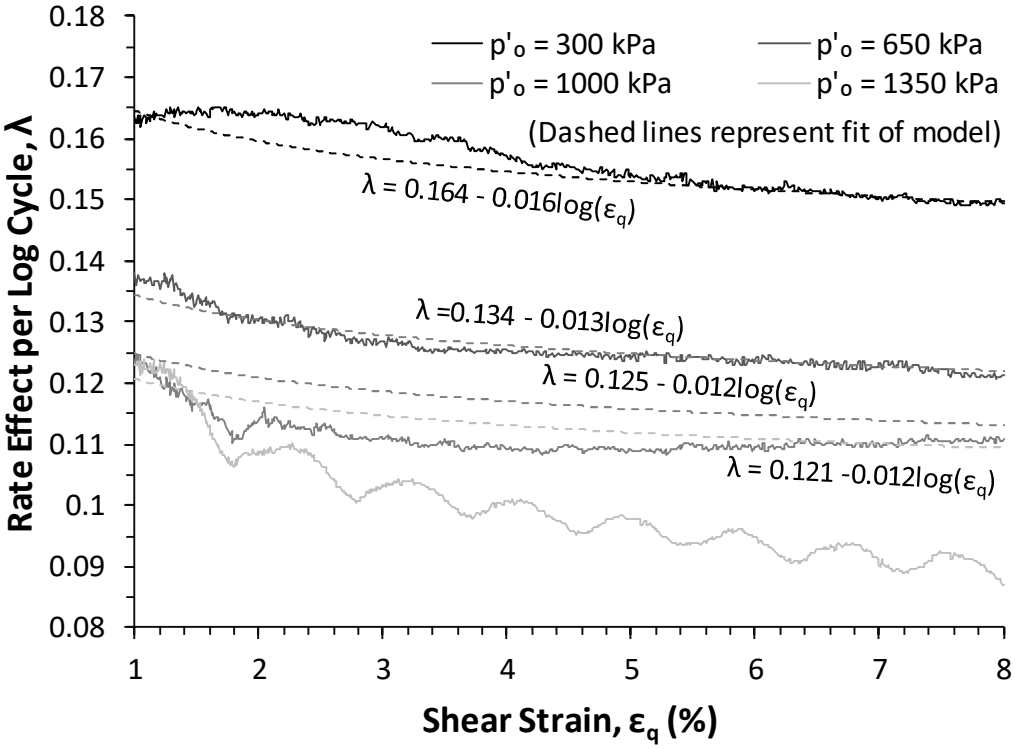

Figure 4-27 – Fit of proposed model to measured rate effects in Kaolin

The coefficients in the equations shown in Figure 4-27 represent the reduction in rate effect per log cycle of strain, $\Delta\lambda_{log(\varepsilon q)}$. By normalising these reductions by the corresponding value of the maximum rate effect ($\lambda_{\varepsilon q=1\%}$), the proportional change in the rate effect per log cycle of strain can be found. Figure 4-28 shows that this normalised change is constant across all of the liquidity indexes tested at -10 % of the maximum rate effect per log cycle strain (i.e. state independent). Using this, Equation 4-23 can be simplified to Equation 4-24.

$$\lambda = (0.120 + 0.43LI^2) \times (1 - 0.10log(\varepsilon_q)) \quad (4\text{-}24)$$

Where:

ε_q is in percent

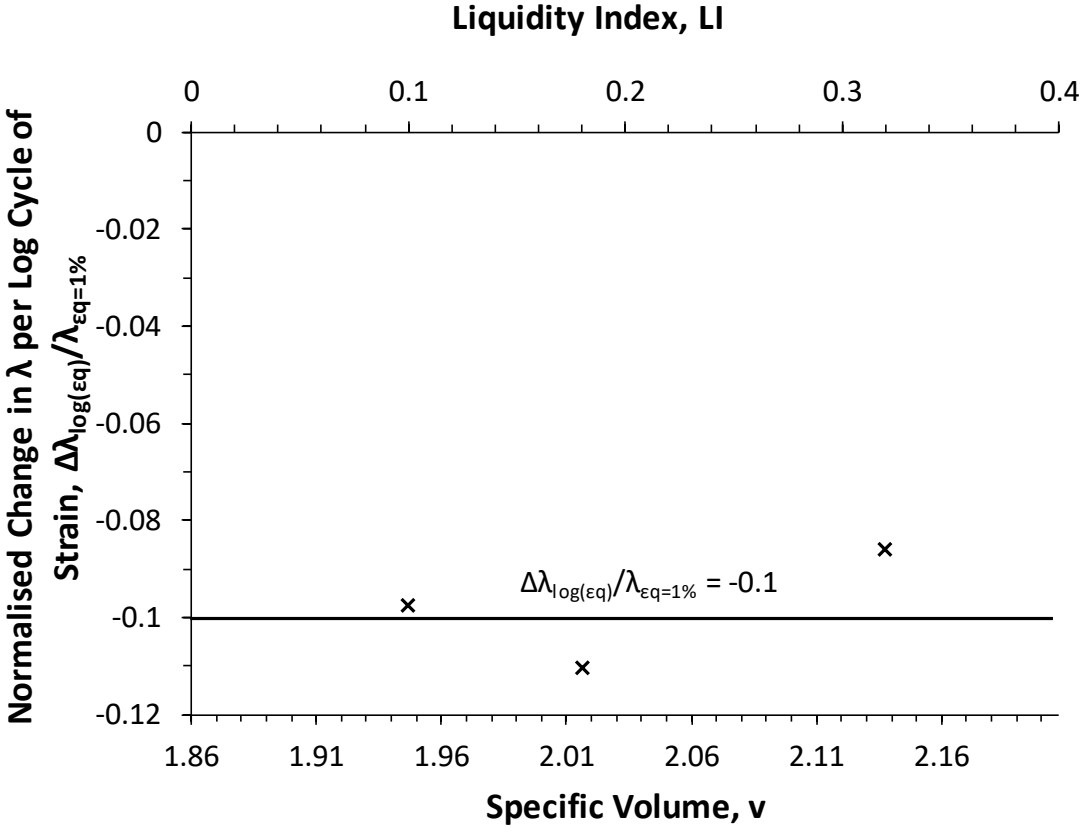

Figure 4-28 – Normalised degradation in rate effect per log cycle of strain post λ_{max}

Figure 4-29 shows a summary of the expected rate effect behaviour of Kaolin throughout the measured strain range using global displacement measurements. In the elastic range below the yield point of the test at the slowest (reference) strain rate, $\varepsilon_{q,EL,ref}$, no rate effects are observed. Between this point and ε_q = 1 %, the rate effect begins to mobilise and reaches the maximum value. After ε_q = 1 %, the rate effect begins to degrade at a rate of approximately

10 % of $\lambda_{\varepsilon q=1\%}$ per log cycle, before localisations mean that it is no longer possible to derive the rate effect, λ, beyond ε_q = 8 to 10 %. The general form of this relationship between rate effects and strain is similar to that observed in field studies such as rapid load testing of piles (Brown, 2008) (Figure 4-30), this suggests that strain-dependent rate effect models developed from element testing could potentially prove useful in field applications.

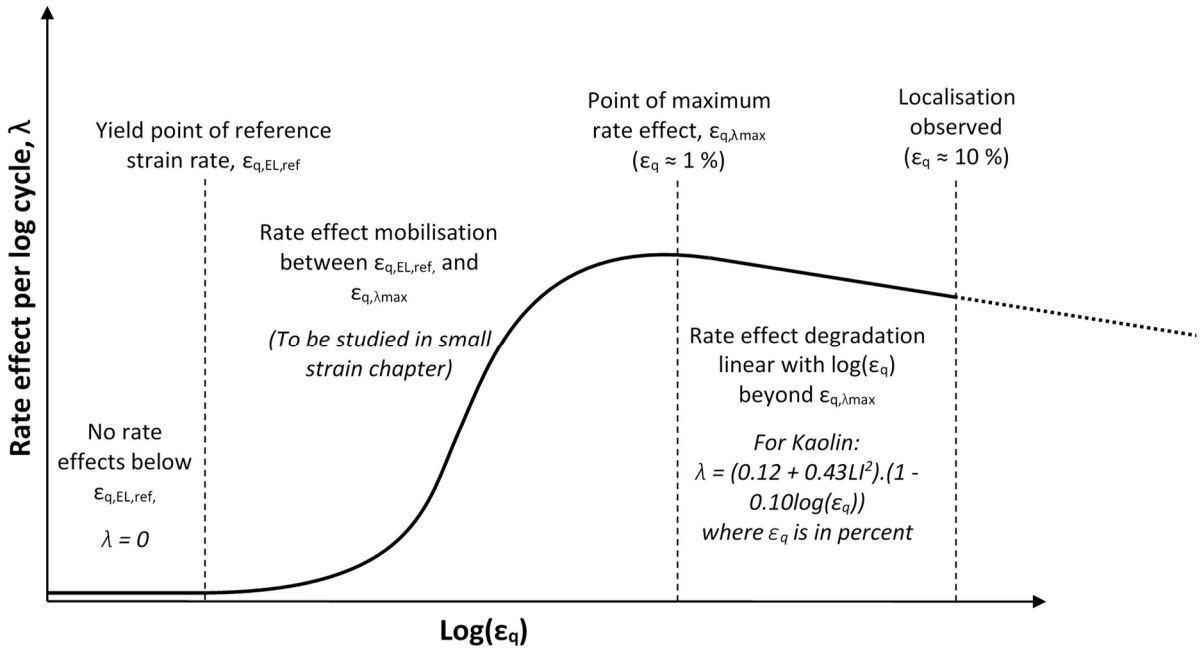

Figure 4-29 – Summary of the variation in rate effect, λ, across the measured strain range based on global displacement measurements (Not to scale)

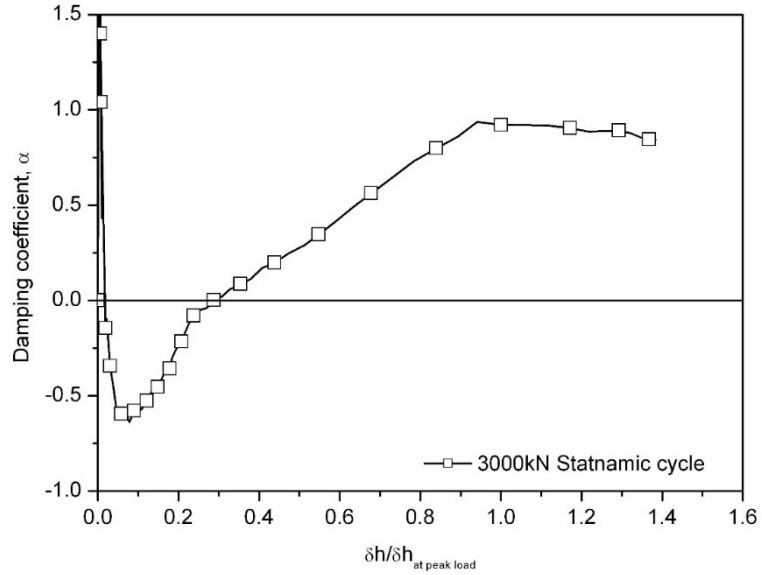

Figure 4-30 – Variation of rate effect (represented by the damping coefficient, α) with normalised displacement from Rapid Load Testing (RLT) of piles in Grimsby Till (Brown, 2008)

It is also important to consider when the use of a strain-based approach for modelling rate effects is beneficial compared to the peak strength based methods most commonly used to date. The answer to this is dependent on the application in question and the desired outcome. Consider as an example, a pile subjected to a rapid load. If the designer wishes only to know whether or not the pile will fail under this rapid load, then a peak strength based approach may be appropriate. For the same example, if the designer wishes to predict the displacement curve which would occur during the rapid load, then a strain-based approach may be more appropriate, as the rate effect which is mobilised would vary with strain (or in this case displacement). In general, for numerical modelling, a strain-based approach is likely to be most useful as it would allow the rate effects in the model to vary for each finite element (if finite element analysis is to be used), depending on the shear strain at any given position in the model at that point in time. For applications where the applied shear strain is low (up to ε_q = 1 %) a strain-based approach to rate effects is essential, due to the fact that (as shown in Figure 4-29) this is the shear strain range where rate effects mobilise, and the rate effect magnitude varies substantially below ε_q = 1 %.

4.2.6. Summary of Large Strain Tests on Kaolin

The large strain testing on Kaolin has identified a number of key aspects of rate effects:

- Viscous undrained strain rate effects on peak strength in Kaolin were found to range from λ_{peak} = 0.16 to 0.10 at p'_0 = 300 kPa and 1350 kPa respectively.
- Strain rate effects have been shown to be dependent on the soil state and this relationship can be described by a correlation between the rate effect per log cycle at peak strength, λ_{peak}, and the liquidity index, LI of the form:

  $$\lambda_{peak} = \lambda_{peak,pl} + \alpha_{peak} LI^2$$

  where $\lambda_{peak,pl}$ is the rate effect per log cycle at the plastic limit and α_{peak} is a material specific parameter which defines the increase in rate effects with LI^2. $\lambda_{peak,pl}$ and α_{peak} were found to be 0.1 and 0.61 respectively for Kaolin.
- Overconsolidation ratio was found to have no observable influence on the magnitude of rate effects at peak strength, other than small increases due to changes in moisture content caused by swelling which are already described by the correlation with liquidity index.
- The strain at which peak deviator stress occurs is dependent on the strain rate, with $\varepsilon_{q,peak}$ reducing from 0.044 - 0.075 at $\dot{\varepsilon}$ = 1000 %/hr to 0.032 - 0.058 at $\dot{\varepsilon}$ = 100,000 %/hr.
- To accurately model rate effects, it is important to compare rate effects using a strain-based definition. Rate effects have been found to be highly strain dependent with the maximum rate effect, λ_{max}, occurring at around ε_q = 0.01 based on large strain measurements.
- The rate effect at ε_q = 0.01, $\lambda_{\varepsilon q=1\%}$, can also be modelling using a correlation with liquidity index:

  $\lambda_{\varepsilon q=1\%} = 0.120 + 0.43LI^2$ for Kaolin

- After ε_q = 0.01 rate effects were found to reduce with log(ε_q), such that for every order of magnitude increase in applied strain, λ reduced by 10 % for Kaolin.

5. Rate Effects on Pore Pressure Evolution in Kaolin

5.1. Pore Pressure Response

The impact of strain rate on pore pressure response is important for understanding the rate dependent effective stress behaviour of clays and, in comparison to the effect of rate effects on the deviator stress response, there is less understanding of the influence of high strain rates on pore pressure evolution (Sabetamal *et al.*, 2016). This includes how the changes in effective stress due to pore pressure evolution contribute to the increase in deviator stress and how the strain rate dependence of pore pressures can be modelled. In particular, there is currently no information on the influence of soil state on pore pressures at high strain rates.

Figure 5-1 shows the excess pore pressures for the normally consolidated undrained CIU tests discussed in Section 4.2 at initial mean effective stresses ranging from p'_o = 300 kPa to 1000 kPa. Usable pore pressures were not available for the tests conducted at p'_o = 1350 kPa due to the fact that a Druck PDCR-81 mid height pore pressure sensor was used in these tests, the response time of which (2 to 3 seconds for 99 % of the applied pressure to be measured when mounted on a clay specimen) was not sufficient for the strain rates investigated (GDS Instruments, 2014). This was discussed previously in Section 3.1.3. Other studies such as Bond *et al.* (1991) found faster response times for PDCR-81 transducers of between 10 and 400 ms, however, this does not take account of the effect of clay particles reducing the permeability of the ceramic filter element when the transducer is installed on a clay specimen (which could significantly increase the response time). The response time of the Honeywell 24PC sensor used for the majority of tests in this study was measured in-situ on a Kaolin specimen. Additionally, test KLN-TU-L3 (p'_o = 300 kPa, $\dot{\varepsilon}$ = 100,000 %/hr) experienced a transducer failure during consolidation, meaning that this data was not available. Figure 5-1 shows, as would be expected, greater pore pressures evolving for higher initial mean effective stresses. However, for any given initial stress, there is a clear trend of reducing pore pressures with increasing axial strain rate. This is in keeping with a number other studies (Sheahan *et al.*, 1996; Zhu and Yin, 2000; Svoboda and McCartney, 2014b; Sudan and Sachan, 2017).

Before continuing, it is important to note that as all of the tests discussed in this chapter are undrained, no volume change occurs. Where a specimen is referred to as having more dilatant

or less contractive tendencies, this refers to the corresponding reduction in pore pressures which, due to the undrained conditions, prevents volume change.

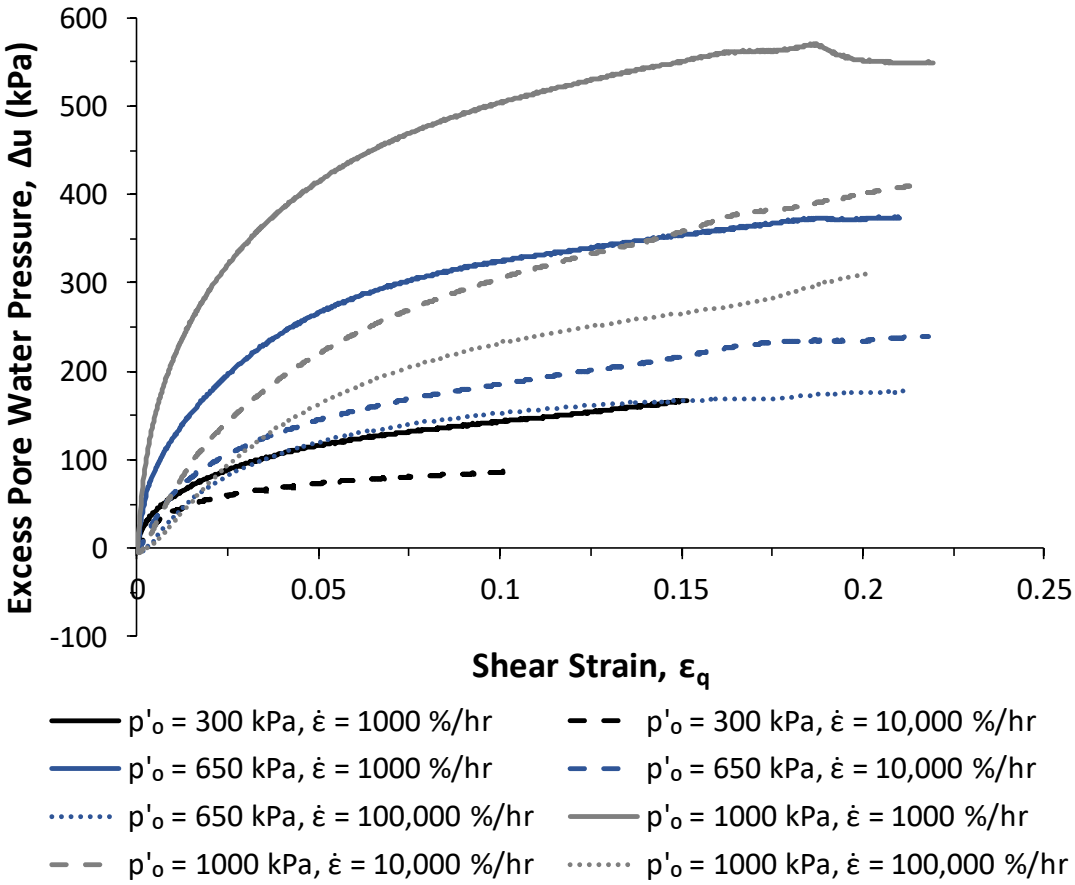

Figure 5-1 – Variation of excess pore pressure with shear strain from undrained triaxial tests on normally consolidated Kaolin

In the triaxial apparatus, the measured excess pore pressure is intrinsically linked to the deviator stress. This is due to the fact that (ignoring for a moment the tendency of the specimen to attempt to either dilate or contract) shearing of the specimen is achieved by increasing the axial stress which in turn generates a deviatoric stress. This increase in the axial stress increases the mean total stress, *p*, on the specimen and creates an additional component of pore pressure which varies throughout the shearing stage (Equation 5-1) depending on the deviator stress acting on the specimen at any given time. This additional pore pressure can mask the change in pore pressures caused by the dilatant or contractive tendency of the specimen, which are of interest.

$$\Delta u = \Delta p = \frac{\Delta \sigma_1}{3} = \frac{\Delta q}{3} \tag{5-1}$$

To account for this effect and consider the true pore pressures generated during shearing of the specimen, the pore pressures discussed from this point onwards will be the excess shear-induced pore pressure, Δu_{si} (Sheahan *et al.*, 1996; Katti *et al.*, 2003), which removes this additional component of excess pore pressure caused by the axial/deviator stress (Equation 5-2). This change also has the benefit that Δu_{si} is equal to $\Delta p'$. Hence a negative value of Δu_{si} indicates the specimen attempting to dilate and a positive value indicates the specimen attempting to contract. For these reasons, it is important to consider the shear-induced (rather than excess) pore pressures when analysing rate effects on pore pressure evolution. Hence, throughout this thesis from this point onwards, the pore pressures referred to will be the shear-induced pore pressures, Δu_{si}.

$$\Delta u_{si} = \Delta u - \frac{q}{3} \tag{5-2}$$

Figure 5-2 shows the variation of the shear-induced pore pressures, Δu_{si}, with shear strain for each of the tests. The shear-induced pore pressures are also shown normalised by p'_o in Figure 5-3. The key difference when compared to Δu is that the shear-induced pore pressures generated at low strains become increasingly negative at higher strain rates; an effect which had been masked by the rapid increase in mean total stress at the beginning of shearing caused by mobilisation of the deviator stress. The strain at which Δu_{si} becomes positive also increases with strain rate, such that at $\dot{\varepsilon}$ = 100,000 %/hr, this point is not reached until ε_q = 0.03 to 0.04. This is in keeping with the findings of Sheahan *et al.* (1996) and Brown *et al.* (2004) who also observed similar initial negative Δu_{si} in the initial stages of shearing. Figure 5-4 shows the pore pressure measured during a constant rate of penetration (CRP) test at 500 mm/s on a 70 mm Ø model pile in a kaolin, sand and silt (KSS) mixture from Brown *et al.* (2004) which demonstrates that these initial negative excess pore pressures are also observed in high strain rate applications such as model pile testing, as well as element tests such as those described by Sheahan *et al.* (1996).

Figure 5-5 shows a comparison of measured shear-induced pore pressures from the normally consolidated triaxial tests on Boston Blue Clay (BBC) by Sheahan *et al.* (1996) (Figure 5-5 (a)) with the triaxial tests on Kaolin in this study at p'_o = 650 kPa (Figure 5-5 (b)) and there are a number of similarities in the data. Firstly, both datasets show no pore pressure changes below $\varepsilon_q \approx 0.0001$, which is close to the yield strain (elastic strain threshold) for the tests conducted

in Kaolin (discussed in more detail in Chapter 6). This is in keeping with the findings of Santagata *et al.* (2005) which showed using triaxial testing at $\dot{\varepsilon}$ = 0.1 to 4 %/hr that below the elastic strain threshold (defined at a slow 'static' strain rate), no shear-induced pore pressures are developed, regardless of the applied strain rate. After this point, both sets of results show negative shear-induced pore pressures developing, which indicates constrained dilation. The reductions in shear-induced pore pressure are larger in this study, which is to be expected due to the higher axial strain rates used ($\dot{\varepsilon}$ = 1000 to 100,000 %/hr).

Whilst the work of Sheahan *et al.* (1996) used significantly lower axial strain rates than those considered here, the similarities provide some confidence in the pore pressure measurements. This indicates that as the strain rate increases, more constrained dilation occurs in the initial stages of shearing, and that this pore pressure suppression may be a key cause of rate effects. This also provides a possible explanation as to why the greatest rate effects are observed at relatively low strains ($\varepsilon_q \approx 0.01$) as shown in Section 4.2. It is interesting to note that although the reduction in Δu_{si} with strain rate first occurs at low strain levels ($\varepsilon_q < 0.01$), the reduction is present throughout the strain range measured.

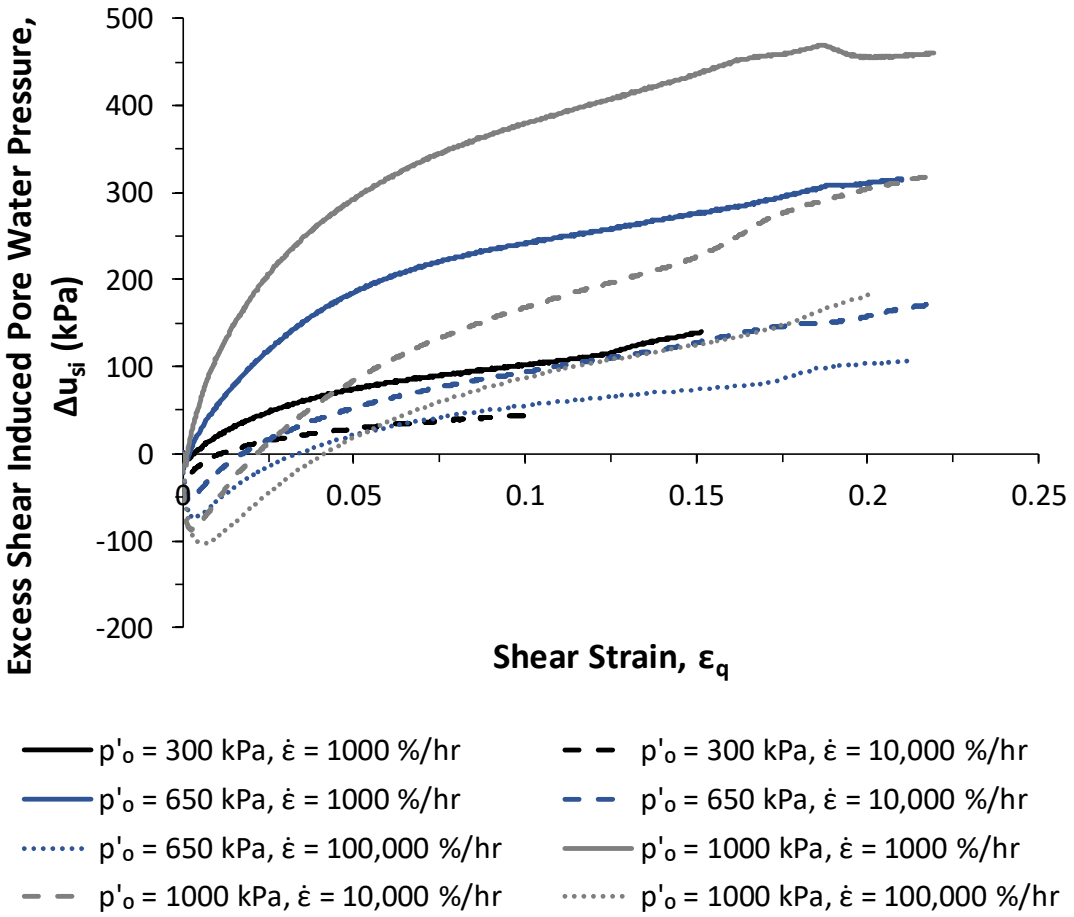

Figure 5-2 – Variation of excess shear-induced pore pressure with shear strain from triaxial tests on normally consolidated kaolin

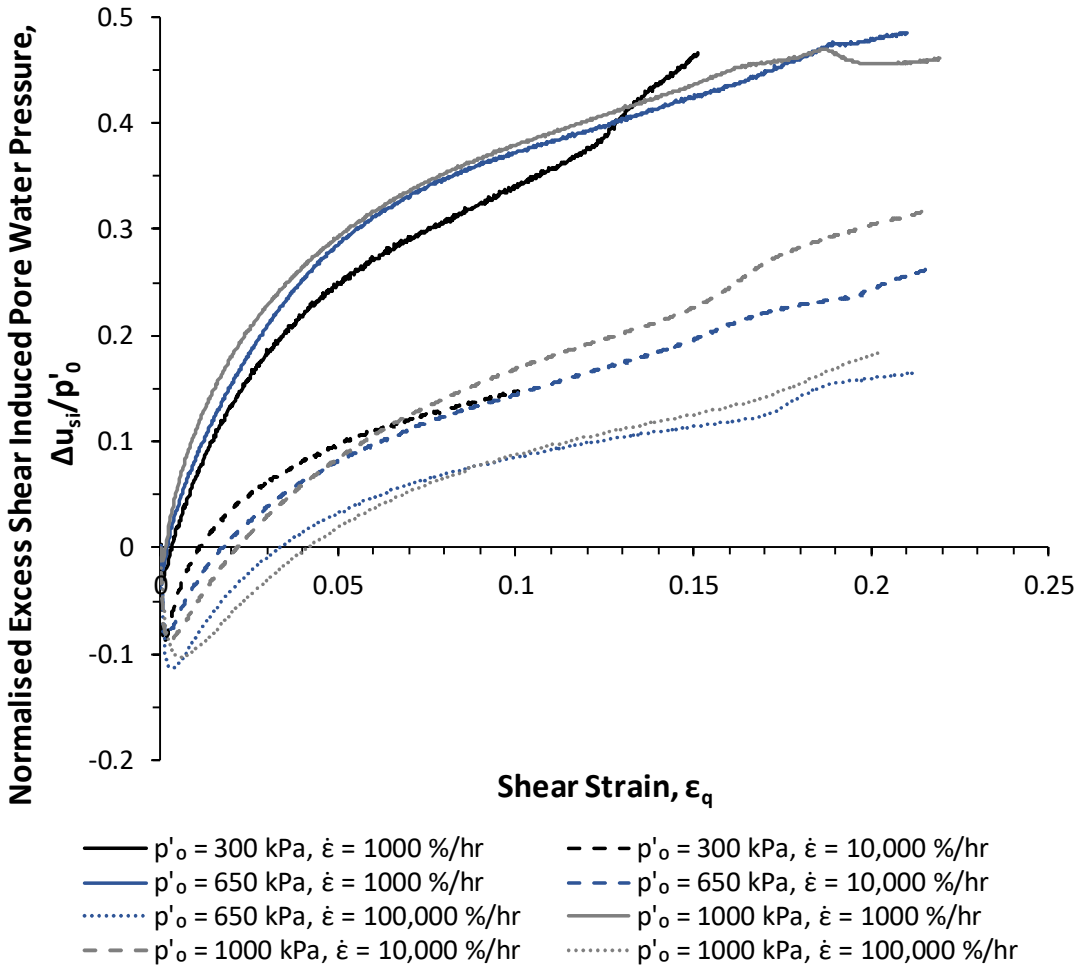

Figure 5-3 – Variation of normalised excess shear-induced pore pressure with shear strain from triaxial tests on normally consolidated kaolin

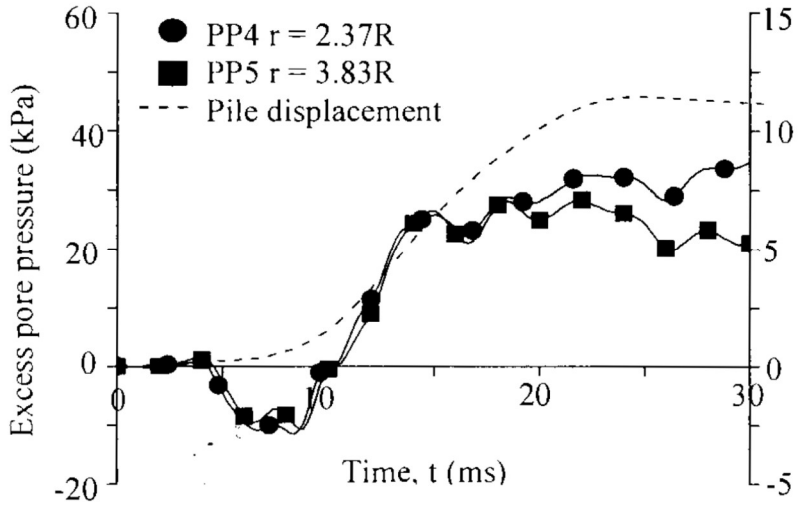

Figure 5-4 – Excess pore pressures measured during a constant rate of penetration test at 500 mm/s on a 70mm diameter model pile in a kaolin, sand and silt (KSS) mixture showing negative initial excess pore pressures (Brown *et al.*, 2004)

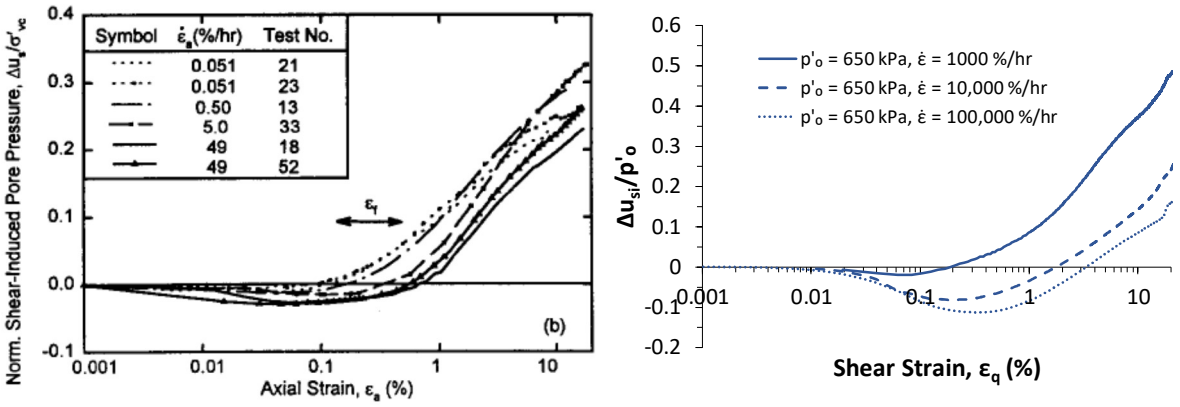

(a) (b)

Figure 5-5 – (a) Variation of normalised shear-induced pore pressure with strain at varying axial strain rates from triaxial tests on Boston Blue Clay (BBC) at OCR = 1 from Sheahan *et al.* (1996) and (b) from triaxial testing of normally consolidated Kaolin (this investigation)

Figure 5-6 shows the excess shear-induced pore pressures at low strain levels (ε_q < 0.01). Similar to the behaviour at greater strain levels, the initial pore pressure suppression due to dilation shows a dependence on both the strain rate and p'_o, with the initial pore pressure suppression increasing with both of these variables. The point of inflection at which the lowest pore pressure occurs ranges from ε_q = 0.0005 to 0.0008 at $\dot{\varepsilon}$ = 1000 %/hr, to ε_q = 0.0033 to 0.0059 at $\dot{\varepsilon}$ = 100,000 %/hr, as shown in Table 5-1.

Table 5-1 – Shear strain at which the lowest value of Δu_{si} occurs

Axial Strain Rate (%/hr)	Initial Mean Effective Stress, p'o (kPa)		
	300	*650*	*1000*
1000	0.0005	0.0006	0.0008
10000	0.0010	0.0019	0.0026
100000	No data	0.0033	0.0059

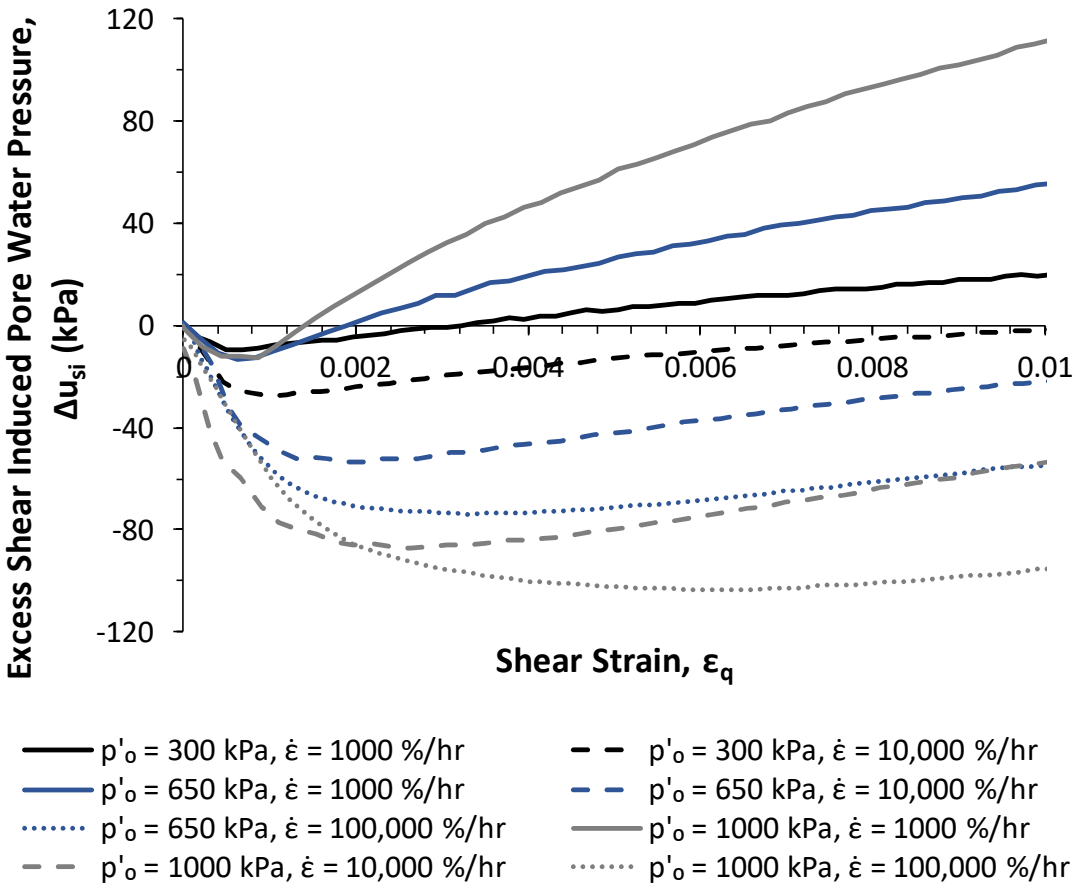

Figure 5-6 – Variation of excess shear-induced pore pressure at low strain levels ($\varepsilon_q < 0.01$)

The point of comparison for strain rate effects on pore pressure development used by the vast majority of studies is the pore pressure at the point of peak deviator stress. Figure 5-7 shows the shear-induced pore pressures at peak deviator stress, $\Delta u_{peak,si}$, normalised by p'_o plotted against the normalised shear strain rate, $\dot{\varepsilon}_q/\dot{\varepsilon}_{q,ref}$, where $\dot{\varepsilon}_{q,ref}$ is the slowest shear strain rate used in each study. From this, it can be seen that these pore pressures reduce approximately linearly with $\log(\dot{\varepsilon}_q/\dot{\varepsilon}_{q,ref})$ according to Equation 5-3. Also shown for comparison are the shear-induced pore pressures presented by Sheahan *et al.* (1996) and Zhu and Yin (2000) on normally consolidated Boston Blue Clay (BBC) and Hong Kong Marine Clay (HKMC), respectively. The pore pressures reported by Zhu and Yin (2000) were not shear-induced pore pressures, but the data shown below has been corrected to account for this.

$$\Delta u_{peak,si}/p'_o = -0.15\log(\dot{\varepsilon}_q/\dot{\varepsilon}_{q,ref}) + 0.30 \quad (5\text{-}3)$$

Aside from the fact that the datasets are from different soils, there are substantial differences between the three series of results shown, which highlight the problematic nature of using

peak deviator stress as a comparison point for pore pressures. Firstly, the pore pressures, even at the reference strain rates, vary substantially in terms of magnitude. The explanation for this lies in the strain at which the peak deviator stresses occur. For the BBC tested by Sheahan *et al.* (1996), the strain at q_{peak} ranged from ε = 0.001 to 0.004 whereas for Zhu and Yin (2000) this is of the order of ε = 0.08 to 0.09 (exact values for the strain at q_{peak} were not reported). For the Kaolin used here, q_{peak} ranged from ε_q = 0.03 to 0.08 as discussed in Chapter 4. As can be seen from Figure 5-2, the pore pressures which evolve at $\varepsilon_q \approx 0.001$ are more than an order of magnitude lower than the pore pressures at $\varepsilon_q \approx 0.1$, which results in the variation in pore pressures at $\dot{\varepsilon}_{q,ref}$ between the three datasets seen in Figure 5-7.

As discussed in Chapter 4, the strain at q_{peak} is also rate dependent for the Kaolin tested, with the strain at q_{peak} reducing from ε = 0.05 to 0.09 at $\dot{\varepsilon}_q$ = 1000 %/hr, to ε = 0.03 to 0.07 at $\dot{\varepsilon}_q$ = 100,000 %/hr. This may also partly account for the fact that the reductions in $\Delta u_{peak,si}$ with shear strain rate reported here are greater than those found by both Sheahan *et al.* (1996) and Zhu and Yin (2000). As the strain at peak reduces with strain rate, this means that the pore pressures at q_{peak} for higher strain rates are derived at lower strain levels, which would again exaggerate the reduction in pore pressures with increasing strain rate found.

Normalising the shear-induced pore pressures by the pore pressure at the reference rate in each of these studies can overcome some of these issues. From Figure 5-8, it can be seen that after this normalisation, the reduction in $\Delta u_{peak,si}$ with shear strain rate is comparable between the results from the Kaolin used here (Equation 5-4) and the BBC tested by Sheahan *et al.* (1996). The reduction from Zhu and Yin (2000) is notably lower, possibly due to the fact that this study used only base pore pressure measurements and did not use lubricated end platens. However, this still leaves the issue of the strain at q_{peak} reducing with strain rate, highlighting the need for a strain-based method for comparing the changes in shear-induced pore pressure with strain rate.

$$\Delta u_{peak,si}/\Delta u_{peak,si,ref} = -0.48\log(\dot{\varepsilon}_q/\dot{\varepsilon}_{q,ref}) + 1.0 \quad (5\text{-}4)$$

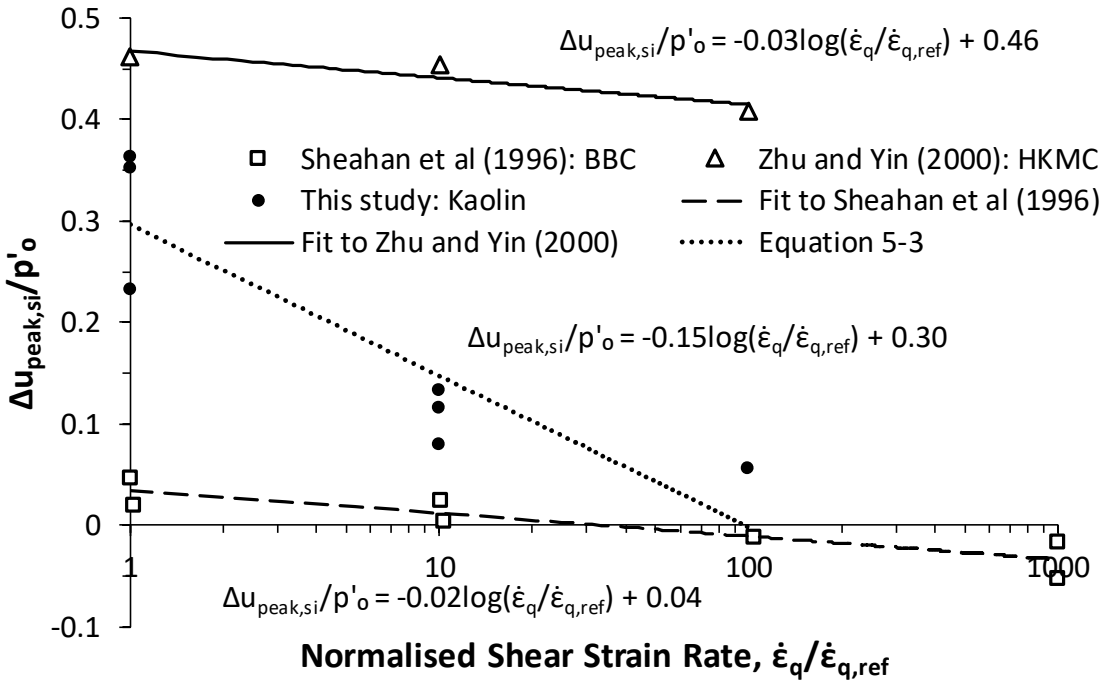

Figure 5-7 – Comparison of shear-induced pore pressure at peak deviator stress in Kaolin with Sheahan *et al.* (1996) and Zhu and Yin (2000)

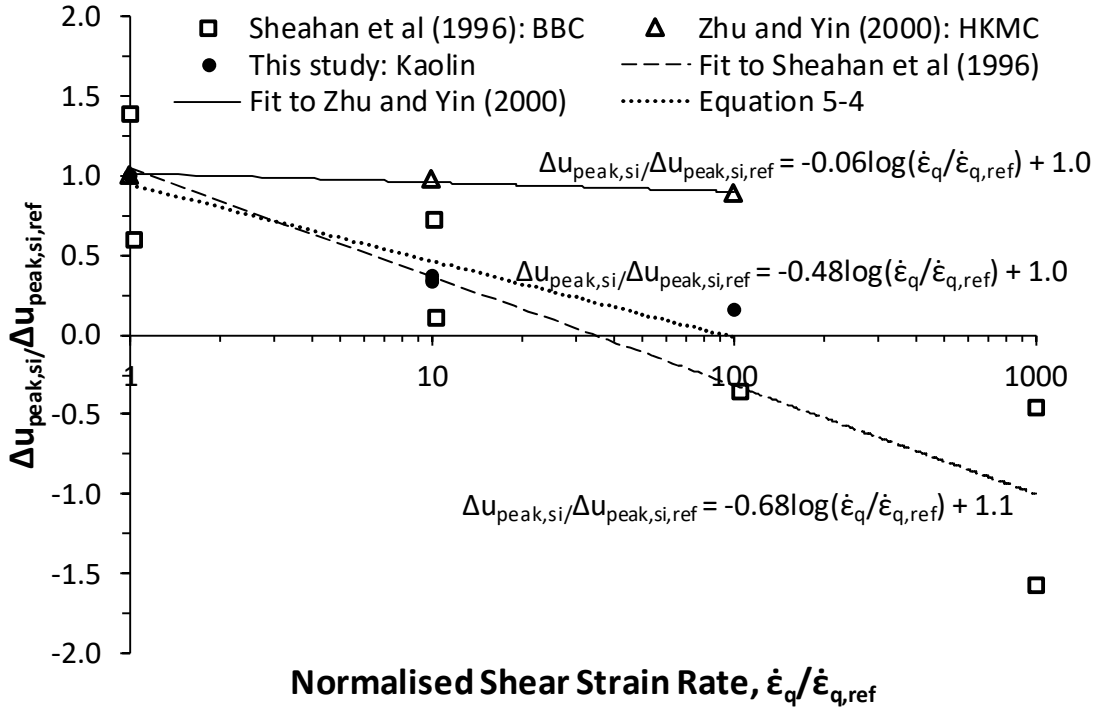

Figure 5-8 – Comparison of normalised shear-induced pore pressure at peak deviator stress in Kaolin with Sheahan *et al.* (1996) and Zhu and Yin (2000)

5.2. Modelling of Pore Pressure Response

To allow the pore pressure variation with strain rate to be investigated, a simple inverse exponential relationship (Equation 5-5) between Δu_{si} and shear strain will be used (Muir Wood, 2011, Personal Correspondence). This assumes that Δu_{si} tends towards a rate dependent final pore pressure denoted $\Delta u_{f,si}$, and the rate at which it tends towards this value is represented by a coefficient, α_u, which is soil specific.

$$\Delta u_{si} = \Delta u_{f,si} (1 - exp[-\alpha_u.\varepsilon_q]) \quad (5\text{-}5)$$

However, this model is based on the response expected at static strain rates and does not account for the initial negative shear-induced pore pressures caused by constrained dilation, meaning that it assumes positive pore pressures will evolve from the onset of shearing. To adjust the model to be able to fit tests conducted at high strain rates, an additional component to represent the initial negative pore pressure, $\Delta u_{dil,si}$, is proposed which will apply an offset to Δu_{si} (Equation 5-6). $\Delta u_{dil,si}$ is a constant determined from each test, with a negative value representing the generation of a negative initial pore pressure. Figure 5-9 shows an example of the definition of $\Delta u_{f,si}$ and $\Delta u_{dil,si}$, which are obtained by the fitting of Equation 5-6 to the measured values of Δu_{si} up to the point of localisation at ε_q = 0.12. It should be noted that $\Delta u_{dil,si}$ is not the minimum pore pressure measured, but the intercept of Equation 5-6 with the y-axis at ε_q = 0. Figure 5-10 shows the impact of the parameter, α_u, with higher values of α_u corresponding to earlier mobilisation of $\Delta u_{f,si}$.

$$\Delta u_{si} = (\Delta u_{f,si} - \Delta u_{dil,si}).(1 - exp[-\alpha_u.\varepsilon_q]) + \Delta u_{dil,si} \quad (5\text{-}6)$$

This inclusion of $\Delta u_{dil,si}$ allows the model to capture the pore pressure response for each test beyond the strain levels shown in Table 5-1 (the data after the strain corresponding to the minimum value of Δu_{si}). Figure 5-11, Figure 5-12 and Figure 5-13 show the fitting of Equation 5-6 to the tests conducted at p'_o = 300, 650 and 1000 kPa, respectively. These show that despite the simplistic nature of the model, it provides a good level of fit to the measured data up until the specimens localise at approximately ε_q = 0.12.

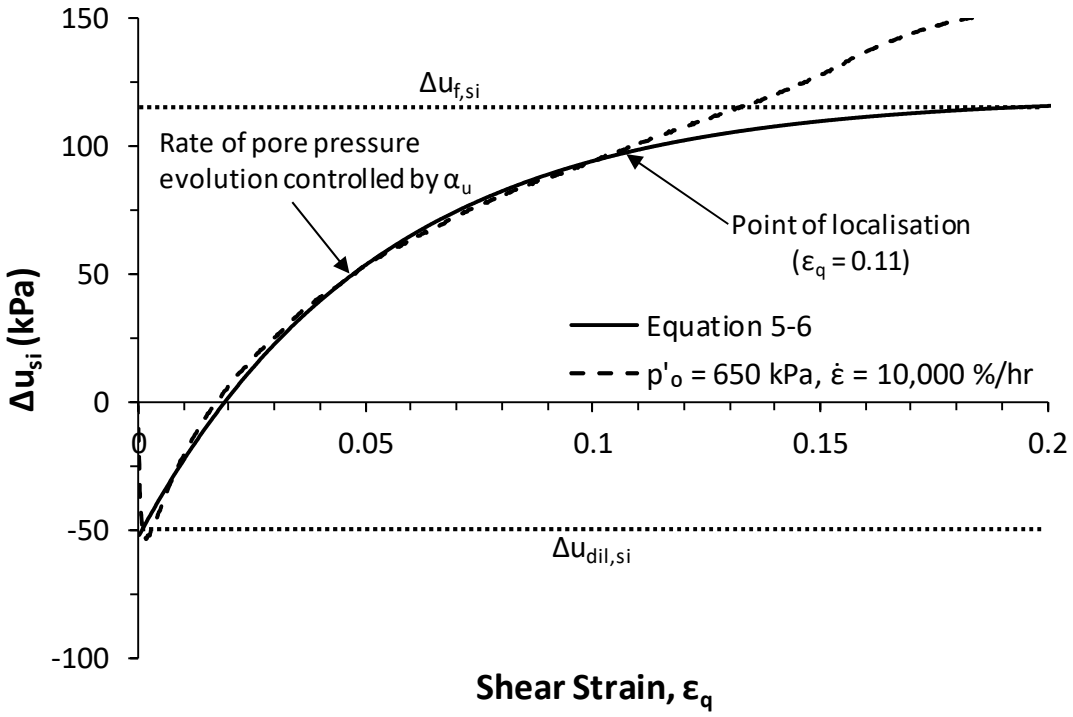

Figure 5-9 – Definition of the parameters $\Delta u_{dil,si}$ and $\Delta u_{f,si}$ using the triaxial test on normally consolidated Kaolin at p'_0 = 650 kPa and $\dot{\epsilon}$ - 10,000 %/hr as an example

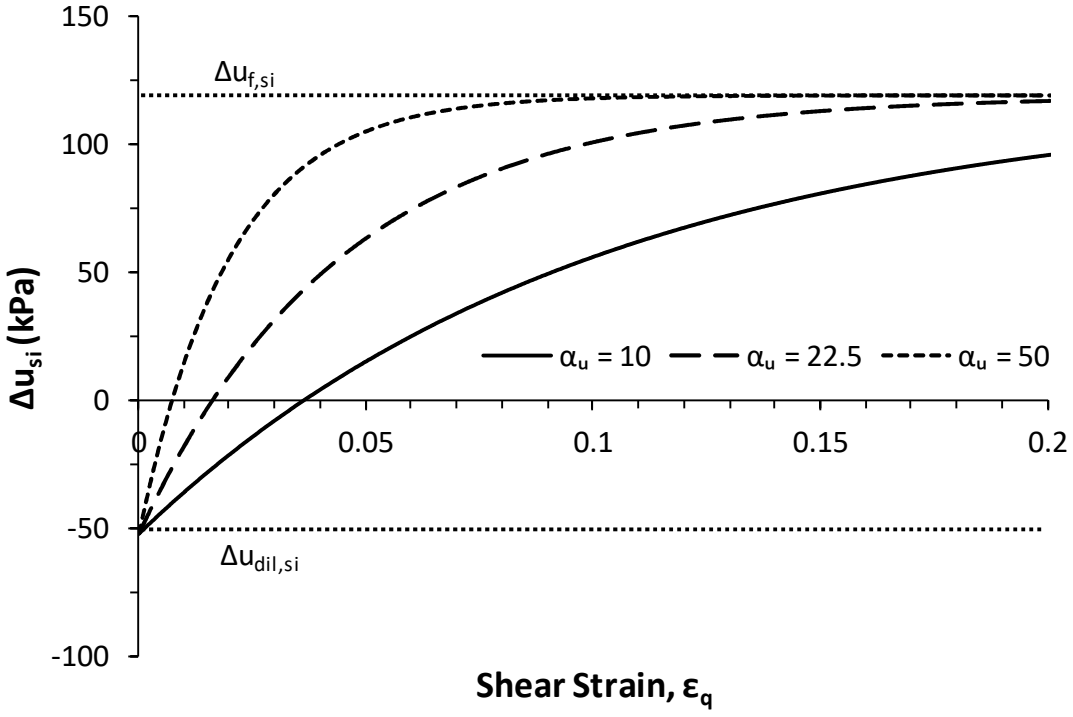

Figure 5-10 – Illustrative example of the impact of three values of α_u on Equation 5-6 for constant values of $\Delta u_{f,si}$ = 119 kPa and $\Delta u_{dil,si}$ = -52 kPa

After localisation occurs, there is a noticeable increase in the measured pore pressures which is due to the effect of localisation on where shearing occurs within the specimen. Up until localisation, the shear strain rate in the soil is relatively even across the specimen. However, after the shear plane forms at around $\varepsilon_q = 0.12$, the shearing begins to focus on this plane. This leads to the strain rate away from the shear plane reducing with increasing strain as more and more of the shearing focusses there (Figure 5-14). This means that the strain rate in the soil adjacent to the pore pressure transducer becomes far lower, tending towards zero if all shearing occurs on the shear plane. It has been shown by a number of studies including Sheahan *et al.* (1996) and Zhu and Yin (2000), as well as in the tests presented here, that higher pore pressures occur at lower strain rates, meaning that as the shearing focusses on the shear plane after localisation, the soil pore pressure adjacent to the PPT increases correspondingly. This results in a 'jump' in the pore pressure in a manner similar to as if an 'isotache' style test was conducted (where multiple shearing stages with different strain rates are conducted on the same specimen).

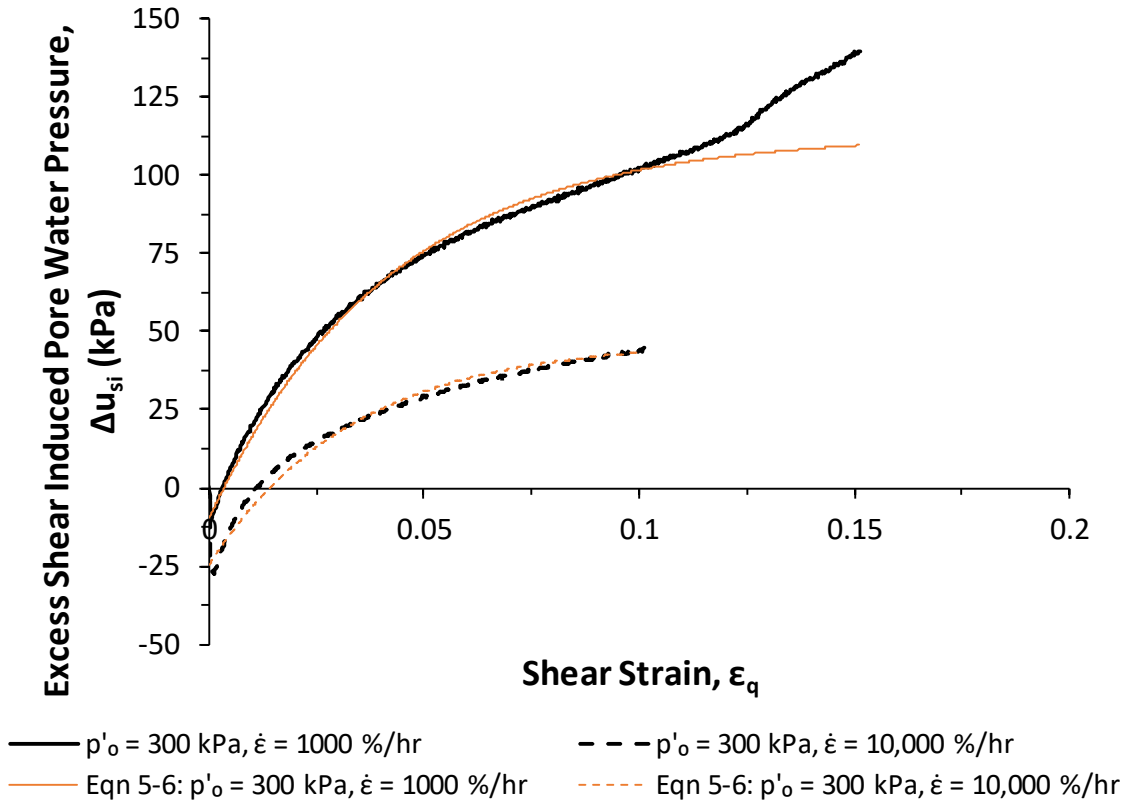

Figure 5-11 – Fitting of hyperbolic model (Equation 5-6) to tests on Kaolin at p'_o = 300 kPa

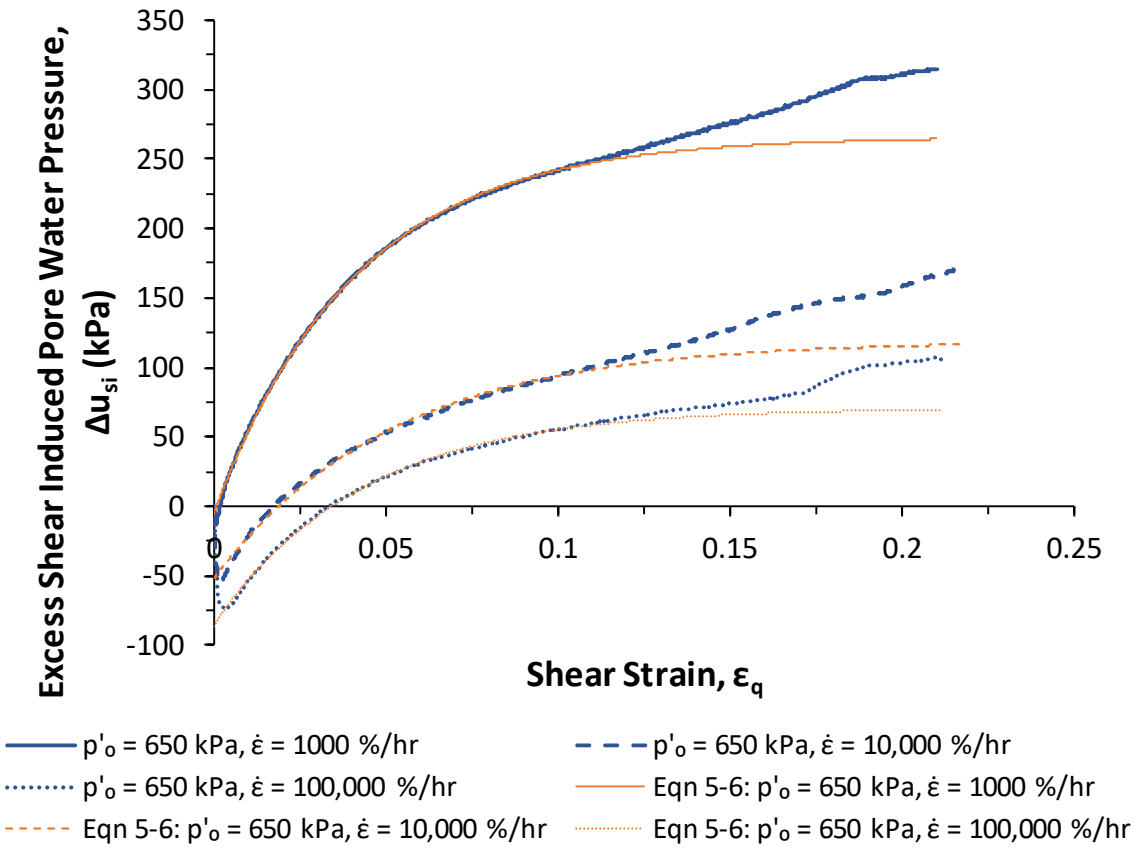

Figure 5-12 – Fitting of hyperbolic model (Equation 5-6) to tests on Kaolin at p'_o = 650 kPa

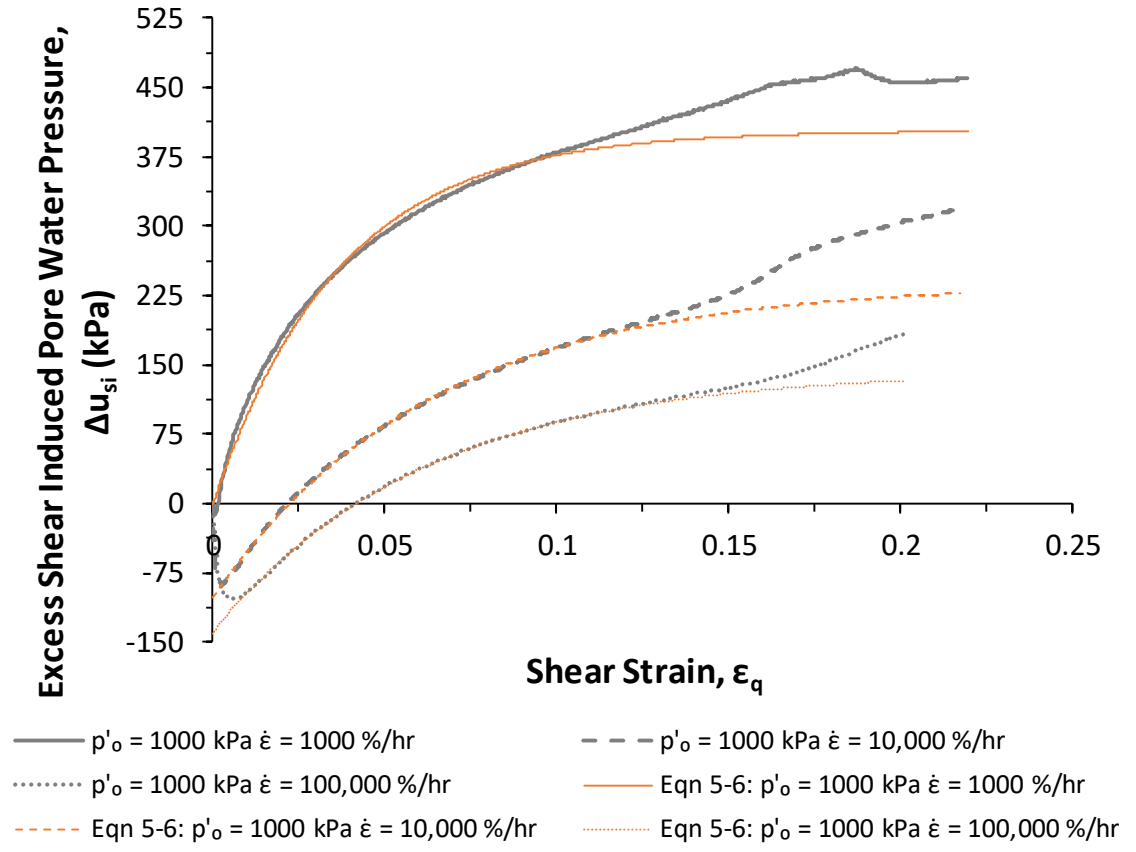

Figure 5-13 – Fitting of hyperbolic model (Equation 5-6) to tests on Kaolin at p'_o = 1000 kPa

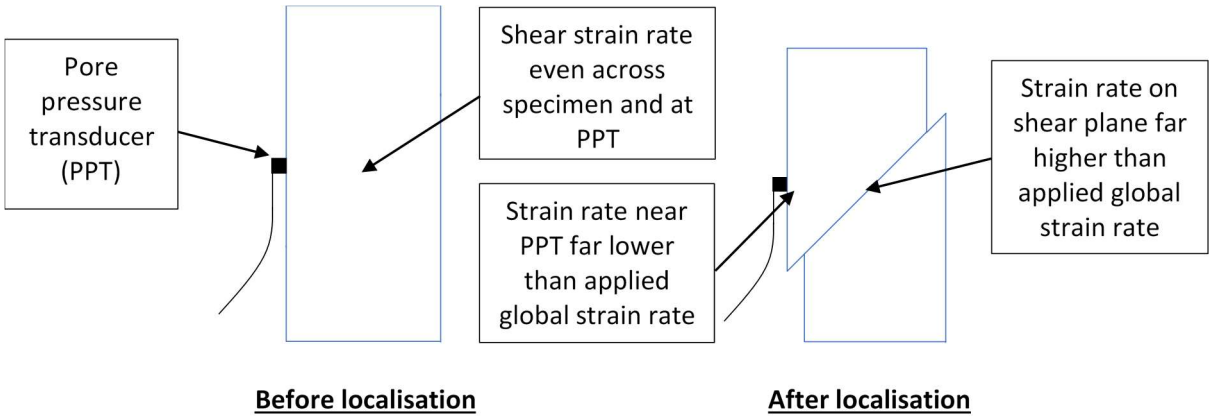

Figure 5-14 – Schematic of localisation of shear strain rates in triaxial specimen before and after shear plane formation

Table 5-2 shows the parameters derived from the fitting process and the expected trends of reducing $\Delta u_{f,si}$ and increasingly negative $\Delta u_{dil,si}$ can be seen as the shear strain rate increases. The variation of these two parameters with strain rate is shown in Figure 5-15 and Figure 5-16. Both $\Delta u_{f,si}$ and $\Delta u_{dil,si}$ appear to vary linearly with the log of shear strain rate, with the reduction in both parameters being greater at higher effective stresses. The reduction in $\Delta u_{f,si}$ ranged from 65 kPa per log cycle at p'_o = 300 kPa to 130 kPa per log cycle at p'_o = 1000 kPa, whilst the reduction in $\Delta u_{dil,si}$ varied from 15 kPa per log cycle to 69 kPa per log cycle, respectively.

The linear relationship of $\Delta u_{f,si}$ with $\log(\dot{\varepsilon}_q)$ is in agreement with the findings of Zhu and Yin (2000) which used Hong Kong Marine Clay, although the magnitude of the reductions observed in this study are greater, possibly due to the higher strain rates used and differences in the materials tested. Nevertheless, the similar form of the relationship provides additional confidence.

The variation of the pore pressure fitting parameter, α_u, with shear strain rate is shown in Figure 5-17. The values for α_u obtained range from 16 to 30, with α_u reducing marginally with $\dot{\varepsilon}_q$ according to Equation 5-7. However, the reduction in α_u is small in comparison to the variability in the data points and may also be due to the lack of a data point for $\dot{\varepsilon}_q$ = 100,000 %/hr at p'_o = 300 kPa. For these reasons, and to simplify the pore pressure evolution model, α_u could be averaged to be a constant value of 22.5 for Kaolin. This simplification means that α_u varies by no more than ±2.5 from Equation 5-7. Additionally, it was initially expected during the development of the model that α_u would be a soil specific material constant (Muir Wood,

2011, Personal Correspondence). Further work would be required to determine α_u for other soils.

$\alpha_u = 33 - 2.8log(\dot{\varepsilon}_q)$ for normally consolidated Kaolin where $\dot{\varepsilon}_q$ is in %/hr (5-7)

Table 5-2 – Parameters derived from hyperbolic pore pressure model fitting

Test Designation	p'o (kPa)	Shear Strain Rate (%/hr)	Model Parameters		
			$\Delta u_{f,si}$ (kPa)	$\Delta u_{dil,si}$ (kPa)	α_u
KLN-TU-L1	300	1000	112.8	-9.6	23.96
KLN-TU-L2	300	10000	46.9	-24.5	29.81
KLN-TU-L4	650	1000	266.0	-5.04	24.30
KLN-TU-L5	650	10000	119.1	-52.1	19.22
KLN-TU-L6	650	100000	70.7	-85.9	23.23
KLN-TU-L7	1000	1000	403.1	0.0	27.23
KLN-TU-L8	1000	10000	238.1	-101.0	15.84
KLN-TU-L9	1000	100000	143.9	-138.5	16.18

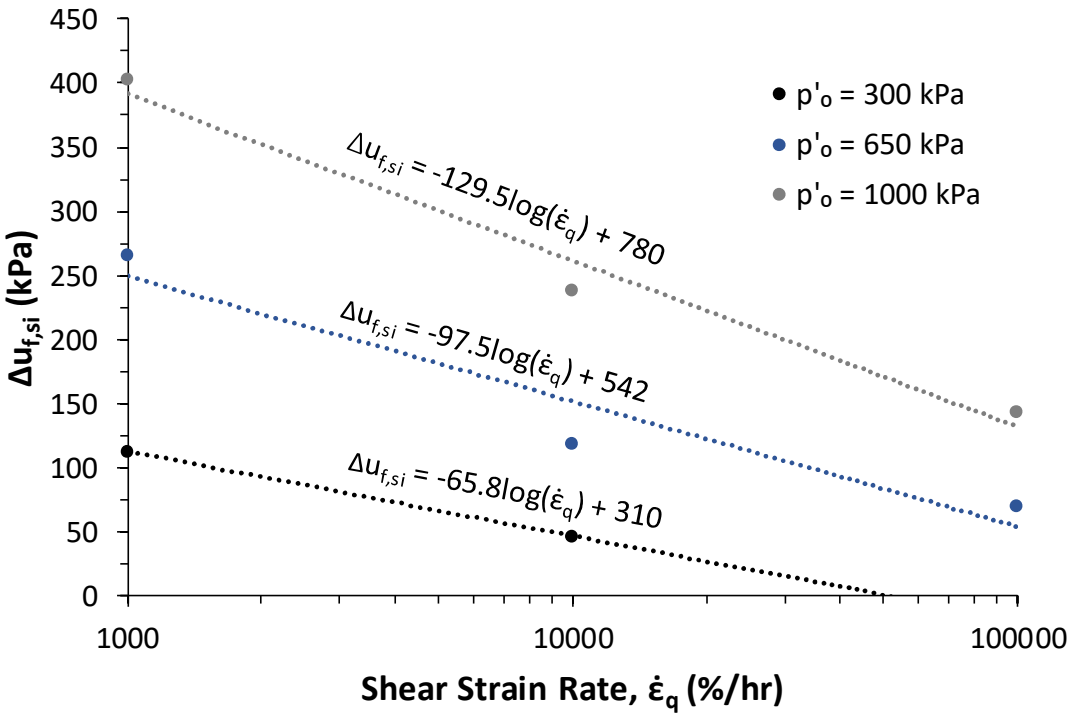

Figure 5-15 – Variation of $\Delta u_{f,si}$ with shear strain rate for normally consolidated Kaolin

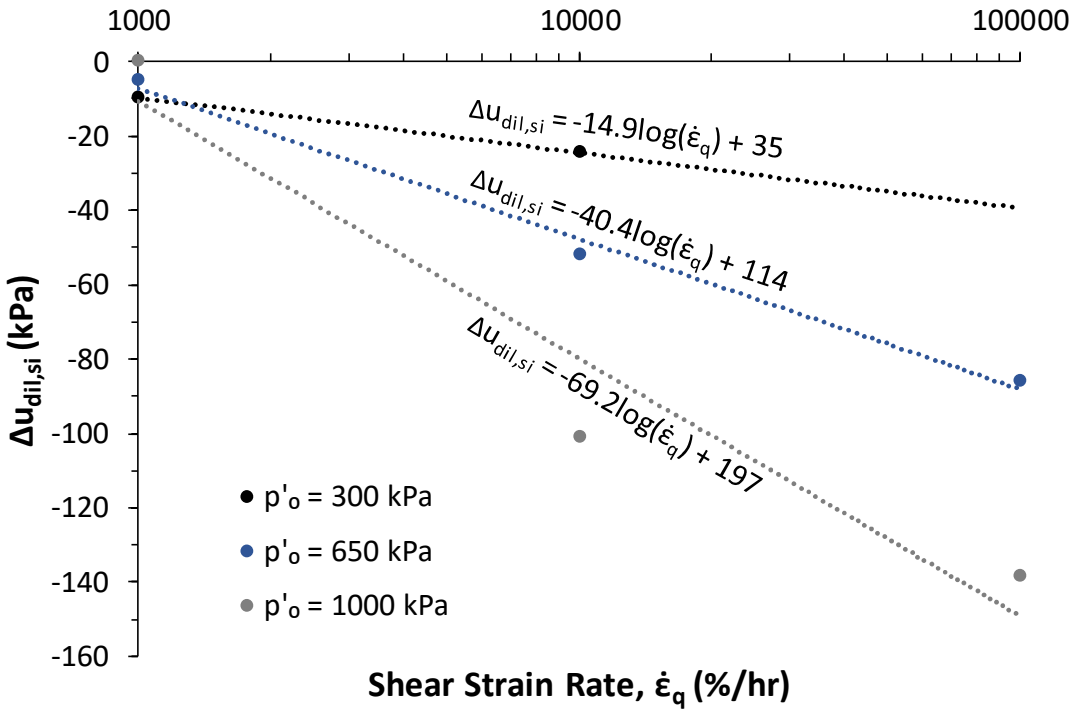

Figure 5-16 – Variation of $\Delta u_{dil,si}$ with shear strain rate for normally consolidated Kaolin

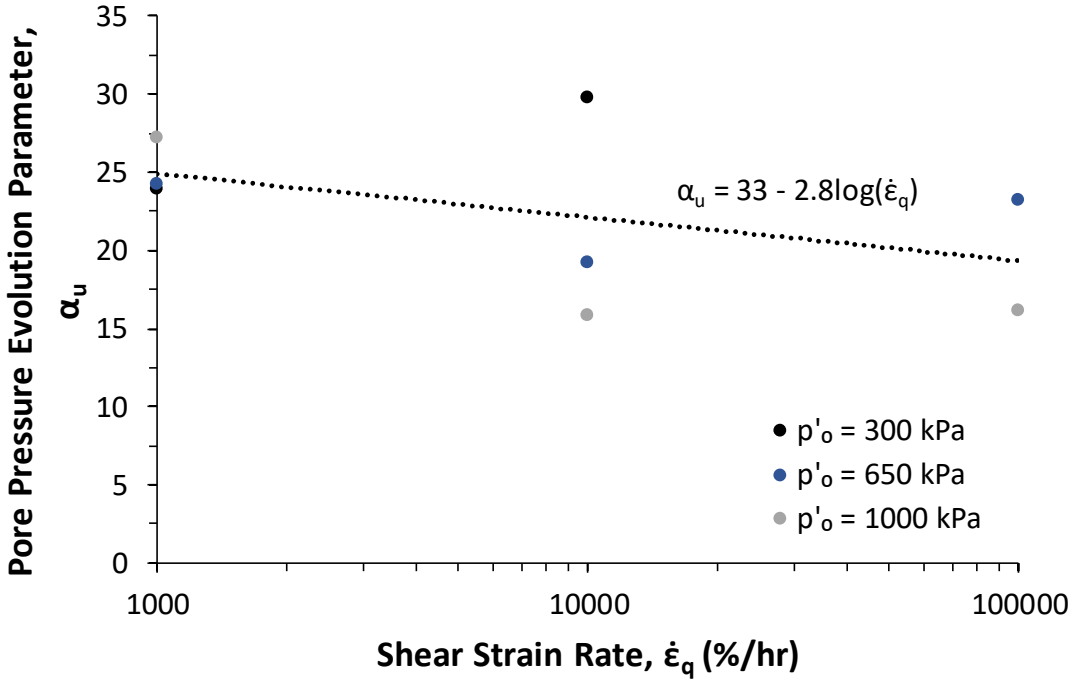

Figure 5-17 – Variation of the pore pressure parameter, α_u, with shear strain rate for normally consolidated Kaolin

Conventionally, shear-induced pore pressures are normalised by p'_o to account for differences in the initial mean effective stress. Figure 5-18 and Figure 5-19 show that despite the varying strain rates and initial mean effective stresses, this normalisation is still successful in bringing together the data points for each value of p'_0 tested when considering both $\Delta u_{f,si}$ and $\Delta u_{dil,si}$. The shear strain rate has also been normalised by the reference strain rate such that the intercept of the semi-log relationships corresponds to the value at the reference shear strain rate of 1000 %/hr. It is shown that for normally consolidated Kaolin at each effective stress, $\Delta u_{f,si}$ and $\Delta u_{dil,si}$ may be represented by Equation 5-8 and Equation 5-9, respectively. Alternatively, a power law can be used to more accurately capture the strain rate dependency of these parameters if required (Equations 5-10 and 5-11).

$$\Delta u_{f,si}/p'_0 = -0.140\log(\dot{\varepsilon}_q/\dot{\varepsilon}_{q,ref}) + 0.375 \quad (5\text{-}8)$$

$$\Delta u_{dil,si}/p'_0 = -0.062\log(\dot{\varepsilon}_q/\dot{\varepsilon}_{q,ref}) - 0.017 \quad (5\text{-}9)$$

$$\Delta u_{f,si}/p'_0 = 0.38(\dot{\varepsilon}_q/\dot{\varepsilon}_{q,ref})^{-0.25} \quad (5\text{-}10)$$

$$\Delta u_{dil,si}/p'_0 = 0.19(\dot{\varepsilon}_q/\dot{\varepsilon}_{q,ref})^{-0.23} - 0.2 \quad (5\text{-}11)$$

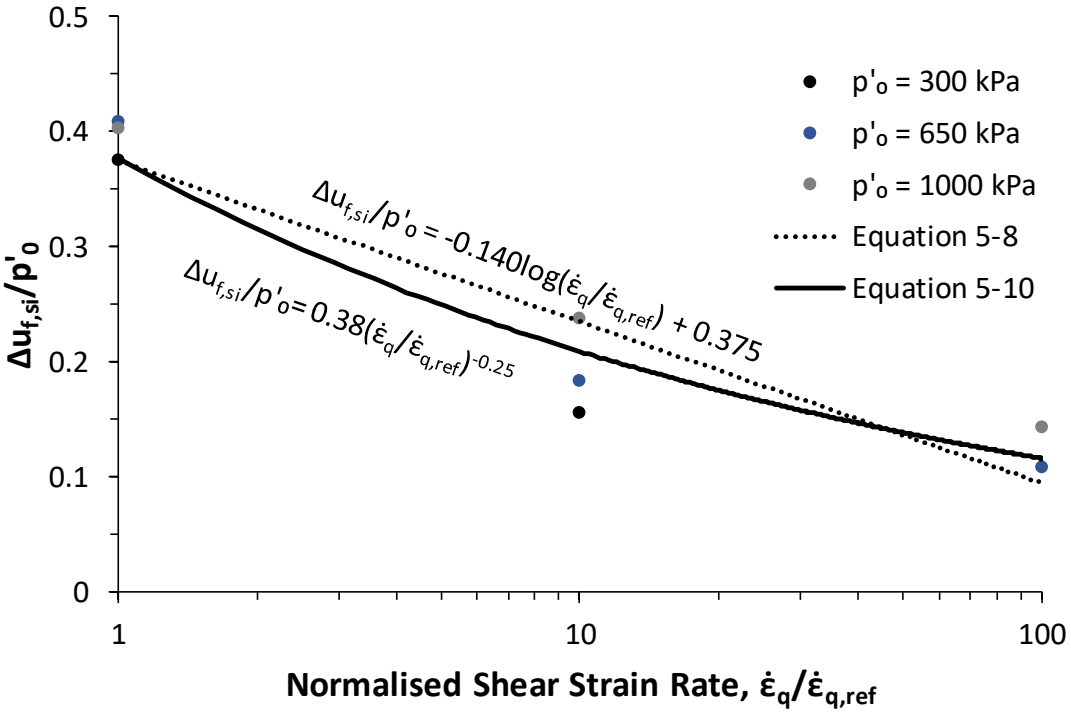

Figure 5-18 – Variation of $\Delta u_{f,si}/p'_0$ with normalised shear strain rate for normally consolidated Kaolin

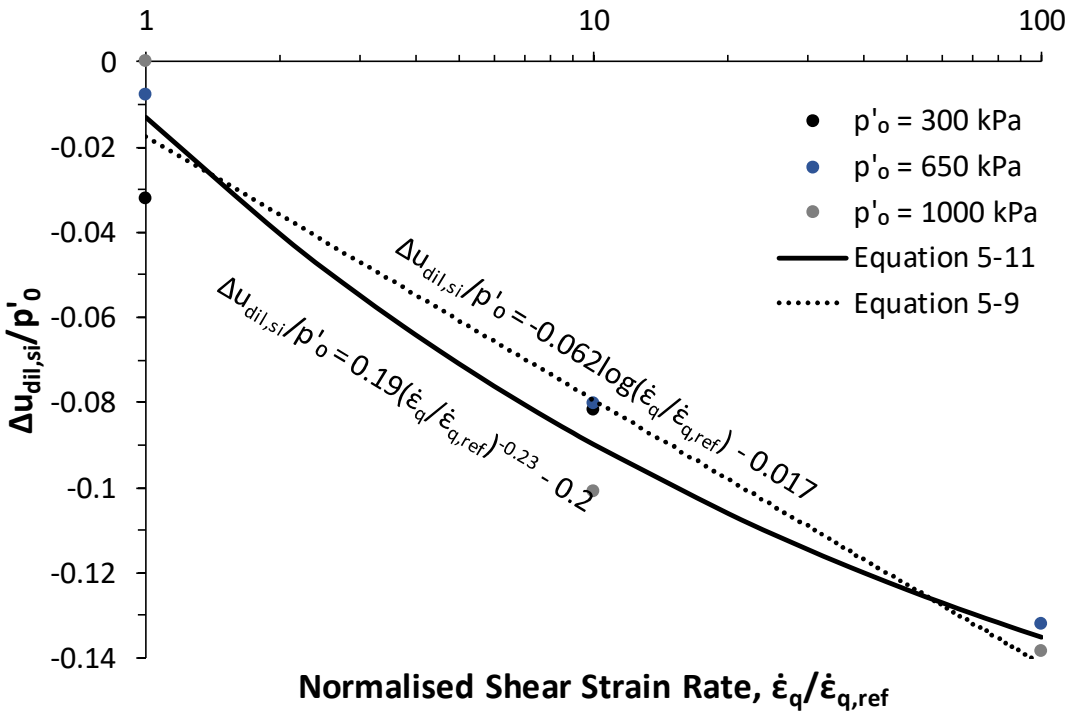

Figure 5-19 – Variation of $\Delta u_{dil,si}/p'_0$ with normalised shear strain rate for normally consolidated Kaolin

A comparison of the final output from the hyperbolic model (Equation 5-6) and the measured pore pressures is shown in Figure 5-20 for each of the strain rates tested. It can be seen that the model provides a reasonable level of fit throughout for $\dot{\varepsilon}$ = 1000 %/hr and 100,000 %/hr, while slightly overestimating the pore pressures in the middle of the shear strain range for $\dot{\varepsilon}$ = 10,000 %/hr.

Whilst the coefficient α_u is empirical, it governs the rate of mobilisation of pore pressure with strain, meaning that it is key to providing additional confidence in the experimental pore pressure measurements. The fact that a constant value of α_u = 22.5 can provide a good level of fit to the data at both the highest and lowest strain rates suggests that there are unlikely to be issues with the response time of the pore pressure transducer (PPT) or pore pressure lags such as those described by Sheahan *et al.* (1996). If a significant delay or lag existed in the pore pressure measurements, this would be expected to lead to a slower rate of mobilisation towards $\Delta u_{f,si}$ and a significantly flatter curve. This behaviour was not observed in the measurements, suggesting that the response time of the new PPT design is sufficient for the rates considered, confirming the detailed analysis of the PPT response time discussed in

Chapter 3. Studies where this 'flattening' (compared to pore pressure measurements at the reference strain rate) of the pore pressure response indicates issues with transducer response times at high strain rates include Quinn (2013) and Sudan and Sachan (2017).

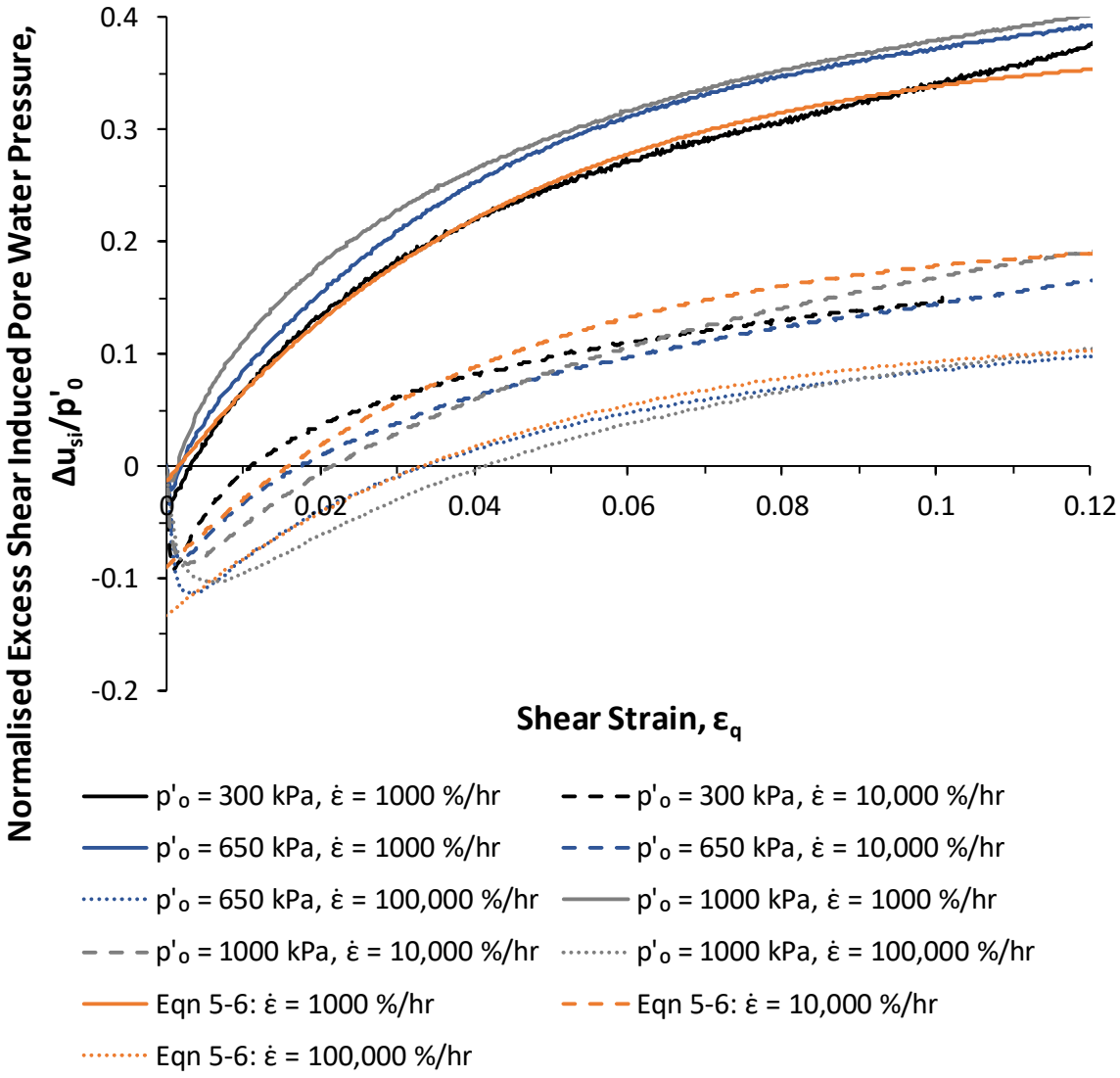

Figure 5-20 – Comparison of hyperbolic model (Equation 5-6) output using Equation 5-10 and 5-11 with measured shear-induced pore pressures in triaxial tests on normally consolidated Kaolin

5.3. Rate Effects on Friction Ratio

The question of whether friction ratios (defined as $\eta = q/p'$) increase or decrease with strain rate has been investigated since the 1950's (Bjerrum *et al.*, 1958) and there is still conflicting evidence of the impact of strain rate on mobilised friction ratios (Sheahan *et al.*, 1996).

Figure 5-21 shows the deviator stress against shear strain response discussed in Chapter 4, normalised by p'_0, for all of the strain rates and effective stresses tested. This shows, for any given initial effective stress, the normalised deviator stress increasing with axial strain rate across all strain levels.

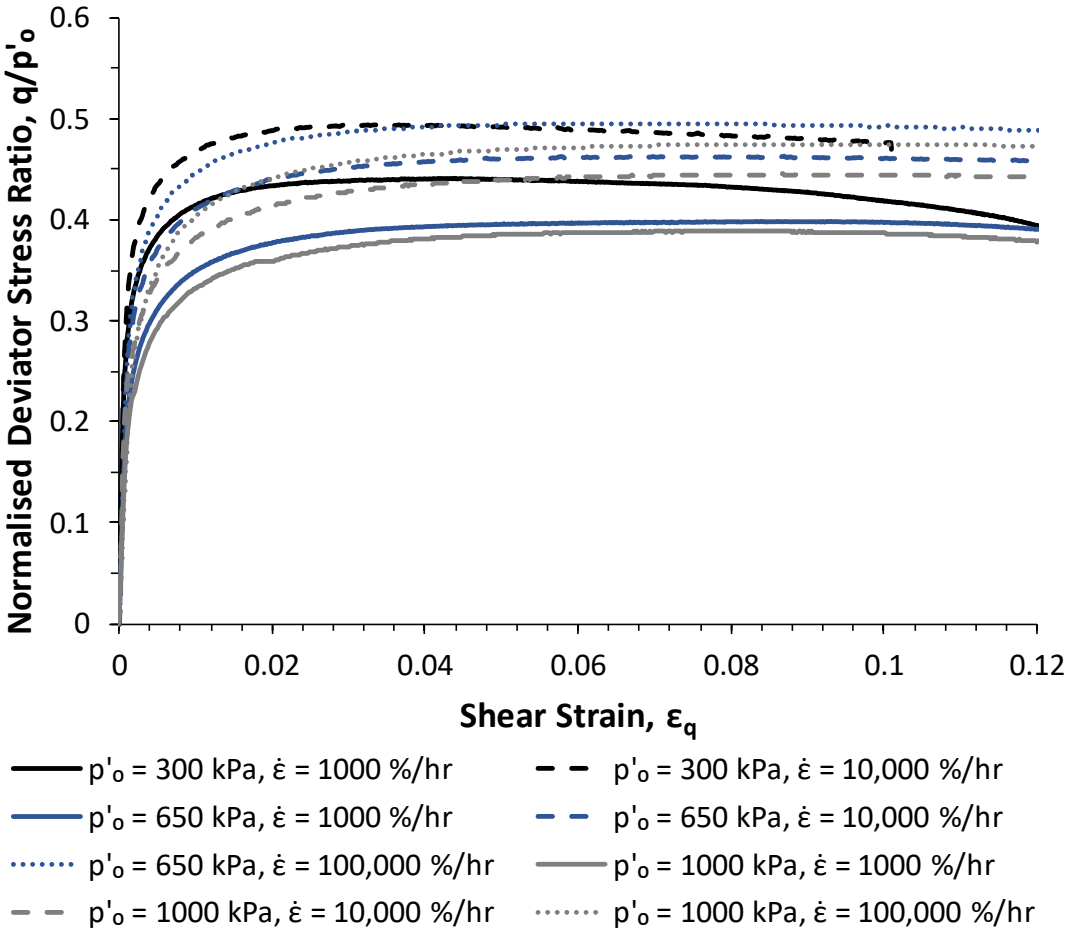

Figure 5-21 – Normalised deviator stress against shear strain for normally consolidated Kaolin

However, when instead normalising the deviator stresses by the measured p' at each strain increment, the importance of the rate-dependent effective stress changes become clear (Figure 5-22). From this, it can be seen that for each value of p'_0, up to approximately $\varepsilon_q = 0.02$ there is a slight increase in friction ratio with strain rate. After $\varepsilon_q = 0.02$, the tests at $\dot{\varepsilon} = 1000$

%/hr begin to generate friction ratios clearly higher than the comparable tests at $\dot{\varepsilon}$ = 10,000 and 100,000 %/hr, between which there was little difference. Comparing tests at the same axial strain rate, it can be seen that tests conducted at lower effective stresses show earlier mobilisation of the effective friction ratio, η, before tending towards a common friction ratio value as the critical state is approached. This is as would be expected given that rate effects are greater at higher liquidity indexes (lower p'_0) and these rate effects reach their maximum value at near ε_q = 0.01 before reducing with strain. The final values which each strain rate tested tends towards with increasing strain correspond to the values of *M,* which are discussed next in Section 5.4.

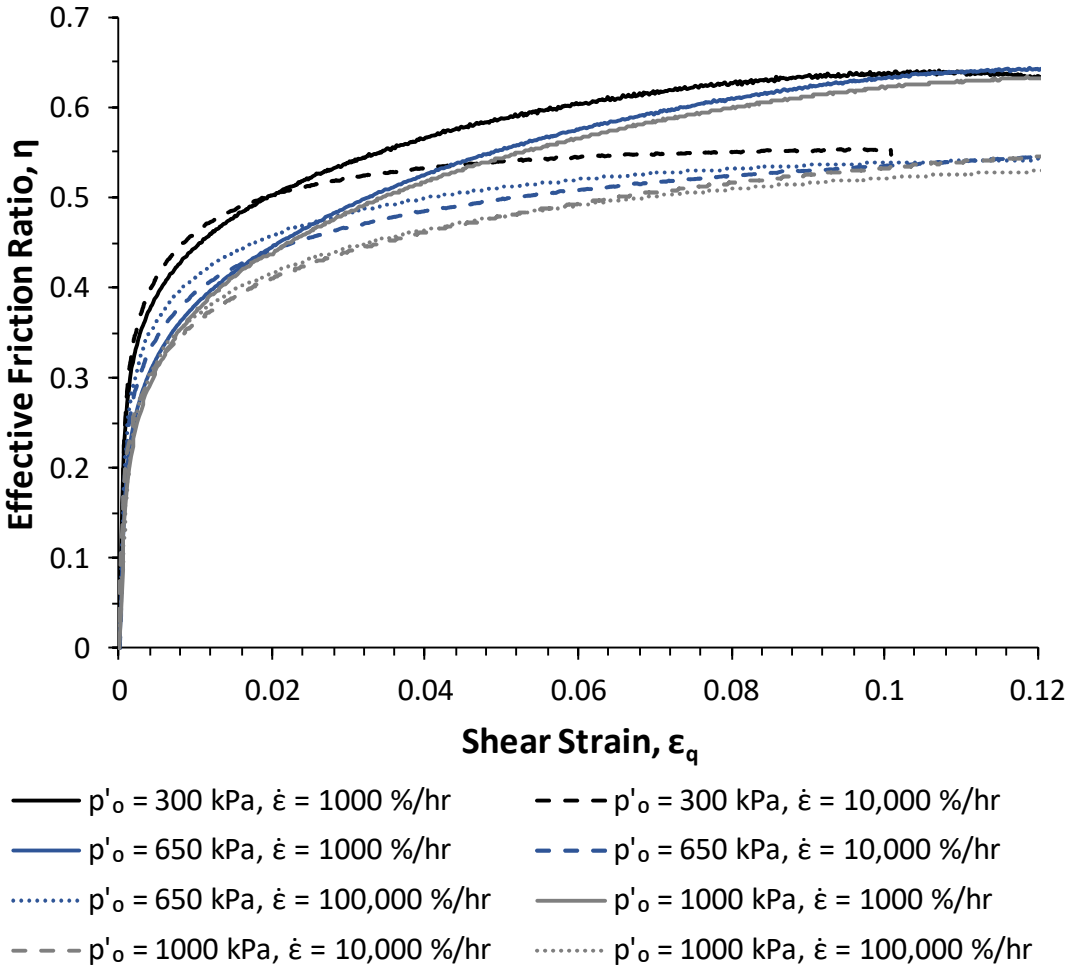

Figure 5-22 – Effective friction ratio, η, (defined as q/p') against shear strain for normally consolidated Kaolin

5.4. Rate Effects in the Critical State Framework

Whilst it is accepted that to reach the 'true' critical state, shear strains of upward of 40 % may be required, the triaxial test (which is typically limited to 20 % strain) is a commonly used method for obtaining critical state parameters. Hence, it is important to consider the impact of the rate dependent deviator stress and pore pressure behaviours, previously discussed, in terms of the critical state framework given its significance in soil mechanics and numerical modelling of soil behaviour.

Figure 5-23 shows the effective stress behaviour of the undrained triaxial tests on Kaolin in *q-p'* space. For comparison, the stress paths from the 38 mm CIU triaxial tests at $\dot{\varepsilon}$ = 1 %/hr are also shown to highlight the changes in the stress paths with axial strain rate. It should be noted that these 38 mm tests were conducted using base pore pressure measurements and without lubricated end platens, which may cause some differences in the stress paths shown. This could allow localised drainage around the central section of the specimen where shearing occurs. Localised drainage could lead to higher measured base pore pressures (as pore fluid migrates from the middle section of the specimen to the ends) and higher measured deviator stresses (as the void ratio reduces in the middle section, again due to pore fluid migration). If this did occur, then it would be likely that the 38 mm testing would slightly overestimate the CSL gradient, *M*. Specimen size effects could also exacerbate this overestimation of *M.* Omar and Sadrekarimi (2015) showed that 38 mm diameter specimens exhibited noticeably higher values of *M* compared to 70 mm diameter triaxial specimens at all initial mean effective stresses (even with lubricated end platens). However, it is noted that Omar and Sadrekarimi (2015) tested Ottawa sand rather than a clay. Possible reasons for this size effect include a greater proportion of the specimen being next to the membrane in smaller specimens (causing additional shear resistance) or the higher probability of specimen imperfections in larger specimens.

From each of the initial mean effective stresses, the tests conducted at $\dot{\varepsilon}$ = 1000 %/hr move approximately upwards to the point of yield, before the increasing pore pressure causes the specimen to move towards an apparent critical state line. The behaviour where the stress path initially follows the total stress path corresponds to the negative shear-induced pore pressures described earlier in this chapter. As previously mentioned, negative shear-induced pore pressures indicate that the specimen initially attempts to dilate, but that this is constrained by the undrained nature of the tests, leading to pore pressure suppression. This effect has been

observed previously in other rate effect studies on normally consolidated soils and was summarised by Jardine *et al.* (2004), as shown in Figure 5-24 (a). Experimental studies which have shown this behaviour include Sheahan *et al.* (1996) using K_0 normally consolidated Boston Blue Clay as shown in Figure 5-24 (b). This also shows the stress paths initially following the total stress path at higher strain rates, until the yield point is reached (which for Boston Blue Clay is also close to the peak shear stress) after which positive pore pressure evolution occurs. Leroueil *et al.* (1985) also considered this issue and suggested that the reason for this behaviour is an apparent rightward shift in the normal consolidation line in *v-ln(p')* space due to the initial dilation, with the strain rate causing the soil to behave as if it is apparently overconsolidated (discussed later in this chapter).

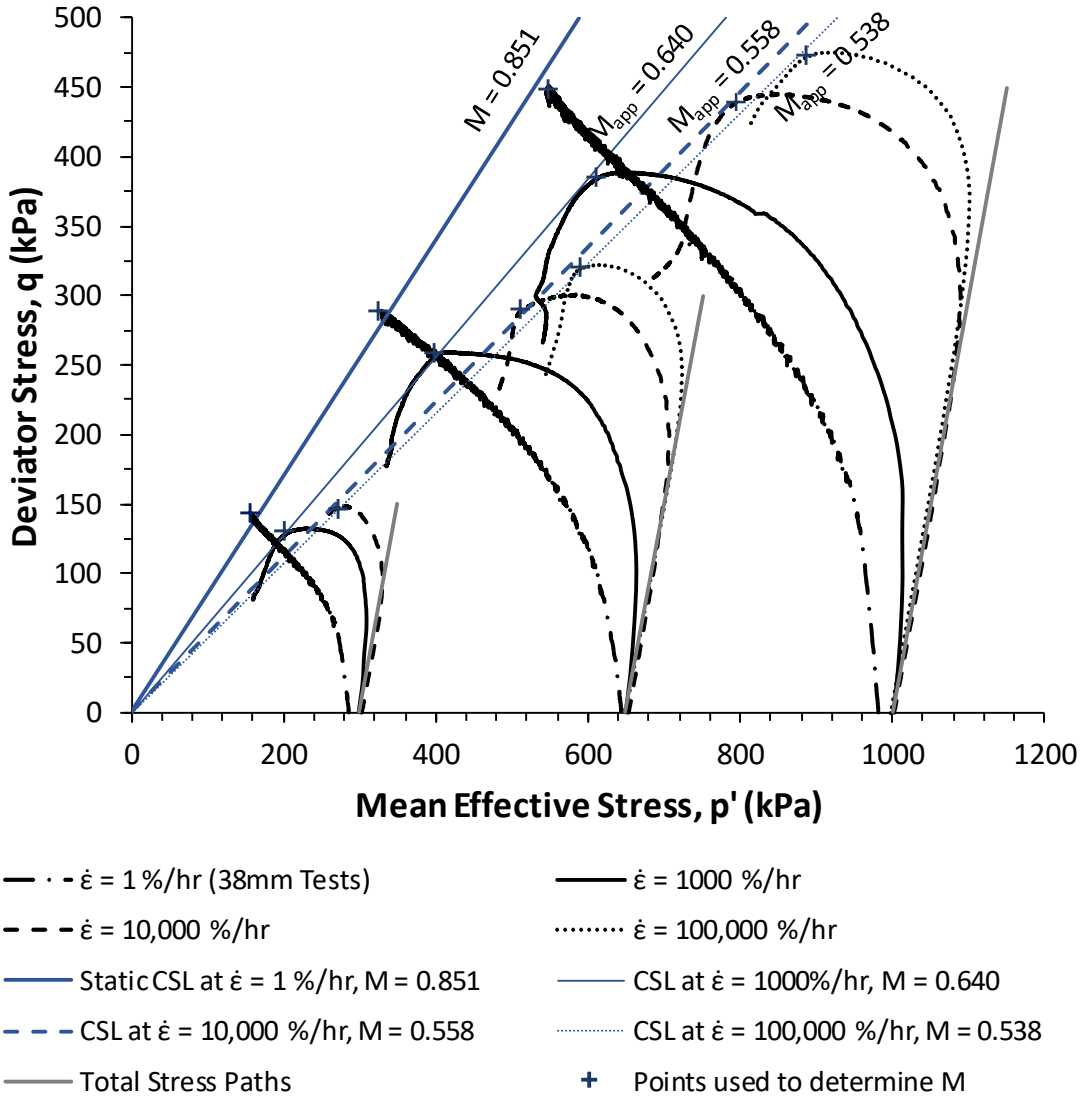

Figure 5-23 – Effective stress response at varying axial strain rates in *q-p'* space for normally consolidated Kaolin

For each of the given strain rates, the specimens all tended towards an apparent critical state line (CSL), denoted M_{app}, after which point localisation occurred and the pore pressures were no longer representative of the specimen as a whole. However, the gradient of the CSL was found to reduce with increasing axial strain rate, ranging from M_{app} = 0.640 to 0.538. These values are lower than the value of M = 0.851 determined from the 'static' characterisation of Kaolin carried out at $\dot{\varepsilon}$ = 1 %/hr. However, it is possible that the differences compared to the value of M derived from the 'static' characterisation are due to the fact that base pore pressure measurements without lubricated end platens were used in the 'static' characterisation. This could potentially mean that the measured pore pressures were not representative of the central section of the specimen where the majority of the shearing occurred, leading to changes in the observed values of M from the 38 mm testing.

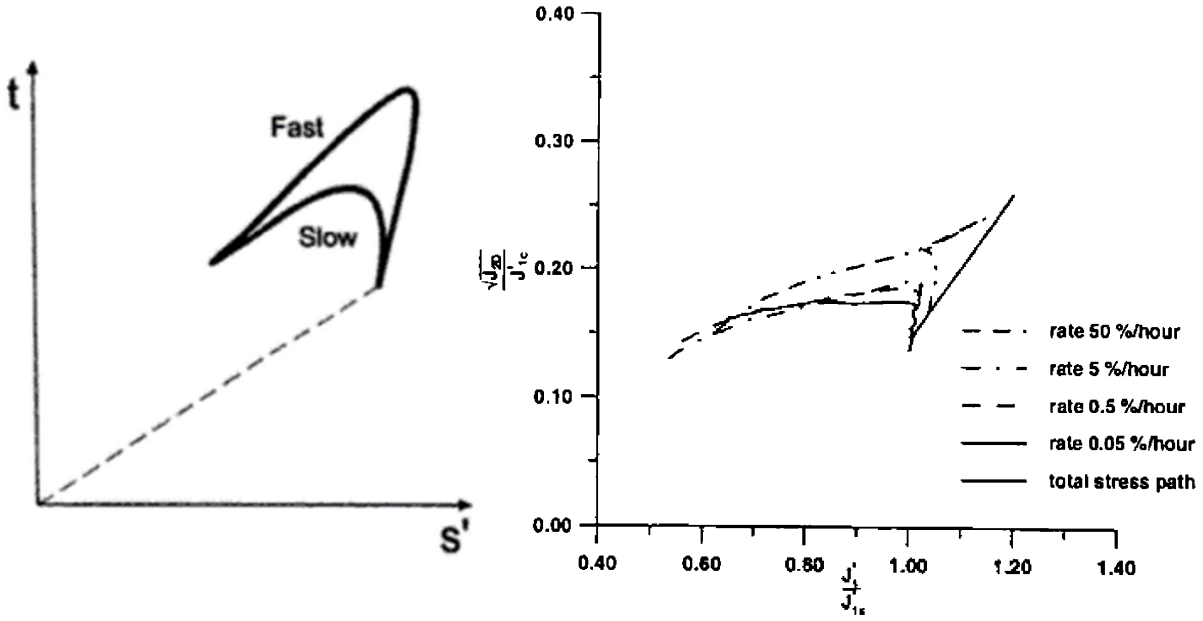

(a) (b)

Figure 5-24 – (a) Illustration of the effect of shear strain rate on the undrained stress path of K_0 normally consolidated clay (Jardine *et al.*, 2004) and (b) undrained tests from Sheahan *et al.* (1996) on K_0 normally consolidated Boston Blue Clay (BBC) showing stress paths initially following the total stress path with increasing strain rate (Katti *et al.*, 2003)

Figure 5-25 shows the apparent variation of the CSL gradient, M_{app}, determined from each individual specimen with shear strain rate. For each strain rate, the specimens tended towards a common value of M regardless of the initial mean effective stress. A greater reduction in M

was observed between $\dot{\varepsilon}_q$ = 1000 and 10,000 %/hr than between $\dot{\varepsilon}_q$ = 10,000 and 100,000 %/hr, and the reduction is best expressed by an exponential relationship (Equation 5-12).

$$M_{app} = 0.54e^{164/\dot{\varepsilon}_q} \quad (5\text{-}12)$$

This apparent reduction in the CSL gradient with strain rate contradicts several previous studies (Sheahan *et al.*, 1996; Li and Baudet, 2016; Mitchell and Soga, 2005) which found no change in *M*. However, these studies considered significantly lower axial strain rates (up to $\dot{\varepsilon}$ = 50 %/hr), and there is currently no information about the effective stress response of clays at strain rates of the order of magnitude considered here. There are also a number of issues with the existing studies mentioned which could impact on their findings. The most detailed study, Li and Baudet (2016), used a Bishop and Wesley cell with only base pressure measurements, which are reported by Sheahan *et al.* (1996) to have a time for 95 % response of 45 to 60 seconds for clays, which may impact on the findings of the study.

Figure 5-26 shows the two relationships from Figure 5-25 extended back to the conventional 'static' reference rate of $\dot{\varepsilon}_q$ = 1 %/hr. If the semi-logarithmic correlation is used, the value of M_{app} predicted is 0.78, which is reasonably close to the 'static' value of *M* = 0.851 based on the 38 mm tests presented in Chapter 3. If Equation 5-12 is used, then M_{app} would exceed *M* at below $\dot{\varepsilon}_q \approx$ 370 %/hr, and an upper limit on M_{app} may be required. The idea of a limit on M_{app} may be in keeping with previous studies discussed in the literature review which showed no change in *M* at up to $\dot{\varepsilon}_q$ = 50 %/hr. In any case, further research would be required to determine the manner in which M_{app} tends back towards *M* at lower shear strain rates.

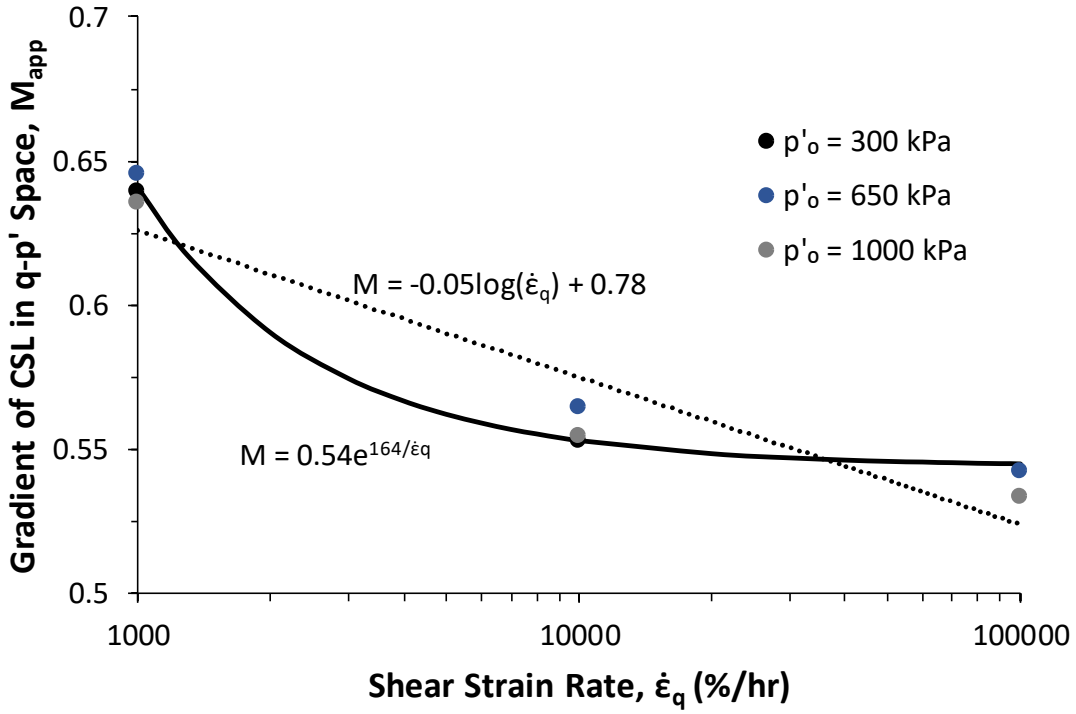

Figure 5-25 – Apparent variation of gradient of CSL in *q-p'* space with shear strain rate for normally consolidated Kaolin

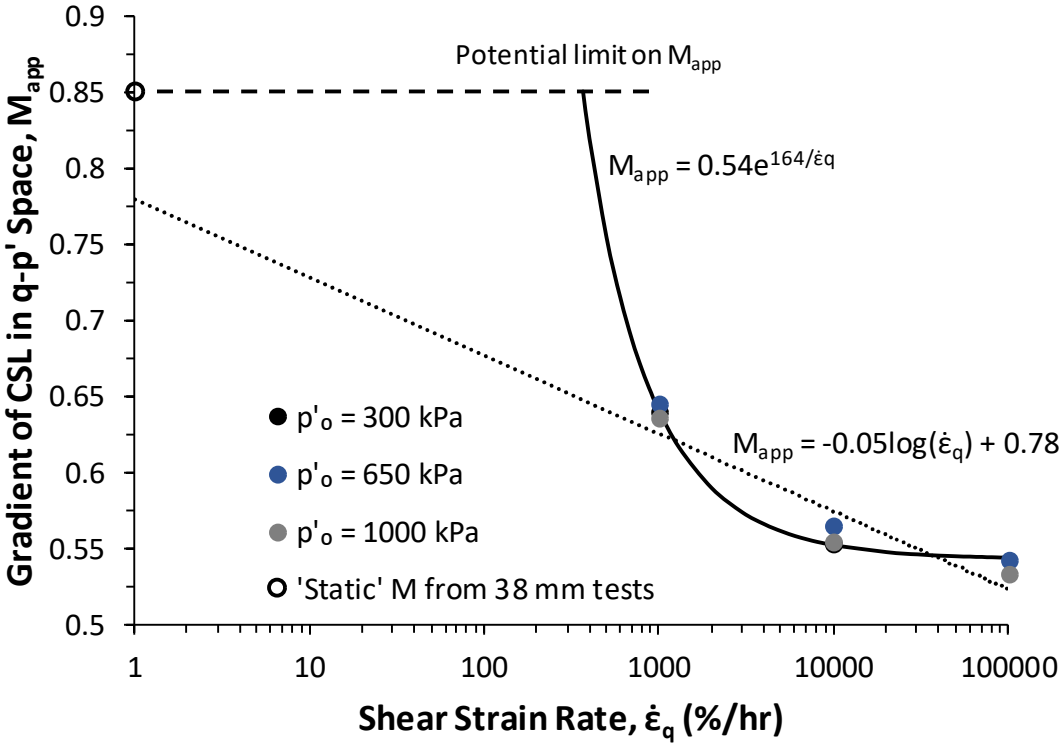

Figure 5-26 – Potential ways in which M_{app} may tend towards M as $\dot{\varepsilon}_q$ reduces to 1 %/hr

There are several possible explanations for this apparent change in *M* which will each be considered:

- Issues associated with pore pressure measurement response at high strain rates
- Localisations within the specimen
- High shear strain rates disrupting the soil structure preventing critical state being reached.

As discussed in the Methodology, careful consideration has been given to ensuring that the response time of the mid-height transducer is suitable. The transducer was found to be able to provide a 95 % pore pressure response within 50 ms and given that in the fastest tests the time to reach critical state is around 350 ms, it would be expected that PPT response times should not be an issue.

Specimen localisations may also impact on the measured pore pressure response (Head and Epps, 2011) when the strain in the sample is focussed away from the location of the pore pressure transducer. However, lubricated ends have been used which should prevent premature localisation. Additionally, if localisations were the cause of the apparent reduction in the CSL gradient, it would be expected that there would be greater variability between the specimens in terms of the value of *M* depending on the proximity of the PPT location to any localisation. This variability was not observed, with good agreement between the tests conducted at any individual strain rate. The issue of shear localisations was also considered in detail by Sachan and Penumadu (2007) using Digital Image Analysis (DIA) of surface deformations in triaxial tests on Kaolin with lubricated end platens. The study found that up until ε_q = 0.11, the shear strain occurred evenly across the surface of the specimen (and hence at the PPT). Only after ε_q = 0.11 did any significant shear localisation occur, which is consistent with the 'jump' in pore pressure measurements presented previously in Figure 5-12. The impact of strain rate on the formation of shear strain localisations was also investigated by Oka *et al.* (2005) who showed using DIA of triaxial tests on Fukakusa clay at axial strain rates from 0.6 to 60 %/hr that as the strain rate was increased, there was no increase in the degree of shear localisation at any given strain level. The results suggested that, if at all, the increasing strain rate slightly reduced the degree of localisation within the specimens.

The final possibility is that the high shear strain rates applied prevent the specimen from reaching the critical state. To consider this possibility, it is important to remember that the critical state line isn't purely a line projected in *q-p'* or *v-ln(p')* space, but has a real meaning in terms of the structure of the soil and the reorientation of the soil particles during shearing. Hattab and Fleureau (2010) investigated how the microstructure and fabric of Kaolin changed with increasing shear strain up to the point the critical state is reached using SEM imaging of triaxial specimens. It was shown that with increasing strain, the soil particles tended towards a preferred orientation (found to be approximately 40° from the horizontal for the material investigated). This preferred orientation of the platy clay particles would represent a more optimal particle packing, allowing the soil structure to either reduce in volume (in a drained test) or generate positive pore pressures (in an undrained test) which would cause the specimen to tend towards the critical state. However, using ring shear testing, Lemos and Vaughan (2000) found that fast shearing disordered the preferred orientation of particles which occurs during shearing. Similar findings were reported by Bromhead (2006) and Fearon *et al.* (2004) using optical microscopy. This raises an important question; if the preferred orientation of the clay particles which occurs as the specimen is sheared towards critical state is thworted, would the specimen reach the critical state line? However, there is little published research considering the influence of high strain rates on the microstructure of clay, and further research would be required to either confirm or refute this possibility. The results of the Scanning Electron Microscopy investigation into the influence of strain rate on the structure of Kaolin are presented in Chapter 7.

Figure 5-27 shows an example of the high strain rate response of Kaolin in *v-p'* space for p'_0 = 650 kPa. The tests have been plotted up to the point of localisation at around ε_q = 0.12. The 'static' CSL derived at $\dot{\varepsilon}$ = 1 %/hr is also shown for comparison. The direction arrows show the movement of the stress path with each specimen initially moving to the right of the NCL. This initial increase in *p'* corresponds to the initial negative shear-induced pore pressures discussed earlier, which indicate constrained dilation. It can be seen that this initial increase in *p'* (or rightwards movement) is greater at higher strain rates. After this point, positive pore pressures develop, and the specimen tends towards critical state. However, the CSL appears to move rightwards (increasing Γ) with strain rate. There was no evidence of a change in the gradient of the CSL, λ_{CSL}, with strain rate and the value of λ_{CSL} = 0.168 determined from both the NCL and

the static CSL was found to fit the high strain rate tests well. Assuming no change in λ_{CSL}, the value of Γ was found to increase from 3.041 to 3.097 as the axial strain rate increased from $\dot{\varepsilon}$ = 1000 %/hr to 100,000 %/hr.

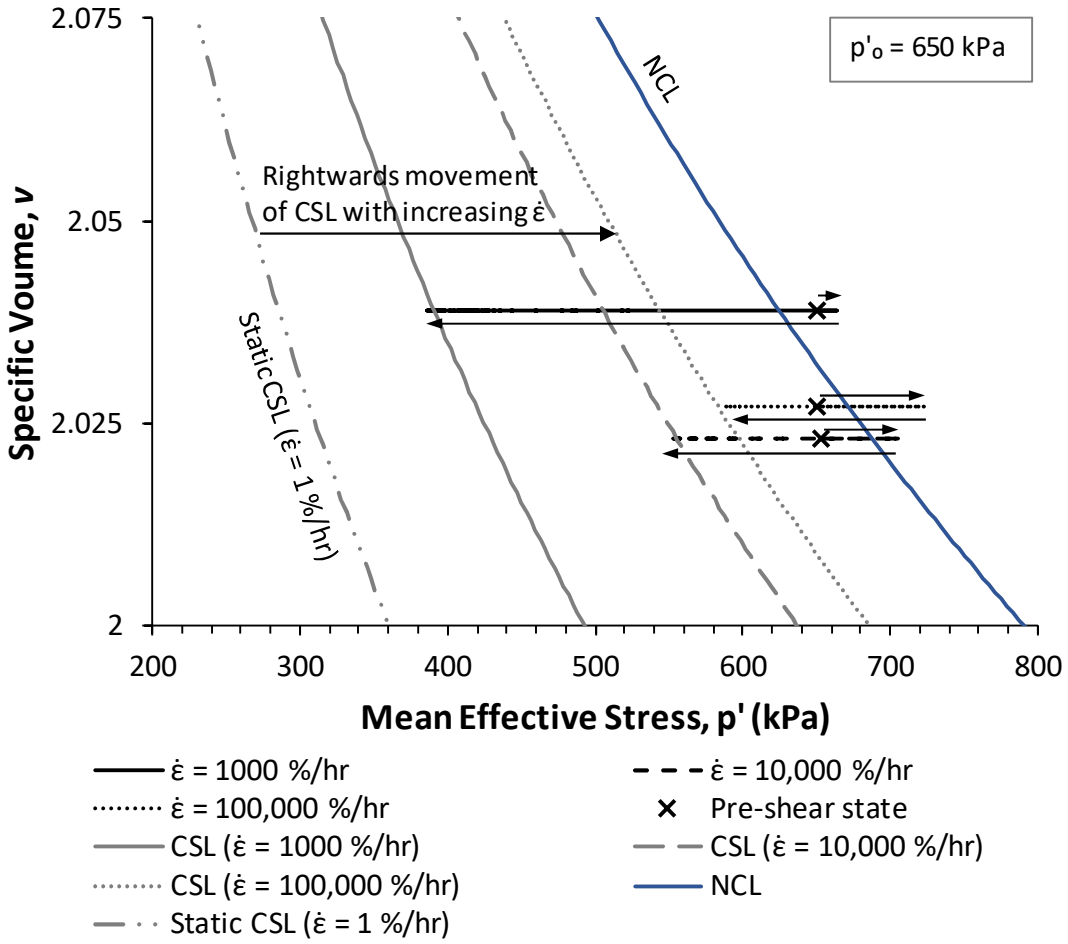

Figure 5-27 – Example of the influence of axial strain rate on the effective stress response of undrained normally consolidated Kaolin at p'_0 = 650 kPa in *v-ln(p')* space showing rightwards movement of the CSL with $\dot{\varepsilon}$ and initial negative shear-induced pore pressures

Figure 5-28 shows the same data from Figure 5-27, but with the inclusion of each of the other values of p'_0 tested. The same behaviour can be seen for each p'_0 tested, with the CSL moving to the right resulting in the CSL intercept, Γ, increasing with axial strain rate.

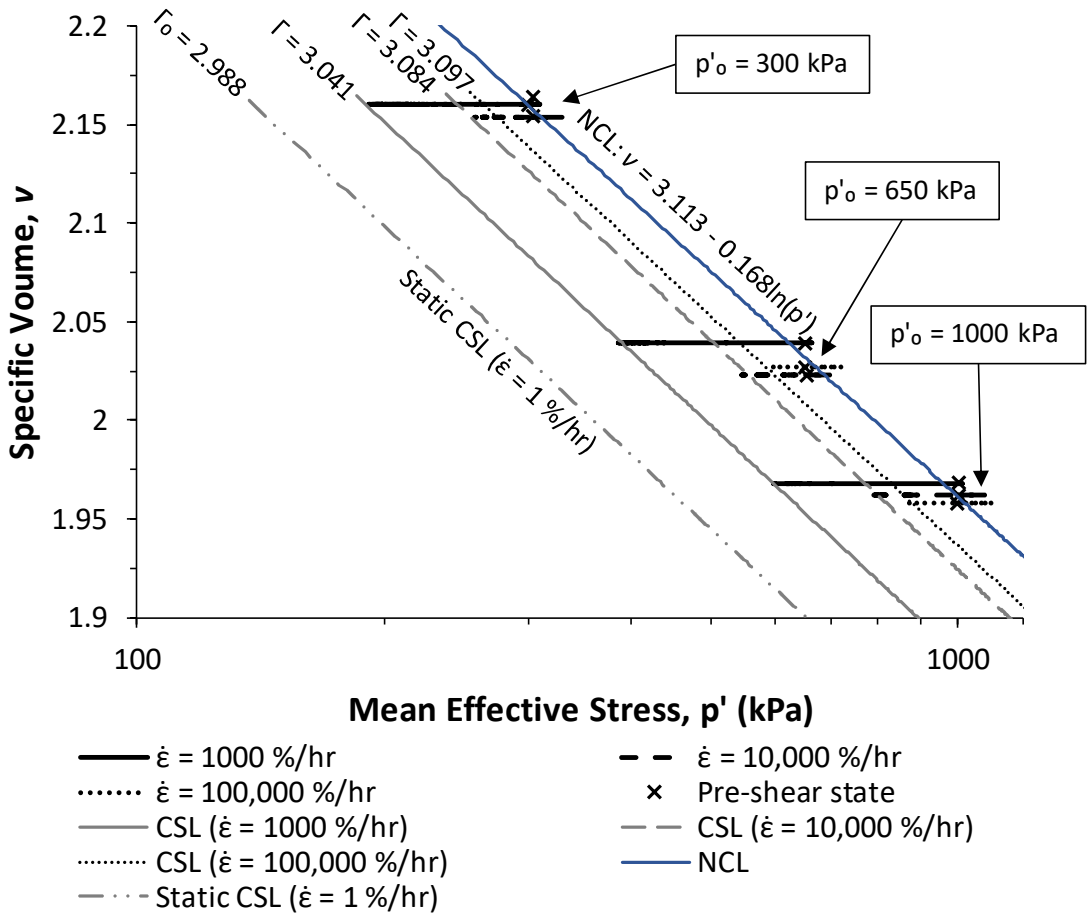

Figure 5-28 – Rate dependency of the CSL in *v-ln(p')* space showing increasing values of Γ with axial strain rate for normally consolidated kaolin

Figure 5-29 shows the variation of Γ with shear strain rate, including the static reference value, Γ_o, at $\dot{\varepsilon}_q$ = 1 %/hr. As can be seen, Γ was found to vary linearly with $log(\dot{\varepsilon})$, and for Kaolin it can be represented by Equation 5-13. The variation of Γ with $\dot{\varepsilon}_q$ has been previously investigated by Martindale *et al.* (2013) using numerical modelling where a constitutive model for strain rate effects was proposed based on the idea that the effect of strain rate is due to a change in the state parameter, Ψ, (defined in Equation 5-14, where N is the NCL intercept), which reduces with increasing shear strain rate. This meant that the intercept of the CSL, Γ, was required to be rate dependent. The idea of modelling rate effects as a change in 'apparent' OCR (which has the effect of reducing the state parameter) that increases with strain rate is not a new one, having been suggested by Leroueil *et al.* (1985) and Katti *et al.* (2003). However, Martindale *et al.* (2013) is the first significant attempt to put this approach in a critical state framework. By incorporating this change in the CSL in *v-ln(p')* space, it was shown that the

results of a number of studies including Sheahan *et al.* (1996), Sorensen *et al.* (2007) and Mukabi and Tatsuoka (1999) could be modelled, both in terms of the deviator stress and the measured pore pressure response.

$\Gamma = 0.023\log(\dot{\varepsilon}_q) + \Gamma_o$ where Γ_o = 2.985 for Kaolin and $\dot{\varepsilon}_q$ is in %/hr (5-13)

$\Psi = N - \Gamma$ for normally consolidated conditions (5-14)

The relationship between Γ and $\dot{\varepsilon}_q$ found by Martindale *et al.* (2013) is shown in Equation 5-15, where Γ_o is the value of Γ at a slow 'static' reference shear strain rate (usually $\dot{\varepsilon}_q$ = 1 %/hr) and C_o is a material dependent parameter which captures the rate dependence. Whilst Martindale *et al.* (2013) is a numerical study, Equation 5-15 is based on analysis of rapid pile tests by one of the authors. The final term, $ln(d_c + 1)$, controls the degradation of rate effects with strain, reducing from a value of 1 at ε_q = 0 to a near zero value at an unspecified extremely high shear strain where the material has fully strain softened. This idea is similar to that discussed previously in Section 4.2.5 where rate effects were found to reduce with $log(\varepsilon_q)$. Zhou and Randolph (2007) suggest that for 95 % of the strain softening to occur, a shear strain of ε_q = 10 to 50 (1000 to 5000 %) is required. This final term does not have a non-numerical solution, meaning that it cannot easily be calculated, and in any case, the highest strain levels considered here of $\varepsilon_q \approx 0.1$ to 0.2 are significantly smaller. If it is assumed that the effect of strain softening in this study is not significant and $ln(d_c + 1) \approx 1$, then Equation 5-15 resolves to Equation 5-16.

$$\Gamma = \Gamma_0\left[1 + C_0\left\{ln(0.1C_0.\dot{\varepsilon}_q + 1)\right\}\left\{ln(d_c + 1)\right\}\right] \text{ where } \dot{\varepsilon}_q \text{ is in \%/hr} \quad (5\text{-}15)$$

$$\Gamma = \Gamma_0 + \Gamma_0.C_0.ln\left(0.1C_0.\dot{\varepsilon}_q + 1\right) \text{ where } C_o = 0.05 \text{ for Kaolin} \quad (5\text{-}16)$$

One of the clays modelled by Martindale *et al.* (2013) was a Kaolin with similar properties to that used here, meaning that the material rate dependency parameter, C_o, was known to be 0.05 for Kaolin. Using this information, the variation of Γ with $\dot{\varepsilon}_q$ found by Martindale *et al.* (2013) has also been shown in Figure 5-29. It should be noted that the only parameter from this study which has been used to determine this is the reference value of the CSL intercept, Γ_o = 2.988, and that the changes in Γ shown are purely based on the material parameter from Martindale *et al.* (2013). The relationship found by Martindale *et al.* (2013) differs slightly in form from Equation 5-13 at low strain rates, which may be due to the fact that some of the studies modelled by Martindale *et al.* (2013) suggested that there is a strain rate below which

rate effects cease and the model has been designed to attempt to capture this. However, at high shear strain rates ($\dot{\varepsilon}_q$ > 100 %/hr), the model predicts that Γ varies linearly with log($\dot{\varepsilon}_q$), as found in this study. Additionally, the increase in Γ per log cycle increase of shear strain rate (Equation 5-17) of 0.021 compares well with the value of 0.023 found here (Equation 5-13), which provides some confidence in the findings. This suggests that the rate effects observed are related to the rightwards shift of the CSL in *v-ln(p')* space (increase in Γ with $\dot{\varepsilon}_q$) and the associated reduction in the state parameter, Ψ.

$$\Gamma = 0.021 log(\dot{\varepsilon}_q) + 2.96 \quad (5\text{-}17)$$

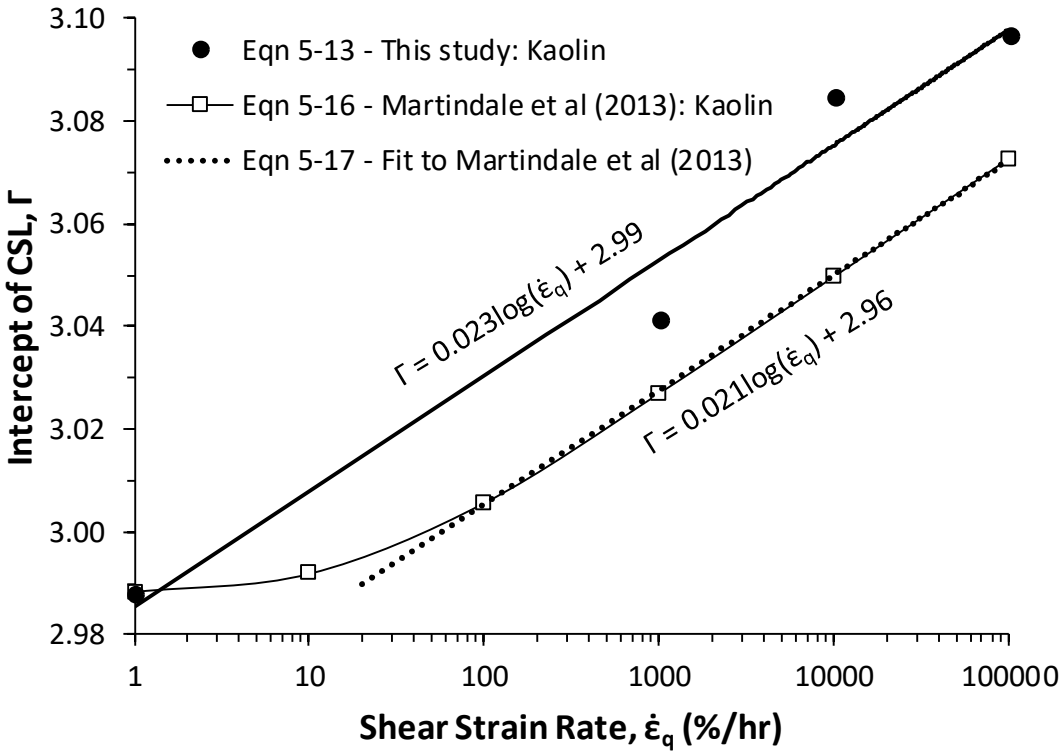

Figure 5-29 – Variation of Γ with shear strain rate for normally consolidated Kaolin

Figure 5-30 and Figure 5-31 show the influence of the changing state parameter with axial strain rate on the pore pressures, $\Delta u_{dil,si}$ and $\Delta u_{f,si}$, derived earlier, with $\Delta u_{dil,si}$ representing the initial reduction in pore pressures and $\Delta u_{f,si}$ corresponding to the final pore pressure which Δu_{si} tends towards at large strains. The state parameter has been calculated using Equation 5-14, where N = 3.113 for Kaolin and Γ is obtained for the corresponding strain rate from Figure 5-28. There is a strong correlation with Ψ for both of these, which indicates that the reductions in pore pressure throughout the strain range measured are due to the reduction in the state parameter with strain rate and less contractive behaviour. Due to the undrained conditions, this results in lower pore pressures.

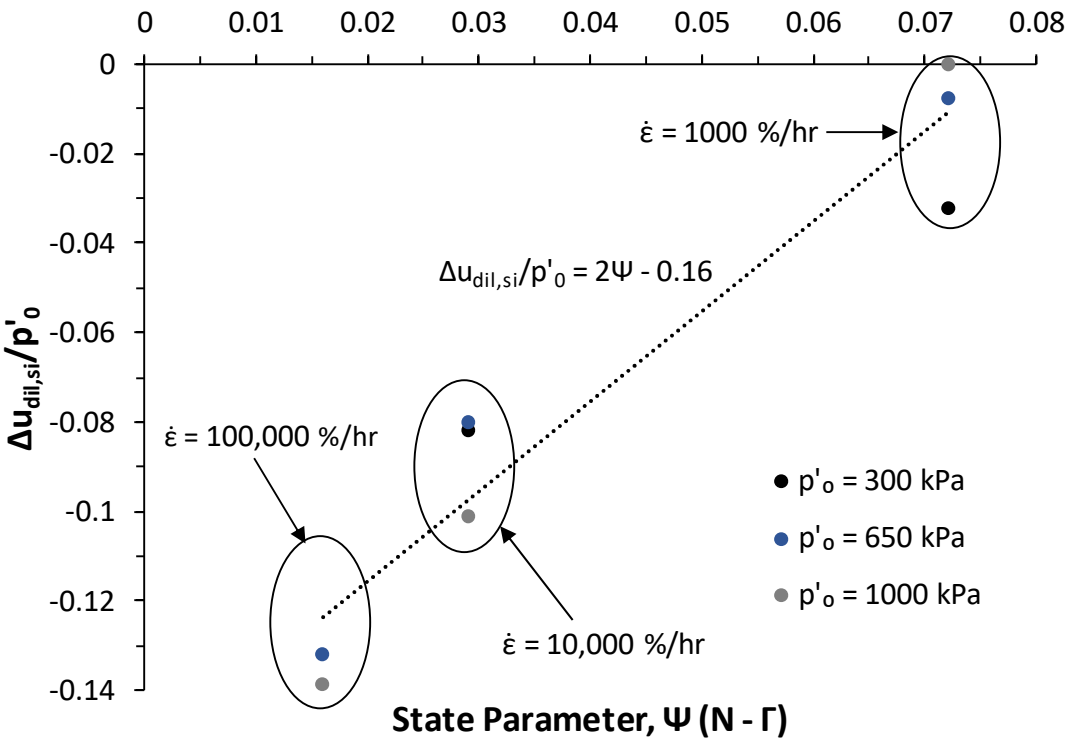

Figure 5-30 – Variation of $\Delta u_{dil,si}/p'_0$ with state parameter, Ψ, for normally consolidated Kaolin

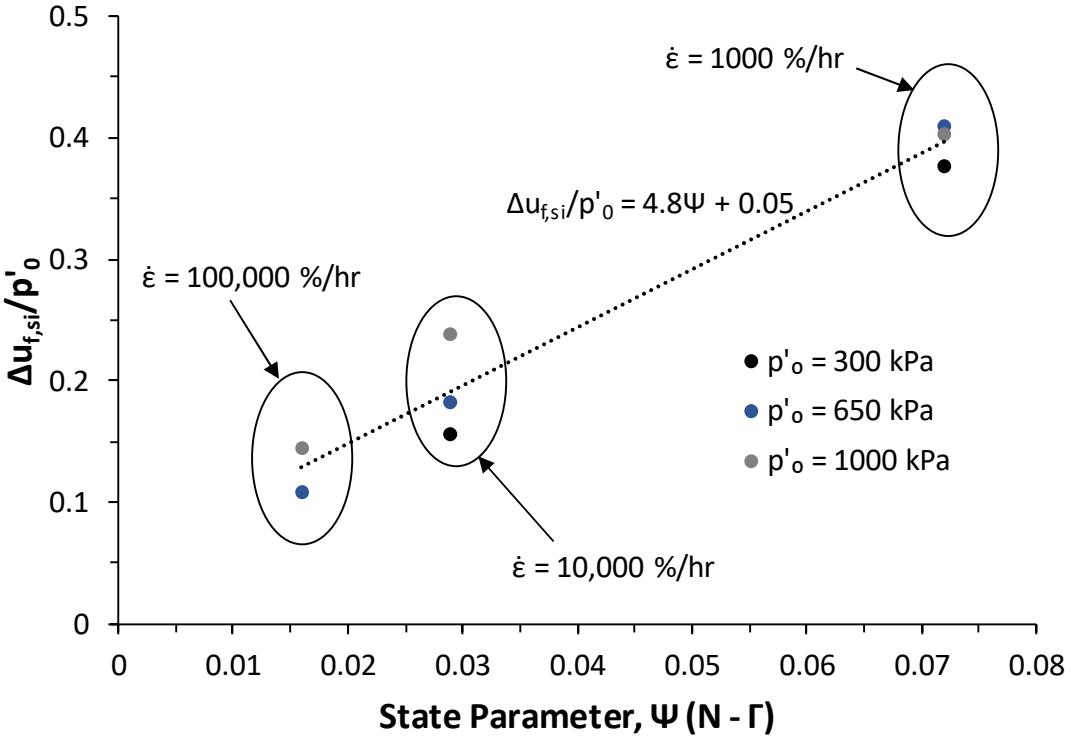

Figure 5-31 – Variation of $\Delta u_{f,si}/p'_0$ with state parameter, Ψ, for normally consolidated Kaolin

The fact that the change in state parameter with strain rate appears to be independent of soil state (or p'_0) (i.e. the critical state line moves without rotating) has important implications for rate effects. By substitution, using the equations of the NCL and CSL (Equations 5-18 and 5-19) and the definition of the state parameter for normal consolidation (Equation 5-14), it can be shown that the effective stress at which a specimen reaches the critical state line, p'_{CSL}, can be represented by Equation 5-20 (assuming undrained conditions). Using the definition of the CSL in q-p' space of $q_{CSL} = Mp'_{CSL}$, the deviator stress at which the CSL is reached, q_{CSL}, is then defined by Equation 5-21. However, as the deviator stress at the reference shear strain rate, $q_{CSL,ref}$, is also proportional to p'_0 (as shown in Chapter 4), this suggests that the rate effect per log cycle, λ, would be a constant value at large strain levels near critical state regardless of soil state. Using the values of M and λ_{CSL} for Kaolin and the change in Ψ with shear strain rate shown in Figure 5-29, Equation 5-21 suggests a constant rate effect of $\lambda \approx 0.12$ for all values of p'_0.

$$v = N - \lambda_{CSL} \ln(p'_0) \tag{5-18}$$

$$v = \Gamma - \lambda_{CSL} \ln(p'_{CSL}) \tag{5-19}$$

$$\frac{p'_{CSL}}{p'_0} = \frac{1}{e^{\left(\frac{\psi}{\lambda_{CSL}}\right)}} \tag{5-20}$$

$$\frac{q_{CSL}}{p'_0} = \frac{M}{e^{\left(\frac{\psi}{\lambda_{CSL}}\right)}} \tag{5-21}$$

In comparison, the rate effects at large strains ($\varepsilon_q = 0.1$) presented in Chapter 4 still showed some soil state dependence, reducing with increasing p'_0 from $\lambda = 0.15$ to 0.11 (although these values are less soil state dependent than the maximum rate effects observed at $\varepsilon_q = 0.01$). A possible explanation for this difference is that these rate effect values were derived at a specific strain of $\varepsilon_q = 0.1$, whereas Equation 5-21 considers only the point at which the CSL is reached.

The question that is then raised is why rate effects at lower strain levels have been found to be soil state dependent? To consider this issue, the changes in effective stress ($\Delta u_{si}/p'_0$) and effective friction ratio at $\varepsilon_q = 0.01$ (where the greatest rate effects were observed) are shown for the three values of p'_0 tested (Figure 5-32 and Figure 5-33). As previously found earlier in this chapter, $\Delta u_{si}/p'_0$ (equal to $\Delta p'/p'_0$) reduced with $\dot{\varepsilon}_q$ according to Equation 5-22 regardless

of the value of p'_0, suggesting the differences in rate effect with soil state are not due to changes in the effective stress.

$$\frac{\Delta u_{si}}{p'_0} = 0.23\left(\dot{\varepsilon}_q / \dot{\varepsilon}_{q,ref}\right)^{-0.30} - 0.15 \tag{5-22}$$

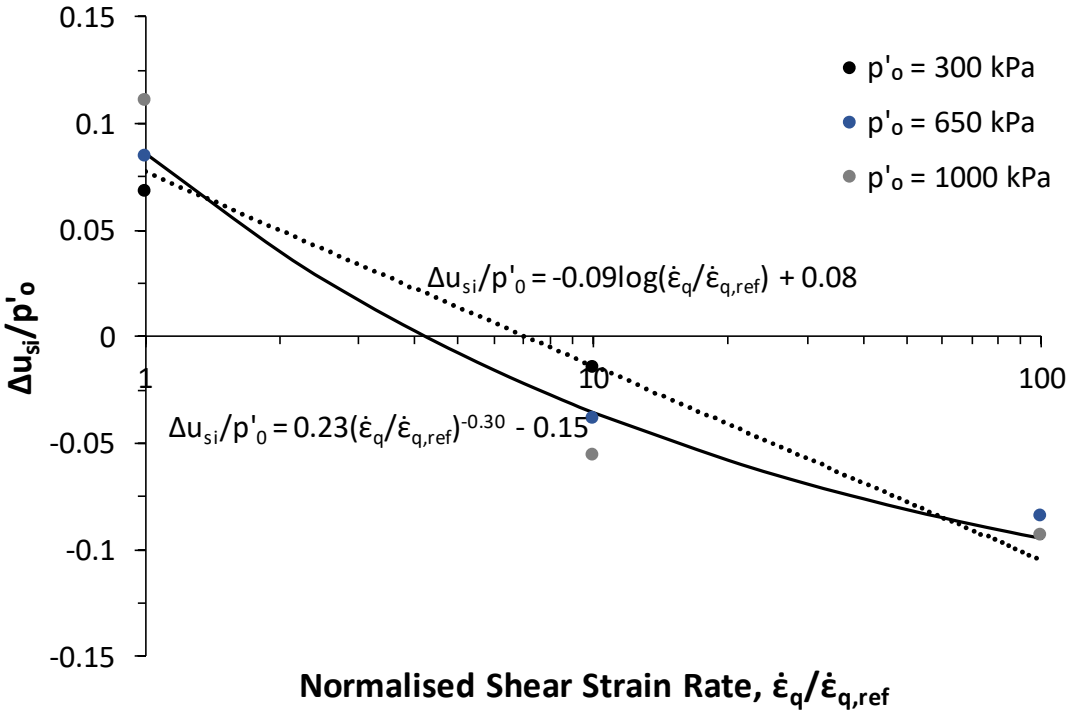

Figure 5-32 – Variation of $\Delta u_{si}/p'_0$ with normalised shear strain rate for normally consolidated Kaolin at ε_q = 0.01

In contrast, the effective friction ratio, q/p', at ε_q = 0.01 showed significant dependence on the soil state, increasing with reducing p'_0 as shown in Figure 5-33. The friction ratio also showed a general trend of increasing with $\dot{\varepsilon}_q$, with these increases being greater at lower initial effective stresses. This provides an explanation for the soil state dependence of rate effects. The deviator stress, q, is related to the effective stress, p', by the effective friction ratio, η, at a given strain (Equation 5-23). Additionally, the change in p' at a given strain is also directly related to Δu_{si}, due to the definition of shear-induced pore pressure (Equation 5-24). Figure 5-33 shows that at ε_q = 0.01, η is higher and shows greater increases with $\dot{\varepsilon}_q$ at lower values of p'_0. Hence, due to this increase in η with $\dot{\varepsilon}_q$, the reduction in Δu_{si} with shear strain rate shown in Figure 5-32 will cause a greater relative increase in q at lower initial mean effective stresses. This greater relative increase in q with $\dot{\varepsilon}_q$ would mean higher values of λ at lower values of p'_0, as observed in Chapter 4. This suggests the soil state dependence of rate effects at low strain levels (of the order of ε_q = 0.01) is due to the dependence of η on p'_0 at these strain levels.

$$q = \eta p' \tag{5-23}$$

$$\Delta p' = -\Delta u_{si} \tag{5-24}$$

Also shown for comparison in Figure 5-33 is the change in effective friction ratio using data from Sheahan *et al.* (1996) for triaxial tests on normally consolidated Boston Blue Clay ($\dot{\varepsilon}$ up to 50 %/hr, $p'_0 \approx 185$ kPa). These friction ratios are at shear strains of $\varepsilon_q = 0.003$, which is the nearest strain level available to the $\varepsilon_q = 0.01$ used for analysis of Kaolin. As can be seen, the increases in the effective friction ratio are similar in magnitude to those found in this study, despite the fact that a different material was tested and a lower value of p'_0 was used.

In summary, the observed reductions in shear-induced pore pressure, Δu_{si} with $\dot{\varepsilon}_q$ are found to be related to a reduction in the state parameter, Ψ, (or increase in Γ) with $\dot{\varepsilon}_q$. These reductions in Δu_{si} appear to be the main mechanism for the increase in deviator stress with strain rate. However, the dependence of rate effects on the initial soil state at low strain levels is not related to differences in the pore pressure generation but is instead due to the fact that rate effects lead to a greater increase in the effective friction angle, η, at lower values of p'_0. This effect reduces with increasing strain as η tends towards M.

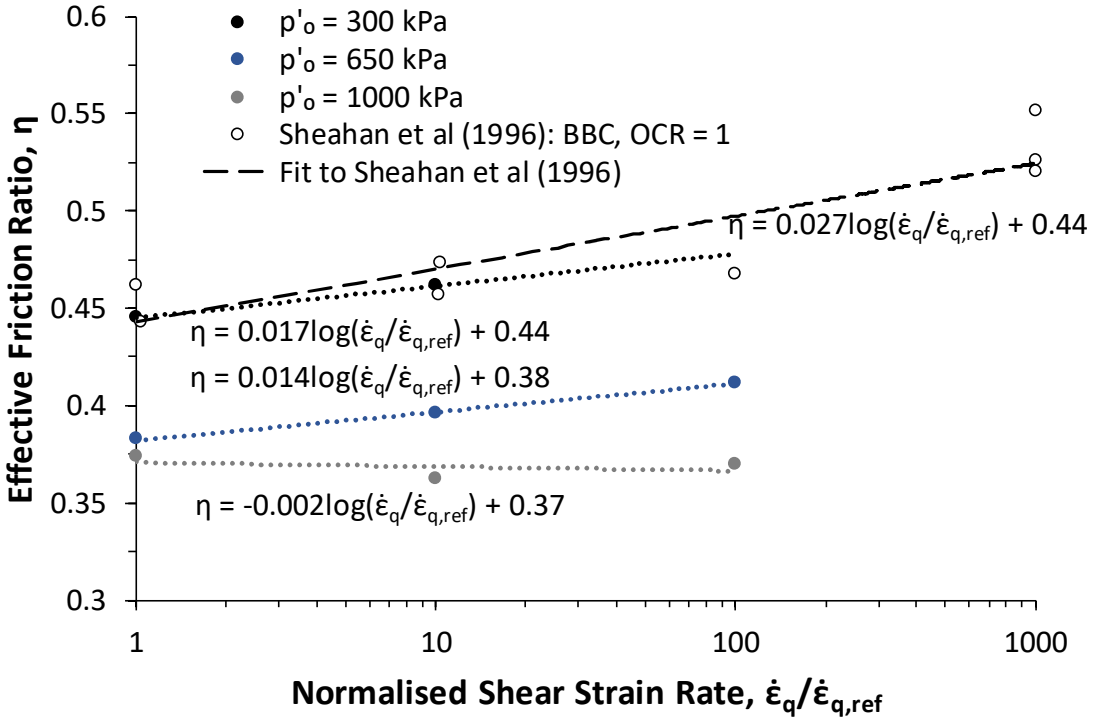

Figure 5-33 – Variation of effective friction ratio, η, with normalised shear strain rate and p'_0 for normally consolidated Kaolin at $\varepsilon_q = 0.01$

5.5. Rate Effects on the Yield Envelope

Using the yield points identified from the large-strain deviator stress against strain data from Chapter 4, the impact of rate effects on the modified cam clay (MCC) yield envelope was investigated. The MCC elliptical yield envelope is defined by Equation 5-25 (excluding the Hvorslev surface which will not be considered here as this would have required a far larger number of overconsolidated tests). In Equation 5-25, p'_{max} is the maximum effective stress experienced by the specimen and p'_0 is the initial effective stress at the start of shearing.

$$\left(\frac{q_y}{p'}\right)^2 = M^2\left(\frac{p'_{max}}{p'} - 1\right) \quad \text{where } p'_{max} = OCR.p'_o \tag{5-25}$$

Theoretically, as the tests conducted were normally consolidated, an overconsolidation ratio (OCR) of 1 would be used to define the yield envelopes. However, the fact that the stress paths initially follow the total stress path before the point of yield in high strain rate tests has implications for this. Due to the greater yield stress and higher effective stress at yield caused by the initial pore pressure suppression discussed earlier, an expansion of the yield envelope with strain rate is required. This effect has been identified by a number of studies (Leroueil *et al.*, 1985; O'Reilly *et al.*, 1989; Martindale *et al.*, 2013) and the only sensible way to fit the MCC yield envelope to the expanded yield points is to vary the value of p'_{max} using an apparent OCR related to the strain rate (Equation 5-26). This approach is not without precedent as several other studies have modelled rate effects using the concept of apparent overconsolidation to simulate the pore pressure suppression that occurs (Katti *et al.*, 2003).

$$\left(\frac{q_y}{p'}\right)^2 = M^2\left(\frac{p'_{max,app}}{p'} - 1\right) \tag{5-26}$$

Using the measured values of the CSL gradient, M_{app}, from Figure 5-25 for each axial strain rate the MCC yield envelopes have been fitted to the observed yield points (which are shown in Figure 5-34) by varying the apparent OCR and identifying the value which causes the yield point and the MCC yield envelope to intersect. The deviator stress and mean effective stress at yield based on the large strain data are denoted q_y and p'_y respectively. This is illustrated schematically in Figure 5-35 for two cases, a slow reference test ($\dot{\varepsilon} \approx 1$ %/hr) and a fast test. In the case of the slow test, the yield stress is small and the effective stress at yield is close to p'_0, meaning that the intercept of the yield envelope with the x-axis, p'_{max}, is close to p'_0, as

conventionally expected. According to Equation 5-25 this would correspond to an OCR of 1. For the fast test, both the yield stress and *p'* at yield are greater, meaning that the intercept of the yield envelope with the x-axis, p'_{max}, is notably higher than p'_0 despite the specimen being normally consolidated. This leads to an OCR of greater than unity in Equation 5-25. Due to the fact that this increase in OCR and p'_{max} is caused by the increasing strain rate rather than real overconsolidation, these values are denoted as 'apparent' (OCR_{app} and $p'_{max,app}$) as shown in Equation 5-27.

$$OCR_{app} = \frac{p'_{max,app}}{p'_0} \tag{5-27}$$

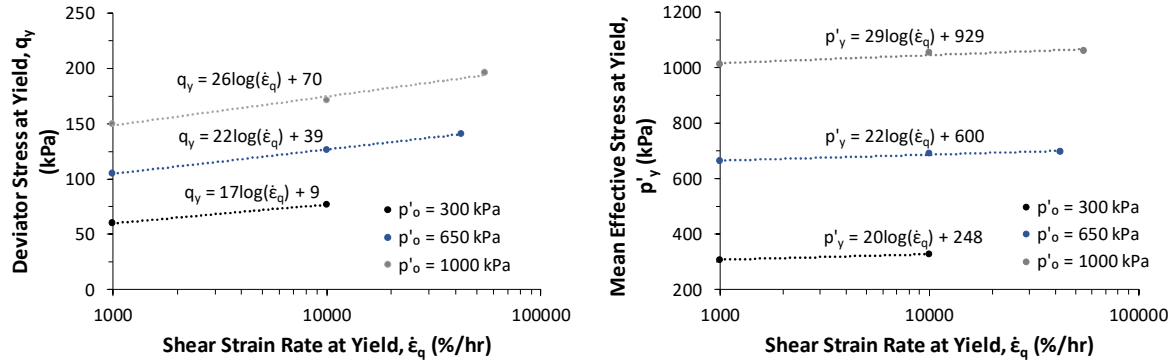

(a) (b)

Figure 5-34 – (a) Variation of deviator stress at yield with shear strain rate and (b) change in mean effective stress with shear strain rate for normally consolidated Kaolin

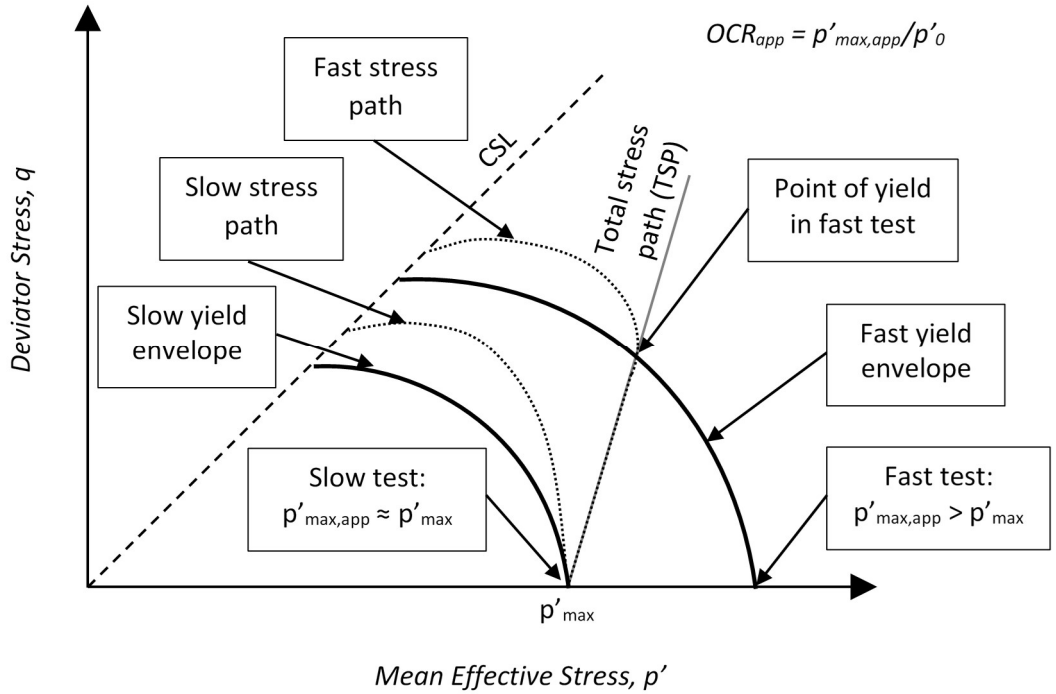

Figure 5-35 – Schematic showing the determination of the apparent OCR, OCR_{app}, from observed yield points and stress paths using Modified Cam Clay (MCC) yield envelopes for normally consolidated specimens

Figure 5-36, Figure 5-37 and Figure 5-38 show the fitted yield envelopes for each of the axial strain rates and initial mean effective stresses tested in *q-p'* space, with each axis normalised by p'_0. This shows that the expansion of the yield envelope with strain rate is greater at lower effective stresses, with the largest changes observed in the tests conducted at p'_0 = 300 kPa. The fitted parameters for the yield envelopes using M_{app} are shown in Table 5-3, with the derived values of OCR_{app} ranging from 1.07 to 1.29. It has been assumed that the overall shape of the MCC yield envelope is rate independent as there is currently no published evidence to the contrary, but this would be an area of recommended future work. This would involve tests at the same effective stresses and axial strain rates considered here, but instead using a range of lightly overconsolidated specimens with static OCR values from 1 to 2. However, the limited number of overconsolidated tests conducted (presented in Section 4.2.3) showed that OCR has no influence on the magnitude of rate effects, which is in agreement with the literature review. This would suggest that the rate effect (q/q_{ref}) would be uniform across the yield envelope, which would expand with strain rate maintaining the same shape and form, although this hypothesis would still require experimental validation.

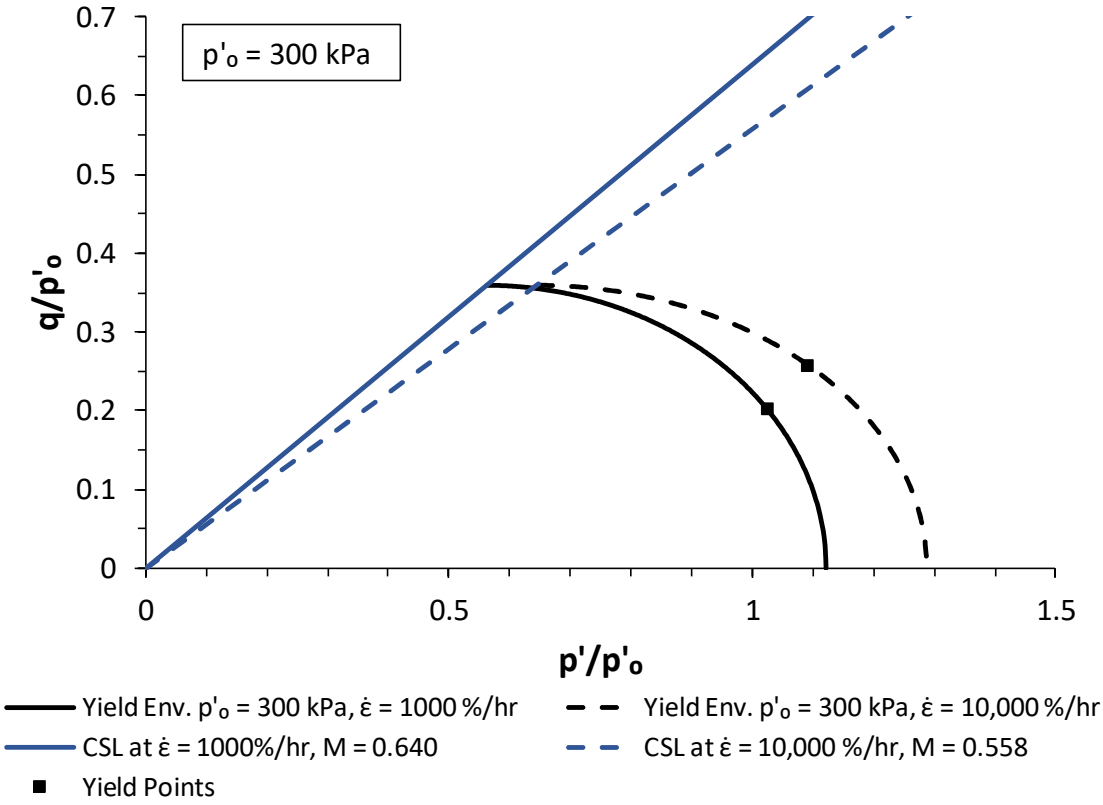

Figure 5-36 – MCC yield envelopes fitted to the experimentally measured yield points using apparent OCR for normally consolidated Kaolin at p'_o = 300 kPa

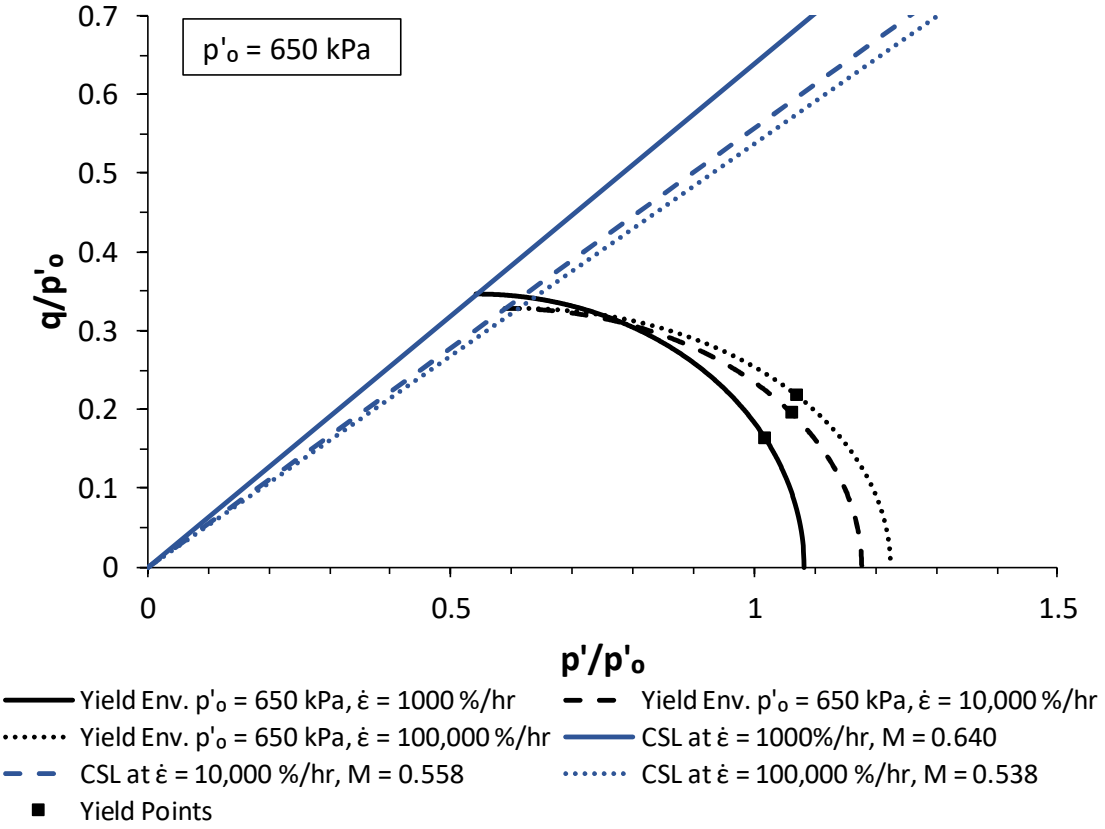

Figure 5-37 – MCC yield envelopes fitted to the experimentally measured yield points using apparent OCR for normally consolidated Kaolin at p'_o = 650 kPa

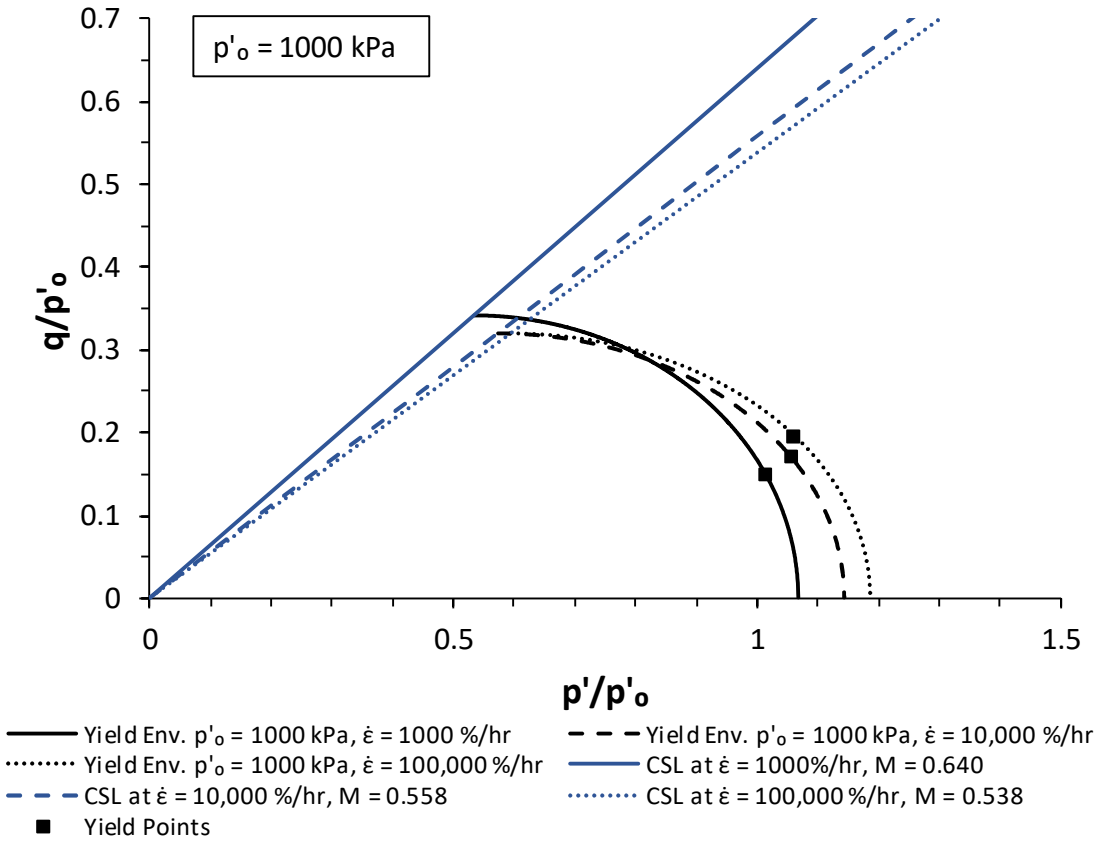

Figure 5-38 – MCC yield envelopes fitted to the experimentally measured yield points using apparent OCR for normally consolidated Kaolin at p'_0 = 1000 kPa

Table 5-3 – MCC yield envelope fitting parameters for normally consolidated Kaolin using M_{app}

Test Designation	p'_0 (kPa)	Axial Strain Rate (%/hr)	MCC Yield Envelope Parameters		
			M_{app}	$p'_{max,app}$ (kPa)	OCR_{app}
KLN-TU-L1	300	1000	0.640	336.5	1.12
KLN-TU-L2	300	10000	0.558	386.0	1.29
KLN-TU-L4	650	1000	0.640	703.6	1.08
KLN-TU-L5	650	10000	0.558	765.7	1.18
KLN-TU-L6	650	100000	0.538	795.5	1.22
KLN-TU-L7	1000	1000	0.640	1066.3	1.07
KLN-TU-L8	1000	10000	0.558	1144.0	1.14
KLN-TU-L9	1000	100000	0.538	1186.1	1.18

OCR_{app} has also been determined using the value of M = 0.861 derived from the 38 mm CIU tests at $\dot{\varepsilon}$ = 1 %/hr for comparison (Table 5-4). These values show the same trend as the values of OCR_{app} derived using M_{app}, with the only difference being that they are slightly lower in magnitude, suggesting that the changes in OCR_{app} with strain rate are not artificially due to the changes in M_{app}. The discussion that follows uses the values of OCR_{app} based on M_{app}, as this is the value of M that derived from the actual stress paths to which the yield envelopes are being fitted.

Table 5-4 – MCC yield envelope fitting parameters for normally consolidated Kaolin using M = 0.861

Test Designation	p'_0 (kPa)	Axial Strain Rate (%/hr)	MCC Yield Envelope Parameters		
			M	$p'_{max,app}$ (kPa)	OCR_{app}
KLN-TU-L1	300	1000	0.861	323.8	1.08
KLN-TU-L2	300	10000	0.861	352.4	1.17
KLN-TU-L4	650	1000	0.861	685.5	1.05
KLN-TU-L5	650	10000	0.861	723.0	1.11
KLN-TU-L6	650	100000	0.861	735.6	1.13
KLN-TU-L7	1000	1000	0.861	1042.1	1.04
KLN-TU-L8	1000	10000	0.861	1092.5	1.09
KLN-TU-L9	1000	100000	0.861	1110.0	1.11

Despite the fact that the change in OCR_{app} with $\dot{\varepsilon}$ has been widely reported, few studies have presented the impact of axial strain rate on the yield envelope in q-p' space. Figure 5-39 shows a comparison of the MCC yield envelopes fitted to data presented by Leroueil and Marques (1996) from one-dimensional constant rate of strain tests (Mascouche clay at p'_0 = 300 kPa, $\dot{\varepsilon}$ = 0.002 to 2 %/hr) with those from Kaolin in the present investigation at the same value of p'_0. The deviator stresses reported in Leroueil and Marques (1996) have been adjusted to account for the fact that Mascouche clay has a far greater (M = 1.27) CSL gradient than Kaolin. This means that the yield envelopes have been scaled vertically to allow comparison. Figure 5-39 shows that, despite the different materials, there is a clear trend in yield envelope expansion with $\dot{\varepsilon}$ over all of the strain rates presented. There is a flattening of the yield envelopes for Kaolin with $\dot{\varepsilon}$, which is due to the fact that M was found to reduce with $\dot{\varepsilon}$ as reported earlier in

this chapter. However, there is insufficient evidence to say whether this flattening actually occurs in reality, and this is an area of recommended future research. There is currently no other data published on yield envelope changes in *q-p'* space at axial strain rates of the order of those used here ($\dot{\varepsilon}$ up to 100,000 %/hr).

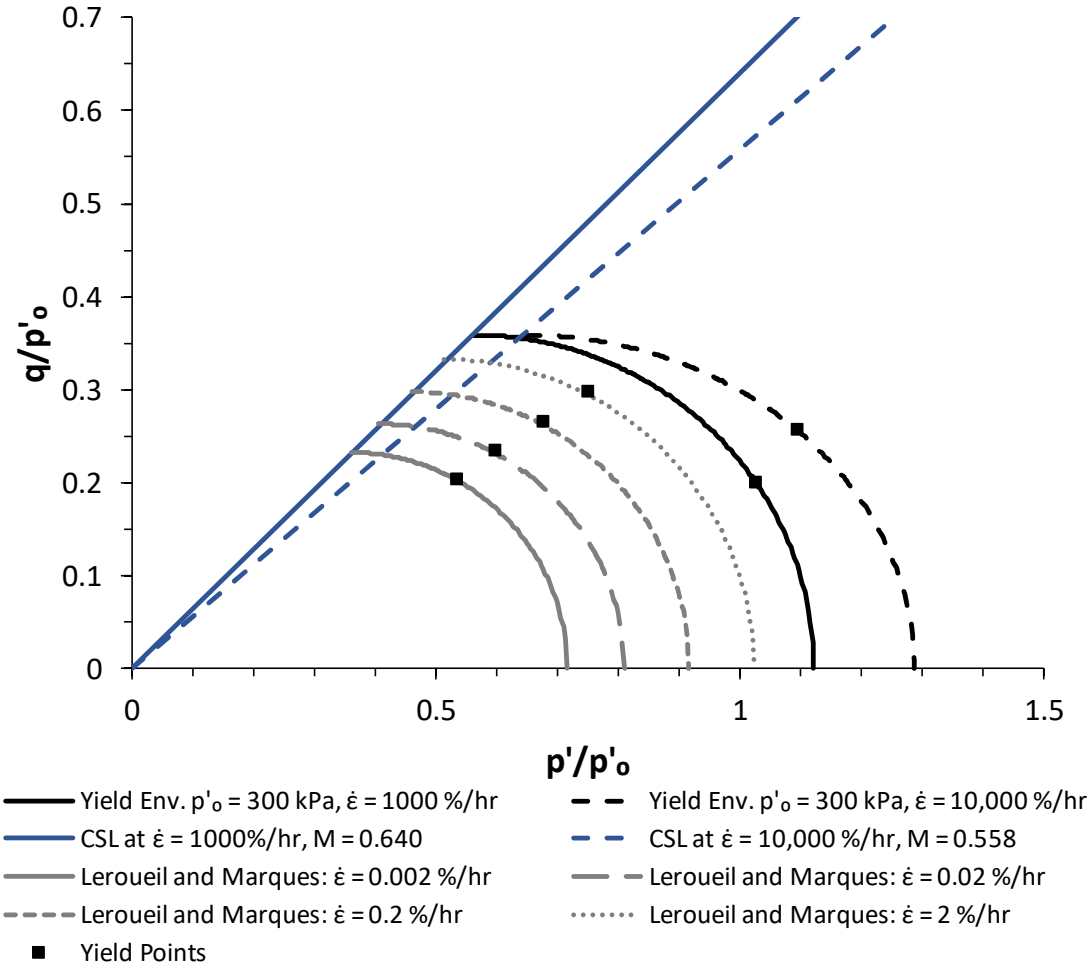

Figure 5-39 – Comparison of derived strain rate dependent yield envelopes from normally consolidated Kaolin with rate dependent yield envelopes for Mascouche clay based on data from Leroueil and Marques (1996) (all at p'_o = 300 kPa)

Figure 5-40 shows the variation of the apparent OCR with shear strain rate for each value of p'_0, which indicates that OCR_{app} varies linearly with $\log(\dot{\varepsilon}_q)$. OCR_{app} was found to be more sensitive to changes in strain rate at lower effective stresses, with the change in OCR_{app} per log cycle of strain rate ranging from 0.165 at p'_0 = 300 kPa to 0.060 at p'_0 = 1000 kPa. The value of OCR_{app} at the reference shear strain rate of $\dot{\varepsilon}_q$ = 1000 %/hr remained higher than unity as, compared to the static shear strain rate of near 1 %/hr on which the MCC model is based, 1000 %/hr is still a relatively high strain rate.

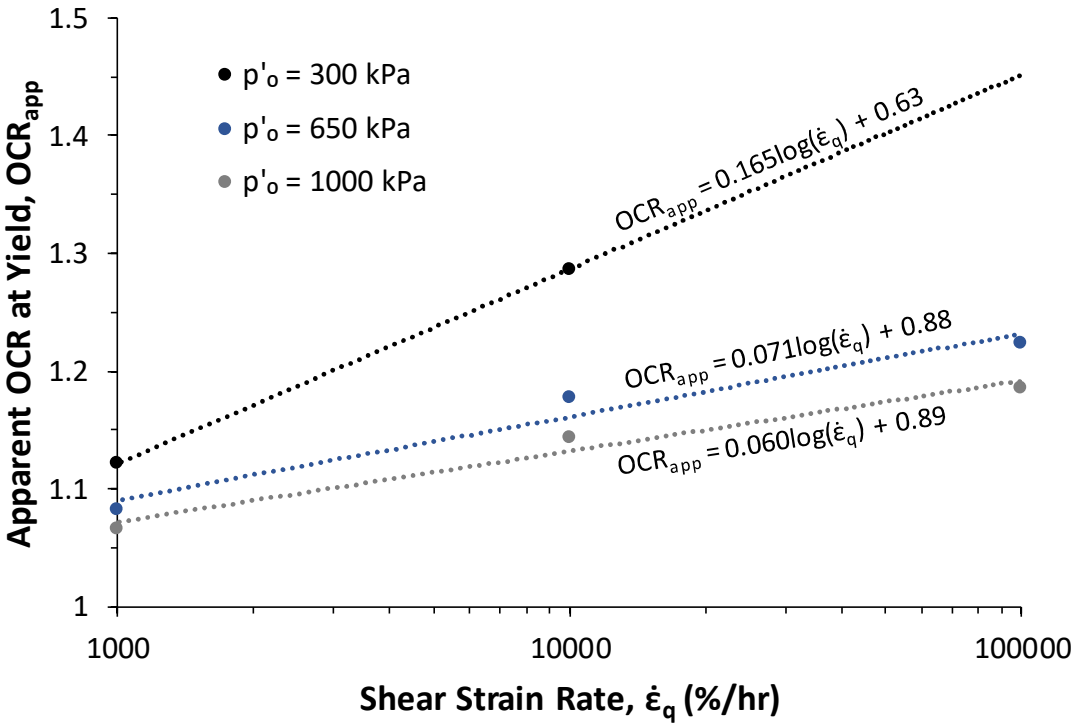

Figure 5-40 – Variation of apparent OCR with shear strain rate for each initial mean effective stress

One issue which required consideration was that the apparent OCR values determined at $\dot{\varepsilon}_q$ = 100,000 %/hr (shown in Figure 5-40) were lower than expected based on the logarithmic relationship with $\dot{\varepsilon}_q$ suggested by other studies such as Katti *et al.* (2003). The reason for this was found to be due to the acceleration of the triaxial system to the required strain rate. As the apparent OCR is derived based on the measured yield points, it is determined at relatively low strain levels. As the strain rate increases, the time from the start of the test until the point of yield reduces correspondingly. It was found that whilst the tests at $\dot{\varepsilon}_q$ = 1000 and 10,000 %/hr were able to reach the desired strain rate well before the yield point, the tests at $\dot{\varepsilon}_q$ = 100,000 %/hr did not reach constant strain rate before ε_q = 0.005 (after $t \approx 50$ milliseconds). The actual shear strain rates achieved at the point of yield were found to be 42,426 and 54,850 %/hr for p'_0 = 650 and 1000 kPa respectively, compared to the desired 100,000 %/hr. The higher value for p'_0 = 1000 kPa is due to the higher strain at which this specimen yielded, allowing more time for system acceleration. Using these corrected shear strain rates, it can be seen that the fit of the logarithmic relationship is improved (Figure 5-41).

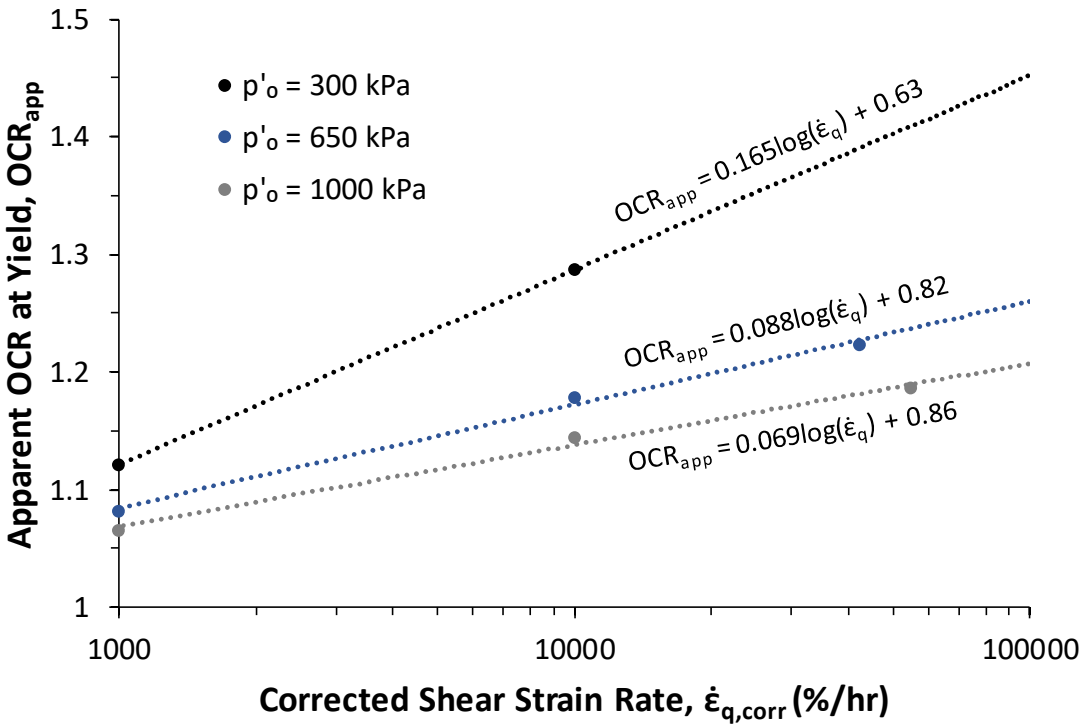

Figure 5-41 – Variation of apparent OCR with corrected shear strain rate for each initial mean effective stress

To allow comparison with other studies, the strain rate and apparent OCR have been normalised by their values at the reference shear strain rate of 1000 %/hr (Figure 5-42). It is proposed that the rate effect on normalised apparent OCR may be represented by Equation 5-28 where the parameter ξ_{ocr} is the rate effect on the normalised OCR_{app} per log cycle similar to λ, the deviator stress rate effect per log cycle. The values for ξ_{ocr} were found to vary from 14.7 to 6.5 % per log cycle. Also shown are the variations in OCR_{app} found by Katti *et al.* (2003) and Leroueil *et al.* (1985). For Katti *et al.* (2003), Equation 5-28 has been applied to the reported values of OCR_{app}. Leroueil *et al.* (1985) and Martindale *et al.* (2013) proposed that OCR_{app} may be modelled by Equation 5-29 and the output from this relationship has been normalised and the best fit of Equation 5-28 has been applied. These compare well with the value of ξ_{ocr} = 0.147 found at p'_0 = 300 kPa, possibly due to the fact that these studies used a similar order of magnitude of initial effective stress, although it is noted that different soils were used.

$$\frac{OCR_{app}}{OCR_{app,ref}} = \xi_{ocr} \, log\left(\frac{\dot{\varepsilon}_q}{\dot{\varepsilon}_{q,ref}}\right) + 1 \tag{5-28}$$

$$OCR_{app} = 1.3\dot{\varepsilon}_q^{\,0.05} \tag{5-29}$$

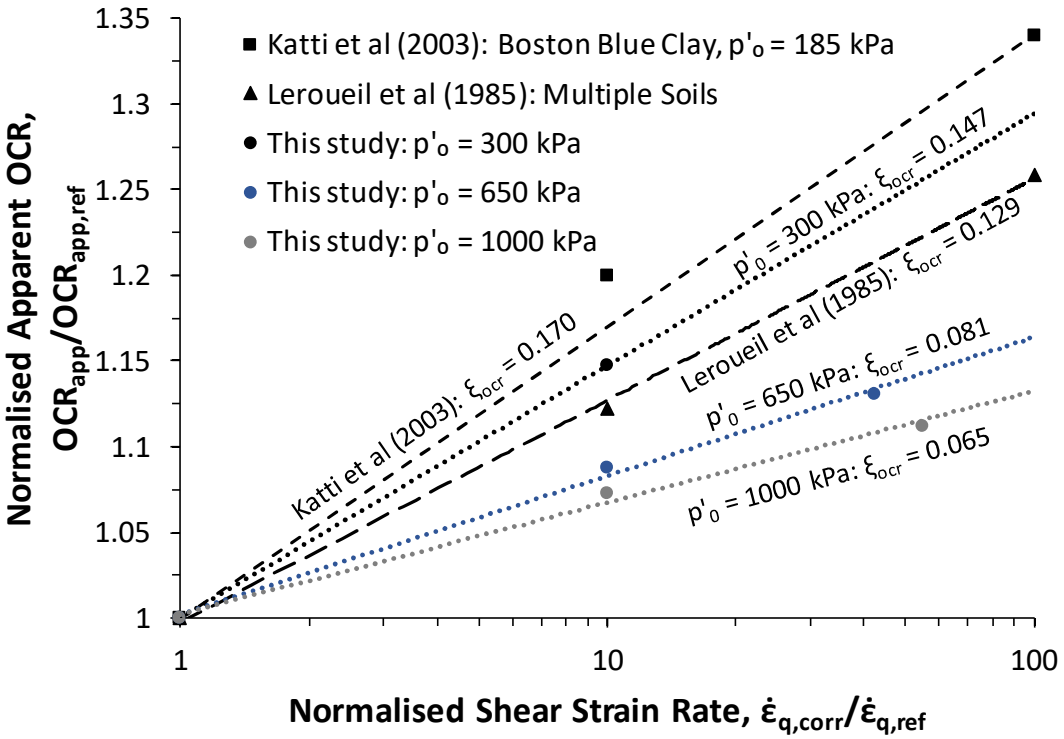

Figure 5-42 – Variation of normalised apparent OCR with normalised shear strain rate

The impact of the soil state on ξ_{ocr} is an area which has not yet been fully researched. Neither Katti *et al.* (2003) nor Leroueil *et al.* (1985) considered how changes in apparent OCR vary with p'_0, meaning that the form of the relationship is not yet known. Given that there are similarities in the variation of ξ_{ocr} with p'_0 to those seen in λ, such as the fact that higher rate effects on ξ_{ocr} are seen at lower effective stresses, the same LI^2 relationship used in Section 4.2.2 has been attempted. Figure 5-43 shows the variation of ξ_{ocr} with liquidity index and as can be seen, an LI^2 relationship provides a good degree of fit to the data. This suggests that, as with λ, the rate of change of ξ_{ocr} appears to reduce with reducing LI (or increasing p'_0) reaching a steady value at the plastic limit of around 0.05. Hence, for isotropically normally consolidated Kaolin, ξ_{ocr} may be represented by Equation 5-30. The only other comparable study for which the liquidity index was available was Katti *et al.* (2003), which is also shown on Figure 5-43. This data point is significantly below the trend found for Kaolin, potentially suggesting that ξ_{OCR} is soil

dependent, as the BBC studied showed lower rate effects on q_{peak} than the kaolin used here. Alternatively, using liquidity index may not be the best variable for comparing ξ_{OCR} between soils. In either case, this is an area where further research is recommended in the future.

By substitution into Equation 5-25, the MCC yield envelope at a strain rate, $\dot{\varepsilon}_q$, can be represented by Equation 5-31 and Equation 5-32. If experimental data for the material to be used is not available, $OCR_{app,ref}$ may be taken to be equal to OCR at $\dot{\varepsilon}_{q,ref}$ = 1 %/hr based on the findings of Leroueil and Marques (1996) and Martindale *et al.* (2013).

$\xi_{OCR} = 0.87LI^2 + 0.053$ for normally consolidated Kaolin (5-30)

$$\left(\frac{q_y}{p'}\right)^2 = M^2\left(\frac{OCR_{app}p'_0}{p'} - 1\right) \tag{5-31}$$

$$OCR_{app} = OCR_{app,ref}\left\{\xi_{OCR}\, log\left(\frac{\dot{\varepsilon}_q}{\dot{\varepsilon}_{q,ref}}\right) + 1\right\} \tag{5-32}$$

Another point to note is that the MCC yield envelope defines the yield surface not just in *q-p'* space, but also in *q-p'-v* space. The value of p'_0 in Equation 5-31 can be represented in terms of the critical state parameters, stress history (p'_{max}) and the specific volume, *v*, as shown in Equation 5-33 by combining and rearranging the equations of the NCL and the unloading line in *v-ln(p')* space. By substituting Equation 5-33 into Equation 5-31, the rate dependent MCC yield envelope in *q-p'* space can be related to specific volume as shown in Equation 5-34.

$$p'_0 = p'_{max}{}^{\left(1-\frac{\lambda}{\kappa}\right)} e^{\left(\frac{N-v}{\kappa}\right)} \tag{5-33}$$

$$\left(\frac{q_y}{p'}\right)^2 = M^2\left(\frac{OCR_{app}p'_{max}{}^{\left(1-\frac{\lambda}{\kappa}\right)} e^{\left(\frac{N-v}{\kappa}\right)}}{p'} - 1\right) \tag{5-34}$$

As an example, the yield surfaces for the Kaolin used in this study based on Equation 5-34 are shown in *q-p'-v* space for two shear strain rates, $\dot{\varepsilon}_q$ = 1000 and 10,000 %/hr (Figure 5-44). The lines on the yield surfaces represent constant volume sections in the *q-p'* plane to allow the shape of the 3D surface to be visualised. From these sections, the same expansion in the yield surface with increasing strain rate previously presented in Figure 5-36 to Figure 5-38 can be seen. This means that for a soil specimen/element, the yield behaviour at any given strain rate

can be captured using one 3D yield surface, which incorporates the effects of current stress level (or specific volume), stress history, and strain rate effects. This also includes the soil state dependence of rate effects at the point of yield as well.

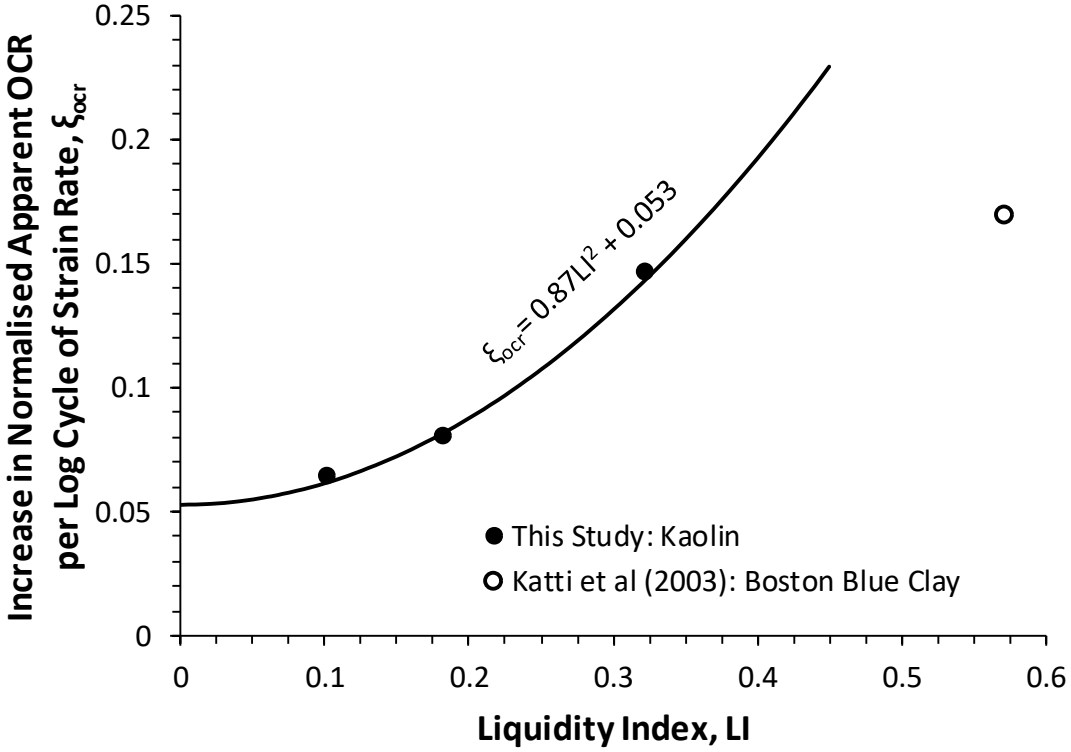

Figure 5-43 – Variation of ξ_{ocr} with liquidity index for normally consolidated Kaolin

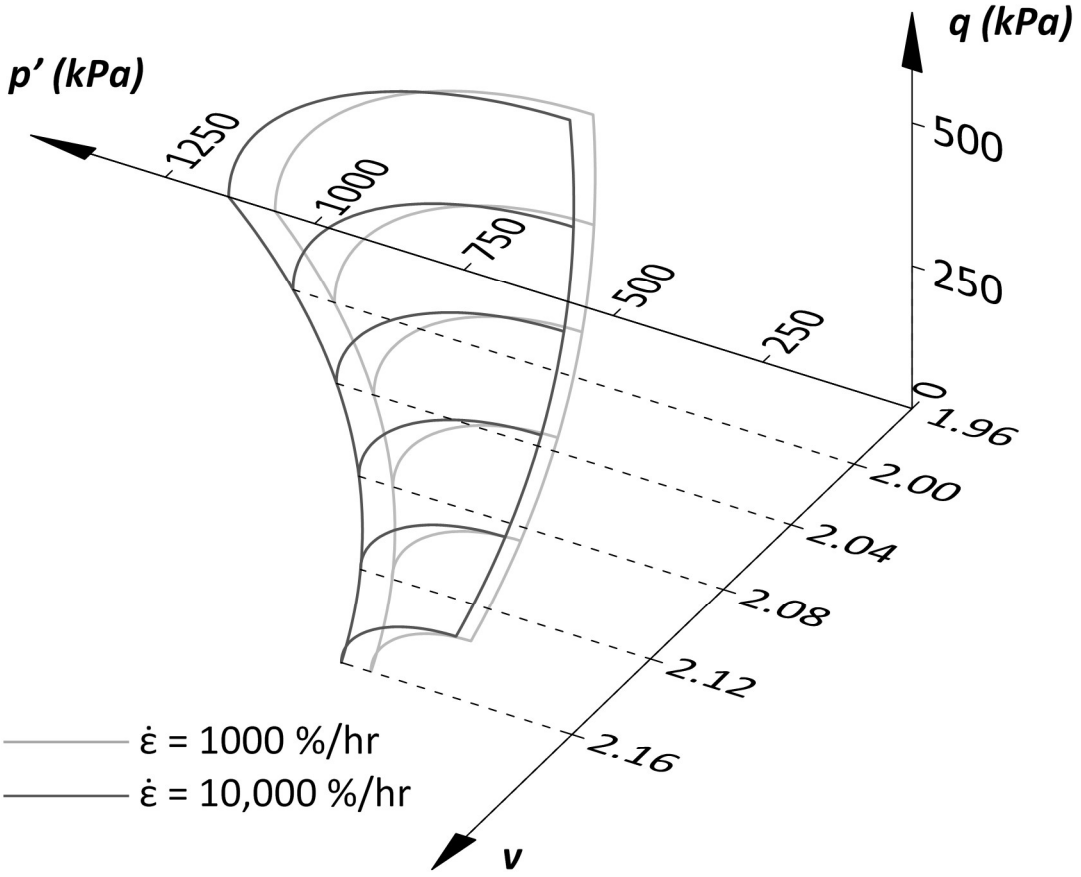

Figure 5-44 – 3D strain rate dependent Modified Cam Clay (MCC) yield surfaces in q-p'-v space at $\dot{\varepsilon}_q$ = 1000 and 10,000 %/hr based on Equation 5-34 for isotropically normally consolidated Kaolin (excluding the Hvorslev surface)

5.6. Summary of Rate Effects on Pore Pressure in Kaolin

The analysis of the pore pressure response and effective stress behaviour of Kaolin at high strain rates has identified the following important conclusions:

- It is important to consider the shear-induced pore pressures when considering the influence of strain rate on pore pressure response as opposed to the excess pore water pressure. This shear-induced pore pressure reflects the true dilatant or contractive tendency of the soil specimen.
- At any given shear strain, increasing strain rates cause a reduction in shear-induced pore pressure which results in the same change in $\Delta u_{si}/p'_0$ regardless of the soil state or initial mean effective stress. This pore pressure reduction appears to be a key reason for the increase in deviator stress with strain rate.
- The shear-induced pore pressure at high strain rates can be captured using simple inverse hyperbolic relationship of the form: $\Delta u_{si} = (\Delta u_{f,si} - \Delta u_{dil,si}).(1 - exp[-\alpha_u.\varepsilon_q]) + \Delta u_{dil,si}$, where α_u is a fitting parameter and $\Delta u_{f,si}$ *and* $\Delta u_{dil,si}$ can be correlated with either the shear strain rate, $\dot{\varepsilon}_q$, or the state parameter, Ψ. This allows the pore pressure at any given stress, strain, and strain rate to be estimated (for normally consolidated specimens).
- The intercept of the CSL in *v-ln(p')* space, Γ, increases with $log(\dot{\varepsilon}_q)$ which leads to a corresponding reduction in the state parameter, Ψ, with strain rate which appears to be the main mechanism behind rate effects. The gradient of the CSL in *v-ln(p')* space, λ_{csl}, was not found to change with shear strain rate.
- The soil state dependence of rate effects observed in Chapter 4 is not due to changes in the effective stress, but is instead caused by increases in the effective friction ratio with strain rate which are greater at lower initial mean effective stresses (or lower p'_0)
- The increase in the yield envelope with strain rate for normally consolidated soil can be modelled by using a Modified Cam Clay (MCC) yield envelope using an 'apparent' increase in OCR. This yield envelope can be implemented in *q-p'-v* space to define a 3D yield surface which accounts for stress level, stress history and strain rate (including the soil state dependence of rate effects at the point of yield).

6. Modelling of Rate Effects at Small Strains

The investigation of rate effects to this point has focussed on the large strain behaviour at shear strains typically greater than 1 %. The use of this large strain data to investigate rate effects at small strain is limited by a number of factors including the use of lubricated end platens, which induce extra compliance, and the resolution of the axial strain measurement from the motor encoder. Since the invention of local on-specimen strain measurement systems such as Hall effect displacement sensors (Clayton *et al.*, 1989), which measure the deformation of the specimen directly, the use of externally measured strains for small strain measurements has become less common. For clarity, strains measured locally on-specimen will be referred to as local strains and strains based on the motor encoder as external strains.

A further series of tests using Hall effect sensors for local strain measurements were carried out at initial mean effective stresses ranging from 300 to 1000 kPa as shown in Table 6-1. The strain applied in these tests was limited to no more than 2 % external axial strain in order to protect the Hall effect sensors from damage and to focus the measured data points (which are limited to 1000 by the GDS DCS as discussed in Chapter 3) in the small strain range. The range of stresses tested is more limited than that carried out for the large strain testing due to the limited range of the Hall effect sensors, even with the adaptations incorporated to extend their measurement range (detailed in Chapter 3). A consequence of this is that tests could not be conducted at p'_0 = 1350 kPa due to the large axial deformations (up to 21 mm) that occurred during consolidation, which could not be accommodated using the Hall effect sensors. Additionally, the tests conducted at $\dot{\varepsilon}$ = 10,000 %/hr (with the exception of p'_0 = 300 kPa) were not usable due to gain control issues during the initial part of the shearing stage.

The focus in this section will be on the impact of rate effects on key parameters which are commonly used to define the soil's behaviour at small strains, along with the key question of the manner in which rate effects mobilise with strain; an aspect which few studies have investigated to date.

Table 6-1 – Programme of small strain triaxial testing on Kaolin

Test Designation	*Test Type*	*Liquidity Index, LI*	*Initial Mean Effective Stress, p'_o (kPa)*	*Axial Strain Rate, $\dot{\varepsilon}$ (%/hr)*	*Back Valve State*	*OCR*
KLN-TU-S1	CIU	0.32	300	1000	Closed	1
KLN-TU-S2	CIU	0.32	300	10000	Closed	1
KLN-TU-S3	CIU	0.32	300	100000	Closed	1
KLN-TU-S4	CIU	0.18	650	1000	Closed	1
KLN-TU-S5*	CIU	0.18	650	10000	Closed	1
KLN-TU-S6	CIU	0.18	650	100000	Closed	1
KLN-TU-S7	CIU	0.10	1000	1000	Closed	1
KLN-TU-S8*	CIU	0.10	1000	10000	Closed	1
KLN-TU-S9	CIU	0.10	1000	100000	Closed	1

* Test data not usable for analysis due to system gain control issues

6.1. Impact on Initial Shear Modulus and Yield Parameters

Figure 6-1 shows the stress-strain behaviour of the small strain tests along with the corresponding secant shear modulus degradation curves in Figure 6-2, all of which are based on the locally measured on-sample strains. The secant shear modulus, *G*, has been defined as shown in Equation 6-1 (Muir Wood, 1990), where ε_q is the deviatoric triaxial shear strain (defined in Chapter 4 and used throughout the thesis).

$$G = \frac{q}{3\varepsilon_q} \tag{6-1}$$

As with the large strain tests, the results show the expected trend of increasing deviator stresses at any given strain with increasing axial strain rate. The only exception to this is the fact that the $\dot{\varepsilon}$ = 10,000 %/hr and 100,000 %/hr tests at p'_0 = 300 kPa displayed a similar response, which is attributed to natural variation between the specimens.

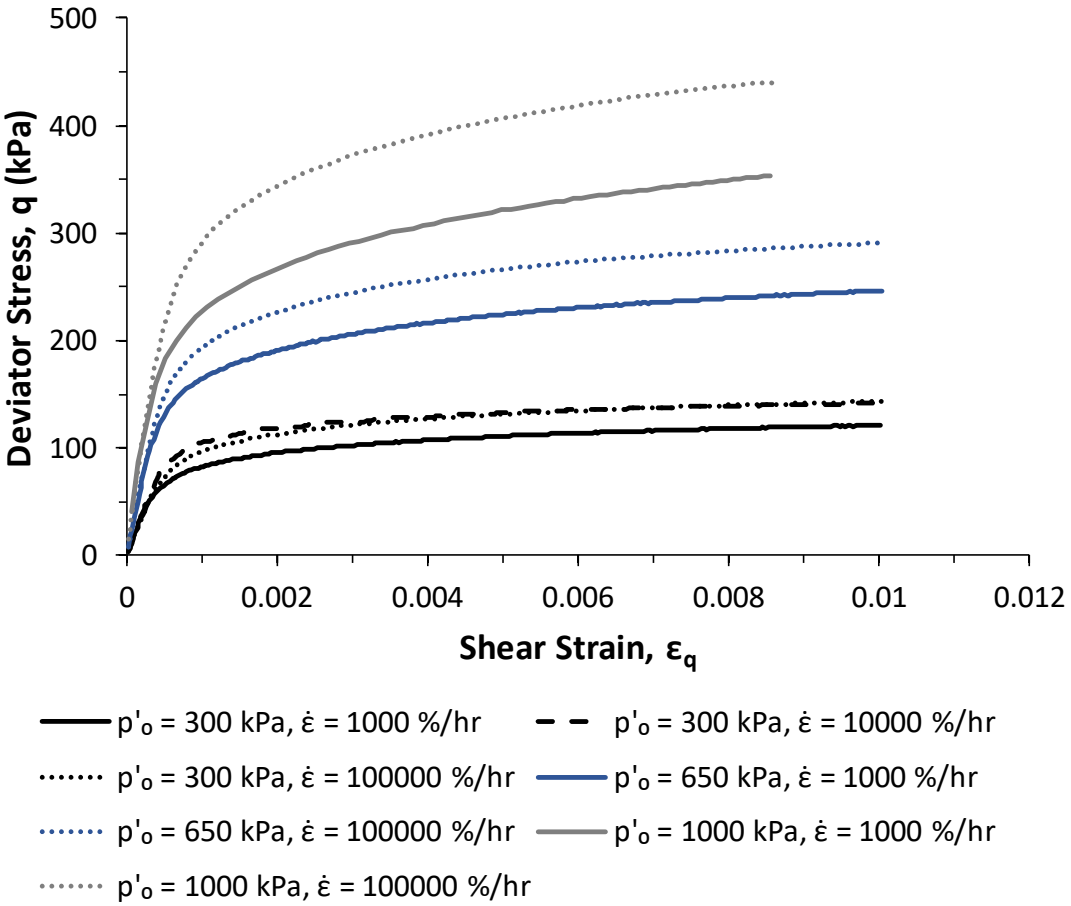

Figure 6-1 – Deviator stress-strain behaviour of small strain triaxial tests on Kaolin up to $\varepsilon_q = 0.01$ and at different axial strain rates and consolidation pressures

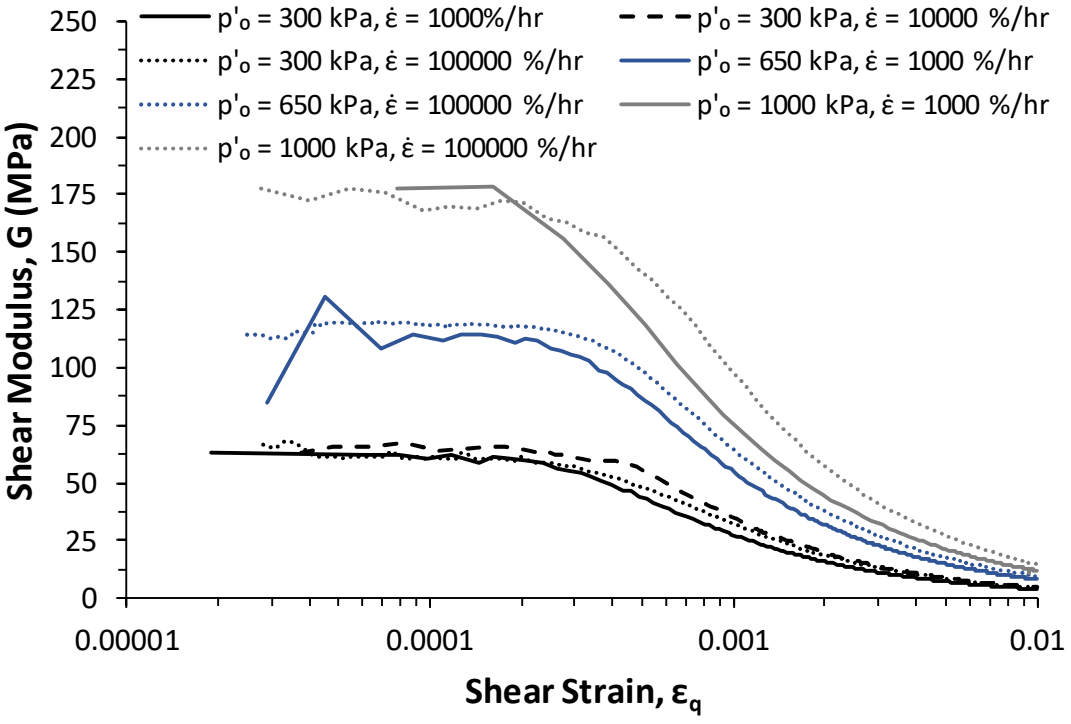

Figure 6-2 – Graph of shear modulus against shear strain for small strain tests on Kaolin at varying rates and consolidation pressures

Figure 6-2 shows the measured shear modulus degradation with strain for each of the specimens. Starting with the initial shear modulus, G_{max}, it can be seen that whilst G_{max} increases with p'_0, the increasing strain rate has no obvious impact beyond the natural variation in the specimens. G_{max} has been taken to be the maximum value of G obtained from the initial Hall effect local strain measurements (i.e. the average of the measured values of G before stiffness degradation was observed). The values of G_{max} range from 64 MPa at p'_0 = 300 kPa to 185 MPa at p'_0 = 1000 kPa. The variation of G_{max} with p'_0 is shown in Figure 6-3, with each of the strain rates annotated separately. This confirms that there is no observable impact of axial strain rate on G_{max}, in keeping with the findings of multiple studies including Sorensen *et al.* (2010). For the Kaolin tested, G_{max} may be represented by Equation 6-2, the form of which has been used by numerous other studies (Equation 6-3). This normalises both G_{max} and p'_0 by the atmospheric pressure, p_a, in order to make the relationship dimensionless (Chow and Airey, 2013; Oztoprak and Bolton, 2013; Sorensen *et al.*, 2010).

$$\frac{G_{max}}{p_a} = 258.9\left(\frac{p'_0}{p_a}\right)^{0.838} \tag{6-2}$$

$$\frac{G_{max}}{p_a} = A\left(\frac{p'_0}{p_a}\right)^{n} \tag{6-3}$$

The values of G_{max} determined from the external large strain data discussed in Chapter 4 have been included in Figure 6-3 for comparison. These values range from 65 % (at p'_0 = 300 kPa) to 33 % (at p'_0 = 1000 kPa) of the locally on-sample measured values suggesting that the use of local strain measurement techniques is even more critical at higher effective stresses. The most likely explanation for this is that the higher stress causes greater compliance in the lubricated end platens, as the silicone grease is displaced from underneath the specimen. Also shown is the G_{max}-p'_0 relationship determined for Kaolin by Chow and Airey (2013) (Equation 6-4), which predicts slightly higher values of G_{max} than those measured here, possibly due to the anisotropic K_0 consolidation used by Chow and Airey (2013) and the different source of the Kaolin.

$$\frac{G_{max}}{p_a} = 432.9\left(\frac{p'_0}{p_a}\right)^{0.709} \tag{6-4}$$

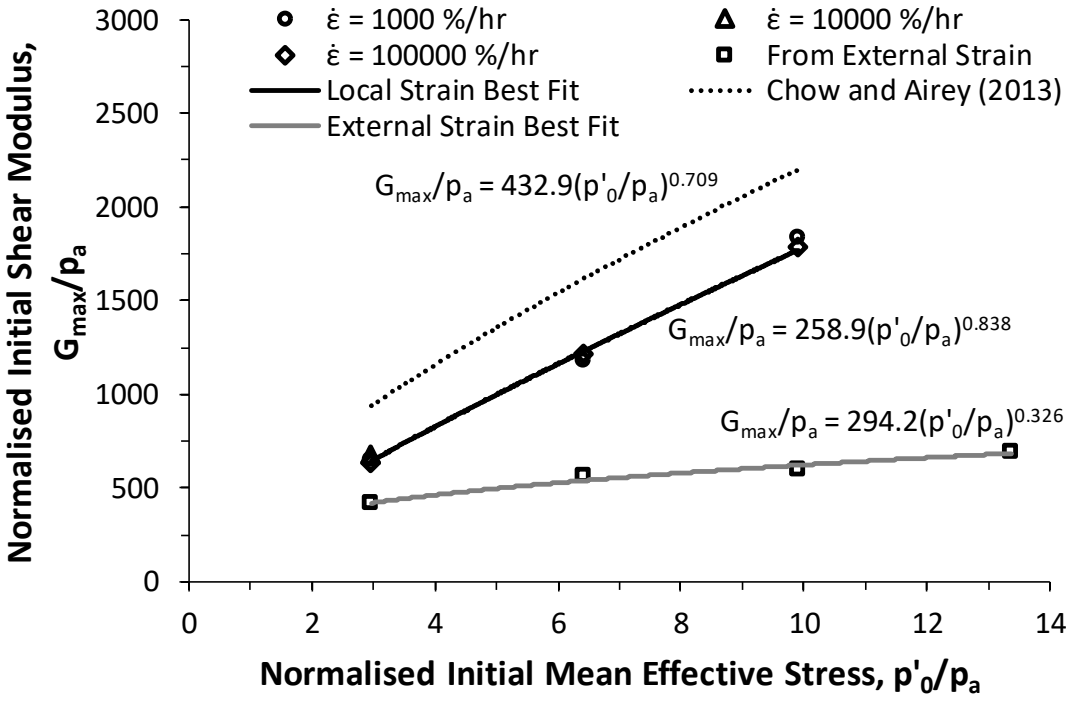

Figure 6-3 – Variation of normalised maximum shear stiffness with initial mean effective stress for Kaolin at varying axial strain rates, comparing local (on sample) and external strain measurements

Two areas of the shear stiffness degradation which can be seen to be impacted by axial strain rate in Figure 6-2 are the point of yield (more specifically the elastic strain threshold, denoted $\varepsilon_{q,EL}$) and the rate of stiffness degradation after yield. Considering the elastic strain threshold first, Table 6-2 shows the yield points identified from the degradation curves, with $\varepsilon_{q,EL}$ increasing with axial strain rate in keeping with the findings of Leroueil *et al.* (1985), Shibuya *et al.* (1996) and Santagata (2008) who also found greater values of $\varepsilon_{q,EL}$ at higher axial strain rates. The definition of yield adopted is that of Jardine (1992) for the Zone 1 (elastic) yield limit. Figure 6-4 shows the variation of the elastic strain threshold with shear strain rate. Error bars are shown based on the error in the measurement resolution of the Hall effect sensors. However, with the consideration of rate effects at low strain levels, it is necessary to consider the actual strain rates achieved, as the system is still accelerating to the target strain rate at small strains near yield. These actual shear strain rates achieved at the point of yield have been denoted $\dot{\varepsilon}_{q,corr}$. Figure 6-5 shows the variation of $\varepsilon_{q,EL}$ with this corrected axial strain rate (defined previously in Chapter 5), indicating that $\varepsilon_{q,EL}$ increases linearly with the log of strain rate and can be described by Equation 6-5.

$$\varepsilon_{q,EL} = 3.4\times10^{-5}\, log(\dot{\varepsilon}_{q,corr}) + 0.00006 \quad (6\text{-}5)$$

Shibuya *et al.* (1996) proposed that the elastic strain threshold could be described by a relationship of the form shown in Equation 6-6. The proposed correlation by Shibuya *et al.* (1996) was unable to match $\varepsilon_{q,EL}$ over the strain rate range considered here, overestimating the yield threshold at higher strain rates. This is most likely related to the fact that Shibuya *et al.* (1996) used axial strain rates more than 3 orders of magnitude lower than those considered here.

$$\varepsilon_{q,EL} = 0.0001\sqrt{\frac{\Delta\varepsilon_a}{\Delta t}} \tag{6-6}$$

where k is a constant and $\frac{\Delta\varepsilon_a}{\Delta t}$ is the axial strain rate in %/min

Robinson and Brown (2013) also studied the impact of rate effects on G_{max} and $\varepsilon_{q,EL}$, and found that $\varepsilon_{q,EL}$ varied with shear strain rate according to Equation 6-7, which estimates that the point of yield would occur at far higher strain levels than those measured here. Significant reductions in G_{max} with $\dot{\varepsilon}$ were also observed. Further investigation found that these findings were due to de-synchronisation and delays in the data acquisition system which adversely affected the results and thus do not reflect the behaviour observed here.

$$\varepsilon_{q,EL} = 0.003\dot{\varepsilon}_q^{0.2} \tag{6-7}$$

Table 6-2 – Measured initial shear moduli and elastic shear strain thresholds

Test Designation	p'_0 (kPa)	Axial Strain Rate (%/hr)	Axial Strain Rate at $\varepsilon_{q,EL}$ (%/hr)	G_{max} (MPa)	Elastic Strain Threshold, $\varepsilon_{q,EL}$
KLN-TU-S1	300	1000	1000	65	0.00016
KLN-TU-S2	300	10000	10000	68	0.00019
KLN-TU-S3	300	100000	23850	64	0.00020
KLN-TU-S4	650	1000	1000	119	0.00017
KLN-TU-S6	650	100000	16016	122	0.00022
KLN-TU-S7	1000	1000	1000	185	0.00016
KLN-TU-S9	1000	100000	17359	180	0.00020

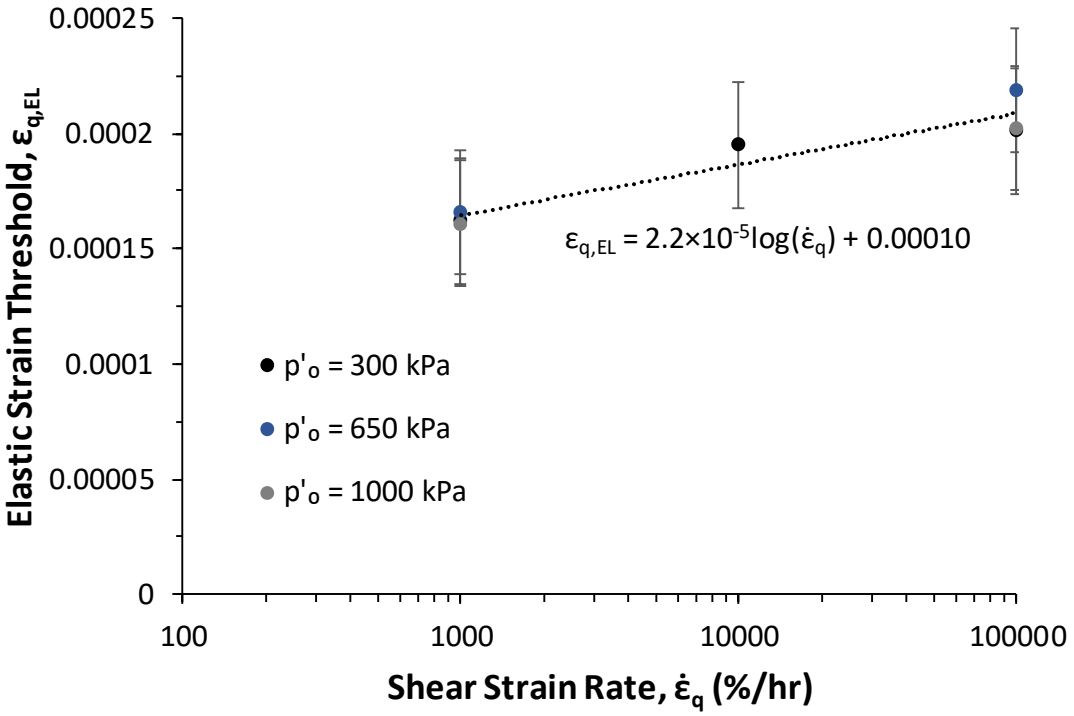

Figure 6-4 – Variation of elastic strain threshold with target shear strain rate for Kaolin at varying initial mean effective stresses

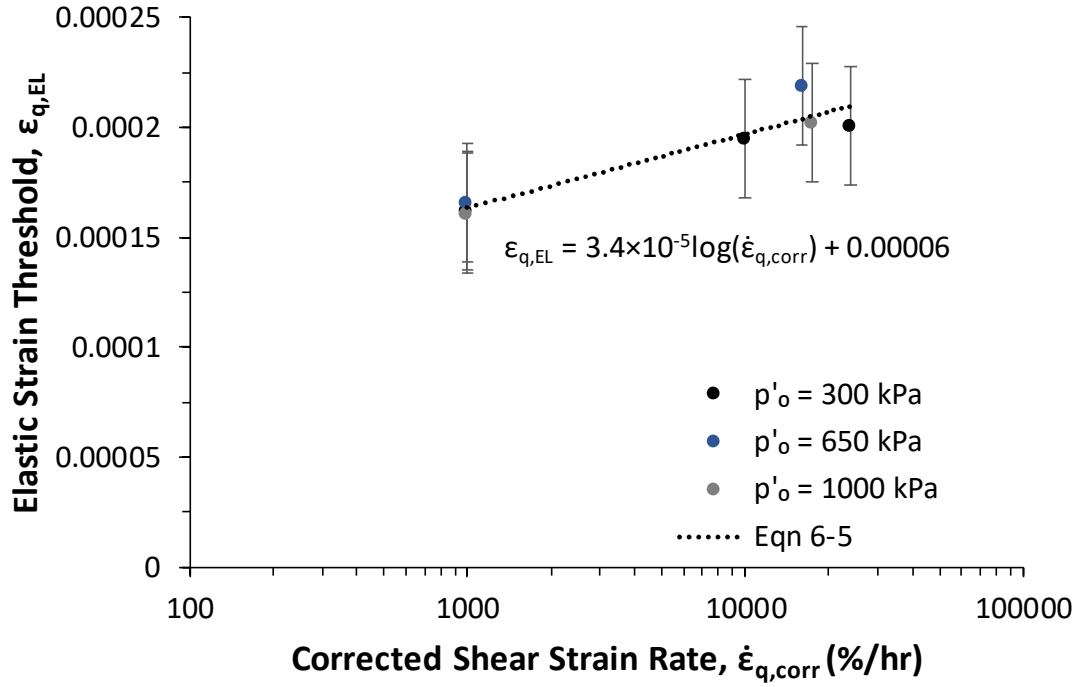

Figure 6-5 – Variation of elastic shear strain threshold with corrected shear strain rate for Kaolin at varying initial mean effective stresses

Figure 6-6 shows a comparison of the variation of elastic strain threshold with shear strain rate from Shibuya *et al.* (1996) (NSF clay, $\dot{\varepsilon}$ = 0.6 to 84 %/hr) and Santagata *et al.* (2007) (Boston Blue Clay, $\dot{\varepsilon}$ = 0.1 to 4 %/hr) with the values from this study. Each of these studies carried out testing at a different range of strain rates, and whilst it should be kept in mind that different clays were tested in each case, it can be seen there is a clear trend that $\varepsilon_{q,EL}$ increases linearly with $log(\dot{\varepsilon}_q)$. This trend is similar to that shown in Equation 6-5. Also shown is the relationship between $\varepsilon_{q,EL}$ and $\dot{\varepsilon}$ suggested by Shibuya *et al.* (1996) (Equation 6-6). Whilst this fits the data reasonably well at lower strain rates (from which it was derived), it significantly overpredicts $\varepsilon_{q,EL}$ at the axial strain rates used in this study. This highlights the importance of deriving correlations at relevant strain rates.

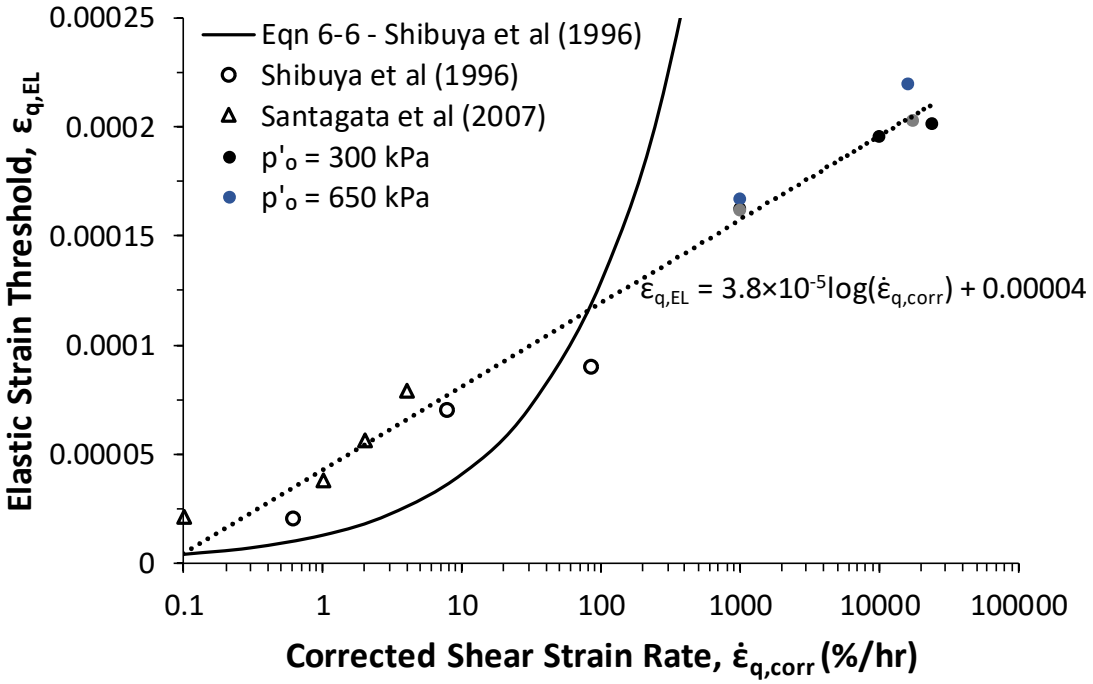

Figure 6-6 – Comparison of the variation of elastic shear strain threshold with shear strain rate from this study on Kaolin with Shibuya *et al.* (1996) (used NSF clay) and Santagata *et al.* (2007) (used Boston Blue Clay, BBC)

By normalising the measured values of $\varepsilon_{q,EL}$ by those at the reference shear strain rate of this study of $\dot{\varepsilon}_q$ = 1000 %/hr, $\varepsilon_{q,EL,ref}$, the effect of strain rate (per log cycle) on the elastic strain threshold can be identified (Figure 6-7). This shows that for every log cycle increase of strain rate, $\varepsilon_{q,EL}$ increases by more than 20 % in Kaolin (Equation 6-8), however, further research is recommended to conclusively identify that the form of the relationship is valid over a wider strain rate range.

$$\frac{\varepsilon_{q,EL}}{\varepsilon_{q,EL,ref}} = 0.208 \log\left(\frac{\dot{\varepsilon}_{q,corr}}{\dot{\varepsilon}_{q,ref}}\right) + 1 \quad (6\text{-}8)$$

where $\varepsilon_{q,EL,ref}$ is the elastic strain threshold at the reference axial strain rate, $\dot{\varepsilon}_{q,ref}$.

For use in practice, it is suggested that Equation 6-8 should be used where a value for $\varepsilon_{q,EL,ref}$ has been experimentally determined at a strain rate appropriate to the application in question. In cases where no value for $\varepsilon_{q,EL,ref}$ is available, Equation 6-5 may be used instead.

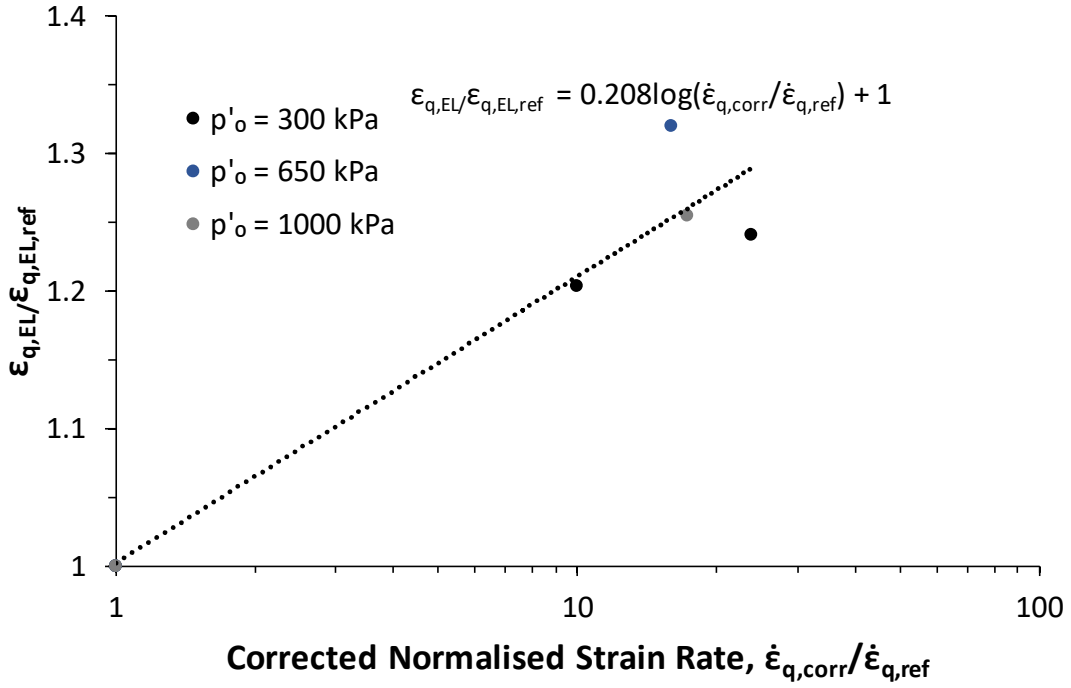

Figure 6-7 – Variation of normalised elastic shear strain threshold with corrected shear strain rate for Kaolin at varying initial mean effective stresses

6.2. Impact on Stiffness Degradation

From Figure 6-2, it was also noted that after the elastic strain threshold, the shear modulus appears to degrade more rapidly with increasing strain rate. Normalising the degradation curves by G_{max} highlights this issue further, showing movement to the right (representing stiffening of the secant shear modulus at any given strain) and increasing gradient of the curves (Figure 6-8). To investigate this issue, it is necessary to fit a model to the degradation curves to allow this effect to be quantified. In this case, the stiffness degradation used in the HS Small

model (Equation 6-9), which was proposed by Hardin and Drnevich (1972) will be used due to its simple nature and widespread use (Plaxis, 2013).

$$\frac{G}{G_{max}} = \frac{1}{1+0.385\left(\frac{\varepsilon_q}{\varepsilon_{q,0.7}}\right)} \tag{6-9}$$

Where $\varepsilon_{q,0.7}$ is the strain at which the shear modulus has degraded to 70 % of G_{max}

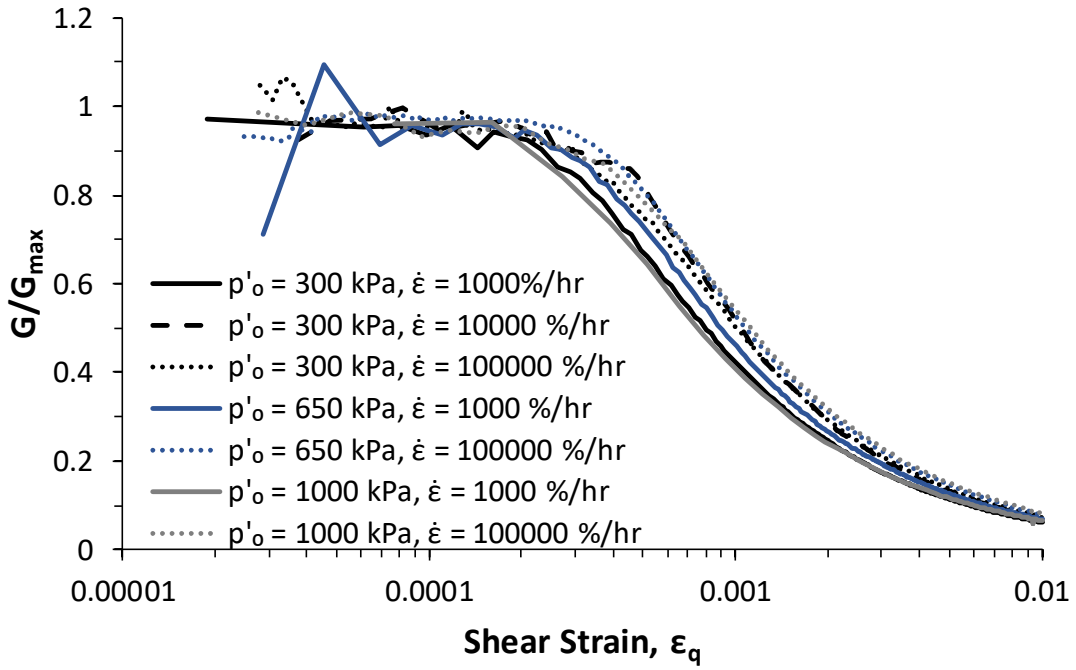

Figure 6-8 – Variation of normalised shear modulus with shear strain at varying axial strain rates for Kaolin at different initial mean effective stresses

Figure 6-9 shows the data from the test conducted at p'_0 = 650 kPa and $\dot{\varepsilon}$ = 100,000 %/hr with Equation 6-9 fitted. This shows that the conventional model (Equation 6-9) underestimates stiffness near the elastic strain threshold, and overestimates stiffness at strains greater than 0.06 %. To overcome this, the Hardin and Drnevich (1972) degradation model may be modified by including a degradation rate parameter, β, (Robinson and Brown, 2013) which controls the rate of degradation, rotating the curve about the point $\varepsilon_{q,0.7}$ (Equation 6-10).

$$\frac{G}{G_{max}} = \frac{1}{1+0.385\left(\frac{\varepsilon_q}{\varepsilon_{q,0.7}}\right)^{\beta}} \tag{6-10}$$

This type of modification has precedent in improving the fit of degradation curves. Vardanega and Bolton (2013) used the same form of equation to modify the degradation curve to provide a better fit to resonant column test data to account for the higher strain rates that occurred when compared to other 'static' tests analysed in the study. In this case of Vardanega and Bolton (2013), the new power was referred to as the curvature parameter, α, although Robinson and Brown (2013) was the first case in which this modification was implemented as a rate dependent parameter.

Equation 6-10 has also been fitted to the data shown in Figure 6-9 using least mean square regression and it can be seen that this provides a noticeably improved fit, although the stiffness is still (slightly) underestimated around the point of yield. Figure 6-10 shows a comparison of both the original model (Equation 6-9) and the revised model's (Equation 6-10) fit to the same data, in terms of the percentage variation from the measured shear modulus with shear strain. The maximum error in the original model is more than 70 % at ε_q = 1 %, and even at ε_q = 0.2 % the variation in G already reaches 40 %. The revised model improves the fit at all strain levels and limits the maximum error to 30 % over the range considered. For strains up to 0.5 %, the error does not exceed 12 %. Hence, it is recommended that for high strain rate testing Equation 6-10 should be used and the degradation rate parameter, β, should be considered. This revised model has been fitted to all of the small strain tests conducted, and the results of the fitting process are shown in Table 6-3, Figure 6-11, Figure 6-12 and Figure 6-13 for each of the effective stresses considered.

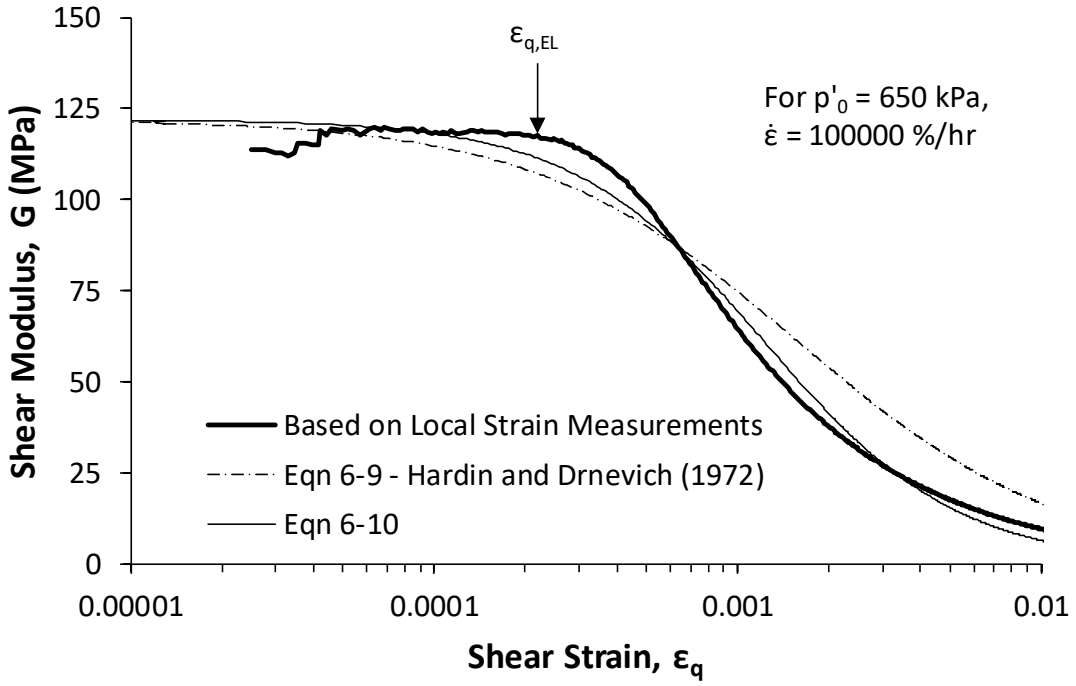

Figure 6-9 – Comparison of Equation 6-9 (Hardin and Drnevich, 1972) and Equation 6-10 with measured shear modulus for Kaolin at p'_0 = 650 kPa and $\dot{\varepsilon}$ = 100,000 %/hr

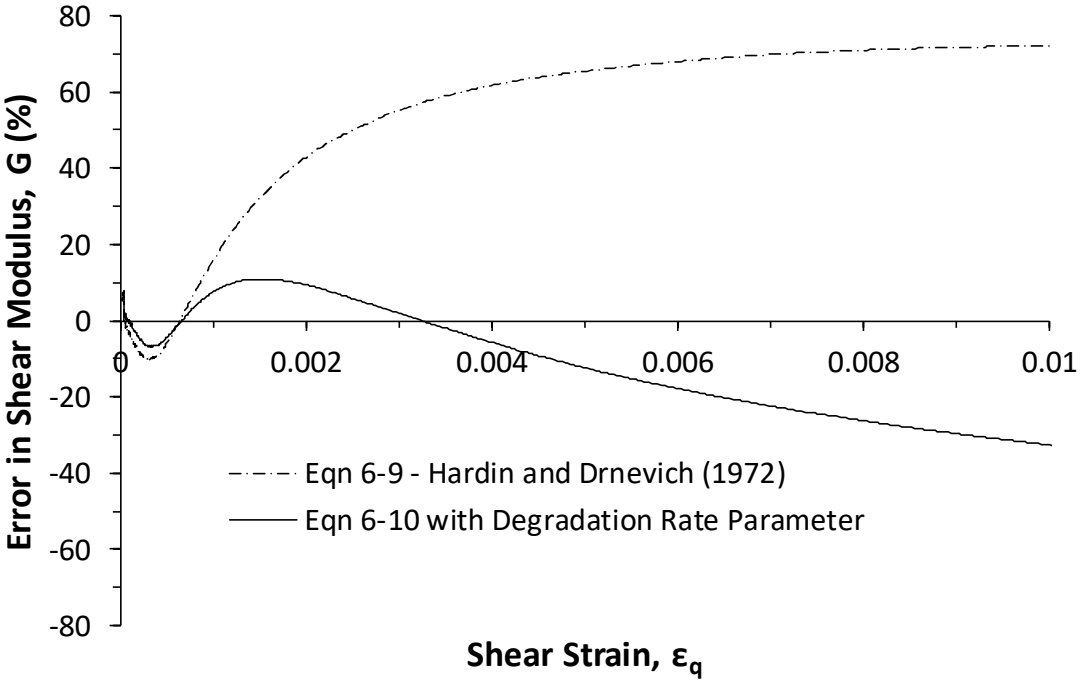

Figure 6-10 – Comparison of error in predicted shear modulus for Equation 6-9 (Hardin and Drnevich, 1972) and Equation 6-10 (Kaolin, p'_0 = 650 kPa, $\dot{\varepsilon}$ = 100,000 %/hr)

Table 6-3 – Revised stiffness degradation model fitting parameters

Test Designation	p'_0 (kPa)	Axial Strain Rate (%/hr)	G_{max} (MPa)	Reference Strain, $\varepsilon_{q,0.7}$	Axial Strain Rate at $\varepsilon_{q,0.7}$ (%/hr)	Deg. Rate Parameter, β
KLN-TU-S1	300	1000	65	0.00042	1000	1.263
KLN-TU-S2	300	10000	68	0.00053	10000	1.307
KLN-TU-S3	300	100000	64	0.00055	44255	1.351
KLN-TU-S4	650	1000	119	0.00049	1000	1.298
KLN-TU-S6	650	100000	122	0.00061	41047	1.368
KLN-TU-S7	1000	1000	185	0.00041	1000	1.227
KLN-TU-S9	1000	100000	180	0.00061	33397	1.308

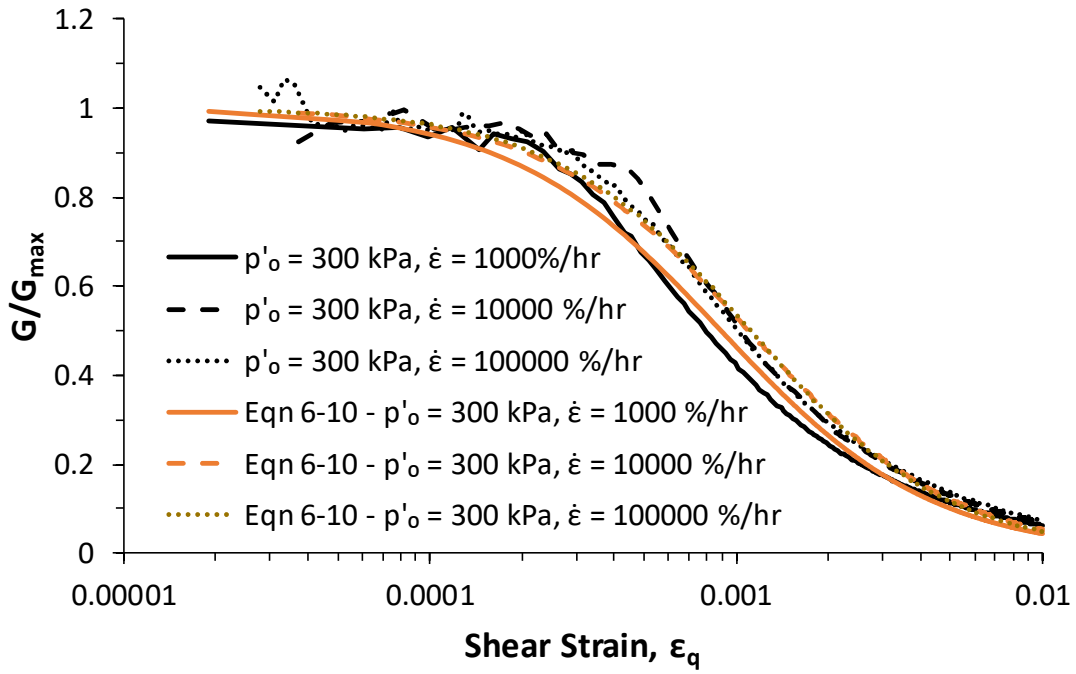

Figure 6-11 – Fit of revised model (Equation 6-10) to tests at varying axial strain rates on Kaolin at p'_0 = 300 kPa

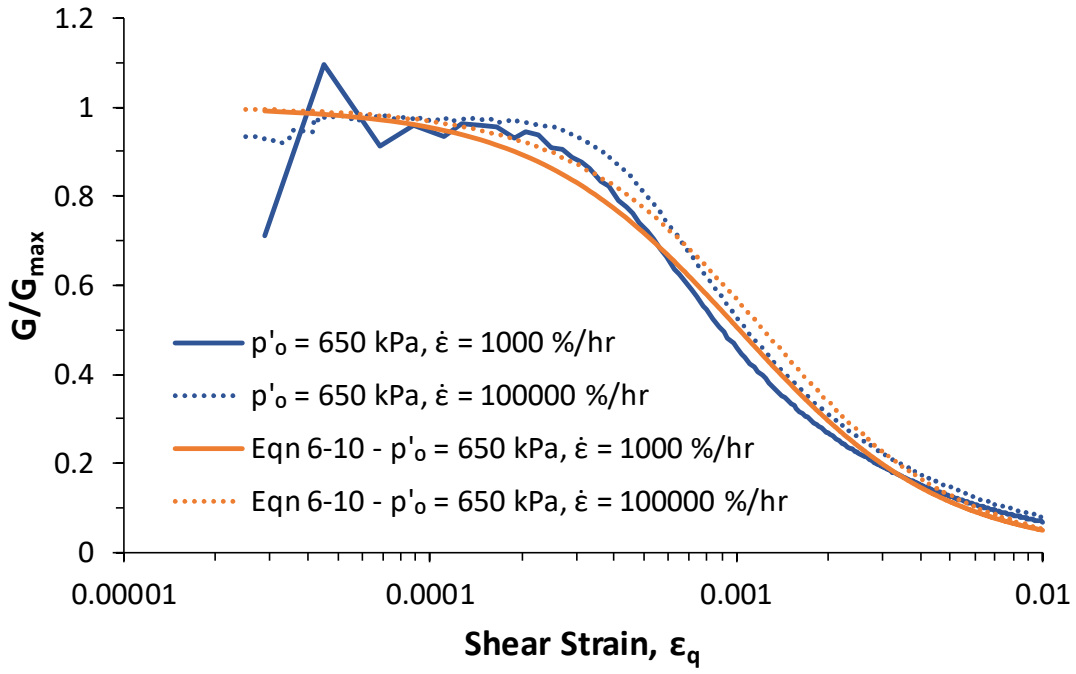

Figure 6-12 – Fit of revised model (Equation 6-10) to tests at varying axial strain rates on Kaolin at p'_0 = 650 kPa

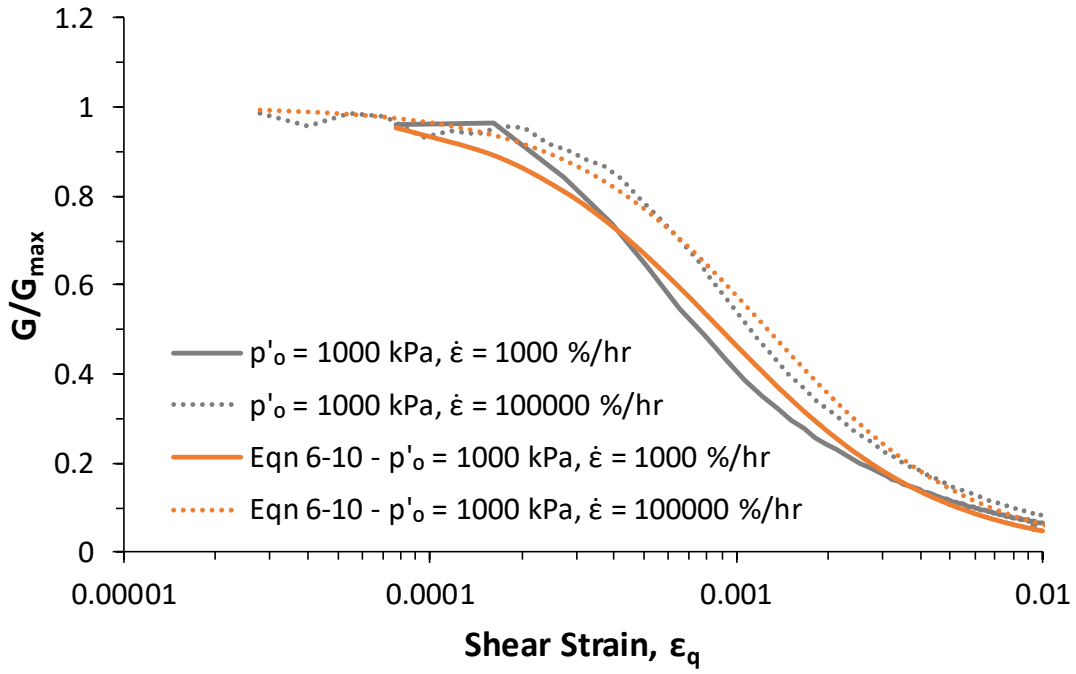

Figure 6-13 – Fit of revised model (Equation 6-10) to tests at varying axial strain rates on Kaolin at p'_0 = 1000 kPa

The results of the fitting process in Table 6-3 show that the reference strain for each of the degradation curves, $\varepsilon_{q,0.7}$, increased with axial strain rate (reflecting the rightwards shift of the degradation curves) and the values identified range from 0.00041 to 0.00061. Figure 6-14 shows that as with $\varepsilon_{q,EL}$, $\varepsilon_{q,0.7}$ increases linearly with log($\dot{\varepsilon}_q$). The strain rates shown are again the corrected shear strain rates which are the actual measured strain rates achieved at $\varepsilon_{q,0.7}$. These are higher than the strain rates achieved at $\varepsilon_{q,EL}$ as the higher strain allows more time for system acceleration. As with $\varepsilon_{q,EL}$, $\varepsilon_{q,0.7}$ also shows no observable variation with initial effective stress, possibly due to the fact that as it is still near to yield, significant effective stress dependent pore pressures have not had the opportunity to develop. $\varepsilon_{q,0.7}$ may be represented by Equation 6-11 below.

$$\varepsilon_{q,0.7} = 9.3\times10^{-5}\, log(\dot{\varepsilon}_{q,corr}) + 0.00016 \tag{6-11}$$

A key check on the consistency of this relationship to ensure its usability is that the value of $\varepsilon_{q,0.7}$ must by definition always be greater than the yield strain, $\varepsilon_{q,EL}$. Many testing programmes or numerical analyses use reference strain rates of around $\dot{\varepsilon}_q$ = 1 %/hr, far lower than those used here, so if the relationship is to be useful, it must still be consistent at these "static" rates. It was found that at $\dot{\varepsilon}_q$ = 1 %/hr, Equations 6-5 and 6-11 produce values of $\varepsilon_{q,0.7}$ = 0.00016 and $\varepsilon_{q,El}$ = 0.00006, meaning the condition is met. It was also identified that on the basis of these relationships, for Kaolin, $\varepsilon_{q,0.7}$ was consistent at 2.7 times greater than $\varepsilon_{q,EL}$ across the strain rate range from $\dot{\varepsilon}_q$ = 1 to 100,000 %/hr (Equation 6-12) for all initial mean effective stresses.

$$\varepsilon_{q,0.7} = 2.7\varepsilon_{q,EL} \tag{6-12}$$

Normalising $\varepsilon_{q,0.7}$ by the value at the reference shear strain rate for this study of $\dot{\varepsilon}_q$ = 1000 %/hr (Figure 6-15), it can be shown that the rate effect on $\varepsilon_{q,0.7}$ is 21.6 % per log cycle (Equation 6-13). This is very similar to the rate effect on $\varepsilon_{q,EL}$, which increases by 20.8 % per log cycle (which is to be expected given that $\varepsilon_{q,0.7}$ and $\varepsilon_{q,EL}$, are proportional to each other as shown in Equation 6-12). As discussed previously, it is recommended that Equation 6-13 be used where a value of $\varepsilon_{q,0.7,ref}$ is available for the application in question, otherwise Equation 6-12 may be used instead.

$$\frac{\varepsilon_{q,0.7}}{\varepsilon_{q,0.7,ref}} = 0.216\, log\left(\frac{\dot{\varepsilon}_{q,corr}}{\dot{\varepsilon}_{q,ref}}\right) + 1 \tag{6-13}$$

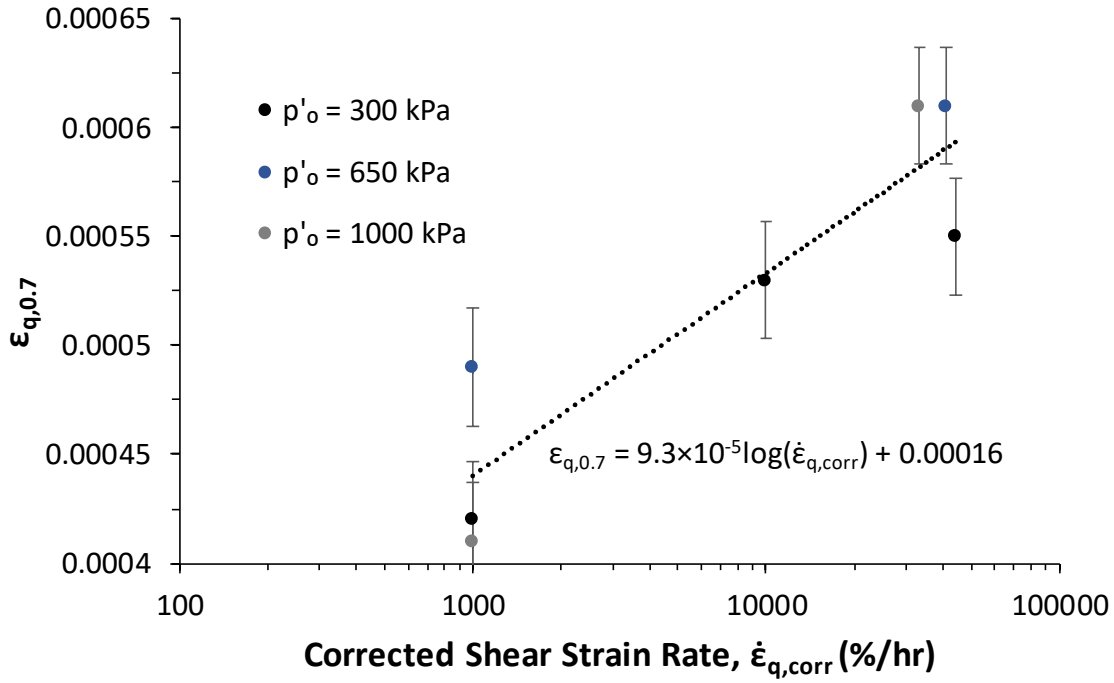

Figure 6-14 – Graph of $\varepsilon_{q,0.7}$ against corrected shear strain rate for Kaolin at varying initial mean effective stresses

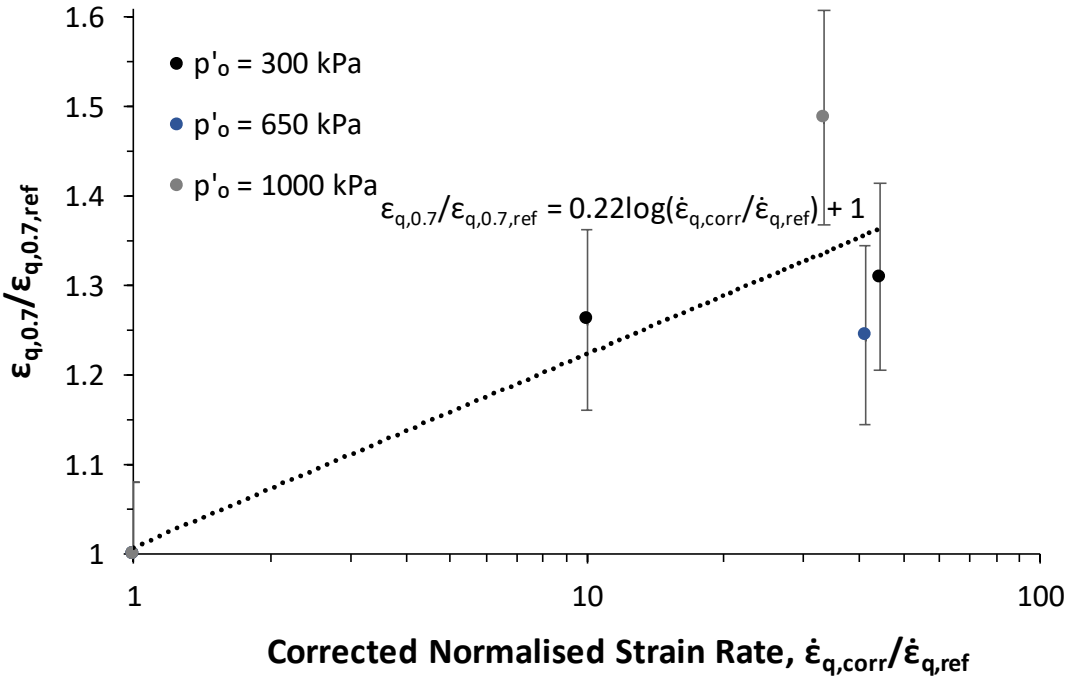

Figure 6-15 – Graph of $\varepsilon_{q,0.7}/\varepsilon_{q,0.7,ref}$ against corrected normalised shear strain rate for Kaolin at varying initial mean effective stresses

Considering the rate dependant degradation parameter, β, Figure 6-16 shows its variation with shear strain rate. The corrected strain rates used were the same as those for $\varepsilon_{q,0.7}$, which is the rotation point of the degradation curve that β modifies. The values determined for β ranged from 1.23 to 1.37. This is higher than the range found by Vardanega and Bolton (2013) of 0.91 to 1.00, due to the significantly higher strain rates used here. In common with all of the other small strain fitting parameters, β again displayed little effective stress dependence and could be represented by a semi-log relationship (Equation 6-14). It should be noted that Equation 6-14 has been fitted through 1 at the base of the semi-log relationship of 1 %/hr. This has the benefit of ensuring that at the "static" shear strain rate of 1 %/hr, the revised degradation model (Equation 6-10) reduces to the original model (Equation 6-9) improving consistency. Hence Equation 6-14 should be used when modelling this aspect of rate effects. If the fitted values of β are extrapolated back to $\dot{\varepsilon}_q$ = 1 %/hr without setting the intercept as 1, this yields a value of β = 1.11. This is still slightly above the range of 0.91 to 1.00 found by Vardanega and Bolton (2013), with the reason for this difference most likely to be uncertainties from extrapolating back over 3 orders of magnitude of shear strain rate.

$$\beta = 0.08 \log(\dot{\varepsilon}_{q,corr}) + 1 \quad (6\text{-}14)$$

The rate effect on β was found to be 4 % per log cycle (Figure 6-17 and Equation 6-15) after normalisation.

$$\beta/\beta_{ref} = 0.04 \log(\dot{\varepsilon}_{q,corr}/\dot{\varepsilon}_{q,ref}) + 1 \quad (6\text{-}15)$$

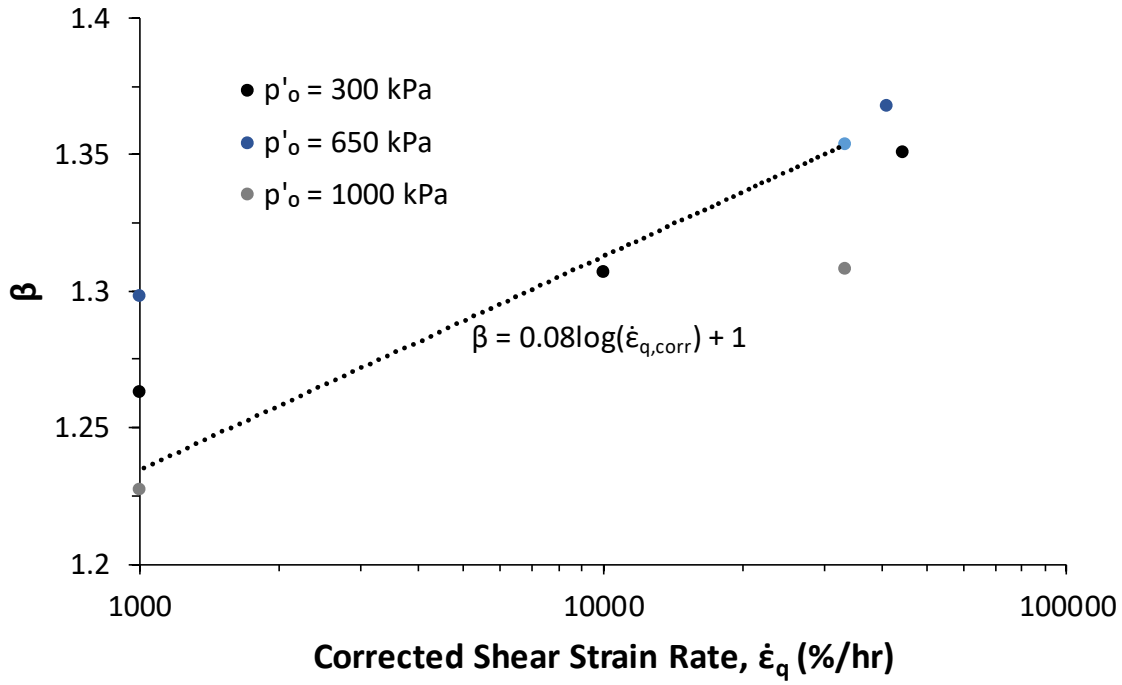

Figure 6-16 – Variation of β with corrected shear strain rate for Kaolin at varying initial mean effective stresses

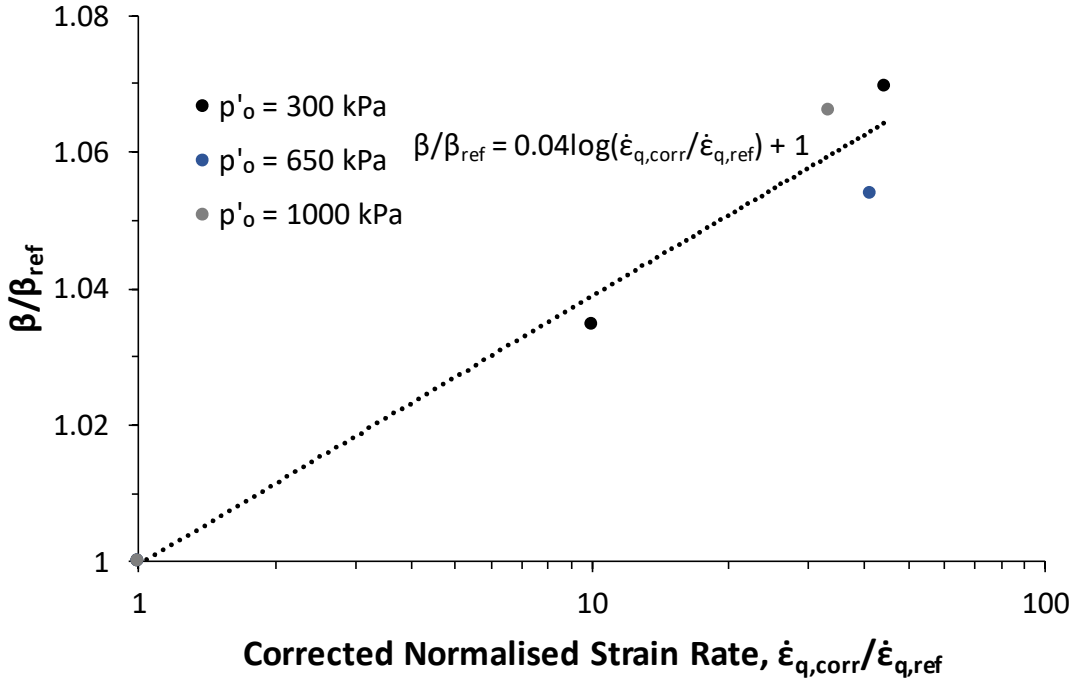

Figure 6-17 – Variation of β/β_{ref} with corrected normalised shear strain rate

6.3. Development of Rate Effects Model for the Full Strain Range

Up to this point, this thesis has identified ways in which rate effects may be modelled at large strains (ε_q > 1 %) and how existing models for stiffness degradation may be improved in order to better model rate effects at small strains (ε_q < 1 %). However, if rate effects are to be modelled in activities which require the entire strain range to be considered, then these two ways of analysing rate effects would lead to inconsistent values at the crossover point. In numerical modelling this discontinuity could cause serious issues, meaning that there is a need to create a model which can capture rate effect behaviour at any strain level consistently.

The impact of strain level on the rate effect per log cycle at large strains (ε_q > 1 %) has been considered in Chapter 4, with rate effects reducing linearly with $log(\varepsilon_q)$. A model for the variation of λ (the rate effect per log cycle) with ε_q is also required for the small strain range. The key features that the model must be able to capture are:

- There is no observable rate effect before the yield point, $\varepsilon_{q,EL}$, (at a reference strain rate).
- Rate effect mobilisation occurs after the yield point.
- A peak rate effect is reached, after which the large strain data indicates that rate effects will degrade.

The mobilisation of rate effects with strain is an area where there is little current research. The most useful research in this area is the database (Table 6-4) compiled by Lo Presti (1996) which includes data from Mukabi *et al.* (1991), Berre and Bjerrum (1972) and Akai *et al.* (1975). Lo Presti *et al.* (1996) proposed that the small strain rate effects are related to the plasticity index, *PI*, for the soils tested and the data set can be split into two cases; high *PI* (*PI* > 30 %) and low *PI* (*PI* < 30 %). For comparison, the Kaolin used in this study has a *PI* of 32.5 %. The rate effect definition used in the dataset is the strain rate coefficient, α_G, (Equation 6-16), which is the rate effect per log cycle on the shear modulus. However, as the secant shear modulus is proportional to the deviator stress, q, (Equation 6-17) for any given strain, the coefficient, α_G, resolves to the same definition as that used for λ (Equation 6-18). The variation of α or λ with ε_q based on the data gathered by Lo Presti *et al.* (1996) is shown in Figure 6-18.

$$\alpha_G\left(\varepsilon_q\right)=\frac{\Delta G(\varepsilon_q)}{\Delta(\log\dot{\varepsilon}_q).G\left(\varepsilon_q,\dot{\varepsilon}_{q,ref}\right)} \tag{6-16}$$

$$G=k\frac{q}{\varepsilon_q} \tag{6-17}$$

$$\lambda=\frac{\Delta q}{\Delta log(\dot{\varepsilon}_q).q_{ref}} \tag{6-18}$$

Table 6-4 – Rate effect mobilisation studies compiled by Lo Presti *et al*. (1996)

Source	*Clay Type*	*Soil Condition*	*Test Type*	*Plasticity Index, PI (%)*	*PI Grouping Applied*
Mukabi *et al.* (1991)	Kaolin	Remoulded, Isotropic	Triaxial Compression	41	High PI
Mukabi *et al.* (1991)	Kaolin	Remoulded, Anisotropic	Triaxial Compression	41	High PI
Lo Presti *et al.* (1996)	Pisa Clay	Reconsolidated, Anisotropic	Torsional Shear & RCT	20-21	Low PI
Lo Presti *et al.* (1996)	Augusta Clay	Reconsolidated, Isotropic	Torsional Shear & RCT	29	Low PI
Berre and Bjerrum (1972)	Drammen Clay	Reconsolidated, Anisotropic	Triaxial Compression	10	Low PI
Akai *et al.* (1975)	Fukakusa Clay	Remoulded, Isotropic	Triaxial Compression	21-27	Low PI

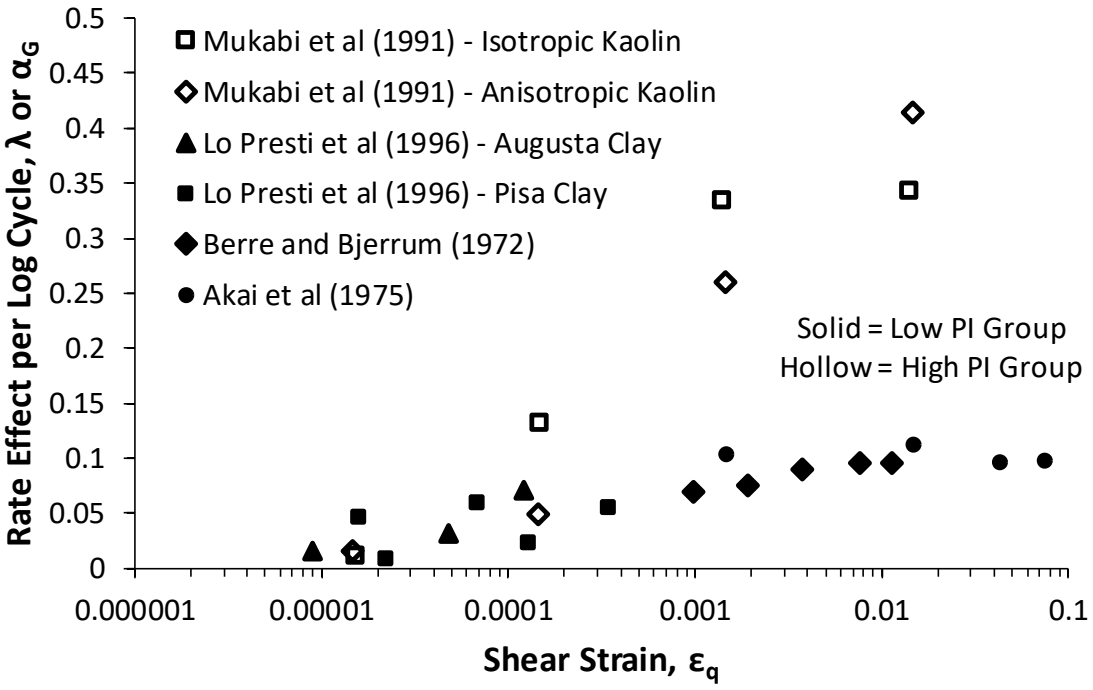

Figure 6-18 – Graph of rate effect mobilisation with strain for data from Lo Presti *et al.* (1996)

To attempt to model the mobilisation of rate effects with strain from Lo Presti *et al.* (1996), a simple hyperbolic curve fit was attempted (Equation 6-19). This is similar to the hyperbolic fit used by Randolph and Hope (2004) to model drainage effects, except with the equation inverted.

$$\frac{\lambda}{\lambda_{max}} = 1 - \frac{1}{1 + c.\varepsilon_q^{\ d}} \tag{6-19}$$

where c and d are empirically derived parameters, and λ_{max} is the maximum value of λ which the rate effect is tending towards.

The usefulness of the equation as a more fundamental model is limited by the fact that the parameters which define it are empirical. However, an analysis of the variation of c and d with $\varepsilon_{q,EL,ref}$ and $\varepsilon_{q,\lambda max}$ shows that when $\varepsilon_{q,EL,ref}$ is taken to be the point at which no more than 1 % of λ_{max} has mobilised and $\varepsilon_{q,\lambda max}$ is defined as the point at which 99 % of λ_{max} has mobilised, c and d are directly related to these key fundamental parameters (Equations 6-20 and 6-21).

$$c = (\varepsilon_{q,EL,ref}.\varepsilon_{q,\lambda max})^{2log\left(\frac{\varepsilon_{q,EL,ref}}{\varepsilon_{q,\lambda max}}\right)^{-1}} \tag{6-20}$$

$$d = 4\log\left(\frac{\varepsilon_{q,\lambda max}}{\varepsilon_{q,EL,ref}}\right)^{-1} \quad (6\text{-}21)$$

To validate that Equation 6-19 can correctly model the mobilisation of rate effects with strain, the equation has been fitted to the high and low *PI* groups from Lo Presti *et al.* (1996). The values for each of the parameters in the equation are shown in Table 6-5. As shown in Figure 6-19, the model captures the measured rate effects at each strain, falling well within the experimental variation of the data. The derived parameters indicate that, as suggested by Vucetic and Dobry (1991) and Lo Presti (1989), the elastic strain threshold, $\varepsilon_{q,EL}$, is greater in clays with a higher plasticity index, *PI*. Interestingly, the high *PI* group exhibits a far greater rate effect (38 % per log cycle) than the low *PI* group (10.3 % per log cycle). The influence of *PI* and other soil material properties on rate effects will be considered further in Chapter 8. However, it should be noted that the reason for the higher rate effects at higher *PI* could in part be related to differences in the experimental approach used in the various studies that comprise the data or other variations between the specimens such as changes in liquidity index of moisture content which have not been accounted for. For each of the *PI* groups, the strain at full rate effect mobilisation, $\varepsilon_{q,\lambda max}$, is similar with values ranging from 1.2 to 1.5 %, although the lack of sufficient data around this point in Lo Presti *et al.* (1996) means that the derived values should be treated with caution.

Table 6-5 – Rate effect mobilisation fitting parameters for high and low *PI* clay groups

Grouping	$\varepsilon_{q,EL,ref}$	$\varepsilon_{q,\lambda max}$	λ_{max}
Low PI (< 30 %)	0.000001	0.015	0.103
High PI (>30 %)	0.000015	0.012	0.380

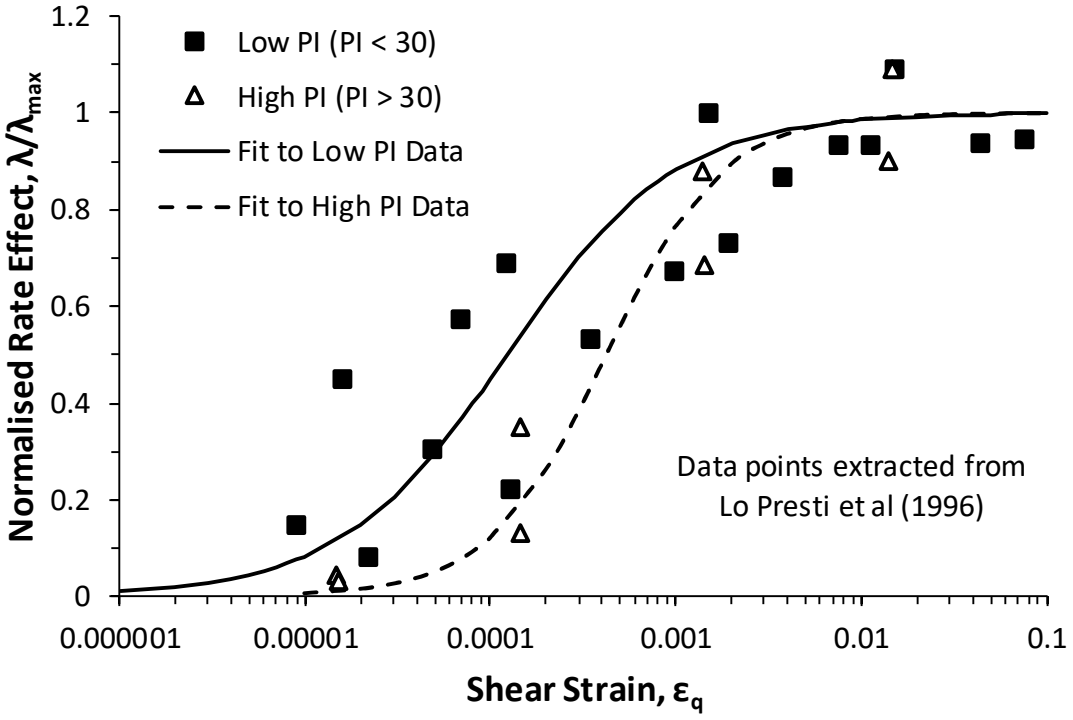

Figure 6-19 – Fitting of proposed rate effect mobilisation model to data from Lo Presti *et al.* (1996)

Up to this stage, the proposed model can capture rate effects up to the point of maximum rate effect. To allow rate effects to be modelled across the full strain range (up to 10 % strain), the rate effect degradation determined from the large strain triaxial testing in Chapter 4 must be included. This can be done by modifying Equation 6-19 to include a linear reduction in rate effect with $log(\varepsilon_q)$ (Equation 6-22). In this, the rate effect degradation is near zero until $\lambda_{\varepsilon q,max}$ after which the rate effect reduces linearly with $log(\varepsilon_q)$ (Figure 6-20). A further empirical parameter, the transition coefficient, ζ, is included in this which determines how rapidly the degradation term is included after $\lambda_{\varepsilon q,max}$ (e.g. a value of 2 means that the degradation would be brought in over ½ a log cycle of strain). $\Delta\lambda_{log}$ is the reduction in λ per log cycle of strain determined in Chapter 4, which is -0.10 for Kaolin (at $\varepsilon_q > 0.01$).

$$\frac{\lambda}{\lambda_{max}} = 1 - \frac{1}{1 + c.\varepsilon_q^{\ d}} + \frac{\Delta\lambda_{log}}{\zeta.ln(10)} sinh^{-1}\left[\left(\varepsilon_q / \varepsilon_{q,\lambda max)}\right)^{\zeta}\right] \quad (6\text{-}22)$$

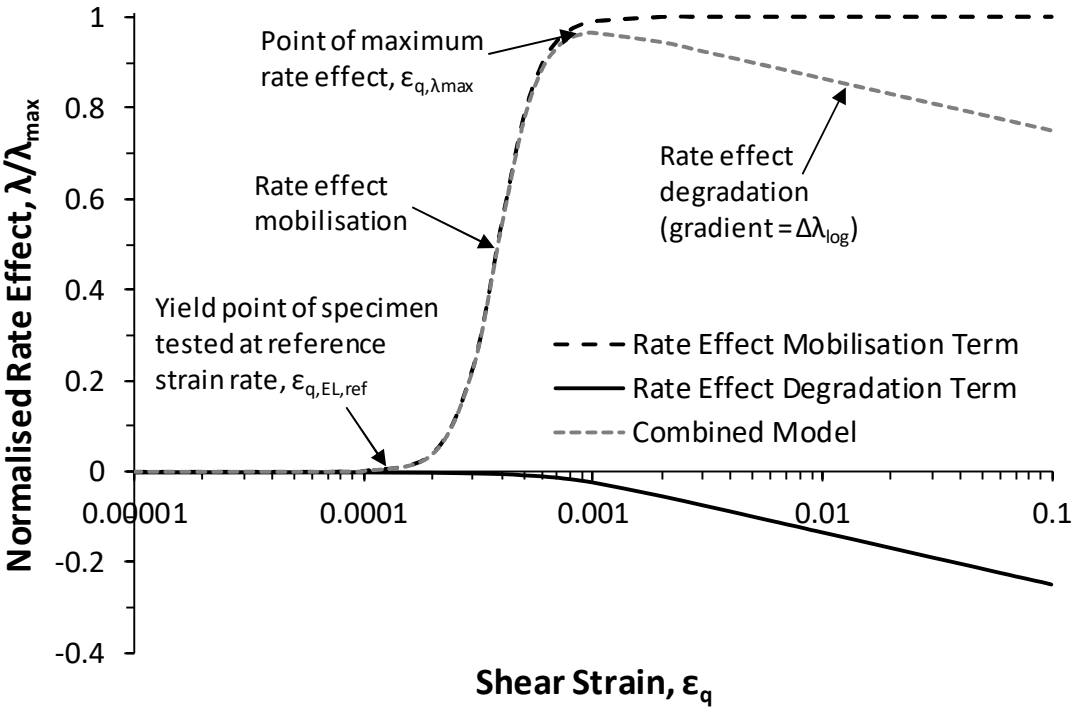

Figure 6-20 – Breakdown of component terms of full strain range rate effect model

6.4. Rate Effect Mobilisation Modelling in Kaolin

The value of λ for each strain level, denoted subscript '*i*', has been determined in the same manner as that used for large strains in Chapter 4 (Equation 6-23) based on the q-ε_q data shown earlier in Figure 6-1.

$$\lambda_i = \frac{\Delta q_i}{\Delta log(\dot{\varepsilon}_q).q_{i,ref}} \tag{6-23}$$

Figure 6-21 shows the variation of λ with strain for the small strain tests on Kaolin. This shows no significant rate effect, with λ being near zero, until the yield of the specimen tested at the reference shear strain rate of 1000 %/hr. There is some variation in λ prior to the point of yield, which is due to natural variations in G_{max} between individual specimens. As discussed previously in Section 6.1, $\varepsilon_{q,EL,ref}$ was found to be effective stress independent and the value for $\varepsilon_{q,EL,ref}$ based on Equation 6-5 has been indicated on Figure 6-21. There is notable noise in the data at this point due to the fact that the measured deviator stresses used in Equation 6-23 at this strain level are themselves small, and also the presence of some variation in initial shear modulus between the specimens. Rate effect mobilisation occurs after this point as expected based on the previously discussed analysis of Lo Presti *et al.* (1996) which has been used to

devise the proposed model. The peak rate effects are typically observed between ε_q = 0.1 and 0.2 %.

The rate effects observed at p'_0 = 650 kPa were significantly lower than expected. Comparison with similar large strain tests showed that the reference test for this effective stress exhibited higher deviator stresses than the comparable large strain test, leading to the lower calculated rate effects. It has not been possible to identify the cause of this. Hence, the data from this effective stress has been excluded from further analysis.

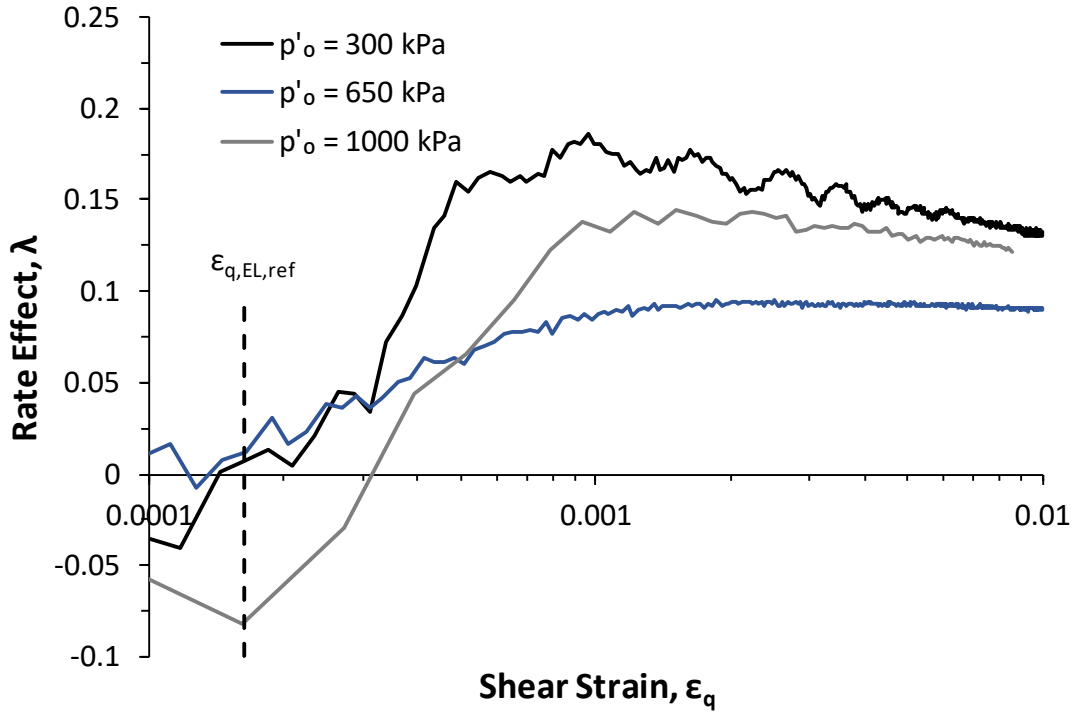

Figure 6-21 – Variation of λ with shear strain from small strain tests on Kaolin

This small strain rate effect data (up to ε_q = 1 %) is shown combined with the large strain data from Chapter 4 (from ε_q = 1 % onwards) in Figure 6-22 and Figure 6-23 for each of the initial mean effective stresses tested. A discontinuity is evident at the interface between the small strain data and the large strain data for p'_o = 300 kPa, in which the rate effect based on the small strain data is significantly lower. Examination of the raw data from the Hall effect sensors for this specific test suggests that at approximately 0.2 % strain the magnet moved away from the face of the Hall effect sensor, which would lead to an underestimation of the measured strains. The data at p'_o = 1000 kPa suggests that the issue was test specific as this data shows good consistency between the measured rate effects at ε_q = 1 % (Figure 1-22).

Also shown in Figure 6-22 and Figure 6-23 is the proposed model (Equation 6-22) fitted to each of the data sets. With the exception of the discontinuity at p'_0 = 300 kPa, the model shows a good level of agreement with the data and is typically able to capture the rate effect behaviour to within 5 % of λ_{max}. The derived values for each of the fitting parameters are shown in Table 6-6.

Table 6-6 – Full strain range rate-effect model fitting parameters for Kaolin

p'o (kPa)	$\varepsilon_{q,EL,ref}$	$\varepsilon_{q,\lambda max}$	λ_{max}	$\Delta\lambda_{log}$	ζ
300	0.000163	0.0011	0.186	-0.100	2
1000	0.000163	0.0013	0.144	-0.125	2

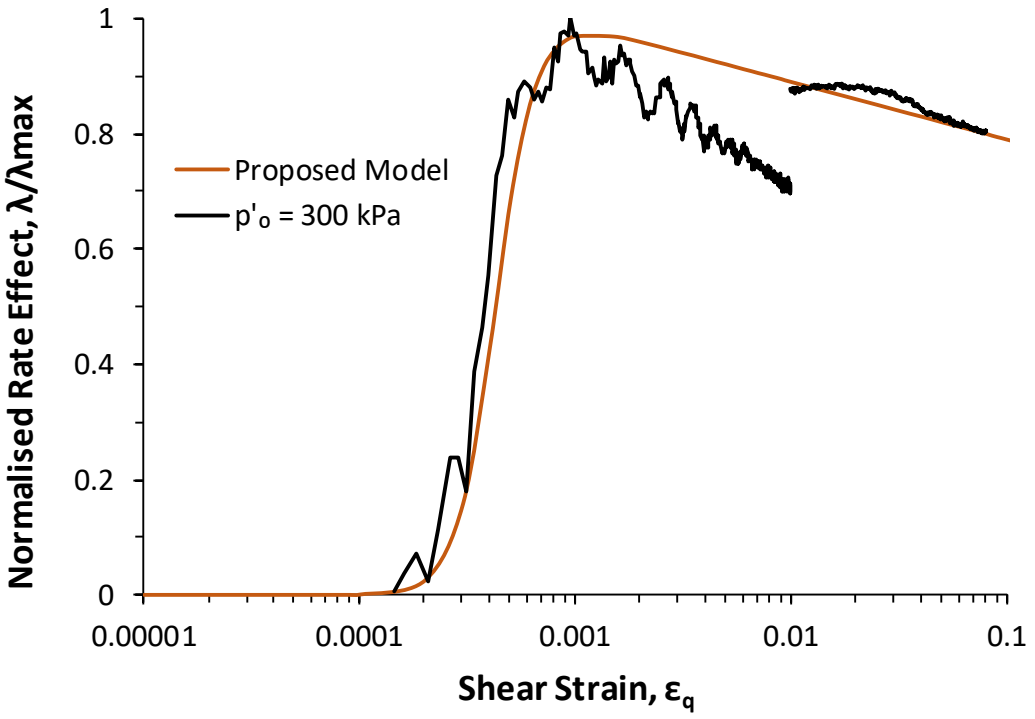

Figure 6-22 – Fitting of rate effect model to combined small and large strain data at p'_0 = 300 kPa

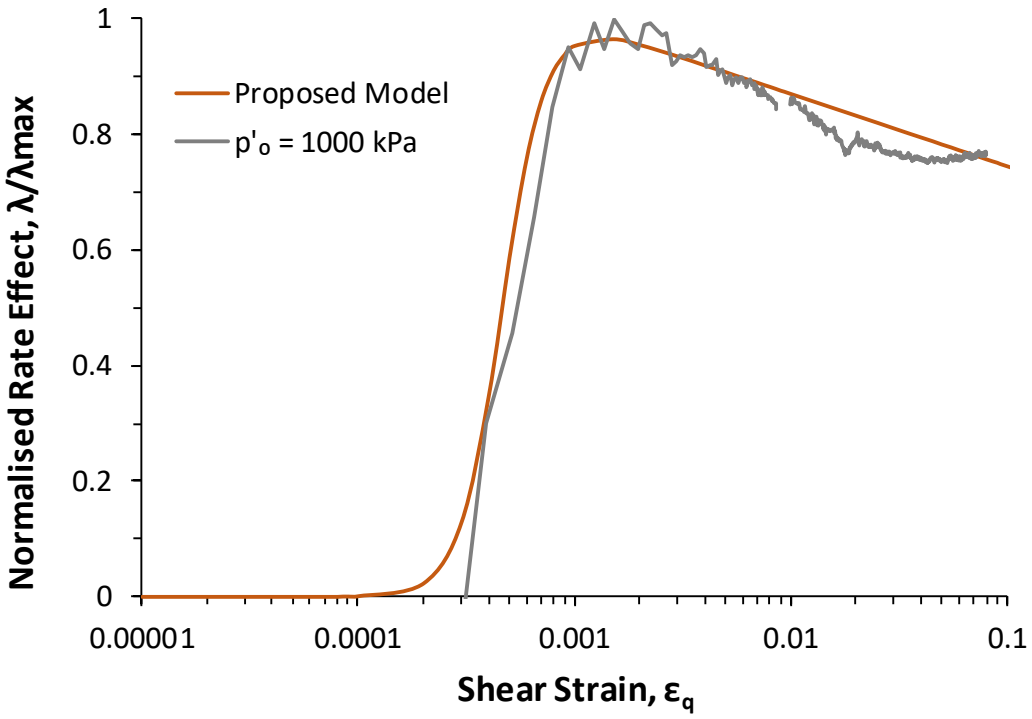

Figure 6-23 – Fitting of rate effect model to combined small and large strain data for p'_o = 1000 kPa

The values of $\varepsilon_{q,EL,ref}$ used are based on Equation 6-5 proposed earlier in this chapter, and it was found that there was no need to alter these from the recommended value. For the effective stresses considered, the strain at which the maximum rate effect occurs, $\varepsilon_{q,\lambda max}$, was found to range from ε_q = 0.11 to 0.13 %, with little effective stress dependence. The small variation that there is may be due to specimen variation and the accuracy limitations of the model fitting process. This suggests that a constant (average) value of $\varepsilon_{q,\lambda max}$ = 0.0012 may be used for Kaolin. The values of $\Delta\lambda_{log}$ range from -0.100 to -0.125, which are close to the value of -0.10 determined from the large strain testing. It is also recommended that a constant value of 2 is used for the transition coefficient, ζ, in all cases.

The measured maximum rate effects were λ = 18.6 and 14.4 % for the p'_o = 300 and 1000 kPa tests respectively. These values are greater than the rate effects determined at ε_q = 1 % from the large strain testing (Figure 6-24). Using an LI^2 model as proposed for the large strain data in Chapter 4, λ_{max} may be represented by Equation 6-24. However, if small strain test data is not available it is recommended that λ_{max} may be estimated from the large strain test data

using Equation 6-25 based on the values of $\lambda_{\varepsilon q=1\%}$ discussed in Chapter 4. This uses the assumption that the degradation of rate effects with $log(\varepsilon_q)$ after $\varepsilon_{q,\lambda max}$ is the same as that determined from the large strain data and back-calculates λ_{max} based on this. The estimation of λ_{max} based on the large strain data using Equation 6-25 is also shown in Figure 6-24, which shows that this provides a reasonably accurate estimation, although the use of measured values of λ_{max} from small strain data is preferable, where available.

$$\lambda_{max} = 0.14 + 0.45LI^2 \quad (6\text{-}24)$$

$$\lambda_{max} = \lambda_{\varepsilon q=1\%} \cdot \left[1 - \Delta\lambda_{log} . log(0.01 / \varepsilon_{q,\lambda max}) \right] \quad (6\text{-}25)$$

where $\Delta\lambda_{log}$ = -0.10 and $\varepsilon_{q,\lambda max}$ = 0.0012 for Kaolin

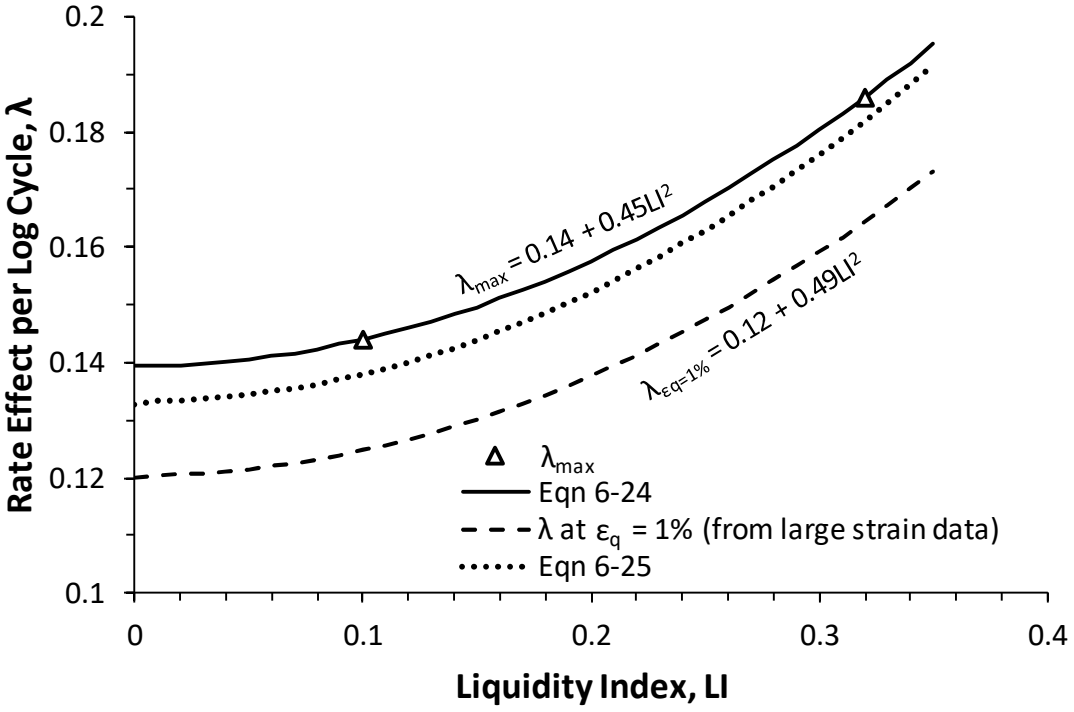

Figure 6-24 – Variation of λ_{max} with liquidity index for Kaolin

6.4.1. Summary of Proposed Model and Parameter Recommendations

A model for capturing the strain level dependence of strain rate effects, which also includes the influence of soil state, at any strain level has been proposed (Figure 6-20). The first step in obtaining the parameters for the model is to determine the reference elastic strain threshold, $\varepsilon_{q,EL,ref}$, which is the elastic strain threshold at the reference strain rate for the study. This key point determines the strain below which the model will predict no strain rate effects. This may either be determined at a slow 'static' strain rate or at the lowest strain rate to be considered. Ideally $\varepsilon_{q,El,ref}$ should be determined from a triaxial test at the reference strain rate, using local on-sample strain measurements. If experimental values are not available, $\varepsilon_{q,El,ref}$ can be estimated using Equation 6-26, which is based on testing of Kaolin in this study.

$$\varepsilon_{q,EL,ref} = 3.4\times10^{-5}\, log(\dot{\varepsilon}_{q,ref}) + 0.00006 \tag{6-26}$$

The next point which needs to be determined is the strain at which the maximum rate effect occurs, $\varepsilon_{q,\lambda max}$, which based on the current evidence is suggested to be taken as a constant value of $\varepsilon_{q,\lambda max}$ = 0.0012, although further research into how this parameter varies in different soils is still required. Using these values, the fitting parameters, *c* and *d* can be calculated using Equations 6-27 and 6-28.

$$c = (\varepsilon_{q,EL,ref}.\varepsilon_{q,\lambda max})^{2\,log\left(\frac{\varepsilon_{q,EL,ref}}{\varepsilon_{q,\lambda max}}\right)^{-1}} \tag{6-27}$$

$$d = 4\,log\left(\frac{\varepsilon_{q,\lambda max}}{\varepsilon_{q,EL,ref}}\right)^{-1} \tag{6-28}$$

The final component of the model's strain dependence is the degradation of the rate effect per log cycle of strain after $\varepsilon_{q,\lambda max}$. This is determined by the gradient, $\Delta\lambda_{log}$ (which is expected to be negative) and a fitting parameter, ζ, which determines how rapidly the degradation is introduced. For Kaolin, $\Delta\lambda_{log}$ may be taken to be -0.115, whilst ζ is recommended to be 2 for all soils. Further discussion of the value of $\Delta\lambda_{log}$ for different clays is given in Chapter 8. These parameters allow the ratio of λ/λ_{max} to be determined for any strain level using Equation 6-29.

$$\frac{\lambda}{\lambda_{max}} = 1 - \frac{1}{1 + c.\varepsilon_q^{\,d}} + \frac{\Delta\lambda_{log}}{\zeta.ln(10)} sinh^{-1}\left[\left(\varepsilon_q / \varepsilon_{q,\lambda max)}\right)^{\zeta}\right] \tag{6-29}$$

The key parameter which sets the magnitude of the predicted rate effects is the maximum rate effect per log cycle, λ_{max} (which occurs at $\varepsilon_{q,\lambda max}$). This is soil state dependent and related to the liquidity index of the soil. For Kaolin, λ_{max} can be calculated using Equation 6-30. Further discussion of the derivation of λ_{max} for other soils is given in Chapter 8. By multiplying the ratio λ/λ_{max} at each strain level by λ_{max}, this allows the rate effect at any given point to be predicted.

$$\lambda_{max} = 0.14 + 0.45LI^2 \quad (6\text{-}30)$$

7. Rate Effect Mechanism Investigation

Thus far, useful models for predicting the rate effect response of Kaolin at both small and large strains have been suggested. However, from a fundamental perspective, there is a need to investigate the mechanism behind rate effects. Primarily due to the fact that there are severe difficulties in imaging high strain rate events at the microscale, the cause behind strain rate effects is very poorly understood (Kwok and Bolton, 2010). Two proposed mechanisms have been identified from the literature review:

- Increases in deviator stress with strain rate due to highly viscous layers of adsorbed water on the surface of clay particles causing greater resistance to inter-particle shear (Rattley *et al.*, 2011; Low, 1961)
- Inter-particle locking at higher strain rates leading to increased contact forces and hence increases in deviator stress (Waitukaitis and Jaeger, 2012; Bi *et al.*, 2011; Richardson, 1963; Wang and Cheng, 2017)

However, in Geotechnical Engineering, the fundamentals of these mechanisms are poorly understood, and it is necessary to turn to the field of granular physics. Interestingly, in granular physics, the same two theories exist for strain rate effects in dense granular suspensions, albeit expressed in different terminology; inter-particle fluid viscosity (Wagner and Brady, 2009) and particle to particle contact (Brown and Jaeger, 2014).

7.1. Fluid Viscosity Mechanism

One of the most commonly suggested mechanisms for rate effects is that a thin film of highly viscous adsorbed water exists on the surface of clay particles, and that increasing strain rate causes additional viscous shear resistance as particles move relative to each other (Rattley *et al.*, 2011; Low, 1961). Due to the small size of the clay particles, physical contact between the particles, and hence mechanical friction, would not normally occur (at slow strain rates) due to the repulsive electrical forces between the clay surface charges (Santamarina and Shin, 2009; Mitchell and Soga, 2005). These surface charges would act to repel adjacent clay particles which would have the same charge. This means that friction between the clay particles would mainly come from the interaction of the electrical charges and from the viscosity of the pore fluid between the particles.

However, the evidence for the high viscosity of the adsorbed layer is conflicting. Studies such as Osipov (2012) infer the existence of the adsorbed layer, however the majority of studies attribute this finding to other effects such as measurement errors (Mitchell and Soga, 2005). The only direct measurements found of the viscosity of adsorbed layers on a clay mineral surface showed that adsorbed water maintains its normal viscosity down to the last molecular layer of thickness from the mineral surface (Christenson *et al.*, 1987; Mitchell and Soga, 2005).

Nevertheless, Wagner and Brady (2009) asserted that even without the existence of a zone of highly viscous pore fluid around the clay particles, normal fluid viscosity could still lead to strain rate effects. This is attributed to the fact that as the particles shear relative to each other, the fluid viscosity causes a drag force on the adjacent particles which draws the particles together. This reduces the distance between the particles and increases the effective viscosity (as the fluid shear rate is focussed over a smaller particle separation) (Brown and Jaeger, 2014). However, Brown and Jaeger (2014) carried out numerical particle simulations on dense, fine granular suspensions and found that these hydrodynamic effects could not fully account for the observed strain rate effects.

7.2. Granular Dilatancy and Particle to Particle Contact Mechanism

In contrast, the mechanism by which particle locking occurs is far more poorly understood. It is still a subject of debate and continues to be a topic of research in other fields such as fluid mechanics and the physics of particle interactions, as observing and measuring its existence is not trivial (Bi *et al.*, 2011; Waitukaitis and Jaeger, 2012). However, it has been attributed as the reason that some DEM models cannot correctly model strain rate effects (Wang and Cheng, 2017).

This mechanism is best described by Brown and Jaeger (2014) who also describe it as “granular dilatancy”. Brown and Jaeger (2014) showed using numerical particle simulations that as dense fine granular suspensions are sheared, increasing shear rates lead to individual particles having more momentum. This causes particles to come into contact (effectively colliding) with adjacent particles and solid to solid frictional contact occurs between them, as their increased momentum overcomes the repulsive forces keeping the particles apart. As these particles effectively lock together, a network of particle to particle contacts forms in the material, which

can carry force. This additional ability to carry the shear forces was thought to be the cause of the observed rate effects.

The idea of granular dilatancy (or particle locking) described by Brown and Jaeger (2014) has a number of key impacts which would be expected to be exhibited. Firstly, it predicts that fine granular materials would exhibit an increased yield stress (and also hence strain) in undrained conditions. This is due to the additional structure caused by the particle to particle contact network at higher strain rates, which more work is required to overcome. This is in keeping with the increasing yield thresholds with strain rate observed in Chapter 6.

Secondly, granular dilatancy leads to dilation of the material with increasing strain rates. As higher strain rates lead to more particle to particle contacts, these 'locked' particles are forced to rotate past each other during shearing, causing dilation of the structure. This was previously described by Richardson (1963), as shown in Figure 7-1. In the case of undrained tests, this would cause negative pore pressures which would restrain the dilation. Again, this was observed in Chapter 5, both in terms of the pore pressure suppression measured and in the rightwards movement of the CSL in *v-ln(p')* space (which represents less contractive behaviour).

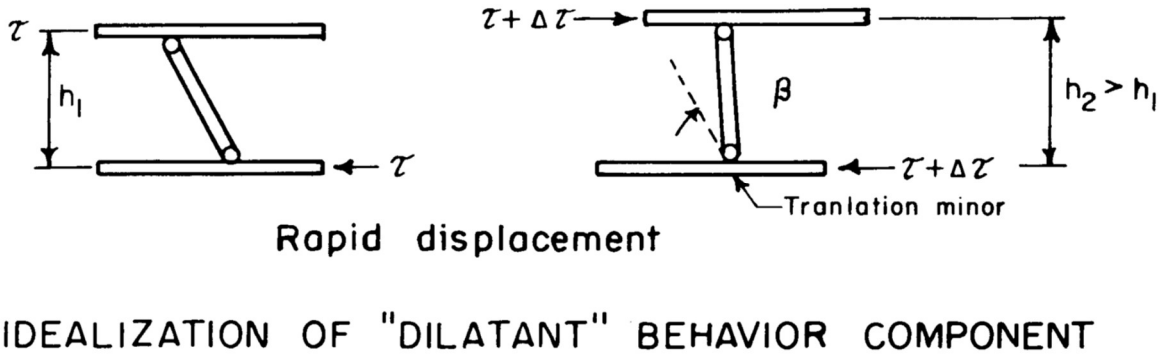

Figure 7-1 – Potential mechanism for dilation of 'locked' particles where particle to particle contact occurs (Richardson, 1963)

Brown and Jaeger (2014) also found that for granular dilatancy, the increase in shear stress with strain rate would be greater in suspensions with higher packing ratios (more densely packed). In terms of the results in this study, this would correspond to higher values of $\Delta q/\log(\dot{\varepsilon})$ at lower void ratios (or higher p'_0). As shown in Chapter 4, this behaviour was observed in Kaolin, with $\Delta q/\log(\dot{\varepsilon}_q)$ (at peak shear strength) increasing from 21 kPa per log cycle

at p'_0 = 300 kPa to 51 kPa per log cycle at p'_0 = 1350 kPa, providing further support to the theory of granular dilatancy being the mechanism behind the rate effects observed here. Whilst this appears to suggest (contrary to the discussion thus far in this thesis) that rate effects increase with p'_0, it is important to note that it is not until $\Delta q/log(\dot{\varepsilon}_q)$ is divided by q_{ref} to give λ that rate effects are seen to reduce with increasing p'_0. This is due to the fact that q_{ref} also increases with p'_0.

One visible indication of granular dilation (which can be observed by eye) mentioned by Brown and Jaeger (2014) is that if the material has been rapidly sheared (in undrained conditions) and the structure attempts to dilate, when the material is exposed to the atmosphere the negative pore pressures lead to the clay particles protruding from the surface of the material (akin to in capillary suction). This causes the surface to refract light differently. This was observed visually in the triaxial specimens after they were removed from the triaxial system and cut in half, particularly around the shear plane where the highest strain rates would have occurred.

One final point on the theory of granular dilatancy is that Brown and Jaeger (2014) presented a state diagram which describes the conditions in which strain rate effects would occur (Figure 7-2). The y axis is shear stress (which the authors also use to represent the shear strain rate as they are inter-related) and the x axis is particle diameter. The hatched area represents the region in which granular dilatancy is possible. The left side is bounded by electrical repulsive forces which keep particles apart, whilst the right side represents the point at which the dilation would overcome capillary suction, which is not relevant to this study as it requires the material being sheared to be open to the air. This diagram suggests that as the size of the particles reduces, higher strain rates are required for granular dilation and particle to particle contact to occur. This is due to the fact that finer particles have less momentum, and their electrostatic repulsion due to surface charges is greater (per unit mass). This is an important prediction which can be tested in Chapter 8 when the results of the testing of different soils are discussed, as it suggests that rate effects would be lower in clays with finer particles. It should be noted, however, that Figure 7-2 is an order of magnitude prediction, as it uses simplistic assumptions (such as assuming the particles are uniformly sized and spherical).

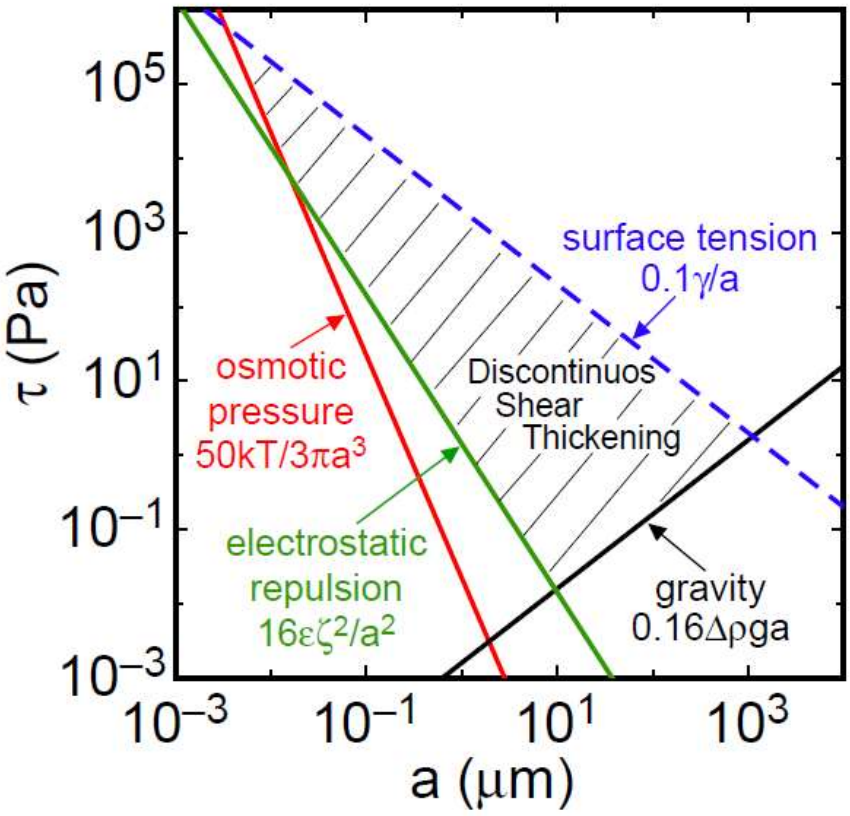

Figure 7-2 – State Diagram for granular dilatancy describing the conditions in which it would occur from Brown and Jaeger (2014) [*sic*]

In summary, the theory of granular dilatancy set out by Brown and Jaeger (2014) presents a possible mechanism by which rate effects occur, and which predicts a number of the behaviours observed in the high strain rate triaxial testing so far. This also suggests that the momentum of the particles is a key factor. Whilst viscous effects cannot fully account for strain rate effects, this does not preclude the possibility that viscous effects contribute to causing the particle to particle contacts which lead to granular dilation.

7.3. Investigation using Scanning Electron Microscopy

Whilst imaging of high strain rate events is not directly possible, it is possible to examine samples from high and low strain rate triaxial specimens which have been flash frozen only a few minutes after shearing to consider if there is any remaining indication in the clay structure as to which of the above mechanisms may be occurring. Three SEM images have been analysed in detail; a sample taken from an unsheared specimen which had been subjected to isotropic consolidation (as a reference), a sample taken from a section of a slow ($\dot{\varepsilon}$ = 1 %/hr, CIU) triaxial test not located near any obvious shear planes (to avoid localised disturbance) and finally a

sample from a similar location of a fast ($\dot{\varepsilon}$ = 100000 %/hr, CIU) triaxial test. These images are shown in Figure 7-3, Figure 7-4 and Figure 7-5, however, it should be noted that these images are not shown correctly orientated to the triaxial specimen due to the screw sample mounting system in the SEM apparatus used. The results of the analyses shown later have been corrected for this effect by using a low zoom image from each sample to identify its specific orientation in the SEM setup.

Using CAD, each particle agglomeration was annotated, allowing the length and orientation of the particle group to be identified. The particle groups were defined as collections of particles which were tightly bound in direct face to face contact and were distinctly visible in the SEM images. Each image (approx. 22 x 32 µm) was found to contain 700 to 1000 identifiable particle flocs. The lengths of each of the particle groups was also identified, allowing the mean length of the particle groups to be found for each case. As the analysis was conducted using CAD, the orientation and length of each individual particle group could be easily exported to text files for analysis. Void spaces within the SEM samples were also annotated, allowing the void area to be estimated. The voids spaces were identified using the fact that the SEM images have a narrow depth of field. This means that the recessed void areas were visible as they were noticeably darker than the surrounding (in plane) particle groups, which were clearly white. The details of each of the SEM images are summarised in Table 7-1.

Table 7-1 – Properties of SEM image analyses of isotropically consolidated Kaolin

SEM Image Description	*Test Axial Strain Rate (%/hr)*	*Initial Mean Effective Stress, p'_o (kPa)*	*Mean Particle Group Length (µm)*	*Area of Voids (µm²)*	*Area of Image (µm²)*
Isotropic	-	300	0.982	359.9	720.9
Slow	1	300	1.153	208.1	720.9
Fast	100000	300	0.971	218.5	720.9

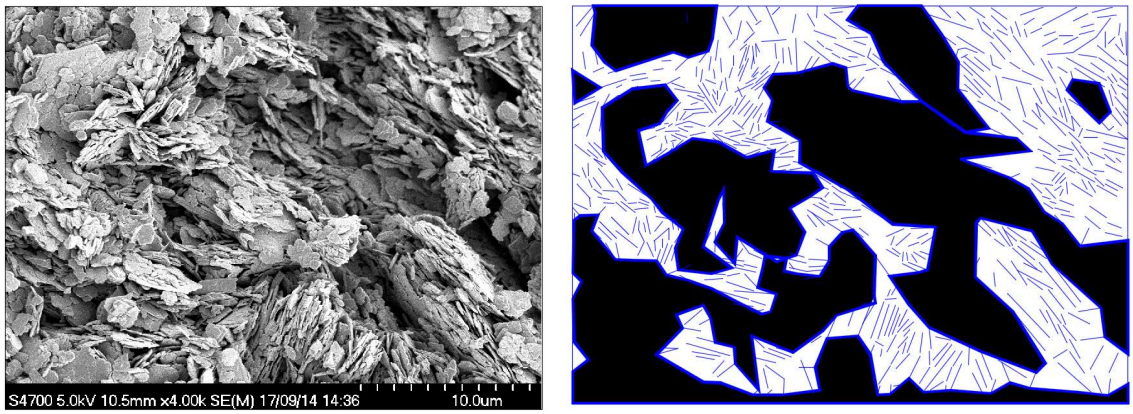

(a) (b)

Figure 7-3 – (a) SEM image of unsheared isotropically consolidated Kaolin triaxial specimen (p'_0 = 300 kPa) and (b) corresponding annotation of particle groups and void areas

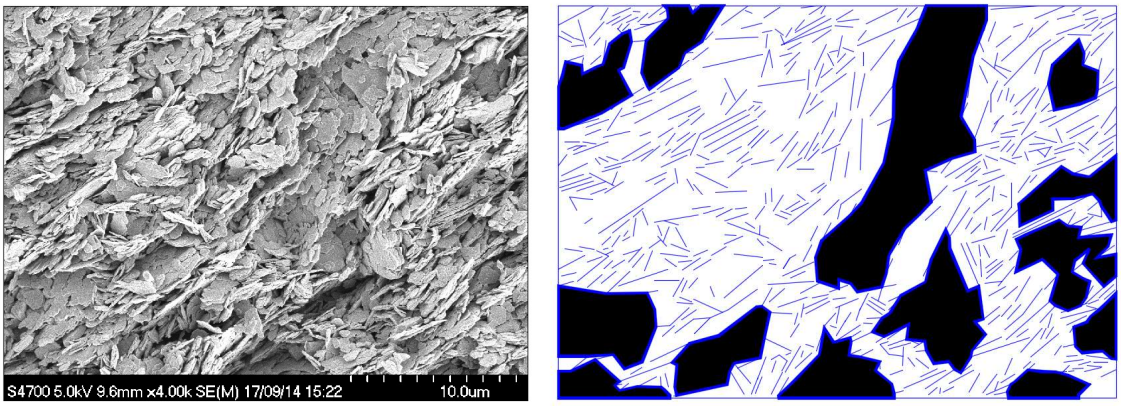

(a) (b)

Figure 7-4 – (a) SEM image of slow sheared isotropically consolidated Kaolin triaxial specimen (p'_0 = 300 kPa, $\dot{\varepsilon}$ = 1 %/hr) and (b) corresponding annotation of particle groups and void areas

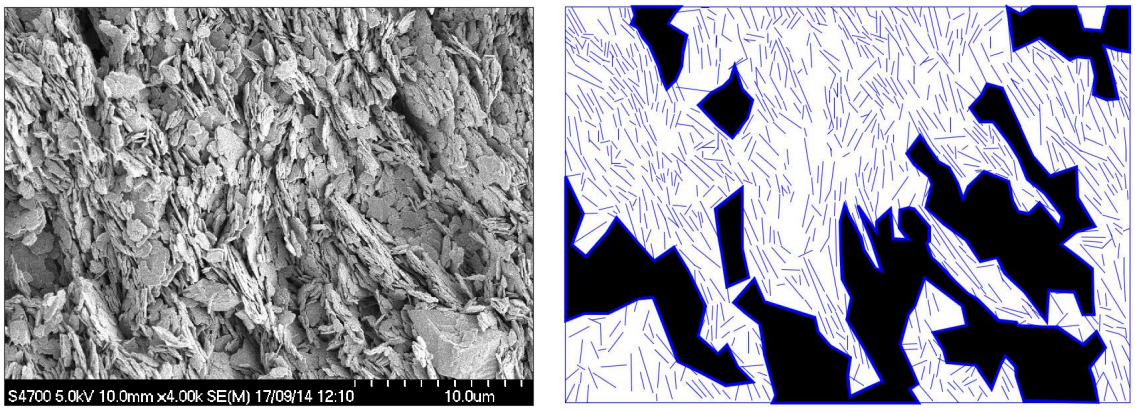

(a) (b)

Figure 7-5 – (a) SEM image of fast sheared isotropically consolidated Kaolin triaxial specimen (p'_0 = 300 kPa, $\dot{\varepsilon}$ = 100000 %/hr) with a quartz particle visible in the bottom right corner and (b) corresponding annotation of particle groups and void areas

To rule out the possibility that the high strain rate events are changing the length of the particle groups within the specimen by breaking down the flocs (into smaller flocs or individual particles), the particle group lengths determined from the SEM analysis have been used to prepare particle size distributions for each of the specimens. These are shown in Figure 7-6. Taking the unsheared isotropic specimen as a reference, the fast sheared specimen displayed no observable reduction in floc length suggesting that no breakdown is occurring. The slow sheared specimen appears to have slightly larger flocs on average compared with both the unsheared and fast sheared specimens, which is most likely to be due to small material variations between the specimens. The PSD analysis indicates that the flocs in clays are so tightly bound that they do not noticeably break down during shearing. Even high shear strain rates of $\dot{\varepsilon}_q$ = 100000 %/hr do not appear to cause significant mechanical changes in the size of the particle flocs.

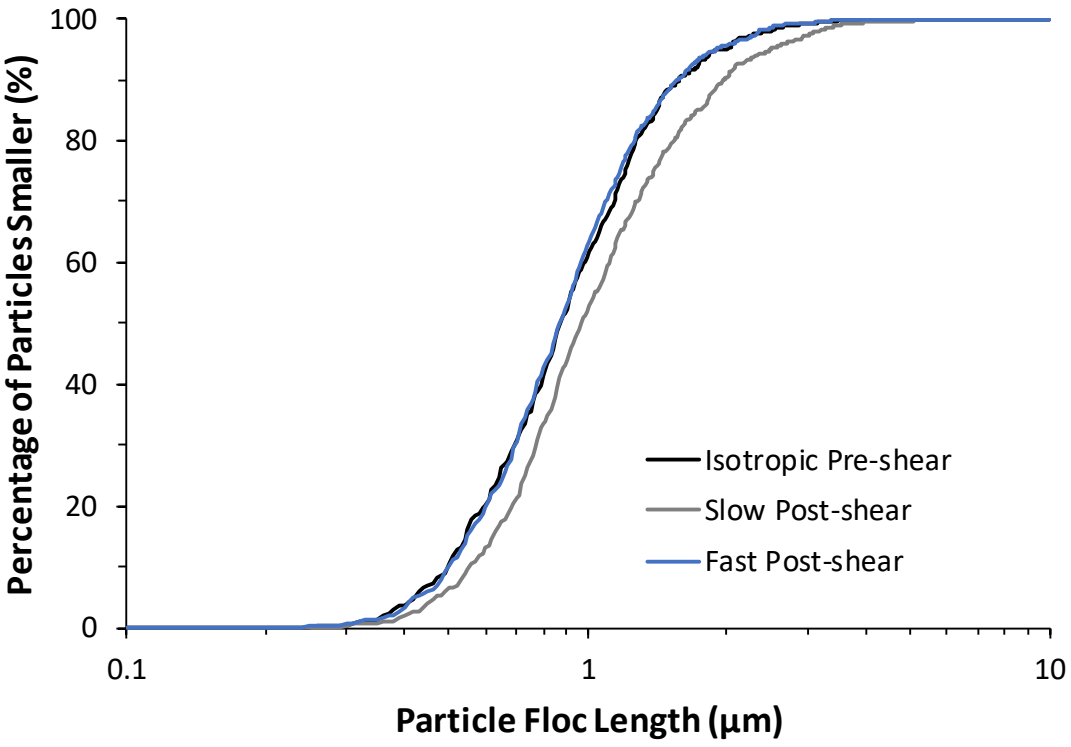

Figure 7-6 – Particle size distributions determined from SEM imagery of Kaolin (p'_0 = 300 kPa) sheared at differing strain rates

Considering the orientation of the particle groups, this may provide an insight into whether particle locking has been occurring, as locked particles in a high strain rate test would be expected to have small differences in their orientation compared to a slower test (Richardson, 1963). Figure 7-7 shows the results of the orientation analysis for each of the SEM images. This has been prepared by rounding the orientation of each of the particle groups identified earlier in Figure 7-3 to Figure 7-5 to the nearest degree, in order to identify the number of particle groups in each degree of orientation. An orientation of 0° has been taken to be aligned to the triaxial specimen's vertical axis. As an example, if all of the particle groups were evenly distributed (completely isotropic) in each degree of orientation, it would be expected that each degree would contain 0.56 % of the particle groups present (100 % divided by the 180 degrees of orientation into which the particles have been split).

Starting with the unsheared isotropic SEM image, it can be seen that the specimen displays no clear preferred orientation, with the percentage of particle groups remaining constant at approximately 0.6 % in each degree increment of orientation. This is close to the 0.56 % that would represent a completely isotropic arrangement. This suggests that, as expected, the specimen is truly isotropic and the effects of the initial 1D consolidation from slurry have been removed by isotropic reconsolidation to a higher stress. In contrast, the slow sheared specimen displays a clear preferred orientation at 70°, as particle groups align themselves parallel to each other as the specimen tends to critical state with shearing. This is close to the angle at which the visible shear plane formed, which was typically at around 60° from vertical. The fast sheared specimen shows a very similar response to the slow sheared specimen, with the amount of preferential orientation being of the same magnitude and peaking at a similar orientation. There is a small offset in the orientation between the slow and fast sheared specimens of approximately 5°, which is attributed to the accuracy with which the small SEM samples (3 mm cubes) can be cut from the triaxial specimen.

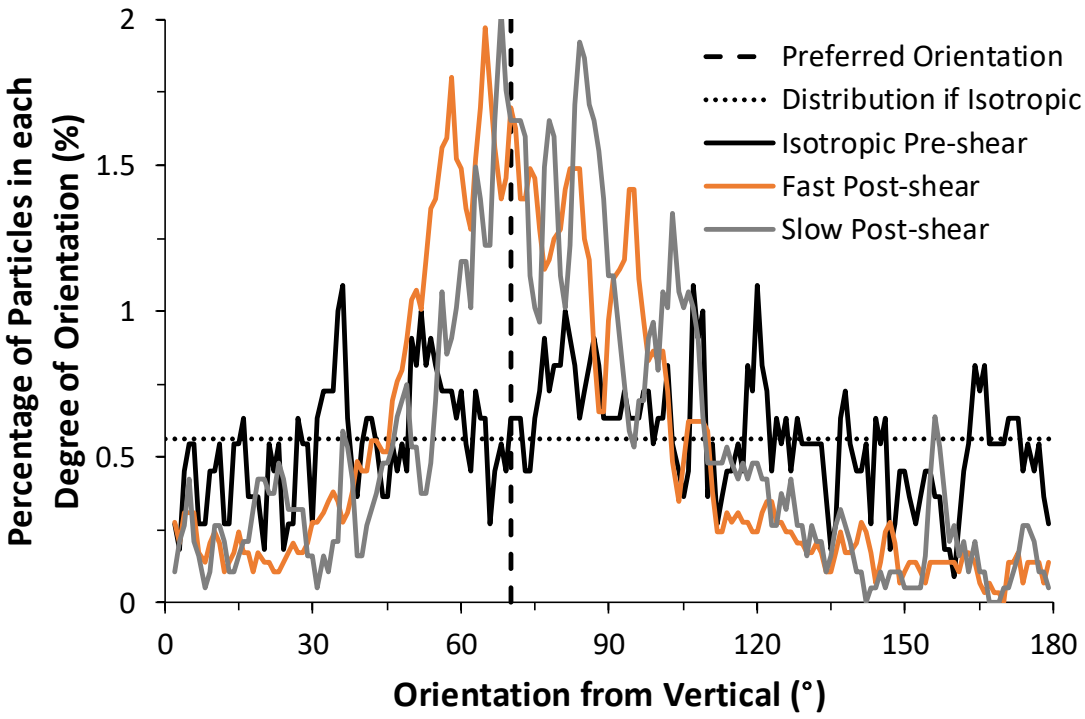

Figure 7-7 – Variation of particle orientation from SEM imagery of Kaolin (p'_0 = 300 kPa) sheared at differing strain rates

From the SEM image orientation analysis, no significant differences were observed between the slow and fast sheared specimens in the approach used here. However, the SEM analysis used here has some limitations which should be kept in mind. Firstly, the SEM analysis considers the size and orientation of the particle groups in an extremely small region of the triaxial specimen, and the assumption is made that the small area imaged is representative of the larger specimen. Whilst the preparation of the SEM specimens used the best available techniques, specimen disturbance is also unlikely to be entirely avoided. A degree of judgement is also used in the identification of the individual particle groups.

Based on the fact that no differences were observed between the SEM images of the fast and slow sheared specimens, evidence of re-orientation due to increasing particle to particle contacts has not been seen. This suggests that either rate effects may be due to fluid viscosity, or possibly that the particle to particle contacts expected by granular dilatancy are released when the shearing stops or when the deviator stress is removed (which occurs during the undocking of the specimen at the end of the test). This would seem sensible as the shear stress which sustains the particle contact would no longer exist, allowing the particles to re-orientate

to a more optimal position. There is some anecdotal evidence to support this theory in Lemos and Vaughan (2000), where it was shown that in ring shear testing of clay soils at high shear strain rates, when rapid shearing is stopped, a sudden increase is pore pressure occurs which was due to the collapse (and subsequent constrained contraction) of the soil structure. This ties in with the increase in shear-induced pore pressures observed in the triaxial testing in this study, when the shear plane formed (and hence when shearing of the location at the PPT was positioned stopped). This was discussed previously in Chapter 5 and suggests a change in the particle contact behaviour occurs when shearing is stopped, or the strain rate is reduced.

8. Potential Methods for Predicting Rate Effects in Different Soils

So far, methods for modelling rate effects at both small and large strains have been proposed and potential causal mechanisms have been investigated. However, the usefulness of these methods may be limited in applications unless the main parameters required can be easily estimated in practice, meaning that simple correlations between rate effect parameters and easily obtainable soil properties are desirable.

Table 8-1 – Programme of triaxial testing on 100 mm specimens of different soils

Test Designation	*Test Type*	*Soil Type*	*Initial Mean Effective Stress, p'_o (kPa)*	*Axial Strain Rate, $\dot{\varepsilon}$ (%/hr)*	*Back Valve State*	*OCR*
H71-TU-L1	CIU	Hyplas 71	300	1000	Closed	1
H71-TU-L2	CIU	Hyplas 71	300	100000	Closed	1
H71-TU-L3	CIU	Hyplas 71	650	1000	Closed	1
H71-TU-L4	CIU	Hyplas 71	650	100000	Closed	1
H71-TU-L5	CIU	Hyplas 71	1000	1000	Closed	1
H71-TU-L6	CIU	Hyplas 71	1000	100000	Closed	1
HAT-TU-L1	CIU	Hymod AT	300	1000	Closed	1
HAT-TU-L2*	CIU	Hymod AT	300	10000	Closed	1
HAT-TU-L3	CIU	Hymod AT	300	100000	Closed	1
HAT-TU-L4	CIU	Hymod AT	650	1000	Closed	1
HAT-TU-L5*	CIU	Hymod AT	650	10000	Closed	1
HAT-TU-L6	CIU	Hymod AT	650	100000	Closed	1
HAT-TU-L7	CIU	Hymod AT	1000	1000	Closed	1
HAT-TU-L8+	CIU	Hymod AT	1000	100000	Closed	1

* Test data not usable for analysis due to gain control issues in strain application

+ Test data not usable for analysis due to slow leakage during test

8.1. Programme for Triaxial Testing of Different Soils

To investigate which soil properties may be good rate-effect indicators, rate effect data from different soils is required. A programme of testing on two further soils, Hyplas 71 and Hymod AT, was carried out at initial mean effective stresses ranging from p'_0 = 300 to 1000 kPa and axial strain rates from $\dot{\varepsilon}$ = 1000 to 100000 %/hr (Table 8-1). Both of these materials are commercially available powdered ball clays from Devon and Dorset respectively. Their characterisation has been described in Chapter 3, but their properties are summarised in Table 8-2 for ease of access, along with those for Kaolin for comparison. Due to severe gain control issues in the tests (denoted * in Table 8-1) conducted at $\dot{\varepsilon}$ = 10,000 %/hr data from these tests was not usable in the analysis. Additionally, test HAT-TU-L8 was subsequently found to have been affected by a slow ongoing leak during the test which altered the sample area calculations, meaning that it was not possible to determine the rate effect in Hymod AT at p'_0 = 1000 kPa.

Before discussing the results of the triaxial testing, it is worthwhile to highlight the differences and similarities of the three clays. The three clays were selected due to their different Atterberg limits. Kaolin and Hymod AT have similar plastic limits of 29.7 and 32.5 %, respectively, whilst the plastic limit of Hyplas 71 is lower at 20.9 %. The liquid limits range from 45.5 to 79.0 % for Hyplas 71 and Hymod AT, respectively. Hymod AT is almost entirely (95 %) clay (<2 µm), whilst Hyplas 71 is only 65 % clay due to the presence of a significant silt fraction in the form of relatively rotund quartz particles. For all of the clays, the amount retained on a 150 µm sieve was no more than 0.5 % (using wet sieving in accordance with BS1377). Hymod AT and Hyplas 71 exhibited very similar permeabilities despite the differences in clay fraction, whilst the permeability of Kaolin was found to be an order of magnitude greater.

The specific surface area of Kaolin was found to be 36.7 m^2/g, whilst Hyplas 71 and Hymod AT had higher *SSA*s of 53.2 and 105.2 m^2/g, respectively. This is due to the fact that these two clays are ball clays (secondary clays), whilst Kaolin is a primary clay. The secondary nature of these ball clays means that they were transported and resedimented after formation from the parent material - a process which preferentially selects finer particles which travel further before settling. This leads to the higher fines contents than Kaolin seen in the particle size distribution (Figure 8-1). Further, evidence of this can be seen in the x-ray diffraction (XRD) analysis results, with Hyplas 71 and Hymod AT containing higher proportions of Illite (28 and

40 %, respectively, compared to only 18 % for Kaolin) and significantly lower Kaolinite proportions (28 and 42 %, respectively, compared to 80 % for Kaolin). Kaolinite is a relatively coarse clay mineral with a specific surface area of 10 to 20 m^2/g, whilst Illite is a fine clay mineral with a specific surface area of 65 to 100 m^2/g, which would be expected to have the most influence on the *SSA* of the three clays. Hyplas 71 was found to contain 44 % Quartz by mass (comparatively large crystals of silt size), explaining the sizeable silt fraction observed in the PSD. In contrast, Kaolin contains only 2 % Quartz by mass.

Table 8-2 – Summary of properties of all clays tested (CSL determined at $\dot{\varepsilon}$ = 1 %/hr)

Property	Kaolin	Hyplas 71	Hymod AT
Plastic Limit, PL (%)	32.5	20.9	29.7
Liquid Limit, LL (%)	65	45.5	79.0
Plasticity Index (%)	32.5	24.6	49.3
Clay Fraction (%)	82	65	95
Activity (%)	39.6	37.8	51.9
Specific Surface Area using Methylene Blue (MB) Spot Method, SSA (m^2/g)	36.7	53.2	105.2
Permeability, k (m/s) *	$0.76x10^{-9}$ to $1.17x10^{-9}$	$0.51x10^{-10}$ to $1.05x10^{-10}$	$0.59x10^{-10}$ to $1.56x10^{-10}$
NCL Gradient, λ_{NCL}	0.168	0.101	0.180
Unload/Reload Line Gradient, κ	0.021	0.046	0.077
NCL Intercept, N $^+$	3.101	2.328	3.125
CSL Intercept, Γ $^+$	2.988	2.268	3.038
Gradient of CSL in q-p' space, M	0.851	0.785	0.569
Reference State Parameter, Ψ_{ref} $^\#$	0.113	0.06	0.087
Proportion of Kaolinite (%)	80	28	42
Proportion of Illite (%)	18	28	40
Proportion of Quartz (%)	2	44	18

* At effective stresses ranging from p' = 300 to 1000 kPa

$^+$ Intercept defined as the specific volume, v, at p' = 1 kPa

$^\#$ For normally consolidated conditions

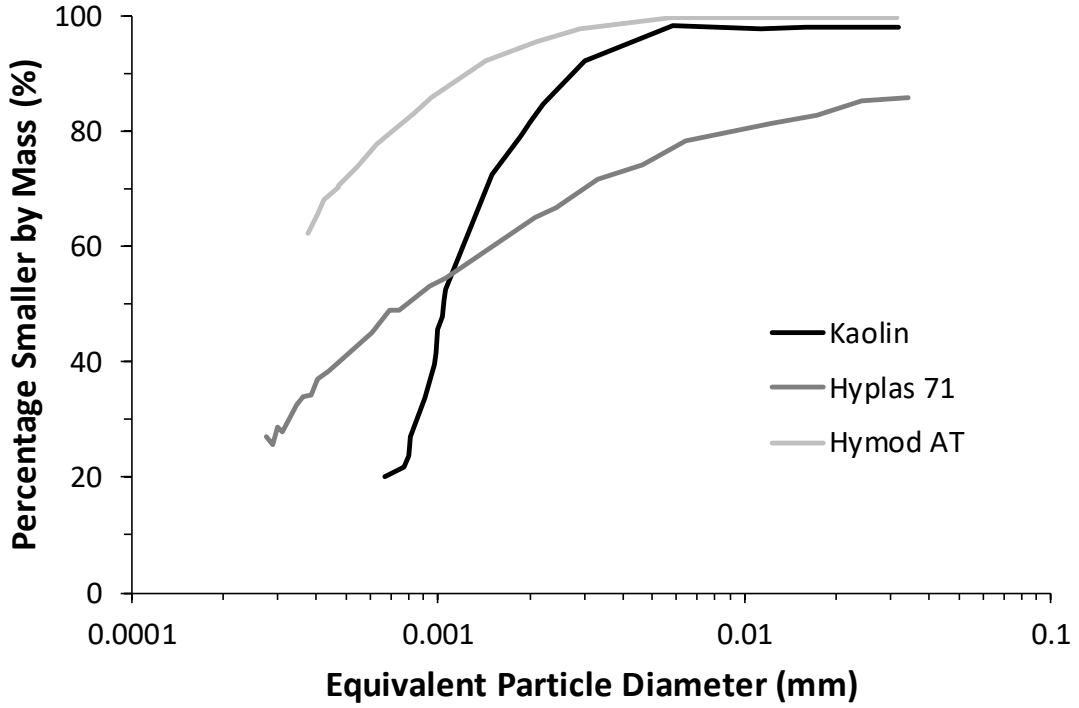

Figure 8-1 – Particle size distribution for the three clays tested from hydrometer testing, showing the differences between the clays due to their varying mineralogy

Turning to the differences in the mechanical properties of the clays, Kaolin and Hymod AT displayed similar consolidation properties in terms of the gradients (λ_{NCL} = 0.168 and 0.180, respectively) and intercepts (N = 3.101 and 3.125, respectively) of the normal consolidation lines in *v-ln(p')* space. Hyplas 71 was significantly less compressible (λ_{NCL} = 0.101) and with a lower intercept of N = 2.238, most likely due to the high silt-sized quartz content. The swelling characteristics of the three clays were each substantially different, with κ ranging from 0.021 for Kaolin, to 0.077 for Hymod AT, which is possibly related to the increasing fine Illite proportion. The critical state line intercept was again similar for Kaolin (Γ = 2.988) and Hymod AT (Γ = 3.038), but notably lower for Hyplas 71 (Γ = 2.268). Finally, all of the clays showed clear differences in the critical state friction ratio, M, with values ranging from 0.851 for Kaolin to 0.569 for Hymod AT.

8.2. Results of Triaxial Testing of Different Soils

Figure 8-2 and Figure 8-3 show the deviator stress variation with shear strain for each of the tests conducted on Hyplas 71 and Hymod AT. These show similar behaviour to that observed in Kaolin, with the deviator stress increasing with axial strain rate. It is also noticeable that the rate effects in Hyplas 71 initially appear greater than those in Hymod AT, but that they also degrade more rapidly with strain. The strain at which localisation occurred using Hyplas 71 ranged from ε_q = 14 to 18 %, compared to ε_q = 8 to 12 % for Hymod AT. For comparison, localisation typically occurred at near ε_q = 12 % in Kaolin meaning that localisation occurs at a slightly lower strain in Hymod AT and a slightly greater strain in Hyplas 71.

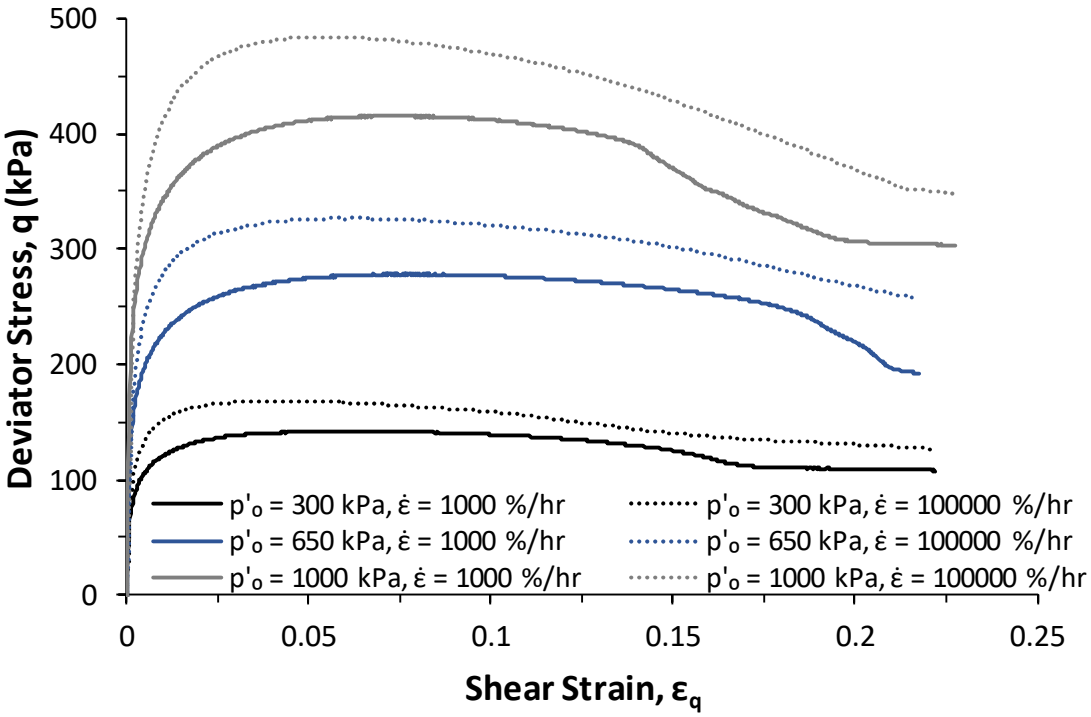

Figure 8-2 – Graph of deviator stress with shear strain for tests on Hyplas 71 at varying initial mean effective stresses and axial strain rates, showing increasing deviator stress with strain rate

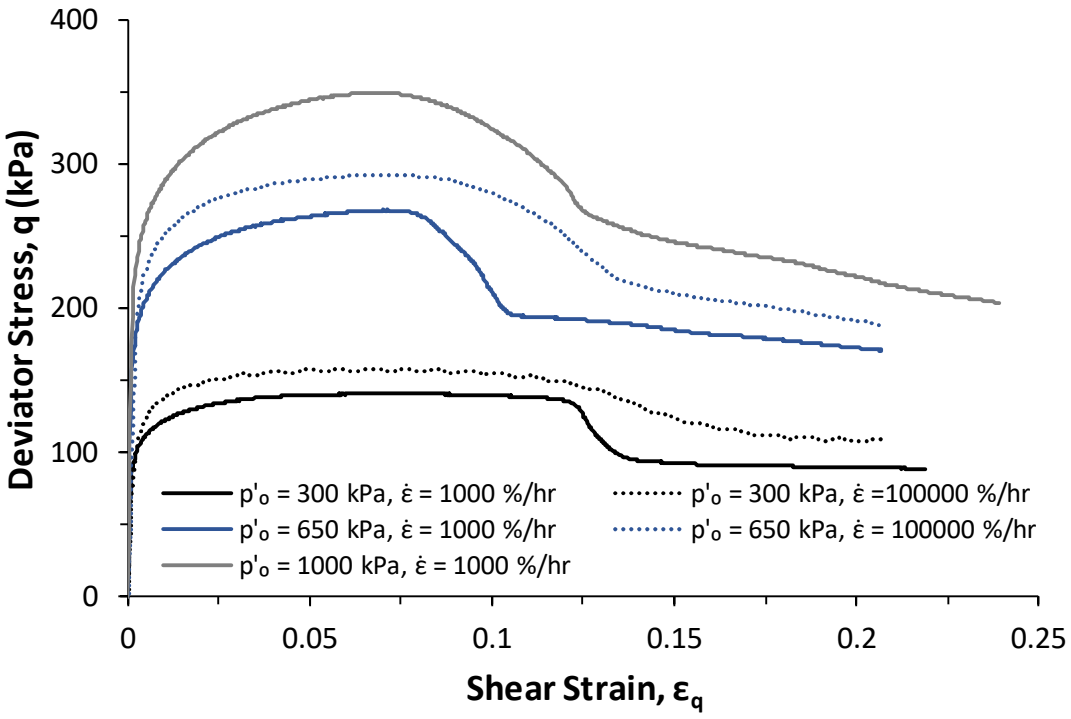

Figure 8-3 – Graph of deviator stress with shear strain for tests on Hymod AT at varying initial mean effective stresses and axial strain rates, showing increasing deviator stress with strain rate

Figure 8-4 and Figure 8-5 show the variation of the deviator stress at 1 % shear strain with shear strain rate and initial mean effective stress for both Hyplas 71 and Hymod AT. Despite the fact that at any given value of p'_0 both clays have very similar deviator stresses at the reference strain rate ($\dot{\varepsilon}_{q,ref}$ = 1000 %/hr), Hyplas 71 shows notably greater increases in the deviator stress with strain rate. For Hyplas 71, this ranges from 16kPa per log cycle at p'_0 = 300 kPa to 34 kPa per log cycle at p'_0 = 1000 kPa, whilst for Hymod AT the increase ranges from only 7 to 13 kPa per log cycle. The derivation of the rate effect per log cycle, $\lambda_{\varepsilon q = 1\%}$, for these two clays at each effective stress is shown in Figure 8-6 and Figure 8-7.

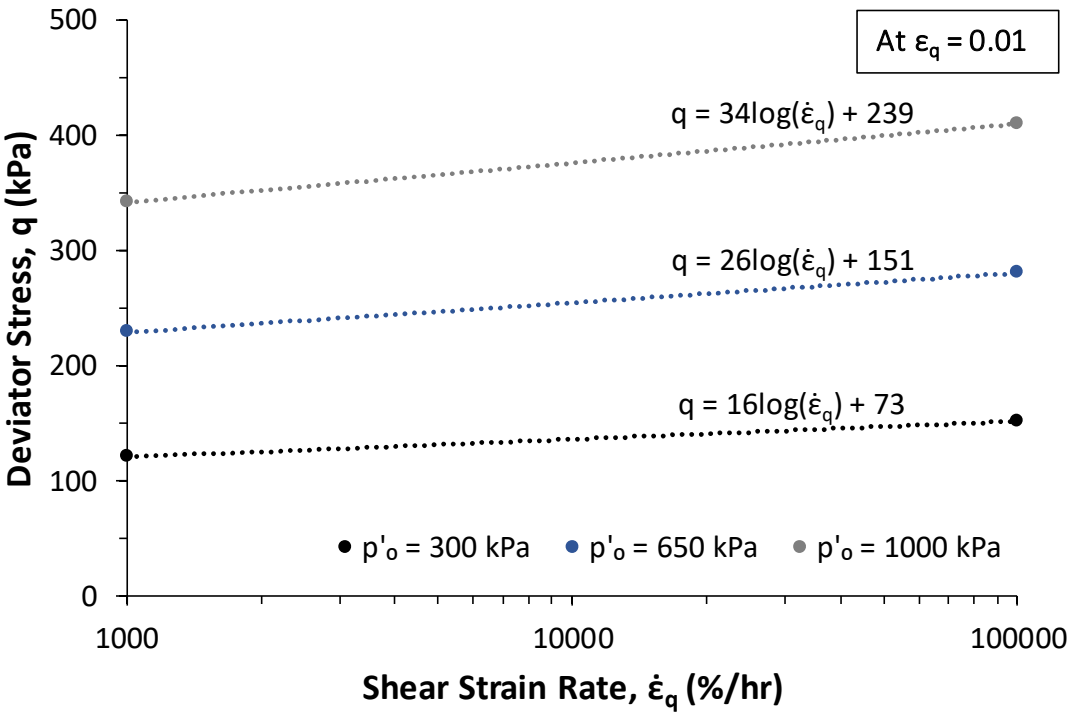

Figure 8-4 – Variation of deviator stress at ε_q = 0.01 with shear strain rate at varying initial mean effective stresses from triaxial testing of Hyplas 71

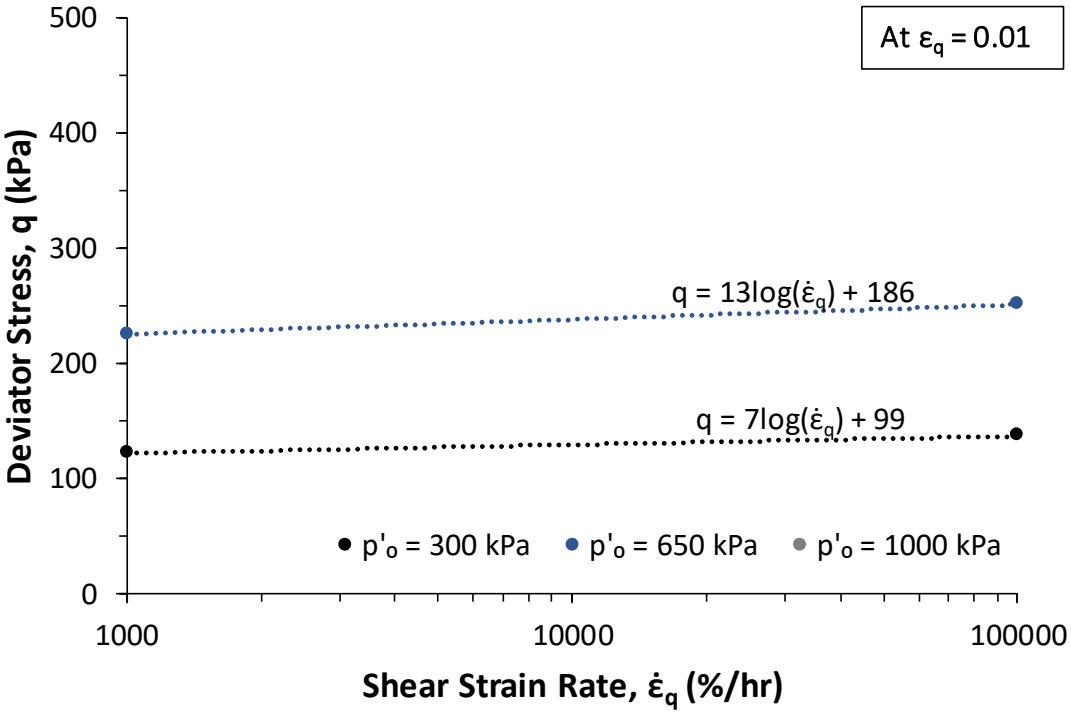

Figure 8-5 – Variation of deviator stress at ε_q = 0.01 with shear strain rate at varying initial mean effective stresses from triaxial testing of Hymod AT

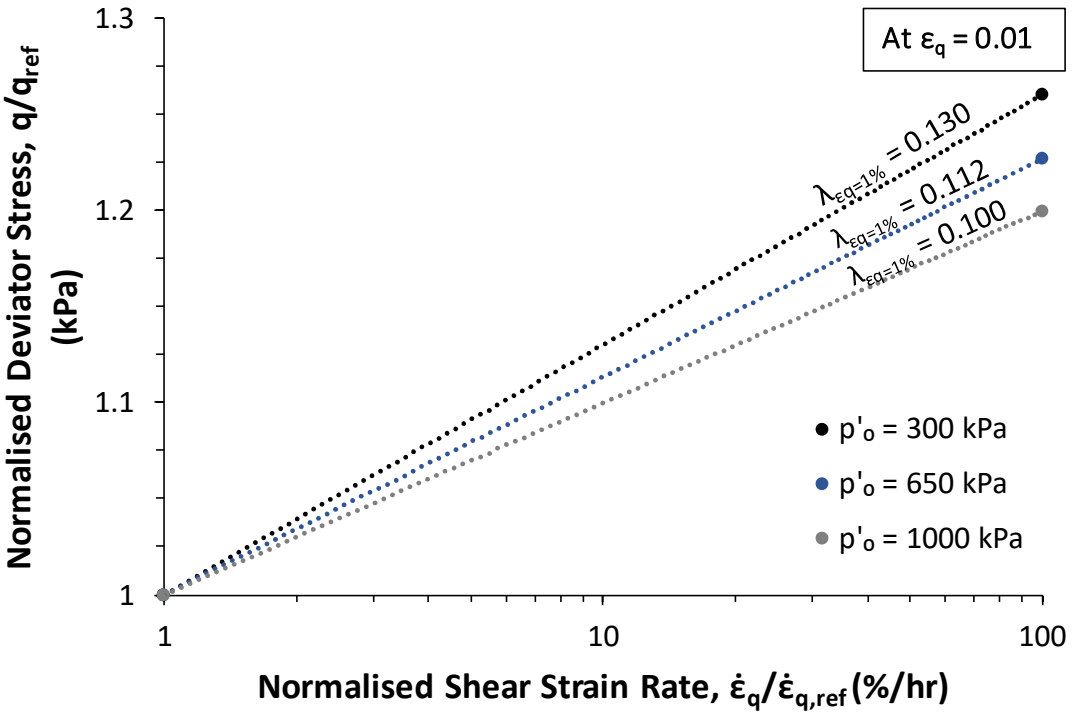

Figure 8-6 – Derivation of $\lambda_{\varepsilon q = 1\%}$ for each effective stress from triaxial testing of Hyplas 71

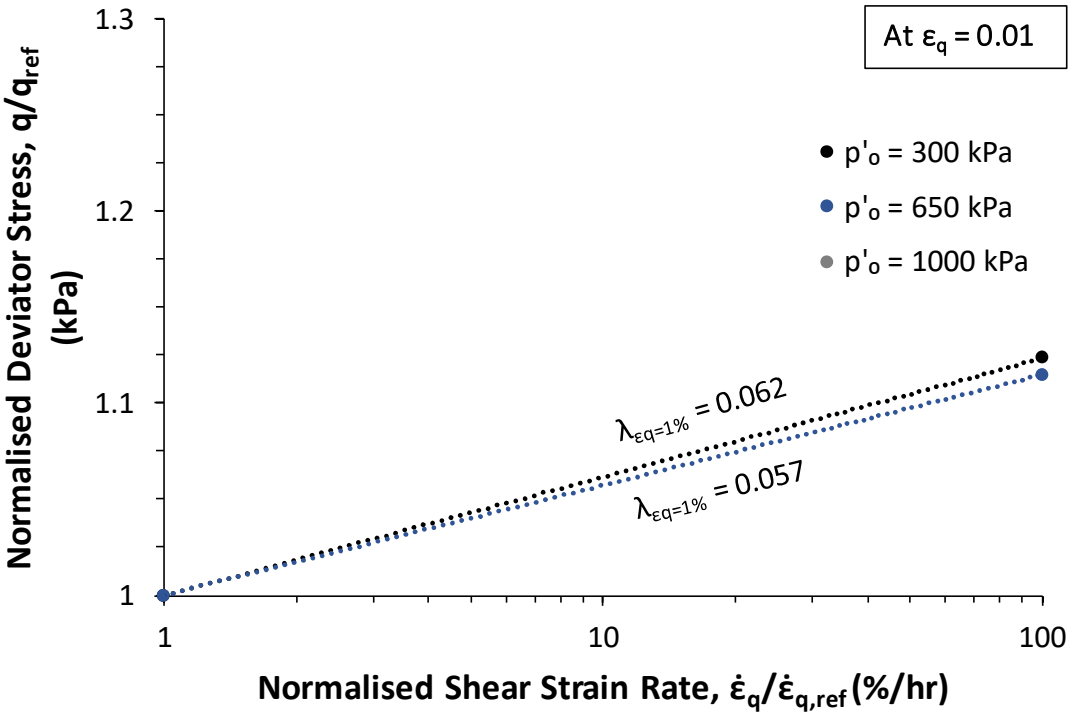

Figure 8-7 – Derivation of $\lambda_{\varepsilon q = 1\%}$ for each effective stress from triaxial testing of Hymod AT

Using the same methodology that was used to derive the variation of the rate effect, λ, with strain for Kaolin at large strains in Chapter 4, the rate effects in Hyplas 71 and Hymod AT have also been determined (Figure 8-8 and Figure 8-9). As with the testing on Kaolin, the values of the rate effect at ε_q = 1 % are broadly representative of the maximum rate effects measured at each p'_0 using the global displacement measurements. The derived values for $\lambda_{\varepsilon q = 1\%}$ are shown in Table 8-3. For comparison, the observed values of $\lambda_{\varepsilon q = 1\%}$ for Kaolin ranged from 0.12 to 0.16 (discussed previously in Chapter 4) which is higher than both Hyplas 71 and Hymod AT. It can also be seen that Hymod AT clearly displays the lowest rate effects, with values for $\lambda_{\varepsilon q = 1\%}$ being approximately half of those for Kaolin.

Table 8-3 – Rate effect per log cycle strain rate at ε_q = 1 % for Hyplas 71 and Hymod AT

p'o (kPa)	*Hyplas 71*			*Hymod AT*		
	Specific Volume, v_o	Liquidity Index	$\lambda_{\varepsilon q=1\%}$	Specific Volume, v_o	Liquidity Index	$\lambda_{\varepsilon q=1\%}$
300	1.738	0.282	0.130	2.049	0.201	0.062
650	1.644	0.138	0.112	1.935	0.114	0.057
1000	1.588	0.052	0.100	-	-	-

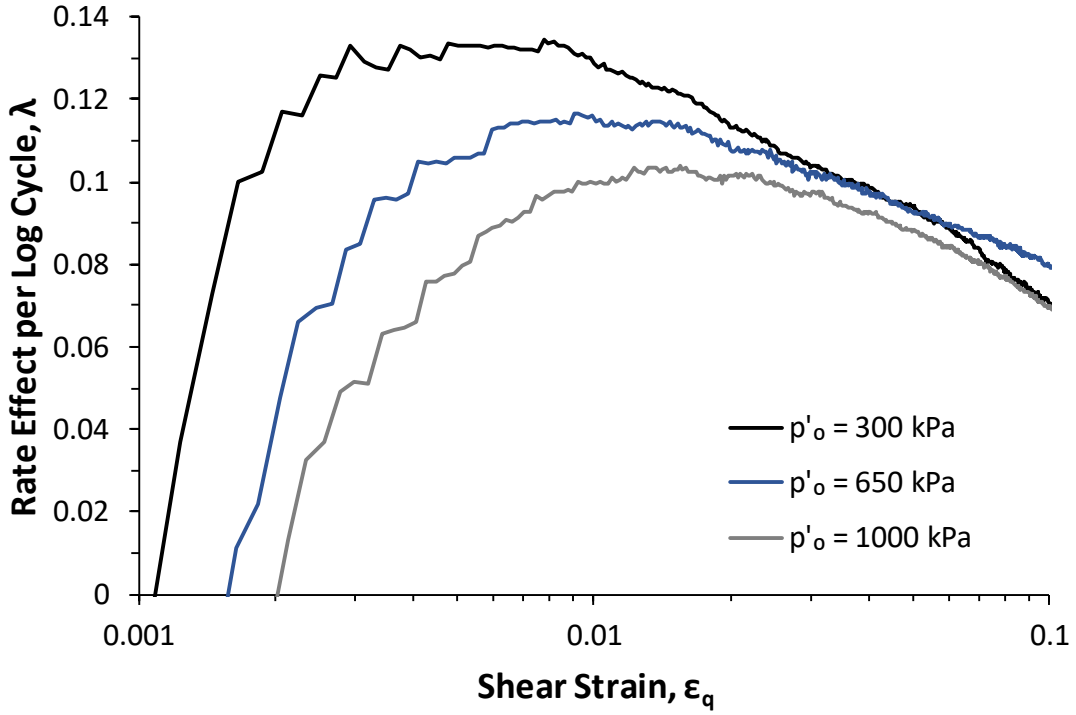

Figure 8-8 – Variation of rate effect per log cycle with shear strain in Hyplas 71 ($\dot{\varepsilon}$ = 1000 to 100000 %/hr)

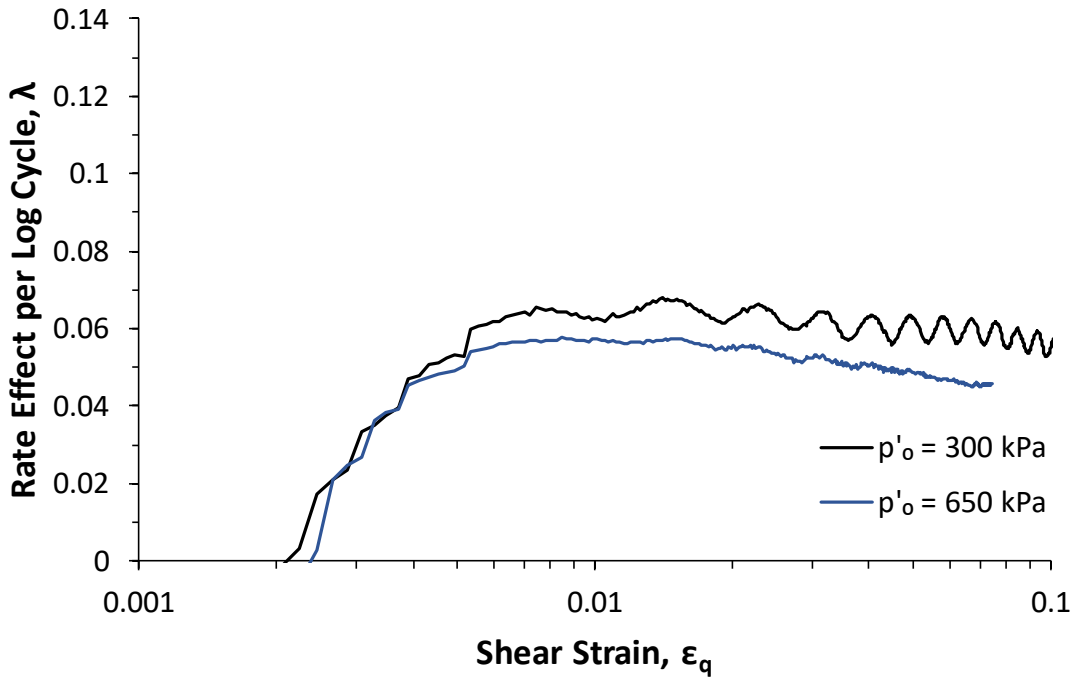

Figure 8-9 – Variation of rate effect per log cycle with shear strain in Hymod AT ($\dot{\epsilon}$ = 1000 to 100000 %/hr)

The variation of $\lambda_{\varepsilon q=1\%}$ with liquidity index for each of the soils tested is shown in Figure 8-10, along with LI^2 relationships which have been fitted to the data for each soil. As with the testing on Kaolin, the LI^2 relationships are of the form shown in Equation 8-1. The derived soil specific parameters are shown in Table 8-4. As can be seen, the highest rate effects at all liquidity indexes occurred in Kaolin, while the lowest rate effects occurred in Hymod AT. Unfortunately, the loss of the test data in Hymod AT at p'_0 = 1000 kPa means that the derived parameters for this soil will likely have a greater degree of uncertainty than the other two soils.

$$\lambda_{\varepsilon q=1\%} = \lambda_{\varepsilon q=1\%,PL} + \alpha_{\varepsilon q=1\%} LI^2 \quad (8\text{-}1)$$

where:

$\lambda_{\varepsilon q=1\%,PL}$ is the rate effect per log cycle at 1 % shear strain at the plastic limit

$\alpha_{\varepsilon q=1\%}$ is a soil specific coefficient which determines the rate of increase of $\lambda_{\varepsilon q=1\%}$ with LI^2

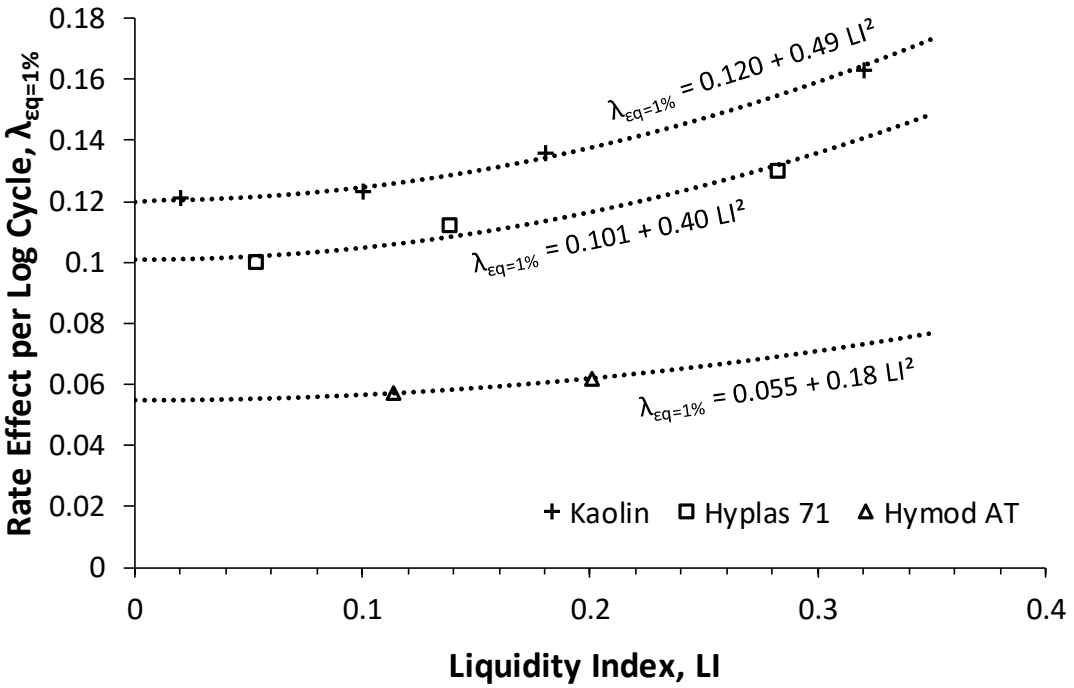

Figure 8-10 – Variation of $\lambda_{\varepsilon q=1\%}$ with liquidity index for all soils tested at axial strain rates from 1000 to 100,000 %/hr

Table 8-4 – Comparison of soil specific rate effect parameters

Soil Type	$\lambda_{\varepsilon q=1\%,PL}$	$\alpha_{\varepsilon q=1\%}$
Kaolin	0.120	0.49
Hyplas 71	0.101	0.40
Hymod AT	0.055	0.18

Figure 8-11 shows the same data presented in Figure 8-10, but with the inclusion of the variation of rate effect with *LI* from Chow and Airey (2011) and Bea (1982). The rate effects observed by Chow and Airey (2011) using free-falling penetrometers in Kaolin are noticeably higher than the other datasets, however, this is not entirely unexpected as the literature review identified that free falling penetrometer studies have a tendency to overestimate rate effects and require a number of other issues to be accounted for (such as inertial effects) which complicate analysis. The data from Bea (1982) based on element testing of Gulf of Mexico clay suggests rate effects similar to those found in this study, with Gulf of Mexico clay displaying rate effects of a magnitude in between Hyplas 71 and Hymod AT.

As shown in Figure 8-12, $\alpha_{\varepsilon q=1\%}$ and $\lambda_{\varepsilon q=1\%,PL}$ appear to be interrelated, suggesting that soils that display the greatest change in rate effect with liquidity index also have the greatest rate effect at the plastic limit. Over the range of soils tested, a simple linear correlation provides a good degree of fit. However, to avoid the implication of negative values of $\alpha_{\varepsilon q=1\%}$ when $\lambda_{\varepsilon q=1\%,PL}$ is below 0.02, a power law (Equation 8-2) is suggested instead.

$$\alpha_{\varepsilon q=1\%} = 7.38\lambda_{\varepsilon q=1\%,PL}^{1.28} \quad (8\text{-}2)$$

Figure 8-12 also includes values of α_{peak} *and* $\lambda_{peak,PL}$ for Gulf of Mexico clay from Bea (1982) for comparison. As can be seen, these values sit below the trend derived from the clays studied here. A possible explanation for this is that Bea (1982) determined rate effects at peak strength rather than at $\varepsilon_{q=1\%}$ (used for the other three clays shown).

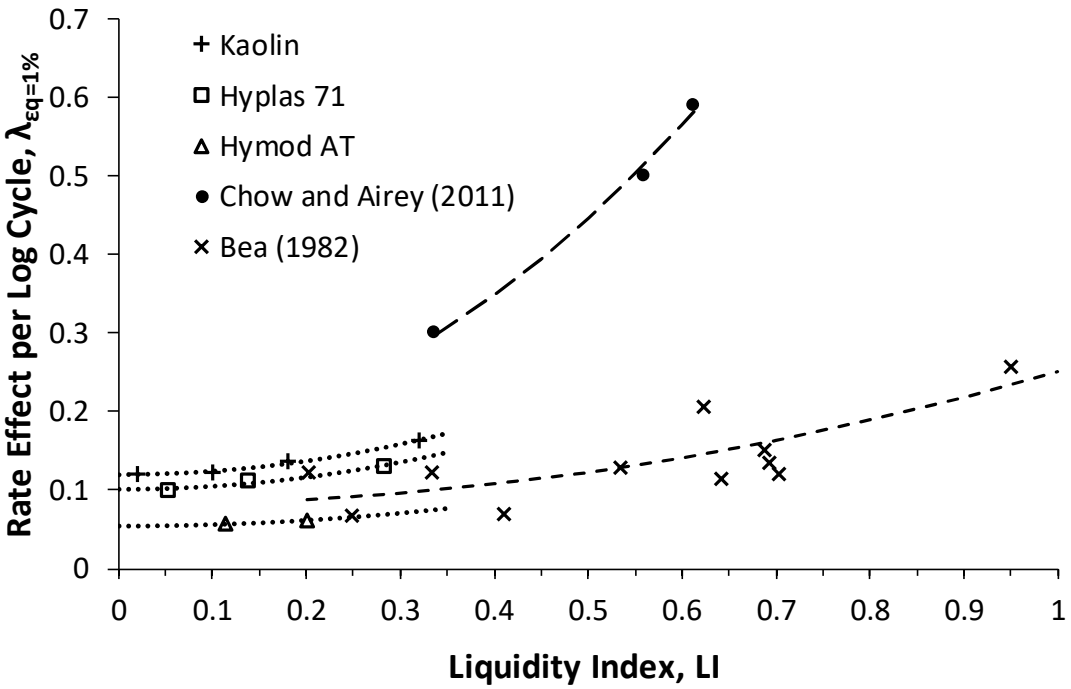

Figure 8-11 – Comparison of the state dependence of rate effects for the three clays tested with the results of Chow and Airey (2011) and Bea (1982)

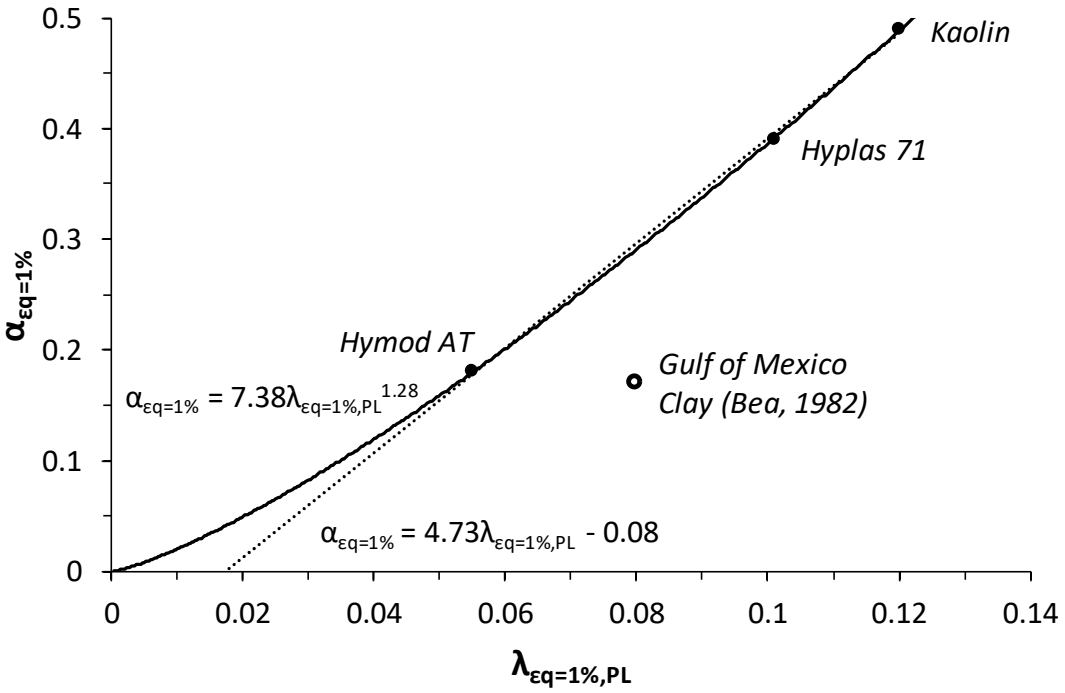

Figure 8-12 – Relationship between $\alpha_{\varepsilon q=1\%}$ and $\lambda_{\varepsilon q=1\%,PL}$, for all soils including comparison with Gulf of Mexico Clay from Bea (1982)

8.3. Rate Effect Parameter Correlations with Soil Properties

The varying properties and rate effect behaviour of the three clays for which rate effect parameters have now been determined means that is possible to investigate whether simple correlations can be good rate effect indicators. In this section, $\alpha_{\varepsilon q=1\%}$ and $\lambda_{\varepsilon q=1\%,PL}$ will be compared with potential indicators that have been suggested in the literature review, as well as to suggest new possible correlations. It is worth restating that $\alpha_{\varepsilon q=1\%}$ and $\lambda_{\varepsilon q=1\%,PL}$ are two state independent parameters which, together, allow the rate effect per log cycle, λ to be estimated at any liquidity index. Care should also be taken not to confuse $\alpha_{\varepsilon q=1\%}$ with the parameter, α, sometimes used in other rate effect studies as a parameter in power law correlations.

As $\alpha_{\varepsilon q=1\%}$ and $\lambda_{\varepsilon q=1\%,PL}$ take into account the effect of soil state and are defined at $\varepsilon_q = 0.01$ (near the strain at which the maximum rate effect occurs), few other studies have sufficient information to allow them to be derived for comparison. Of the studies considered earlier in

the Literature Review (Chapter 2) and Chapter 4, only Chow and Airey (2011) and Bea (1982) have enough information to account for the state dependence of rate effects (testing at multiple liquidity indexes). However, Chow and Airey used free-falling penetrometers to investigate rate effects, meaning that the values for λ derived correspond to very high strain levels, making these results incompatible with the parameters from this element testing study. Bea (1982) used data from element testing at comparable strain levels, but no notable soil characterisation was provided, preventing this study's inclusion in the correlations between rate effect parameters and soil properties which follows. Unfortunately, this means that no published studies exist with sufficient information to be used for comparison, highlighting the need for the rate effect correlations, which will now be discussed.

Plasticity index (*PI*) has often been suggested as a possible rate effect indicator, partly due to its widespread use in industry. Briaud *et al.* (1984) and Powell and Brown (2006) have suggested that rate effects increase with plasticity index. In the case of Briaud *et al.* (1984), this was in the form of a viscous exponent, *n*, (Equation 8-3) while Powell and Brown (2006) proposed a power law (Equation 8-4).

$$\frac{S_{u1}}{S_{u2}} = \left(\frac{t_2}{t_1}\right)^n \tag{8-3}$$

where *t* is the time to failure and *n = 0.035 + 0.00066 PI*

$$\frac{\tau_d}{\tau_s} = 1 + \alpha\left(\frac{v}{v_0}\right)^\beta - \alpha\left(\frac{v_s}{v_0}\right)^\beta \tag{8-4}$$

where α = 0.03 *PI* + 0.5, β = 0.2 for clay and v_0 is a reference velocity of 1 m/s

Figure 8-13 shows the variation of the rate effect parameters derived from this study with Plasticity Index. As can be seen there is no clear trend and if anything, the rate effect appears to reduce with *PI*. This is in keeping with the findings of Graham *et al.* (1983), which suggested that rate effects are independent of *PI*. One possibility that may explain this difference in findings is that the studies by Briaud *et al.* (1984) and Powell and Brown (2006) did not take into account the impact of soil state (*LI*) on the measured rate effects, as plasticity index is often given in case studies but not necessarily insitu moisture content conditions (and thus it is not always possible to determine the liquidity index.)

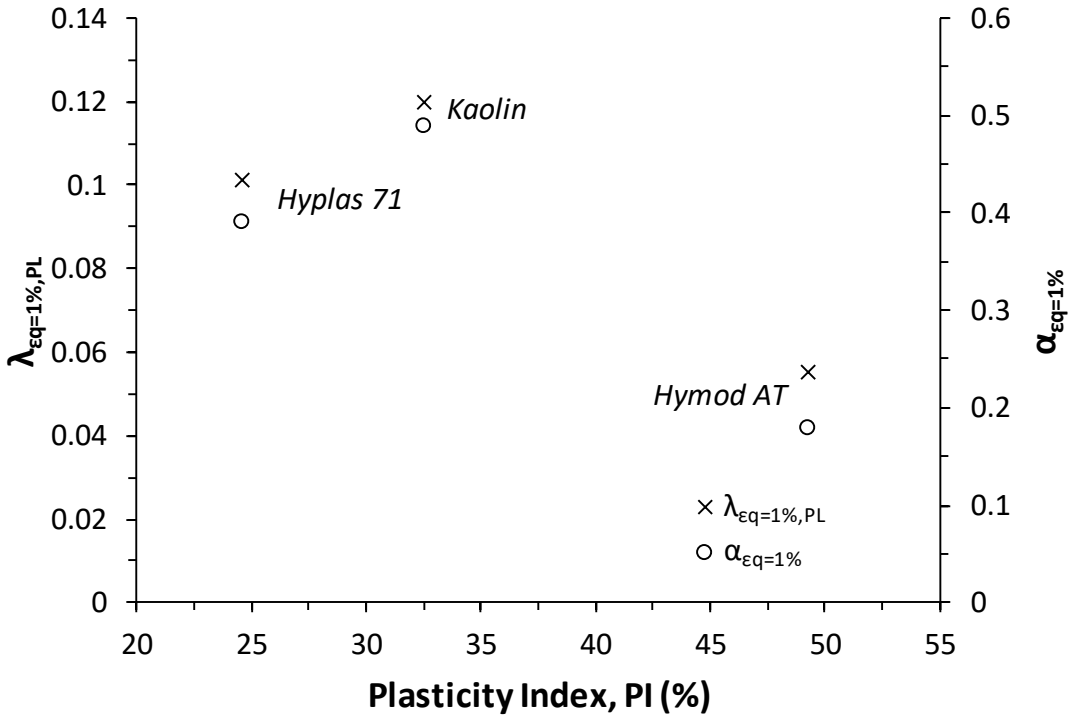

Figure 8-13 – Variation of derived rate effect parameters with plasticity index for all soils

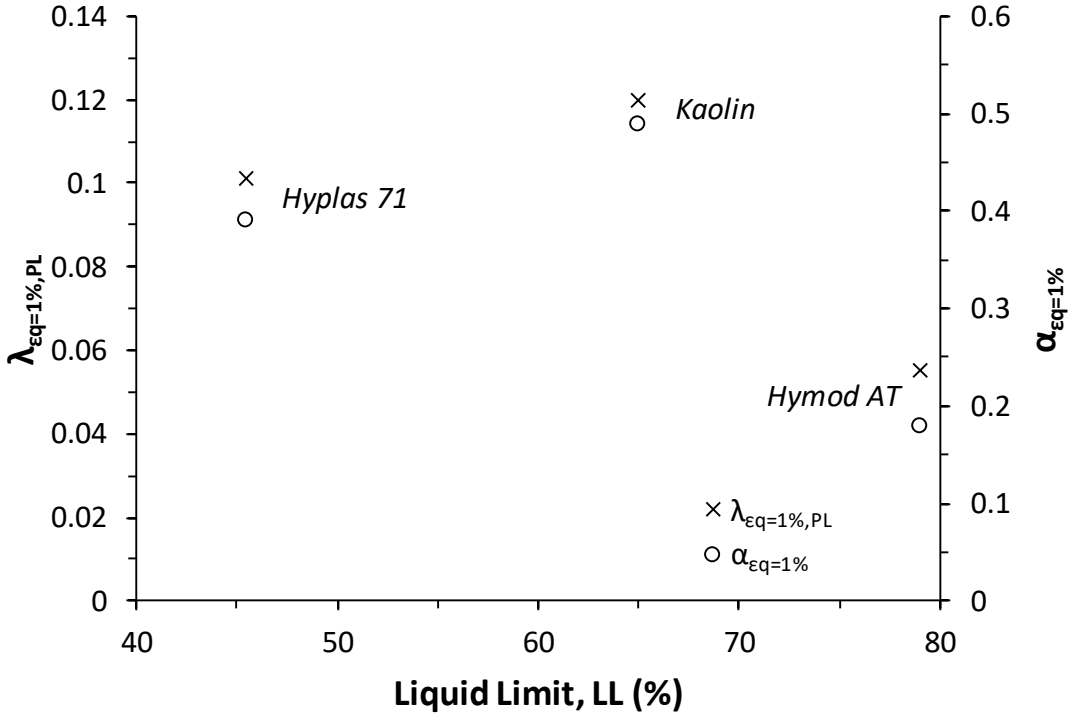

Figure 8-14 – Variation of derived rate effect parameters with liquid limit for all soils

Figure 8-14 shows the variation of the rate effect parameters with liquid limit, which Krieg and Goldscheider (1998) suggested could be used as a rate effect indicator. It was proposed that the viscosity index (proportional to λ_{peak}) increased with *LL*, although a specific correlation was not provided. As shown in Figure 8-14, there is no clear correlation between the liquid limit and the measured rate effect parameters. A number of other properties related to the Atterberg limits were also investigated including the plastic limit, clay fraction and activity, however, as with *PI* and *LL*, there was no useful rate effect correlation.

The specific surface area (*SSA*) of clays is influenced by the shape and size of the particles which constitute it, and which may have an influence of the magnitude of the observed rate effects. From Figure 8-15 it can be seen that there is a distinct correlation between the rate effect parameters and *SSA*, with rate effects reducing with increasing *SSA* (Equation 8-5 and Equation 8-6). This provides some further insight into which of the possible mechanisms is causing the rate effects, as if rate effects are due to highly viscous adsorbed layers on the surface of the clay particles, it may be expected that soils with higher surface areas would exhibit greater rate effects because of the greater proportion of volume consisting of viscous adsorbed layers (Rattley *et al.*, 2011). The data shows that the opposite is true, and that soils with a lower specific surface area, meaning larger particles with a greater inertia and potential for particle to particle contact, show greater rate effects. This may reinforce the evidence that inter-particle locking is a possible mechanism in rate effects.

$$\lambda_{\varepsilon q=1\%,PL} = 0.184e^{-0.011\ SSA} \quad (8\text{-}5)$$

$$\alpha_{\varepsilon q=1\%} = 0.845e^{-0.015\ SSA} \quad (8\text{-}6)$$

Whilst the study only covers three soils, and a larger number of soils would be required to provide a broader database, *SSA* does appear to be a good indicator of rate effect potential and has the benefits of being simple, inexpensive and quick to obtain using Methylene Blue spot testing. It should however be noted that using methods such as N_2 BET adsorption to measure surface areas provides data which would not be suitable for use in the above correlations, as it excludes internal surface areas. Specific surface area information is not readily available in many of the published rate effect studies making comparison with the work of others difficult. It was also found that the *SSA* did not correlate with any of the other indicators investigated, with the exception of the CSL gradient, *M*.

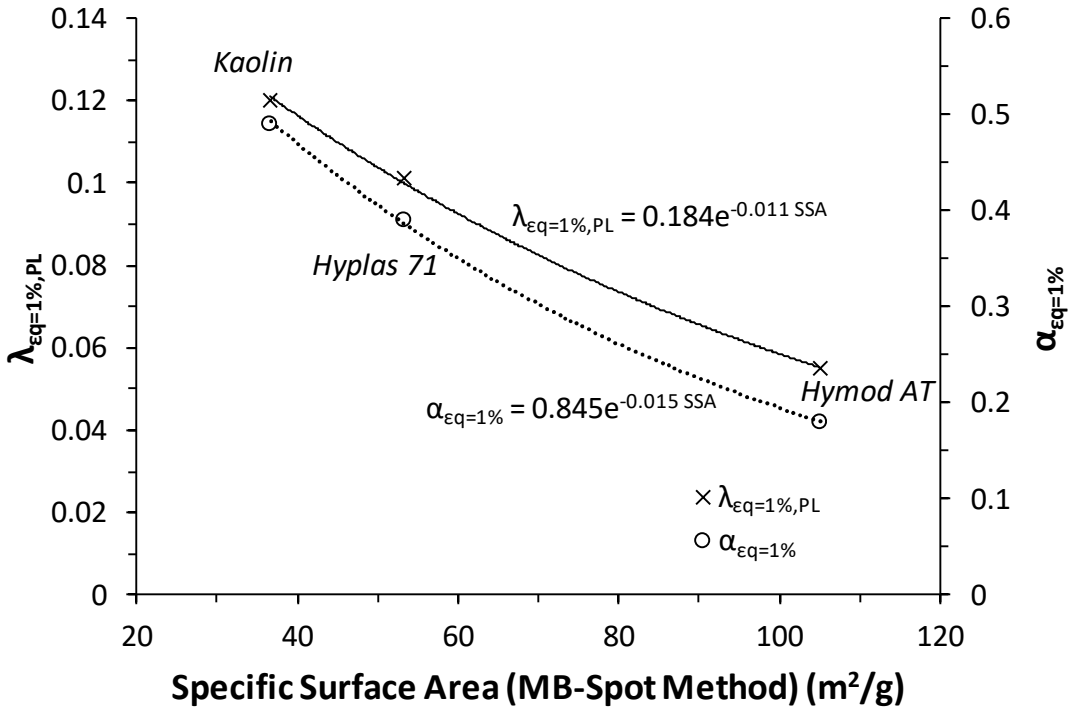

Figure 8-15 – Variation of derived rate effect parameters from all soils with specific surface area measured using methylene blue spot testing

Various critical state parameters for the soils tested including N, Γ, λ_{CSL}, M_{CSL} and the state parameter, Ψ_{ref} were also compared with $\lambda_{\varepsilon q=1\%,PL}$ and $\alpha_{\varepsilon q=1\%}$, however, only the gradient of the critical state line in q-p' space, M_{CSL} provided a usable correlation (Figure 8-16). $\lambda_{\varepsilon q=1\%,PL}$ and $\alpha_{\varepsilon q=1\%}$ were found to vary according to Equation 8-7 and Equation 8-8, with both parameters increasing with M_{CSL}. This suggests that rate effects are greater in soils with a greater inter-particle friction ratio, which influences the global friction ratio of the soil, M_{CSL} (Mitchell and Soga, 2005).

$$\lambda_{\varepsilon q=1\%,PL} = 0.16 M_{CSL}^{1.92} \quad (8\text{-}7)$$

$$\alpha_{\varepsilon q=1\%} = 0.72 M_{CSL}^{2.46} \quad (8\text{-}8)$$

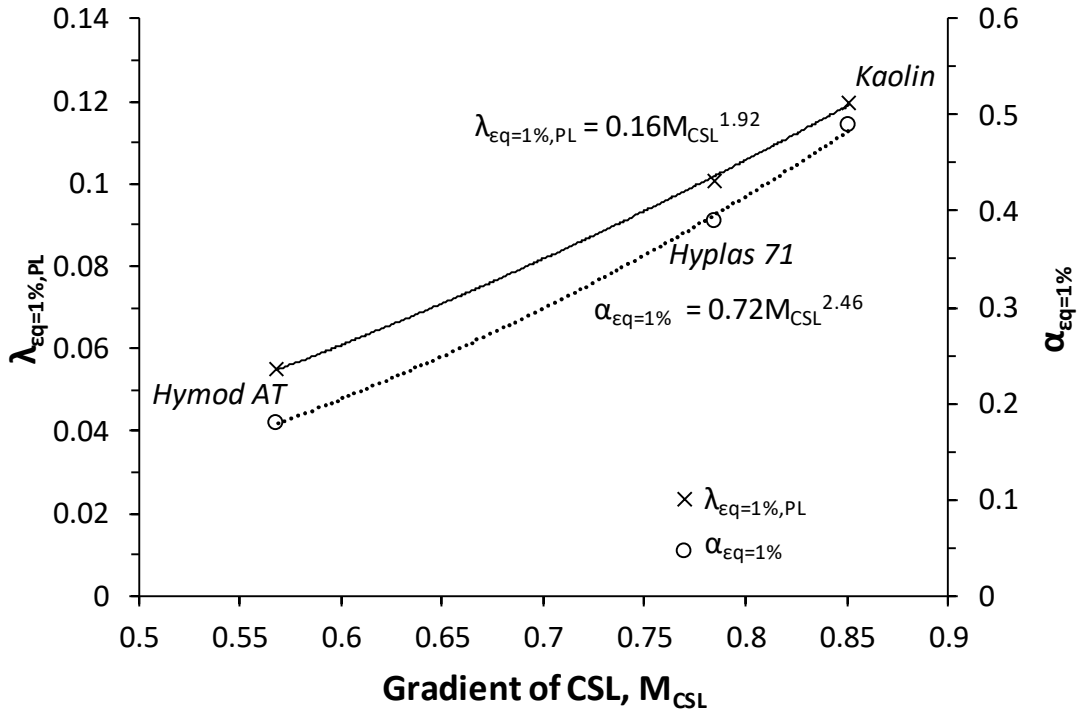

Figure 8-16 – Variation of derived rate effect parameters from all soils with the critical state line gradient M_{CSL} (M_{CSL} determined at $\dot{\varepsilon}_q$ = 1 %/hr)

The reasons why both *M* and *SSA* correlate with the rate effect parameters may be due to the fact that *M* and *SSA* are themselves inter-related. Figure 8-17 shows the relationship between *M* and *SSA* for the three clays used in this study, with *M* reducing with increasing *SSA*. Similar findings were shown by Moore (1991), where ring shear tests were conducted on two pure clay minerals with known *SSA*. It was found that Kaolinite (*SSA* = 10-20 m^2/g) showed a far higher residual friction ratio than Montmorillonite (*SSA* = 800 m^2/g) as shown in Figure 8-18. Moore (1991) attributed this to the fact that lower specific surface areas correspond to larger particles which exhibit higher friction ratios. Further evidence of the correlation between *SSA* and *M* can also be seen in Muir Wood (1990) (Figure 8-19). Whilst the correlation shown is between *M* and plasticity index, it can be seen that the clay minerals shown with lower *SSA*, exhibit higher values of *M*. *M* and *SSA* are useful as rate effect indicators as they are both state independent.

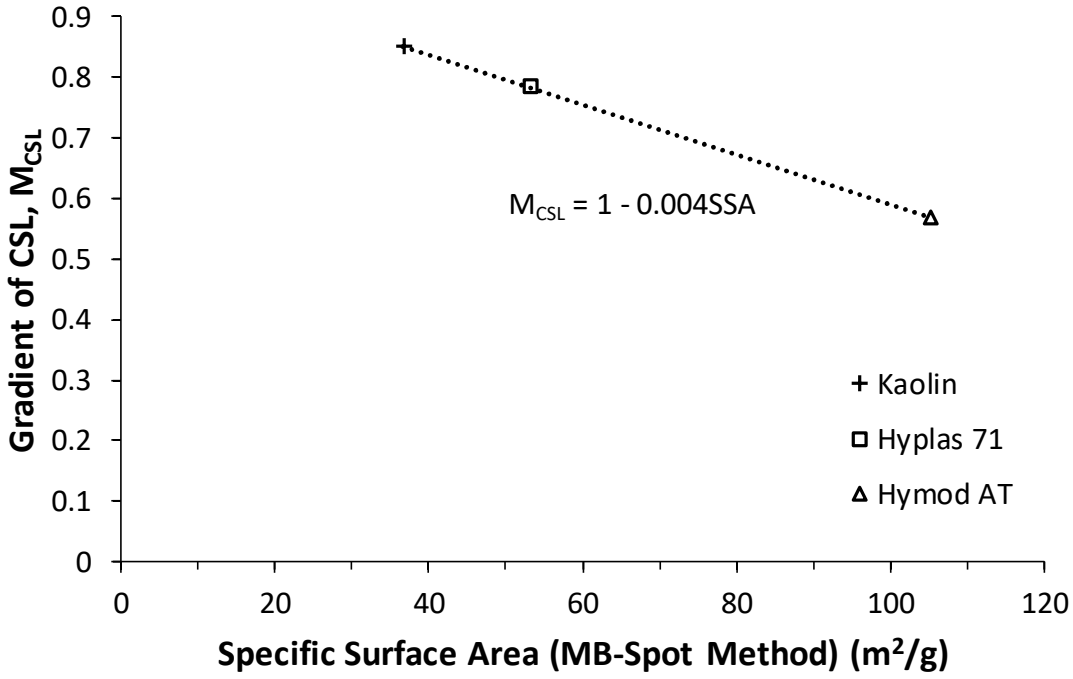

Figure 8-17 – Correlation between *M* and *SSA* for the three clays tested

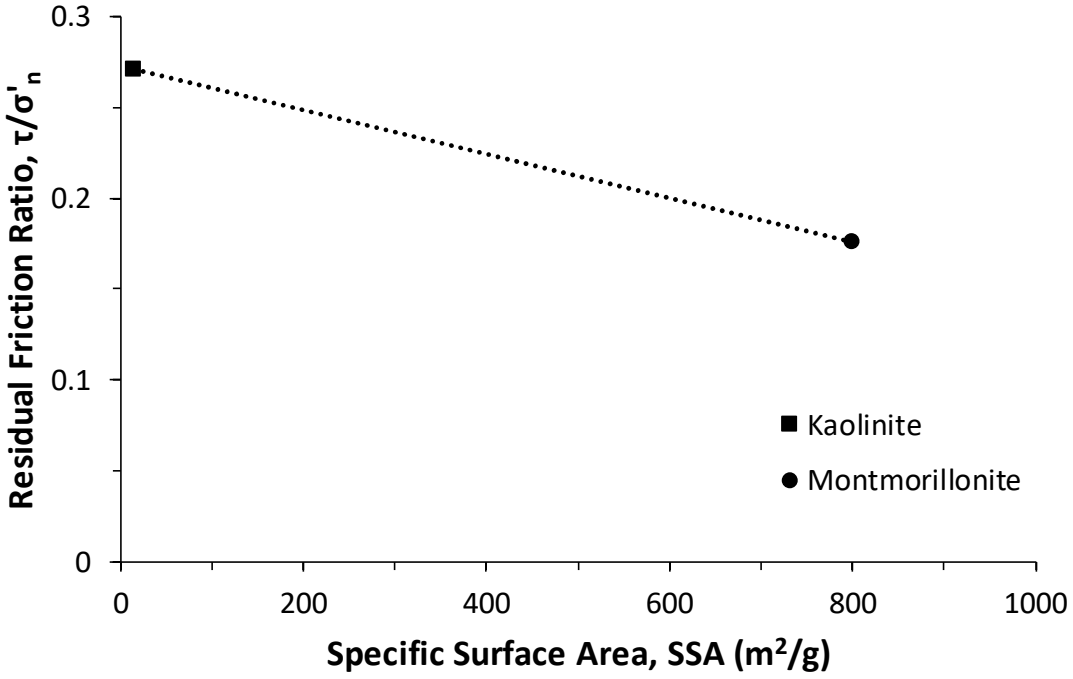

Figure 8-18 – Correlation between residual friction ratio and *SSA* based on data from Moore (1991)

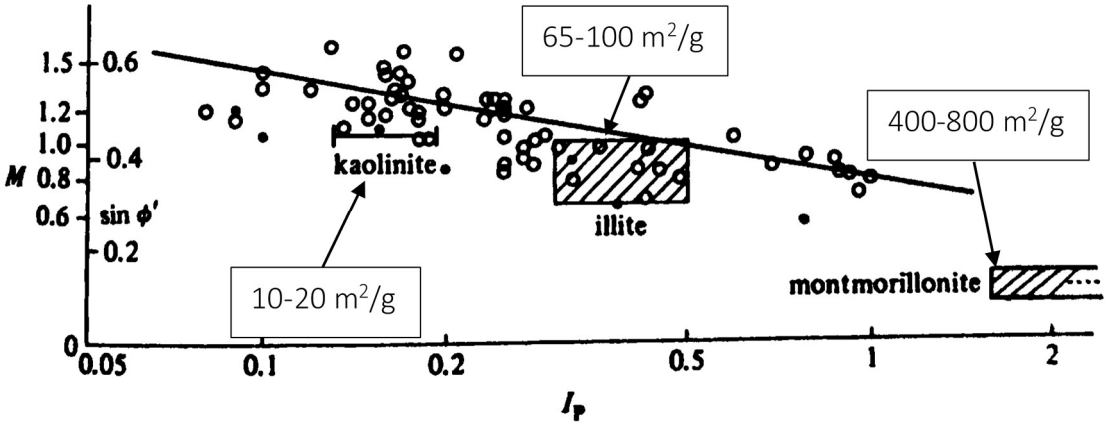

Figure 8-19 – Further evidence for the relationship between *M* and *SSA* based on the sin(ϕ') – *PI* correlation in Muir Wood (1990)

Finally, the mineralogy of the soils has been considered to identify if any specific mineral is influencing the rate effects. The three soils all consist of varying proportions of three common minerals; Kaolinite, Illite and Quartz, which have plotted against $\lambda_{\varepsilon q=1\%,PL}$ and $\alpha_{\varepsilon q=1\%}$ in Figure 8-20, Figure 8-21 and Figure 8-22. The only mineral to have a clear influence on the rate effects is the proportion of Illite, however, this is most likely related to the fact that the Illite portion has a controlling impact on the specific surface area of the clays. Illite has a specific surface area of 65 - 100 m^2/g (Mitchell and Soga, 2005), which is nearly an order of magnitude higher than Kaolinite (10 - 20 m^2/g). This means that the Illite dominates the specific surface area measurements discussed previously.

As discussed in Chapter 7, the rate effect mechanism proposed by Brown and Jaeger (2014) of granular dilatancy/inter-particle contact predicts that for smaller particles (which would have a higher specific surface area), the electrostatic repulsive forces keeping particles apart are greater per unit mass than larger particles. This means that at a given strain rate, smaller particles are less likely to have solid particle to particle contact and would exhibit less rate effects. As the Illite particles are substantially smaller than Kaolinite, it would be expected that soils with a substantial Illite proportion would show lower rate effects.

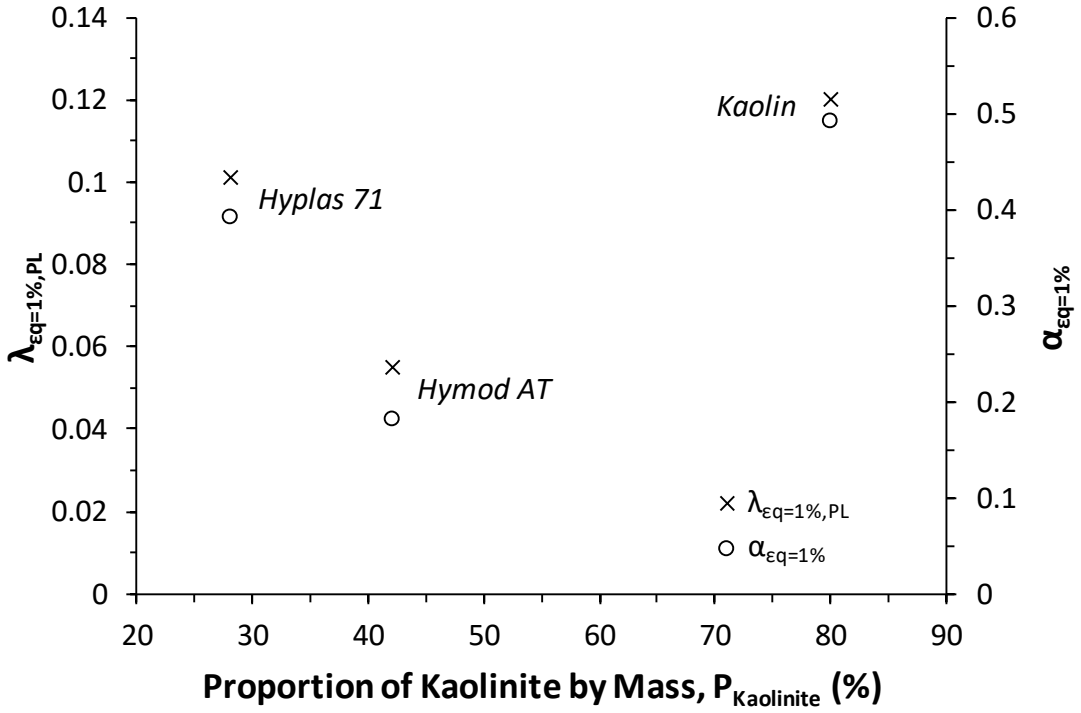

Figure 8-20 – Variation of derived rate effect parameters from all soils with the proportion of Kaolinite

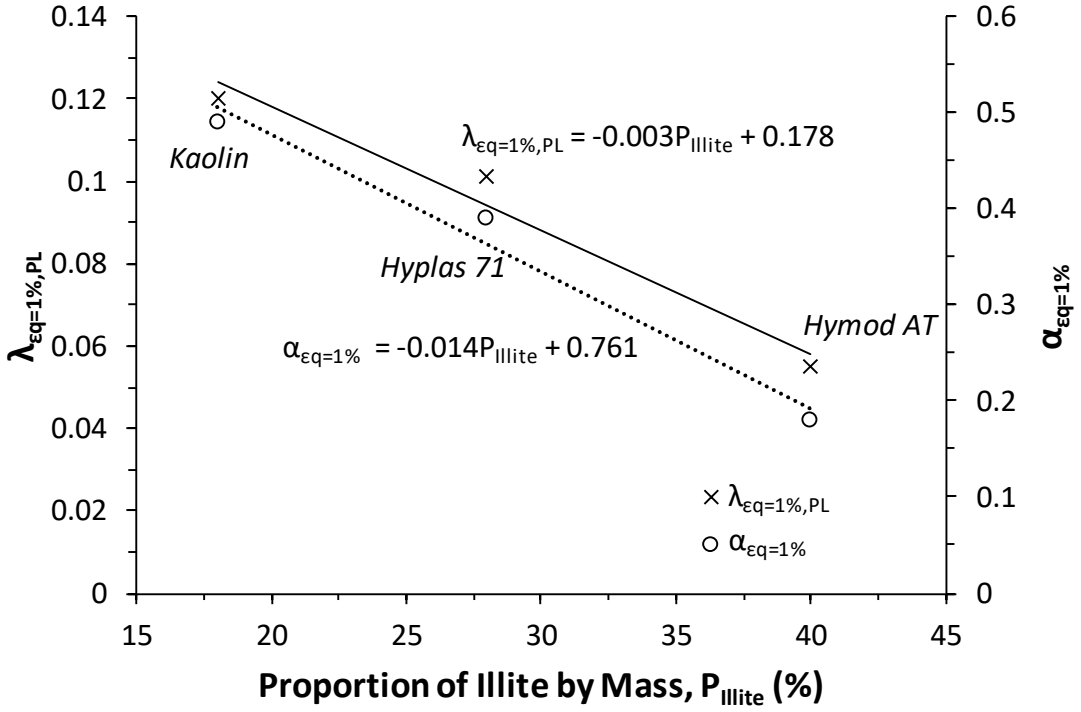

Figure 8-21 – Variation of derived rate effect parameters from all soils with the proportion of Illite

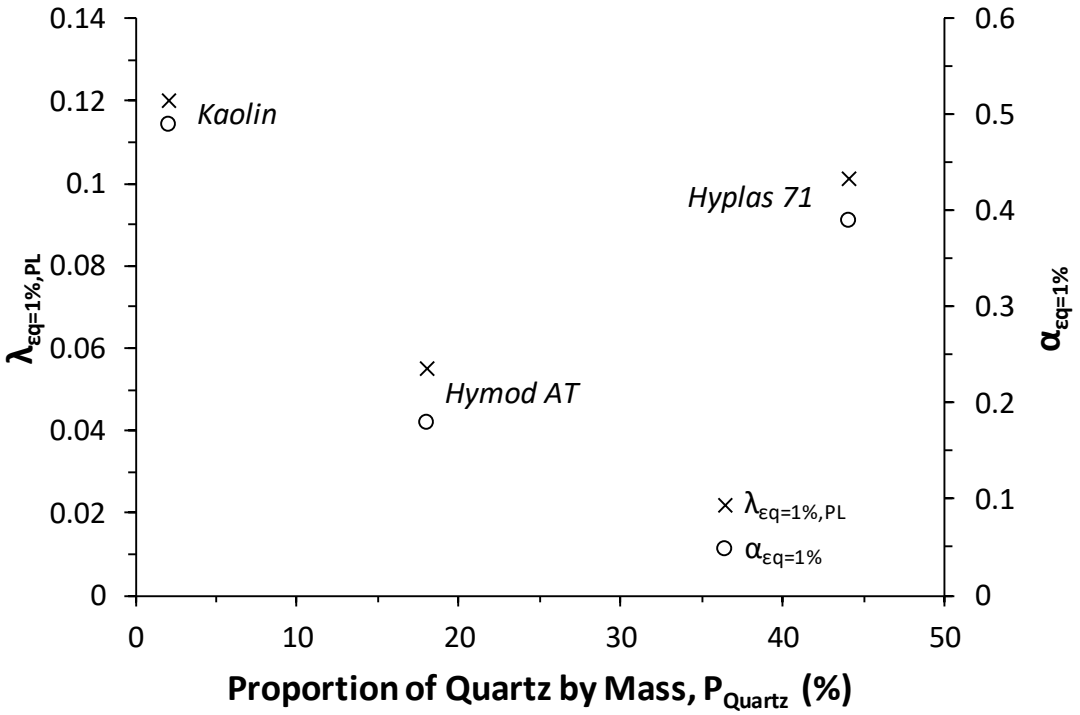

Figure 8-22 – Variation of derived rate effect parameters from all soil with the proportion of Quartz

8.4. Rate Effect Degradation Parameter Correlation with Soil Properties

It has been shown that there are potential indicators of rate effects which can be used to estimate the magnitude of the rate effect which clays will exhibit. However, the other significant parameter required to model rate effect behaviour using the proposed strain-based model is the rate at which the rate effect degrades with increasing strain. Figure 8-23 and Figure 8-24 show the determination of the rate effect degradation with $log(\varepsilon_q)$ for Hyplas 71 and Hymod AT, respectively, in the same manner as that used for Kaolin in Chapter 4. In the analysis of the data for Hyplas 71, it was necessary to restrict the shear strain to values greater than ε_q = 1.5 % as the maximum rate effect from large strain measurements appears to occur at a slightly larger strain than Kaolin. The maximum shear strain used in both clays was taken to be either ε_q = 10 % or the final point before the impact of localisation became apparent. The oscillations in the Hymod AT data are due to extremely small variations in the shearing rate caused by gain control issues. The changes in λ per log cycle increase in shear strain, $\Delta\lambda_{log(\varepsilon q)}$, for each clay and effective stress tested are summarised in Table 8-5, which also includes the values for Kaolin for reference.

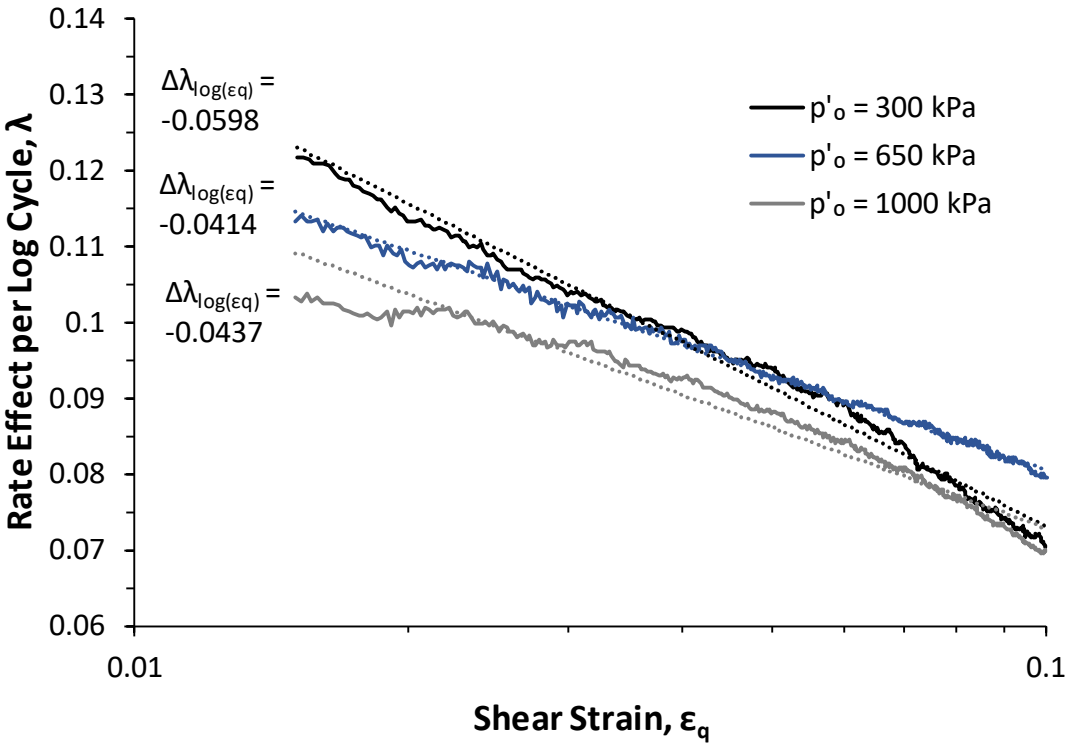

Figure 8-23 – Rate effect degradation in Hyplas 71 with shear strain

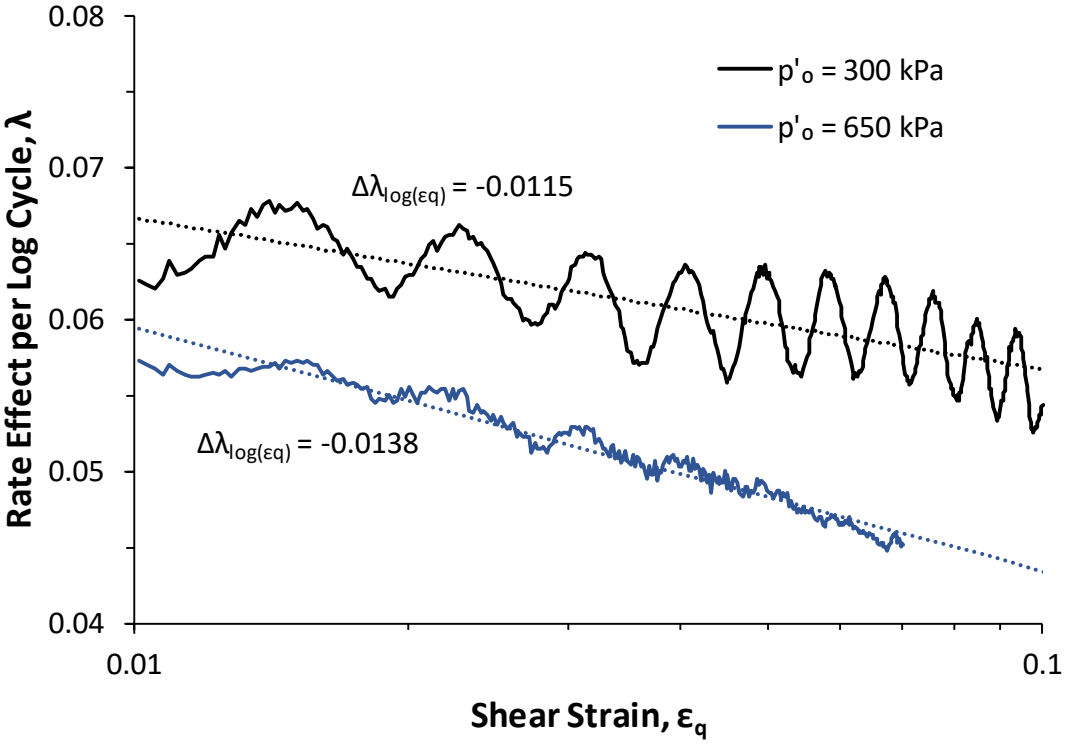

Figure 8-24 – Rate effect degradation in Hymod AT with shear strain

Table 8-5 – Rate effect change per log cycle increase in shear strain for all clays

p'_0 (kPa)	Kaolin		Hyplas 71		Hymod AT	
	LI	$\Delta\lambda_{log(\varepsilon q)}$	*LI*	$\Delta\lambda_{log(\varepsilon q)}$	*LI*	$\Delta\lambda_{log(\varepsilon q)}$
300	0.32	-0.014	0.28	-0.060	0.20	-0.012
650	0.18	-0.015	0.14	-0.041	0.11	-0.014
1000	0.10	-0.012	0.05	-0.044	0.06	-

Figure 8-25 shows these values normalised by the rate effect at ε_q = 1 %, so that the relative change can be identified. The average reduction in $\lambda_{\varepsilon q=1\%}$ for each log cycle of shear strain ranges from 10 % for Kaolin to 43 % for Hyplas 71. There was no clear impact of liquidity index on these values, suggesting that an average value of $\Delta\lambda_{log(\varepsilon q)}/\lambda_{\varepsilon q=1\%}$ for each clay may be used in the absence of further information.

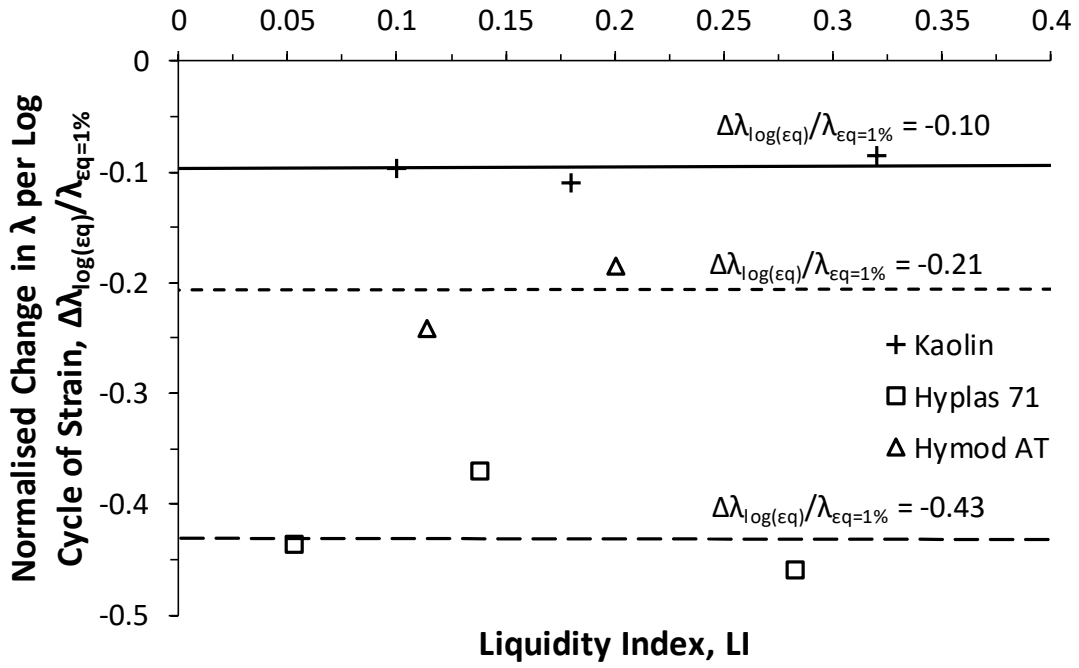

Figure 8-25 – Graph of normalised change in rate effect per log cycle increase in shear strain with liquidity index showing the state independence of rate effect degradation from CIU tests

The parameters discussed previously which have been used to find correlations with $\lambda_{\varepsilon q=1\%,PL}$ and $\alpha_{\varepsilon q=1\%}$ were also compared with the values of $\Delta\lambda_{log(\varepsilon q)}/\lambda_{\varepsilon q=1\%}$. The only parameters which showed a correlation with the rate effect degradation were the plastic limit and the quartz proportion. Figure 8-26 and Equation 8-9 show the relationship between $\Delta\lambda_{log(\varepsilon q)}/\lambda_{\varepsilon q=1\%}$ and the measured plastic limits for the three clays, suggesting that the degradation of rate effects with strain is greatest at lower plastic limits, with the greatest degradation observed in Hyplas 71 (43.7 % per log cycle) which has a plastic limit of 20.9 %. This correlation has not been suggested previously by other literature and the reasons for it are not clear, although it should be noted that very few studies have considered the factors which influence rate effect degradation.

$$\Delta\lambda_{log(\varepsilon q)}/\lambda_{\varepsilon q=1\%} = 0.028PL - 1 \quad (8\text{-}9)$$

A possible explanation for the link with plastic limit is suggested by the fact that the rate effect degradation has also been found to be correlated with the quartz content of the clays (Figure 8-27 and Equation 8-10). The quartz proportion (denoted P_{Quartz}) appears to be related to the plastic limit of the clays, with the plastic limit reducing with quartz content as shown in Figure 8-28. As the quartz is present in the clay as relatively large rotund crystals of silt size, it would be expected to have little or no cohesion or plasticity. Hence, it would be intuitive that the amount of quartz would influence the plastic limit. This raises the possibility that it could be the presence of the quartz crystals (or other non-plastic fines) which controls the rate effect degradation rather than the plastic limit. The presence of larger particles in clays is a factor which has previously been investigated as a possible control on rate effect degradation.

$$\Delta\lambda_{log(\varepsilon q)}/\lambda_{\varepsilon q=1\%} = -0.008P_{Quartz} - 0.08 \quad (8\text{-}10)$$

It is recommended that, where possible, XRD testing should be carried out to measure quartz content when investigating rate effects (although the specialist equipment for this is not always readily available). Firstly, this would allow Equation 8-10 to be used which avoids the use of the plastic limit in estimating the rate effect degradation, as the plastic limit is more subjectively determined and can vary depending on the test operator. Secondly, this additional data in future research could provide further insight into whether the plastic limit or the quartz content is the true controlling factor in rate effect degradation.

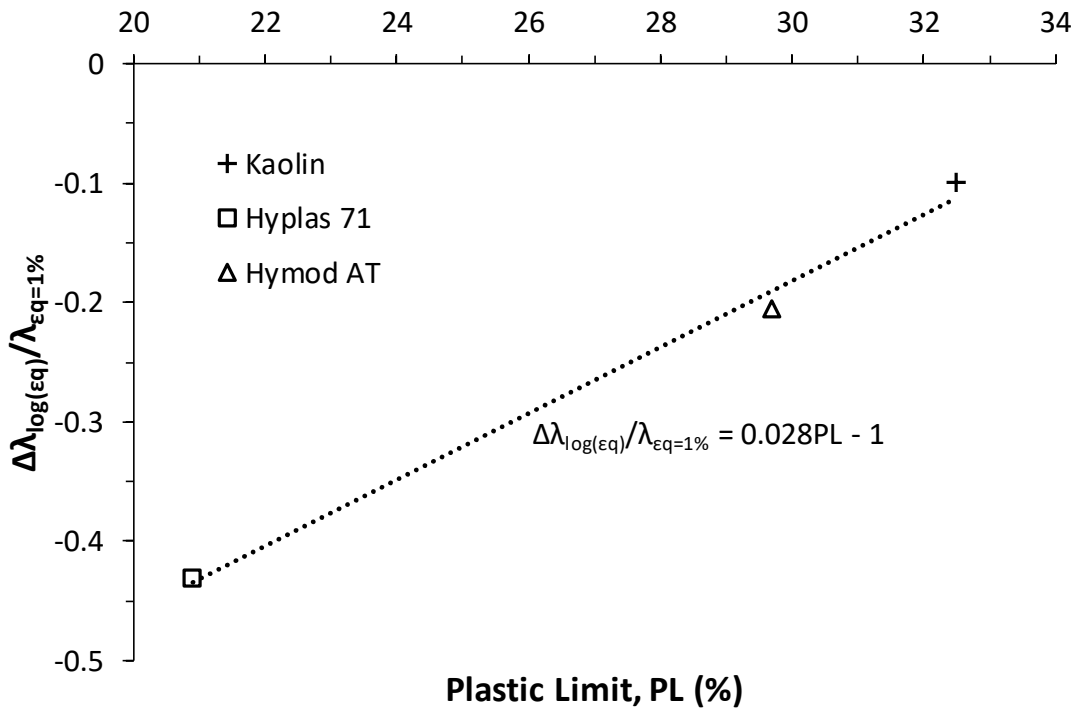

Figure 8-26 – Variation of normalised rate effect degradation with plastic limit showing reducing rate effect degradation with increasing plastic limit

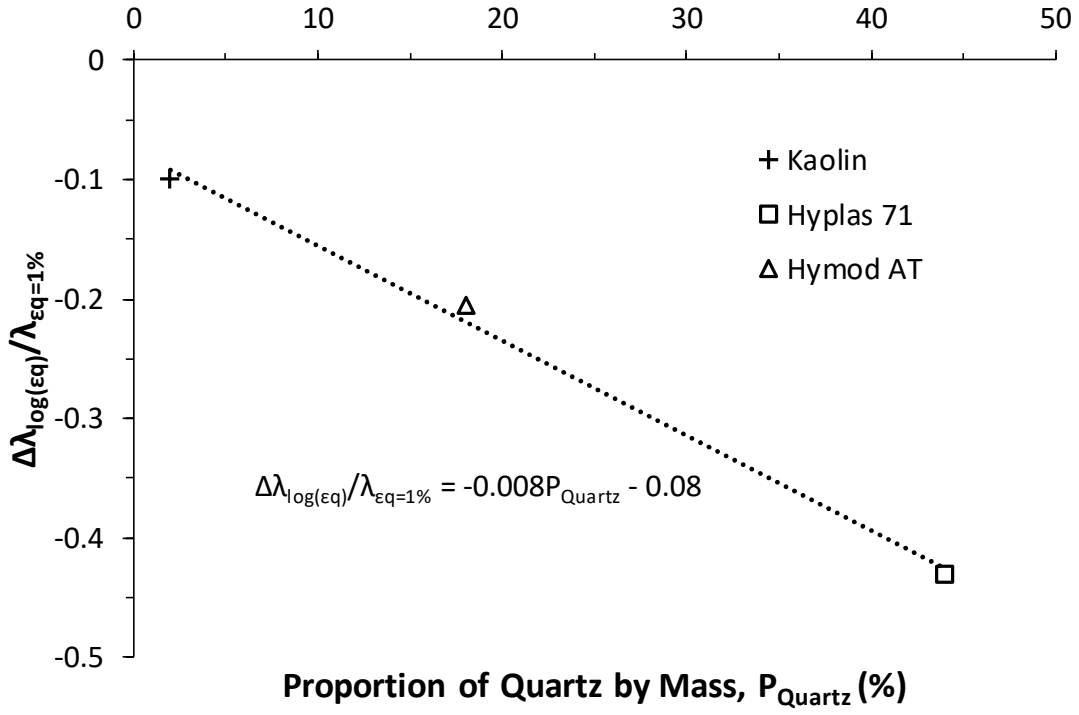

Figure 8-27 – Variation of normalised rate effect degradation with quartz proportion by mass showing greater rate effect degradation at higher quartz proportions

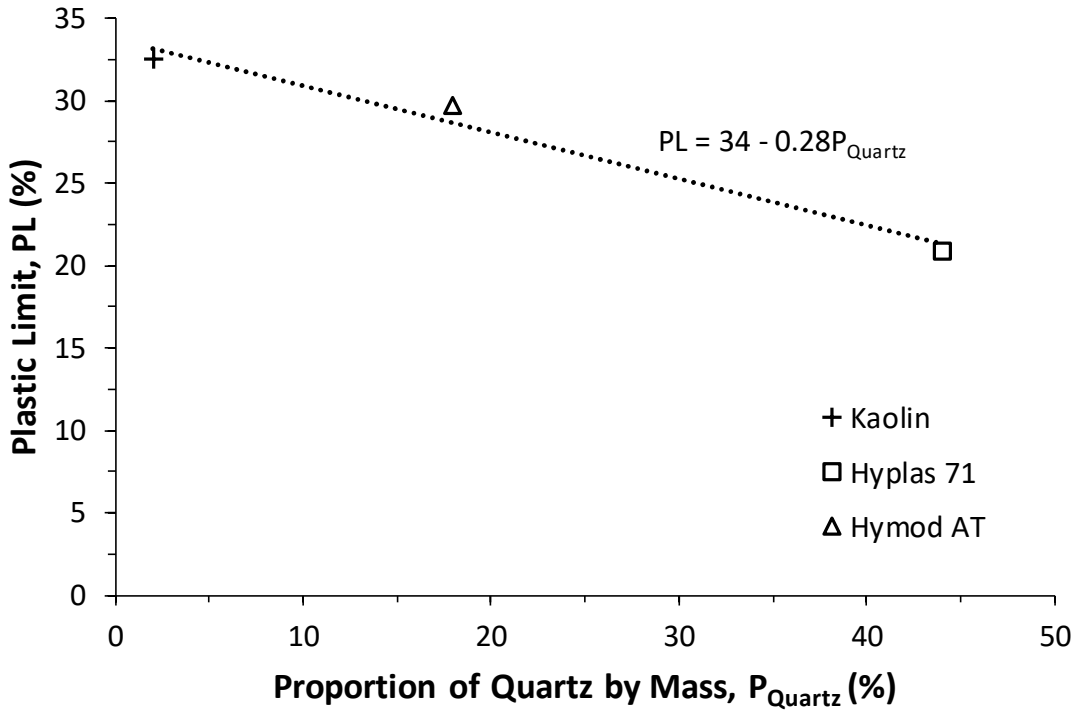

Figure 8-28 – Correlation between plastic limit and quartz proportion by mass showing the reduction in plastic limit due to the presence of the silt-sized rotund quartz particles

As the clay shears, the SEM imaging of Kaolin in Chapter 7 suggests that the clay particle groups tend towards a preferred orientation and increasingly align parallel to each other. This would tend to reduce the interaction between the clay mineral particles, meaning less potential for particle interaction (and possibly less particle to particle contacts as discussed in Chapter 7). Hence, it could be suggested that as the clay particles tend towards a preferred orientation with increasing shear, the rate effect may be expected to reduce, leading to rate effect degradation with strain. Lupini *et al.* (1981) and Lemos and Vaughan (2000) investigated the shearing mechanisms which occur at high strain rates using ring shear testing of a wide variety of soils. It was found that while platy clay particles would align and form a 'sliding' shear mechanism, the presence of larger (by an order of magnitude compared to the clay particles) rotund particles (such as the quartz crystals found here) prevented the preferred orientation from occurring by disrupting the sliding mechanism. However, if this was occurring, it would be expected that the rate effect degradation would be greatest for Kaolin, which has the least quartz content. In Figure 8-27, it can be seen that the opposite is observed. This suggests the

mechanistic changes seen in Lupini *et al.* (1981) and Lemos and Vaughan (2000) may be specific to the pre-formed shear planes and interfaces used in these studies.

Further research would be required to determine the reasons why the quartz content changes the rate effect degradation with strain. One possibility which could warrant further investigation could be related to the possible rate effect mechanism suggested by Brown and Jaeger (2014). As discussed in Chapter 7, Brown and Jaeger suggested that rate effects are due to increasing particle interaction at high shear strain rates leading to a network of solid, frictional particle to particle contacts which cause the observe increases in shear strength. It is possible that the movement of the comparatively massive quartz particles with increasing strain destroys these force-carrying networks leading to a reduction in the rate effect with increasing strain. However, there is currently insufficient evidence to either confirm or refute this idea.

9. Conclusions

9.1. Introduction

Strain rate effects are important considerations in a number of geotechnical applications, such as rapid load testing of piles, free falling penetrometers and deep penetrating anchors, where the increase in deviator stress with strain rate influences analysis. Currently, there is a lack of sufficient understanding of the controls and influences of rate effects, which is a barrier to more accurate analysis and predictions for these activities.

This thesis has set out the findings of a programme of high strain rate triaxial testing on three clays for a range of initial mean effective stresses and axial strain rates, including rapid pore pressure measurements and local on-sample strain measurements. It has been shown that observed rate effects are influenced by a number of factors, including the soil state (in terms of the liquidity index) and the applied strain level. Correlations and models have been proposed which allow each of these factors to be accounted for, and an integrated model which allows rate effects to be estimated at any strain level and soil state, without the need to use separate models for the small and large strain ranges, has been proposed. Rate effects were found to vary significantly between the three clays tested, and correlations with potential rate effect indicators, which allow the magnitude of rate effects to be predicted for a given soil, are suggested. Consideration of the evidence from the testing programme suggests that rate effects are due to increasing particle to particle contacts at high shear strain rates (otherwise described as rate dependent granular dilatancy).

9.2. Rate Effects in Kaolin at Large Strains

The programme of triaxial testing on Kaolin highlighted a number of key aspects of rate effects:

1. Viscous undrained strain rate effects on peak strength in Kaolin were found to be dependent on the soil state and ranged from λ_{peak} = 0.16 to 0.10 at p'_0 = 300 kPa and 1350 kPa, respectively. These rate effects were found to vary with LI^2.
2. Overconsolidation ratio was found to have no observable influence on the magnitude of rate effects at peak strength, other than small increases due to changes in moisture content caused by swelling, which are already described by the correlation with liquidity index.

3. The strain at which peak deviator stress occurs is dependent on the strain rate. Hence, it is important to compare rate effects using a strain-based definition as rate effects have been found to be highly strain dependent. The maximum rate effect, λ_{max}, occurs around ε_q = 0.01 based on large strain measurements. The rate effect at ε_q = 0.01, $\lambda_{\varepsilon q=1\%}$, also varies with LI^2.
4. After ε_q = 0.01 rate effects were found to reduce with $log(\varepsilon_q)$, such that for every order of magnitude increase in applied strain, λ reduced by 10 % for Kaolin.

Chapter 4 investigated how rate effects change depending on soil state (*LI*), and developed a model to account for this change. The maximum rate effect was shown to occur around ε_q = 0.01, after which rate effects degrade with increasing strain.

9.3. Rate Effects on Pore Pressure Evolution in Kaolin

The analysis of the pore pressure response and effective stress behaviour of Kaolin at high strain rates has identified the following important conclusions:

1. It is important to consider shear-induced pore pressures when considering rate effects (rather than excess pore water pressure). This shear-induced pore pressure reflects the true dilatant or contractive tendency of the soil specimen.
2. At any given shear strain, $\Delta u_{si}/p'_0$ reduces with shear strain rate. This reduction is soil state independent and is a key reason for the increase in deviator stress with strain rate.
3. The shear-induced pore pressure at high strain rates can be captured using a simple inverse hyperbolic relationship which can be correlated with either the shear strain rate, $\dot{\varepsilon}_q$, or the state parameter, Ψ. This allows the pore pressure at any given stress, strain, and strain rate to be estimated (for normally consolidated specimens).
4. The intercept of the CSL in *v-ln(p')* space, Γ, increases with $log(\dot{\varepsilon}_q)$, which leads to a corresponding reduction in the state parameter, Ψ, with strain rate, which appears to be the main mechanism behind rate effects. The gradient of the CSL in *v-ln(p')* space, λ_{csl}, was not found to change with strain rate.
5. The soil state dependence of rate effects is caused by increases in the effective friction ratio with strain rate, which are greater at lower initial mean effective stresses (or lower p'_0).

6. The increase in the size of the yield envelope with strain rate for normally consolidated soil can be modelled by using a Modified Cam Clay (MCC) yield envelope using an 'apparent' increase in OCR. This yield envelope can be implemented in *q-p'-v* space to define a 3D yield surface which accounts for stress level, stress history and strain rate (including the soil state dependence of rate effects at the point of yield).

Chapter 5 considered the impact of strain rate on pore pressure and effective stress. Ways to model the shear-induced pore pressures at high shear strain rates were presented, and the implications of these pore pressure changes on the critical state framework were discussed.

9.4. Modelling of Rate Effects at Small Strains

Strain rate effects were found to have several notable influences on the small-strain response of Kaolin, which are summarised below.

1. The initial shear modulus, G_{max}, is rate independent meaning that below the elastic strain threshold, $\varepsilon_{q,EL}$, no observable strain rate effects occur.
2. In contrast, the elastic strain threshold is rate dependent and increases with $log(\dot{\varepsilon}_q)$. This yield point (at the reference shear strain rate) defines the strain after which rate effects begin to develop.
3. Existing Hardin and Drnevich (1972) type stiffness degradation models cannot accurately capture the degradation of the shear modulus with strain at high strain rates. An improvement to this type of model has been suggested to allow the rate dependence of stiffness degradation to be modelled.
4. A model for the mobilisation of rate effects after the point of yield and up until the point of maximum rate effect has been proposed. This has been validated against the local Hall effect small strain measurements, as well as existing published data.
5. To allow rate effects to be captured throughout the strain range, an integrated model has been proposed which allows the rate effect to be modelled regardless of whether the strain in question is below the elastic strain threshold, during rate effect mobilisation, or even during rate effect degradation at large strains. This includes accounting for the influence of soil state on rate effects.

Chapter 6 covered the development of an integrated rate effects model which accounts for both soil state and the variation in rate effects with strain, from small through to large strains,

without the discrepancies which could occur if separate models were to be used. An improved stiffness degradation model was also presented.

9.5. Rate Effect Mechanism Investigation

Discussion of the potential rate effect mechanism(s) and the supporting evidence identified the following conclusions:

1. Two potential mechanisms appear in the existing literature; fluid viscosity or inter-particle locking (also described as granular dilatancy). Fluid viscosity suggests rate effects are due to rate dependent viscous drag forces as adjacent particles shear relative to each other, whilst inter-particle locking attributes rate effects to increasing particle interaction at higher strain rates, which leads to more force-carrying solid, frictional particle to particle contacts (as electrostatic repulsive forces are overcome).
2. Existing literature does not support the idea of an area of high viscosity adsorbed pore fluid on clay particle surfaces, often suggested as an explanation for rate effects. Other studies have also shown that fluid viscosity cannot fully account for the magnitude of rate effects observed on its own.
3. Rate dependent "granular dilatancy" as described by Brown and Jaeger (2014) predicts a number of key impacts on fine dense suspension behaviour with increasing strain rate. Each of these behaviours was observed in the triaxial testing programme described in this thesis.
4. Granular dilatancy would suggest lower rate effects in finer soils as these smaller particles would have less momentum and greater surface areas and repulsive forces (per unit mass).
5. Scanning electron microscopy of flash frozen samples from triaxial specimens sheared at $\dot{\varepsilon}$ = 1 %/hr and 100,000 %/hr found no observable differences between the specimens in terms of the orientation of the particle flocs/groups or their size.

Chapter 7 considered the two main mechanisms proposed in literature as the cause of rate effects, and identifies the implications of these mechanisms which could suggest they are occurring.

9.6. Potential Methods for Predicting Rate Effects in Different Soils

In this section, the rate effect parameters $\lambda_{\varepsilon q=1\%,pl}$ and $\alpha_{\varepsilon q=1\%}$ were correlated with potential rate effect indicators to determine parameters which could be used to predict the magnitude of rate effects in different soils.

1. Triaxial testing of two further clays at $\dot{\varepsilon}$ = 1000 to 100,000 %/hr identified that significant differences in rate effects can be seen between different clays. Rate effects range from $\lambda_{\varepsilon q=1\%}$ = 0.10 to 0.13 for Hyplas 71 and $\lambda_{\varepsilon q=1\%}$ = 0.05 to 0.06 for Hymod AT (compared to $\lambda_{\varepsilon q=1\%}$ = 0.12 to 0.16 for Kaolin). Hymod AT showed by far the lowest rate effects.
2. The state independent rate effect parameters, $\lambda_{\varepsilon q=1\%,pl}$ and $\alpha_{\varepsilon q=1\%}$, were not found to correlate well with the Atterberg limits. Except for the specific surface area (*SSA*) and the critical state friction ratio, *M*, no other potential indicators were found to have useful correlations.
3. The specific surface area (*SSA*) and the critical state friction ratio, *M*, were both shown to correlate well with the observed rate effects and could potentially be good rate effect indicators. The rate effect parameters were found to reduce with increasing *SSA*, suggesting granular dilatancy is the mechanism underlying rate effects. *M* has also previously been shown by other studies to be related to *SSA*, explaining the observed correlation with the rate effect parameters, which increase with *M*.
4. Each of the three clays tested consisted of three main minerals; Kaolinite, Illite and Quartz. The Illite proportion was found to have a significant effect on the observed rate effects, due to the fact that it is an order of magnitude finer in size than the other minerals and hence controls the specific surface area of the clays. The lowest rate effects were observed in Hymod AT, which had the highest Illite content (40 %). The fine Illite proportion clearly reduces the observed rate effects.
5. The rate at which λ degrades at strains beyond $\varepsilon_{q,\lambda max}$ was also found to vary between the three clays, but was not related to $\lambda_{\varepsilon q=1\%,pl}$ and $\alpha_{\varepsilon q=1\%}$. Instead, the degradation of rate effects was found to be related to the quartz proportion in the clays.

Models which allow the effect of the material properties on rate effects to be accounted for were presented in Chapter 8. Combined with the integrated model presented in Chapter 6, this allows the rate effect of any clay soil to be predicted at any given soil state for any shear

strain level. The only information required to use this model is the result of a simple, rapid and inexpensive methylene blue spot test for *SSA* and a disturbed soil sample to determine the in-situ liquidity index.

10. Recommendations for Future Work

10.1. Areas for Future Research

The research described here has attempted to cover many aspects of rate effects, however, the scope inevitably had to be limited to deliver a sensible programme of research.

The research has found that in terms of soil state, rate effects vary with the square of liquidity index, LI^2, although liquidity indexes greater than 0.32 have not been investigated. Further testing at lower initial effective stresses would provide a greater range of liquidity indexes, providing greater confidence in the proposed LI^2 relationship and also allowing for its use in near-surface activities and softer soils where rate effects may be expected to be far greater.

Likewise, the proposed rate effect indicators, such as Specific Surface Area (*SSA*), suggested here, are based on the three soils tested. Testing of additional clays would increase the confidence in the correlations with these parameters, especially if those clays include minerals other than Kaolinite, Illite and Quartz. The clays selected for future testing should also be chosen carefully to have widely varying geotechnical properties, where possible.

One question, which has been raised by this research, is the impact of the silt fraction commonly present in clays on rate effects. Even the supposedly 'pure' clays tested here have varying silt components. Silts are an area where there is perhaps even less rate effect information than that available for clays. A study is recommended using one type of clay, into which at least three different proportions of silts are added. This would allow the impact of the silt on the parameters which are believed to be good rate effect indicators (eg *SSA* or *M*) to be separated from the impact of the silt portion on the measured rate effects; a deconvolution which has not been possible in this study. A similar programme could also be conducted for sand proportions.

The specimens used in this study have all been isotropically consolidated. This was mainly due to the fact that before the impact of anisotropy on rate effects can be considered, a good understanding of rate effects in isotropic conditions is first required. A study to consider whether there is any effect of anisotropy would represent an important step towards the accurate prediction of rate effects in real world conditions, where anisotropy is an important consideration. This research also concluded that there is no observable impact of OCR on rate

effects based on a limited number of tests, so further testing of overconsolidated soils at a greater range of OCRs could provide more confidence in this assertion. Other potential avenues for research include the impact of ageing of specimens on the observed rate effects and methods for estimating rate effects in soils with significant organic components.

Finally, the purpose of the research was to develop useful methods for predicting rate effects for use in real world applications. A number of class A predictions would provide further confidence in these methods and potentially improve their adoption.

10.2. Further Investigation of the Rate Effect Mechanism

Some avenues which could provide further insight into the mechanism behind rate effects were identified during the study. One avenue of particular interest would be to further investigate the influence of the clay minerals on rate effects. In Chapter 8, Illite was shown to influence (reduce) the observed rate effects, most likely as it was controlling the *SSA* of the clay. Testing of specimens consisting of only one clay mineral would allow the influence of each mineral on rate effects to be found. This could indicate whether the impact of mineralogy is due to the varying *SSA* or other variables related to the specific mineral.

The cause of the wide variation in the manner that rate effects reduce with increasing strain (after the maximum rate effect) could also be investigated further. One of the potential explanations for this is that at large strains, the movement of the silt sized quartz crystals (large particles compared to the clay particle size) destroys the network of solid force-carrying particle to particle contacts, which are a possible explanation for rate effects. Post-shear SEM imaging of the clay which showed the greatest rate effect reductions with strain, Hyplas 71, may provide confirmation of this theory. The study into the impact of silt proportion described earlier in this chapter could also assist with this, as it would show whether the rate effect degradation increases with silt content. This would be expected if the comparatively large particles are indeed responsible for the degradation.

The cause of the dependency of rate effects on soil state could also be better understood using further SEM imaging of Kaolin. The imaging conducted in this study was entirely at p'_0 = 300 kPa, and a similar programme of SEM imaging at a higher effective stress would allow comparison of and highlight any changes in the soil structure or particle floc properties. This may allow potential causes of the reducing rate effects at lower liquidity indexes to be found.

10.3. Equipment Improvements

One of the primary reasons for unusable data in a few of the high-speed element tests was gain control issues, which caused minute oscillations in the application of the axial strain rate to the sample, under certain conditions. This in turn led to small variations in the observed rate effects, often at $\dot{\varepsilon}$ = 10000 %/hr. Whilst it was possible to manually adjust the gain settings to an extent, the issue tended to be dependent on the individual specimen installed and its stiffness as well as the strain rate, making gain adjustments unfeasible. An adaptation to the MiniDYN system to incorporate automatic gain tuning would prevent the control issues affecting the data in any future testing programme and would be highly recommended by the author. In this case, the system would be able to monitor the stiffness of the specimen during consolidation when suction caps are connected, and the gain settings would be automatically adjusted prior to shearing. Such an adaptation is now provided by the system manufacturer, GDS Instruments, although there is still a technical question as to whether this would be possible via a firmware upgrade, or whether some hardware changes would be required.

Another system issue which limited productivity was the fact that the system was limited to 1000 data points per dynamic test stage, meaning that in the shearing stage, a large strain (up to ε = 20 %) triaxial test may only contain two or three data points before yield in some cases. This was the main reason that the small strain rate effect investigation described in this study required a separate programme of small strain (up to $\varepsilon \approx 2$ %) triaxial testing, to focus the available data points at low strain levels. If this issue could be overcome, it would be possible to combine future small strain and large strain rate effect investigations into one triaxial testing programme, doubling productivity. This could be done either by a system upgrade to the GDS DCS by the manufacturer, or by using a high speed external data acquisition system to log sensor outputs alongside the GDS DCS.

Another issue related to this is that the holders used to mount the local Hall effect sensors to the triaxial specimen are susceptible to damage if large strains are applied, particularly if a shear plane forms. This is due to the fact that the existing holders are unable to accommodate lateral movement or rotation. Modification of the sensor holders to avoid damage would overcome this issue. A prototype of a new axial Hall effect holder has already been developed using 3D printing and has been tested, meaning only a new design for the radial holder is

required. Once these have been developed, the designs can be transferred to a more durable 3D printing material for use.

Specimen consolidation times could also be improved through the use of filter paper drains which are more resistant to effective stress when wet. This is due to the fact that the stress (from the consolidation pressure) on the filter paper compresses the pores, making the drains less permeable. Sometimes hardened cellulose papers can be used to overcome this issue. In tests conducted at higher effective stresses, there were some indications that the permeability of the filter drains was reducing, and slightly longer consolidation times were required. However, sourcing these papers in sufficiently large sizes to make the filter drains can be problematic. It should also be considered that using a filter paper with a stronger structure could lead to reinforcing effects on the specimen which would need to be quantified.

Appendix 1 – Material Source Information

Speswhite Kaolin

Powdered primary kaolin clay (Speswhite^{TM})

Source Deposit: *Various (South West England)*

Quarry Site: *Various (South West England)*

Manufacturer: Imerys Filtration and Additives Europe
Par Moor Centre
Par Moor Road
Par
Cornwall
PL24 2SQ
United Kingdom
Tel: +44 1726 818000
www.imerys-filtration.com

Supplier: WhitChem Ltd
23 Albert Street,
Newcastle-under-Lyme
Staffordshire
ST5 1JP
United Kingdom
Tel: +44 1782 711777
www.whitchem.co.uk

Hyplas 71

Powdered natural secondary ball clay from Devon (Hyplas™ 71)

Source Deposit: Bovey Basin, Devon, United Kingdom

Quarry Site: Imerys Minerals Ltd
Higher Brocks Plantation
Old Newton Road
Teigngrace
Newton Abbot
Devon
TQ12 6QZ
United Kingdom
Tel: +44 1626 822366

Manufacturer: Imerys Ceramics
Shelton New Road,
Cliffe Vale,
Stoke on Trent
Staffordshire
ST4 7AR
United Kingdom
Tel: +44 1782 748620
www.imerys-ceramics.com

Supplier: Clayman Supplies
Morells Barn
Lower Bognor Road
Lagness
Chichester
West Sussex
PO20 1LR
United Kingdom
Tel: +44 1243 265845
www.claymansupplies.co.uk

Hymod AT

Powdered natural secondary ball clay from Dorset (Hymod™ AT)

Source Deposit: Wareham Basin (Furzeyground), Dorset, United Kingdom

Quarry Site: Imerys Minerals Ltd
Furzebrook Works
Furzebrook Road
Wareham
Dorset
BH20 5AR
United Kingdom
Tel: +44 1929 552146

Manufacturer: Imerys Filtration and Additives Europe
Par Moor Centre
Par Moor Road
Par
Cornwall
PL24 2SQ
United Kingdom
Tel: +44 1726 818000
www.imerys-filtration.com

Supplier: Clayman Supplies
Morells Barn
Lower Bognor Road
Lagness
Chichester
West Sussex
PO20 1LR
United Kingdom
Tel: +44 1243 265845
www.claymansupplies.co.uk

Appendix 2 – Equipment Calibration

GDS MiniDYN 100 mm High Speed Triaxial System		
Transducer	Calibration Method	Comments
Global platen displacement from GDS MiniDYN motor encoder	Calibration from manufacturer's calibration sheet	Calibration factor confirmed using RS Pro digital caliper (0.01 mm resolution) over full displacement range
Axial load from GDS STALC9 5 kN submersible load cell	UKAS traceable calibration by manufacturer	Calibration confirmed up to 1 kN using laboratory weights
Cell pressure from GDS STDDPC pressure controller	UKAS traceable calibration by manufacturer (Latest calibration Jan 2018)	Calibration confirmed using external Sherbourne pressure transducer
Back pressure from GDS STDDPC pressure controller	Calibration by manufacturer	Calibration confirmed to match cell pressure controller to within 0.5 %
External Sherbourne cell pressure transducer	Calibrated from manufacturer's calibration sheet	Calibration confirmed to match cell pressure controller to within 0.5 %
Druck PDCR81 mid-height pore pressure transducer	Calibrated to match cell pressure controller inside triaxial cell	-
Honeywell 24PCGFA6G mid-height pore pressure	Calibrated to match cell pressure controller inside triaxial cell	-
GDS Hall effect local strain sensors	Calibrated to match global platen displacement	Calibrated by mounting Hall effect sensors to base platen and fixing magnets to frame on MiniDYN, to allow accurate displacements to be applied and measured

GDS 38 mm Stress Path Cell		
Transducer	Calibration Method	Comments
Global platen displacement from external LVDT	Calibration using RS Pro digital caliper (0.01 mm resolution)	Calibrated over full displacement range, with a linear best-fit applied
Axial load from GDS STALC9 10 kN submersible load cell	Calibration from manufacturer's calibration sheet	Calibration confirmed up to 1 kN using laboratory weights
Cell pressure from GDS ADVDPC pressure controller	Calibration by manufacturer	Calibration confirmed to match cell pressure controller on MiniDYN high speed system to within 0.5 %
Back pressure from GDS ADVDPC pressure controller	Calibration by manufacturer	Calibration confirmed to match cell pressure controller to within 0.5 %
Base cell pressure transducer	Calibrated to match cell pressure controller	-

References

Abelev, A. and Valent, P. (2013) Strain-rate dependence of strength of the Gulf of Mexico soft sediments. *IEEE Journal of Oceanic Engineering*, **38**(1), 25-31.

Akai, K., Adachi, T. and Ando, N. (1975) Existence of a unique stress-strain-time relation of clays. *Soils and Foundations*, **15**(1), 1-16.

Anderson, K.H. (1993) Clay behaviour under irregular cyclic loading. *Publication 189*, Norges Geotekniske Institutt, 1-14.

Atkinson, J.H. (2000) Non-linear soil stiffness in routine design. *Géotechnique*, **50**(5), 487-508.

Atkinson, J. (2007) *The Mechanics of Soils and Foundations (Second Edition)*, Taylor and Francis, Abingdon.

Balderas-Meca, J. (2004) Rate effects of rapid loading in clay soils. *PhD Thesis*, University of Sheffield, UK.

Bea, R.G. (1982) Soil strain rate effects on axial pile capacity. *Proc. 2nd Int. Conf. on Numerical Methods in Offshore Eng.,* 107-132.

Berre, T. and Bjerrum, L. (1972) Shear strength of normally consolidated clays. *Proceedings of the ICSMFE*, Moscow, 39-49.

Bertalot, D. (2013) Seismic behaviour of shallow foundations on layered liquefiable soils. *PhD Thesis,* University of Dundee, Dundee, UK.

Bi, D., Zhang, J., Chakraborty, B. and Behringer, R.P. (2011) Jamming by shear. *Nature,* **480**, 355-358.

Biscontin, G. and Pestana, J.M. (2001) Influence of peripheral velocity on vane shear strength of an artificial clay. *Geotechnical Testing Journal*, **24**(4), 423-429.

Bjerrum, L., Simons, N. and Torblaa, I. (1958) The effect of time on the shear strength of a soft marine clay. *Proceedings of the Brussels Conference on Earth Pressure Problems*, 148-158.

Bond, A.J., Jardine, R.J. and Dalton, J.C.P. (1991) Design and performance of the Imperial College instrumented pile. *Geotechnical Testing Journal*, **14**(4), 413-424.

Boukpeti, N., White, D.J., Randolph, M.F. and Low H.E. (2012) Strength of fine-grained soils at the solid-fluid transition. *Géotechnique*, 62(3), 213-226.

Briaud, J-L. and Garland, E. (1985) Loading rate method for pile response in clay. *Journal of Geotechnical Engineering*, ASCE, 111(3), 319-335.

Bromhead, E.N. (2006) *The stability of slopes*, CRC Press.

Brown, E. and Jaeger, H.M. (2014) Shear thickening in concentrated suspensions: phenomenology, mechanisms, and relations to jamming. *Reports on Progress in Physics*, IOP, 77(4), Article Number 046602.

Brown, M.J. (2004) The rapid load testing of piles in fine grained soils. *PhD Thesis*, University of Sheffield, UK.

Brown, M.J. (2008) Recommendations for statnamic use and interpretation of piles installed in clay. *Rapid Load Testing on Piles*, CRC Press, London, 23-36.

Brown, M.J., Hyde, A.F.L. and Anderson, W.F. (2006) Analysis of a rapid load test on an instrumented bored pile in clay. *Géotechnique*, 56(9), 627-638.

Brown, M.J. and Hyde, A.F.L. (2008a) Rate effects from pile shaft resistance measurements. *Canadian Geotechnical Journal*, 45, 425-431.

Brown, M.J. and Hyde, A.F.L. (2008b) High penetration rate CPT to determine damping parameters for rapid load pile testing. *Geotechnical and Geophysical Site Characterisation*, Taylor and Francis, London, 657-663.

Brown, M.J. and Powell, J.J.M. (2013) Comparison of rapid load test analysis techniques in clay soils. *Journal of Geotechnical and Geoenvironmental Engineering,* 139 (1), 152-161.

Chow, S.H. and Airey, D.W. (2011) Rate effects in free falling penetrometer tests. *Proceedings of the International Symposium on Deformation Characteristics of Geomaterials*, September 1-3, Seoul, Korea, 592-599.

Chow, S.H. and Airey, D.W. (2013) Soil strength characterisation using free-falling penetrometers. *Géotechnique,* 63 (13), 1311-1143.

Chow, S.H., O'Loughlin, C.D., White, D.J. and Randolph, M.F. (2017) An extended interpretation of the free-fall piezocone test in clay. *Géotechnique*, **67**(12), 1090-1103.

Christenson, H.K., Israelachvili, J.N. and Pashley, R.M. (1987) Properties of capillary fluids at the microscopic level*, SPE Reservoir Engineering*, **2**(2), 155-165

Chung, S.F., Randolph, M.F. and Schneider, J.A. (2006) Effect of penetration rate on penetrometer resistance in clay. *Journal of Geotechnical and Geoenvironmental Engineering*, ASCE, **132**(9), 1188-1196.

Clayton, C.R.I. and Khatrush, S.A. (1986) A new device for measuring local axial strains on triaxial specimens. *Géotechnique*, **36**(4), 593-597.

Clayton, C.R.I., Khatrush, S.A., Bica, A.V.D. and Siddique, A. (1989) The use of Hall effect semiconductors in geotechnical instrumentation. *Geotechnical Testing Journal*, **12**(1), 69-76.

Colreavy, C., O'Loughlin, C.D. and Randolph, M.F. (2016) Estimating consolidation parameters from field piezoball tests. *Géotechnique*, **66**(4), 333-343.

Dayal, U. and Allen, J.H. (1975) The effect of penetration rate on the strength of remolded clay and sand samples. *Canadian Geotechnical Journal*, **12**, 336-348.

Di Benedetto, H. and Tatsuoka, F. (1997) Small strain behaviour of geomaterials: modelling of strain rate effects. *Soils and Foundations*, **37**(2), 127-138.

Diaz-Rodriguez, J.A. and Martinez-Vasquez, J.J. (2005) Strain rate behavior of Mexico City soils. *Proceedings of the 16th International Conference on Soil Mechanics and Geotechnical Engineering (16th ICSMGE)*, Osaka, Japan, 333-336.

Einav, I. and Randolph, M.F. (2005) Combining upper bound and strain path methods for evaluating penetration resistance, *International Journal of Numerical Methods in Engineering,* **63**(14), 1991-2016.

Eyring, H. (1936) Viscosity, plasticity and diffusion as examples of absolute reaction rates. *Journal of Chemical Physics*, **4**(4), 283-291.

Fearon, R.E., Chandler, R.J. and Bommer, J.J. (2004) An investigation of the mechanisms which control soil behaviour at fast rates of displacement. *Advances in Geotechnical Engineering: The Skempton conference*, Thomas Telford, London, UK, 441-452.

Finnie, I.M.S and Randolph, M.F. (1994) Punch-through and liquefaction induced failure of shallow foundations on calcareous sediments. *Proceedings of the International Conference on Behavior of Offshore Structures*, BOSS '94, Boston, USA, 217-230.

Fourie, A.B. and Xiaobi, D. (1991) Advantages of midheight pore pressure measurements in undrained triaxial testing. *Geotechnical Testing Journal*, **14**(2), 138-145.

Gasparre, A. (2005) Advanced laboratory characterisation of London clay. *PhD Thesis*, Imperial College London, UK.

GDS Instruments Ltd. (2014) *Mid plane pore pressure probe: datasheet.* GDS Instruments, Hook, UK.

GDS Instruments Ltd (2018) *Advanced dynamic triaxial testing system (DYNTTS) datasheet*. GDS Instruments, Hook, UK.

Graham, J., Crooks, J.H.A. and Bell, A.L. (1983) Time effects on the stress -strain behaviour of natural soft clays. *Géotechnique*, **33**(3), 327-340.

Hardin, B.O. and Drnevich, V.P. (1972) Shear modulus and damping in soils: measurement and parameter effects. *Journal of the ASCE Soil Mechanics and Foundations Division*, **98**(SM6), 603-624.

Hattab, M. and Fleureau, J-M. (2010) Experimental study of kaolin particle orientation mechanism. *Géotechnique*, **60**(5), 323-331.

Head, K.H. and Epps, R.J. (2011) *Manual of Soil Laboratory Testing – Volume II: Permeability, Shear Strength and Compressibility Tests.* Whittles Publishing, Caithness, Scotland.

Head, K.H. and Epps, R.J. (2014) *Manual of Soil Laboratory Testing – Volume III: Effective Stress Tests.* Whittles Publishing, Caithness, Scotland.

Henkel, D.J. and Gilbert, G.D. (1952) The effect of the rubber membrane on the measured triaxial compression strength of clay samples. *Géotechnique*, **3**(1), 20-29.

Holzer, L., Münch, B., Rizzi, M., Wepf, R., Marschall, P. and Graule, T. (2010) 3D-microstructure analysis of hydrated bentonite with cryo-stabilized pore water. *Applied Clay Science,* **47**, 330-342.

Huggett, J.M. and Shaw, H.F. (1997) Field emission scanning electron microscopy – a high resolution technique for the study of clay minerals in sediments. *Clay Minerals,* **32**, 197-203.

Jardine, R.J. (1992) Some observations on the kinematic nature of soil stiffness. *Soils and Foundations*, **32**(2), 111-124.

Jardine, R.J., Gens, A., Hight, D.W. and Coop, M.R. (2004) Developments in understanding soil behaviour. *Advances in Geotechnical Engineering: The Skempton Conference*, Thomas Telford, London, UK, 103-206.

Karimi-Lotfabad, S. and Gray, M.R. (2000) Characterization of contaminated soils using confocal laser scanning microscopy and cryogenic-scanning electron microscopy. *Environmental Science and Technology,* **34** (16), 3408-3414.

Katti, D.R., Tang, J. and Yazdani, S. (2003) Undrained response of clays to varying strain rate. *Journal of Geotechnical and Geoenvironmental Engineering*, ASCE, **129**(3), 278-282.

Krieg, S. and Goldscheider, M. (1998) Bodenviskosität und ihr Einfluβ auf das Tragverhalten von Pfählen. *Bautechnik 75*, Ernst und Sohn, 806-820. (In German)

Kulhawy, F.H. and Mayne, P.W. (1990) Manual on estimating soil properties for foundation design. *Report EL-6800*, Electric Power Research Institute, Palo Alto, California, USA.

Kwok, C-Y. and Bolton, M.D. (2010) DEM simulations of thermally activated creep in soils. *Géotechnique*, **60**(6), 425-433.

Lehane, B.M., O'Loughlin, C.D., Gaudin, C. and Randolph, M.F. (2009) Rate effects on penetrometer resistance in kaolin. *Géotechnique*, **59**(1), 41-52.

Lemos, L.J.L. and Vaughan, P.R. (2000) Clay-interface shear resistance. *Geotechnique*, **50**(1), 55-64.

Leroueil, S., Kabbaj, M., Tavenas, F. and Bouchard, R. (1985) Stress-strain rate relation for the compressibility of sensitive natural clays. *Géotechnique*, **35**(2), 159-180.

Leroueil, S. and Marques, M.E.S. (1996) Importance of strain rate and temperature effects in geotechnical engineering. *Geotechnical Special Publication*, ASCE, **61**, 1-59.

Leroueil, S., Tavenas, F., Rochelle, P.L. and Tremblay, M. (1988) Influence of filter paper and leakage on triaxial testing. *Advanced Triaxial Testing of Soil and Rock: ASTM STP 977,* American Society for Testing and Materials, Philadelphia, USA.

Li, P.Q. and Baudet, B.A. (2016) Strain rate dependence of the critical state line of reconstituted clays. *Géotechnique Letters*, **6**, 66-71.

Lo Presti, D.C.F. (1989) Proprieta dinamiche dei terreni, *Proceedings XIV Conferenza Geotecnica di Torino*, Department of Structural Engineering, Politecnico di Torino. (In Italian)

Lo Presti, D.C.F., Jamiolkowski, M., Pallara, O. and Cavallaro, A. (1996) Rate and creep effect on the stiffness of soils. *Measuring and Modelling Time Dependent Soil Behaviour,* ASCE, 166-180.

Low, P.F. (1961) The physical chemistry of clay-water interaction. *Advances in Agronomy*, **13**(1), 269-327.

Lupini, J.F., Skinner, A.E. and Vaughan, P.R. (1981) The drained residual strength of cohesive soils. *Géotechnique*, **31**(2), 181-213.

Martindale, H., Chakraborty, T. and Basu, D. (2013) A strain-rate dependent clay constitutive model with parametric sensitivity and uncertainty quantification. *Journal of Geotechnical and Geological Engineering*, **31**, 229-248.

Meehan, C.L., Brandon, T.L. and Duncan, J.M. (2008) Measuring "fast" shear strengths along slickensided surfaces in the Bromhead ring shear. *Geotechnical Testing Journal*, ASTM, **31**(3), 239-242.

Mitchell, J.K. and Soga, K. (2005) *Fundamentals of Soil Behavior.* John Wiley and Sons, Hoboken, New Jersey, USA.

Monroy, R., Zdravkovic, L., and Ridley, A. (2010) Evolution of microstructure in compacted London Clay during wetting and loading. *Géotechnique,* **60** (2), 105-119.

Moore, R. (1991) The chemical and mineralogical controls upon the residual strength of pure and natural clays. *Géotechnique*, **41**(1), 35-47.

Moore, D.M. and Reynolds, R.C. (1997) *X-ray Diffraction and the Identification and Analysis of Clay Minerals.* Oxford University Press, New York, USA.

Morton, J.P., O'Loughlin, C.D. and White, D.J. (2016) Estimation of soil strength in fine-grained soils by instrumented free-fall sphere tests. *Géotechnique*, **66**(12), 959-968.

Mun, W., Teixeira, T., Balci, M.C., Svoboda, J. and McCartney, J.S. (2016) Rate effects on the undrained shear strength of compacted clay. *Soils and Foundations*, **56**(4), 719-731.

Muir Wood, D. (1990) *Soil Behaviour and Critical State Soil Mechanics*, Cambridge University Press.

Muir Wood, D. (2011) Personal Correspondence.

Mukabi, J.N., Tatsuoka, F. and Hirose, K. (1991) Effect of strain rate on small strain stiffness of Kaolin in CU triaxial compression. *Proceedings of the 26th Japan National Conference on Soil Mechanics and Foundation Engineering*, Nagano, 659-662.

Mukabi, J.N. and Tatsuoka, F. (1999) Influence of reconsolidation stress history and strain rate on the behaviour of kaolin over a wide range of strain. *Proceedings of the 12th African Regional Conference: Geotechnics for Developing Africa*, 365-377.

Nakase, A. and Kamei, T. (1986) Influence of strain rate on undrained shear characteristics of K_0-conolidated cohesive soils. *Soils and Foundations*, **26**(1), 85-95.

Nanda, S., Sivakumar, V., Hoyer, P., Bradshaw, A., Gavin, K.G., Gerkus, H., Jalilvand, S., Gilbert, R.B., Doherty, P. and Fanning, J. (2017) Effects of strain rates on the undrained shear strength of kaolin. *Geotechnical Testing Journal*, **40**(6), 951-962.

O'Kelly, B.C., Vardanega, P.J. and Haigh, S.K. (2018) Use of fall cones to determine Atterberg limits: a review. *Géotechnique*, **68**(10), 843-856.

O'Loughlin, C.D., Richardson, M.D. and Randolph, M.F. (2009) Centrifuge tests on dynamically installed anchors. *Proceedings of the 28th International Conference on Ocean, Offshore and Arctic Engineering,* Honolulu, Hawaii, USA.

O'Loughlin, C.D., Richardson, M.D., Randolph, M.F and Gaudin, C. (2013) Penetration of dynamically installed anchors in clay. *Géotechnique*, **63**(11), 909-919.

O'Reilly, M.P. (1991) Cyclic load testing of soils. *Cyclic loading of soil: from theory to design,* Blackie, Glasgow, 71-121.

O'Reilly, M.P., Brown, S.F. and Overy, R.F. (1989) Viscous effects observed in tests on an anisotropically normally consolidated silty clay. *Géotechnique*, 39(1), 153-158.

Oka, F., Kodaka, T., Kimoto, S., Ichinose, T. and Higo, Y. (2005) Strain localization of rectangular clay specimen under undrained triaxial compression conditions. *Proceedings of the International Conference on Soil Mechanics and Geotechnical Engineering (ICSMGE)*, Osaka, Japan, 16(2), 841-844.

Omar, T. and Sadrekarimi (2015) Effect of triaxial specimen size on engineering design and analysis. *International Journal of Geo-Engineering*, 6(5), 1-17.

Osipov, V.I. (2012) Nanofilms of adsorbed water in clay: mechanism of formation and properties. *Water Resources*, Pleiades Publishing, 39(7), 709-721.

Overy, R.F. (1982) The behaviour of anisotropically consolidated silty clay under cyclic loading. *PhD Thesis,* University of Nottingham, Nottingham, UK.

Oztoprak, S. and Bolton, M.D. (2013) Stiffness of sands through a laboratory test database. *Géotechnique*, 63(1), 54-70.

Plaxis (2013) *Material Models Manual*. Plaxis BV, Delft, The Netherlands.

Quinn, T. (2013) Rate effects in fine grained soils. *PhD Thesis*, University of Dundee, UK.

Quinn, T.A.C. and Brown, M.J. (2011) Effect of strain rate on isotropically consolidated kaolin over a wide range of strain rates in the triaxial apparatus. *Proceedings of the International Symposium on Deformation Characteristics of Geomaterials*, September 1-3, Seoul, Korea, 607-613.

Rae, P., Trujillo, C. and Lovato, M. (2009) The Young's modulus of 1018 steel and 6061-T6 aluminium measured from quasi-static to elastic precursor strain-rates. *Report LA-UR-03627*, Los Alamos National Laboratory (LANL), Los Alamos, New Mexico, USA, 1-5.

Randolph, M. and Hope, S. (2004) Effect of cone velocity on cone resistance and excess pore pressures. *Engineering Practice and Performance of Soft Deposits*, IS-OSAKA 2004, 147-152.

Rattley, M.J., Hill, A.J., Thomas, S. and Sampurno, B. (2011) Strain rate dependent simple shear behaviour of deepwater sediments in offshore Angola. *Frontiers in Offshore Geotechnics II*, Taylor & Francis, 377-382.

Reeves, G.M., Sims, I. and Cripps, J.C. (2006) *Clay Minerals Used in Construction.* Geological Society of London, London, UK.

Richardson, A.R. (1963) The relationship of the effective stress-strain behaviour of a saturated clay to the rate of strain, *DSc Thesis*, Massachusetts Institute of Technology, Massachusetts, USA.

Richardson, A.M. and Whitman, R.V. (1963) Effect of strain-rate upon undrained shear resistance of a saturated remoulded fat clay. *Géotechnique*, **13**(4), 310-324.

Rietveld, H.M. (1969) A profile refinement method for nuclear and magnetic structures. *Journal of Applied Crystallography,* **2**, 65-71.

Robinson, S. and Brown, M.J. (2013) Towards a framework for the prediction of installation rate effects. *Proceedings of the International Conference on Installation Effects in Geotechnical Engineering,* CRC Press, 128-134.

Rowe, P.W. and Barden, L. (1964) Importance of free ends in triaxial testing. *Journal of the Soil Mechanics Division*, ASCE, **90**(SM1), 1-27.

Sabetamal, H., Carter, J.P., Nazem, M. and Sloan, S.W. (2016) Numerical study of the effects of strain rate on the behaviour of dynamically penetrating anchors in clay. *7th International Conference on Computational Methods, ICCM2016,* Berkeley, California, USA.

Sachan, A. and Penumadu, D. (2007) Strain localization in solid cylindrical clay specimens using digital image analysis (DIA) technique. *Soils and Foundations*, **47**(1), 67-78.

Santagata, M. (2008) Effects of stress history on the stiffness of a soft clay. *Proceedings of the 4th International Symposium on Deformation Characteristics of Geomaterials,* IS Atlanta '08, Atlanta, 95-123.

Santagata, M., Germaine, J.T. and Ladd, C.C. (2005) Factors affecting the initial stiffness of cohesive soils. *Journal of Geotechnical and Geoenvironmental Engineering*, ASCE, **131**(4), 430-441.

Santagata, M., Germaine, J.T. and Ladd, C.C. (2007) Small-strain nonlinearity of normally consolidated clay. *Journal of Geotechnical and Geoenvironmental Engineering*, ASCE, **133**(1), 72-82.

Santamarina, J.C., Klein, K.A., Wang, Y.H. and Prencke, E. (2002) Specific surface: determination and relevance. *Canadian Geotechnical Journal,* **39**, 233-241.

Santamarina, J.C. (2005) Particle-level phenomena and macroscale soil behavior. In *Deformation Characteristics of Geomaterials,* Taylor and Francis, London, 145-154.

Santamarina, J.C. and Shin, H. (2009) Friction in granular media. *Meso-scale Shear Physics in Earthquake and Landslide Mechanics,* CRC Press, London, UK, 157-188.

Sheahan, T.C., Ladd, C.C. and Germaine, J.T. (1996) Rate-dependent undrained shear behaviour of saturated clay. *Journal of Geotechnical Engineering*, ASCE, **122**(2), 99-108.

Sheng, D., Westerberg, H., Mattsson, H. and Axelsson, K. (1997) Effects of end restraint and strain rate in triaxial tests. *Computers and Geotechnics*, **21**(3), 163-182.

Shibuya, S., Mitachi, T., Hosomi, A. and Hwang, S.C. (1996) Strain rate effects on stress strain behaviour of clay as observed in monotonic and cyclic triaxial tests. *Measuring and Modelling Time Dependent Soil Behaviour: ASCE GSP*, **61**, 214-227.

Sivakumar, V., O'Kelly, B.C., Henderson, L., Moorhead, C. and Chow, S-H. (2016) Measuring the plastic limit of fine soils: an experimental study. *Proceedings of the Institution of Civil Engineers - Geotechnical Engineering*, **168**(GE1), 53-64.

Sorensen, K.K., Baudet, B.A. and Simpson, B. (2007) Influence of structure on the time-dependent behaviour of a stiff sedimentary clay. *Géotechnique*, **57**(1), 113-124.

Sorensen, K.K., Baudet, B.A. and Simpson, B. (2010) Influence of strain rate and acceleration on the behaviour of reconstituted clays at small strains. *Géotechnique,* **60**(10), 751-763.

Steenfelt, J.S. (1993) Sliding resistance for foundations on clay till. *Predictive soil mechanics*, Thomas Telford, London, 664-684.

Steiner, A., Kopf, A.J., L' Heureux, J-S., Kreiter, S., Stegmann, S., Haflidason, H. and Moerz, T. (2014) In situ dynamic piezocone penetrometer tests in natural clayey soils – a reappraisal of strain-rate corrections. *Canadian Geotechnical Journal*, **51**, 272-288.

Stone, K.J.L. and Phan, K.D. (1995) Cone penetration tests near the plastic limit. *Géotechnique*, **45**(1), 155-158.

Sudan, G.K. and Sachan, A. (2017) Effect of strain rate on pore pressure evolution and effective stress path of soft soil under different stress history conditions. *International Journal of Geotechnical Engineering*, Taylor and Francis, **11**(1), 62-71.

Svoboda, J.S. and McCartney, J.S. (2014a) Shearing rate effects on dense sand and compacted clay. *Dynamic Behaviour of Materials*, Society for Experimental Mechanics, **1**, 389-395.

Svoboda, J.S. and McCartney, J.S. (2014b) Impact of strain rate on the shear strength and pore water pressure generation of saturated and unsaturated compacted clay. *ASCE Geotechnical Special Publication*, 1453-1462.

Tatsuoka, F. and Shibuya, S. (1992) Deformation characteristics of soils and rocks from field and laboratory tests. *Proceedings of the 9th Asian Regional Conference on Soil Mechanics and Foundation Engineering*, Bangkok, Thailand, **2**, 101-170.

Tika, T.E., Vaughan, P.R. and Lemos, L.J.L.J. (1996) Fast shearing of pre-existing shear zones in soil. *Géotechnique*, **46**(2), 197-233.

Vardenega, P.J. and Bolton, M.D. (2013) Stiffness of clays and silts: normalizing shear modulus and shear strain. *Journal of Geotechnical and Geoenvironmental Engineering*, **139**(9), 1575-1589.

Vucetic, M. and Dobry, R. (1991) Effect of soil plasticity on cyclic response. *Journal of Geotechnical Engineering,* ASCE, **117**(1), 89-107.

Waitukaitis, S.R. and Jaeger, H.M. (2012) Impact-activated solidification of dense suspensions via dynamic jamming fronts. *Nature*, **487**, 205-209.

Wagner, N.J. and Brady, J.F. (2009) Shear thickening in colloidal dispersions, *Physics Today*, **62**(10), 27-32.

Whitman, R.V. (1957) The behaviour of soils under transient loadings. *Proceedings of the 4th International Conference on Soil Mechanics and Foundation Engineering (ICSMFE)*, 1, 207-210.

Yimsiri, S. and Soga, K. (2002) A review of local strain measurement systems for triaxial testing of soils. *Journal of Southeast Asian Geotechnical Society*, **33**, 41-52.

Yukselen-Aksoy, Y. and Kaya, A. (2013) Specific surface area effect on compressibility behaviour of clayey soils. *Proceedings of the Institution of Civil Engineers - Geotechnical Engineering,* **166** (1), 76-87.

Zhou, H. and Randolph, M.F. (2007) Computational techniques and shear band development for cylindrical and spherical penetrometers in strain-softening clay. *International Journal of Geomechanics*, ASCE, **7**(4), 287-295.

Zhu. H. and Randolph, M.F. (2011) Numerical analysis of a cylinder moving through rate-dependent undrained soil. *Ocean Engineering*, **38**(7), 943-953.

Zhu, J-G. and Yin, J-H. (2000) Strain-rate-dependent stress-strain behaviour of overconsolidated Hong Kong marine clay. *Canadian Geotechnical Journal*, **37**, 1272-1282.